LA-3241

C.3

LOS ALAMOS SCIENTIFIC LABORATORY
of the
University of California
LOS ALAMOS • NEW MEXICO

PHERMEX: A Pulsed High-Energy

Radiographic Machine Emitting X-Rays

This report expresses the opinions of the author or authors and does not necessarily reflect the opinions or views of the Los Alamos Scientific Laboratory.

LOS ALAMOS SCIENTIFIC LABORATORY
of the
University of California
LOS ALAMOS • NEW MEXICO

Report distributed: May 15, 1967

PHERMEX: A Pulsed High-Energy
Radiographic Machine Emitting X-Rays

by

Douglas Venable
D. O. Dickman
J. N. Hardwick
E. D. Bush, Jr.
R. W. Taylor
T. J. Boyd
J. R. Ruhe
E. J. Schneider
B. T. Rogers
H. G. Worstell

Douglas Venable, Editor

1

PREFACE

PHERMEX is a high current, high energy electron accelerator that provides very intense but short bursts of gamma rays for flash radiographic studies of explosives and explosive-driven metal systems. This project represents the culmination of many years of effort both in formulating design concepts and in actual construction. Indeed, an extensive report could be written on each aspect of this effort. However, this report discusses only the salient design aspects and the capability of PHERMEX as an electron accelerator and a source of penetrating gamma rays for flash radiography.

Two mutually dependent studies provided the basis for design concepts of this facility. One of these experimentally demonstrated the physical feasibility of performing accurate radiodensitometric measurements of mass density distributions in certain simple geometric configurations of explosives and metals. These configurations were also those from which data could be extracted easily. The results of this study indicated that density distributions could be determined within a few percent in sections as thick as ten mean free paths. A small source of adequately penetrating gamma rays is necessary, the precision being established primarily by the source size and by the radiation flux per unit area transmitted through the specimen. The second study investigated other aspects of the overall problem. It considered (1) the optimum bremsstrahlung spectrum, hence the appropriate electron beam energy, (2) the radiation source size as well as the quantity and momentum distribution of electronic charge that must be deposited on a radiation target to ensure statistically significant radiographic measurements, and (3) the feasibility of constructing an electron accelerator which could accomplish this task.

Consideration of the radiographic needs demonstrated that the proposed high explosive experiments could be carried out satisfactorily with the radiation generated by 5 to 10 μcoul of nominally 20 MeV electrons falling upon a tungsten target in 0.2 to 0.1 μsec or less. Thus the basic accelerator problem involved accelerating very high current electron streams in stored-energy standing wave accelerator structures. Indeed, this was the first time that this problem of accelerating high current beams had been examined and treated quantitatively. The results of this work demonstrated that an electron accelerator that could accelerate several hundred amperes to the desired energy was practical. These results also established the basic design parameters of this accelerator.

The accompanying figure illustrates the growth in radiation output as measured in Roentgen per pulse. Although this figure demonstrates a rather high level of achievement, the ultimate capability of PHERMEX has not been reached. Further improvements are being pursued.

At present PHERMEX may be characterized by the following parameters. This operating level was attained in the spring of 1966:

Beam energy	27 MeV
Beam current at target	30 A
Pulse length	0.2 μsec (or 0.1 μsec)
Radiation output (at 1 m)	30 R (or 10 R)
Radiation source diameter	3 mm
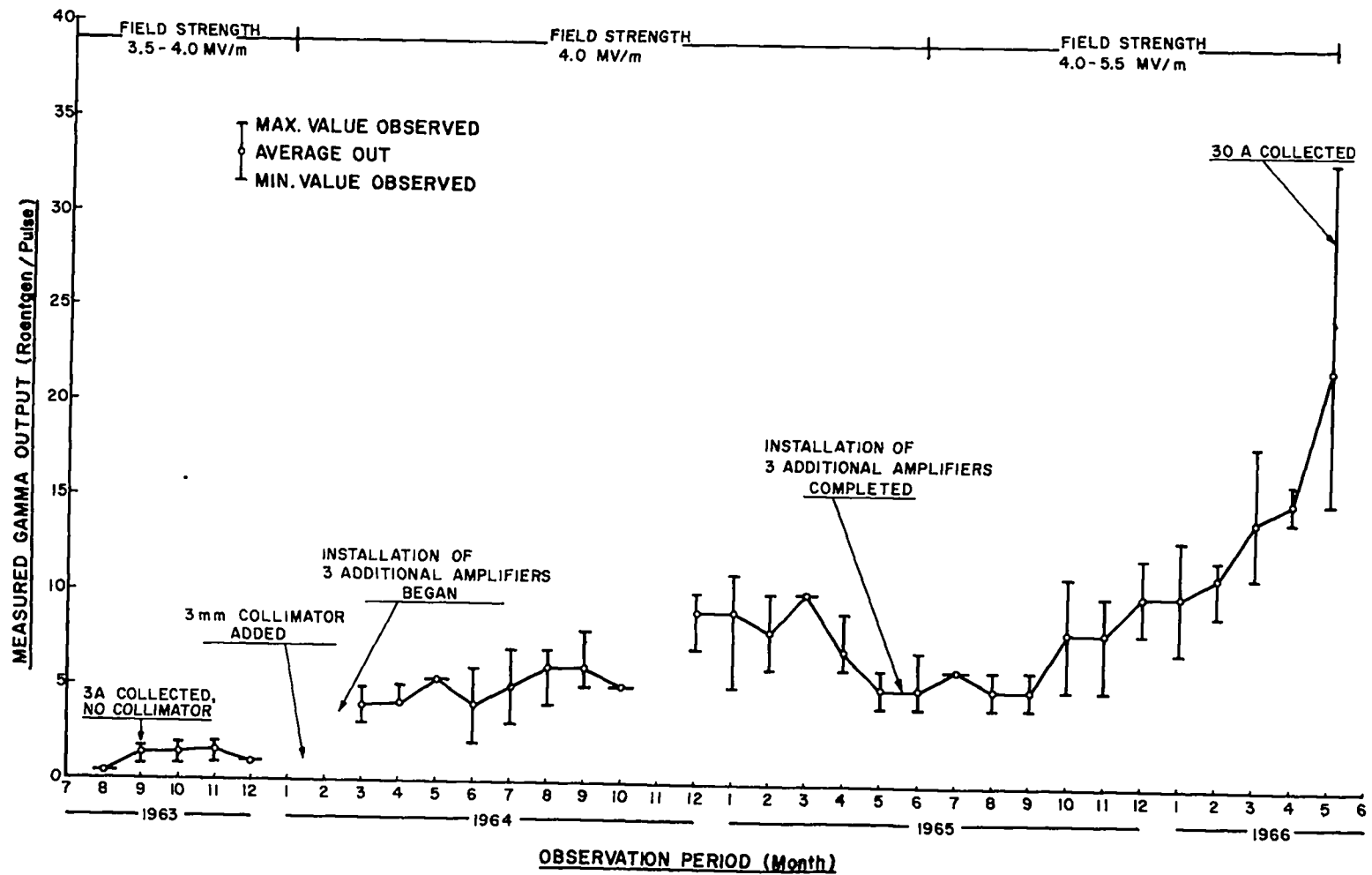
PHERMEX growth record.

All of this activity, which ranged from the exploration of concepts to a working flash radiographic facility, was carried out in GMX-Division of the Los Alamos Scientific Laboratory with the encouragement, support, and stimulation of its Division Leader, D. P. MacDougall. The first two feasibility studies, executed in Group GMX-7 under R. L. Spaulding, were performed by Leo F. Perry, Glenn E. Seay, and Douglas Venable. This phase of the work was completed early in 1952. The design of hardware, construction, and procurement began in March 1957; the first radiographic experiment with high explosives was performed in August 1963. This phase of the activity was carried out in Group GMX-11, which was administered by F. R. Tesche until June 1965.

The principal technical participants in this later activity are represented by the authors of the various chapters. These people carried the responsibilities for the respective areas of endeavor reported herein. Many others contributed to the success of this venture, unfortunately too many to enumerate completely. However, special reference is made to a few of these:

Members of Group T-1 who contributed heavily to the successful formulation of major computer codes were Ivan J. Cherry, Thomas L. Jordan, and Carol Reed. R. J. Watts of K-Division and Haskel Sheinberg of Group CMB-6 participated in the development of electron guns and large diameter impregnated cathodes, respectively. G. H. Tenney of Group GMX-1 and P. D. Edwards, now in Group MP-5, provided by far the greatest portion of the nondestructive testing of both materials and welds. Indeed, GMX-1 developed the ultrasonic scanning device for testing all the critical copper clad steel plates that were used to fabricate the vacuum vessels. The authors are particularly indebted to the following people for their contributions: W. R. Field, D. H. Janney, H. P. Lindberg, R. E. Stapleton, and E. M. Sandoval of Group GMX-11; C. R. Emigh, R. R. Stevens, and F. R. Tesche of MP-Division; and M. E. Ennis of W-Division.

George Wheeler, now of the Brookhaven National Laboratory, served as consultant on high power radiofrequency generators during the construction period. W. A. Sandberg provided some of the mechanical engineering design studies for the large vacuum vessels.

R. G. Shreffler, formerly the Associate Division Leader of GMX-Division, provided much of the initial drive for this program.

It is also a pleasure to thank Lee Shlaer of GMX-11 for typing the manuscript and the members of Group D-6 for proofreading and other editorial services.

<div align="right">

Douglas Venable, GMX-11
Editor

</div>

CONTENTS

8

TABLES

FIGURES

Frontispiece

11

12

Chapter I

INTRODUCTION

by
Douglas Venable

It is the purpose of this report to discuss the development of PHERMEX as an electron linear accelerator that provides very intense short bursts of bremsstrahlung for precision flash radiography of explosive-driven systems. Flash radiography, as a diagnostic technique, for implementing experiments relevant to detonation wave and shock wave phenomena is by no means new;[1.1-1.18] this field continues to be very rewarding. The first serious applications began nearly three decades ago, continuing into World War II. As revealed by postwar reports the United States and Germany had made very nearly identical progress in techniques of low energy flash radiography, or skiagraphy, applied to explosives and explosive-driven metal systems. However, by 1950 it was still evident that available flash radiographic equipment and techniques were insufficient to perform precision flash radiography which demanded both accurate resolution of edges and discontinuities and accurate resolution of areal mass density distributions. Notwithstanding this apparent deficiency, a study was initiated at the Los Alamos Scientific Laboratory to determine the feasibility of achieving quantitative radiodensitometry as well as constructing a pulsed electron accelerator which would provide the proper bremsstrahlung spectrum, flux, and spot size needed for precision flash radiodensitometry of thick sections of high atomic number materials.

Although this preliminary study[1.19] was not reported in the open literature, it literally formed the backbone of this entire program, in that it established beyond doubt the feasibility of obtaining high quality flash radiographs. It clearly demonstrated that, even when using film, precision determination of areal distributions of mass density in very thick sections, greater than ten mean-free-paths thick, is not only physically feasible with adequate flux but also practical with a variety of object configurations, provided careful control is exercised over alignment, penumbra effects, geometric symmetry, scattered radiation, detector latitude,[1.20] and calibration techniques, along with a host of other problems. Thus the feasibility of performing precision radiography, as defined above, was established.

The second objective of this early study was accomplished also. It was shown that an x-ray machine, capable of performing many of the tasks of interest to this laboratory, could be fabricated from existing facilities using known techniques. This phase of the study provided rough specifications of the electron beam energy and the amount of charge that must be delivered to a target to satisfy the flux requirements of precision thick-section radiography. Radiation pulse length, as prescribed by specific experimental objectives, then defined the electron beam current. The resulting values of current implied high space charge fields which represented one of the most serious limitations in the electron optics of the proposed device. Considerable computational work was done at that time using card programmed electronic computers to solve the equations of motion of electrons in high current beams which were accelerated in radiofrequency fields.

This groundwork demonstrated that a high current electron accelerator capable of generating very intense bursts of bremsstrahlung having suitable properties was feasible then. However, this project formally began with the initiation of detailed design and construction in 1957, at which time both techniques and equipment had matured, resulting in a far superior facility than could have been built in 1952.

It was intended that this x-ray machine should have the capacity of performing certain precision tasks within a well-defined range of radiography of detonating explosives and explosive-driven metal systems. At one extreme of

this range lies the more or less conventional flash skiagraphy or shadow radiography; at the other lies flash radiodensitometry requiring penetration through various thicknesses of material, particularly material of high atomic number such as uranium. Densitometry as used here applies to the quantitative determination of areal mass distribution. A flash x-ray source of sufficient intensity to penetrate desired thicknesses of uranium, for example, and which also provides an adequate signal-to-noise ratio for densitometry would be sufficient for most of the contemplated skiagraphic work. Therefore attention was focused upon a radiographic machine which would most nearly satisfy the more severe densitometric requirments. Experimental parameters of penetration experiments dictated that the x-ray spectrum must be rich in 3 to 4 MeV quanta. Pulse length and radiation transmission through the experimental materials then establish the required electron beam current for an acceptable absorption statistical error.

Precision radiography requires accurate resolution of edges and discontinuities as well as mass density distributions. Precision is degraded by many things, but especially by scattered radiation. In this sense scattered radiation, which increases with object thickness, serves to establish a practical upper limit of object thickness that can be radiographed usefully.

Static radiographic experiments using film[1,19] demonstrated that with certain geometrical shapes and with considerable experimental care the resolution of areal density can be held to within 2 percent for objects approaching thicknesses as great as ten mean free paths for the incident radiation.

The error of resolution associated with scattered radiation increases very rapidly with mean free paths for thick sections. Furthermore, the usefulness of information also decreases very rapidly as the errors increase beyond several percent. Therefore a reasonable practical upper limit of object thickness was established at about ten mean free paths. Generally speaking PHERMEX, at present, is capable of performing precision flash radiography in objects about four mean-free-paths thick when using conventional film techniques and about ten mean-free-paths thick when using electronic detectors.

A dichotomy of radiographic experiments had to be considered when designing this flash x-ray machine. One class of experiments demands peak radiation flux per unit area distributed over a region significantly smaller than the radiographic object, whereas the second class requires a high average flux completely irradiating the region of interest.

In experiments of the first class high intensities are obtained by simply increasing the beam energy that both narrows the radiation cone and increases the radiation production efficiency. Indeed this is one of the primary selling points for present day traveling wave electron accelerators as radiation generators. In this class a figure of merit for relative output intensities of x-ray machines can be defined as the ratio of beam current at an arbitrarily chosen standard energy to the beam current at some other energy that will produce the same useful axial radiation intensity. Such a relative figure of merit, shown in Fig. 1.1, has been determined as a function of energy
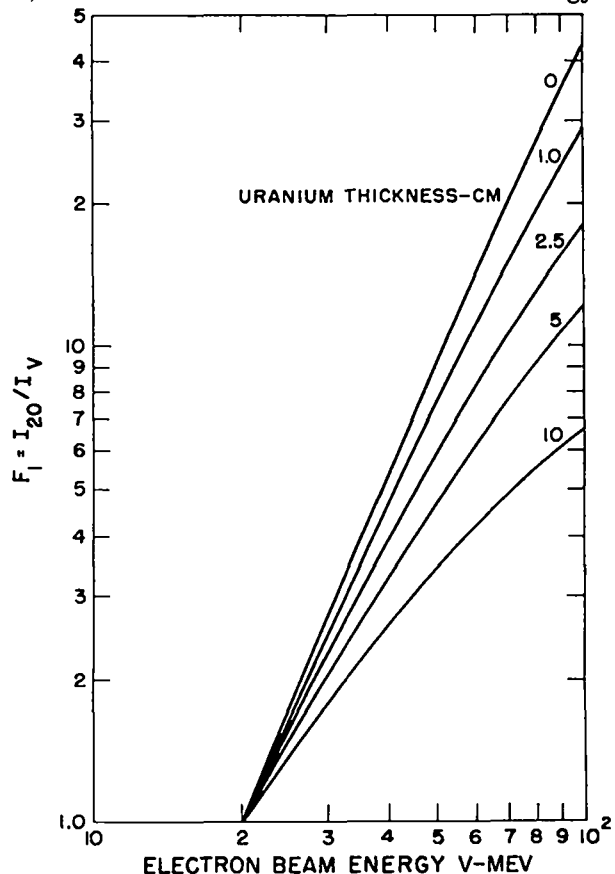
Fig. 1. 1.   A figure of merit for radiographic machines where maximum useful radiation intensity is demanded.

16

for the two radiographic extremes: skiagraphy, wherein only shadow profiles are obtained, and densitometry, using a standard energy of 20 MeV. For instance, a 20 MeV electron beam must have 5.4 times the current of a 40 MeV beam to be equally useful for skiagraphic service. On the other hand, the current of a 20 MeV electron beam need be only 2.6 times as great to provide the same useful transmitted radiation intensity as a 40 MeV electron beam when radiographically penetrating 10 cm of uranium. Therefore, for this class of radiography, high electron beam energies are important.

Another, even more important, figure of merit is defined for the second class of radiographic experiments in which not the relative intensity but the total useful flux transmitted through the experimental object is considered. It is this latter figure of merit that is paramount when radiographing a fixed size thick object. It is also this figure of merit that is most applicable to PHERMEX experiments. In this case there is a much less favorable energy advantage since it is the production efficiency of 3 to 4 MeV quanta that is significant in whole object penetration experiments with uranium or 4 to 8 MeV quanta for iron objects. This may be seen by comparing the figures of merit presented in Figs. 1.1 and 1.2. Again, examining the radiation generated by 20 and 40 MeV electron beams, one finds that a 20 MeV beam must have 35 percent more current than a 40 MeV beam in order to generate the same skiagraphically useful radiation flux. On the other hand, for radiographic penetration of 10 cm of uranium, the 40 MeV beam must have about 1.5 times the current of the 20 MeV machine. The higher energy machines offer no obvious advantage for whole object radiodensitometry when penetrating thick sections of uranium; real gains in radiation intensity are obtained by increasing the electron beam current. Similar data are plotted in Fig. 1.3 for the case of radiodensitometry with iron. Here higher energies provide at best only a modest gain. These figures of merit were derived from data given in Chapter 2.

It was whole-object thick-section radiodensitometry in detonating explosives and explosive-driven metal systems for which this flash x-ray machine was initially designed and built. The radiation flux for single pulse radiography
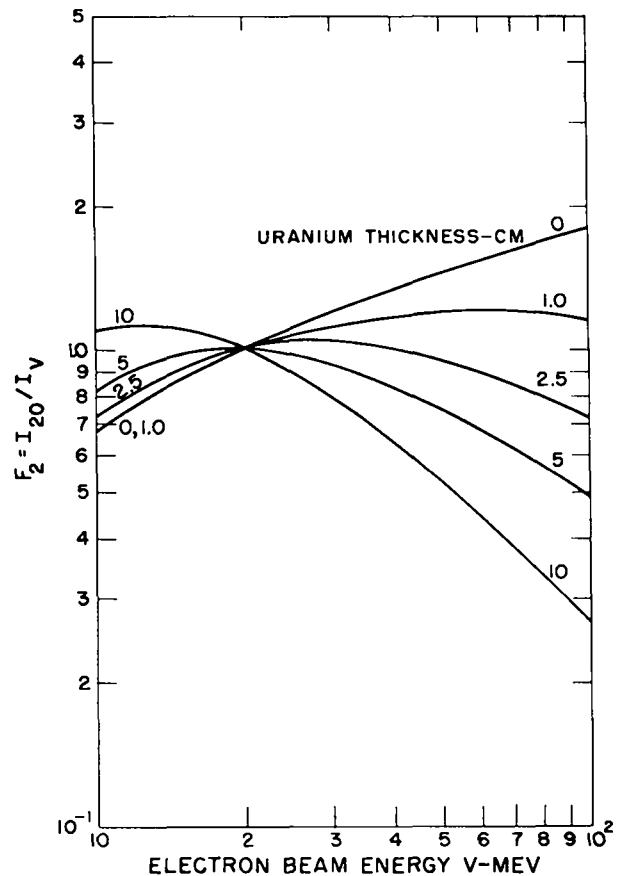
Fig. 1. 2. A figure of merit for radiographic machines where maximum useful radiation flux is required to penetrate uranium.

that is required to overcome the statistical uncertainties of some of the more difficult of the contemplated experiments is equivalent to that generated by a 20 MeV electron beam, delivering 5 to 10 μcoul or more to a 3 mm diameter tungsten target in times like 0.2 to 0.1 μsec or less. These figures do not by any stretch of the imagination represent a maximum useful flux, but rather an acceptable practical lower limit above which the utility of such a device is well established. Although Fig. 1.2 suggests that 15 MeV might be the most favorable energy for thick section radiodensitometry of high atomic number materials, 20 MeV was chosen as the nominal beam energy of this machine, representing an acceptable compromise when considering all aspects of the contemplated radiographic experiments. This conclusion is in rough agreement with Kerst and Adams[1,21] who carried out extensive radiography studies in the 3 to 20 MeV bremsstrahlung range.

17

Fig. 1. 3. A figure of merit for radiographic machines where maximum useful radiation flux is required to penetrate iron.

The chart shows axes: vertical axis labeled $F_2 = I_{20}/I_V$ with values 10^{-1} to 5, horizontal axis labeled ELECTRON BEAM ENERGY V-MEV from 10 to 10^2. Curves labeled IRON THICKNESS—CM with values 0 and 10.

fined as that number needed to perform a given radiographic task within prescribed limits of allowable error. Parameters which are needed to minimize the ratio of the number of high energy electrons delivered to a suitable target to the number of useful quanta required to perform an experiment are discussed. The information needed to provide estimates of answers to these problems is presented. This includes a survey of bremsstrahlung production as a function of both electron energy and target material, the intensity-angle distribution of the useful radiation, and the transmission and spectral degradation of bremsstrahlung through materials which are possible candidates for experimental systems. The most important parameter in this study is the electron energy that was varied from 5 to 100 MeV. Target materials ranged from beryllium to uranium, with tungsten chosen as most suitable because of its refractory properties and its high efficiency for bremsstrahlung production. In short, Chapter 2 is concerned with the determination of the most favorable radiation spectrum and the total flux required to perform statistically significant thick section flash radiography.

The radiation flux and hence the electron beam energy and target current required to solve a certain class of flash radiographic problems can be obtained most satisfactorily by means of a standing wave accelerator. Chapter 3 discusses the design parameters for an accelerator of this kind which most economically assure the delivery of the required charge to a target. Hence this chapter is directed primarily toward considerations of particle and cavity energetics, field strength limitations and choice of wavelength, equations of motion, optimum injection parameters, the spatial distribution of energy and momentum among the electrons of the ejected beam, and final focusing. In essence, the development of particle energetics and electron trajectories is effected by following representative points in classical phase space from their source on a cathode to their termini which must lie either on walls of the accelerator system or on the target. Space charge is included as a perturbation. As is illustrated in Fig. 1.4, a representative point is one which is typically found initially at the point r_0, θ_0, z_0 in configuration space at which time, t_0, the momentum components are p_{r0}, $p_{\theta0}$, p_{z0}. The equations of motion are discussed in this chapter, along with analytic description of the aperture defect,

Thus a minimum desirable electron beam power at the target is roughly 1000 MW, with a beam kinetic energy of about 100 joules. For a radiation production efficiency of about 42 percent, the maximum power in the 20 MeV bremsstrahlung beam would be about 420 MW.

The high current electron beam accelerator that has the most attractive characteristics and that can most nearly satisfy the specifications of the desired x-ray machine is the standing wave accelerator, in which electromagnetic energy can be stored at a modest rate by means of conventional radiofrequency amplifiers, and subsequently energy can be extracted by an electron beam at a greater rate.

Chapter 2 then discusses the economical production of useful quanta within a suitable spatial distribution. The number of useful quanta is de-

18

azimuthally symmetrical magnetic focusing fields, space charge effects, and the cavity accelerating fields.
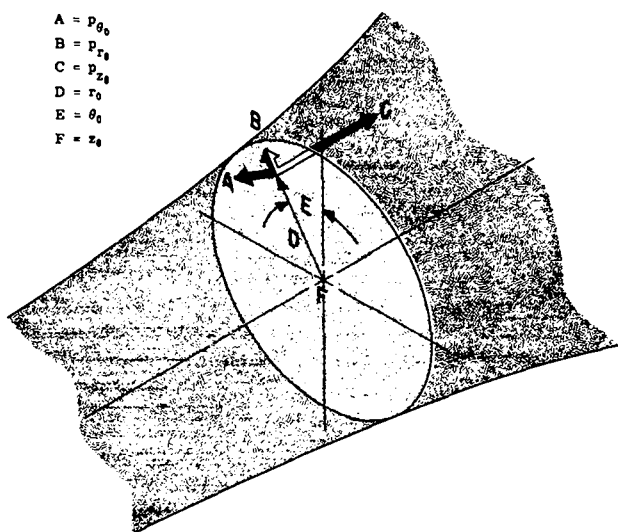
Fig. 1. 4. An initial representative point in the injected electron beam.

Several computational models have been used to describe electron flow through PHERMEX cavities. In two of these schemes the beam was conceptually divided into many smaller regions of charge. To each region was assigned an effective charge center. Then each charge center was treated as a point charge in one case and a ring of charge in the other case. The interactions of all these elements of charge with one another and with the cavity fields were computed and referred to a frame of reference fixed in the accelerator. Much useful information was obtained, especially relevant to space charge effects.

Yet another model was tried in which the electron beam was considered as a charge bunch whose effective charge center was constrained to move along the axis of the cavity. In order to describe space charge effects as well as off-axis particle motion, a test charge was followed computationally throughout the cavity system of fields. This model also yielded considerable information, not only on space charge effects but also on

the important problem of phase focusing and phase defocusing. The model that has been used most extensively is that whose analytic description is provided in Chapter 3. It is this model for which an elegant computer code was written.

Chapter 4 presents a detailed working description of this code, called GRAPE SEED III. Numerical data from GRAPE SEED III provided much of the guidance for detailed design of the electron optical system of PHERMEX by means of a very extensive parameter variation study. A report of some of this latter work is found in Chapter 5. Here it was determined that the optimum injector convergence angle for the machine was very nearly zero. Beam trajectories were examined as functions of injection phase angle, radius, and energy, and also as functions of beam current, peak accelerating field, and confining magnetic fields. These results may be seen in the trajectory plots illustrated in that chapter.

Chapter 6 pertains to the development of the electron optical components of PHERMEX. It includes the electron source, beam preparation, injection optics, some of the optical properties of the accelerator cavities, ejection optics, final focusing, and the production of the desired bremsstrahlung beam.

The nature of the half-wavelength-cavity standing wave accelerator system of PHERMEX, when operating with continuous injection, is such that only about one-third of the charge that is injected continuously over one cycle can be ejected from the first cavity. Of this ejected charge, only a fraction is physically accessible to a remotely located small target. This latter fraction depends upon many factors, the principal ones being the method of final focusing and the distance from the ejection aperture to the target. However, in the case of PHERMEX, blast protection demanded that the target be located about 11 meters away from the last cavity. As a result of this constraint, only about one-eighth of the continuously injected charge is accessible to the 3 mm diameter target. The pre-established pulse length of 0.2 μsec and the required charge then suggest a target beam current of about 20 A or greater. Thus, if nature is otherwise sufficiently kind, a continuously injected electron beam current of 200 to 300 A should be adequate. This has proved to be the case.

19

It is recognized that greater optical efficiency can be achieved with suitable beam preparation such as bunching; however, the resultant gains in output radiation flux are at best only moderate. Therefore, until less expensive and simpler schemes for enhancing the bremsstrahlung output are exhausted, continuous injection appears to be the most practical.

As with most electron optics, no one component is completely independent of any of the others. Therefore, the design of the overall electron optical system required careful considerations of the electron beam at every point between the cathode and target, including the characteristics of lenses as well as those of the cavities which behave as time variable refractive optical entities.

A minimum number of lenses was employed to assure the required optical conditions. Since both beam radius and convergence are important upon injection, two lenses are needed to provide optimum beam preparation for continuous injection, allowing some degree of flexibility. Likewise, since the beam incident upon the target must lie within given radius and convergence ranges to satisfy both radiographic space resolution and the desired bremsstrahlung intensity-angle distribution, two lenses are needed also in the ejection optical system. More than two static lenses in either region offer redundancy.

Except for the electron beam flow within the electron gun and in some regions of the cavities, paraxial optics is maintained throughout PHERMEX. Paraxial optics here means that beam convergence angles, as viewed from a frame fixed in the beam, are constrained to lie within one-tenth radian. In regions free from externally imposed electromagnetic fields, the trajectory equation, as discussed in Appendix B of Chapter 6, can be normalized and reduced to a simple second-order differential equation.

$$\frac{d^2R}{dZ^2} = \frac{1}{2R}$$

(1.1)

where

$$\frac{dR}{dZ} = \frac{1}{\delta} \frac{dr}{dz}$$

(1.2)

The validity of this scheme of beam design is well recognized for nonrelativistic electron optics. Its extension to the relativistic case has proven to be worthwhile as indicated by the results of tests with PHERMEX injectors. Indeed, results of experiments, reported later in the text, demonstrate that for high current electron beams, 200 to 300 A, these simple considerations adequately predicted beam behavior.

Magnetostatic lenses were used throughout. These were short strong focusing devices possessing azimuthal symmetry. Quadrupole lenses are not compatible with high current circular cross section beams wherein space charge forces are significant. Lens design was based upon the following simple formulation for the necessary ampere-turns for this type of lens of focal length f.

$$NI = 9.82 \times 10^{-3}\left[\frac{b}{f} V(V + 2\mu) \right]^{1/2}$$

(1.3)

An effective value for the lens radius, b, can be obtained from electrolytic tank plots or, with somewhat less precision, from field plots made on conducting paper.

Extensive calculations were made to determine the most favorable conditions for (a) time-independent injection, (b) continuous but time-variable injection, and (c) bunching. The results of this work, discussed in Chapter 5, served as a guide for defining suitable ranges of beam radii and convergences at injection for a given achievable ejected beam energy and current. These optimum conditions were those which assured the greatest useful radiation flux output, demonstrating the intimate connection among all the optical components.

The next step was that of designing a suitable electron gun. This course of action was accompanied by detailed supporting calculations which accounted for additional information needed for complete gun design. Nonrelativistic gun design techniques, employed at first, are discussed in Appendix A of Chapter 6. These concepts were applied to a low voltage electron gun model, which was designed to emit continuously 16 A at 70 keV, representing a perveance of about 10^{-6}. Indeed, pulses as long as 1 msec were used

in the early experiments. Results of experimental tests with this gun verified basic gun design procedures.

The cathodes used for this work were impregnated ones, the Type B originally developed by Phillips.[1,22] This type was preferred over all others that were considered at that time because of its high emission current density capability, low operational temperature, long term stability, resistance to poisoning, and the dimensional precision with which these cathodes can be fabricated. At the beginning of this project large diameter impregnated cathodes (Type B) were not available commercially. Cathodes up to 12.5 cm in diameter were made by the metallurgical group, CMB-6, of the Los Alamos Scientific Laboratory (LASL). Since that time these devices have become available through industrial facilities at reasonable costs.

The first gun model was of conventional Pierce design, and used a 5 cm diameter cathode capable of emitting greater than 150 A. At the time of design it was not known what voltage pulse this gun structure would tolerate. Therefore, once the design characteristics had been found suitable, this gun was operated under pulsed conditions with 0.2 μsec pulses that could be varied continuously up to 300 kV. Initially, internal electrical breakdown was experienced between the cathode field forming electrode and the anode. Slight modifications were made in the geometry of this region which eliminated this problem without seriously affecting either the perveance or the beam flow characteristics. Before attaining 300 kV, external breakdown had to be suppressed. This was done by encapsulating the external insulator with a cloud of SF_6, at local atmospheric pressure, containing this gas in a plastic bag. This scheme has proved very satisfactory and is used frequently in other similar applications. An ejected gun current of about 165 A was achieved at 300 keV. The original perveance of the 70 keV version of this gun was preserved to a first approximation.

As indicated earlier, two magnetic lenses are needed to provide suitable adjustments of both beam radius and beam convergence at injection. Two scale model lenses, clad with cold rolled steel, were built and tested in a geometry similar to that expected to be used in the final machine. This half-scale injector demonstrated that about 90% of the gun current could be injected into the first cavity satisfactorily.

The Pierce gun with its 5 cm diameter cathode and the injector lens system was scaled up by a factor of two. A commercially fabricated 600 kV, 275 ohm, 0.2 μsec pulser was selected to drive this gun.

PHERMEX cavities are excited by means of nine very high power radiofrequency amplifiers. These 1 MW level generators are capable of being driven at a rate of fifteen 3 msec long pulses per second. After about 1 msec the cavity fields reach equilibrium; at an appropriate time during the ensuing 2 msec the electron gun is energized to inject charge continuously into the first cavity. Some of this charge passes through the three cavities and emerges with a peak energy of about 27 MeV. Typical operating conditions consist in injecting about 200 amperes into the first cavity for 0.2 μsec. By virtue of the nature of this kind of accelerator, the first cavity rejects all but about one-third of the charge injected per cycle. Fortunately it is the higher energy charge which is favored and injected into the subsequent cavities in turn. Chapter 7 describes the radiofrequency power generation, details of intercavity phasing, operating procedures, and personnel safety.

This entire radiographic facility owes much of its success to the thorough considerations of the mechanical engineering problems. These ranged from designing the blast-proof bunkers which house the accelerator to the deionized water cooling system for removing heat from the anodes of the final amplifiers. Of course, the amplifiers themselves, as well as the cavities and the vacuum system, fall into this category. Solutions to some of these problems are presented in Chapter 8. Mechanical alignment of the entire electron optical complex, one of the most difficult problems, is discussed in Chapter 9. A very high vacuum is required before efficient electron optics can be achieved. This vacuum system was another feature unique to the mechanical engineering aspects of PHERMEX; this part of the work is included in Chapter 10.

Many of the details of the accelerator can be identified in Fig. 1.5, a model of PHERMEX, while the frontispiece gives an excellent view of the PHERMEX site and complex of buildings.
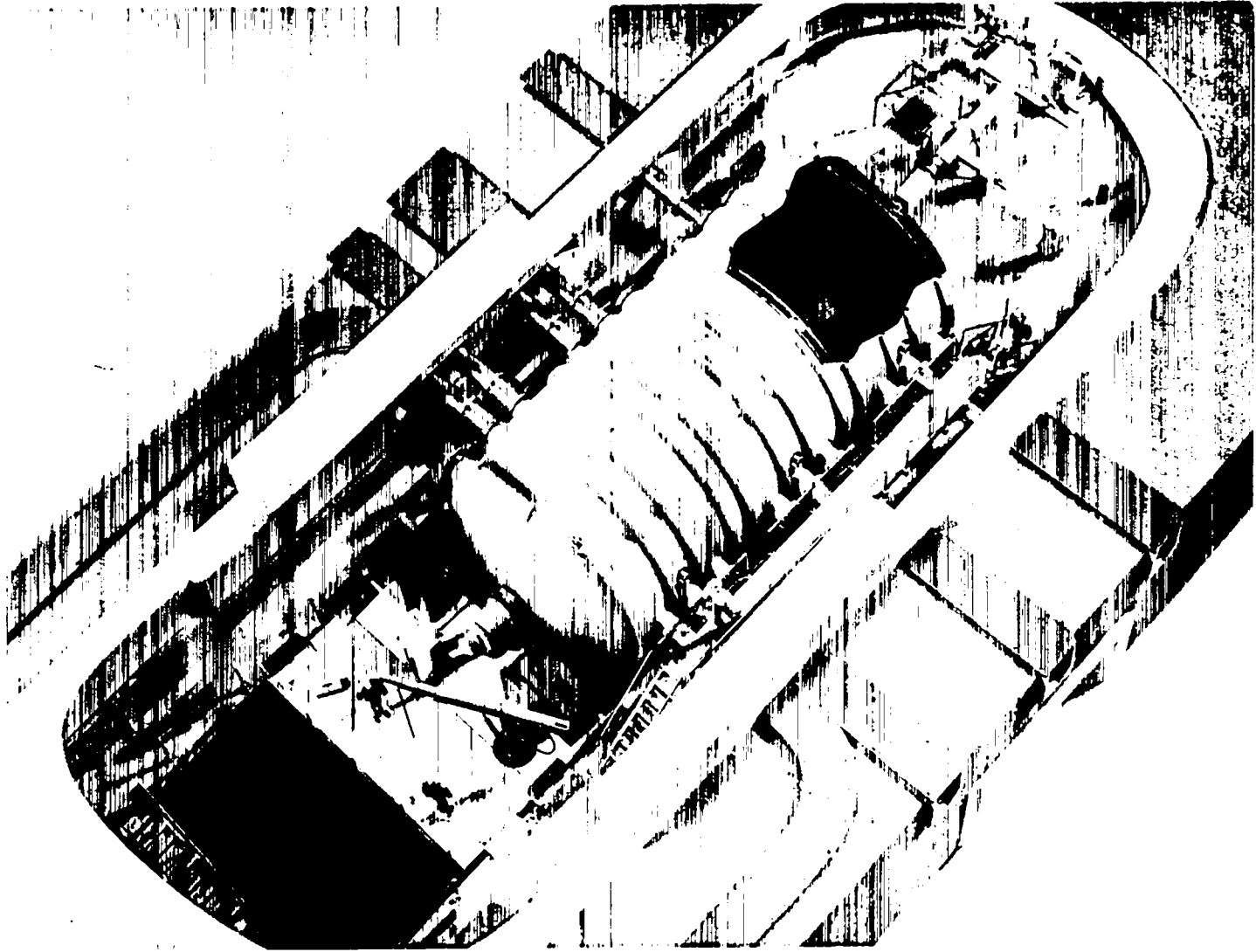
Fig. 1. 5. Scale model of PHERMEX.

NOTES AND REFERENCES

1. 1. David Hawkins, *Manhattan District History; Project Y, the Los Alamos Project; Vol. I,* Los Alamos Scientific Laboratory Report LAMS-2532, 1946 and 47.

1. 2. V. A. Zukerman, *Compt. Rend. (Doklady)* **40**, 267 (1943).

1. 3. L. E. Simon, *German Research in World War II,* John Wiley and Sons, 1947.

1. 4. J. C. Clark, *Phys. Rev.* **72**, 741(A) (1947); *J. Appl. Phys.* **20**, 363 (1949); *Am. Soc. Test. Mat. Special Technical Publication No. 96* (1950).

1. 5. W. Schaaffs and F. Trendelenburg, Z. *Naturforsch.* **4a**, 463 (1949) and **5a**, 132 (1950); Z. *Physik* **137**, 200 (1954) and **142**, 642 (1955).

1. 6. R. Schall, Z. *Angew. Phys.* **2**, 83 and 252 (1950); **4**. 291 (1952); Z. *Naturforsch.* **8a**, 676 (1953).

1. 7. G. Thomer, Z. *Angew. Phys.* **5**, 217 (1953).

1. 8. W. Schaaffs and K. H. Herrmann, Z. *Angew, Phys.* **6**, 23 (1954).

1. 9. R. Schall and G. Thomer, Z. *Physik* **142**, 632 (1955).

1.10. W. Schaaffs, Z. *Physik* **142**, 642 (1955).

1.11. V. A. Zukerman and M. A. Manakov, *Soviet Phys-Tech. Phys.* **2**, 353 (1957).

1.12. R. Schall, *Explosivstoffe* **6**, 120 (1958).

1.13. W. N. Hess, M. D. Martin, G. C. McFarland, W. A. Rutz, and J. A. Welch, *Rev. Sci. Instr.* **30**, 794 (1959).

1.14. F. J. Grundhauser, W. P. Dyke, and S. D. Bennett, *J. Soc. Motion Picture Television Engrs.* (USA) **70**, 435 (1961).

1.15. L. V. Al'tshuler and A. P. Petrunin, *Soviet Phys.-Tech. Phys.* **6**, 516 (1961).

1.16. R. Schall and G. Thomer, *Flash Radiographic Measurement of the Shock Compressibility of Magnesium Alloy, Lucite, and Polyethylene,* Air Force Special Weapons Center, Report AFSWC-TOR-62-134 (October 1962).

1.17. A. S. Balchan, *J. Appl. Phys.* **34**, 241 (1963).

1.18. A. S. Balchan and G. R. Cowan, *Rev. Sci. Instr.* **35**, 937 (1964).

1.19. Most of this work, performed at the Los Alamos Scientific Laboratory by Leo F. Perry, Glenn E. Seay, and Douglas Venable, was completed in 1952.

1.20. N. C. Miller and J. D. Steely, AECU-2721 (Oct. 1953), U.S. Government Printing Office, Washington, D. C.

1.21. D. W. Kerst and G. D. Adams, *Final Report on 3 to 20 Million Volt Radiography,* OSRD-1333, March 1, 1943, University of Illinois, Urbana, Illinois.

1.22. Roberto Levi, *J. Appl. Phys.* **24**, 233 (1953).

Chapter 2

THE RADIATION PROBLEM

by
Douglas Venable

Where experiments permit sufficient freedom of choice of parameters as well as component arrangement, an optimum radiographic thickness would correspond to two mean free paths for the traversing radiation. For instance, for a given number of available monoenergetic quanta incident per unit area upon an object, the minimum statistical uncertainty for measuring density changes occurs when the radiographic thickness is two mean free paths. However, in most cases a line spectrum of sufficient intensity is not available for flash radiography of dense matter; in practice, only continua are available. Therefore, similar considerations must be given to the available radiation spectra. This concept was worked out theoretically and confirmed experimentally for a low energy continuum spectrum.[2.1]

If the spectral distribution is defined by the function $\phi(V)$, then the transmission of this spectrum through matter of density ρ and thickness x is given by

$$T = \frac{\int_0^{V_0} e^{-\mu\rho x}\phi(V)\ dV}{\int_0^{V_0} \phi(V)\ dV}$$

(2.1)

where the absorption coefficient μ is a function of the energy and of the material. The mass absorption coefficient is assumed to be negligibly dependent upon interatomic distances for the compressions that can be achieved by means of present day laboratory facilities, even using high explosive systems, although Bainbridge, Goldhaber, and Wilson[2.2] have shown that a change in μ might be expected at sufficiently high compressions. For the continuum spectrum case, the fractional uncertainty in measuring changes in the product of density and thickness, $\rho x = t$, can be written

$$\frac{\Delta t}{t}\sqrt{n_0} = -\frac{1}{\bar{\mu}tT^{1/2}}$$

(2.2)

where a mean value of $\bar{\mu}$ is defined as

$$\bar{\mu} = -T^{-1}\frac{dT}{dt}$$

(2.3)

and n_0 is the number of useful incident quanta. The extension to a monoenergetic spectrum is obvious, where $\bar{\mu} = \mu$.

Equation (2.2) is illustrated by Fig. 2.1 for the case of tungsten bremsstrahlung transmitted through $\bar{\mu}\rho x$ mean free paths in uranium, uranium being chosen as representative of one extreme case. It is seen that an optimum thickness, minimizing the ordinate, is still roughly two mean free paths. Furthermore, it is clear that for thick sections the choice of an optimum spectrum is decidedly not critical.
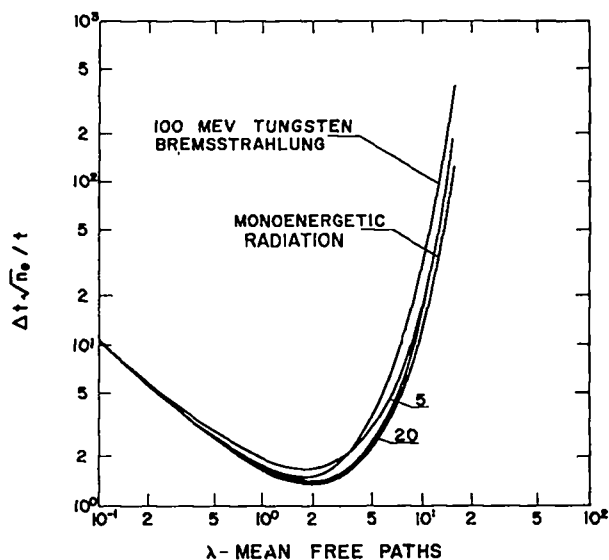
Fig. 2. 1. Statistical uncertainty in radiographic measurements of density.

Precise unfolding of radiographic data depends also upon the symmetry of the object. In the case of flash radiography of shock waves and detonation waves, it is most desirable to use sufficiently large objects so that hydrodynamic perturbations do not seriously disturb measurements of the primary phenomenon. For example, measurements of the density variation behind a detonation wave are affected by wave curvature. By suitable choice of geometry and explosive charge size, this perturbation can be reduced, hopefully to a negligible amount. Experimental conditions then usually determine whether a section will be radiographically thick or thin. For purposes of discussion here, thick sections are those which are many mean free paths thick.

Therefore, the first problem is to find the optimum spectrum needed to satisfy the average requirements of a large class of experiments, and hence to find the most suitable energy, V_0, of the electron beam generating the radiation. Once the spectrum is established, permissible statistical uncertainties, object size, and experimental geometry dictate the radiation flux, the radiation intensity-angle distribution, and the target size. The flux that engulfs an object is determined by the charge delivered to the target at energy V_0, target thickness and material, and the convergence of the electron beam incident upon the target. Radiation pulse length and target charge prescribe the electron beam current; desired space resolution for a given target-to-object distance and a given object-to-detector distance finally fix the target size as well as target current density. The beam convergence angle at the target should be less than the bremsstrahlung angle to ensure maximum on-axis radiation intensity.

The radiation beam parameters completely define the electron beam, i.e., the space-time momentum and density distribution among electrons incident upon the target. Indirectly then, the parameters describe the characteristics of an electron accelerator that is needed to achieve the desired electron distribution. The accelerator design parameters are discussed in Chapter 3. In short, it is essential to understand target design, radiation production, and radiation intensity-angle distribution, as well as the transmission and spectral degradation of radiation passing through matter.

Because of the number of variables that cannot be easily accounted for analytically, such as environment and object scatter, noise-to-signal ratio, radiation intensity-angle distribution, and spectral response of detectors, it is clear that extremely precise computations were not warranted. Instead, a wide latitude of parameters was employed to provide adequate coverage of the problems anticipated in experimental designs, radiation sources, radiation shields, and even electron beam collimators.

Section I, the basis for the rest of this chapter, discusses the energy loss gradient, i.e., the rate of electron energy loss per unit path length in various materials. Energy losses ascribable to both radiation production and ionization effects are considered for electron energies ranging from 5 to 100 MeV and for materials having atomic numbers from 4 to 92.

The next step in the computations determined the integral of the energy loss gradient, taking into account both the radiation and ionization loss rates, in order to obtain the electron energy as a function of the average depth of penetration. The integral distribution of the energy loss is given so that one can determine what fraction of the electron energy has been converted into heat, which might damage the target, and what fraction into bremsstrahlung. These data establish the upper limit to the radiation production efficiency. In addition to self-absorption within the target, one can determine the actual production efficiency and the spectral distribution of the radiation emerging from a target of thickness t.

A useful adjunct to the energy loss gradient data is the electron range. Here, the range is defined as that effective path length at the end of which an average electron has lost all of its initial energy, through radiation and ionization (see discussion in Section II); straggling is not considered important. Electron range determinations for several elements are calculated in Section III.

A detailed determination of the emerging radiation spectrum and intensity-angle distribution from a thick target requires evaluation, over the total target thickness, of the effects in all thin targets of thickness dx at x ascribed to (a) the bremsstrahlung angular distribution, (b) the electron scattering function, and (c) the radiation

absorption in the remaining target thickness, t — x. Although this computation has not been carried out completely, the basic conditions have been established. Measurements of the intensity-angle distribution of the radiation from PHERMEX are presented in Section IV. To a first approximation, the spectrum-angular distribution is not important to PHERMEX problems; and this aspect of the overall problem was not treated.

Therefore, a naive approach to the transmission and spectral degradation of radiation employs the thin target bremsstrahlung spectrum (see discussion in Section V). This approach is somewhat erroneous when the spectrum is applied to radiography of thin sections, because the low energy portion of the spectrum becomes an important feature needing more extensive consideration. On the other hand, for thick sections (even thicker than one-half mean free path for the radiation) this choice of an emerging spectrum is more than adequate to describe transmission phenomena for purposes of radiography. Thus, extensive refinement of the description of thick target radiation is unnecessary when unfolding data from the typical flash radiographic experiments planned for PHERMEX. Ultimately, experimental reliability must be assured by suitable calibration, using theory merely as a guide.

The computational study investigated a variety of elements with atomic numbers varying from 4 to 92, and also provided data on materials that are very poor generators of bremsstrahlung and, therefore, could serve as excellent electron shields or electron beam collimators. These data also indicate that some material such as mercury vapor or xenon gas could serve as useful self-healing targets for situations where very high electron beam current densities and, hence, high areal energy dispositions cause solid targets to explode or to ablate badly. Notwithstanding other possibilities and conditions, the most favorable target material for PHERMEX still appears to be the refractory metal, tungsten.

I. ELECTRON ENERGY LOSS GRADIENTS FOR SEVERAL ELEMENTS

Radiation production, intensity-angle distribution, emitted spectral distribution, and electron energy loss within targets are of prime importance to thick section flash radiography. An understand-ing of these phenomena as a function of such parameters as electron kinetic energy and target material and thickness is needed to enable one to make better estimates of the capability of flash x-ray machines, to facilitate establishment of the design of radiation shields, electron shields, and targets, and to determine the electron beam requirements for a given experiment as a function of the geometry and other constraints. For example, one may need to know what target thickness and material define an optimum target for certain problems. In some instances, an optimum target is that target which yields the greatest intensity of radiation directed along the axis of the electron beam and, concurrently considering the refractory properties of the material, has a long, useful lifetime.

A study of the relevant parameters began with computations of electron energy loss gradients for 12 elements that might conceivably be employed as target materials: Be, Ne, Al, Ar, Cu, Kr, Mo, Xe, W, Hg, Pb, and U. Energy loss gradients were computed for energies ranging up to 100 MeV. These data are presented in Fig. 2.2.

The computations of the radiation production process also reflect the energy degradation experienced by an electron traversing matter, accounting for ionizing as well as radiative collisions.[2,3] The results of these computations are also shown in Fig. 2.2; the results of the critical energy computations are given in Fig. 2.3, which also indicates that energy for which radiation and ionization loss gradients are equal for various elements.

The cross-section formulae consolidated in Reference 2.3 have been used with a slightly different notation. These formulae and the appropriate operations on them were coded for the IBM-704 by Group T-1 at Los Alamos. The formulations for these computations are given below.

Ionization loss gradient:

$$\left(\frac{dE}{dt}\right)_{COLL} = \frac{k_1}{1 - \left(\frac{\mu}{U}\right)^2}$$

$$\times \left[\ln \frac{(U^2 - \mu^2)(U - \mu)}{k_2} \right.$$

$$+ \left(\frac{\mu}{U}\right)^2 + \frac{1}{8}\left(1 - \frac{\mu}{U}\right)^2$$

$$\left. - \left(\frac{\mu}{U}\right)\left(2 - \frac{\mu}{U}\right) \ln 2 \right] \tag{2.4}$$

Radiation cross section:

$$\phi_2 = k_3 \left[1 + (1 - v)^2 - \frac{2}{3}(1 - v) \right]$$

$$\times \left[\ln\left(\frac{2U}{v} \cdot \frac{1 - v}{v}\right) - \frac{1}{2} \right], \quad \gamma \gg 1 \tag{2.5}$$

$$\phi_3 = k_3 \left\{ \left[1 + (1 - v)^2 - \frac{2}{3}(1 - v) \right] \right.$$

$$\left. \times \ln\left(\frac{183}{Z^{1/3}}\right) + \frac{1}{9}(1 - v) \right\}, \quad \gamma \approx 0 \tag{2.6}$$

$$\phi_4 = k_3 \left\{ [1 + (1 - v)^2] \left[\frac{f_1(\gamma)}{4} - \ln Z^{1/3} \right] \right.$$

$$\left. - \frac{2}{3}(1 - v)\left[\frac{f_2(\gamma)}{4} - \ln Z^{1/3}\right] \right\},$$

$$\gamma < 2 \tag{2.7}$$

$$\phi_5 = k_3 \left[1 + (1 - v)^2 - \frac{2}{3}(1 - v) \right]$$

$$\times \left[\ln\left(\frac{2U}{\mu} \cdot \frac{1 - v}{v}\right) - \frac{1}{2} - C(\gamma) \right],$$

$$2 \le \gamma < 15 \tag{2.8}$$

where

$U = E + \mu$, total energy of electron

$\mu = 0.5109$ MeV, rest energy of electron

$$0 \le v \le \left(1 - \frac{\mu}{U}\right) = \frac{E}{U} = v_{max} \tag{2.9}$$

$$\gamma = \frac{100}{Z^{1/3}} \frac{\mu}{U} \frac{v}{1 - v} \tag{2.10}$$

Radiation loss gradient:

$$\left(\frac{dE}{dt}\right)_{RAD} = U \int_0^{v_{max}} \phi \, dv \tag{2.11}$$

The computation was carried out for energies between 2 and 100 MeV in steps of 0.5 MeV. For each value of V, v ranged from 0 to v_{max} in steps of 0.01. Similar computations were made for V ranging from 0.05 to 2 MeV in steps of 0.05, and for each V, v ranged from 0 to v_{max} in steps of 0.005.

The functions f_1, f_2, and C were taken from Reference 2.3, and are shown in Figs. 2.4 and 2.5.

The constants, k_1, k_2, and k_3, are listed in Table 2.1.

It is recognized that the validity of these computations becomes questionable when applied to the low range of electron energies. However, the computations were carried out to provide an approximate guide for further work.

II. PENETRATION AND ENERGY BALANCE FOR ELECTRONS TRAVERSING MATTER

The computations discussed in the preceding section have been amplified to account for the depth of penetration of the electrons and the degradation of their initial energy.

The average energy loss suffered by electrons after traversing X g/cm² of matter is

$$U_T = \int_0^t \left(\frac{dE}{dt}\right)_{TOT} dt \tag{2.12}$$
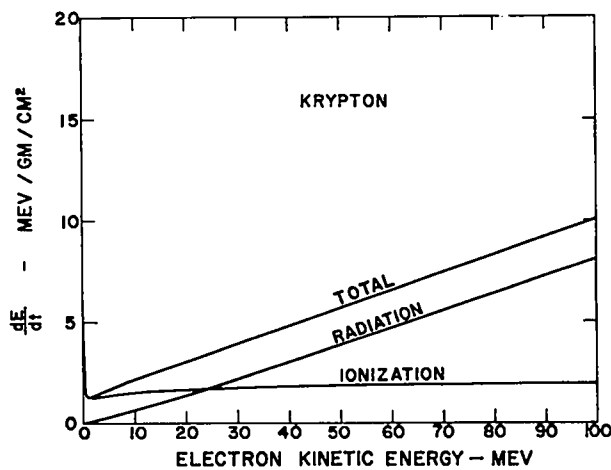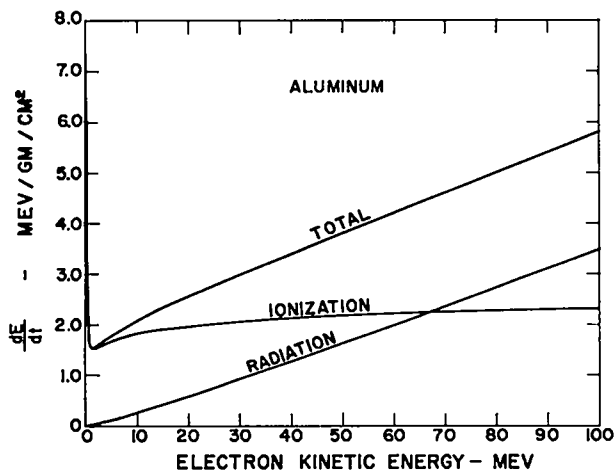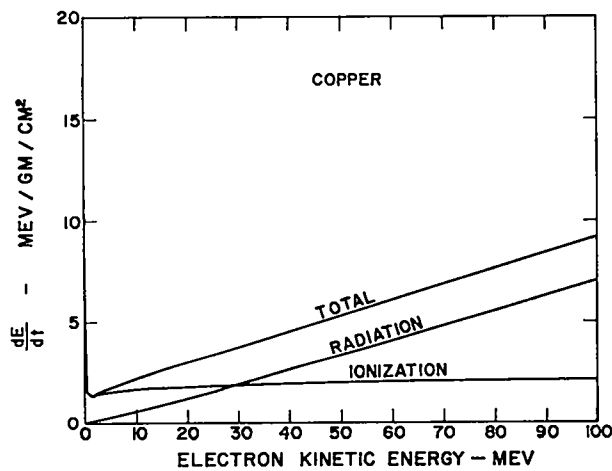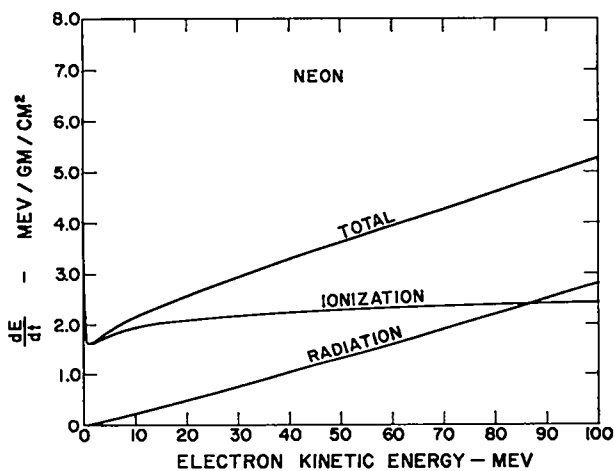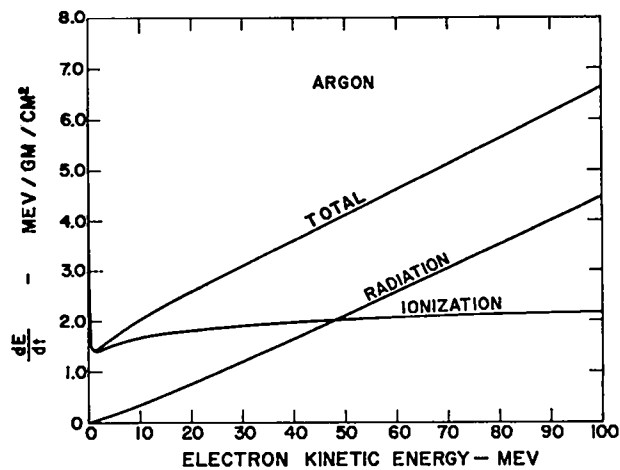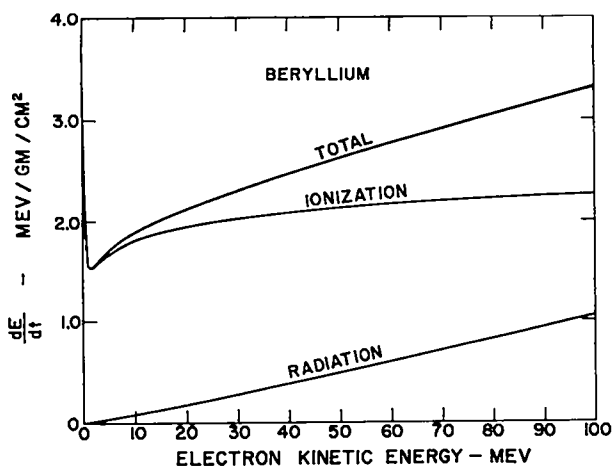
Fig. 2. 2.   Electron energy loss gradients in various materials.

28

Fig. 2. 2. Continued.

29

OTHER ELEMENTS	ATOMIC NUMBER	CRITICAL ENERGY—MEV
Be	4	218.7
Ne	10	87.3
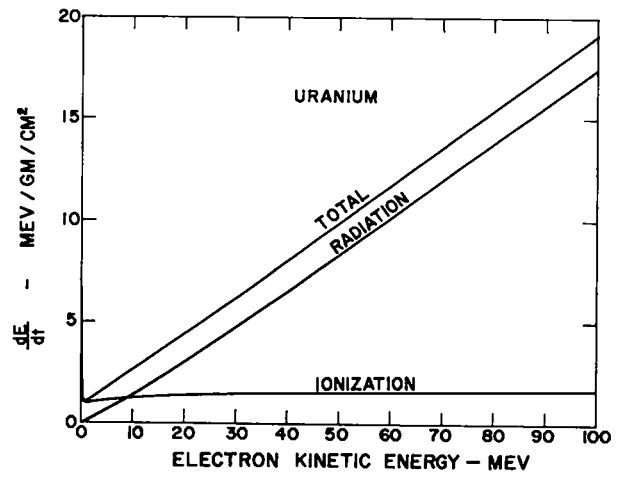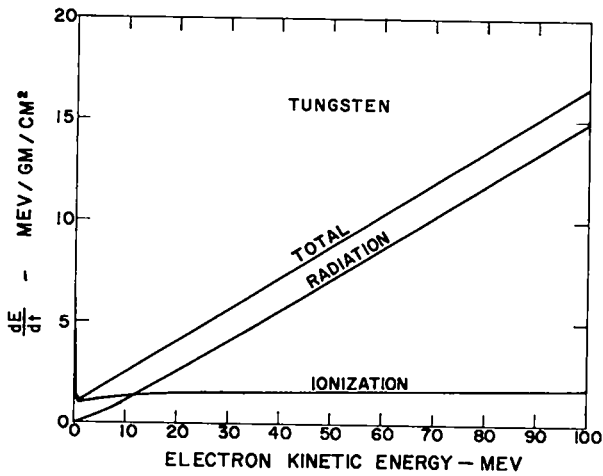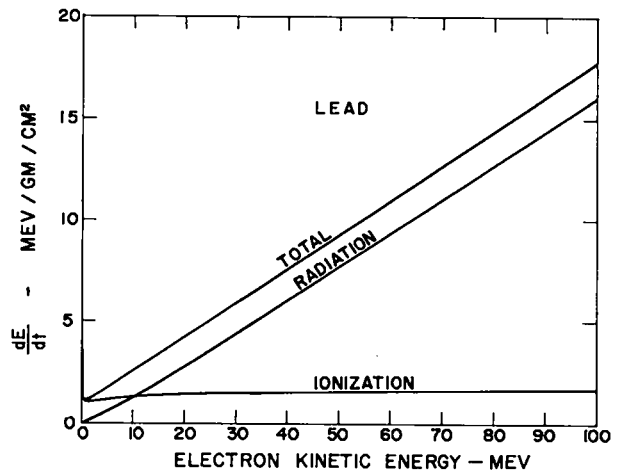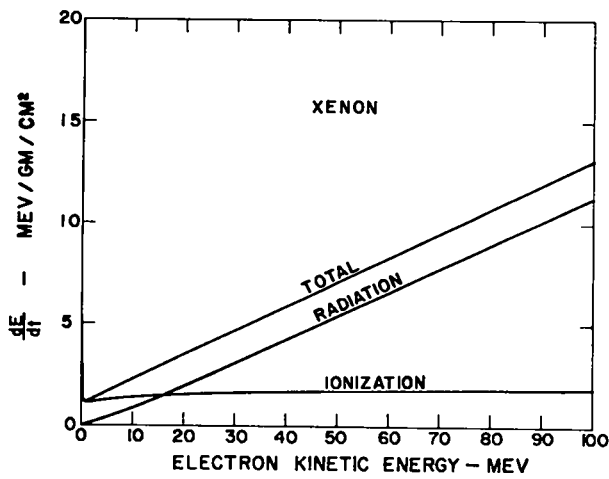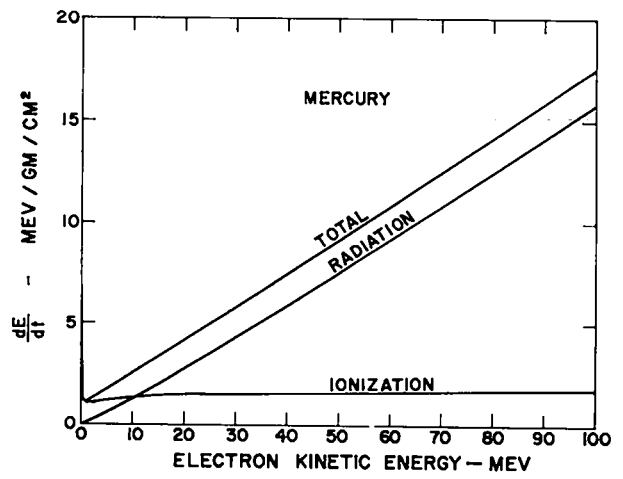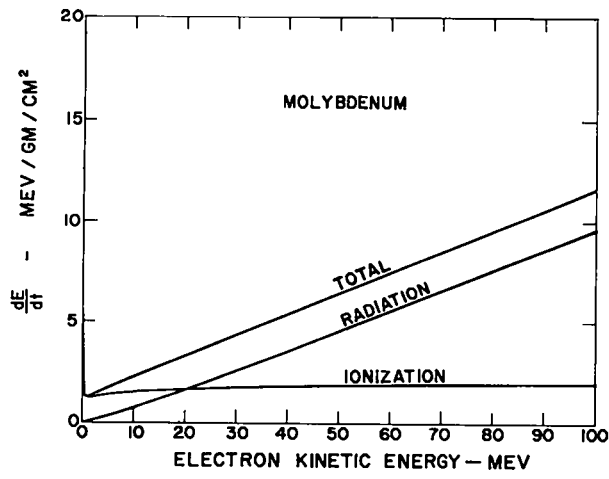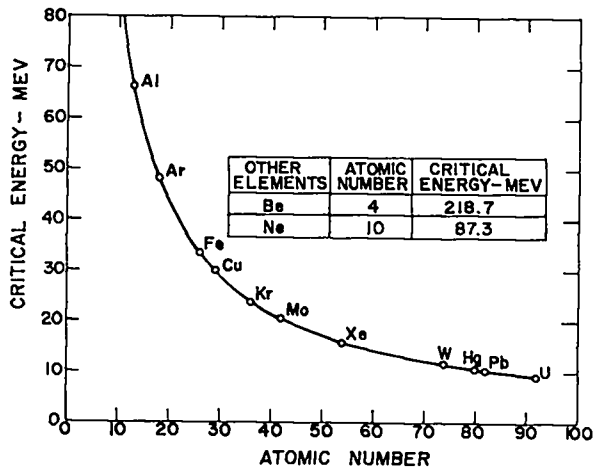
Fig. 2. 3.   Critical energy vs atomic number.
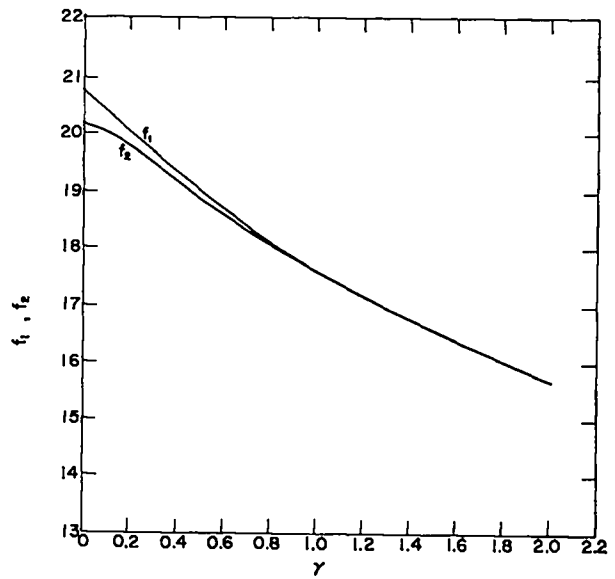
Fig. 2. 4.   The functions f_1, f_2 vs γ.
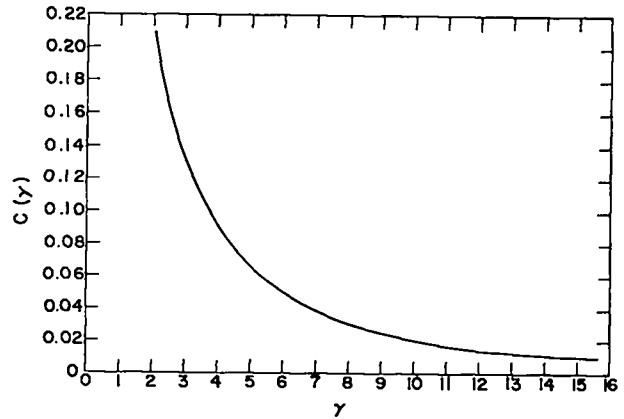
Fig. 2. 5.   The function $C(\gamma)$ vs γ.

Table 2.1
Parameters for Equations 2.4-2.8

Element	Z	k_1	k_2	k_3
Be	4	6.81313×10^{-2}	3.72773×10^{-9}	2.47808×10^{-3}
Ne	10	7.60624×10^{-2}	1.12653×10^{-8}	6.91639×10^{-3}
Al	13	7.39703×10^{-2}	2.28372×10^{-8}	8.74400×10^{-3}
Ar	18	6.91794×10^{-2}	3.31063×10^{-8}	1.13229×10^{-2}
Cu	29	2.00659×10^{-2}	7.75546×10^{-8}	1.84726×10^{-2}
Kr	36	6.59499×10^{-2}	1.21620×10^{-7}	2.15887×10^{-2}
Mo	42	6.71986×10^{-2}	1.52560×10^{-7}	2.56637×10^{-2}
Xe	54	6.31371×10^{-2}	2.55450×10^{-7}	3.10019×10^{-2}
W	74	6.17673×10^{-2}	4.73594×10^{-7}	4.15623×10^{-2}
Hg	80	6.12199×10^{-2}	4.72480×10^{-7}	4.45311×10^{-2}
Pb	82	6.07518×10^{-2}	5.08148×10^{-7}	4.52983×10^{-2}
U	92	5.93252×10^{-2}	6.69741×10^{-7}	4.96291×10^{-2}

Correspondingly, that portion of the total energy loss which has gone into ionization and that which has gone into radiation after the electron has gone a distance X g/cm² may be written

$$U_{COLL} = \int_0^t \left(\frac{dE}{dt}\right)_{COLL} dt$$

(2.13)

and

$$U_{RAD} = \int_0^t \left(\frac{dE}{dt}\right)_{RAD} dt$$

(2.14)

Proper account has been taken of the energy degradation as the particles pass through matter.

Results of these calculations are presented in Figs. 2.6 through 2.13, covering energies from 5 to 100 MeV for electrons traversing various thicknesses of Be, Ne, Al, Ar, Cu, Kr, Mo, Xe, W, Hg, Pb, and U.

III. ELECTRON RANGE IN SEVERAL ELEMENTS

The electron ranges for the elements Be, Ne, Al, Ar, Cu, Kr, Mo, Xe, W, Hg, Pb, and U were computed from the expression

$$R = \int_0^{E_0} \frac{dE}{\left(\dfrac{dE}{dt}\right)_{TOT}}$$

(2.15)

where

E_0 = kinetic energy of incident electron

$\left(\dfrac{dE}{dt}\right)_{TOT}$ = total energy loss gradient, radiation plus ionization, MeV/(g/cm²)

(2.16)

The results of these computations are given in Fig. 2.14.

IV. RADIATION INTENSITY-ANGLE DISTRIBUTION

Bremsstrahlung from high energy electrons is, by nature, highly directional, having a sharply defined angular spread about the direction of motion of the charged particles generating it. Furthermore, as these particles wander through the material of the target, they experience both elastic and inelastic scattering collisions, with the distribution of the former being predominant in defining the intensity-angle distribution of radiation emerging from thick targets.

One of the first calculations that must be made is an estimate of the optimum target thickness. Here, the optimum target is defined as one which generates a maximum on-axis radiation intensity. A more appropriate definition, however, is that thickness which generates the greatest forward intensity having the most favorable energy distribution for the particular radiographic experiment being considered. Simple calculations demonstrate that the first definition of an optimum thickness target is adequate for thick section radiography. Therefore, since PHERMEX was designed primarily for penetrating thick sections, the naive definition is the one of importance here.

Considerable effort has been made to understand the phenomena of electron penetration of matter, as well as of the intensity-angle distribution of the bremsstrahlung generated.[2.4-2.13] More detailed theory of the on-axis and the off-axis bremsstrahlung has been worked out thoroughly by Emigh[2.14] at Los Alamos. No attempt is made here to extend present theories, but merely to provide an adequate guide for target design.

The total bremsstrahlung flux generated per coulomb by electrons of kinetic energy V_0 incident upon a target of thickness t and material Z can be obtained from the preceding sections of this chapter. However, two modifications are needed to determine the emerging radiation spectrum, flux, and intensity-angle distribution. Neglecting the intensity-angle distribution for the moment, the emerging spectrum and flux for target thicknesses sensibly less than one radiation length are easily obtained by considering the target as being composed of a large number of thin targets, dx.

31
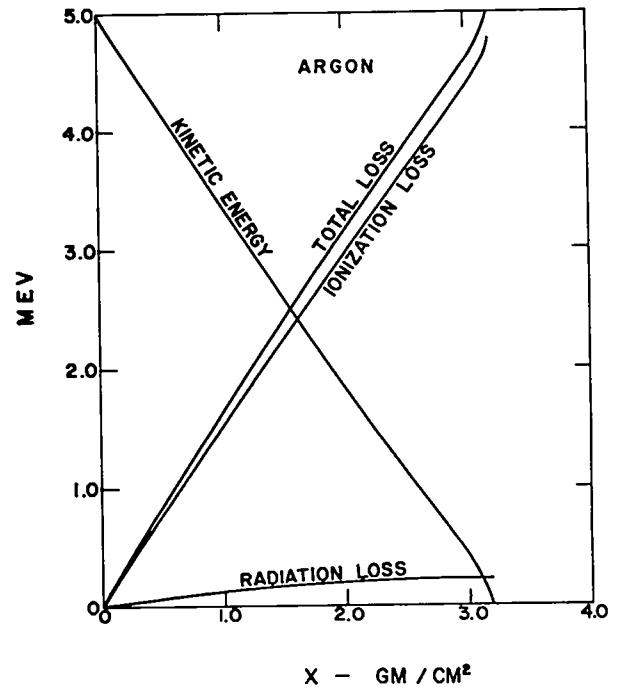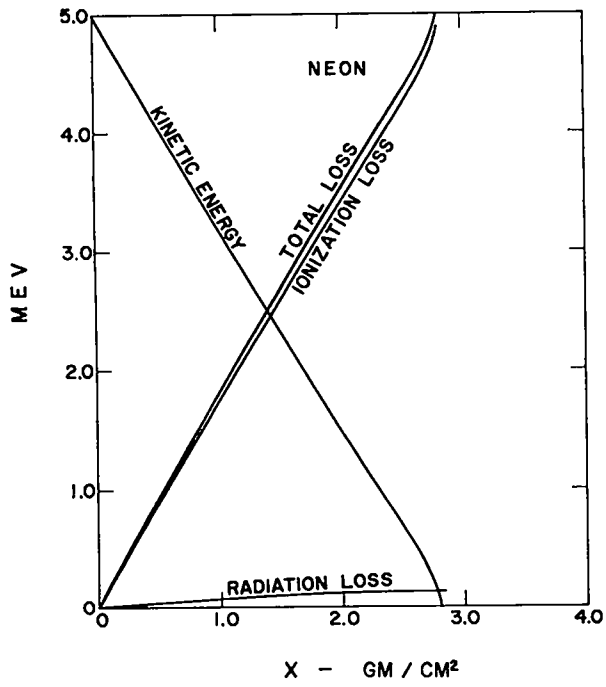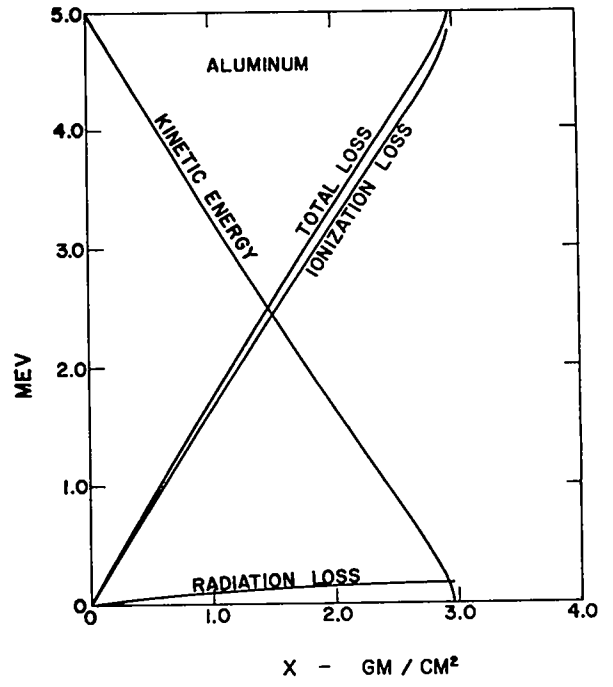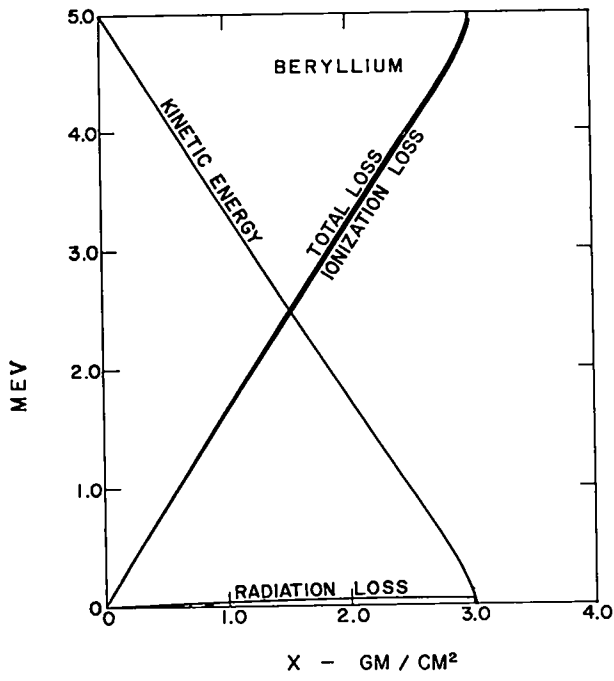
Fig. 2. 6.   5 MeV electron losses and penetration vs thickness.

Fig. 2. 6.   Continued.

33

Fig. 2. 6. Continued.

34
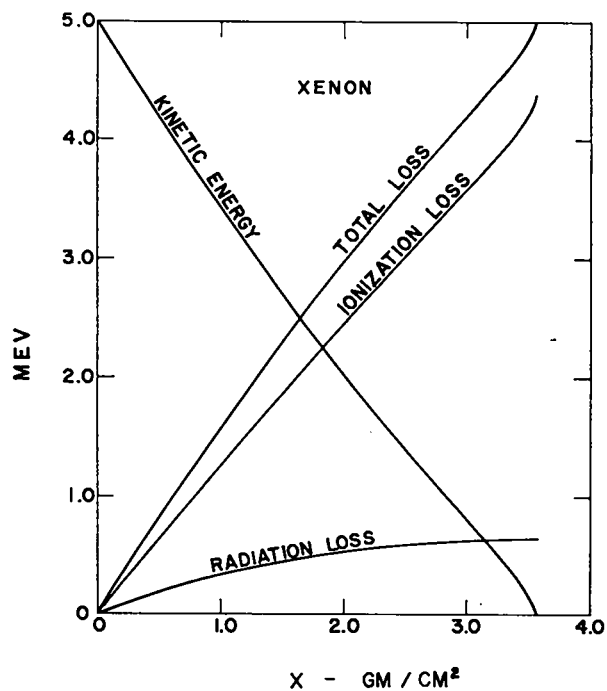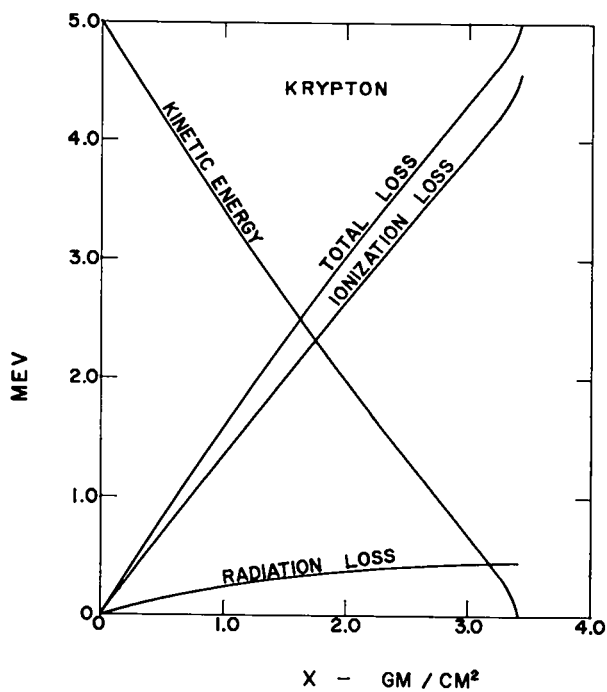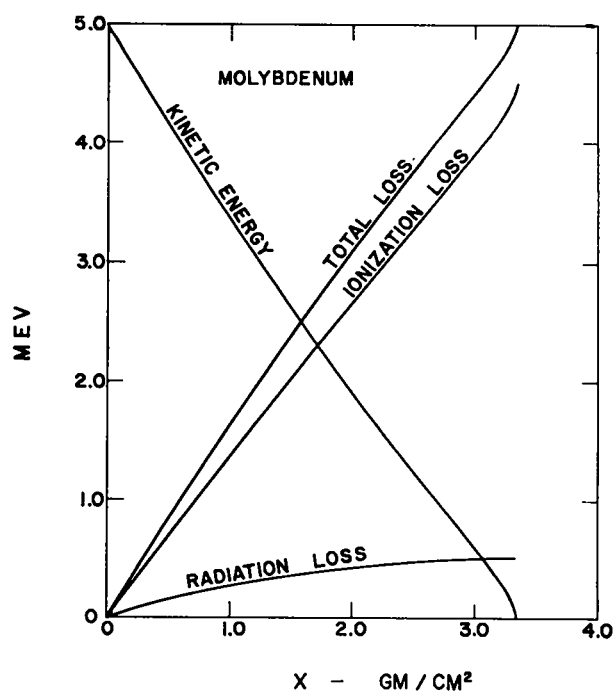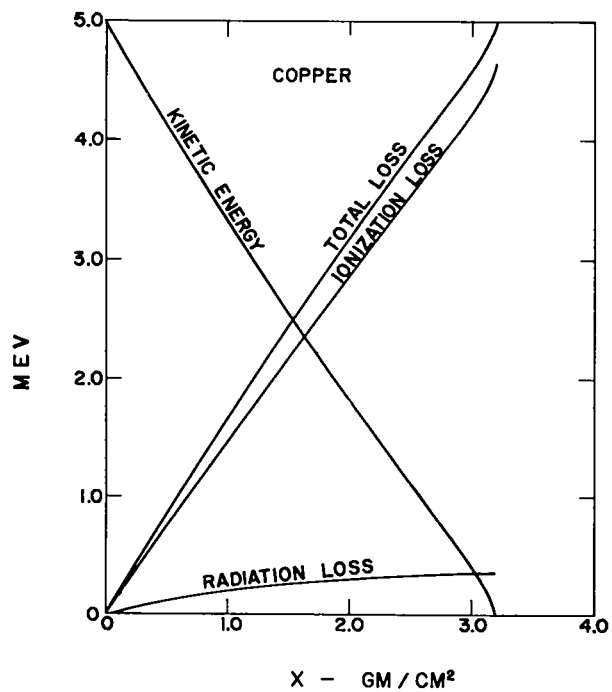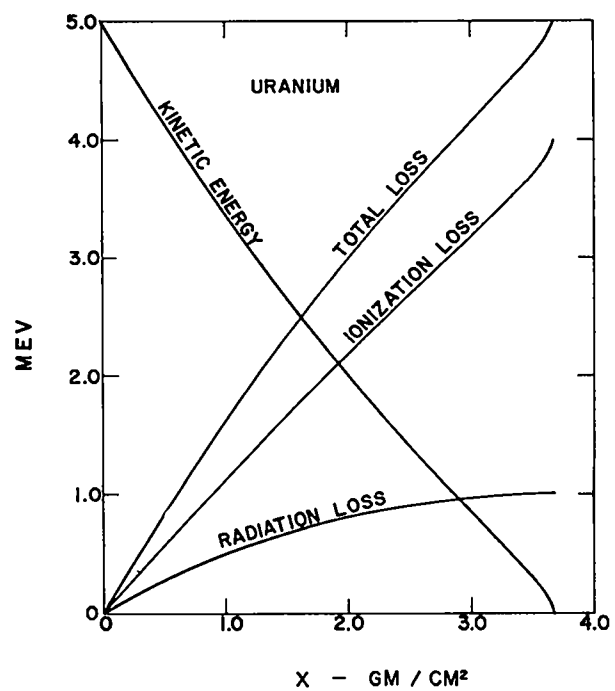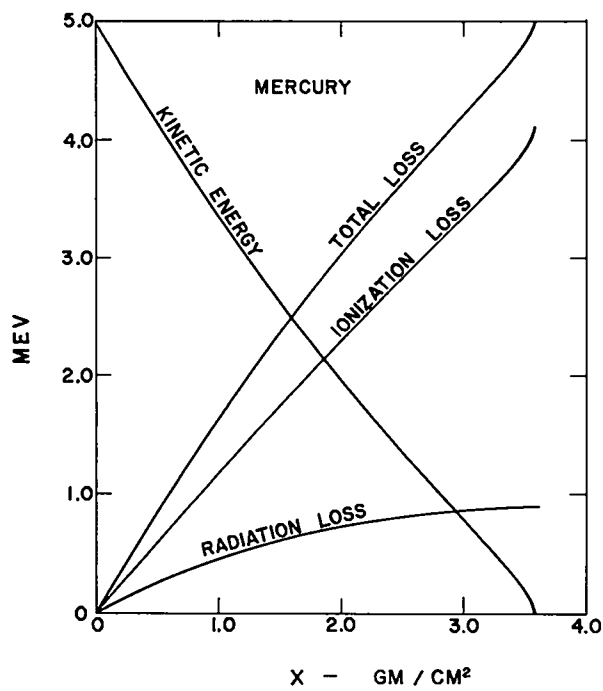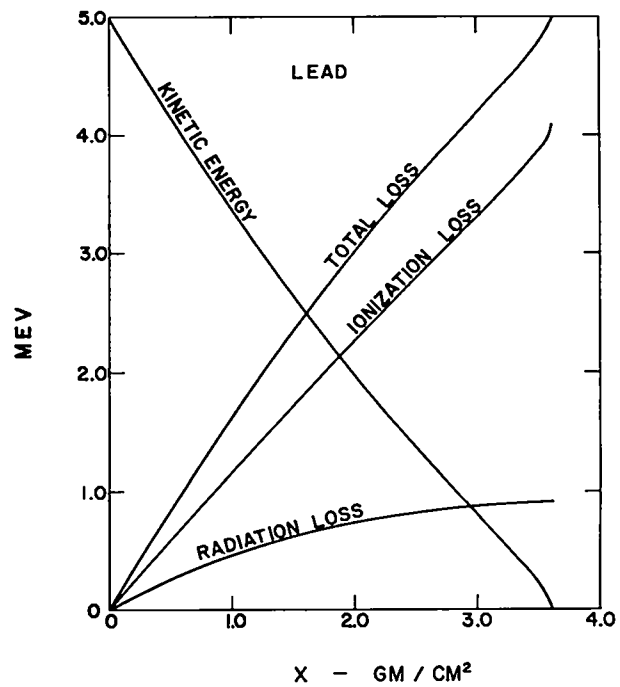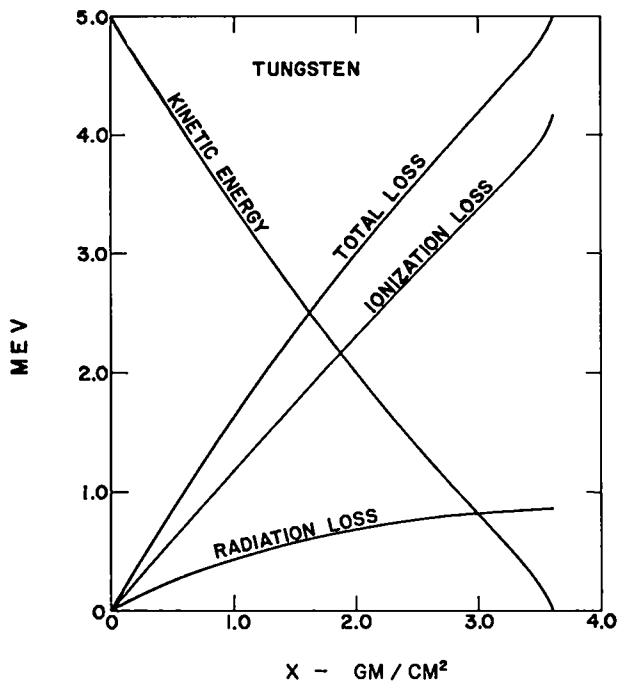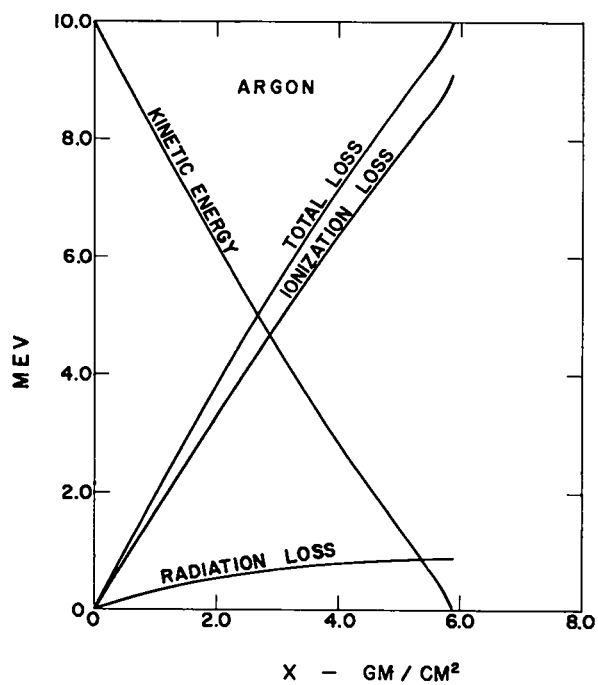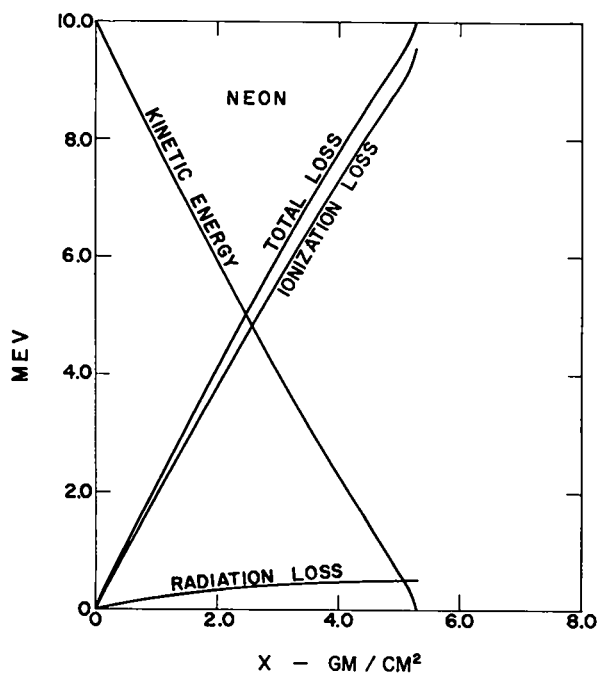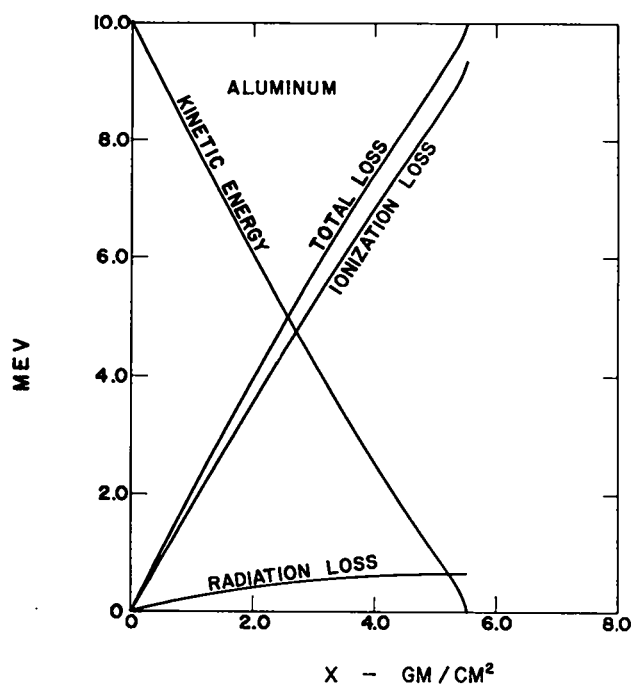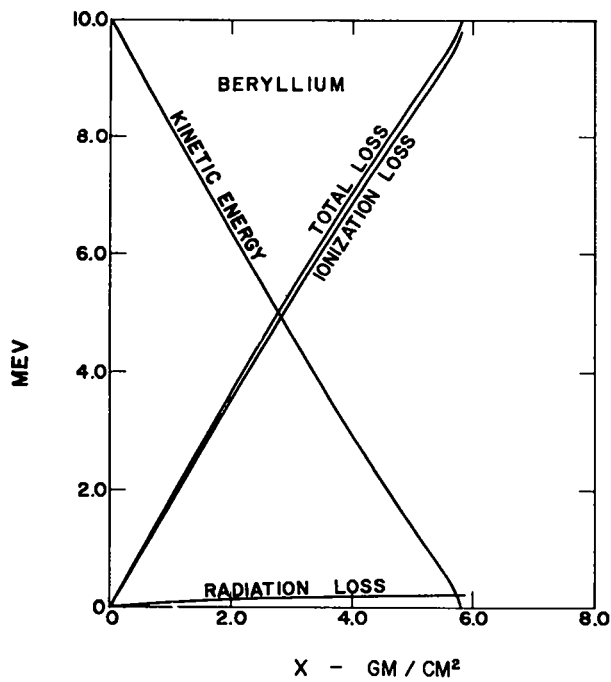
Fig. 2. 7.   10 MeV electron losses and penetration vs thickness.
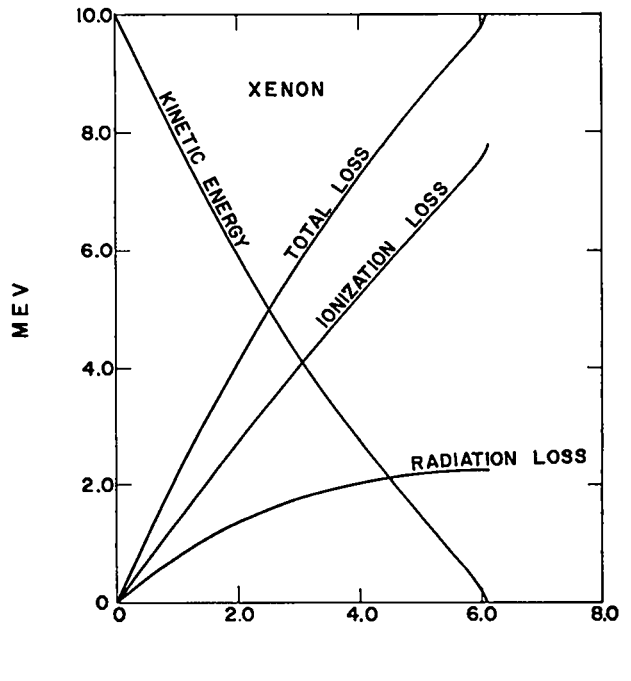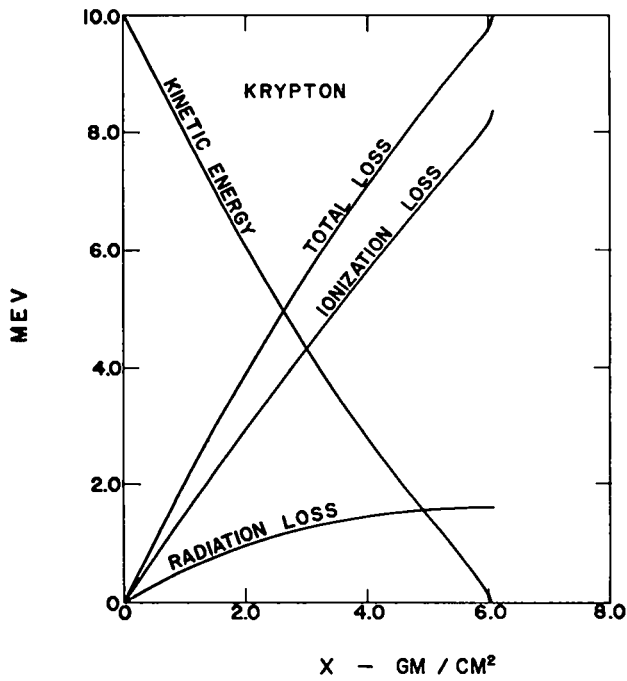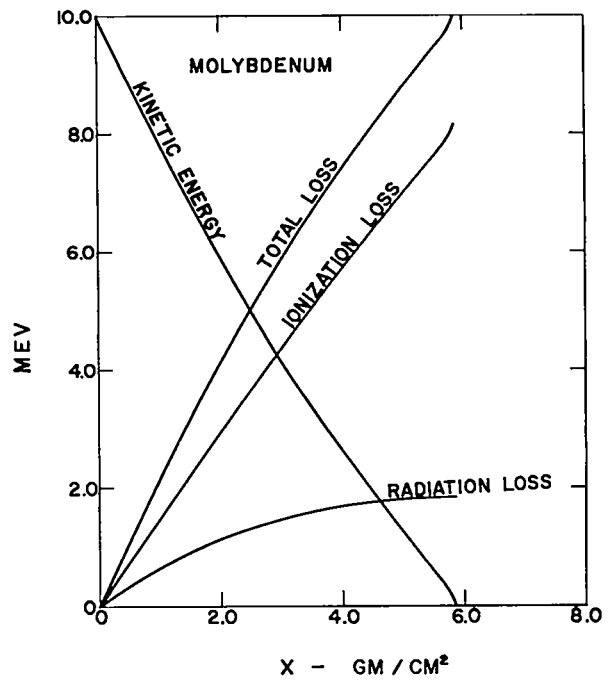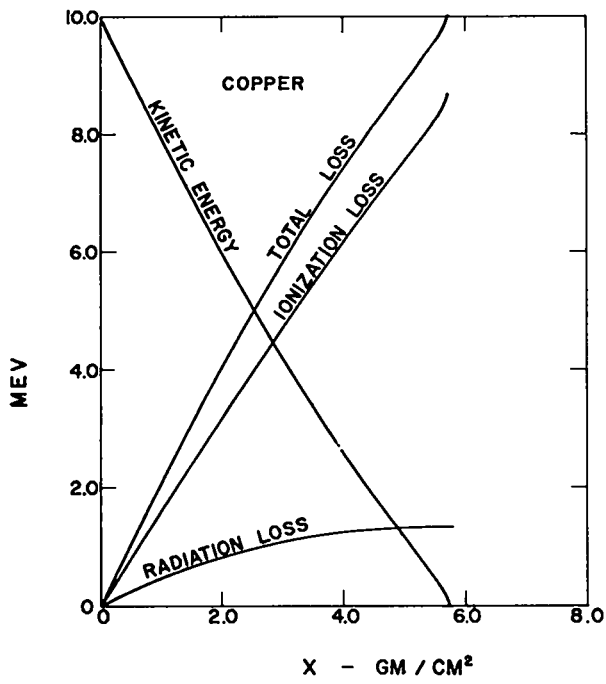
Fig. 2. 7. Continued.
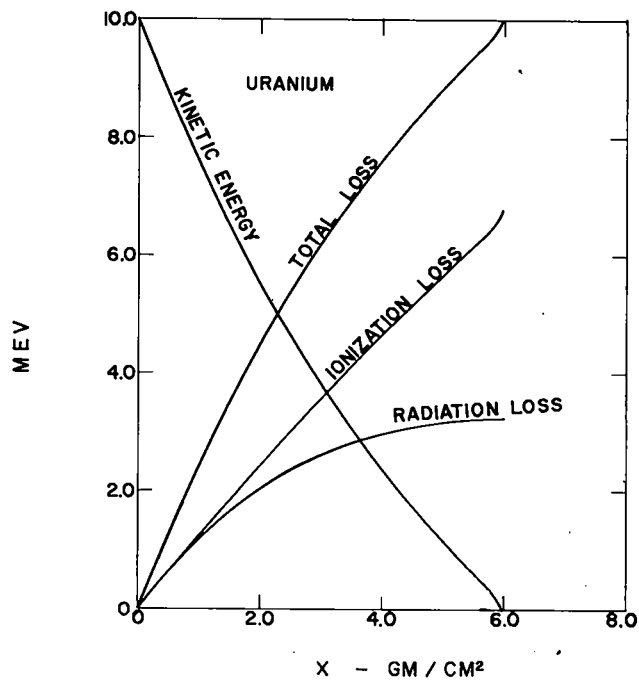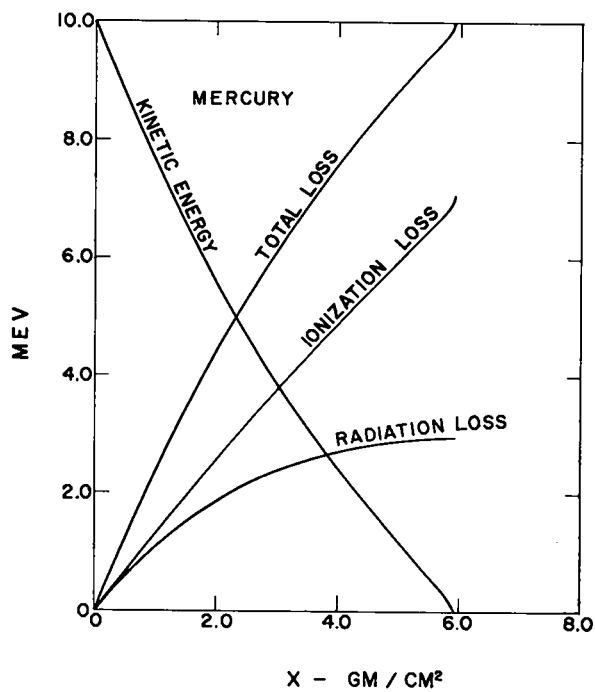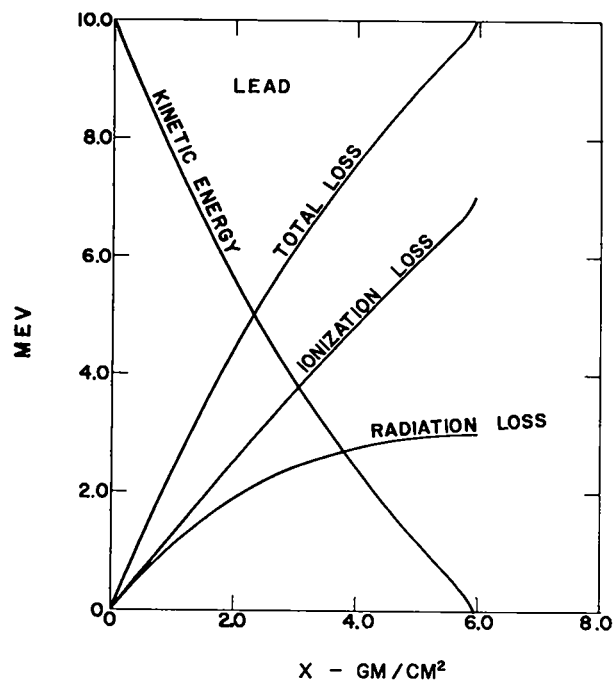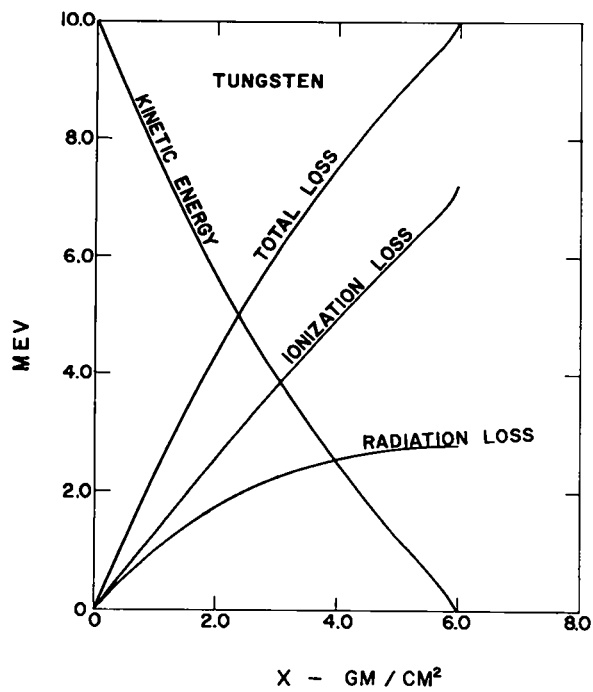
Fig. 2. 7. Continued.
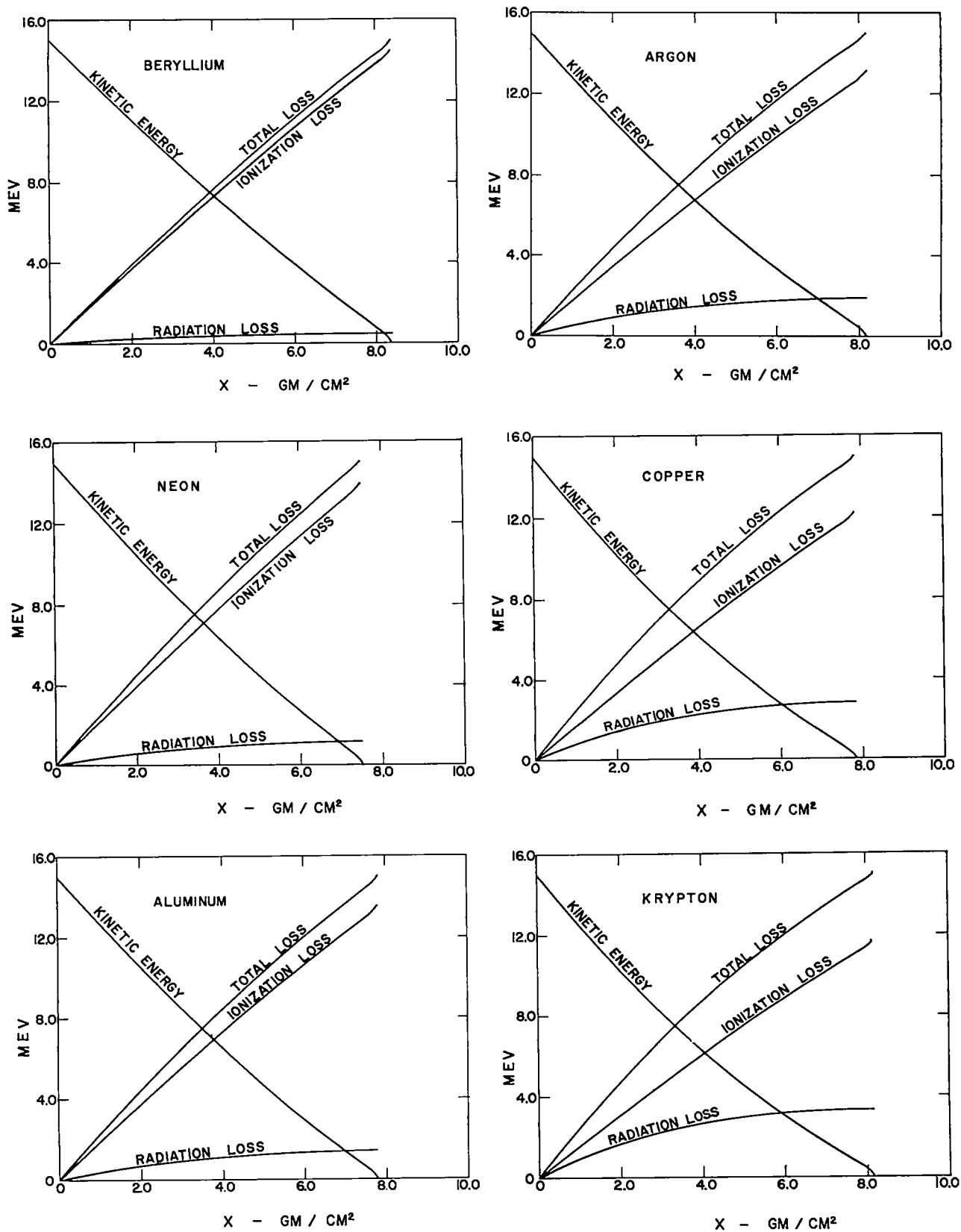
Fig. 2. 8.   15 MeV electron losses and penetration vs thickness.
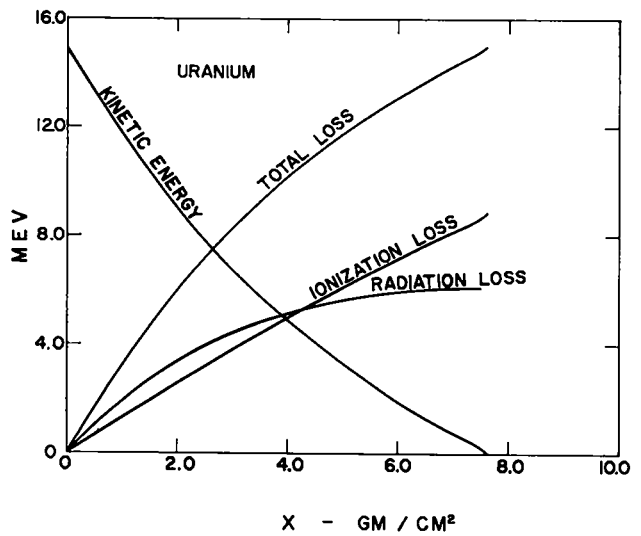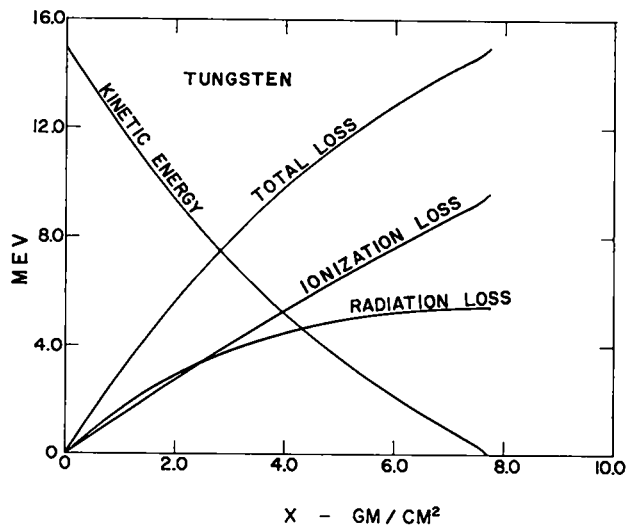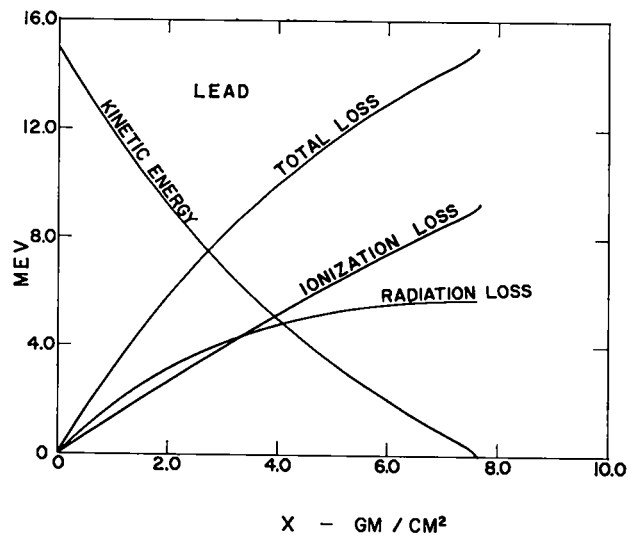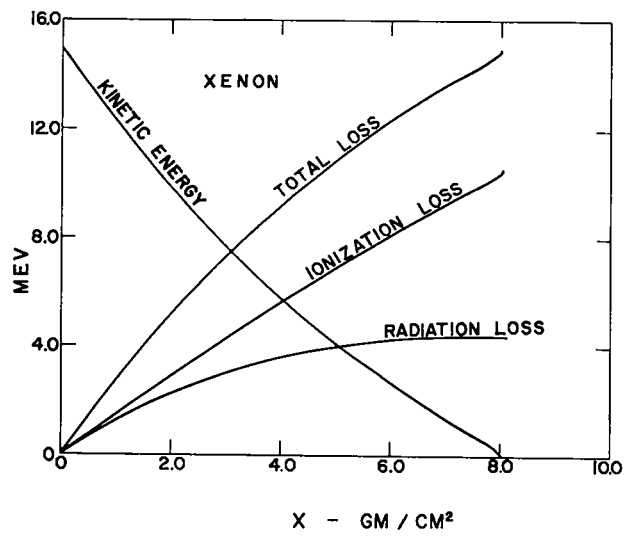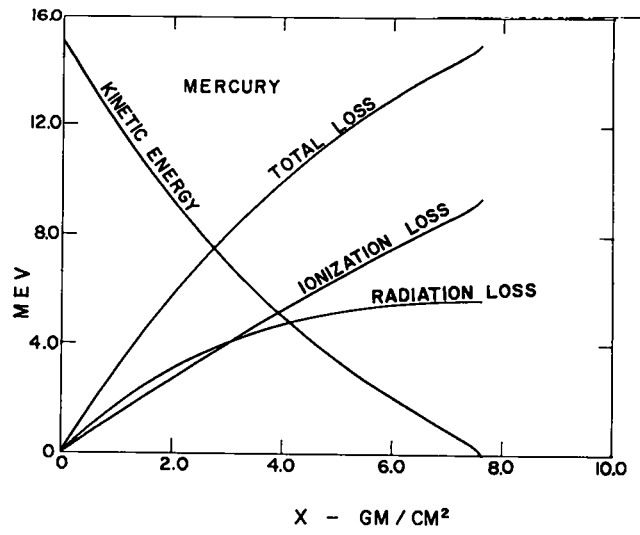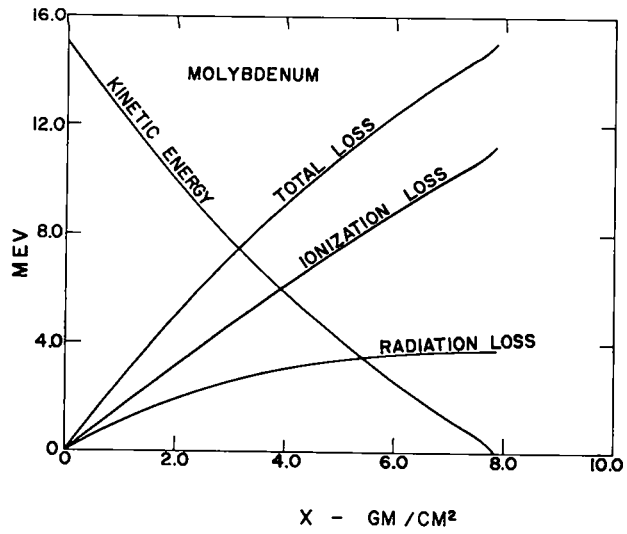
Fig. 2. 8. Continued.
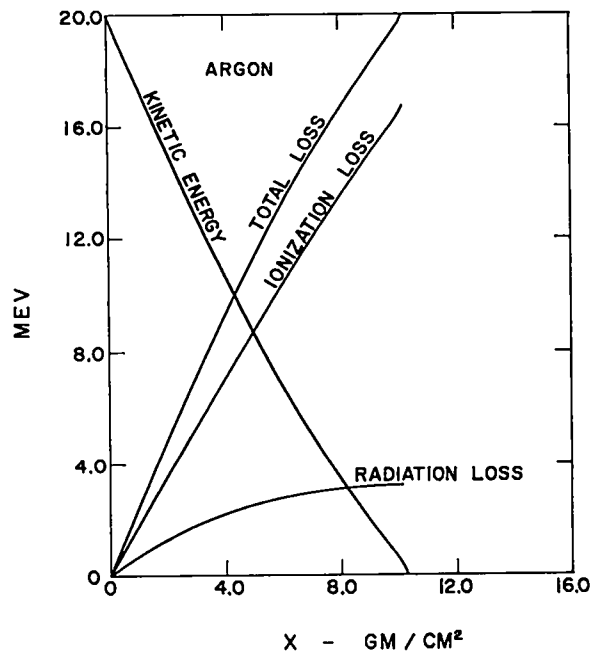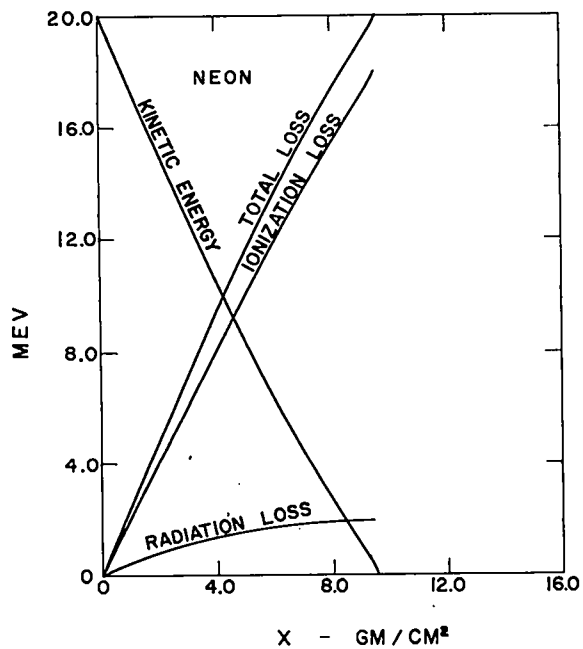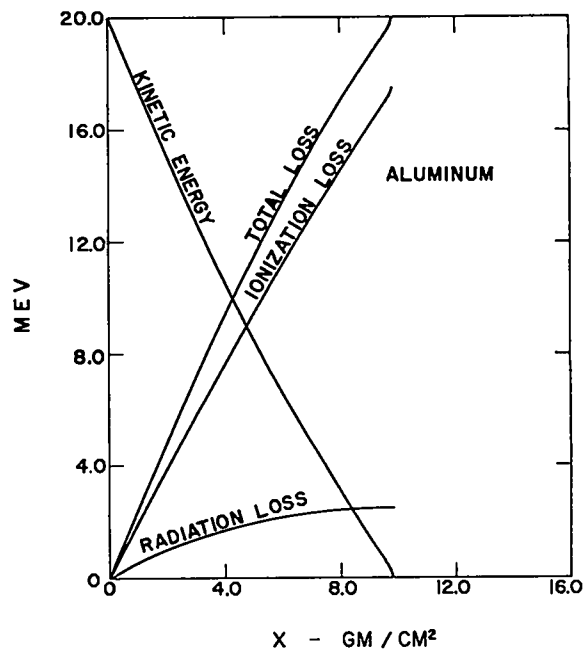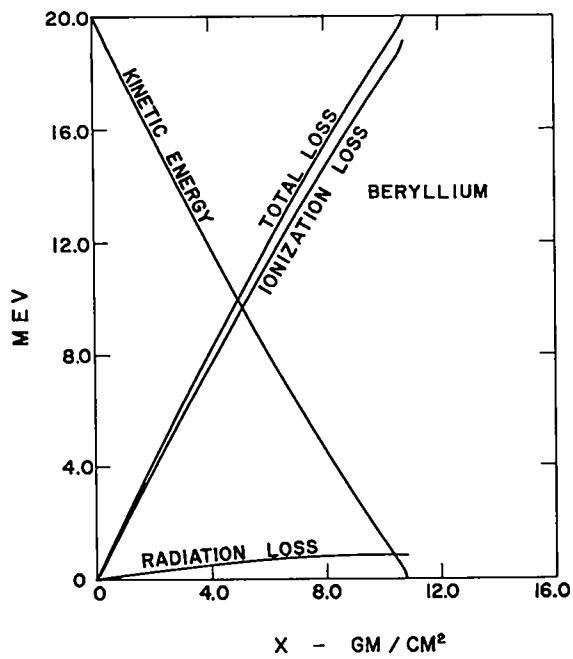
Fig. 2. 9.   20 MeV electron losses and penetration vs thickness.
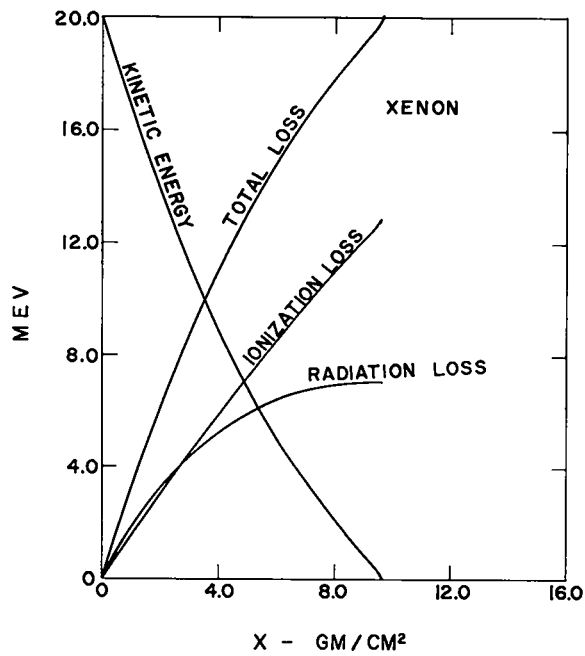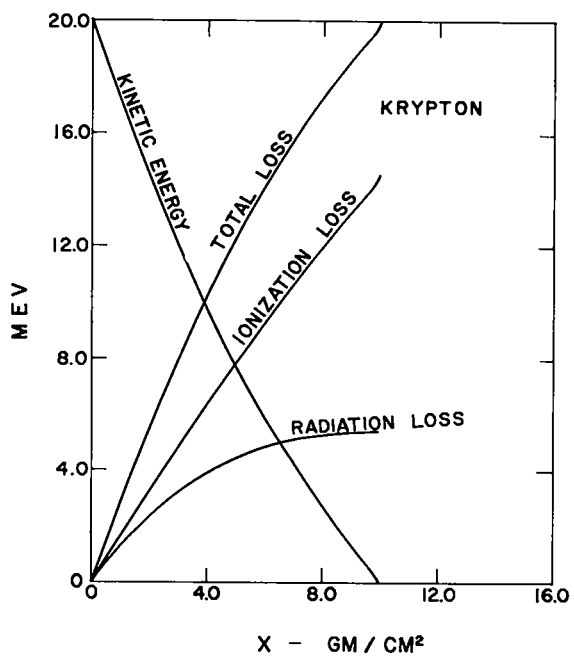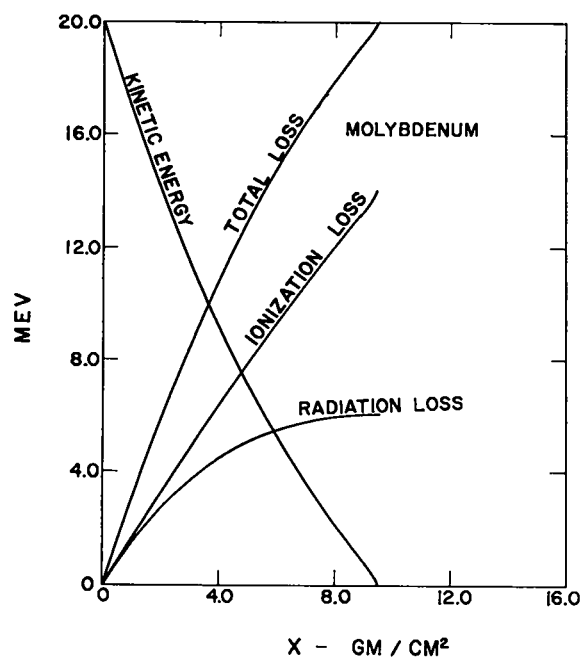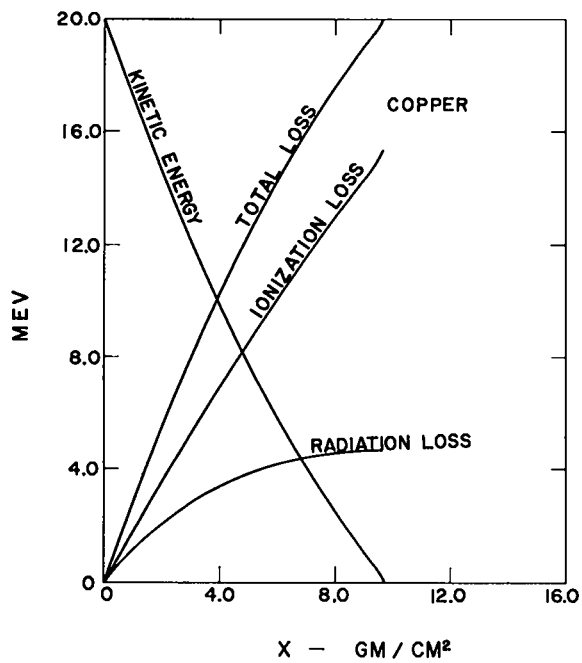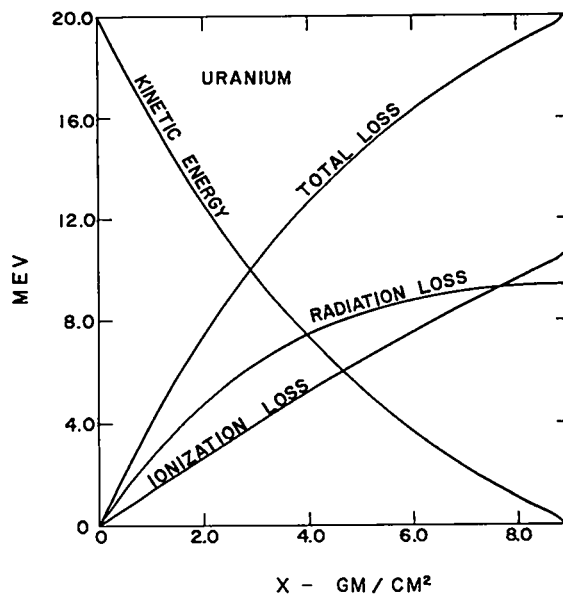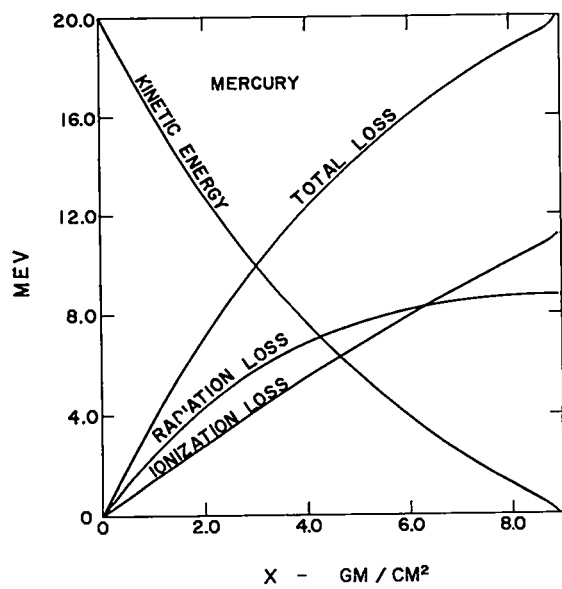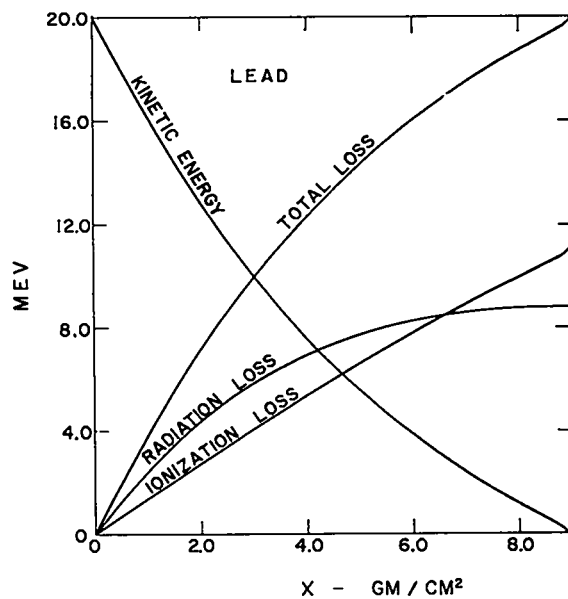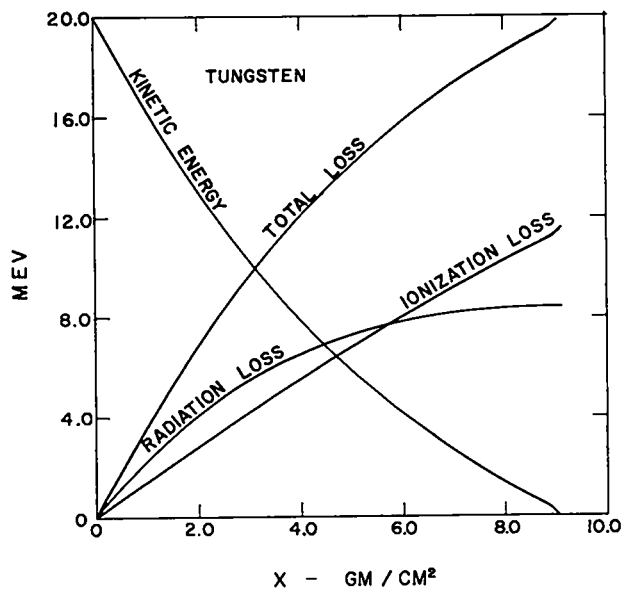
Fig. 2. 9.   Continued.

Fig. 2. 9. Continued.

42
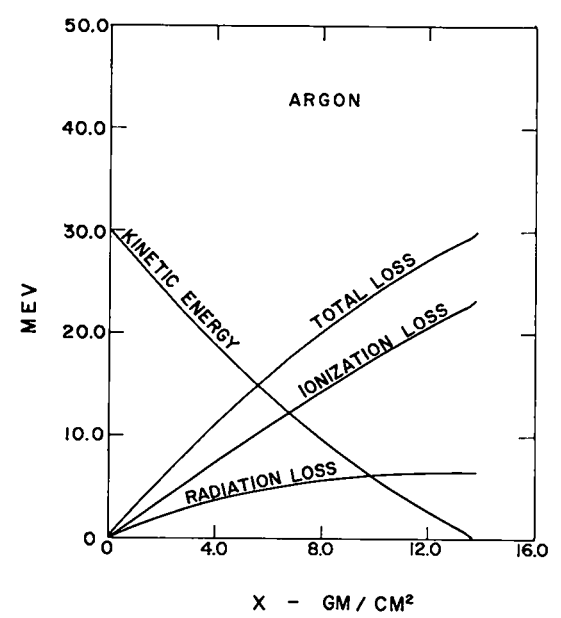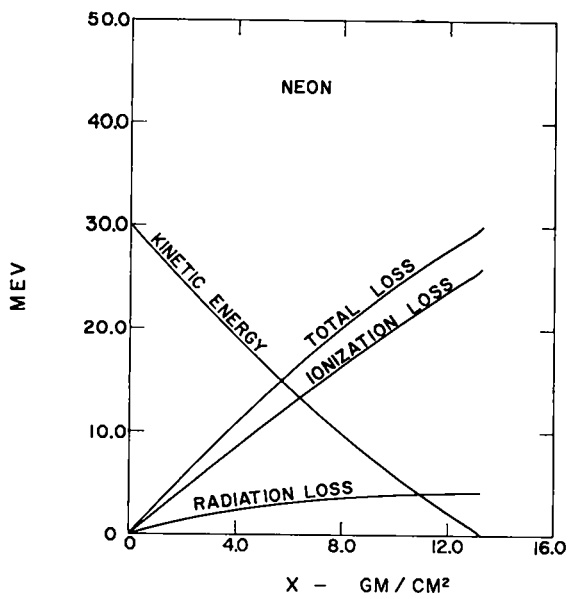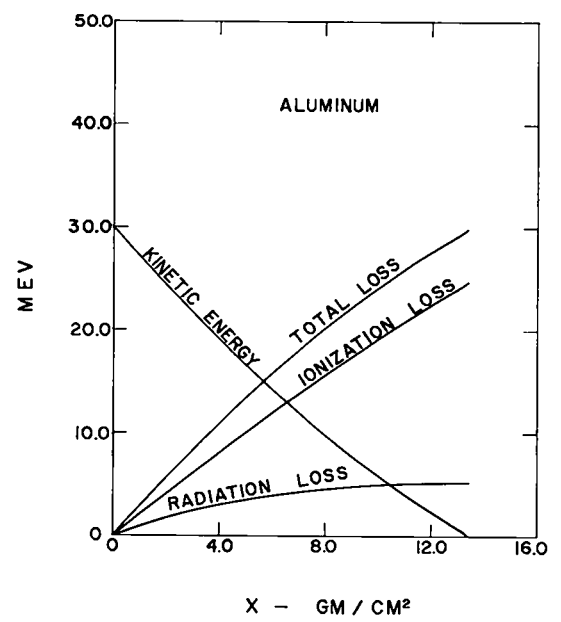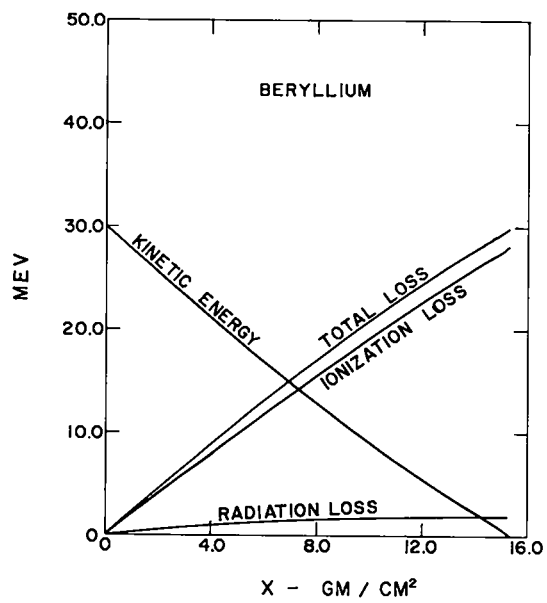
Fig. 2.10   30 MeV electron losses and penetration vs thickness.

Fig. 2.10. Continued.

44
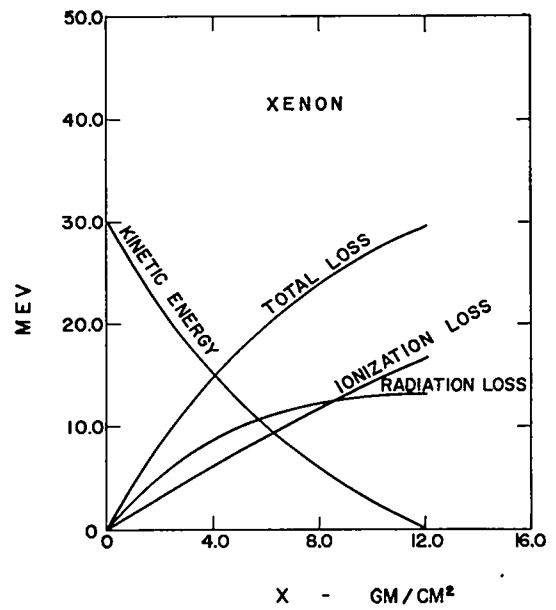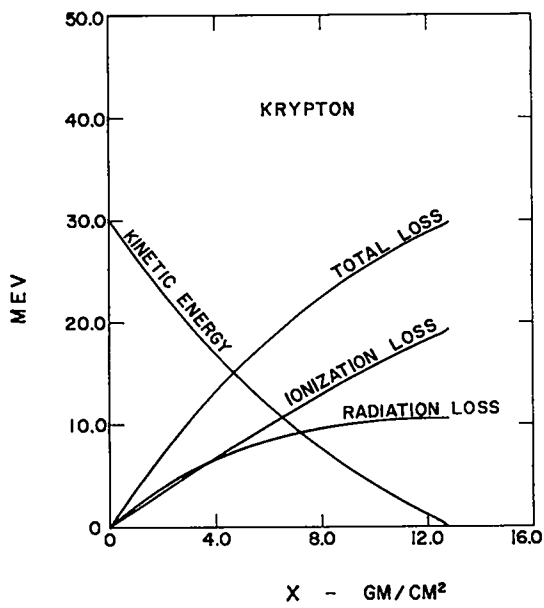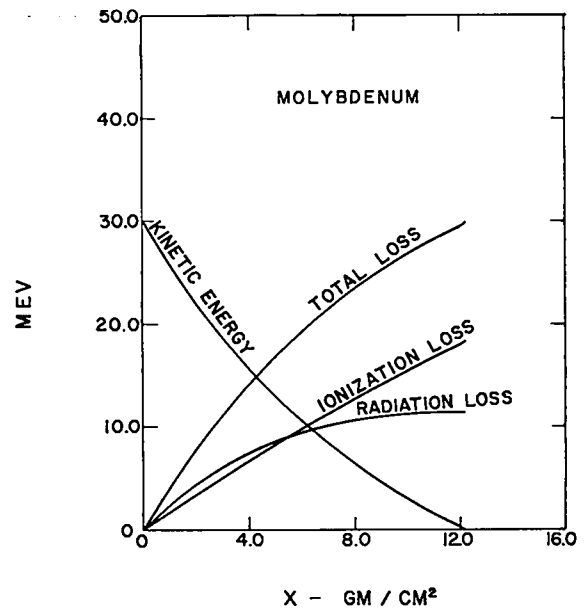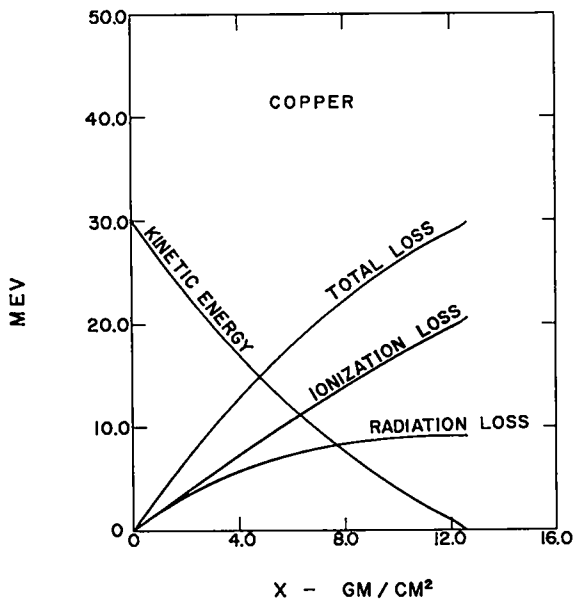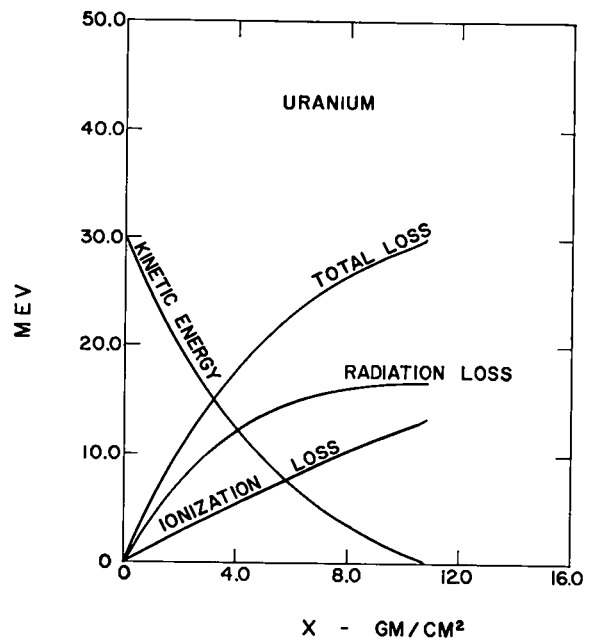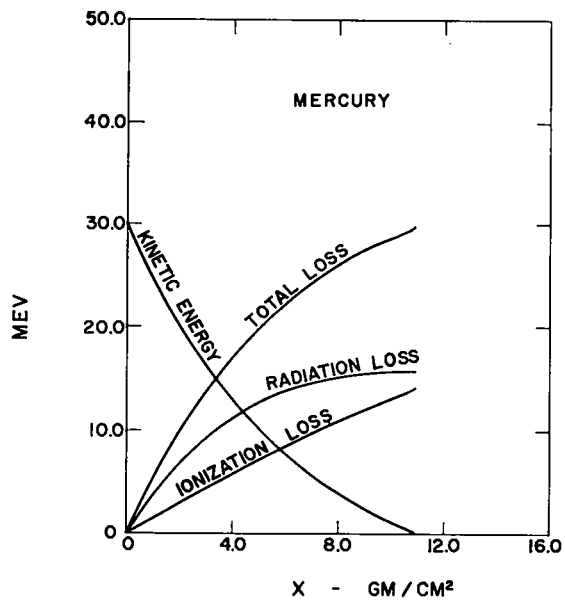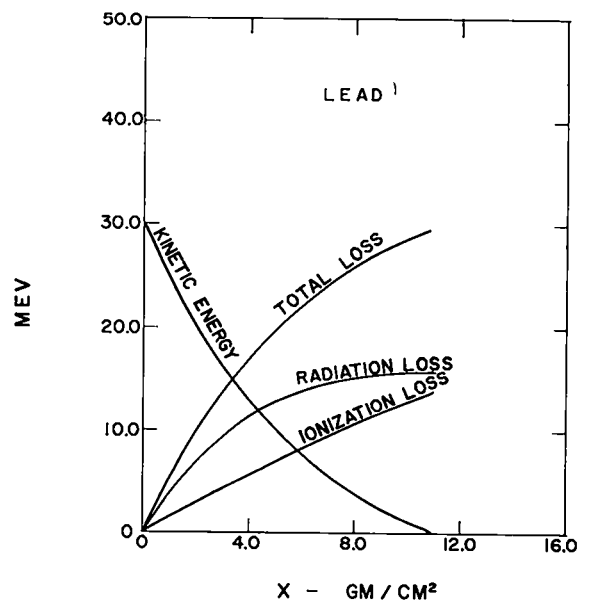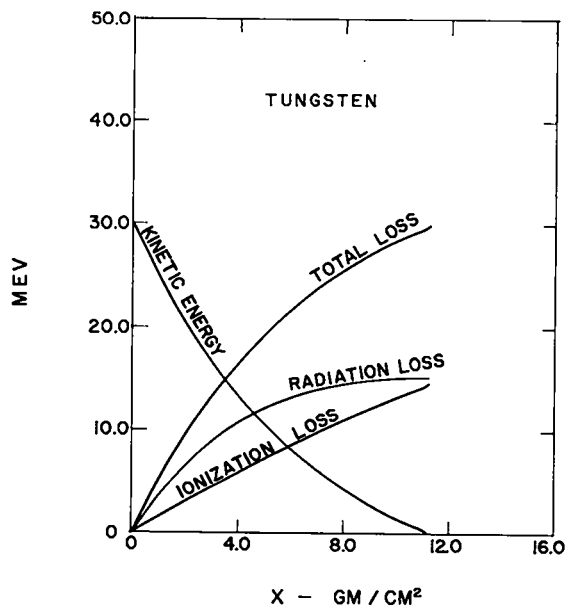
Fig. 2.10.   Continued.
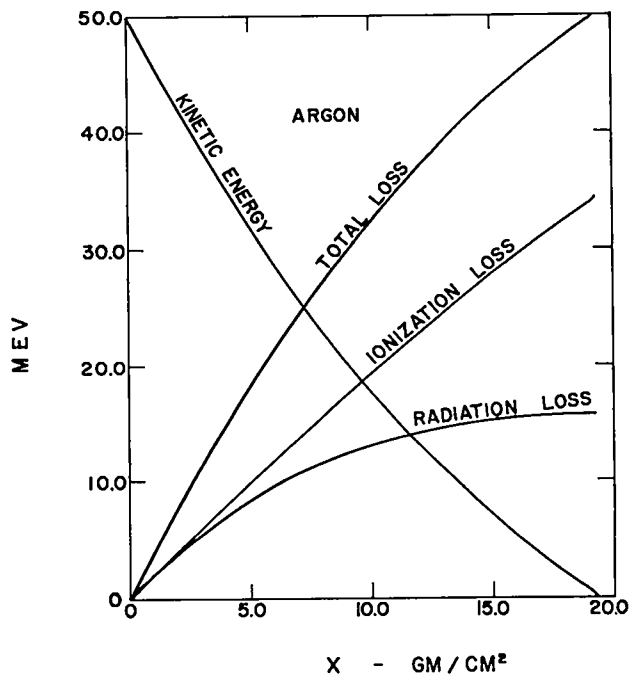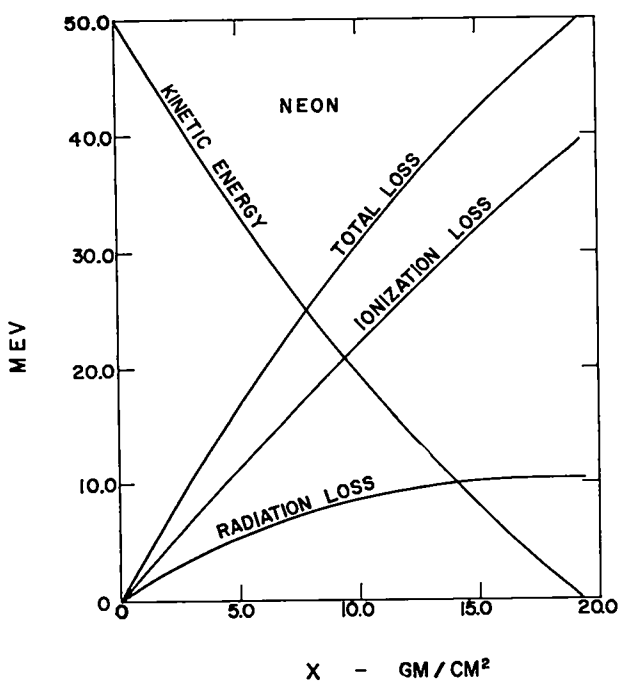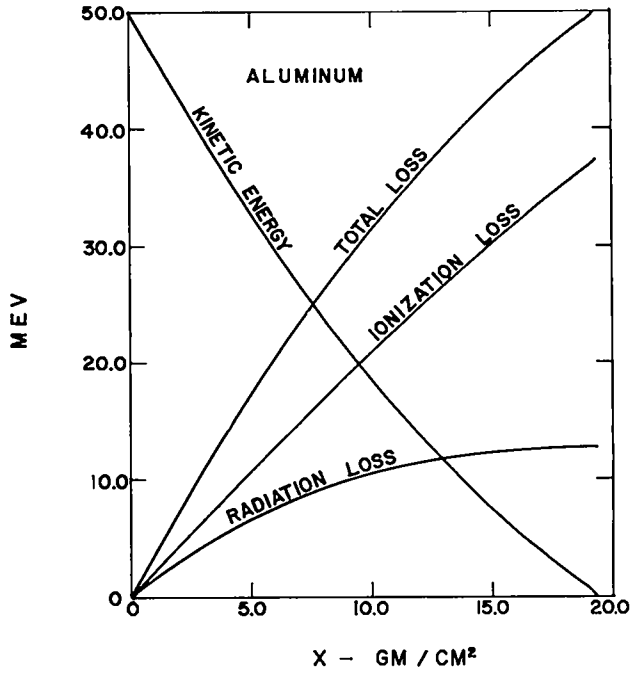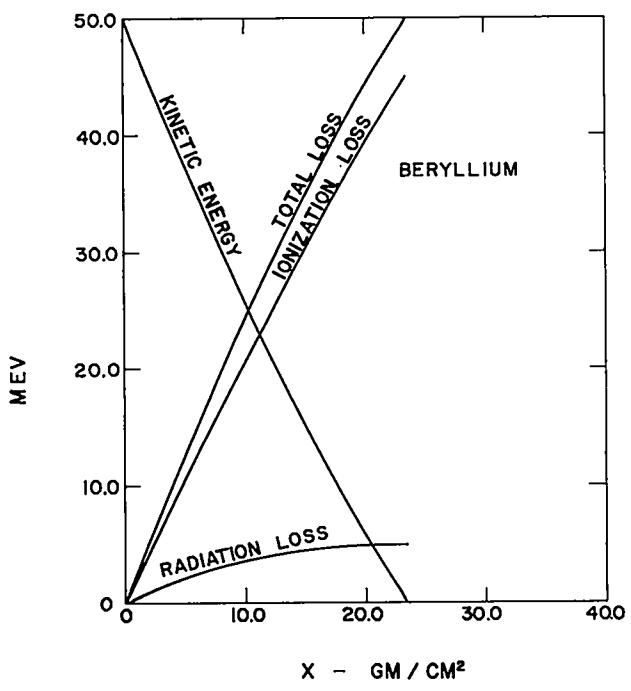
Fig. 2.11. 50 MeV electron losses and penetration vs thickness.

Fig. 2.11.   Continued.

47

Fig. 2.11. Continued.

48
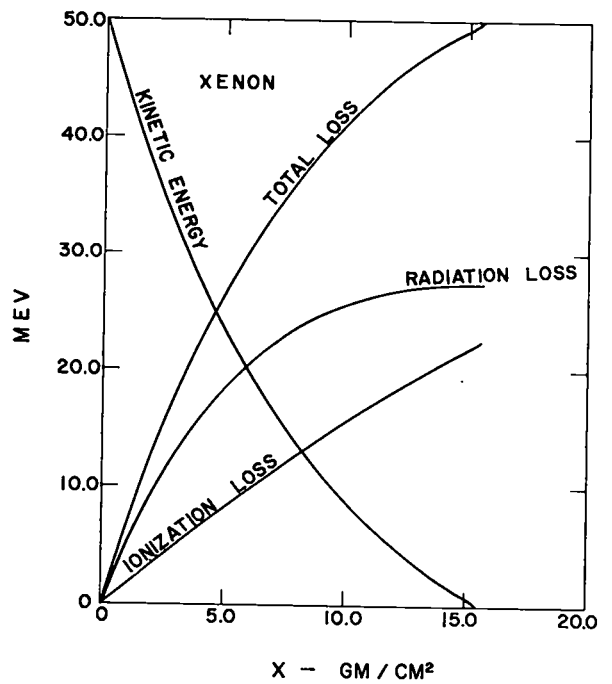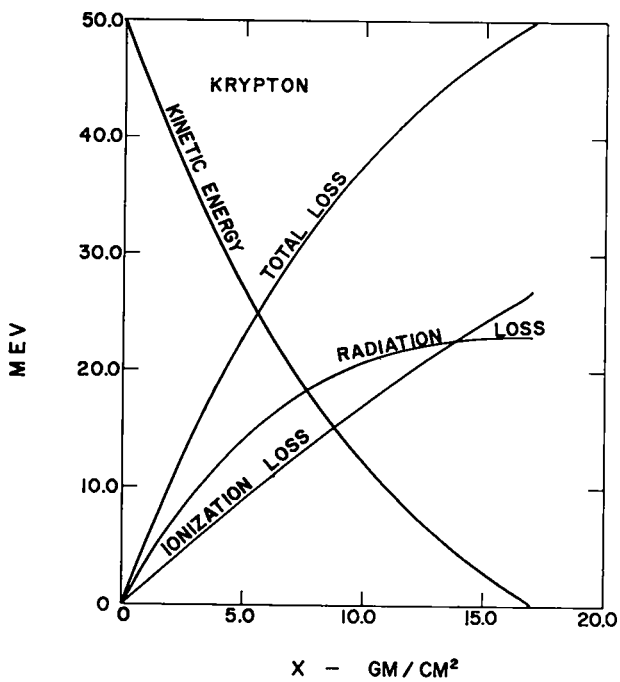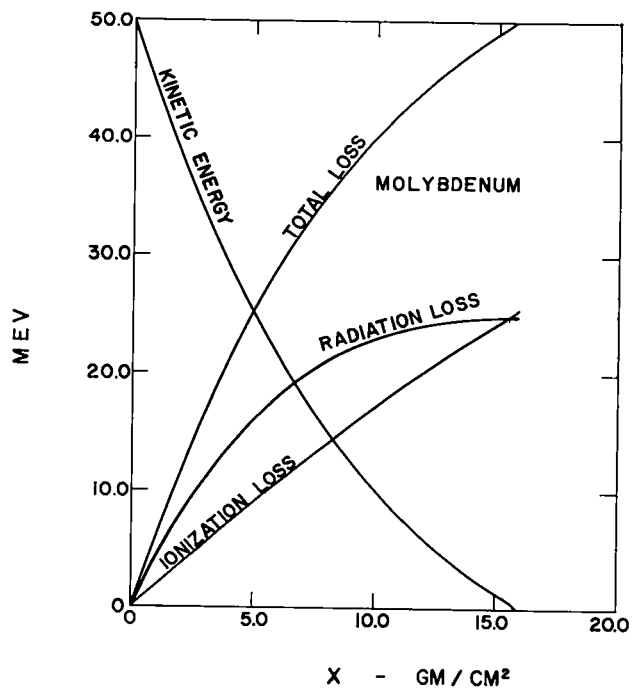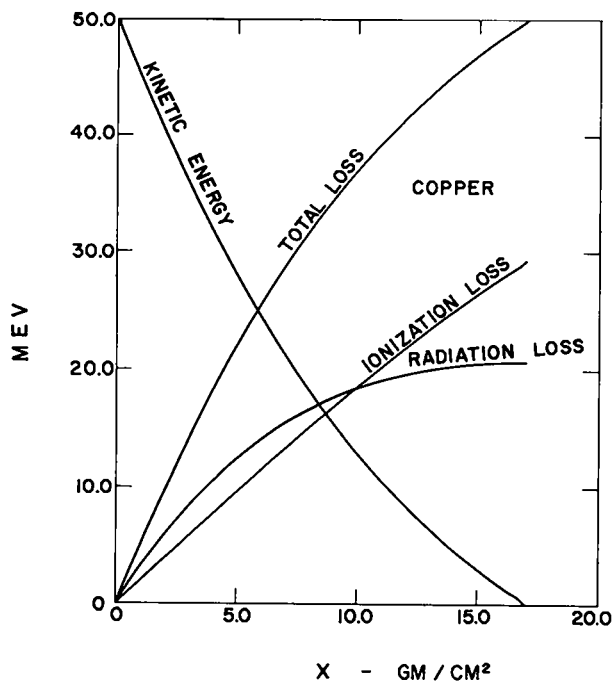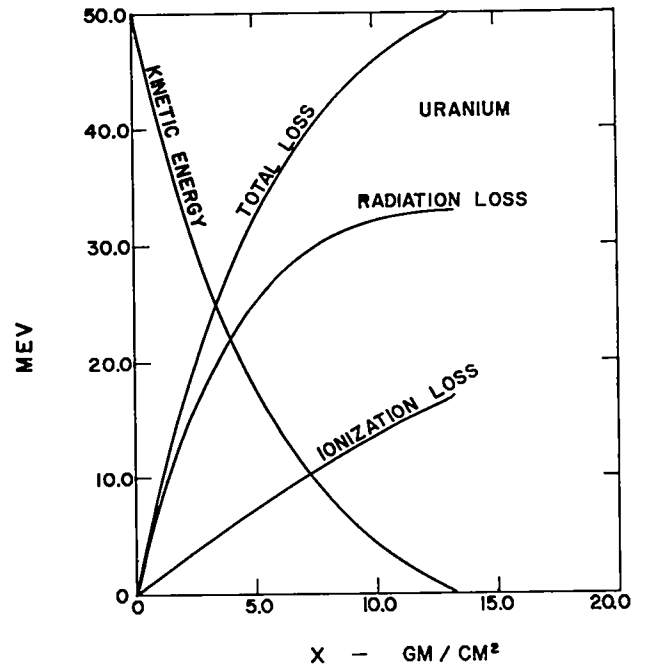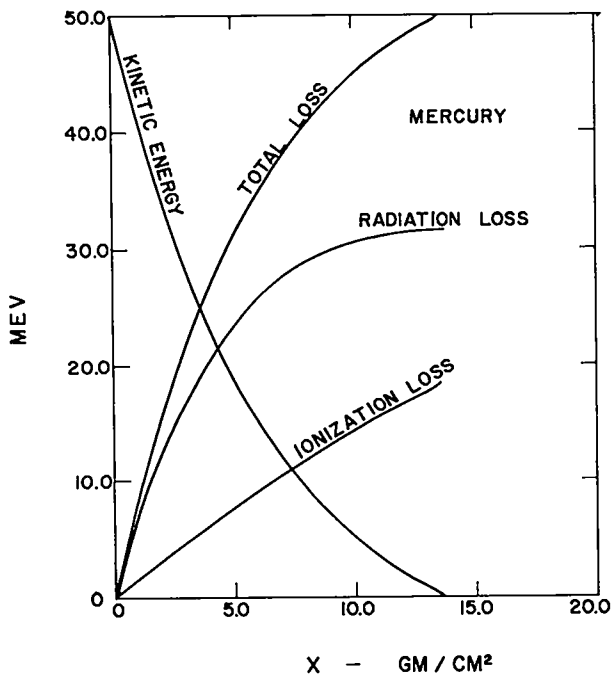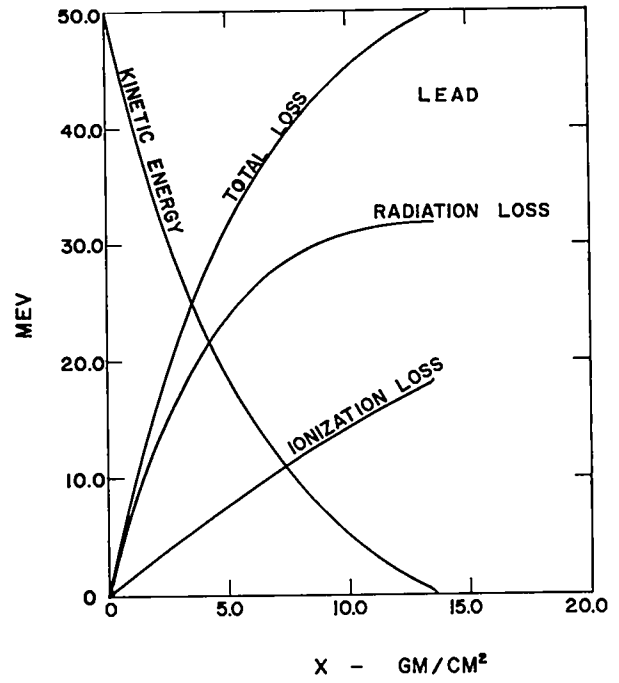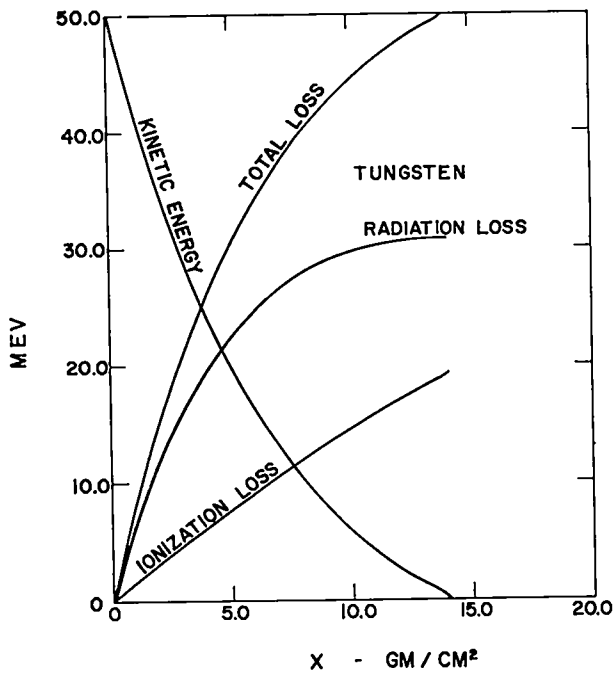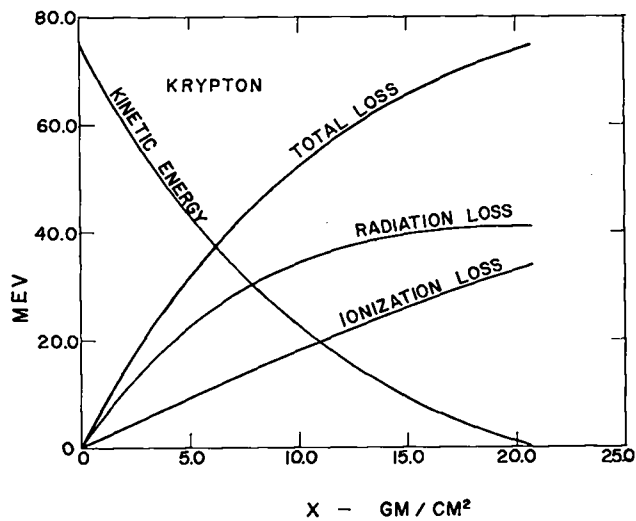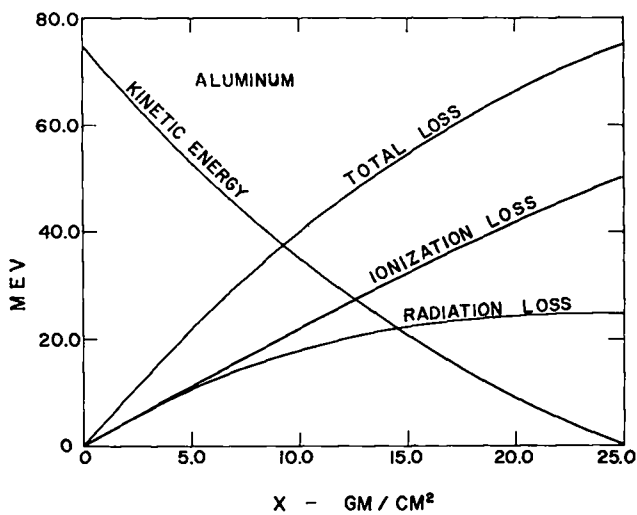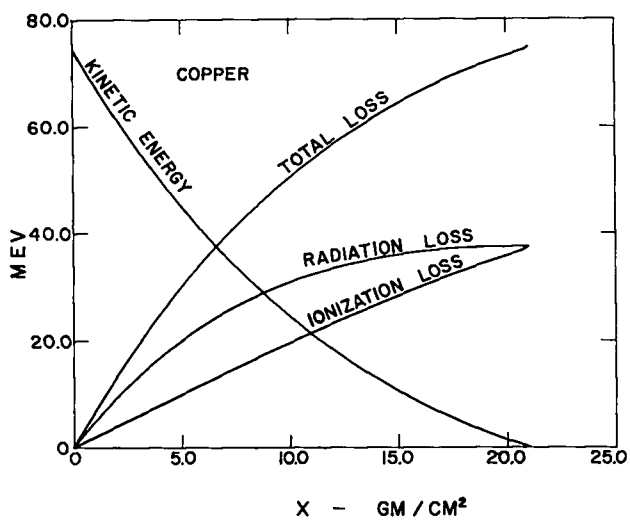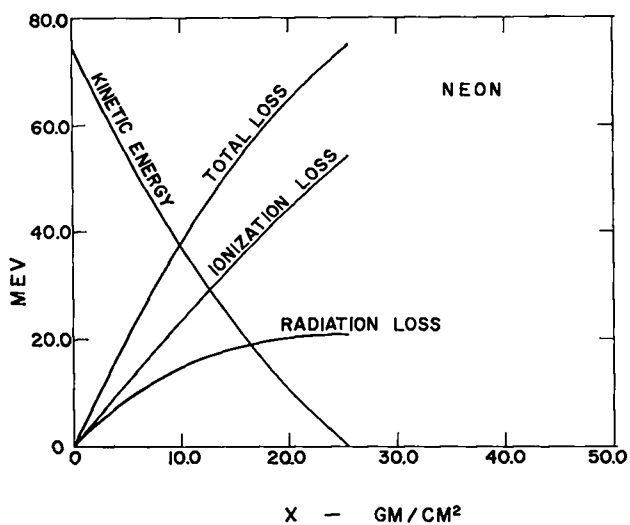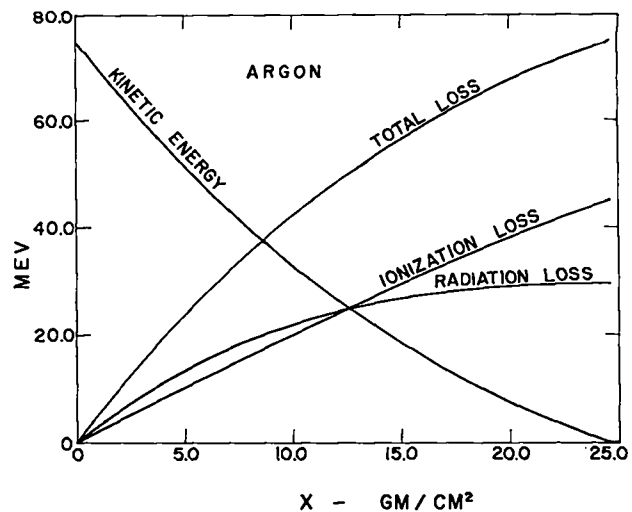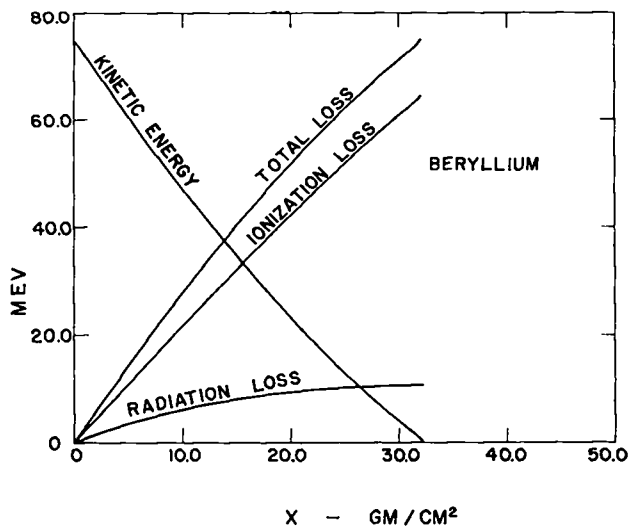
Fig. 2.12. 75 MeV electron losses and penetration vs thickness.

Fig. 2.12. Continued.

50
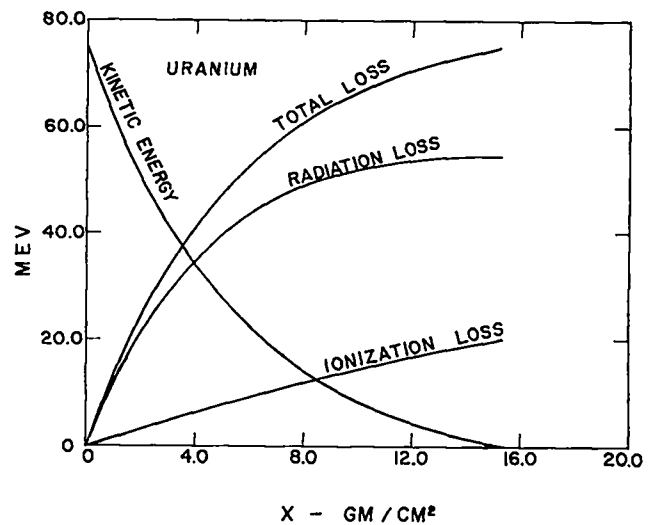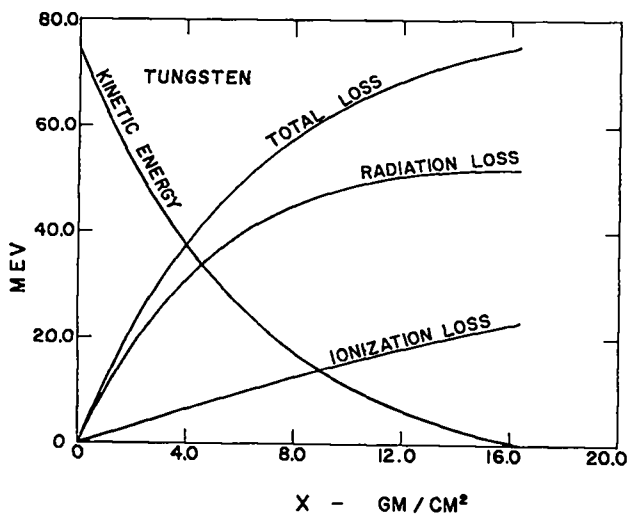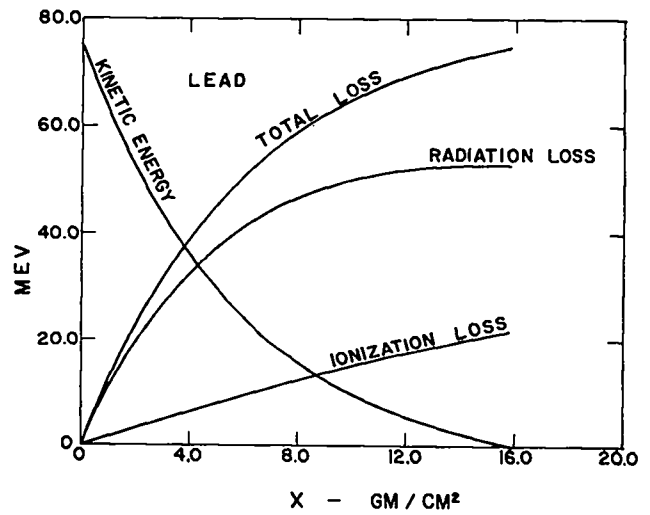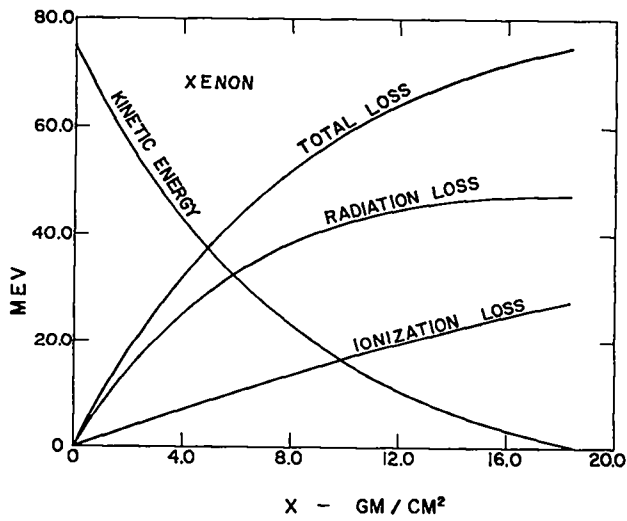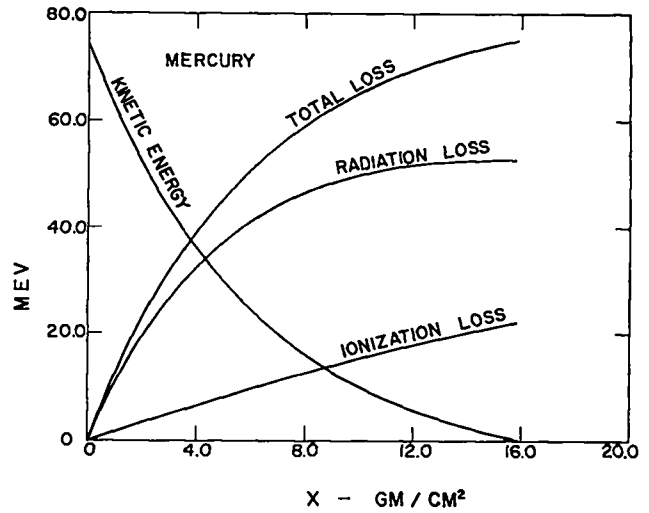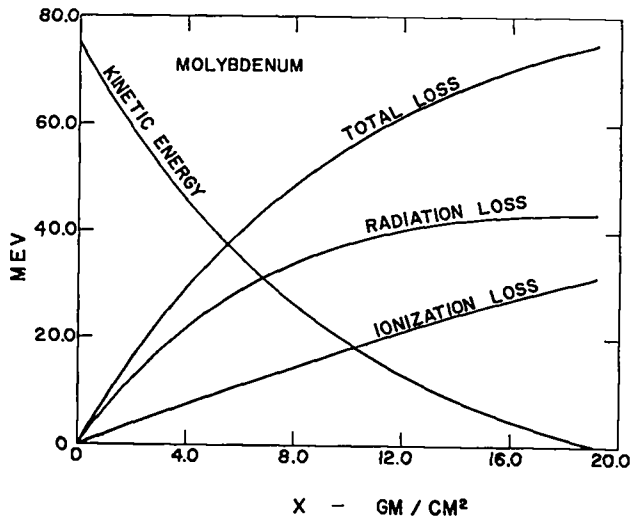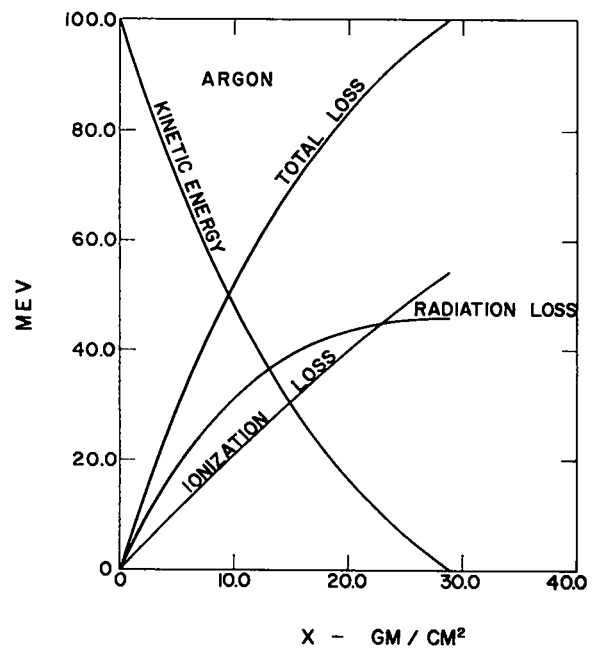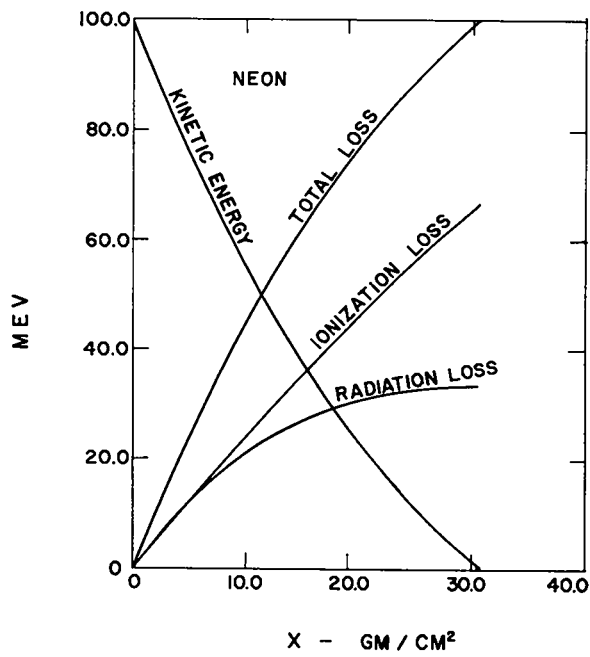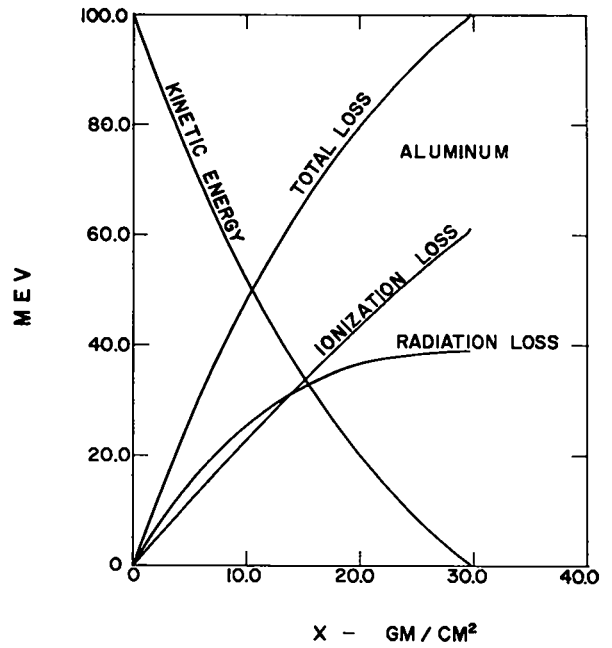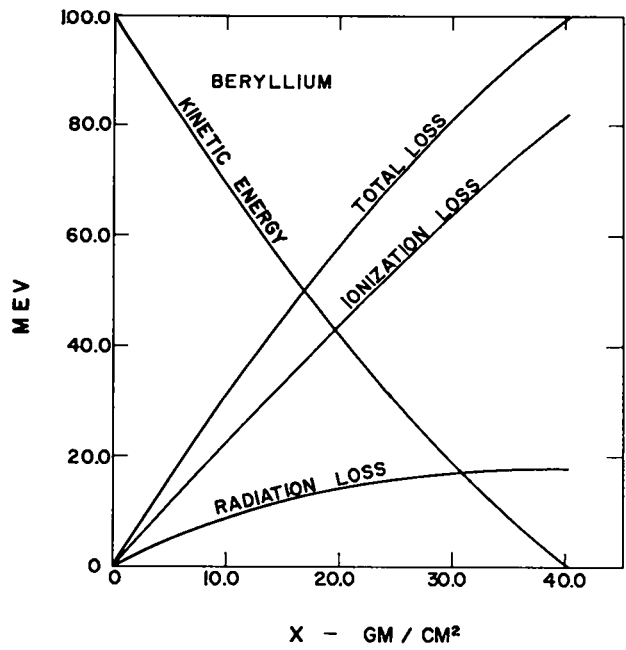
Fig. 2.13. 100 MeV electron losses and penetration vs thickness.

Fig. 2.13. Continued.

52

Fig. 2.13. Continued.

53
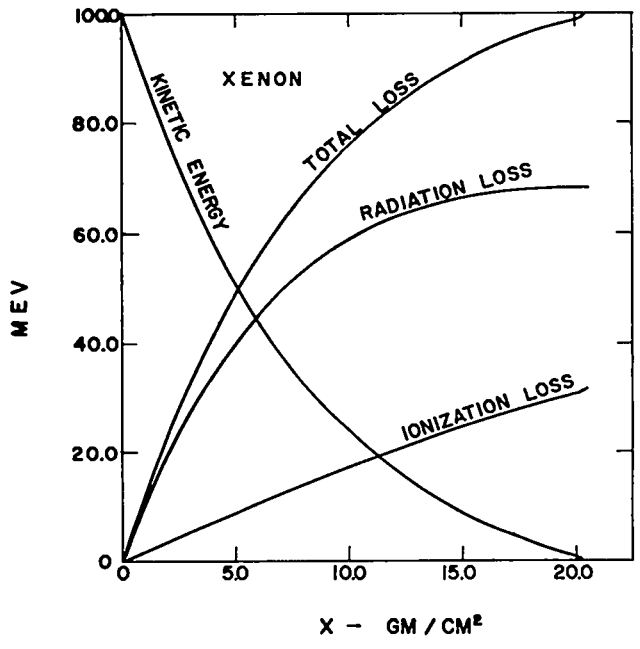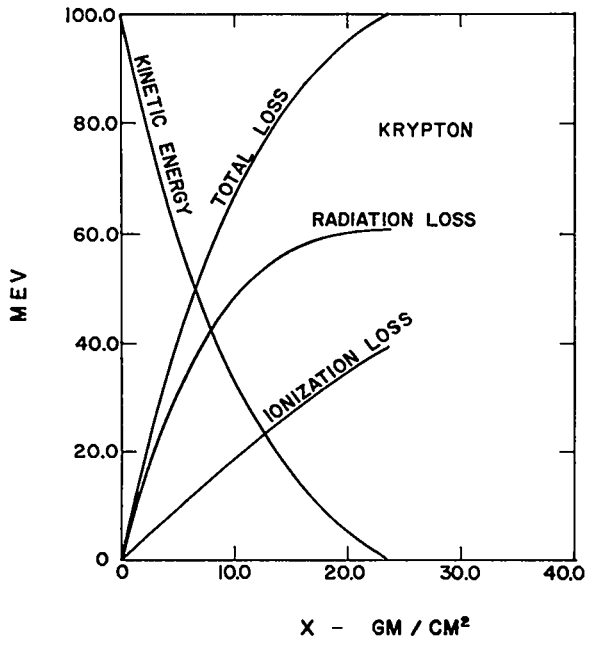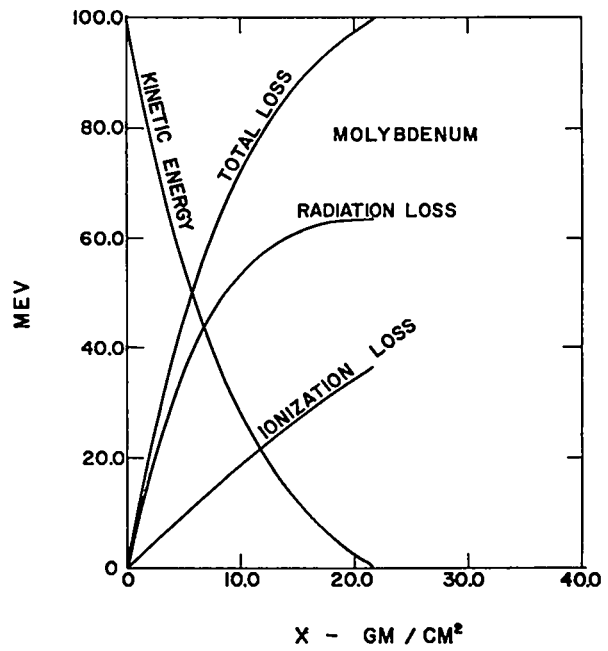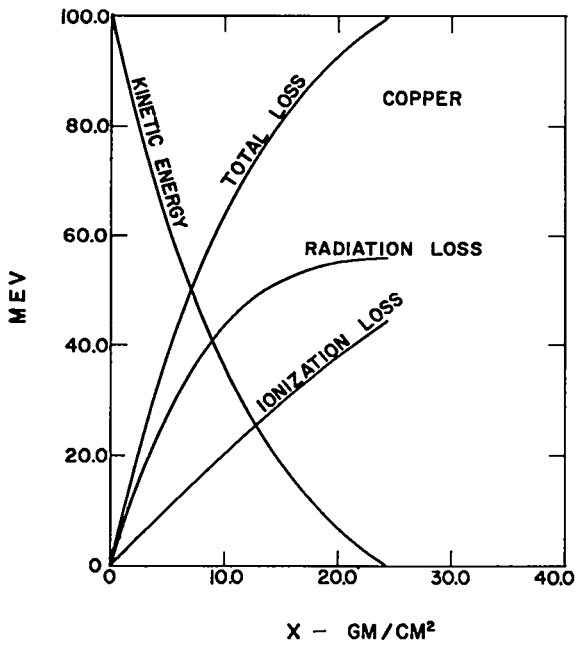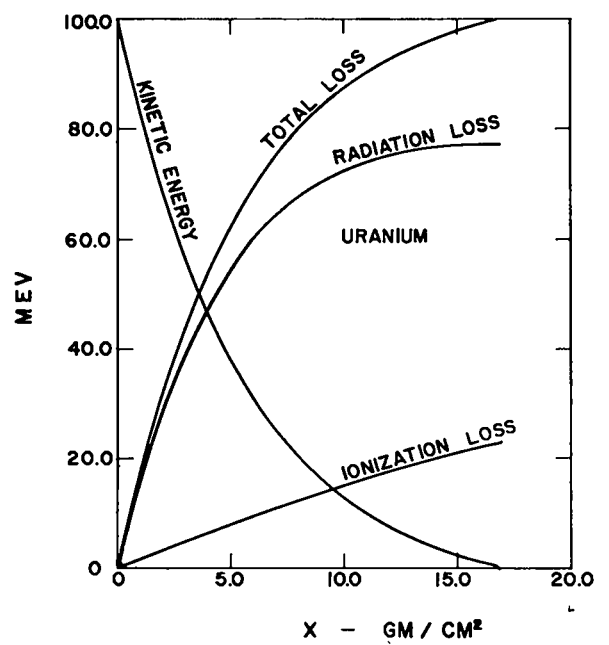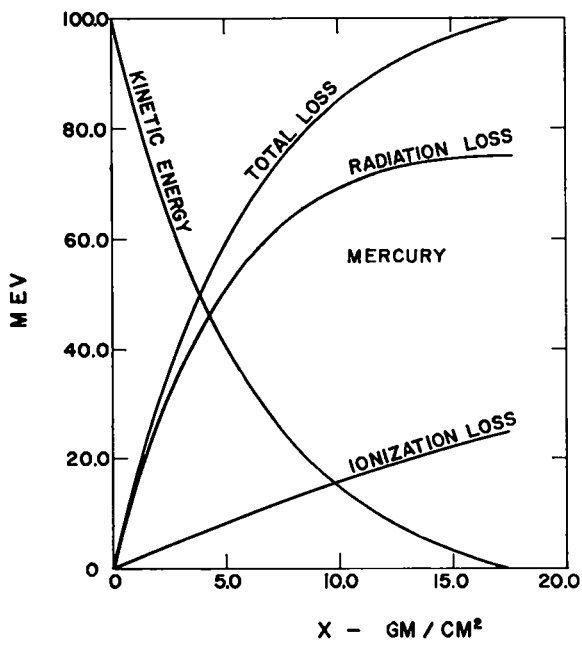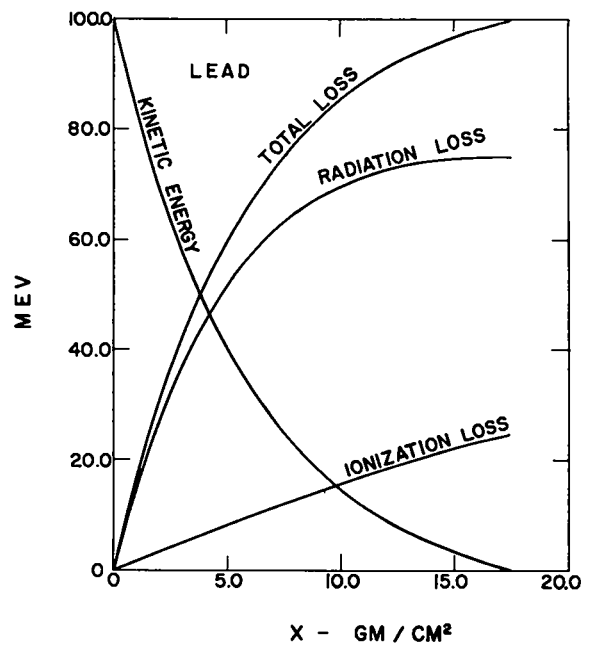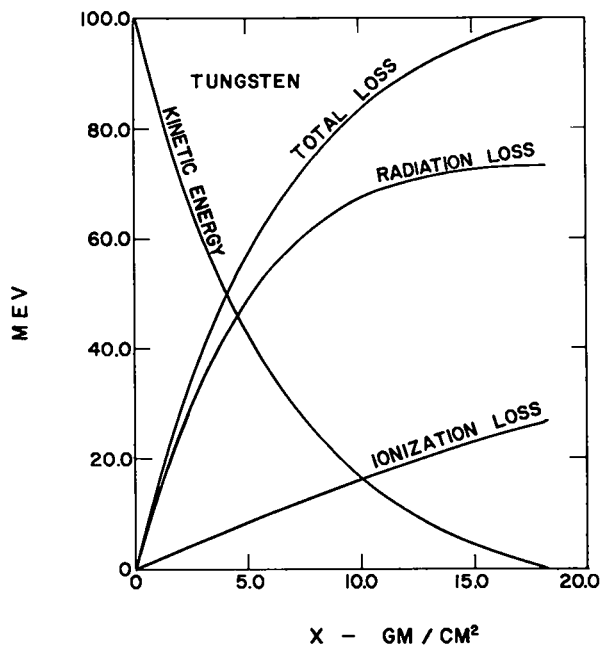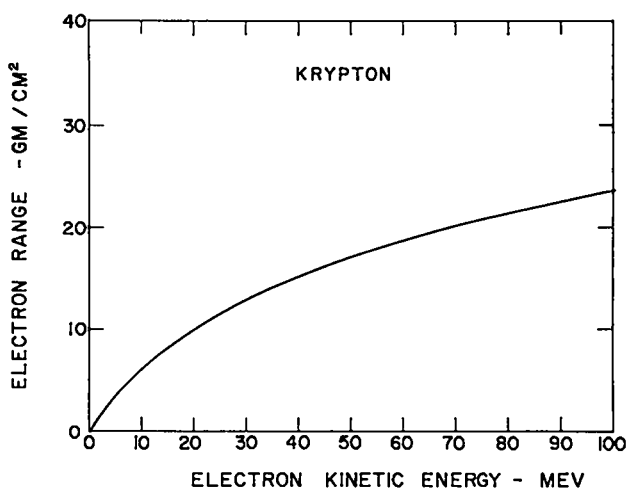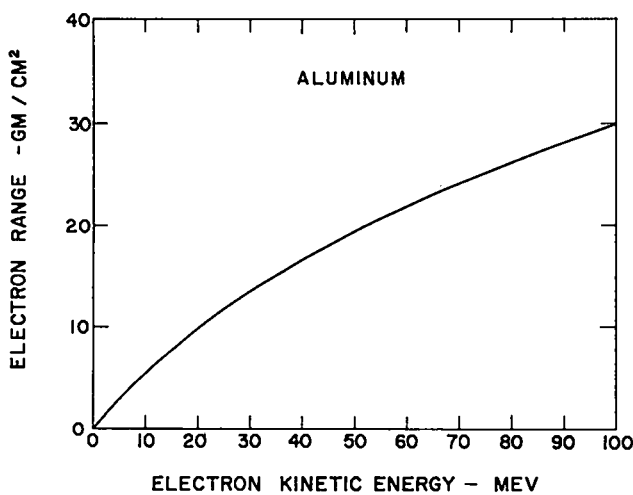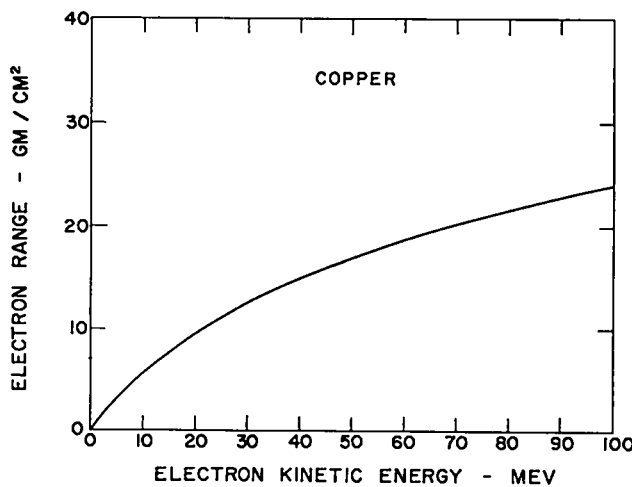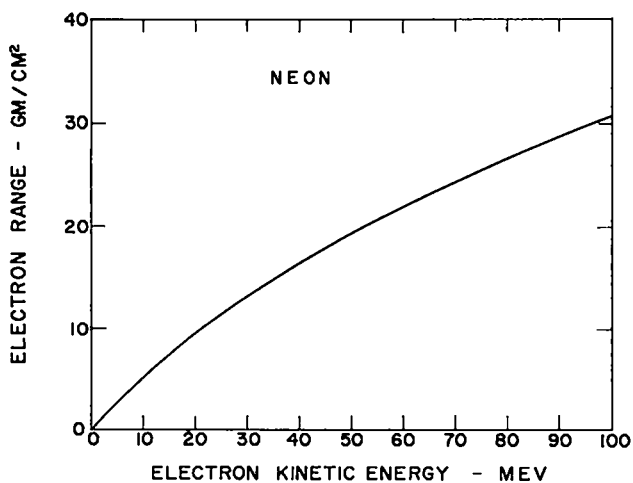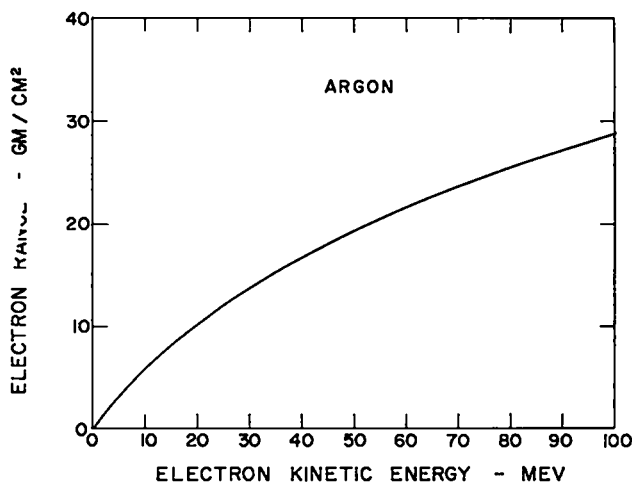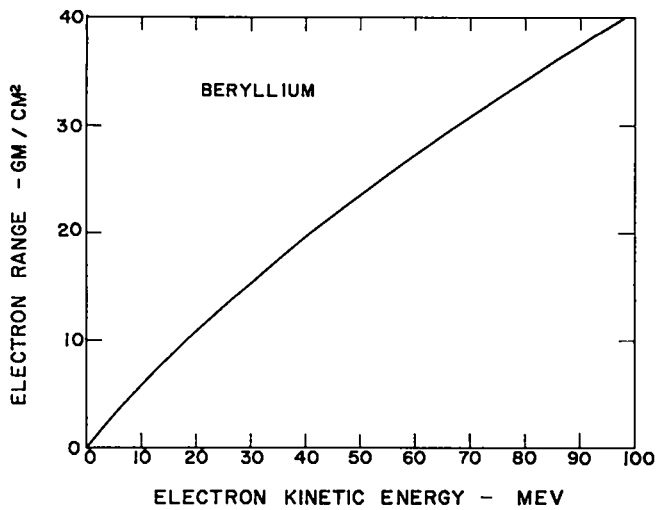
Fig. 2.14. Electron range in various materials.

Fig. 2.14.   Continued.

55
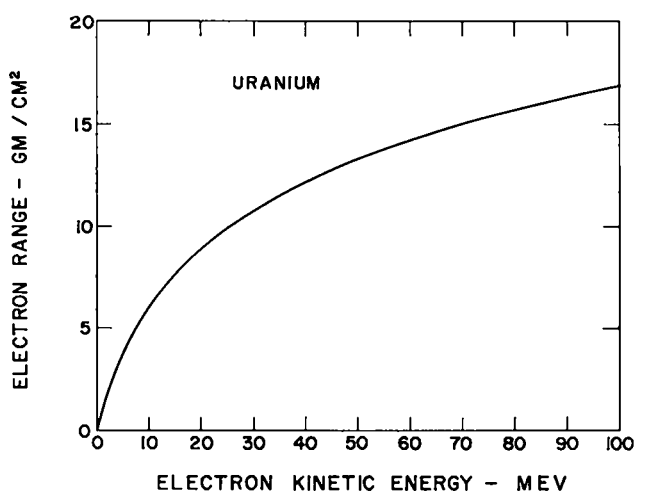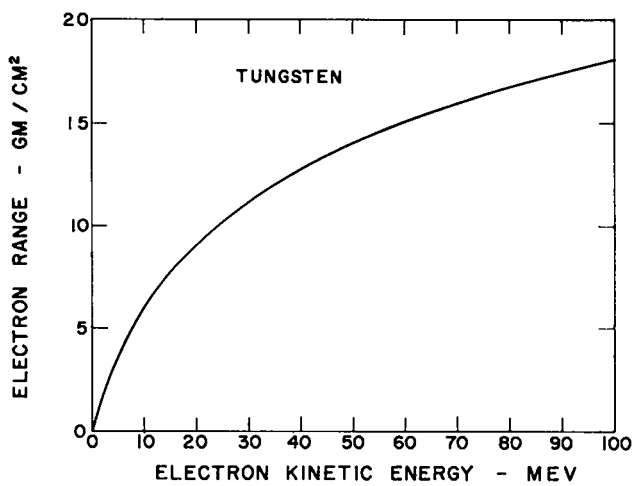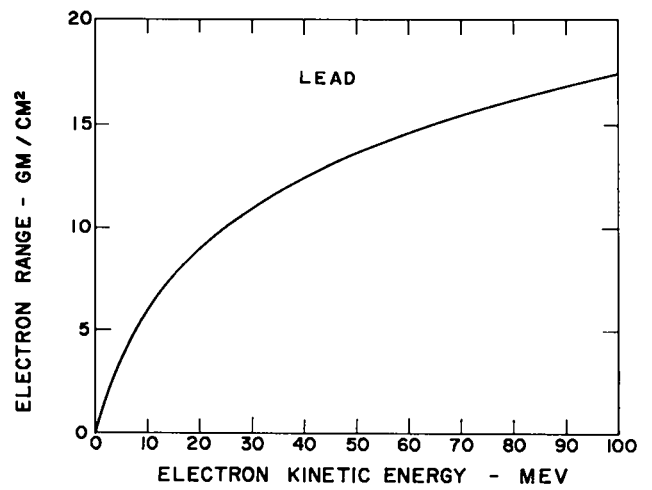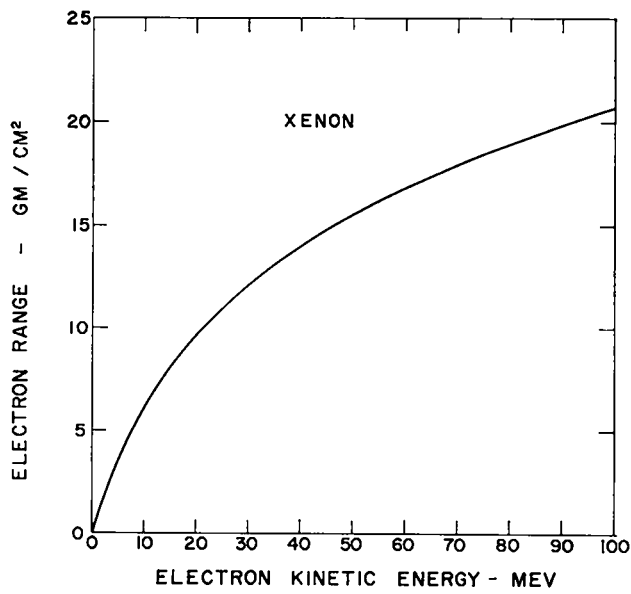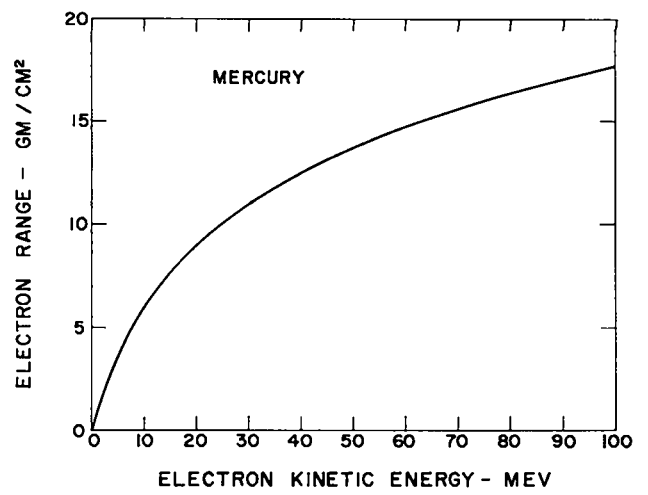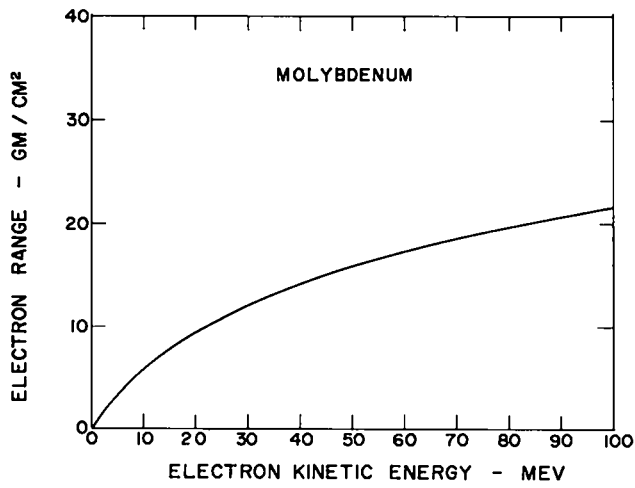
Bremsstrahlung generated by electrons of energy V(x) in the elemental target, dx at x, is subsequently attenuated preferentially in traversing the remaining target thickness, t — x. By accounting for the absorption coefficient of the target material and the spectrum generated in dx, the modified spectrum of the emerging primary radiation can be determined approximately. It is the low energy end of the spectrum which is most grossly modified; however, because this portion of the spectrum is also the least useful, its adulteration is unimportant.

Unless the target is very thick, the radiation intensity-angle distribution is substantially unaffected by the internal radiation absorption process. For thin targets, e.g., less than one-tenth radiation length thick, the radiation distribution is suitably defined by the convolution of both the bremsstrahlung production-angle function and the electron scattering function, providing there is no significant degradation of the electron energy in traversing the target.[2.11] For target thicknesses greater than that for which the effective electron scattering angle is as much as five to six times the bremsstrahlung angle, there is no significant contribution to the useful on-axis radiation intensity. Thus, beginning with this thickness, except for radiation absorption within the target, the on-axis intensity is, to a first approximation, independent of target thickness.

The on-axis relative intensity has been computed for tungsten (Z = 74) targets of various thicknesses for electrons having an initial energy of 20 MeV. Figure 2.15 illustrates the results of this work. It is noted that this conclusion is in close agreement with the gold (Z = 79) target discussed by Lanzl and Hanson.[2.15] Intensity-angle distributions measured at Los Alamos with film techniques were found to agree sufficiently well with calculations[2.11] to confirm this naive method of target design.

Figure 2.16 shows typical intensity-angle distribution curves determined from film data for normal density tungsten targets having thickness ranges from 1.2 to 4.8 mm. A more fundamental question concerns the intensity-angle distribution of the useful portion of the spectrum, namely that

portion which is transmitted through thick sections of, say, uranium. This distribution has been measured for radiation that has traversed about 10 cm of uranium (see Fig. 2.17). It is seen that this distribution is very nearly the same as that for the unadulterated spectrum.
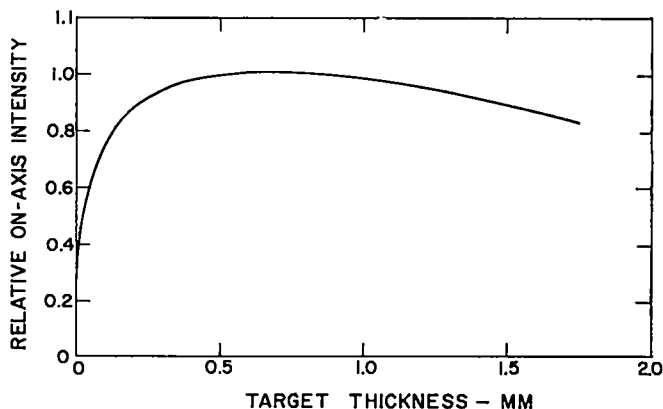
Fig. 2.15. Relative on-axis radiation intensity vs target thickness for 20 MeV bremsstrahlung.
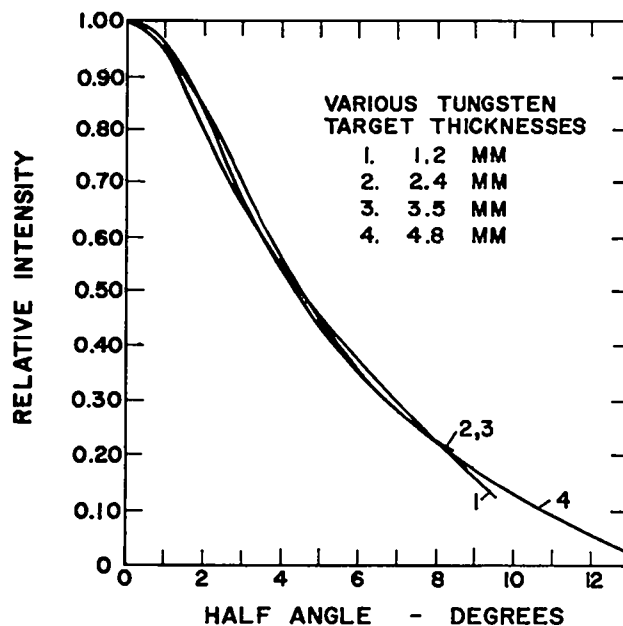
Fig. 2.16. Experimentally determined intensity-angle distribution for 20 MeV bremsstrahlung with no absorber.

56
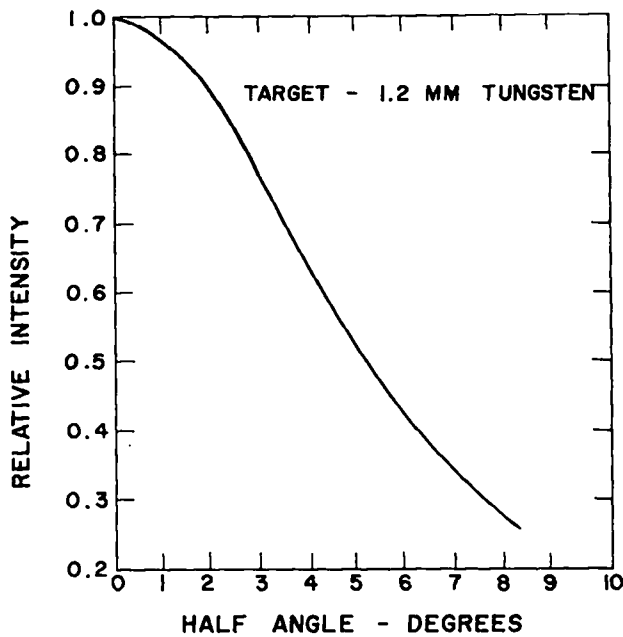
Fig. 2.17. Experimentally determined intensity-angle distribution for 20 MeV bremsstrahlung after passing through 10 cm of uranium.

V. TRANSMISSION AND SPECTRAL DEGRADATION OF BREMSSTRAHLUNG TRAVERSING MATTER

Transmission of the bremsstrahlung continuum through the substances reported here is of particular interest to persons engaged in the flash radiography of explosive-driven metal systems. Computations have been carried out by Group T-1 at Los Alamos to determine the transmission of bremsstrahlung through beryllium, aluminum, uranium, and the high explosive Composition B. Unadulterated bremsstrahlung from 5, 10, 15, 20, 30, 50, 75, and 100 MeV electrons incident on tungsten has been investigated. Self-absorption effects of targets have not been treated here.

Since the distribution of radiation in the bremsstrahlung lies in a continuum, the transmission of this radiation through matter is described by:

$$T = \frac{\displaystyle\int_0^{V_{max}} e^{-\mu\rho x}\phi_0(v)\ dv}{\displaystyle\int_0^{V_{max}} \phi_0(v)\ dv}$$

$$(2.17)$$

where

$\phi_0(v)$ = initial intensity distribution of the radiation emitted by a target, defined in Section I

μ = $\mu(v)$ = mass absorption coefficient,[2.16] cm^2/g

ρ = density of absorber, g/cm^3

x = linear thickness of absorber, cm

v = W/U

W = quantum energy

U = sum of kinetic and rest energies of electron producing radiation

The integral in the denominator is proportional to the primary energy incident upon the absorber, whereas the numerator is proportional to the transmitted primary radiation. As an example, a plot of $\phi_0(v)$ is shown in Fig. 2.18 for the unadulterated 5 MeV bremsstrahlung spectrum emitted by a thin tungsten target. The product $e^{-\mu\rho x}\phi_0(v)$ represents the spectral distribution of the radiation as a function of the properties and thickness of the absorber.

In addition to the results of the transmission calculations, plots of the spectral distributions at various thicknesses of these materials are also given in Figs. 2.19 through 2.89. This information enables one to follow both spectral degradation and attenuation with increasing absorber thickness. Furthermore, the data facilitate calculations in the event one desires to consider transmission through several layers of various thicknesses of these materials.
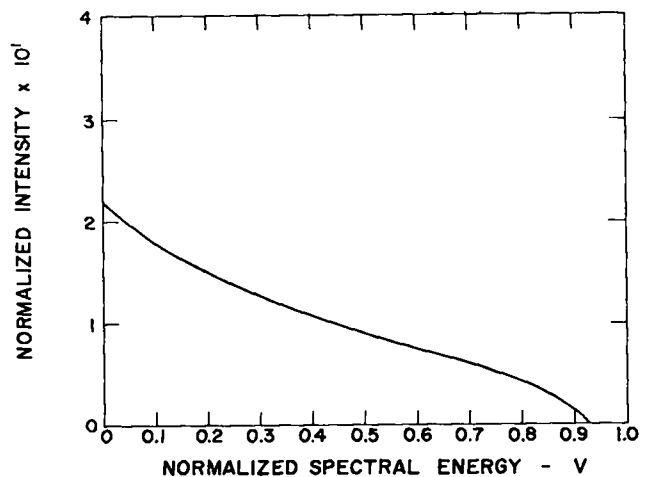
Fig. 2.18. Unadulterated 5 MeV tungsten bremsstrahlung spectrum.
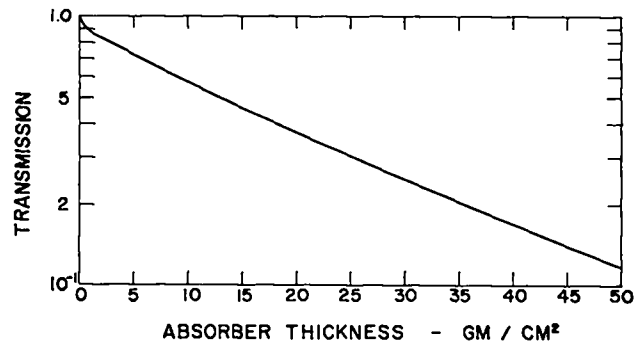
Fig. 2.19. Transmission of 5 MeV tungsten brems-
strahlung through beryllium.
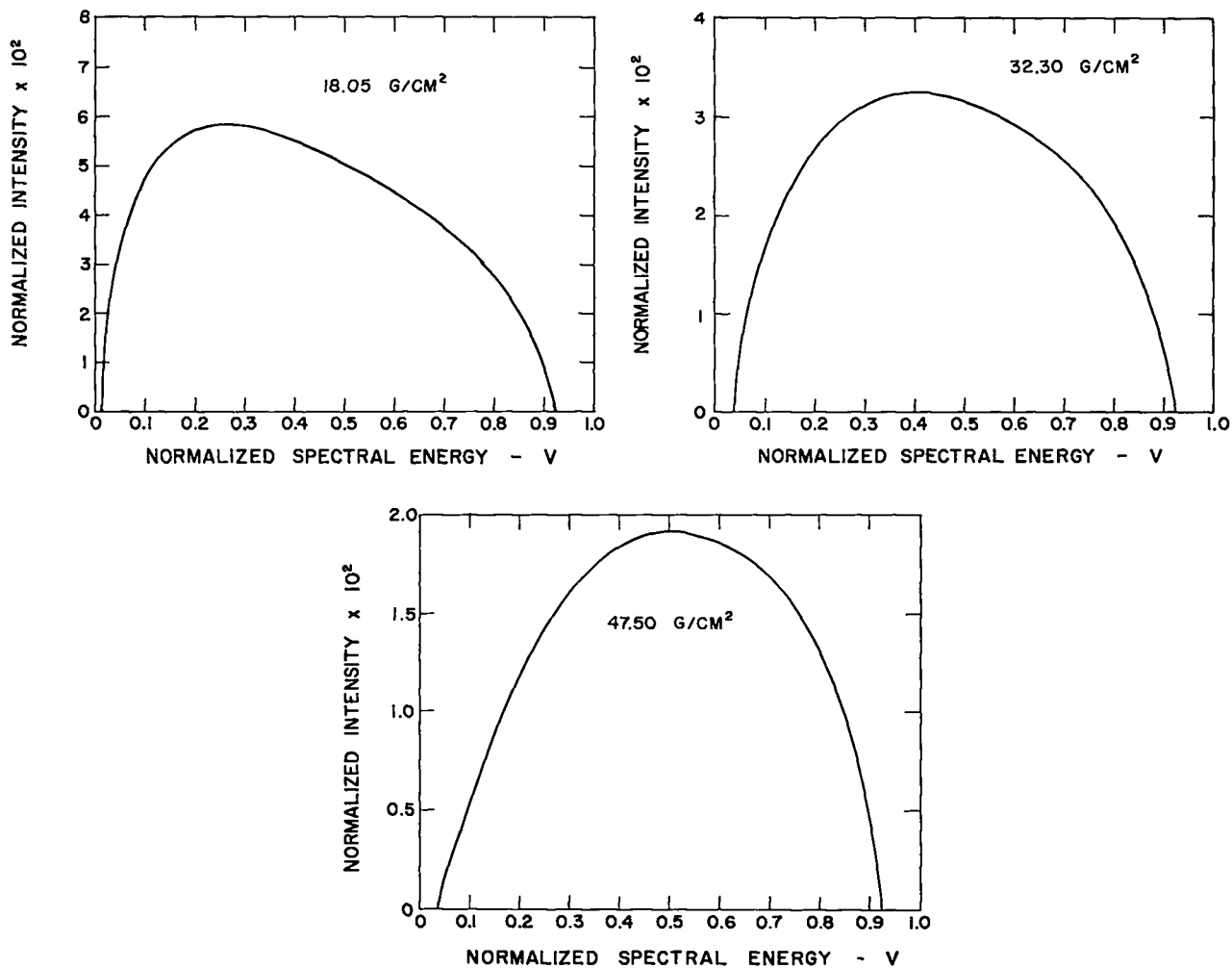
Fig. 2.20. Degraded 5 MeV tungsten bremsstrahlung spectrum after traversing various thicknesses of beryllium.

58
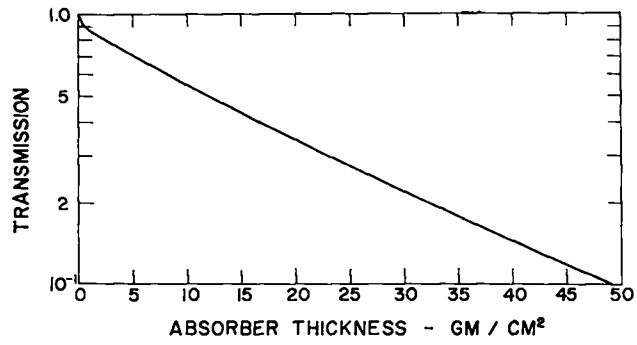
Fig. 2.21. Transmission of 5 MeV tungsten bremsstrahlung through aluminum.
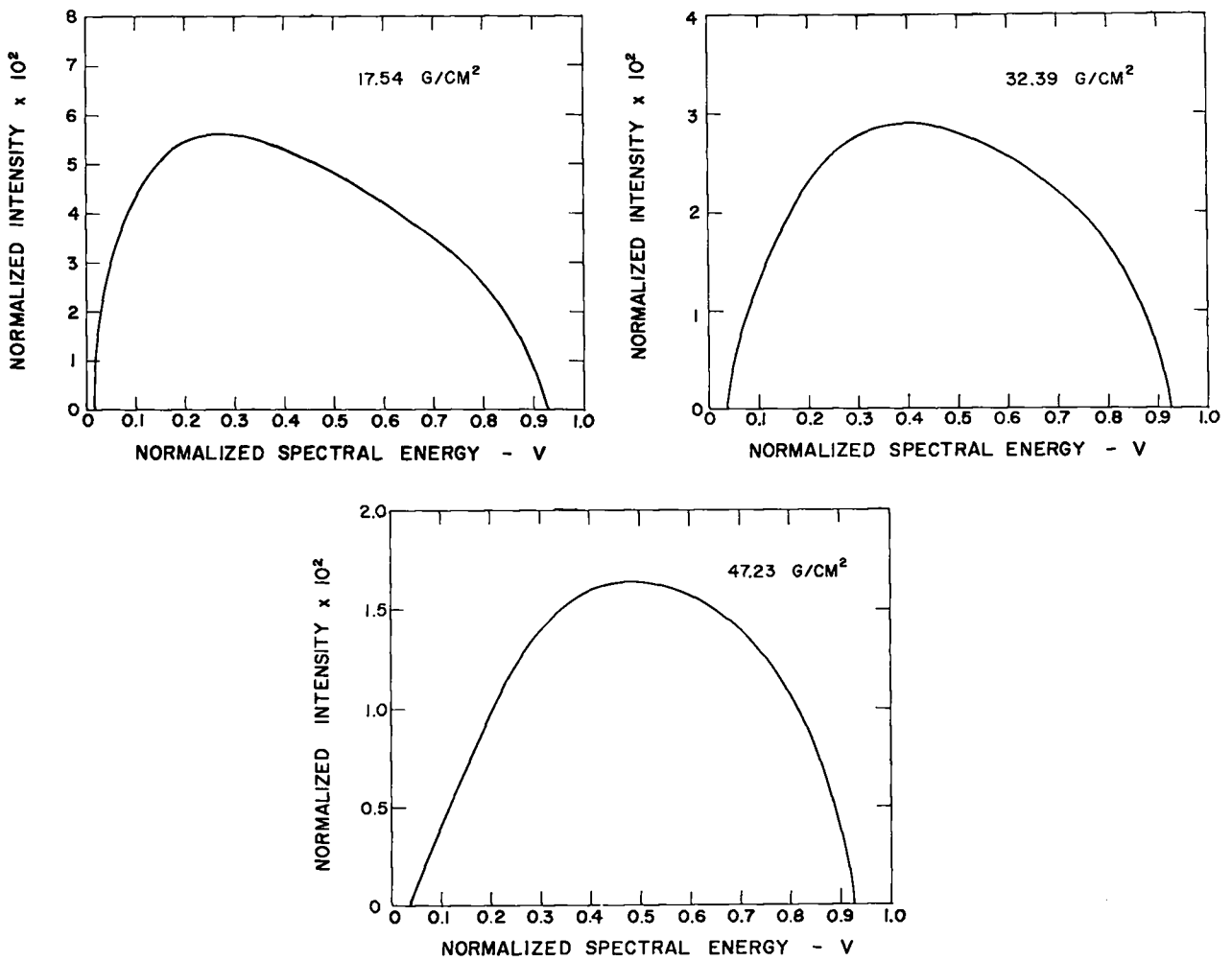
Fig. 2.22. Degraded 5 MeV tungsten bremsstrahlung spectrum after traversing various thicknesses of aluminum.

59
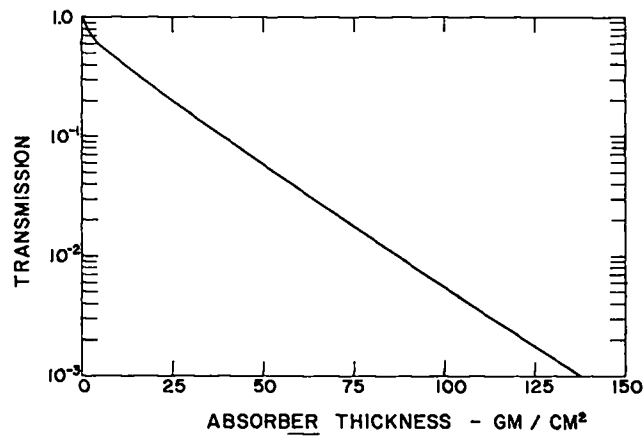
Fig. 2.23. Transmission of 5 MeV tungsten bremsstrahlung through uranium. For 135 g/cm^2 $\leq$ thickness $\leq$ 567 g/cm^2, $\log_{10}$ T$\cong$ $-0.01982t - 0.36940$.
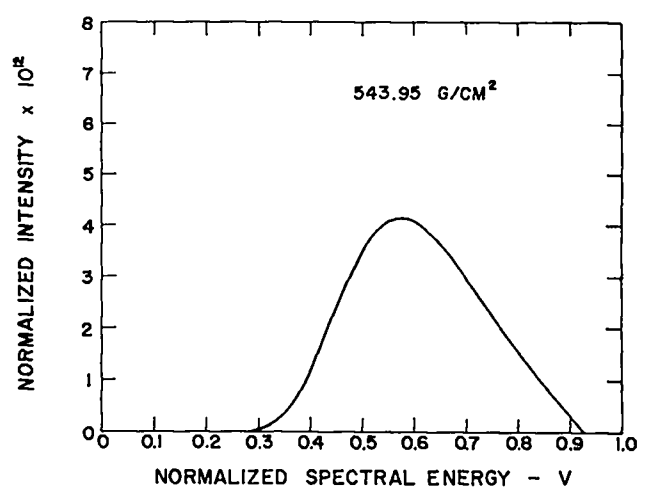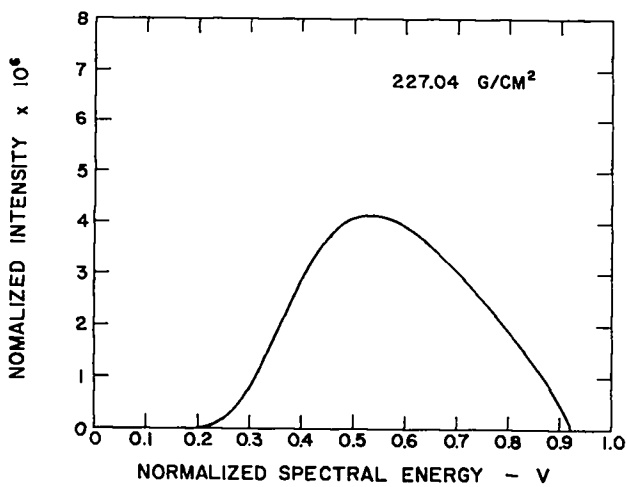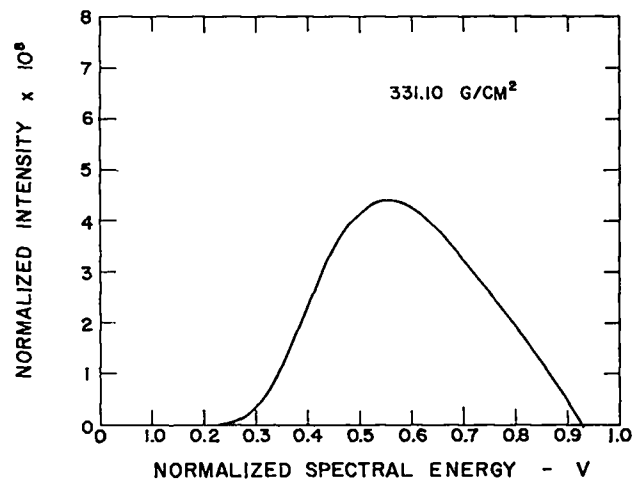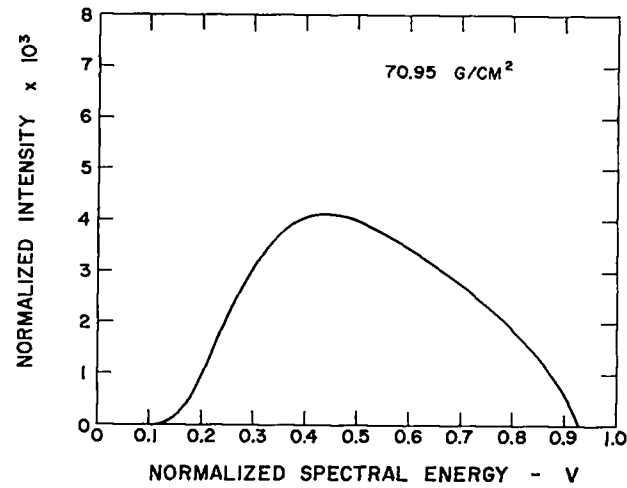
Fig. 2.24. Degraded 5 MeV tungsten bremsstrahlung spectrum after traversing various thicknesses of uranium.

60
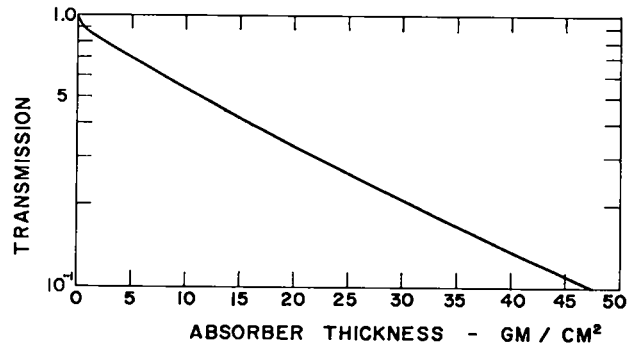
Fig. 2.25. Transmission of 5 MeV tungsten brems-
strahlung through Composition B.
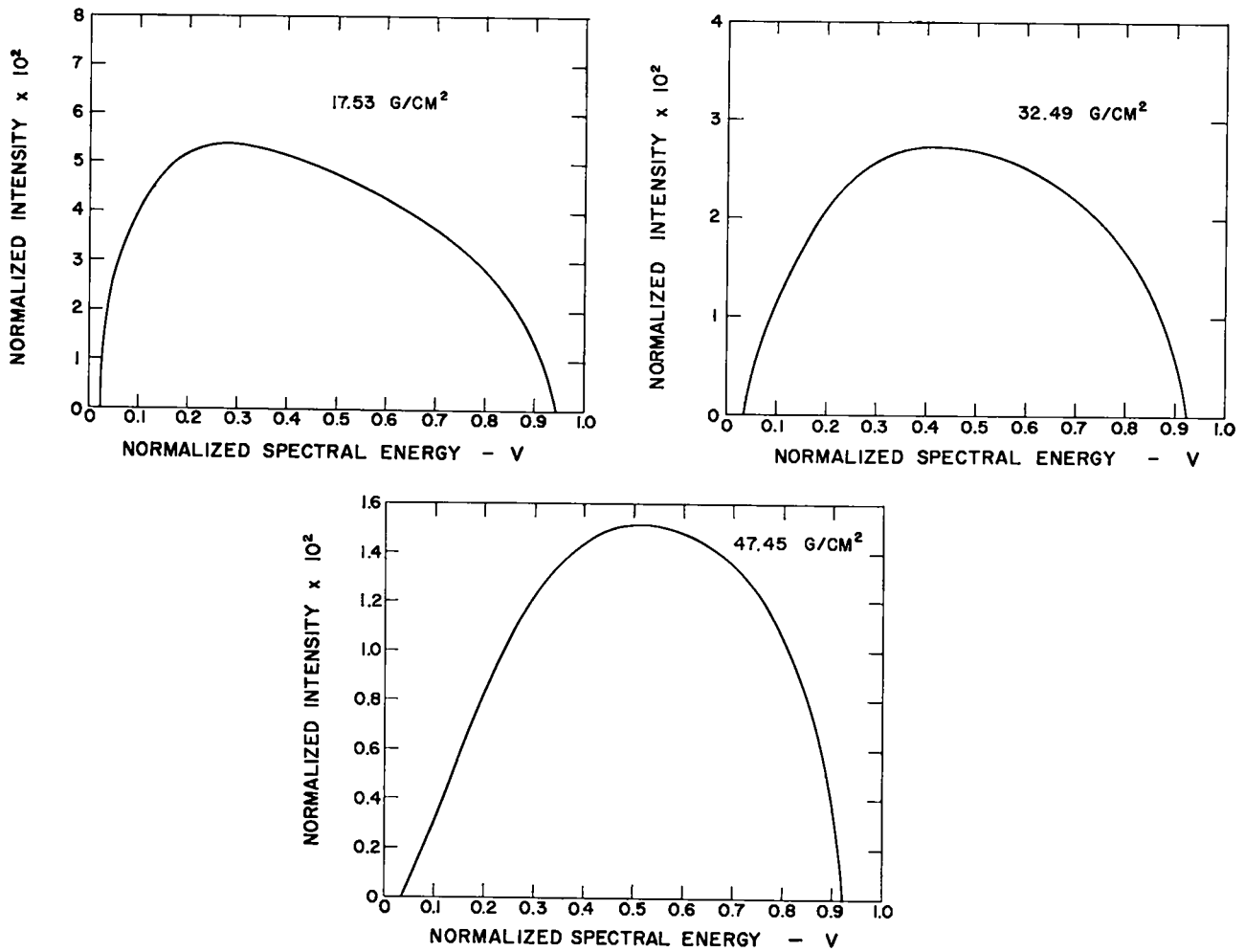
Fig. 2.26. Degraded 5 MeV tungsten bremsstrahlung spectrum after traversing various thicknesses of Composi-
tion B.

61
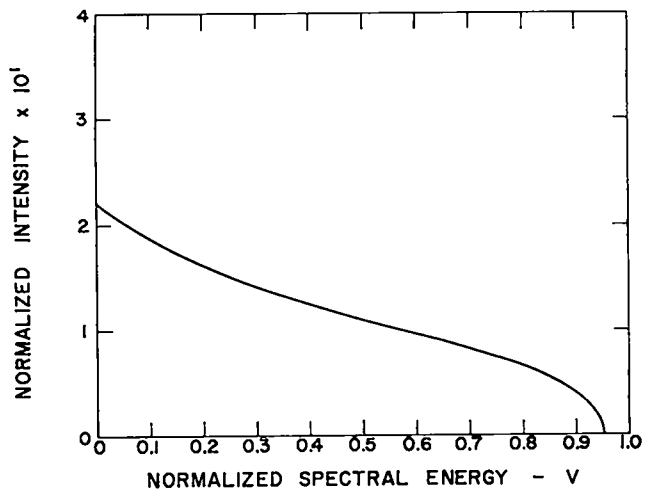
Fig. 2.27. Unadulterated 10 MeV tungsten bremsstrahlung spectrum.
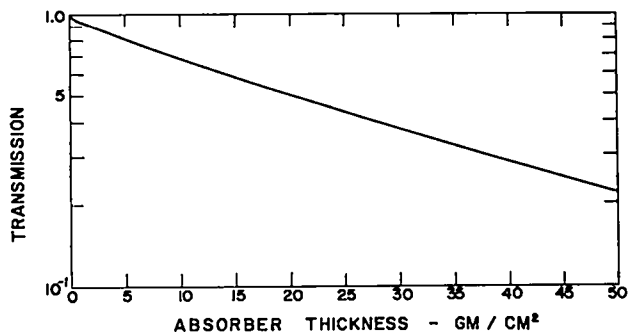
Fig. 2.28. Transmission of 10 MeV tungsten bremsstrahlung through beryllium.
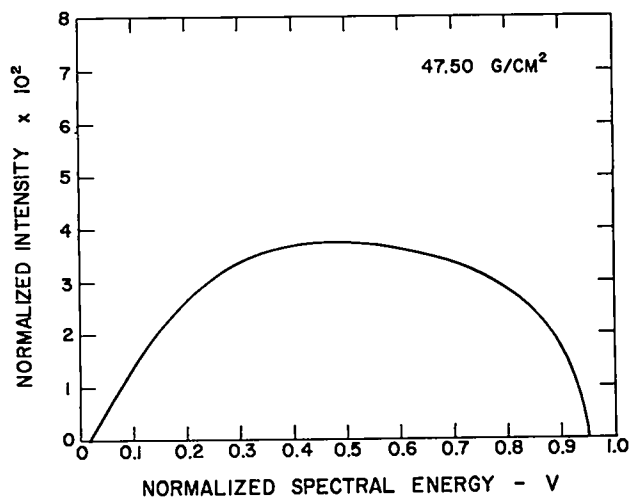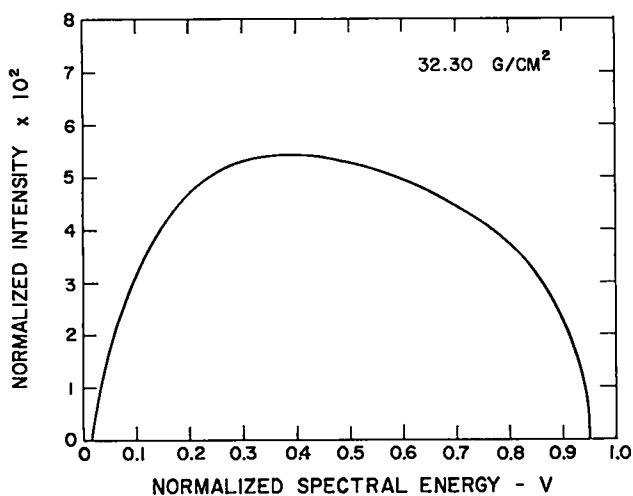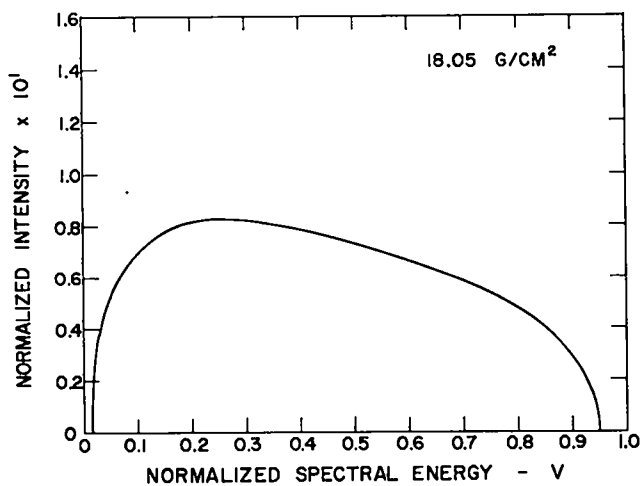
Fig. 2.29 Degraded 10 MeV tungsten bremsstrahlung spectrum after traversing various thicknesses of beryllium.
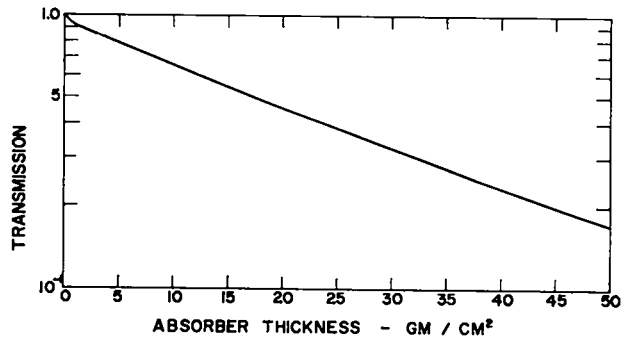
Fig. 2.30. Transmission of 10 MeV tungsten brems-
strahlung through aluminum.
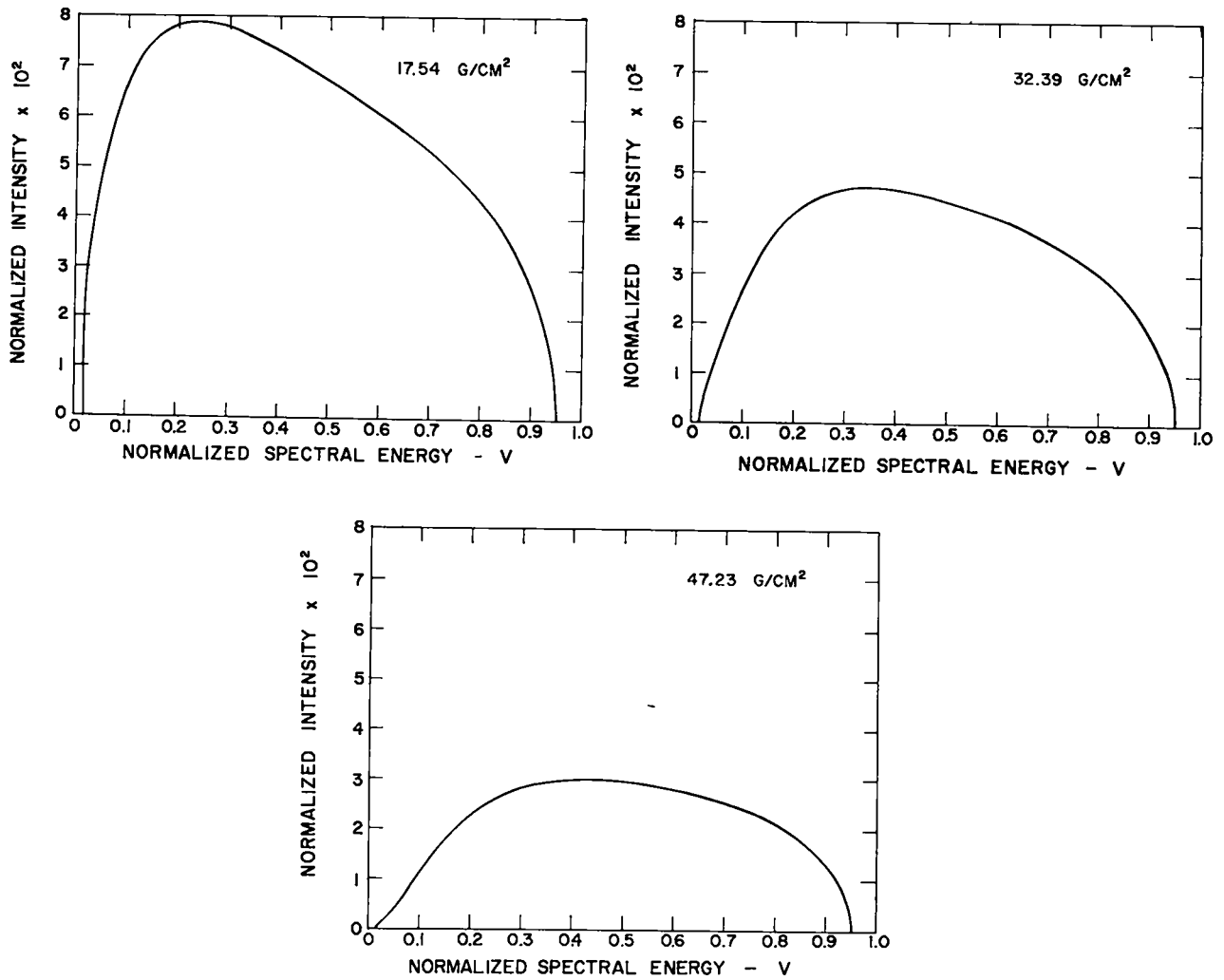
Fig. 2.31. Degraded 10 MeV tungsten bremsstrahlung spectrum after traversing various thicknesses of aluminum.
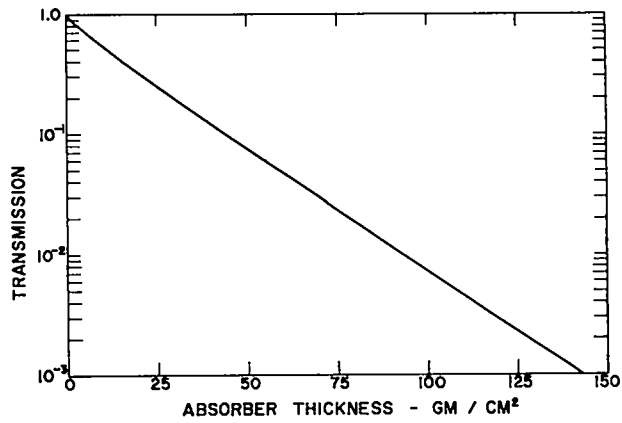
Fig. 2.32. Transmission of 10 MeV tungsten brems-
strahlung through uranium. For thickness
> 140 g/cm^2, $\log_{10} T \cong -0.01956t - 0.2029$.
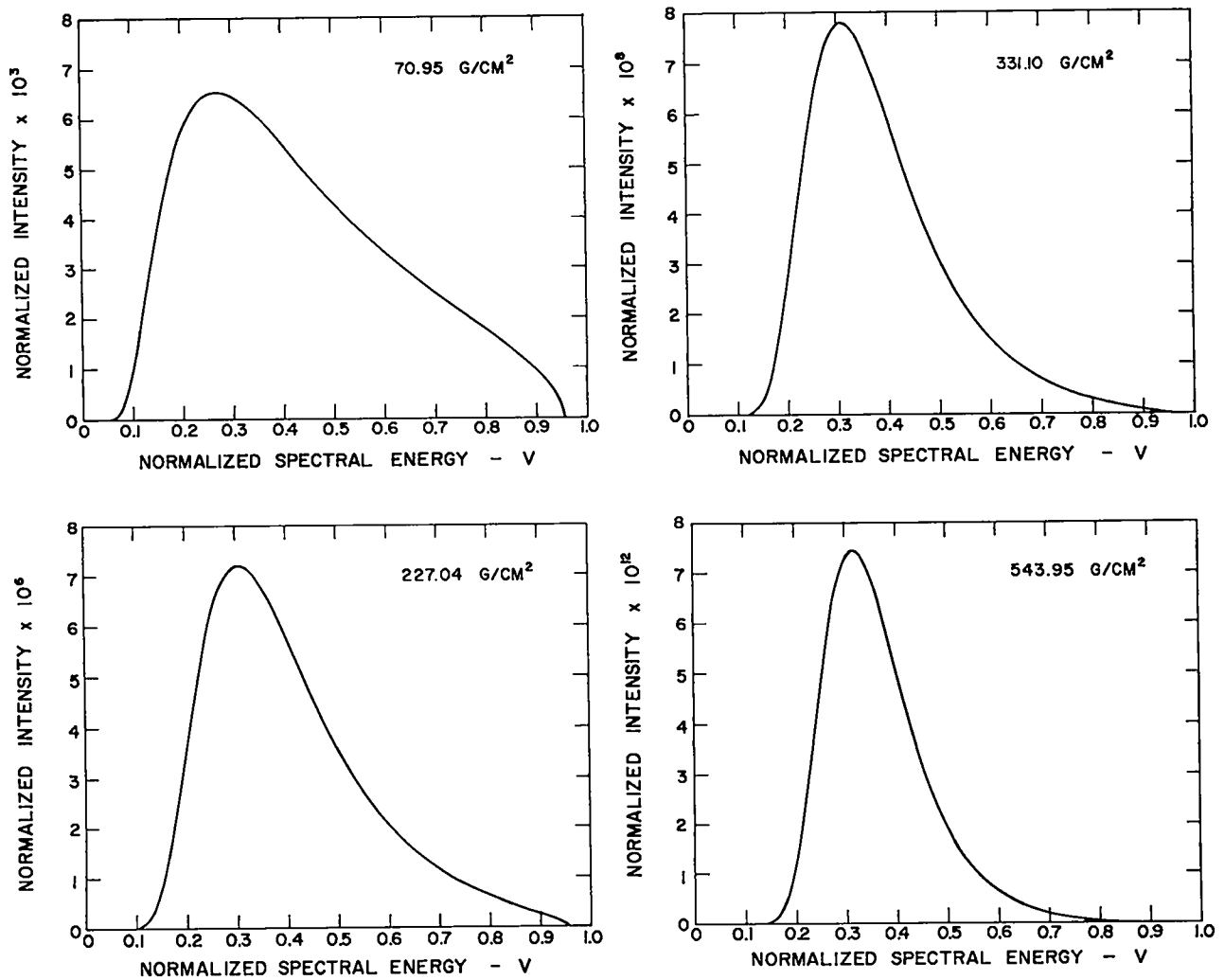
Fig. 2.33. Degraded 10 MeV tungsten bremsstrahlung spectrum after transversing various thicknesses of uranium.
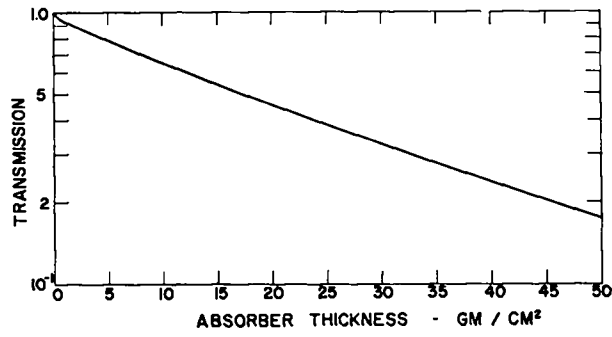
Fig. 2.34. Transmission of 10 MeV tungsten bremsstrahlung through Composition B.
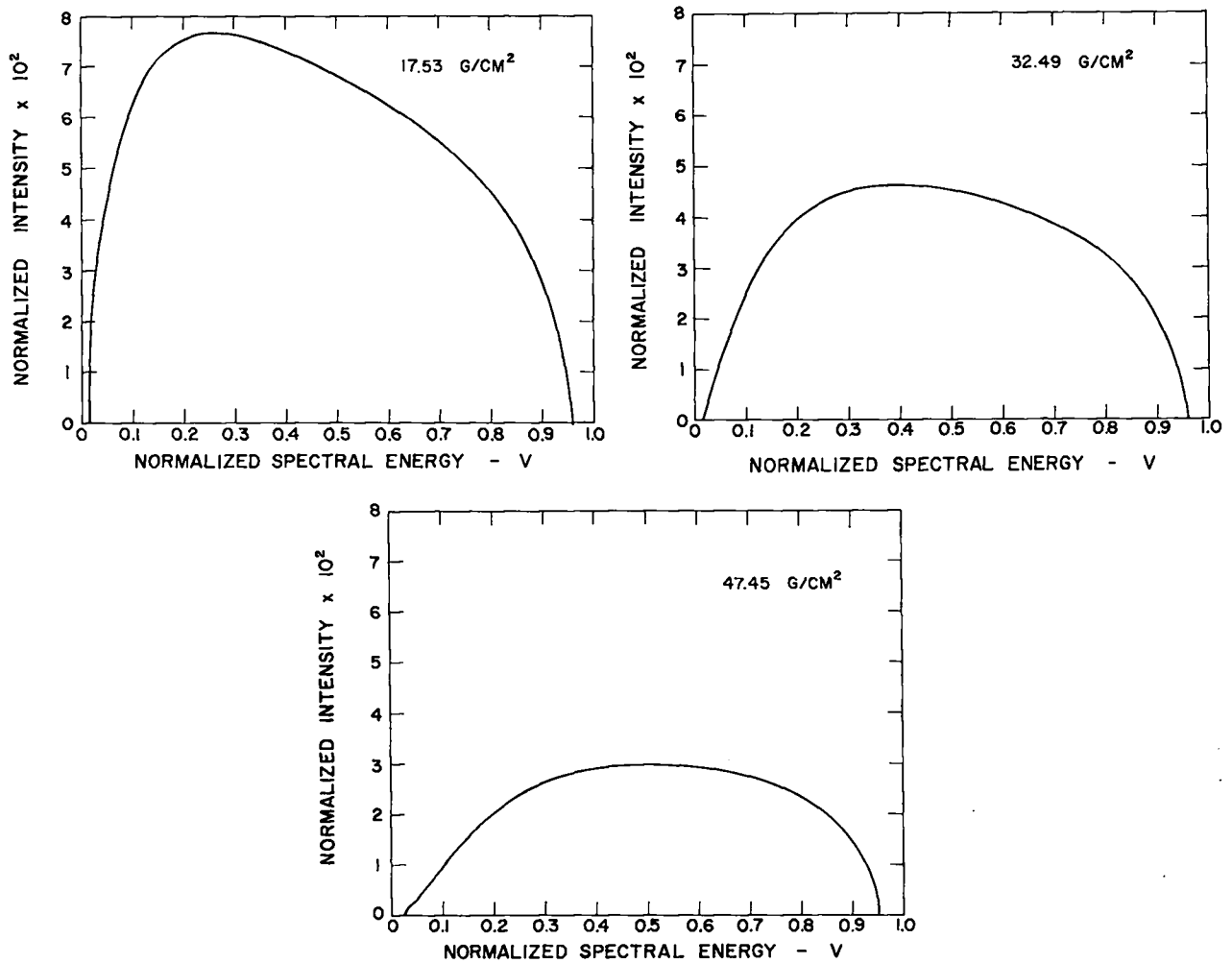
Fig. 2.35. Degraded 10 MeV tungsten bremsstrahlung spectrum after traversing various thicknesses of Composition B.
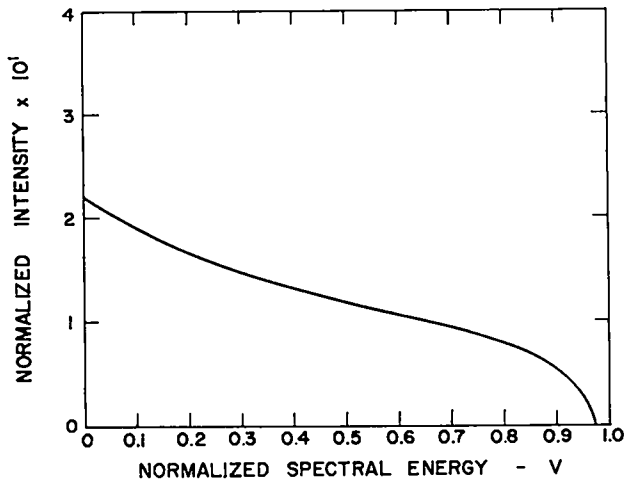
Fig. 2.36. Unadulterated 15 MeV tungsten brems-
strahlung spectrum.
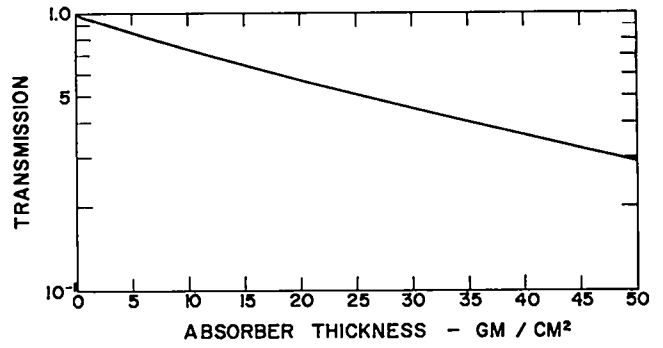
Fig. 2.37. Transmission of 15 MeV tungsten brems-
strahlung through beryllium.
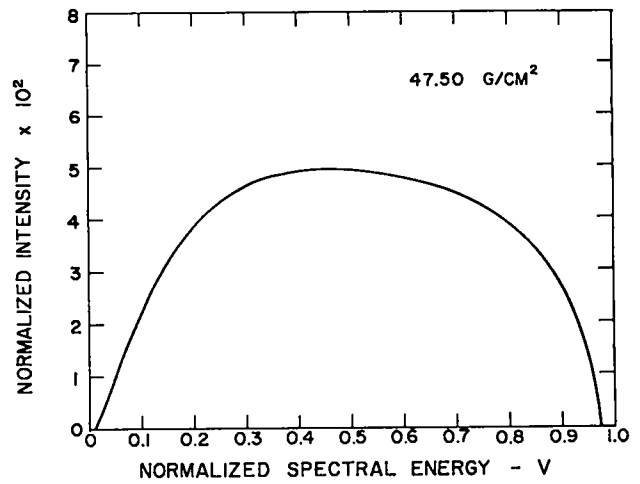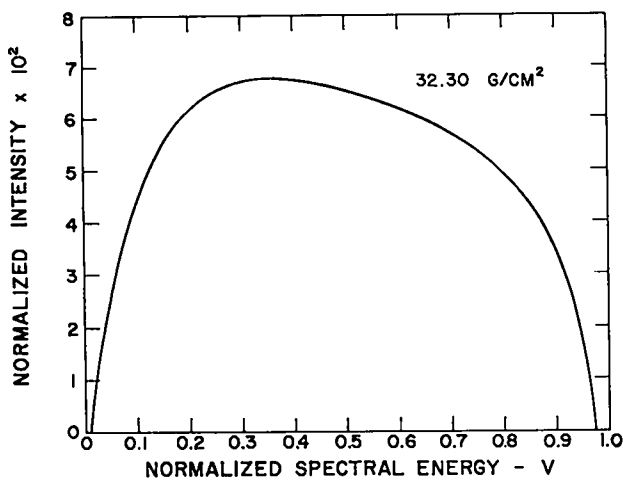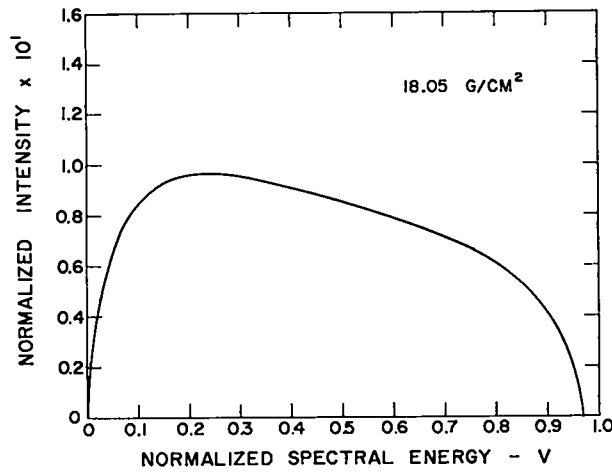
Fig. 2.38. Degraded 15 MeV tungsten bremsstrahlung spectrum after traversing various thicknesses of beryllium.
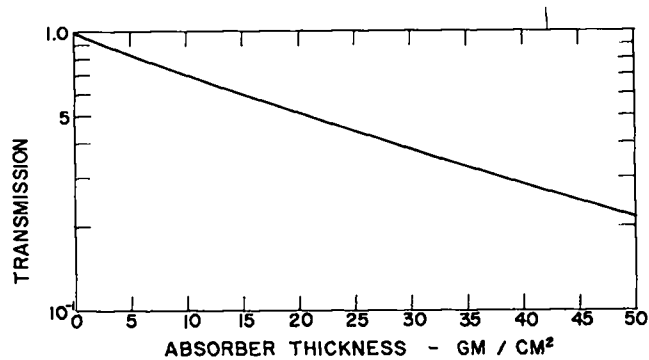
Fig. 2.39. Transmission of 15 MeV tungsten brems-
strahlung through aluminum.
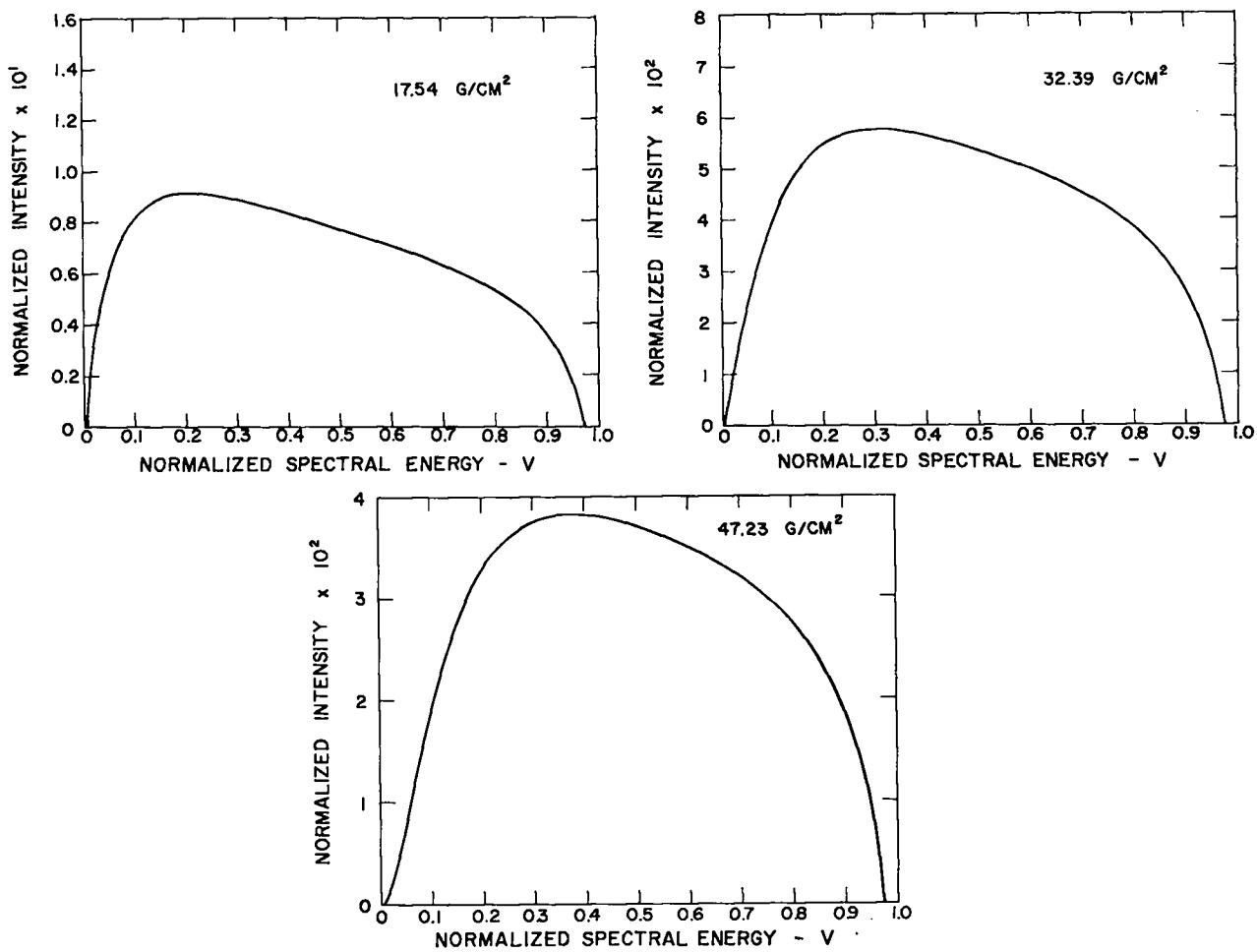
Fig. 2.40 Degraded 15 MeV tungsten bremsstrahlung spectrum after traversing various thicknesses of aluminum.
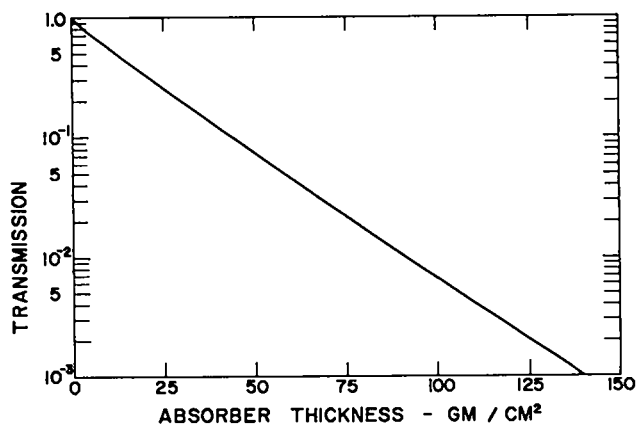
Fig. 2.41. Transmission of 15 MeV tungsten brems-
strahlung through uranium. For 140 g/cm^2
$\leq$ thickness $\leq$ 567 g/cm^2, $\log_{10}$ T$\cong$
$-0.0196t - 0.3009$.
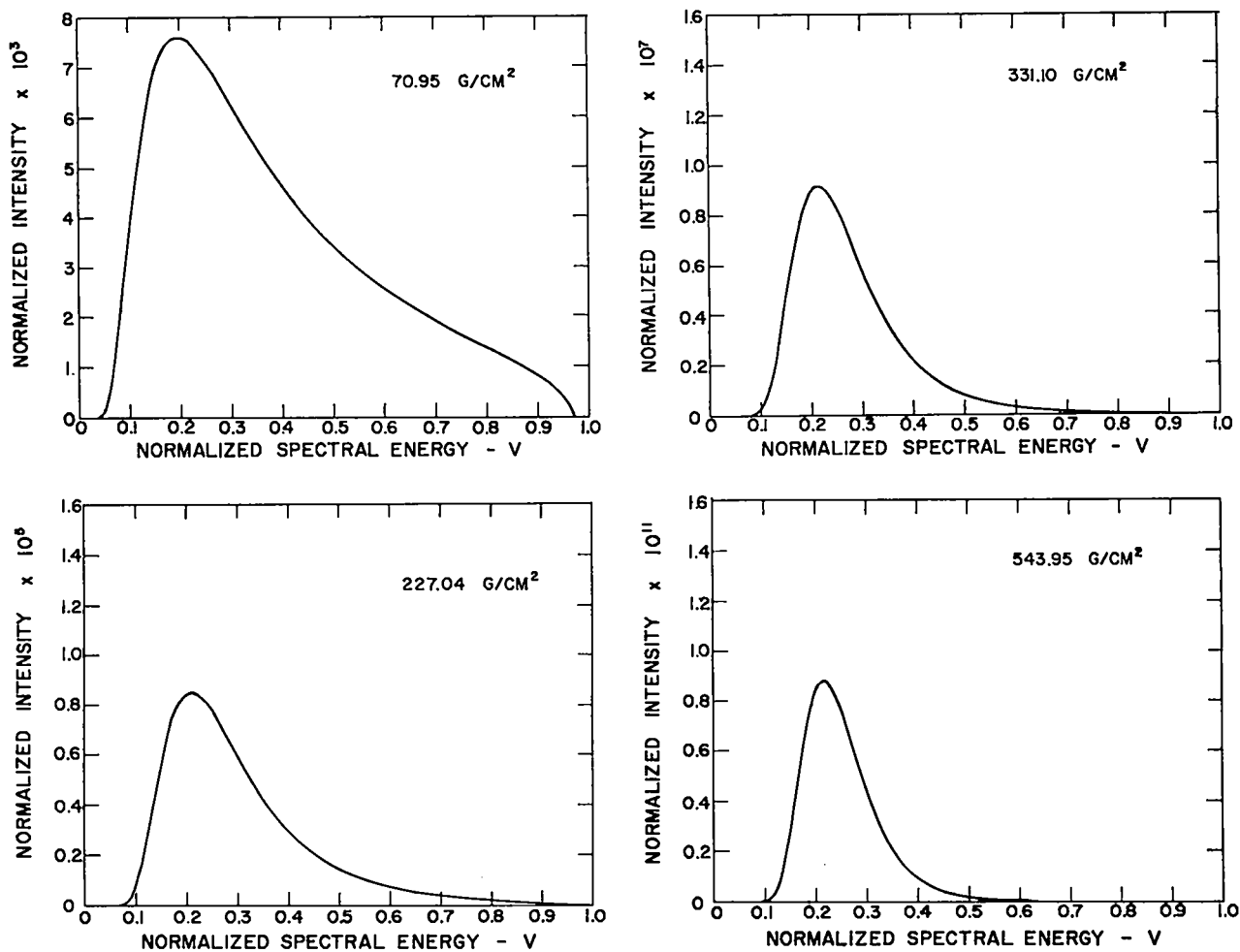
Fig. 2.42 Degraded 15 MeV tungsten bremsstrahlung spectrum after traversing various thicknesses of uranium.

68
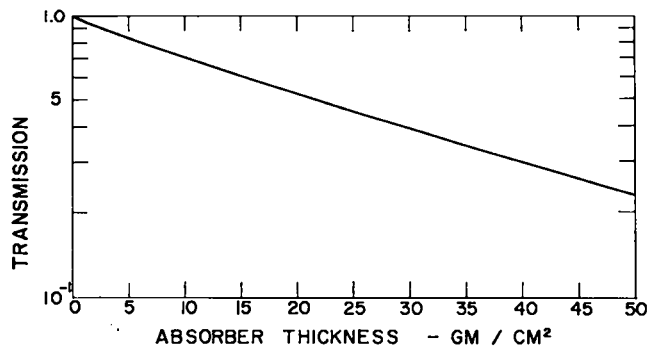
Fig. 2.43. Transmission of 15 MeV tungsten brems-
strahlung through Composition B.
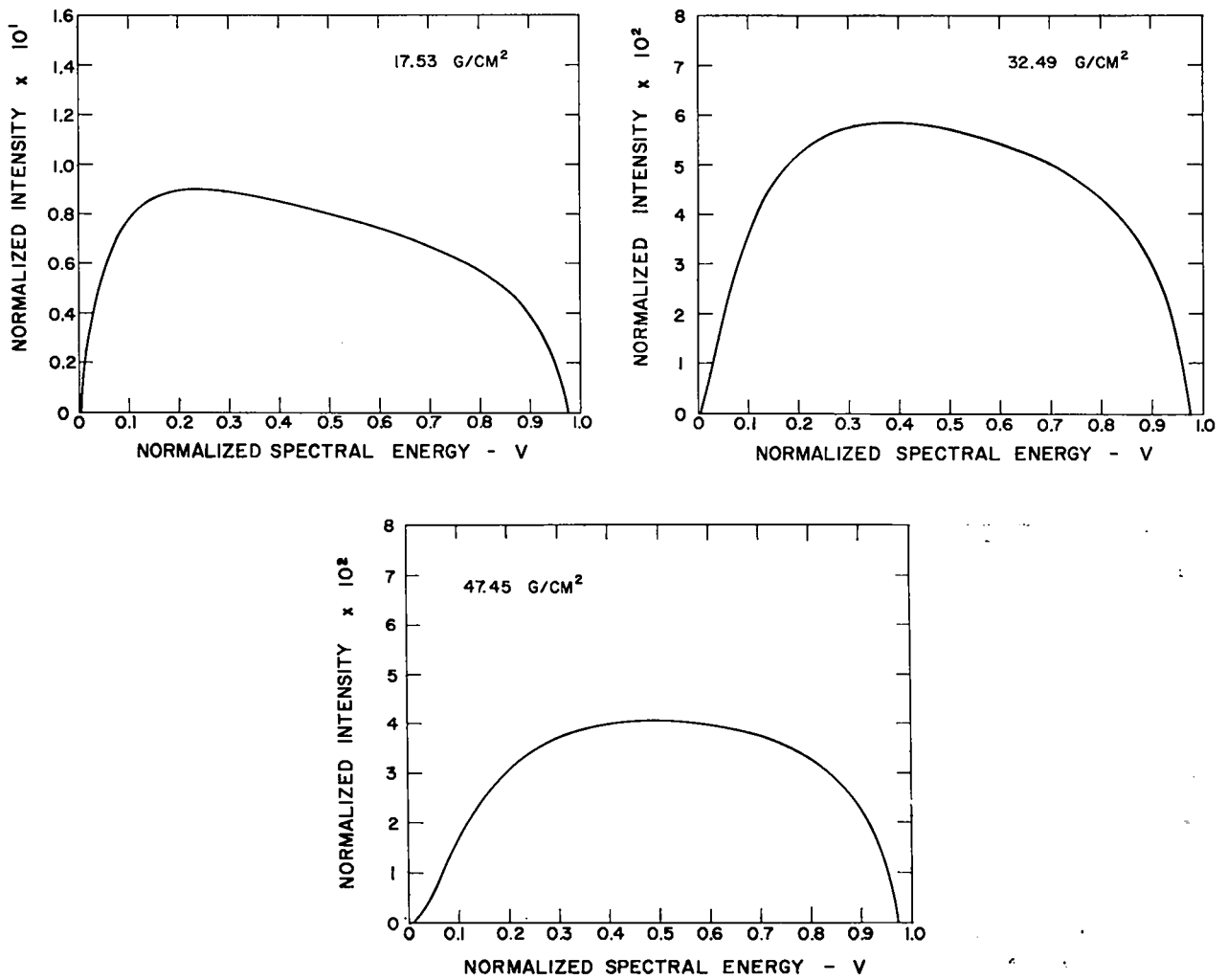
Fig. 2.44   Degraded 15 MeV tungsten bremsstrahlung spectrum after traversing various thicknesses of Composi-
tion B.
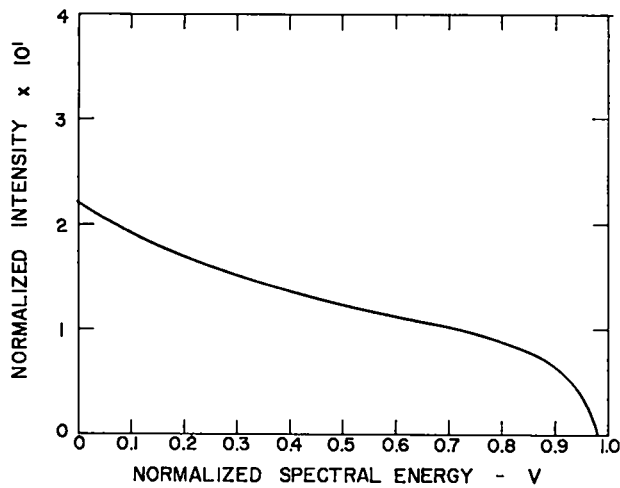
Fig. 2.45. Unadulterated 20 MeV tungsten brems-
strahlung spectrum.
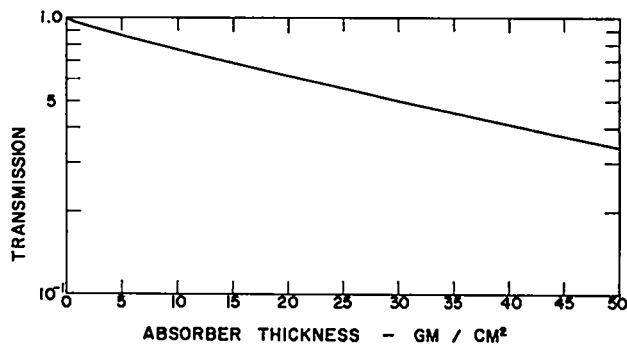
Fig. 2.46. Transmission of 20 MeV tungsten brems-
strahlung through beryllium.
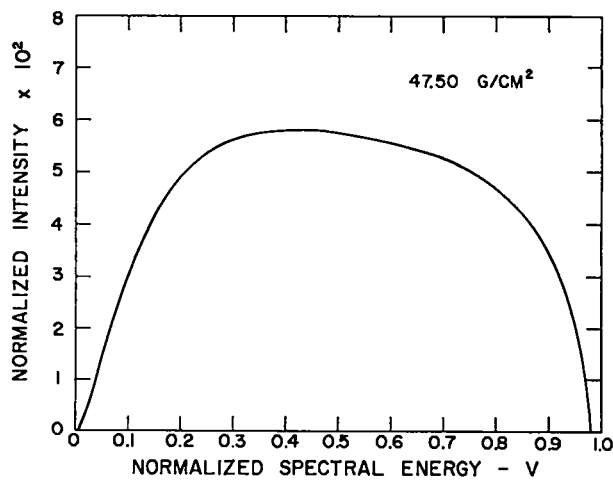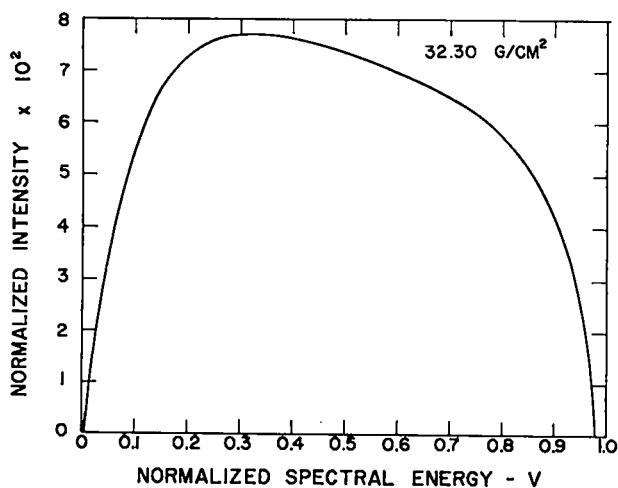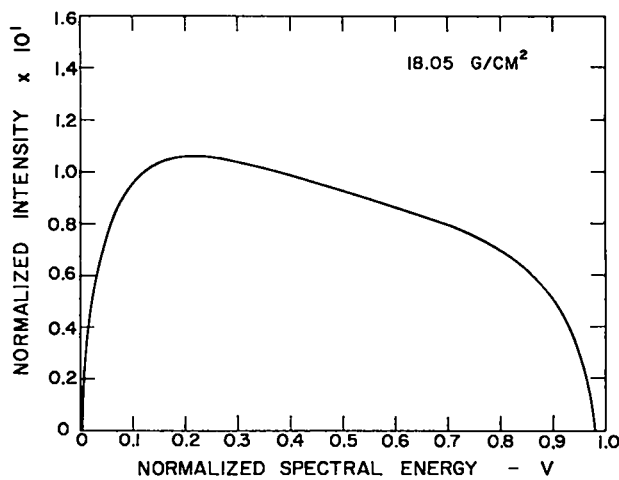
Fig. 2.47. Degraded 20 MeV tungsten bremsstrahlung spectrum after traversing various thicknesses of beryllium.
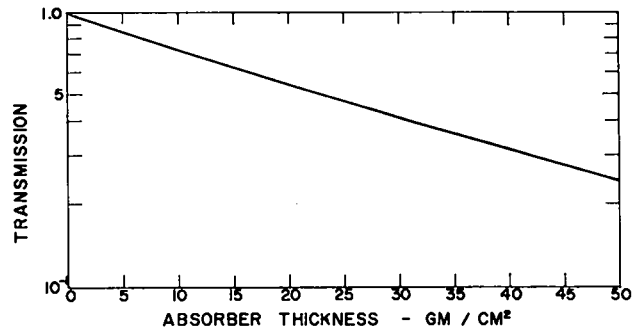
Fig. 2.48. Transmission of 20 MeV tungsten brems-
strahlung through aluminum.
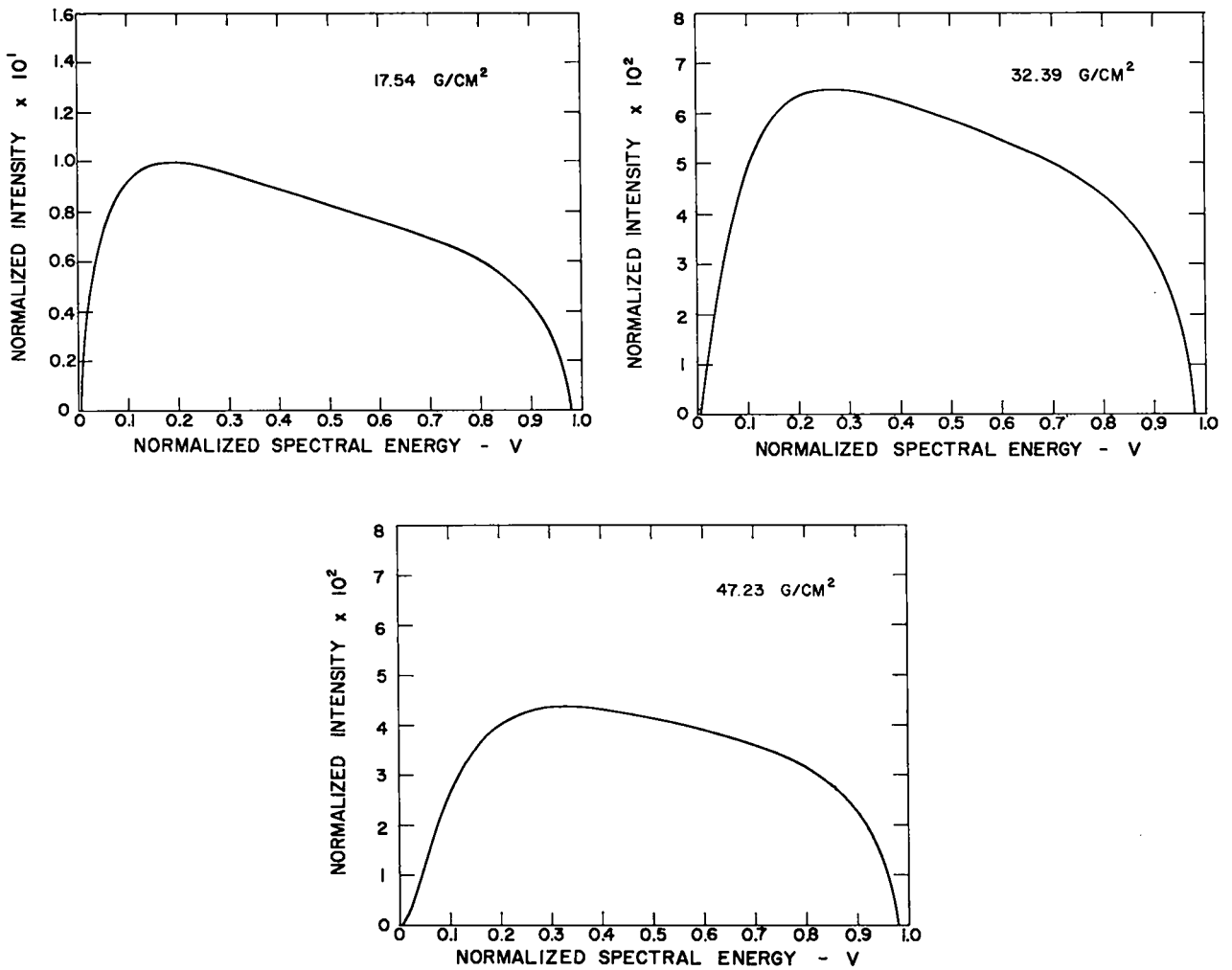
Fig. 2.49. Degraded 20 MeV tungsten bremsstrahlung spectrum after traversing various thicknesses of aluminum.
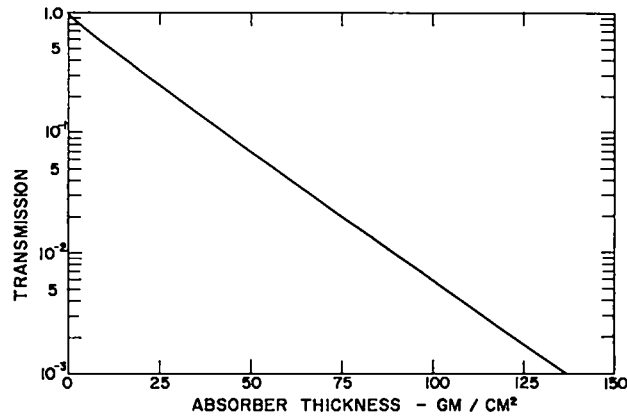
Fig. 2.50. Transmission of 20 MeV tungsten brems-
strahlung through uranium. For 137 g/cm²
$\leq$ thickness $\leq$ 567 g/cm², $\log_{10}$ T$\cong$
$\overline{1.34236} \times 10^{-6}t^2 - 2.06771 \times 10^{-2}t -$
0.20082.
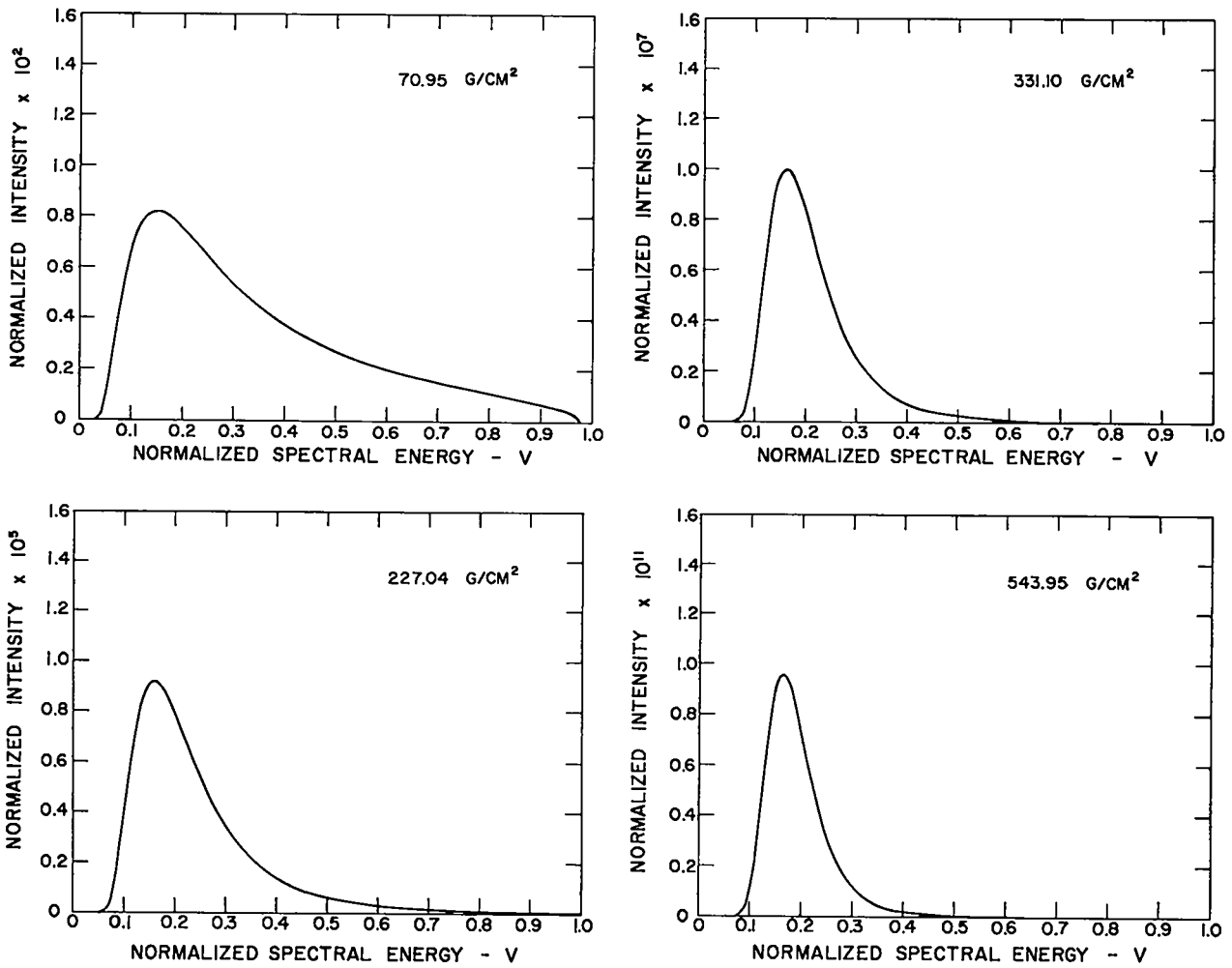
Fig. 2.51. Degraded 20 MeV tungsten bremsstrahlung spectrum after traversing various thicknesses of uranium.

72
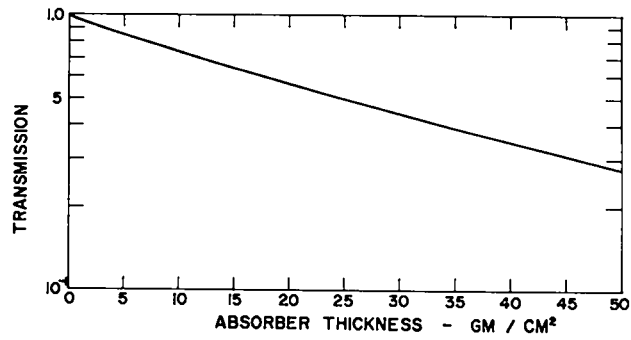
Fig. 2.52. Transmission of 20 MeV tungsten brems-
strahlung through Composition B.
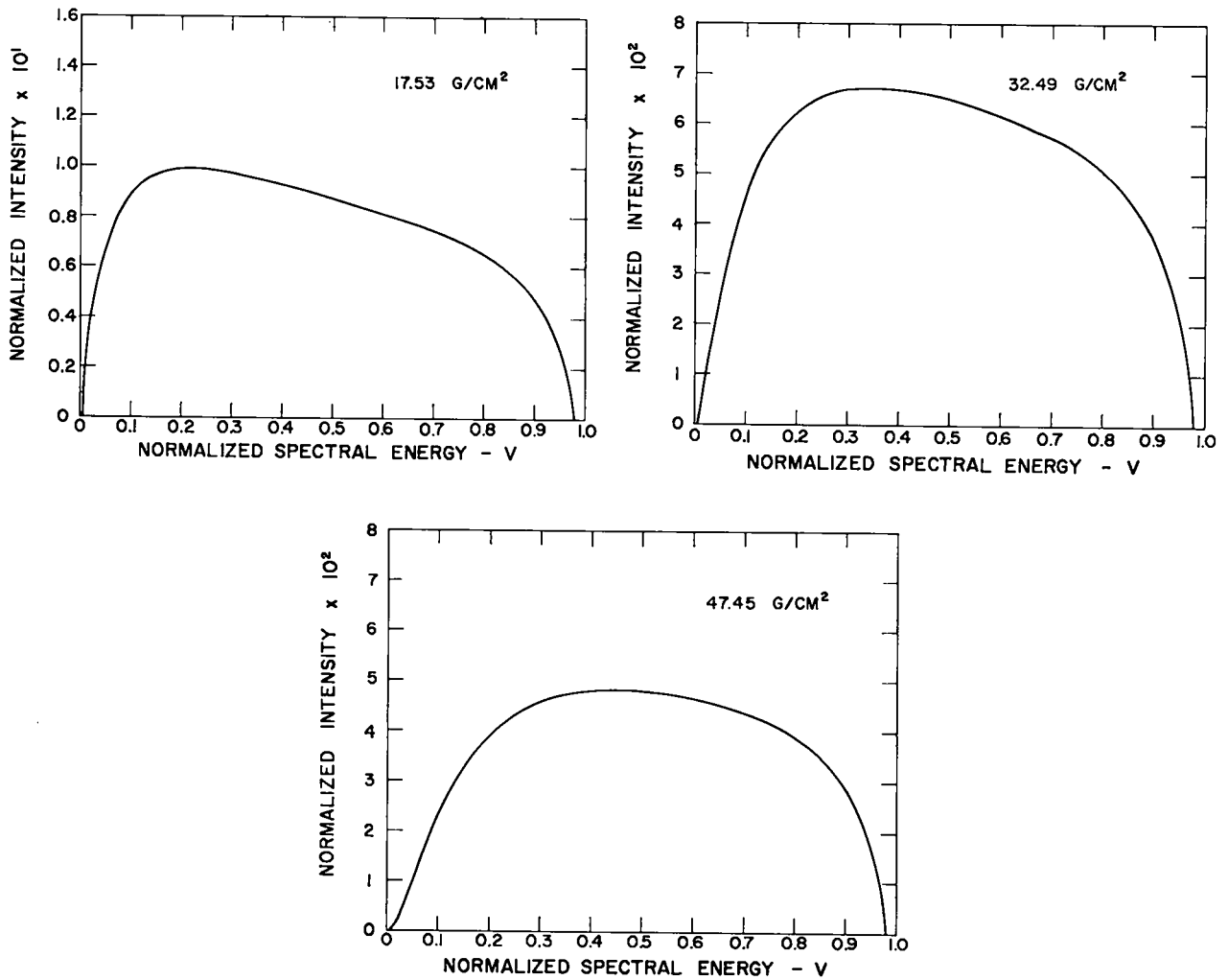
Fig. 2.53. Degraded 20 MeV tungsten bremsstrahlung spectrum after traversing various thicknesses of Composi-
tion B.

73
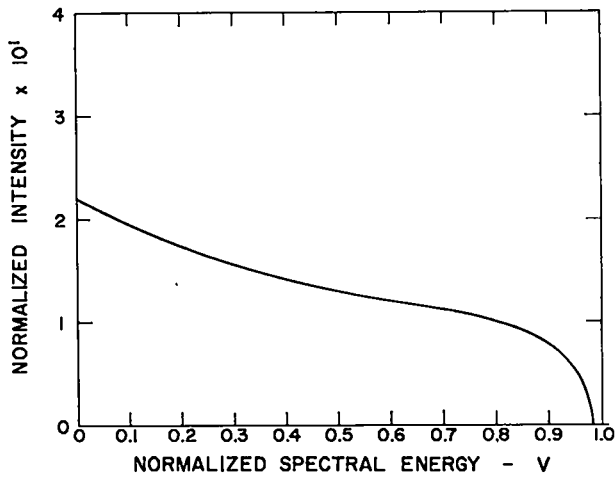
Fig. 2.54. Unadulterated 30 MeV tungsten brems-
strahlung spectrum.
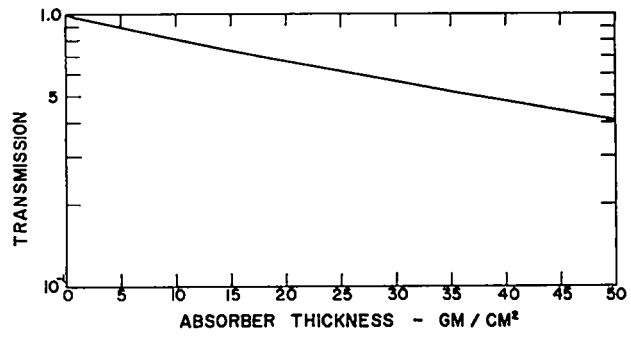
Fig. 2.55. Transmission of 30 MeV tungsten brems-
strahlung through beryllium.
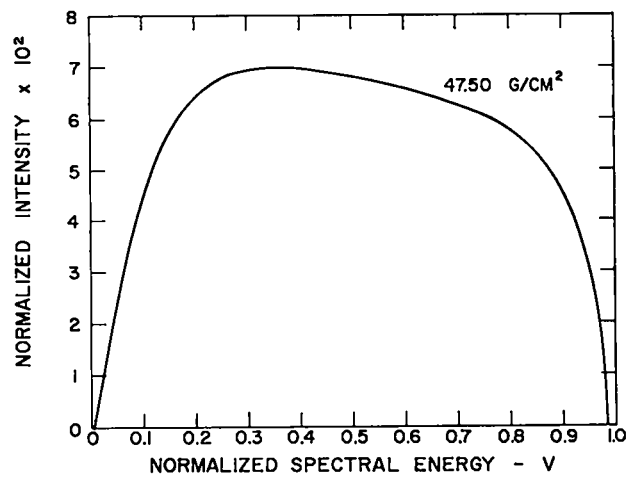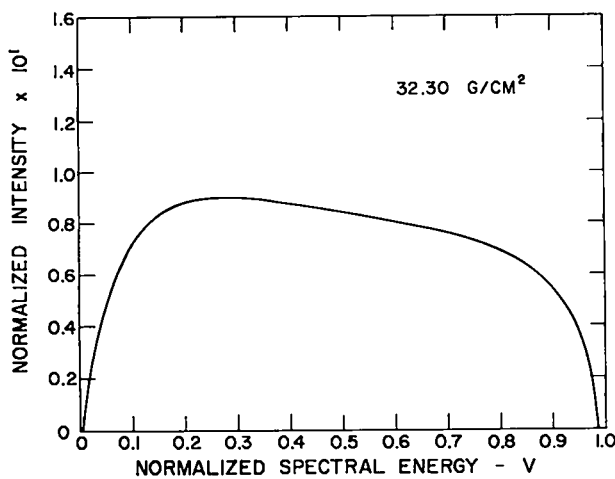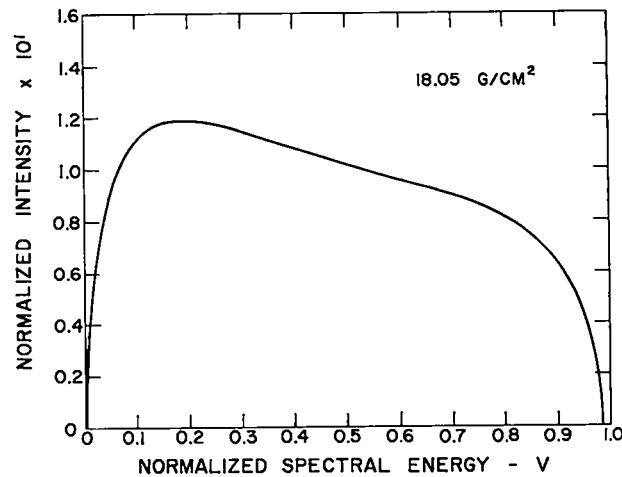
Fig. 2.56. Degraded 30 MeV tungsten bremsstrahlung spectrum after traversing various thicknesses of beryllium.
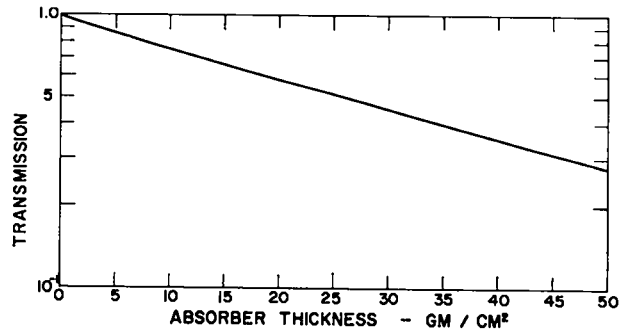
Fig. 2.57. Transmission of 30 MeV tungsten bremsstrahlung through aluminum.
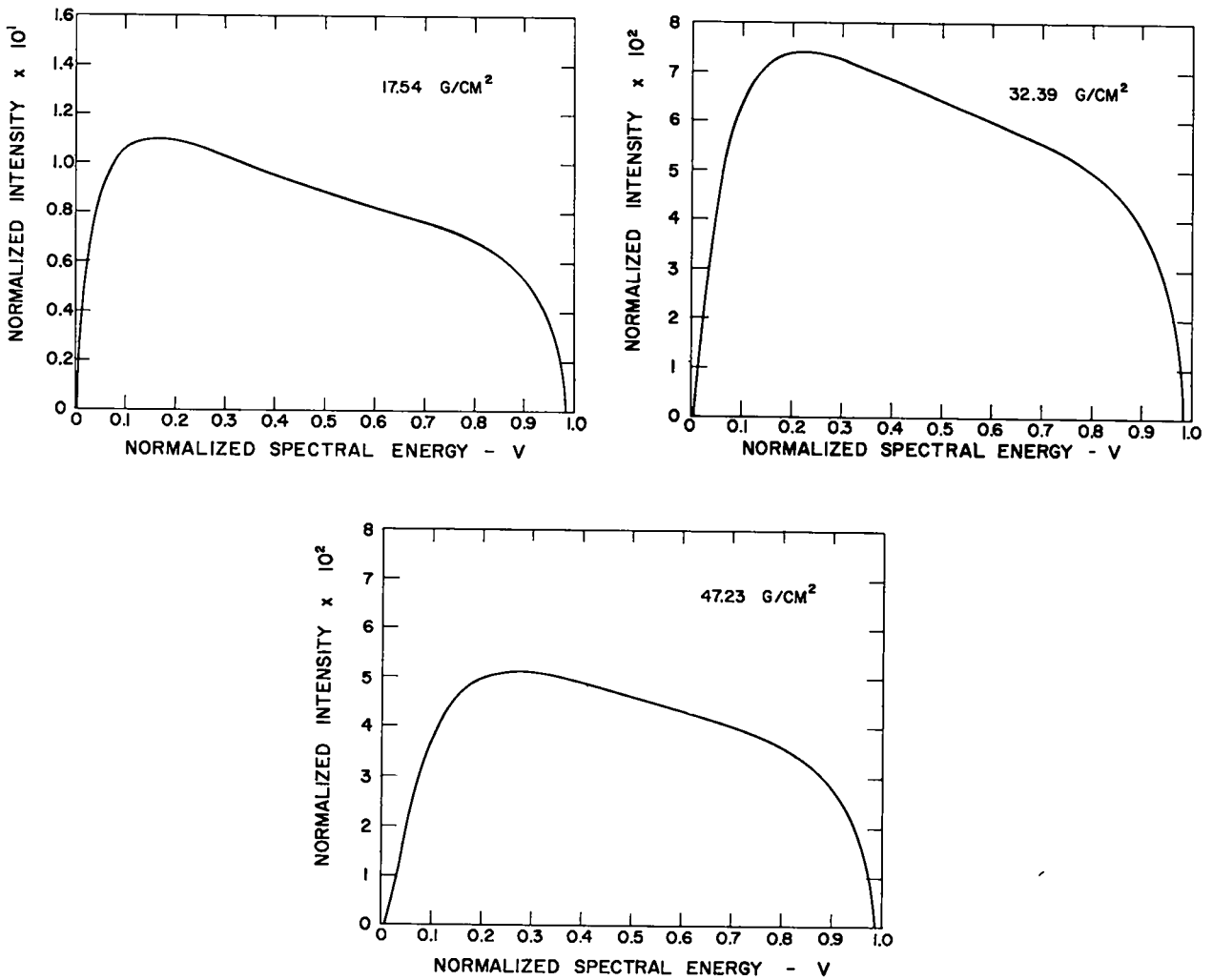
Fig. 2.58. Degraded 30 MeV tungsten bremsstrahlung spectrum after traversing various thicknesses of aluminum.
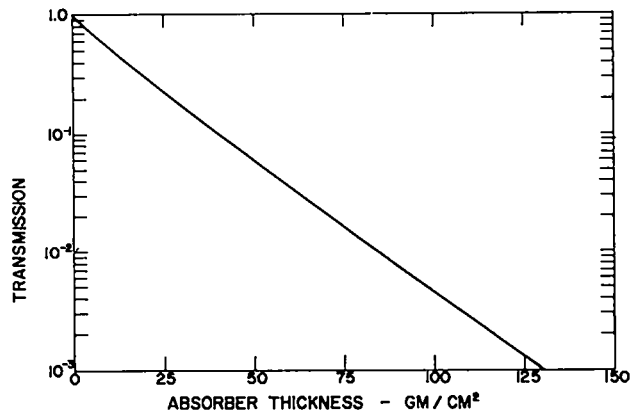
Fig. 2.59. Transmission of 30 MeV tungsten brems-
strahlung through uranium. For 130 g/cm²
$\leq$ thickness $\leq$ 567 g/cm², $\log_{10}$ T$\cong$
$\overline{1.56008} \times 10^{-6}t^2 - 2.07979 \times 10^{-2}t - 0.34227.$
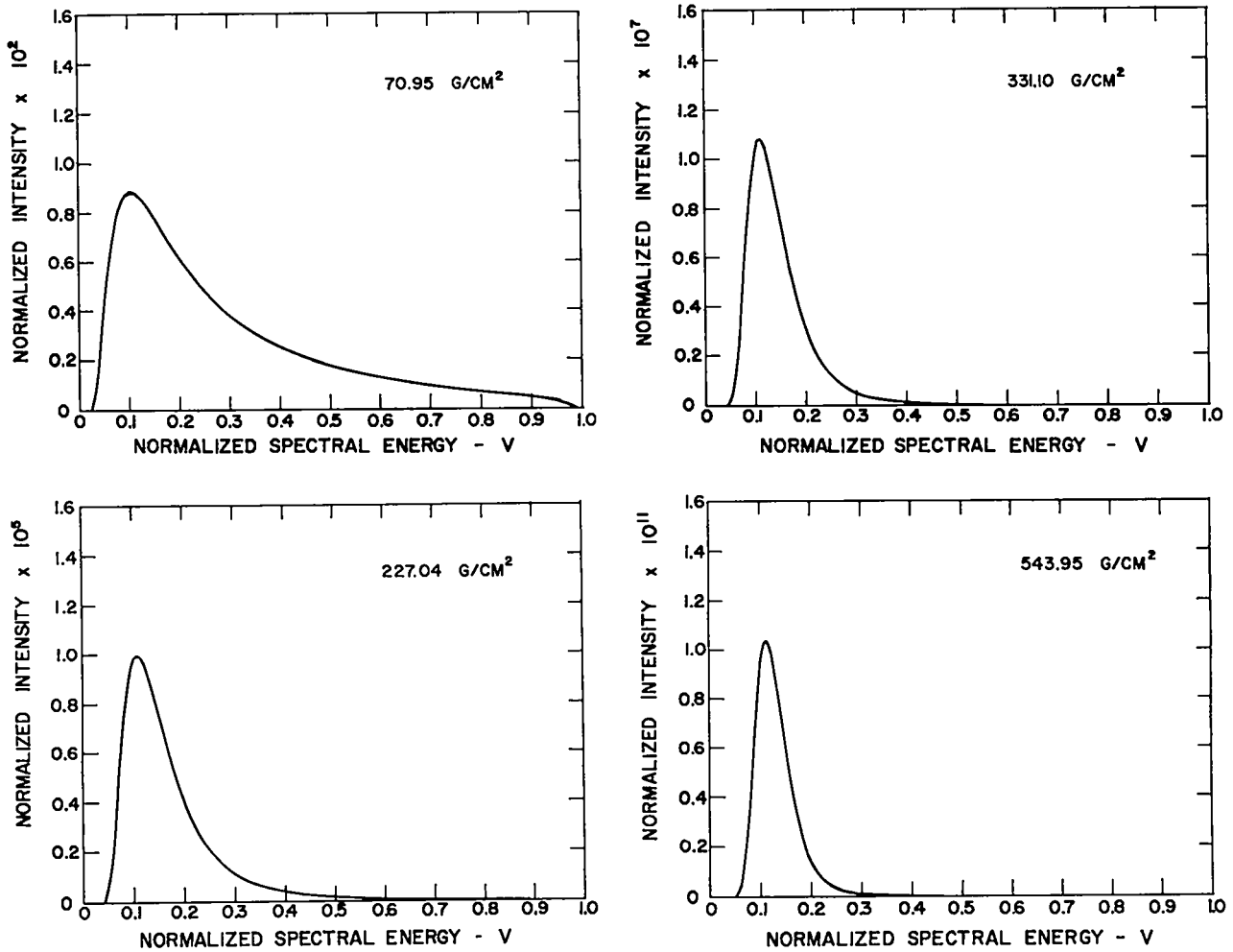
Fig. 2.60. Degraded 30 MeV tungsten bremsstrahlung spectrum after traversing various thicknesses of uranium.
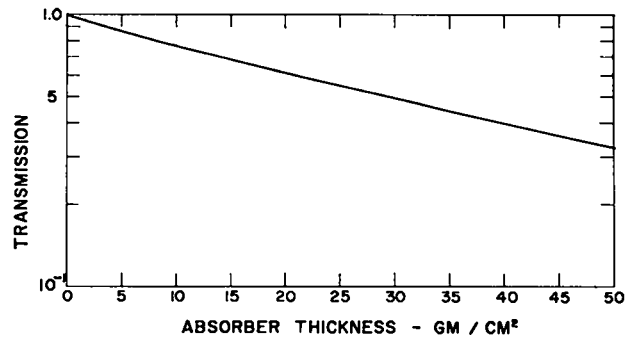
Fig. 2.61. Transmission of 30 MeV tungsten brems-
strahlung through Composition B.
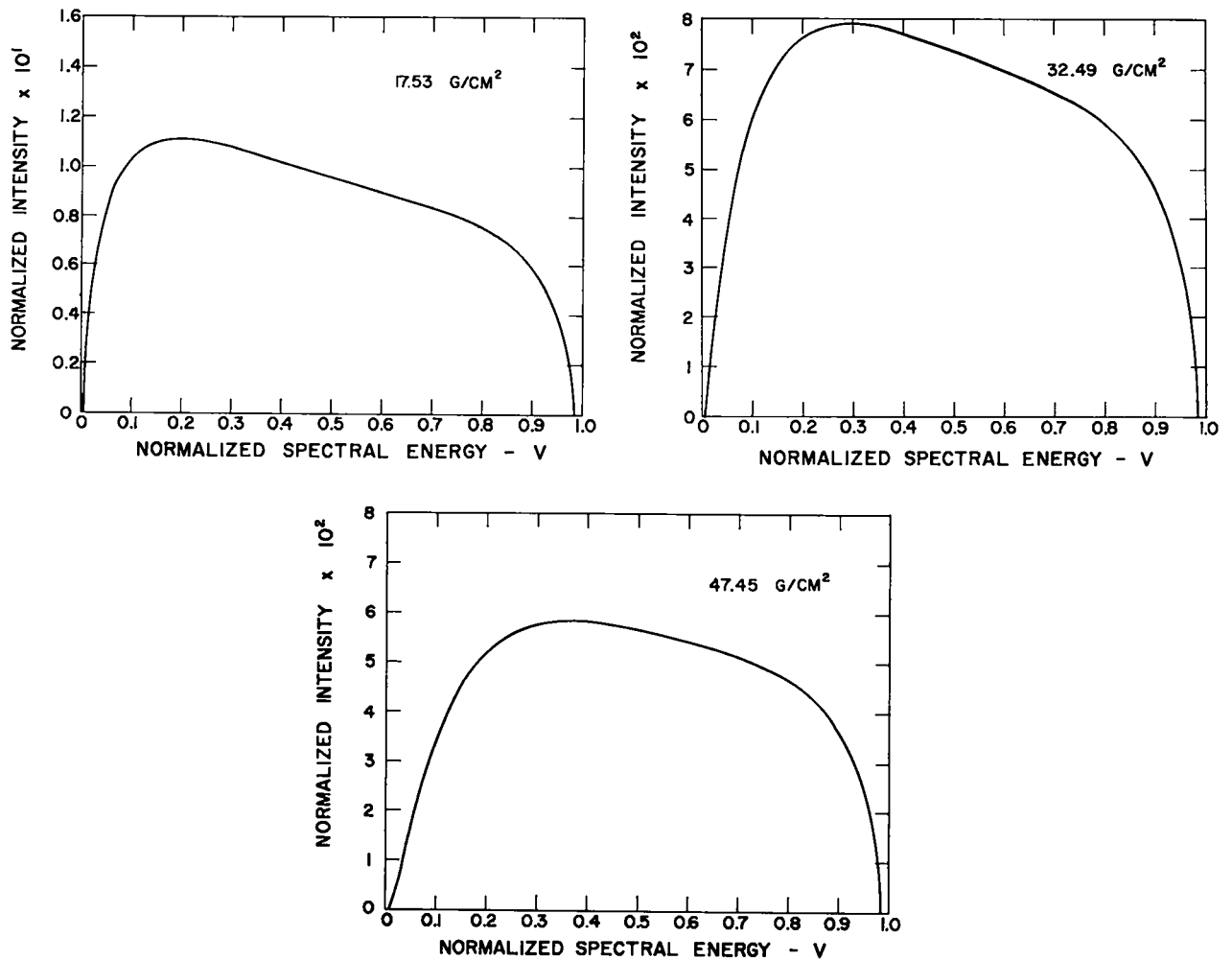
Fig. 2.62. Degraded 30 MeV tungsten bremsstrahlung spectrum after traversing various thicknesses of Composi-
tion B.

77
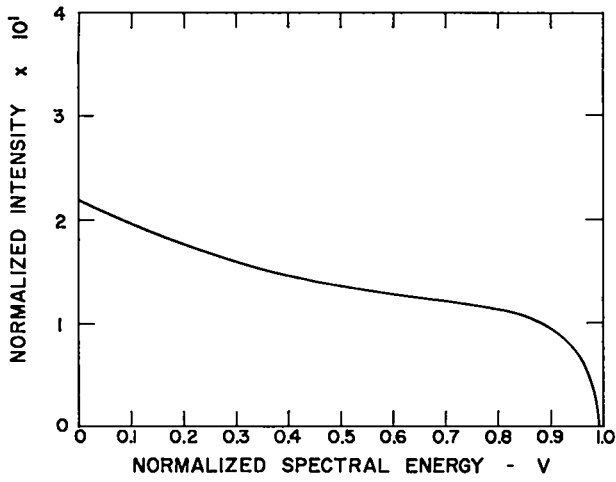
Fig. 2.63. Unadulterated 50 MeV tungsten brems-
strahlung spectrum.
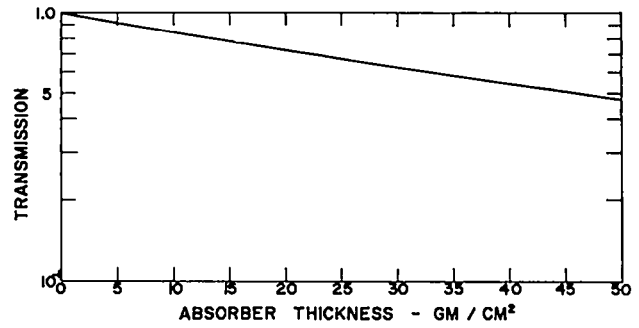
Fig. 2.64. Transmission of 50 MeV tungsten brems-
strahlung through beryllium.
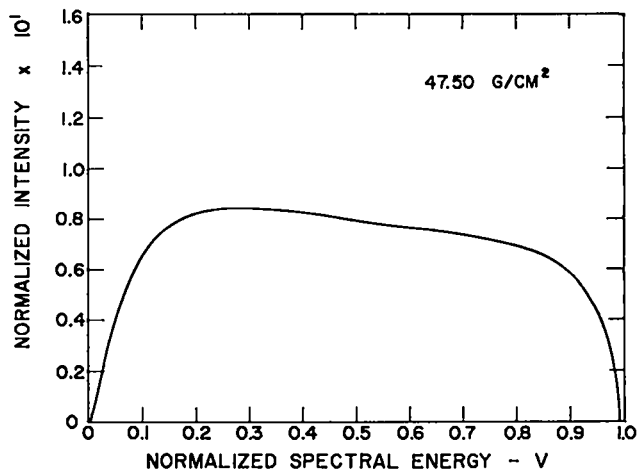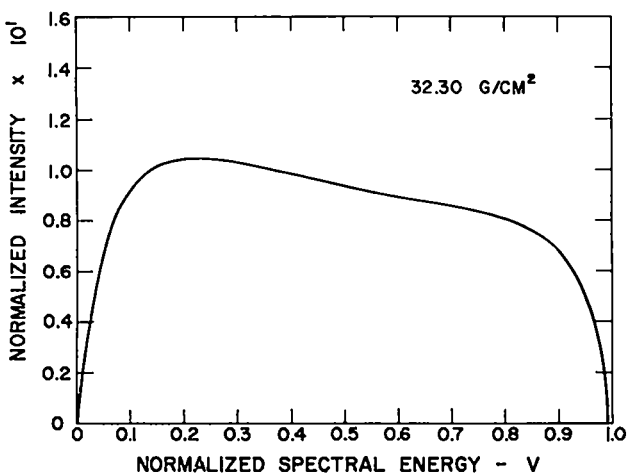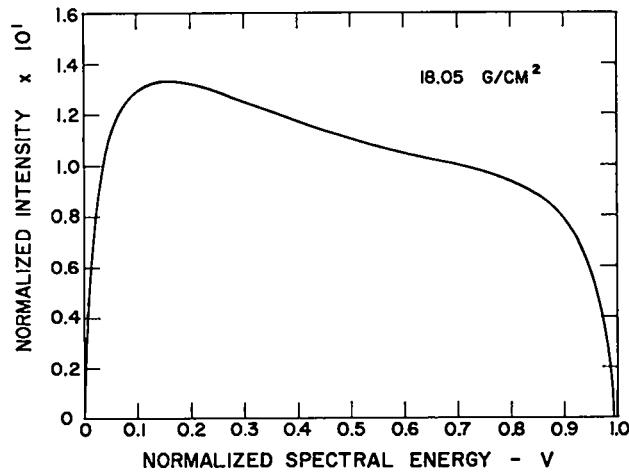
Fig. 2.65. Degraded 50 MeV tungsten bremsstrahlung spectrum after traversing various thicknesses of beryllium.

78
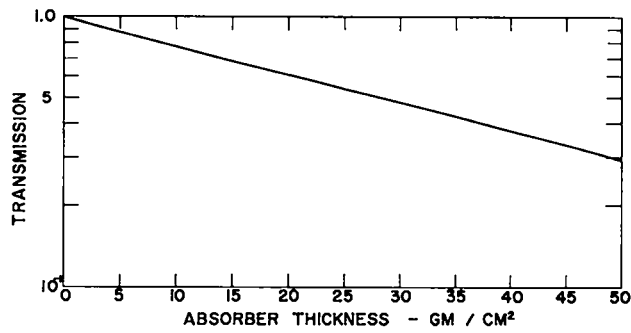
Fig. 2.66. Transmission of 50 MeV tungsten brems-
strahlung through aluminum.
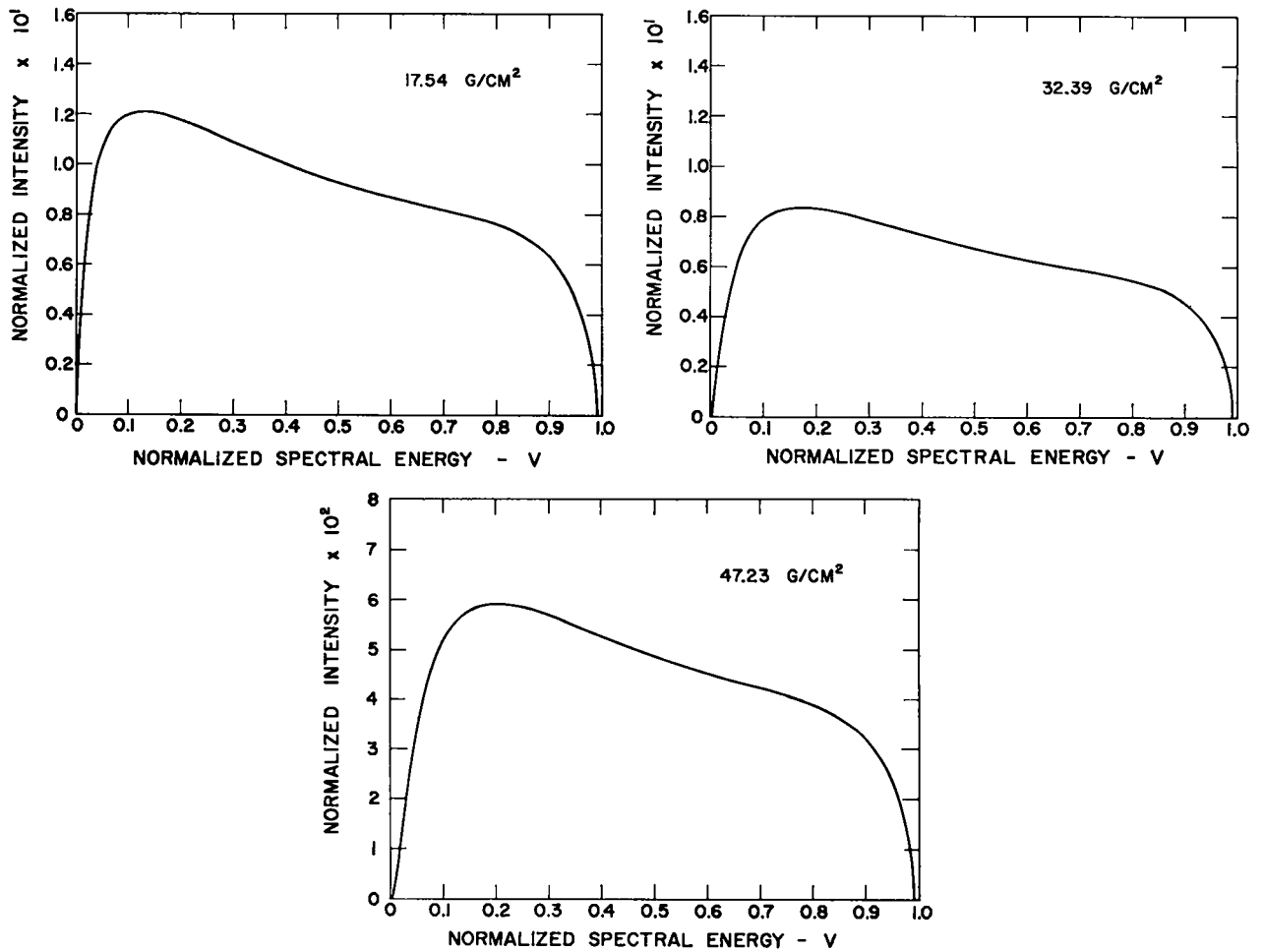
Fig. 2.67. Degraded 50 MeV tungsten bremsstrahlung spectrum after transversing various thicknesses of aluminum.

79
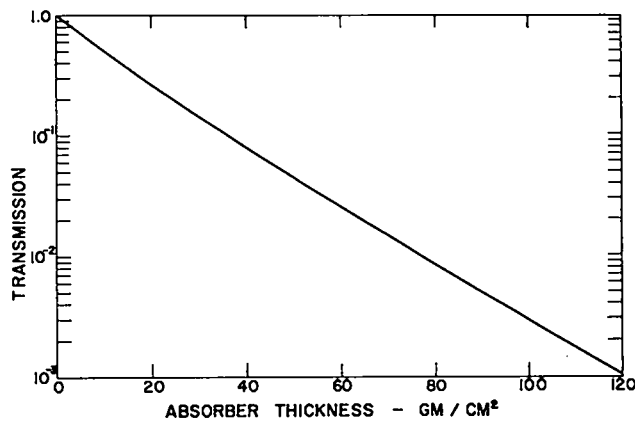
Fig. 2.68. Transmission of 50 MeV tungsten brems-
strahlung through uranium. For 120 g/cm²
$\leq$ thickness $\leq$ 567 g/cm², $\log_{10}$ T$\cong$
$2.39523 \times 10^{-6}t^2 - 2.14976 \times 10^{-2}t - 0.43243$.
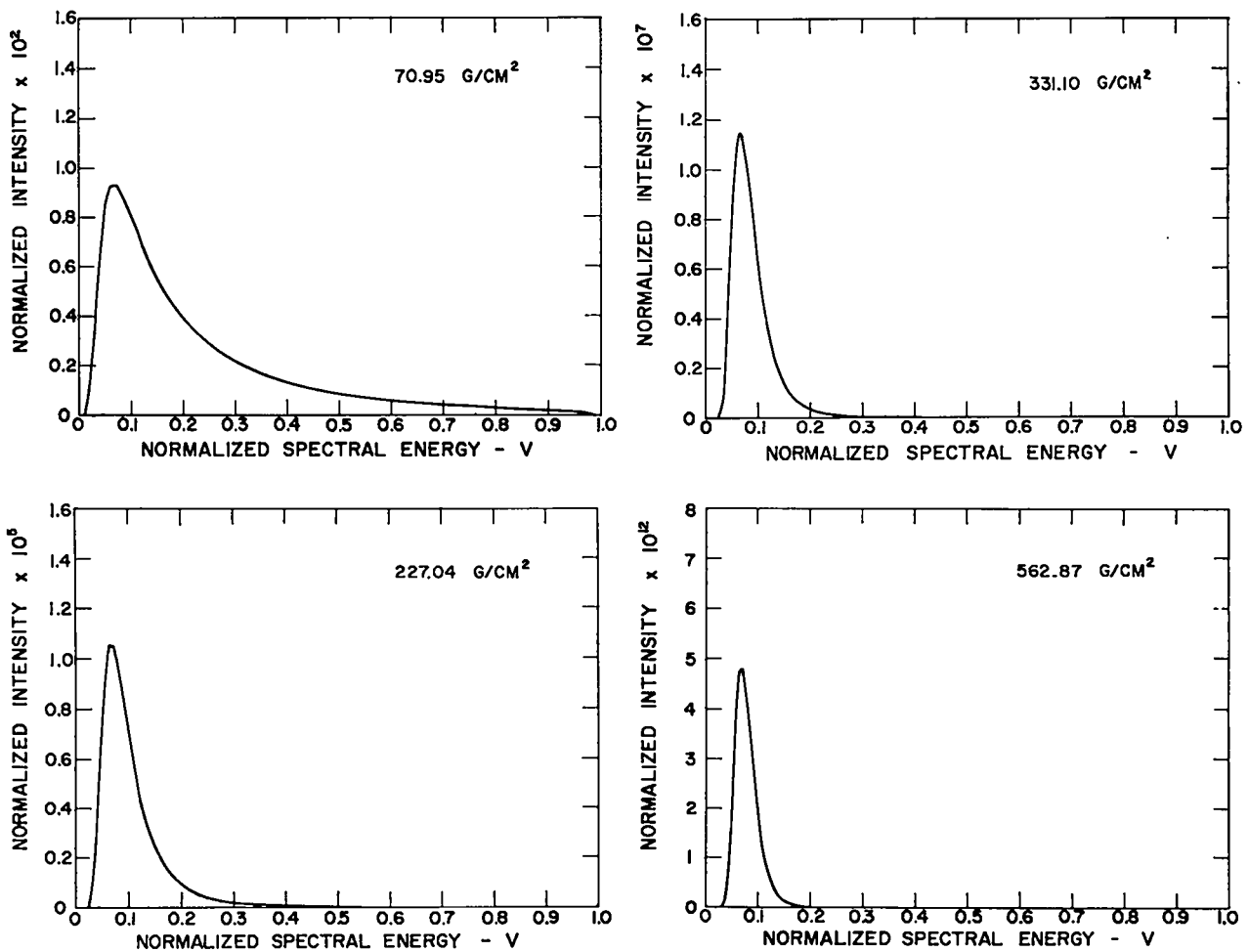
Fig. 2.69. Degraded 50 MeV tungsten bremsstrahlung spectrum after traversing various thicknesses of uranium.

80
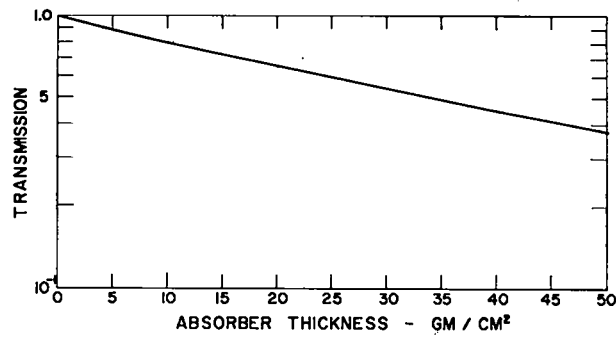
Fig. 2.70. Transmission of 50 MeV tungsten brems-
strahlung through Composition B.
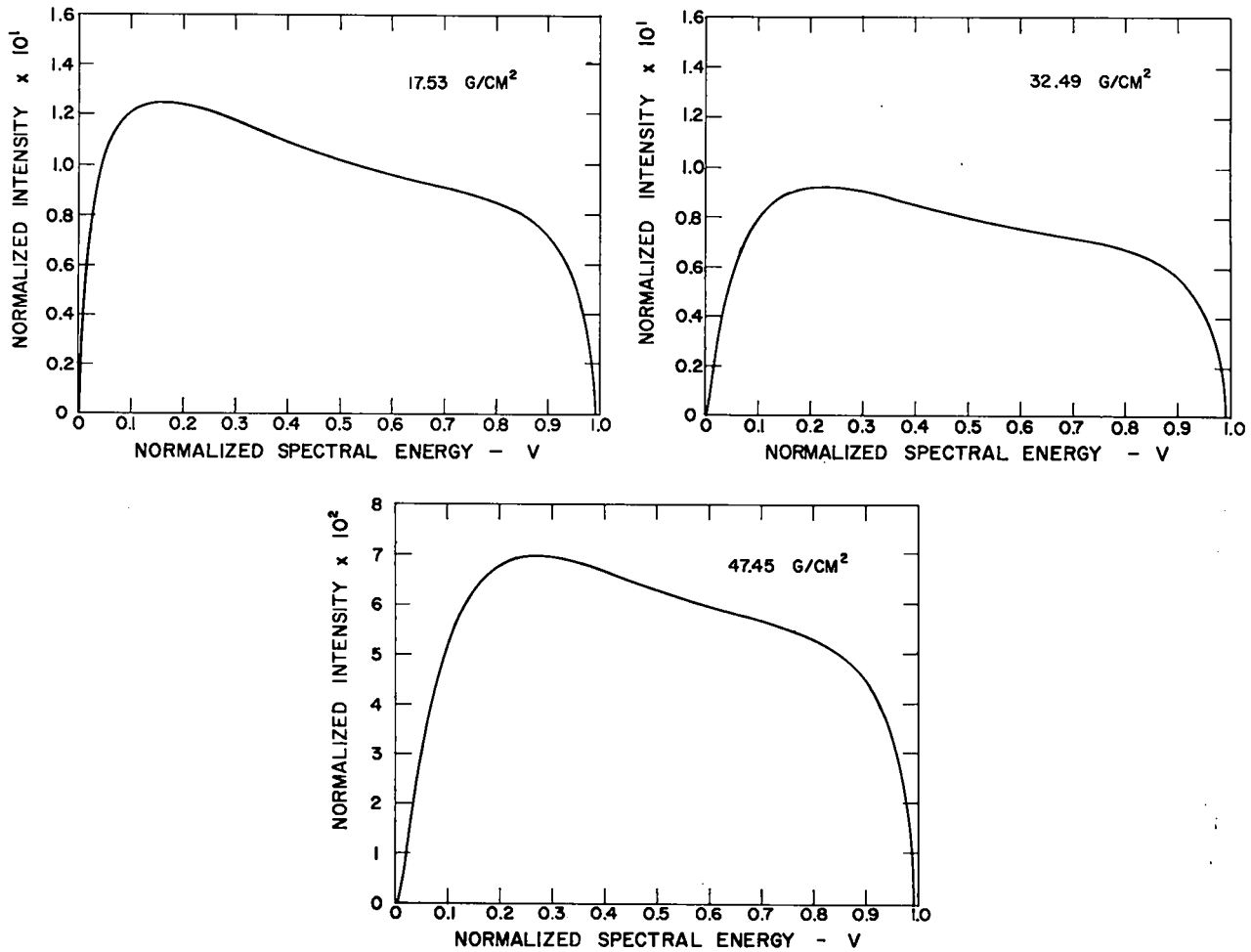
Fig. 2.71. Degraded 50 MeV tungsten bremsstrahlung spectrum after traversing various thicknesses of Composi-
tion B.

81
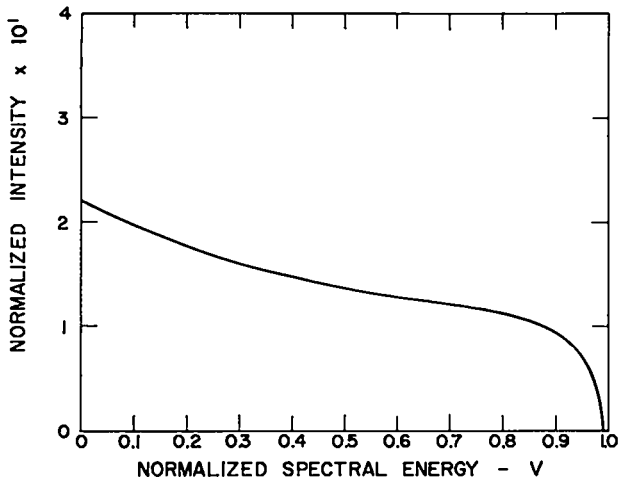
Fig. 2.72. Unadulterated 75 MeV tungsten bremsstrahlung spectrum.
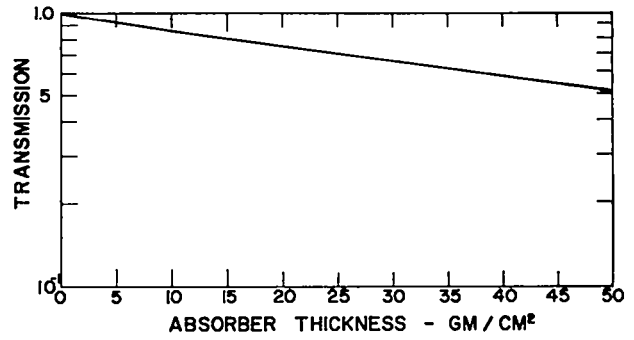
Fig. 2.73. Transmission of 75 MeV tungsten bremsstrahlung through beryllium.
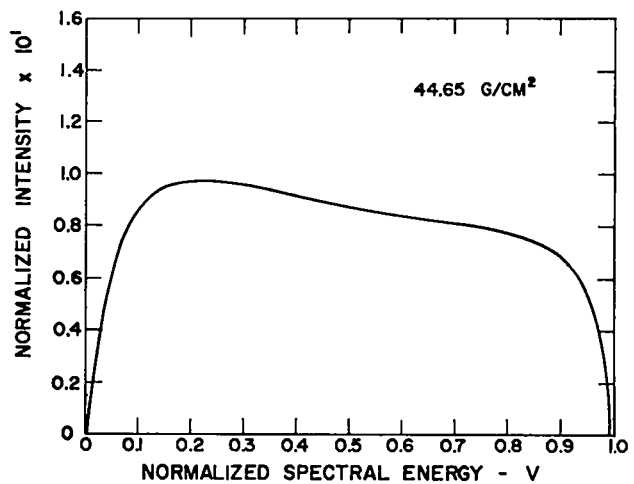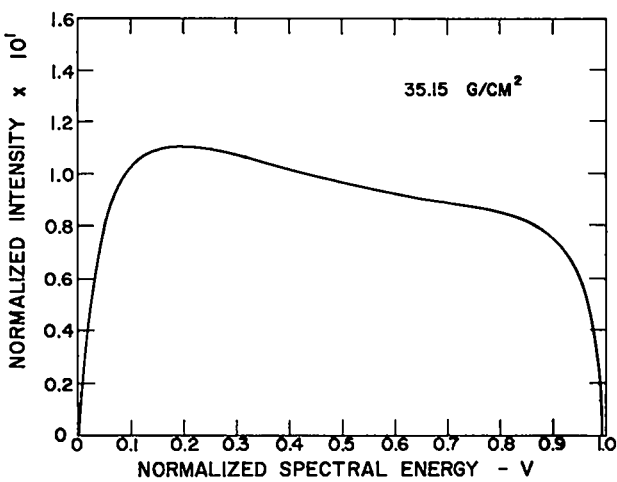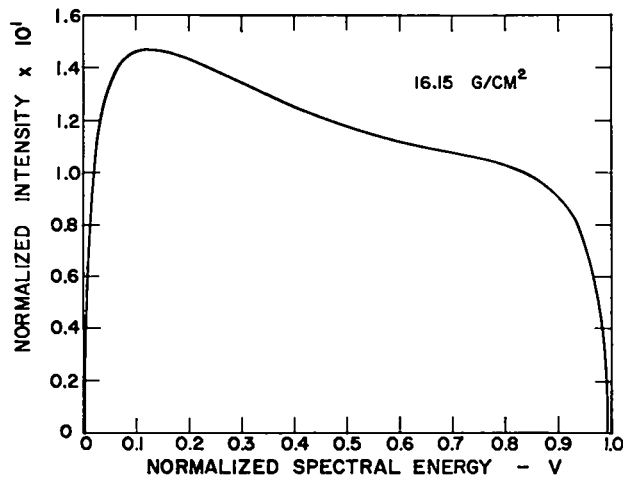
Fig. 2.74. Degraded 75 MeV tungsten bremsstrahlung spectrum after traversing various thicknesses of beryllium.
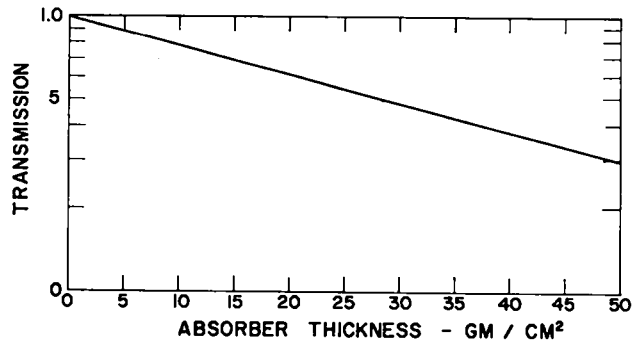
Fig. 2.75. Transmission of 75 MeV tungsten brems-
strahlung through aluminum.
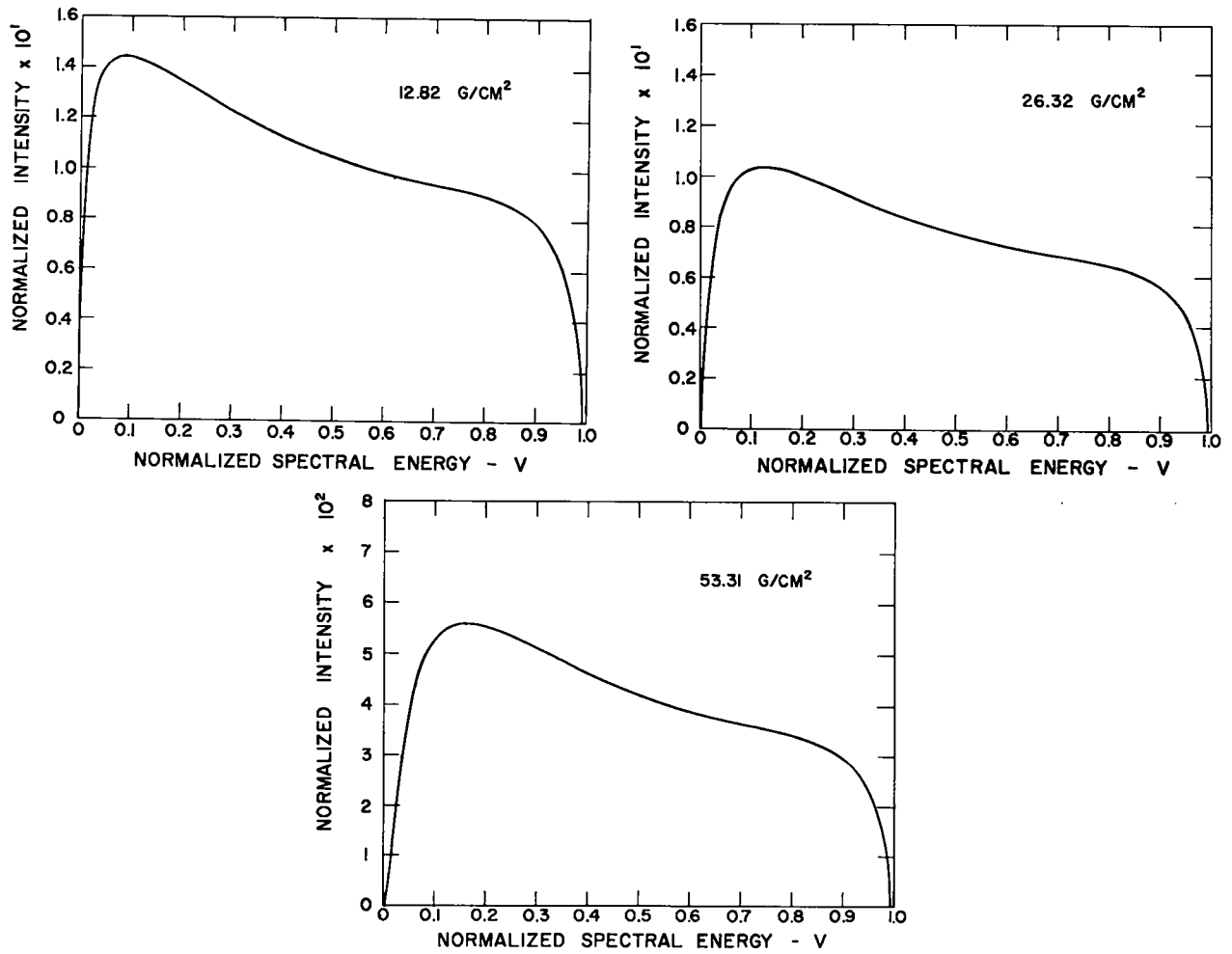
Fig. 2.76. Degraded 75 MeV tungsten bremsstrahlung spectrum after traversing various thicknesses of aluminum.

83
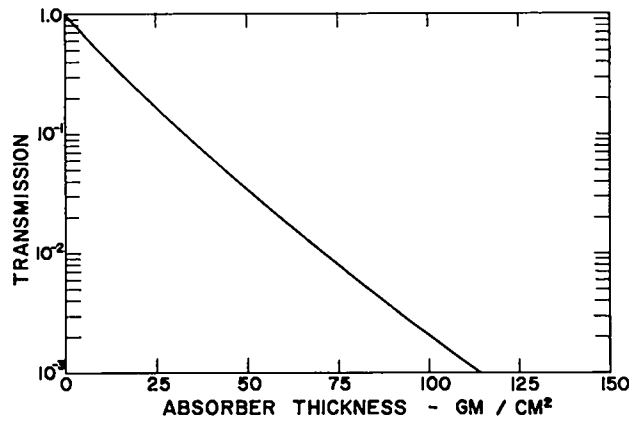
Fig. 2.77. Transmission of 75 MeV tungsten brems-
strahlung through uranium. For 115 g/cm²
$\leq$ thickness $\leq$ 567 g/cm², $\log_{10}$ T$\cong$
$\overline{1.77891} \times 10^{-6}t^2 - 2.10109 \times 10^{-2}t - 0.68008$.
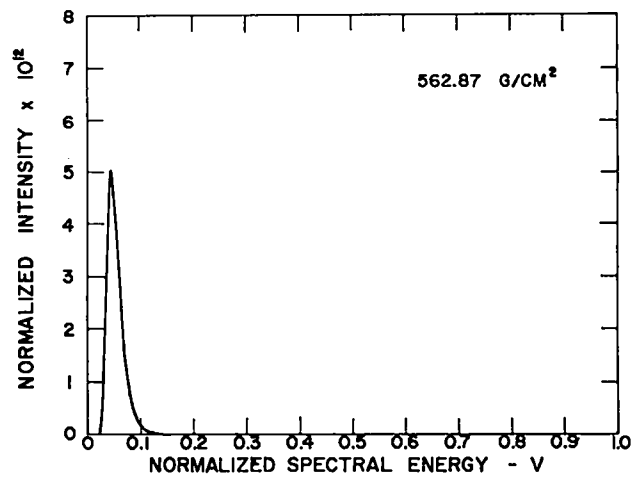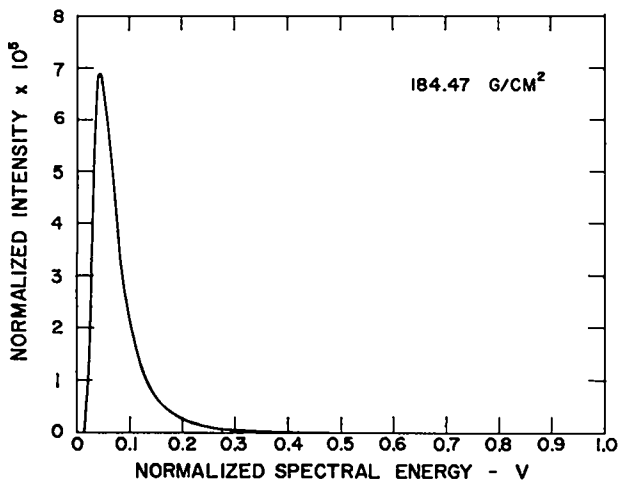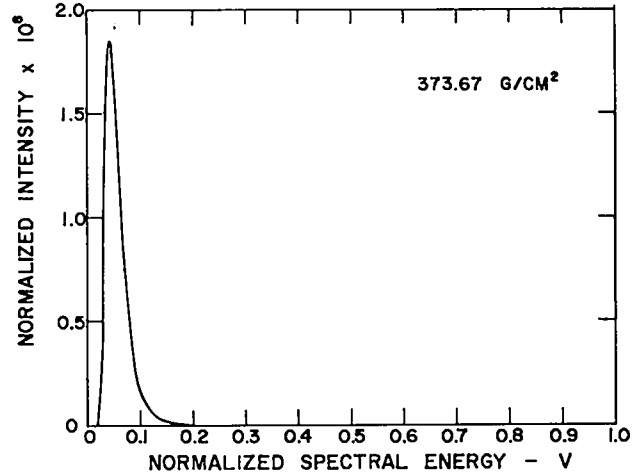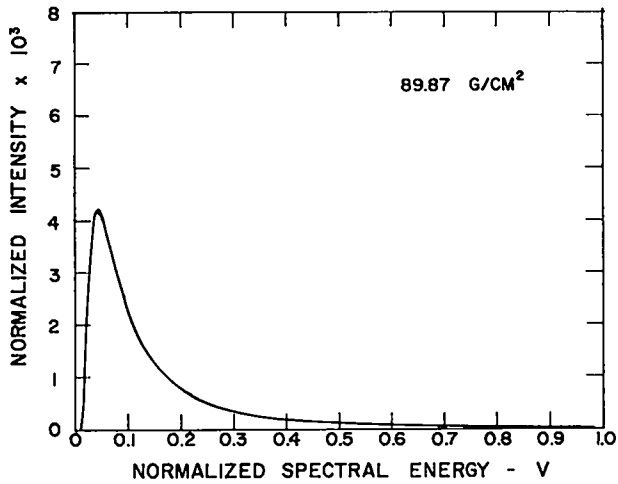
Fig. 2.78. Degraded 75 MeV tungsten bremsstrahlung spectrum after traversing various thicknesses of uranium.
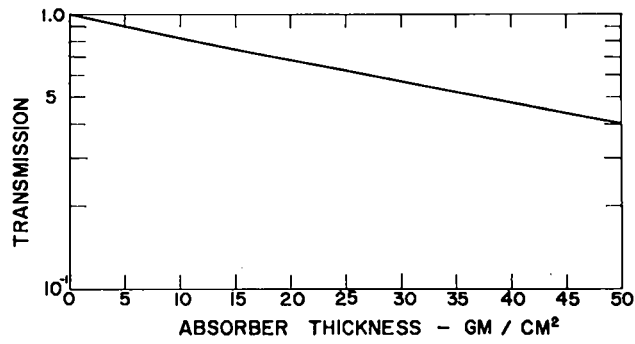
Fig. 2.79. Transmission of 75 MeV tungsten bremsstrahlung through Composition B.
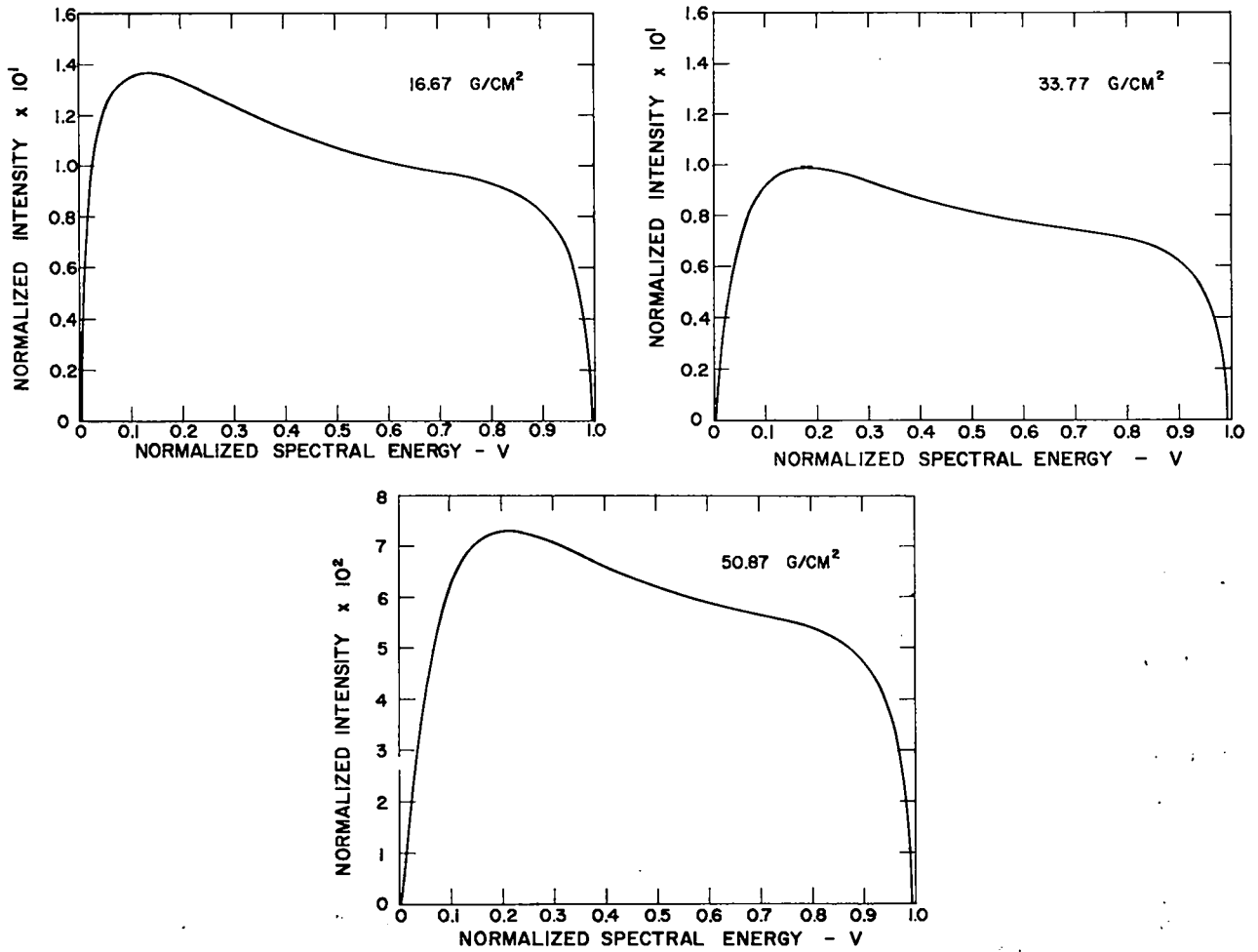
Fig. 2.80. Degraded 75 MeV tungsten bremsstrahlung spectrum after traversing various thicknesses of Composition B.

85
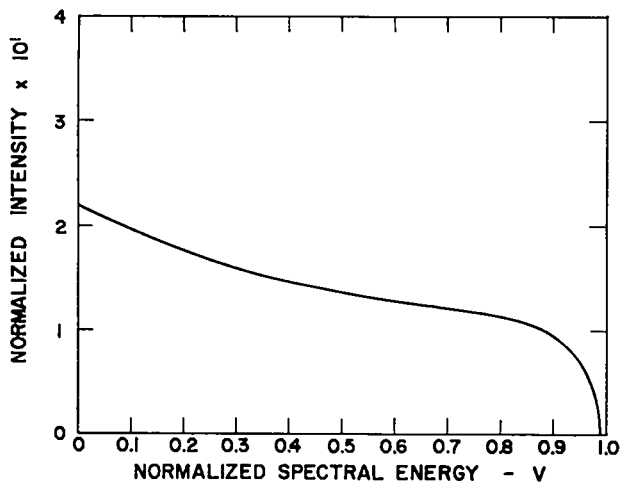
Fig. 2.81. Unadulterated 100 MeV tungsten brems-
strahlung spectrum.
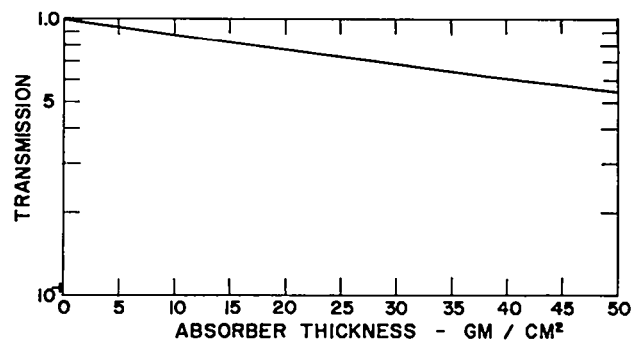
Fig. 2.82. Transmission of 100 MeV tungsten brems-
strahlung through beryllium.
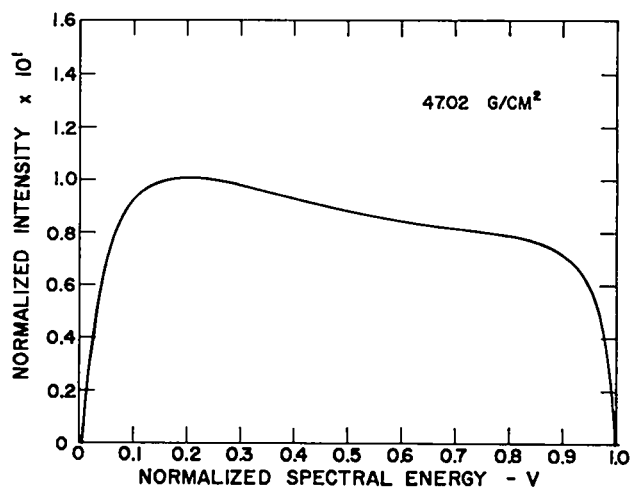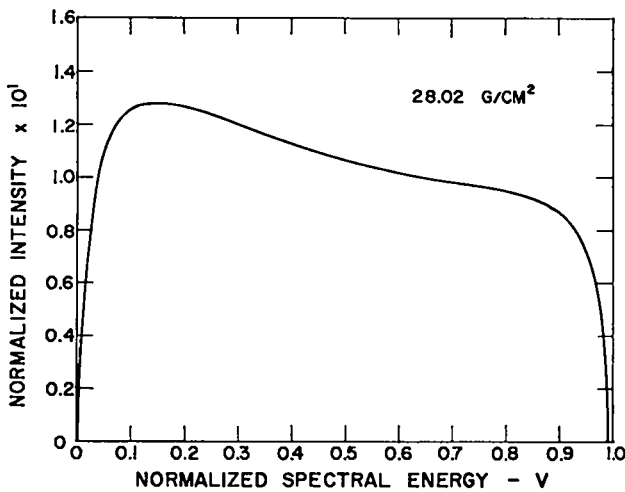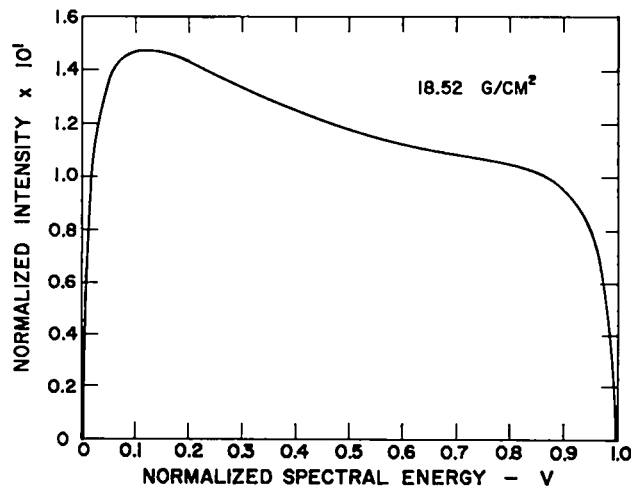
Fig. 2.83. Degraded 100 MeV tungsten bremsstrahlung spectrum after traversing various thicknesses of beryllium.
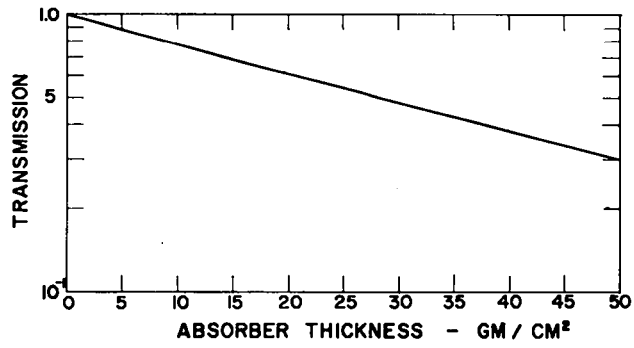
Fig. 2.84. Transmission of 100 MeV tungsten brems-
strahlung through aluminum.
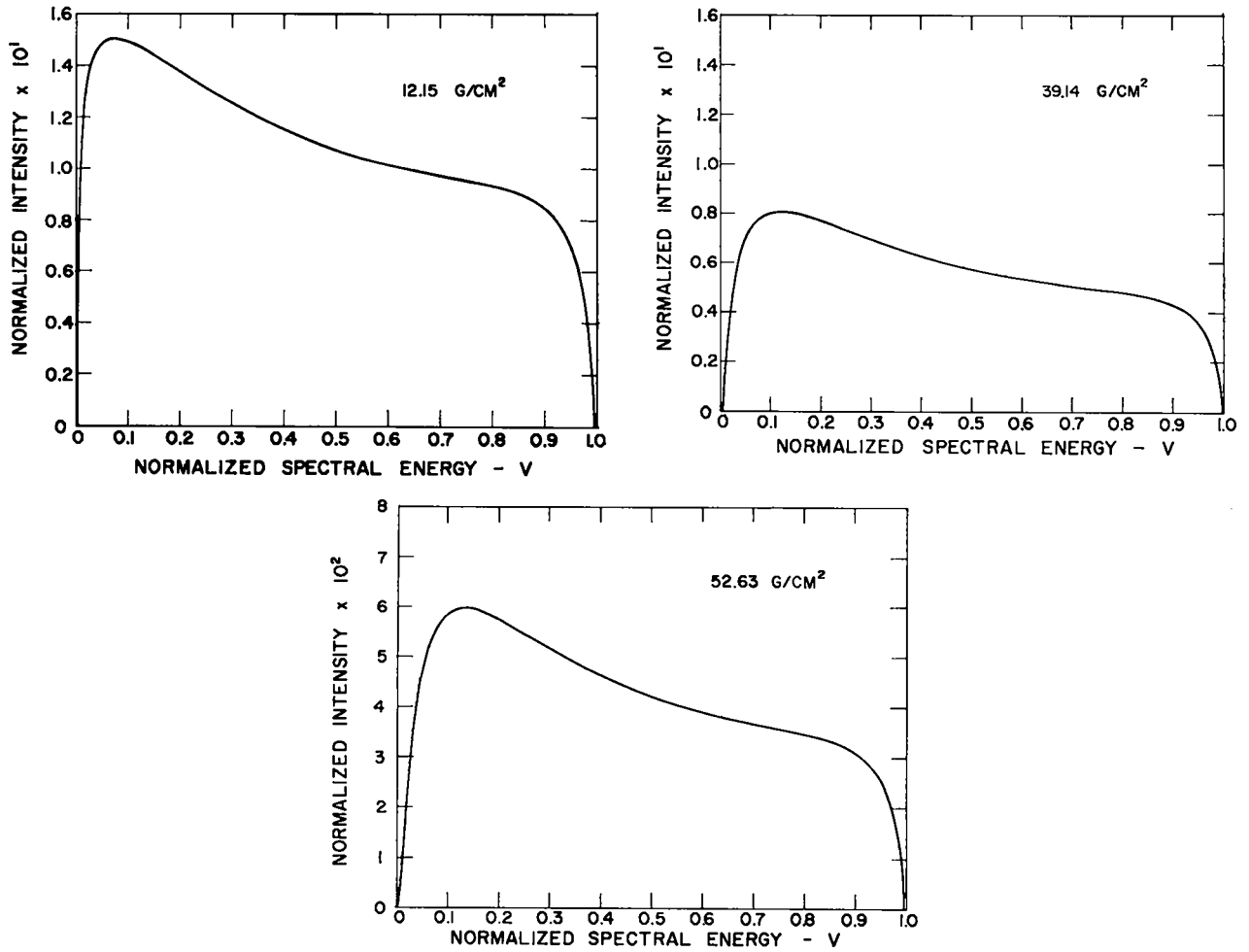
Fig. 2.85. Degraded 100 MeV tungsten bremsstrahlung spectrum after traversing various thicknesses of aluminum.
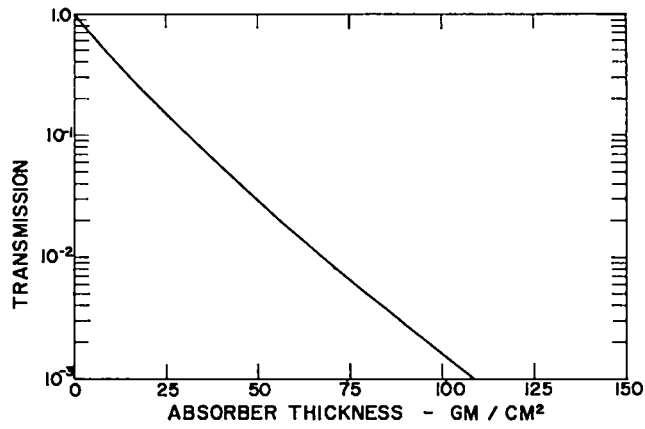
Fig. 2.86. Transmission of 100 MeV tungsten brems-
strahlung through uranium. For 110 g/cm²
$\leq$ thickness $\leq$ 567 g/cm², $\log_{10}$ T$\cong$
$\overline{1.75576}$ $\times$ $10^{-6}t^2$ — 2.10026 $\times$ $10^{-2}t$ —
0.80442.
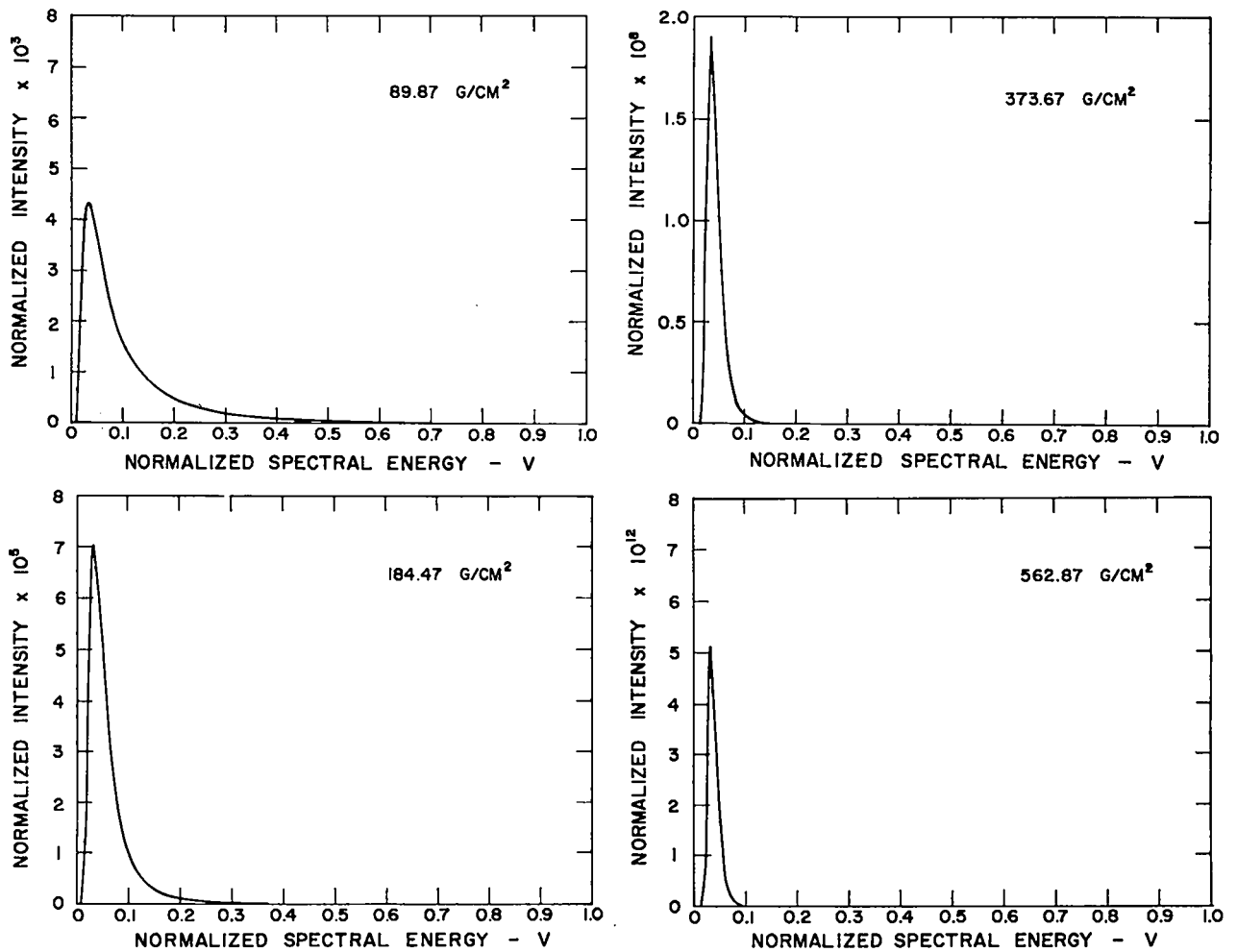
Fig. 2.87. Degraded 100 MeV tungsten bremsstrahlung spectrum after traversing various thicknesses of uranium.

88
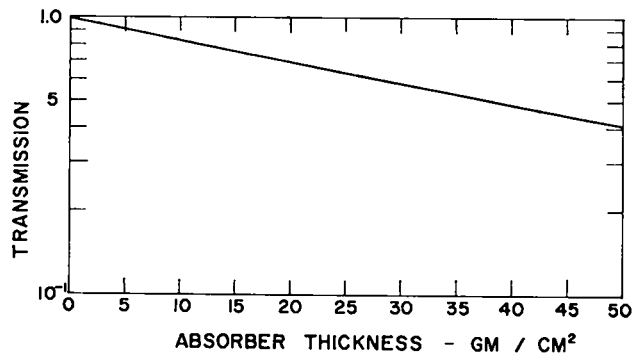
Fig. 2.88.   Transmission of 100 MeV tungsten brems-
strahlung through Composition B.
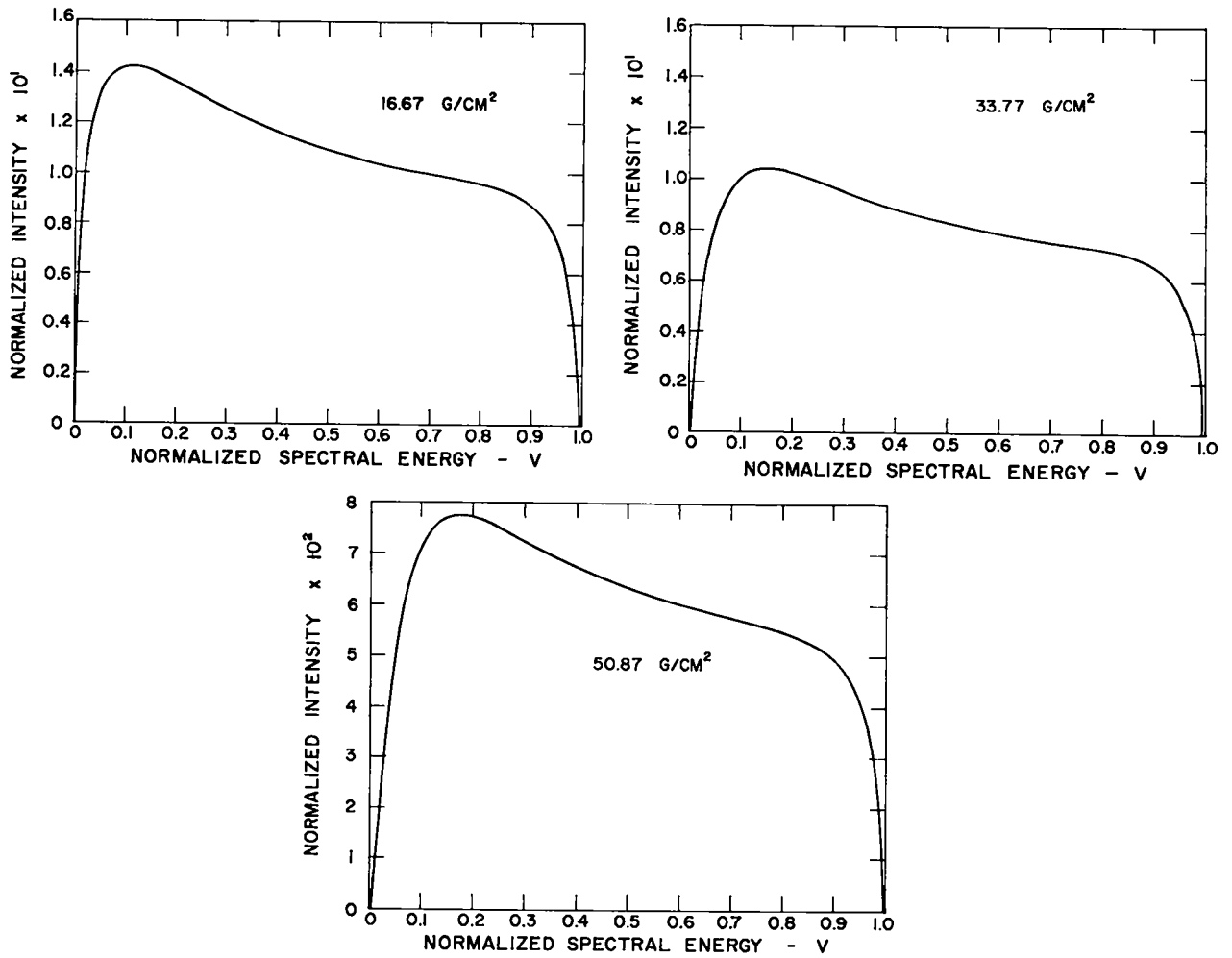
Fig. 2.89.   Degraded 100 MeV tungsten bremsstrahlung spectrum after traversing various thicknesses of Composi-
tion B.

89

NOTES AND REFERENCES

2. 1. Douglas Venable and Leo F. Perry, *Phys. Rev.* **94**, 784(A) (1954).

2. 2. K. T. Bainbridge, M. Goldhaber, and E. Wilson, *Phys. Rev.* **84**, 1260(L) (1951).

2. 3. E. Segre, Ed., *Experimental Nuclear Physics, Vol. 1*, John Wiley and Sons, New York, 1953.

2. 4. F. Bloch, *Ann. Phys.* **16**, 285 (1933) and *Z. Physik* **81**, 363 (1933).

2. 5. H. Bethe and W. Heitler, *Proc. Roy. Soc. (London)* **A146**, 83 (1934).

2. 6. B. Rossi and K. Greisen, *Rev. Mod. Phys.* **13**, 240 (1941).

2. 7. W. Heitler, *The Quantum Theory of Radiation*, 2nd Ed., Oxford University Press, London, 1944.

2. 8. E. J. Williams, *Proc. Roy. Soc. (London)* **A169**, 531 (1939) and *Phys. Rev.* **58**, 292 (1940).

2. 9. G. Molière, *Z. Naturforsch.* **3a**, 78 (1948).

2.10. L. I. Schiff, *Phys. Rev.* **70**, 87 (1946) and **83**, 252 (1951).

2.11. J. D. Lawson, *Proc. Phys. Soc (London)* **A63**, 653 and 780 (1950); *Phil. Mag.* **43**, 306 (1952); *Brit. J. Appl. Phys.* **3**, 219 (1952); and *Nucleonics* **10**, 61 (1952).

2.12. E. G. Muirhead, B. M. Spencer, and H. Lichtblau, *Proc. Phys. Soc. (London)* **A65**, 59 (1952).

2.13. H. Kulenkampff, M. Scheer, and R. Schittenhelm, *Z. Physik* **129**, 202 (1951).

2.14. C. Robert Emigh, LASL, private communications, 1962-64.

2.15. L. Lanzl and A. Hanson, *Phys. Rev.* **83**, 959 (1951).

2.16. K. Siegbahn, Ed., *Beta- and Gamma-Ray Spectroscopy*, Interscience, New York, 1955.

Chapter 3

PHERMEX DESIGN PARAMETERS

by
Douglas Venable

In designing a device such as PHERMEX, two mutually dependent characteristics of the electron stream must be examined. The first of these pertains to the energy spectrum of the ejected electron beam; hence it is related to the energy initially stored in the electromagnetic fields of the accelerator structure and the interaction between these electrons and the fields. The second concerns the selection of stable orbits; hence it is related to the equations of motion and to some extent to the initial distribution of the electromagnetic fields.

The energy extracted from the cavity by the electron beam must be consistent with both the energy stored and the tolerable momentum distribution among the ejected electrons. Once the lower limit of the permissible stored energy has been fixed, the product of wavelength, λ, and peak field strength, E_o, is determined for a given cavity length. An upper limit to field strength in a high vacuum is set where the electron field emission current excessively depletes the stored energy and seriously overloads the rf generators driving the cavity. This limit depends on the properties of the electron emitting surfaces and on the field strength distribution normal to these surfaces. Attainable field strength is more likely to be limited, practically, by rf power amplifier cost and, possibly, by the method of coupling power into the cavity. On the other hand, there is obviously a sensible lower limit to useful field strengths, below which electrical breakdown never occurs; there is no advantage in having lower fields.

As electrons are accelerated, energy flows into them from the electromagnetic field. The result is a depletion of the stored energy and, hence, a decrease in the strength of the accelerating fields. A cycle-to-cycle decay of the electric field strength implies a cycle-to-cycle spread in the space and time distribution of the vector momentum components of the ejected electrons, and hence an aperiodic variation in momentum distribution.

The three-dimensional equations of motion describe particle trajectories through a cavity. These equations account for aperture defects and space charge, both treated as perturbations. An axial magnetic field, as well as the magnetic fields from single-turn loops of arbitrary size — concentric with the cavity — are included to facilitate a study of the effects of various combinations of confining magnetic fields and magnetic lenses. The equations simply describe the motion of an arbitrary electron located on or within a long beam injected into the cavity. This concept, which simplifies the description of radial space charge, neglects axial space charge effects. However, this latter defect is not important in the case of particles injected relativistically about optimum injection phase angles. Injection is discussed in Chapter 5, where beam preparation methods for both continuous and bunched injection are examined; and the advantages and disadvantages of these two general methods of injection are presented.

Before optical devices can be designed to focus the ejected beam to a target, the spatial distribution of momentum among the ejected electrons must be known. This aspect of the accelerator optics is also examined.

91

I. PARTICLE ENERGY — PARAXIAL OPTICS APPROACH

A particle i of charge q_i gains or loses kinetic energy when interacting with electromagnetic fields. The energy of such a particle is given by the energy equation

$$\frac{dU}{dt} = q_i \left(\frac{\partial \psi_i}{\partial t} + \mathbf{u}_i \cdot \mathbf{E}_i \right)$$

(3.1a)

or by an integration of the equations of motion

$$m_0 \frac{d}{dt} \left(\frac{\mathbf{u}_i}{\sqrt{1 - \beta^2}} \right) = q_i (\mathbf{E}_i + \mathbf{u}_i \times \mathbf{B}_i)$$

(3.1b)

For the present discussion, it is sufficient to consider the special case of a particle constrained to the axis. The particle is injected with an energy V_0 into a cavity of length L, where the exciting wavelength is λ, and the peak electric field strength is E_0. In general, the energy of such an on-axis electron, after it has been in transit

$$\Delta\phi = \phi - \phi_0 = \omega \Delta t$$

(3.2)

is given by

$$V = \mu \left[1 + \left\{ \left[\left(\frac{V_0}{\mu} + 1 \right)^2 - 1 \right]^{1/2} \right. \right.$$
$$\left. \left. + \frac{V_g}{2\mu} (\cos\phi_0 - \cos\phi) \right\}^2 \right]^{1/2} - \mu$$

(3.3)

where the axial position z and $\Delta\phi$ are related by

Under the appropriate conditions the electron energy gain $V - V_0$ can approach the limit

$$V_g = \frac{E_0\lambda}{\pi}$$

(3.5)

The cavity length for which this occurs is $\lambda/2$ for a relativistic injection energy, V_0. Aside from the rf drive capability to achieve a predefined E_0, the physical limitation in Eq. (3.5) is that imposed by electron field emission. In reasonably well-prepared systems, the limiting electric field strength may well exceed 50 MV/m in nominal half-wavelength cavities.

For on-axis particles, E_i in Eq. (3.1) is simply $E_0 \sin\phi$, $\phi = \omega t$. The transit angle, $\Delta\phi$, accounts not only for the transit time for an electron to move along the cavity axis toward the far wall, but also for multiple excursions. Thus, V corresponds to the ejection energy only when $\Delta\phi$ is the transit angle across the cavity. It is clear that there is an infinitude of values of ϕ_0, $\Delta\phi$, V_0, and V_g for which an electron cannot reach the far wall of a cavity of length $z = L$ but is turned around somewhere between the bounding end walls and driven into the upstream wall where $z = 0$. Indeed, once L is fixed, $\Delta\phi$ is defined by Eq. (3.4).

Because Eq. (3.3) is general, neglecting space charge effects, it is worthwhile to present in Fig. 3.1 a plot of the peak energy gain, $V_{max} - V_0$, as a function of V_g for several cavity lengths expressed in terms of fractional wavelengths. Superimposed on this figure are points obtained from the literature representing electric field strength values that have been achieved.[3.1-3.4]

$$z = \frac{\lambda}{2\pi} \int_{\phi_0}^{\phi} \frac{\left[\left(\frac{V_0}{\mu} + 1 \right)^2 - 1 \right]^{1/2} + \frac{V_g}{2\pi} (\cos\phi_0 - \cos\phi)}{\left[1 + \left\{ \left[\left(\frac{V_0}{\mu} + 1 \right)^2 - 1 \right]^{1/2} + \frac{V_g}{2\mu} (\cos\phi_0 - \cos\phi) \right\}^2 \right]^{1/2}} \, d\phi$$

(3.4)
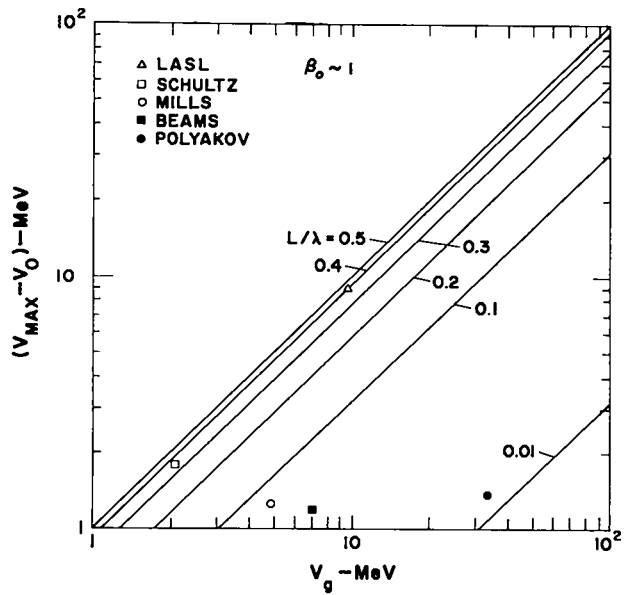
Fig. 3. 1. Beam energy gain vs V_g for relativistic injection.

The numerical data in Fig. 3.1 apply to relativistic injection where $\beta_0 \sim 1$. However, it is not always feasible to enjoy such a large value of β_0 upon injection into the first cavity of an accelerator. Consideration is given to low energy injection in Fig. 3.2, where $\beta_0 = 0$. It is seen
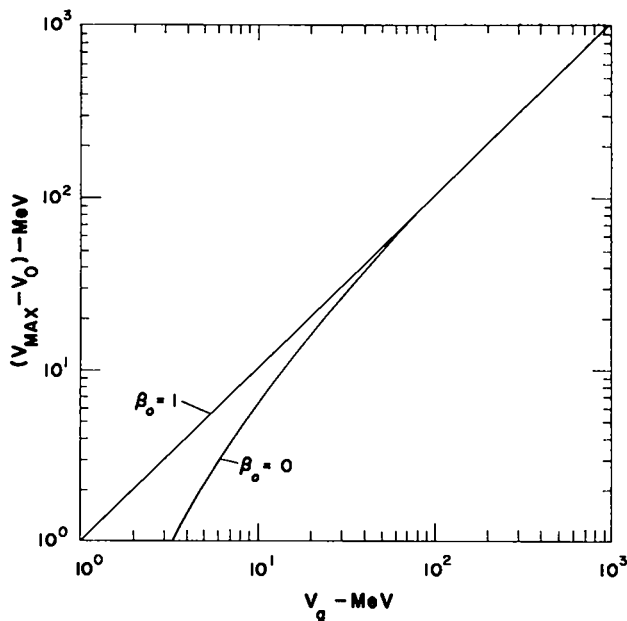
Fig. 3. 2. Comparison of energy gain for relativistic and nonrelativistic injection.

that the voltage gain for nominal half-wavelength cavities is not a strong function of injection energies when V_g is greater than, say, 10 MeV. In a half-wavelength, 50 Mc cavity this value of V_g corresponds to about 5 MV/m field strength.

In those cavities where injection is not sensibly relativistic, nor paraxial, consideration must be given to all the details of the trajectories, since the transit time angle $\Delta\phi$ and particle energy can be seriously affected by off-axis excursions. Even so, Eqs. (3.3) and (3.5) describing the energy of on-axis particles prove very useful for general design purposes. Complete three-dimensional trajectory calculations have demonstrated that, for paraxial optics, where beam radii are very much less than one wavelength, these two energy equations are excellent approximations. In the presence of large space charge forces, the paraxial assumptions become less and less accurate, as will be discussed later.

Another way of displaying the physical meaning of Eqs. (3.3) and (3.4) for paraxial particles is shown in Fig. 3.3 and these curves indicate the energy spread found among the electrons that arrive at the end of a single 50 Mc cavity of length L/λ when injection takes place over a finite range of phase angles, $\Delta\phi_0$. These curves also illustrate the range of E_0, hence V_g, beyond which the effect of V_0 is unimportant for on-axis electrons. The most important conclusion that can be drawn from this discussion is that for paraxial optics, the optical efficiency — defined here as the ratio of ejected charge to injected charge — increases significantly with V_0. This is also true in the general case of off-axis trajectories. For very short bunches of electrons there is an optimum injection phase angle for a given cavity length, the optimum being that phase angle for which the terminal energy, V_t, is a maximum; the maximum terminal energy is also given in the curves of Fig. 3.3.
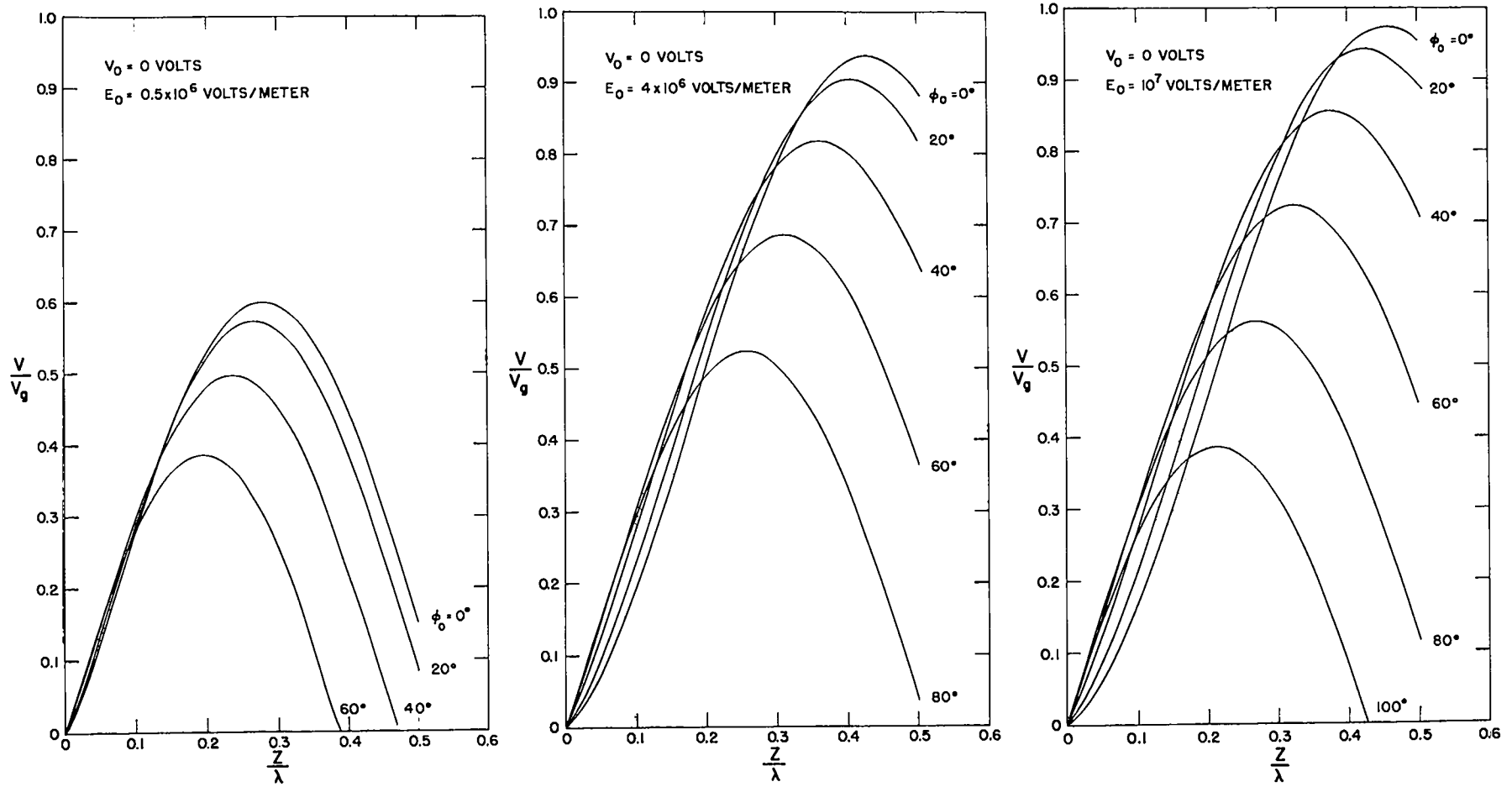
Fig. 3. 3.   Electron energy vs cavity length for several injection parameters.
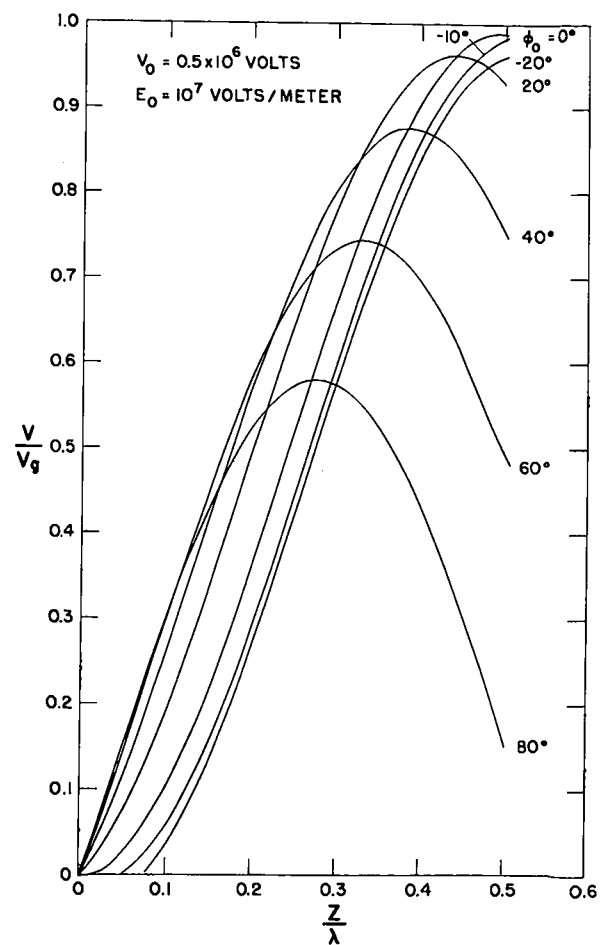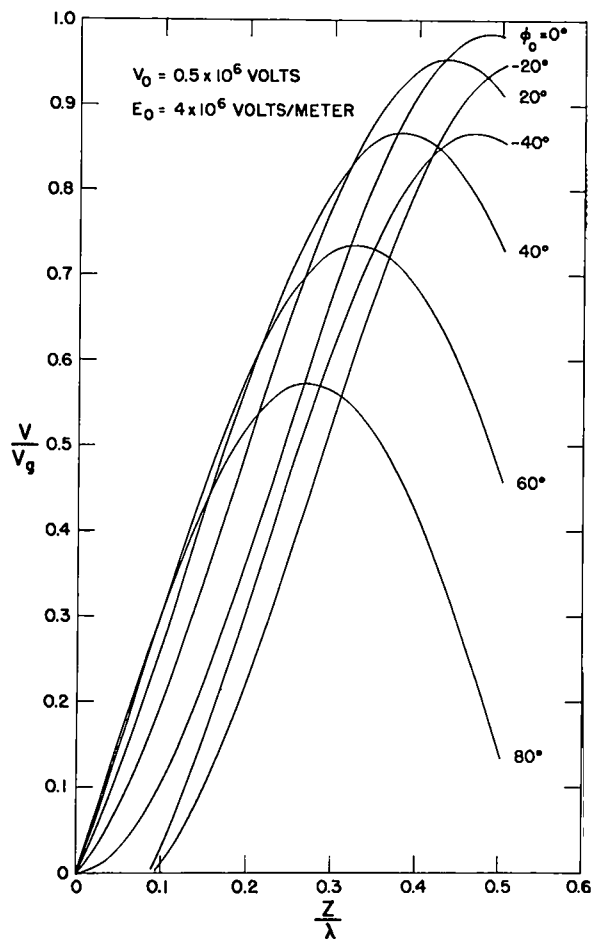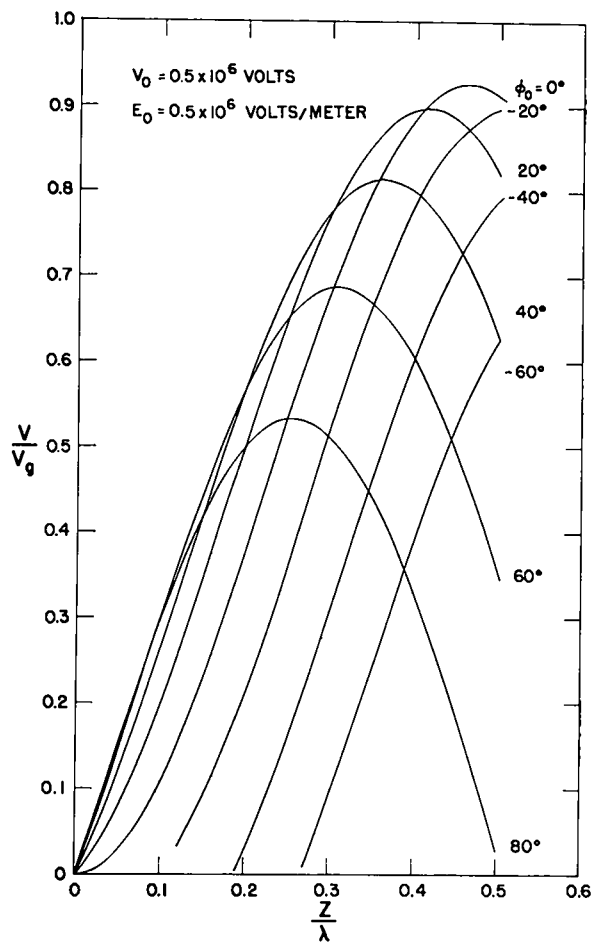
Fig. 3. 3.   Continued.
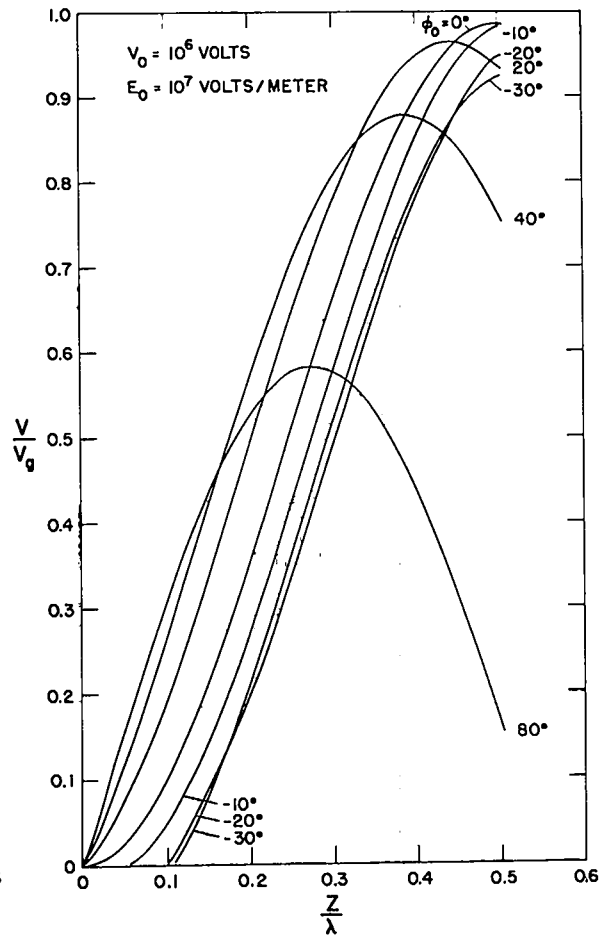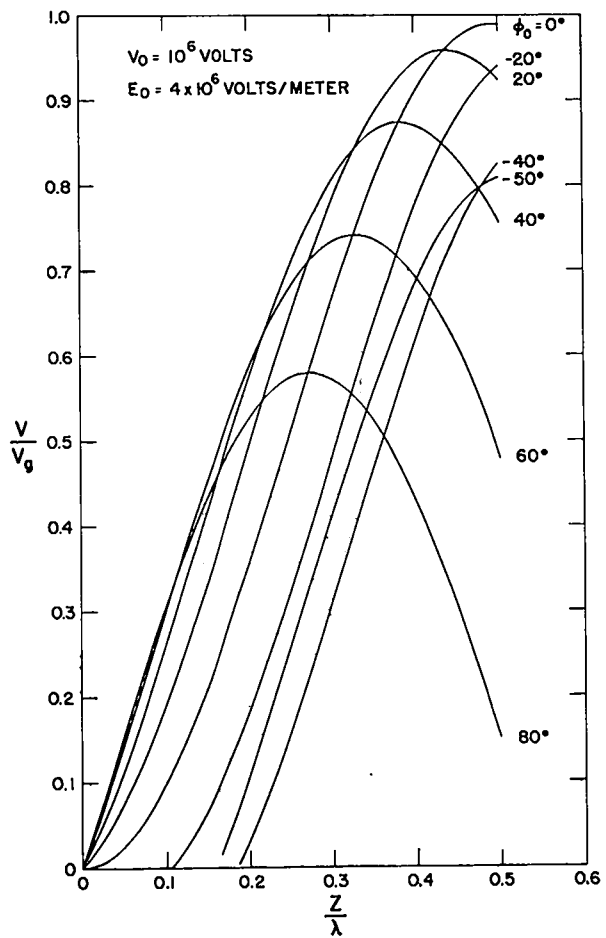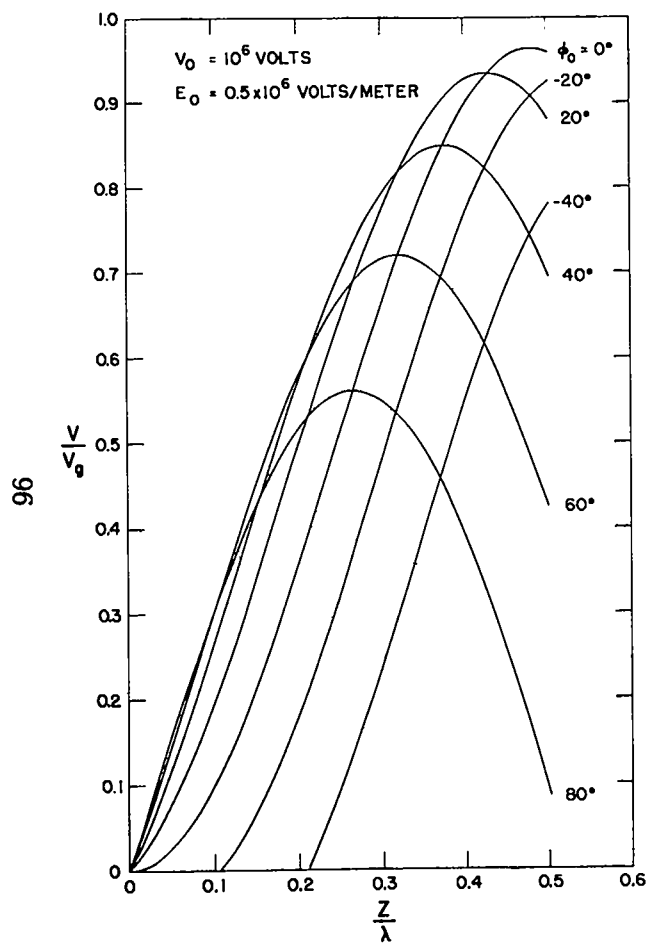
Fig. 3. 3.   Continued.
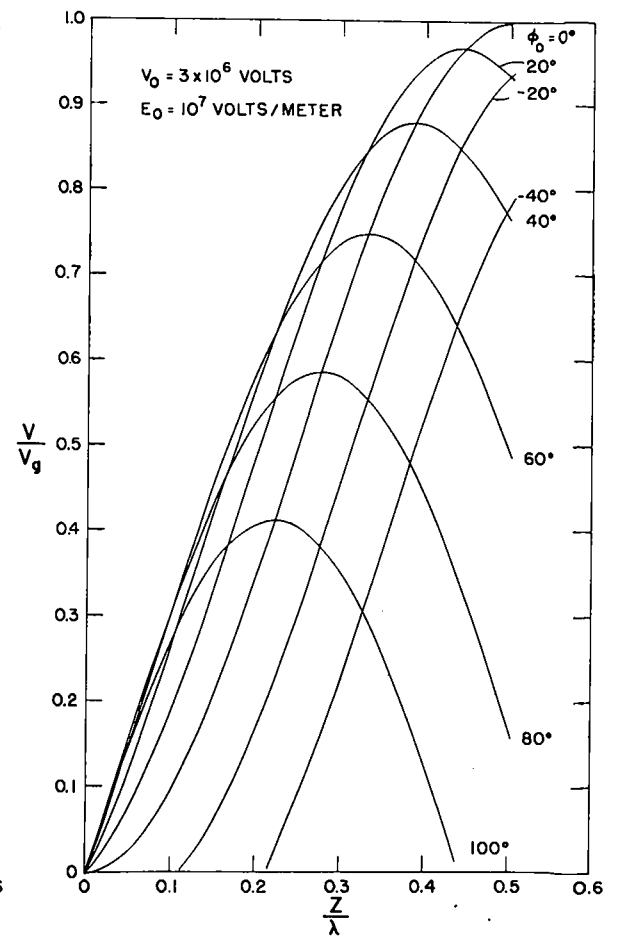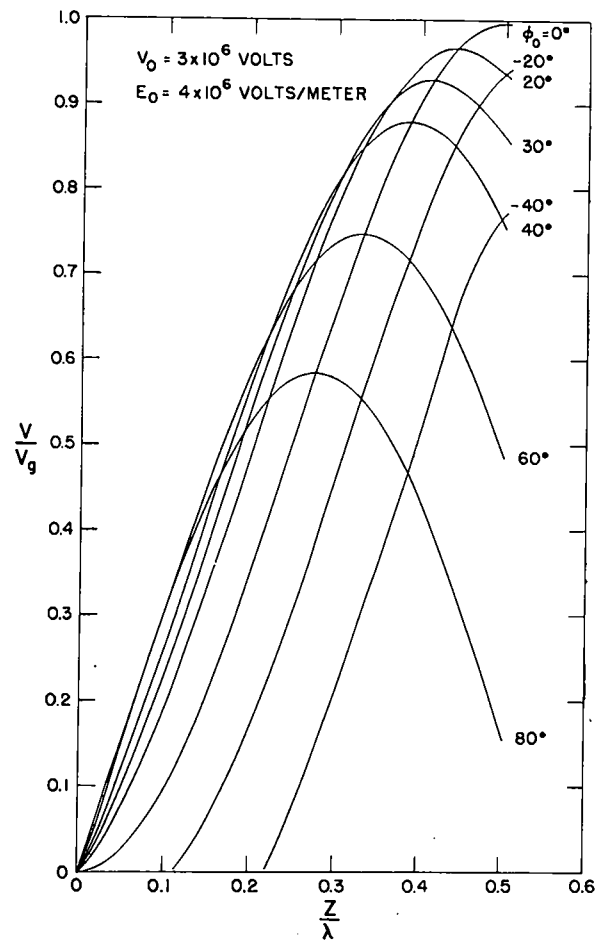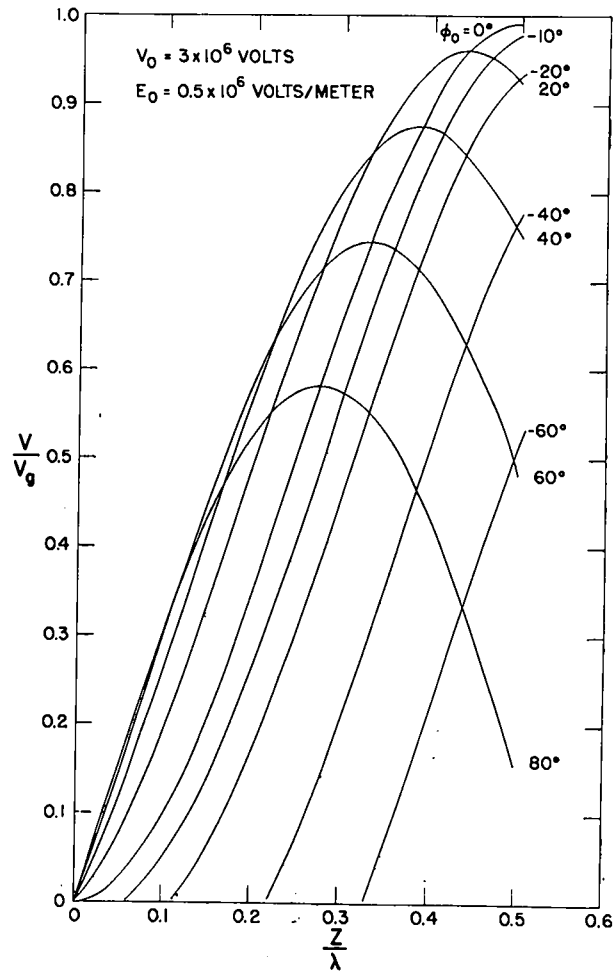
Fig. 3. 3.   Continued.

II. FIELD STRENGTH E_0, WAVELENGTH λ, AND NUMBER OF CAVITIES N

Radiation flux and spectral requirements define, approximately, the quantity of charge, $\triangle q_t$, and the terminal energy, V_t, of the electron beam that must be focused on a target of given material. Thus, the kinetic energy of the beam at the target must be

$$\triangle U_t = \triangle q_t V_t$$

(3.6)

The properties of the ejection electron optical system, including target diameter, further dictate that permissible field variations associated with energy extraction should not exceed some fraction of the initial field strength. In the absence of serious phase defocusing due to axial space charge forces, the optical efficiency, η, of an N-cavity, standing wave accelerator can be made to approach unity if suitably prepared electron bunches are injected within a small angular range about the optimum injection phase angle. These conditions imply that there is a maximum fraction, ξ, of the stored energy that an electron beam may be permitted to extract.

Once ξ has been fixed, the stored energy, hence the product of field strength and the square of the wavelength, can be established simply in this ideal case for each of the N cavities. However, nontrivial space charge effects are inherent with high average beam currents. Hence, the accelerator injector-to-target optical efficiency, η, is always less than unity. In accounting for both ξ and η, the total stored energy must be at least

$$U_0 = \frac{\triangle q_t V_t}{\eta \xi}$$

(3.7)

For a tandem array of appropriately phased, half-wavelength cavities having equal field strengths

$$V_t = N \frac{E_0 \lambda}{\pi}$$

(3.8)

If the cavity length is set proportional to the wavelength, then

$$U_0 = N\kappa E_0^2 \lambda^3$$

(3.9)

It is necessary to determine the basic accelerator parameters E_0, λ, and N. Equations (3.7) through (3.9) define $\lambda^2 E_0$ but not N. An obvious lower limit to N is unity, requiring $E_0\lambda$ to be a maximum. The choice of E_0 for a single cavity then must be consistent with the limiting breakdown field strength within that particular accelerator structure and also with the ability to excite this structure to the desired field strengths. Although the choice of λ depends upon E_0, a lower limit on λ already may be fixed, in a practical sense, by the availability and costs of rf components. An upper limit to N also may be determined from that choice of field strength below which electrical breakdown will certainly never occur in highly evacuated, half-wavelength cavities. Consistent with the acceptability of an extrapolation of Kilpatrick's criterion,[3.5] a maximum number of cavities can be established.

In the case of PHERMEX, calculations of trajectories of representative electrons in high current, bunched beams traversing cavities indicated that η might be as great as 0.8 for feasible injector systems. The properties of the exit optical system limit ξ to a value no greater than 0.1. Thus, the total stored energy should be about 2500 J, and $NE_0\lambda$ should be about $2\pi \times 10^7$ V. The maximum number of half-wavelength cavities was then determined, from Kilpatrick's criterion, to be three for E_0 and λ of about 3.8×10^6 V/m, and 6 m, respectively. Relationships among various parameters are shown in Fig. 3.4. The values of E_0, λ, and N obtained here provided an adequate starting point for more detailed calculations of the final cavity length, field strength, and suitable injection parameters.

A λ of 6 m was fixed early in order to begin designing rf power amplifiers. Because the optimum cavity length is actually somewhat less than a half wavelength, as determined from these simple concepts, a greater value of E_0 is needed. Indeed, for this case, E_0 must be more nearly 4×10^6 V/m. To illustrate this last point the computational data shown in Fig. 3.4 are presented specifically in Fig. 3.5 for 50 Mc cavities of several lengths, where $\beta_0 \sim 1$. Also included for reference are an extrapolation of Kilpatrick's criterion and an experimental point obtained at Los Alamos.

When the original design parameters of this machine were established, more worldly factors than technical ones dictated the choice of operating wavelength. There existed no reliable, rugged tubes with adequate power and duty-factor ratings suitable for this service that were capable of long pulse megawatt power levels at wavelengths less than about 4 to 5 m. On the other hand, the *physical size of a cavity system operating at wavelengths greater than 7 to 8 m was highly unattractive for this particular application.* Thus, the operating wavelength was chosen to be 6 m, a choice compatible with existing technology and commercially available equipment. Hence, it was consistent with minimizing development work.

Fig. 3. 5. Beam energy gain vs field strength for $\lambda = 6$ m.

III. DIMINUTION OF STORED ENERGY

Energy continually flows between cavity fields and injected electrons. In general, the terminal energy of an electron does not represent the maximum energy it acquired during its flight. The energy, $(\Delta U_i)_{max}$, is defined here as the maximum energy gained by the ith electron during the jth excursion, energy being radiated by the electron when it is decelerated. More than one excursion may occur before the particle is lost to the bounding walls. Obviously, this may happen during multiple excursions in which an injected particle may first be accelerated, then be slowed down, fail to reach the far wall, and finally be turned around and driven upstream.

The portion of the deceleration radiation energy that has suitable frequency components and phase relations with respect to cavity fields will reinforce the fundamental cavity fields or excite other modes. However, in high-Q cavities without coherent deceleration, this reradiation could, at best, represent a discouragingly small fraction of the deceleration energy. Therefore, field reinforcement is neglected in the following discussions. Cavity field depletion measurements substantiate this conclusion.

WAVE LENGTH—METERS

Fig. 3. 4. Field strength requirements vs operating wavelength for various numbers of half-wavelength cavities.

99

The maximum energy, ΔU, extracted from the cavity fields by the injected charge, i.e., the beam loading per cycle, is obtained by summing all $(\Delta U_i)_{max}$ experienced both by particles injected during one period and by residual particles that were injected earlier. This includes those $(\Delta U_i)_{max}$ which also arise as a result of multiple excursions. In general, there is no closed analytic expression that describes $(\Delta U_i)_{max}$; however, these values may be obtained through numerical integration of the equations of motion. Indeed, this is the method that was employed for the electrons in nonparaxial beams. For the case of paraxial optics, neglecting cavity wall losses and the input power, the field energy diminution, ΔU, associated with the charge, Δq, injected during one cycle can be written as the product of Δq and a mean energy $\overline{V}$ defined below. Here, ΔU is limited to a small fraction of the stored energy.

$$\Delta U = \Delta q \overline{V}$$
(3.10)

where

$$\Delta q = I_0 \tau f$$

is the charge injected at a constant rate, I_0, over a fraction, f, of a cycle of period τ; and where

$$\overline{V} = E_0 L \int_{\phi_{01}}^{\phi_{02}} g(\phi_0, \Delta\phi) \, d\phi$$
(3.11)

is the mean energy gain of the particles that are injected over the phase angle range ϕ_{01} to ϕ_{02}, accounting for multiple excursions. The term $g(\phi_0, \Delta\phi)$ is a weighting function, determined from numerical computations. This term also accounts for those maxima of $(V - V_0)$ which are permitted for a given transit angle, $\Delta\phi$. Although, for on-axis trajectories, $\Delta\phi$ is an implicit function of V_0, ϕ_0, L, and λ, it is also a weak function of E_0, and, over limited ranges of E_0, permits Eq. (3.11) to be reduced to

$$\overline{V} = k_0 + k_1 E_0^\alpha, \quad \alpha = 1 + \epsilon$$
(3.12)

The constants k_0 and k_1 include the cavity length, L, and depend upon the range of injection phase angles, $\Delta\phi_0 = \phi_{02} - \phi_{01}$. For off-axis trajectories,

$\Delta\phi$ is a strong function of r_0, $\dot{r}_0$, and $\dot{\theta}_0$. Therefore, in general, Eq. (3.11) must be rewritten to include these other parameters. Figure 3.6 shows $\overline{V}$ of Eq. (3.11) for the on-axis conditions of $\Delta\phi_0 = 2\pi$, L = 2.6 m, and $V_0 = 0.5, 1, 2$, and 3 MeV. The term ϵ is a computable number and smaller than unity when injecting over all possible ϕ_0. For sufficiently short electron bunches injected about the optimum phase angle, ϵ approaches zero. Only then does the sum of particle terminal energies correspond to the energy extracted from the electromagnetic fields. Figure 3.6 also illustrates $\overline{V}$ for the case of $\epsilon = 0$, i.e., for injection of short bunches around the optimum phase angle.

On the other hand, when charge injection occurs at a constant rate over an entire cycle, considerable deceleration radiation is generated. If this radiation is absorbed coherently by the cavity in the operating mode, then the net energy extracted per cycle from the electromagnetic fields is the time average of the terminal energies. Experimental studies of field depletion in long cavities clearly demonstrated that there is very little if any field reinforcement from this mechanism.

Of particular interest to PHERMEX design is the fractional energy depletion per cycle per unit current injected. If the initial stored energy is

$$U_0 = k_2 E_0^2$$
(3.13)

where k_2 includes a term λ^2 and the cavity length, L, then, if it is assumed that deceleration radiation does not reinforce the cavity fields,

$$\frac{\Delta U / U_0}{I_0} = \frac{\tau f}{k_2} (k_0 E_0^{-2} + k_1 E_0^{\alpha-2})$$
(3.14)

Typical examples are illustrated in Fig. 3.7 for a 2.6 m long, 50 Mc cavity into which 0.5, 1, 2, and 3 MeV beams are injected over all phase angles. The case of bunched injection about the optimum injection phase angle is shown also.
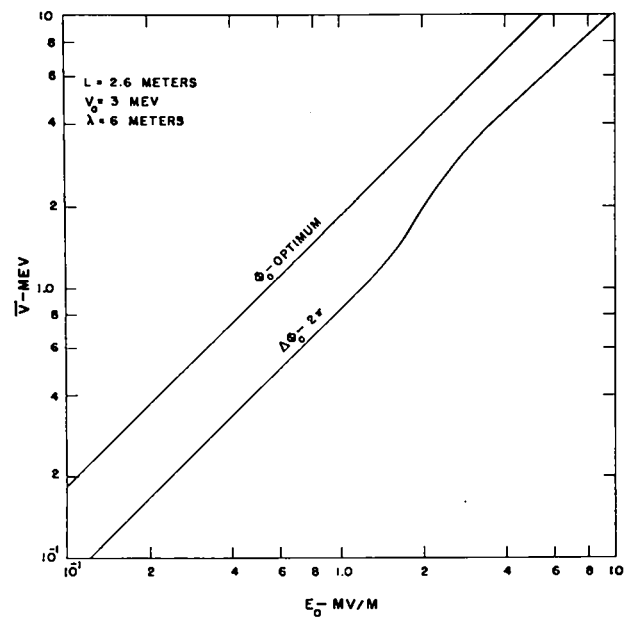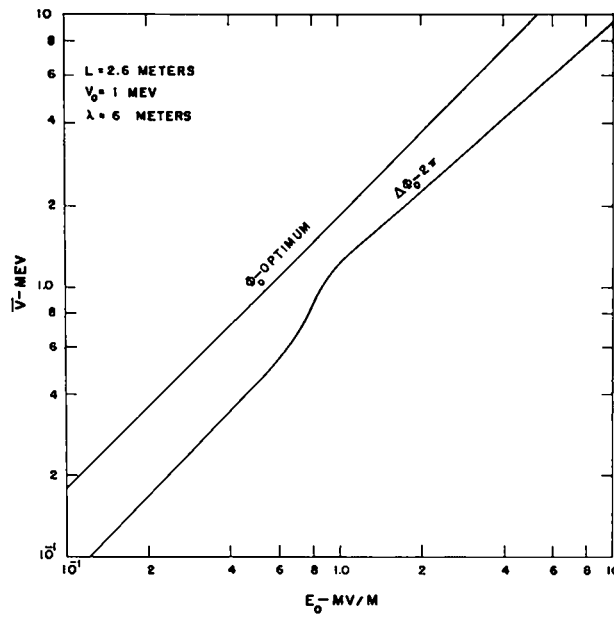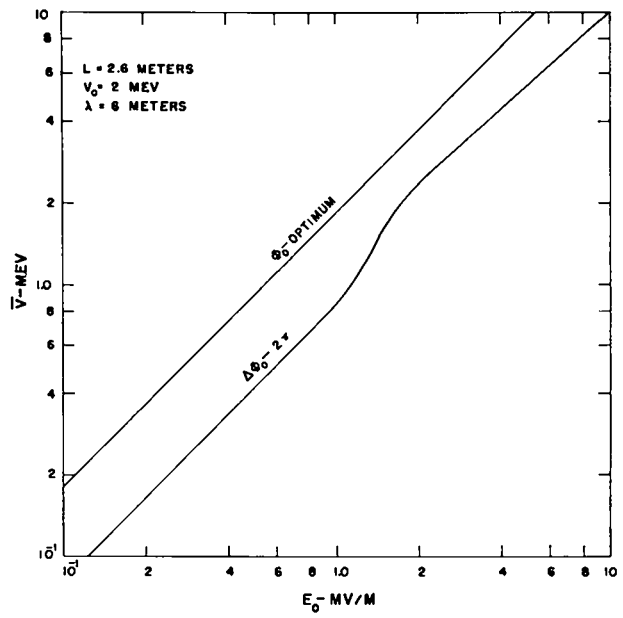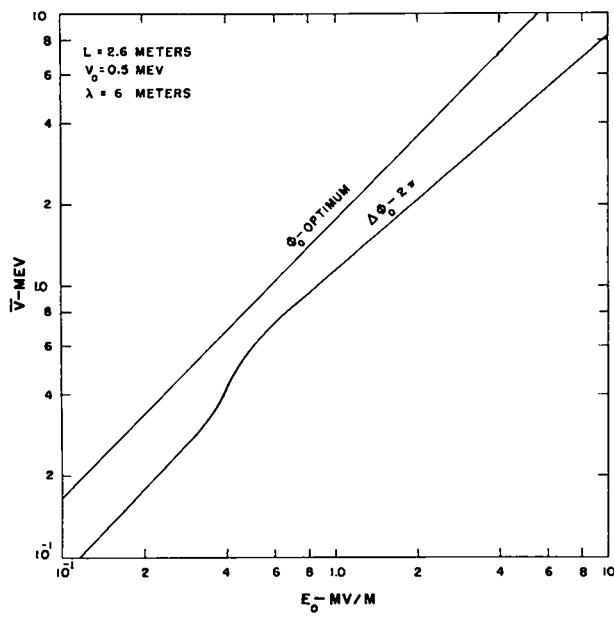
Fig. 3. 6. Mean energy/electron extracted/cycle from cavity.

101
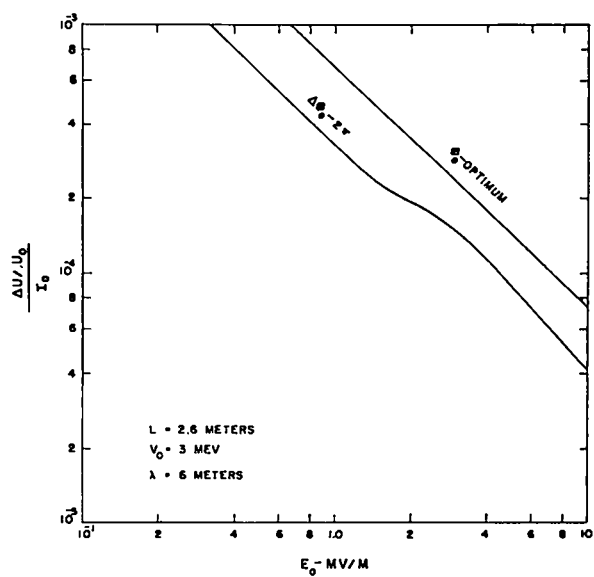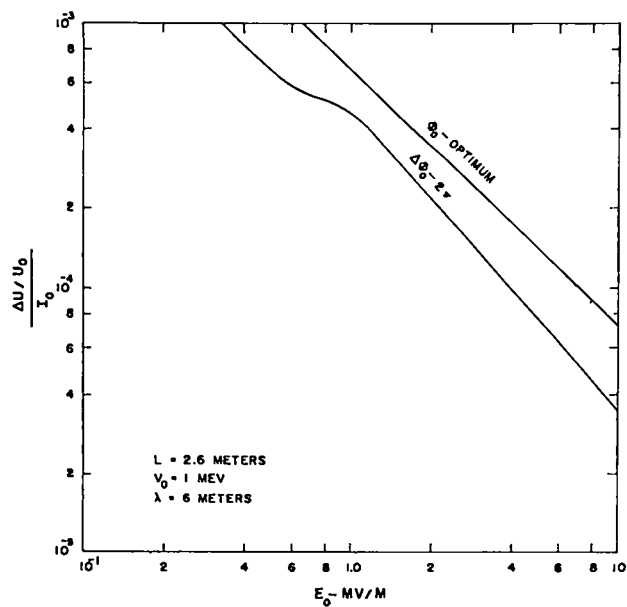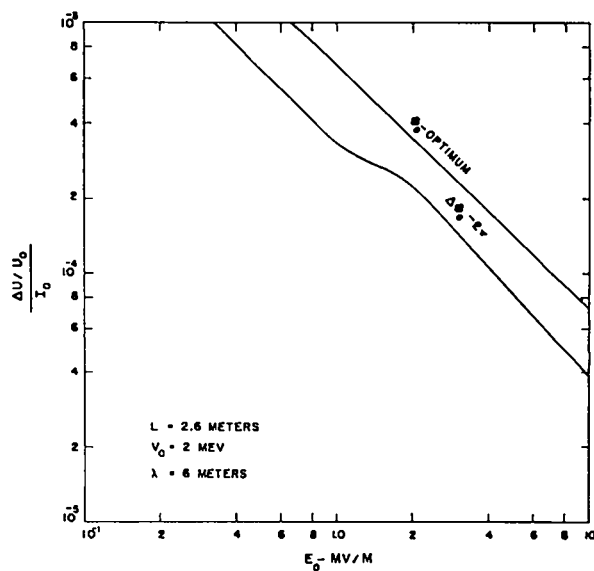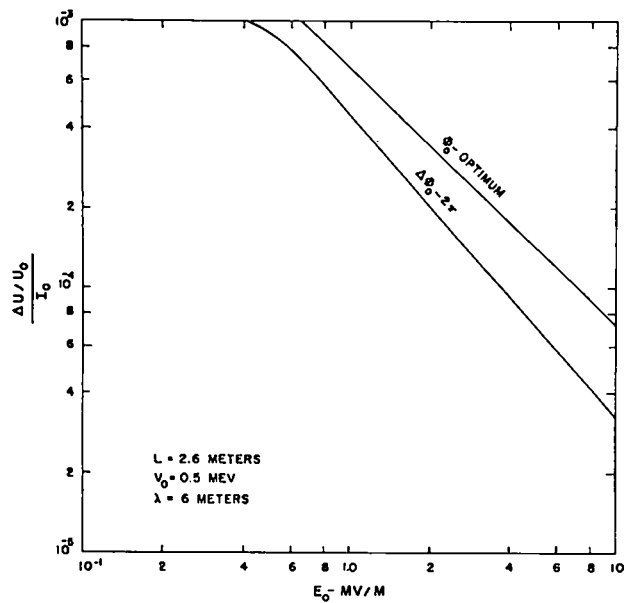
Fig. 3. 7. Fractional stored energy depleted/cycle/ampere.

102

These data are within a few percent of those existing for the same conditions, except $L = 2.4$ m, corresponding to the length of the experimental prototype cavity.[3.6]

The total fractional energy depletion over j cycles is

$$\sum_{i}^{j} \frac{\Delta U_i}{U_0} = 1 - \frac{E^2}{E_0^2}$$

(3.15)

If the fractional energy depletion per cycle is small, and Eq. (3.12) is a valid description of $\overline{V}$, then the cycle-to-cycle fields can be determined from the recursion formula

$$E_{i+1} = E_i \left[1 - \frac{\Delta q}{2k_2} (k_0 E_i^{-2} + k_1 E_i^{\alpha-2}) \right]$$

(3.16)

The injection current is included in the term Δq, as indicated by Eq. (3.10).

Consider the case of the experimental cavity $L = 2.4$ m, where $V_0 = 0.5$ MeV, and $\phi_{02} - \phi_{01} = 2\pi$. Figure 3.8 illustrates the fractional energy depletion over 10 cycles as a function of peak field strength and a constant injected beam current, I_0. Experimental points were obtained for which the fractional energy depletion over 10 cycles, $(\Delta U/U_0)_{10}$, was determined from oscilloscope traces of field decay. A typical cathode-ray oscilloscope trace of the field depletion is shown in Fig. 3.9.

Electric field strength is directly proportional to the output voltage of a pickup loop located at the cavity wall. Furthermore, the difference between the peak electron energy and the injection energy can be computed precisely. A beta-ray spectrometer was used to calibrate E_0. The value for I_0 was obtained from the experimentally determined volt-ampere characteristics of the injector.

To a close approximation, Eq. (3.15), using Eq. (3.16) where adequate, has been confirmed for a total fractional energy depletion as great as 50% over 10 cycles. Indeed, this result of the diagnostics agrees closely with the small-signal theory predictions used here.

It is noted that $U_0/\Delta U$, whose inverse is seen in Eq. (3.14), is a measure of the loaded Q of the cavity. Within a reasonable approximation, these expressions for energy depletion also agree with the work of Khizhnyak et al.[3.7]

Energy considerations, although necessary, are insufficient. Except in a gross sense, they contribute nothing to a description of those electron trajectories that are ultimately accessible to the target. However, if the cycle-to-cycle energy extraction, hence the field decay, is too great, beam trajectories must be considered for each cycle during which beam injection occurs. For completeness, the equations of motion must be solved quite generally. Thus, for a given set of injection and operating parameters, the spatial momentum distribution among particles can be determined for any time. Of the beam particles injected continuously during any one cycle, only a fraction is accessible to the target. Although the differential equations of motion describe at any instant of time where a particle wants to go, it is the integral solution that tells where a particle has been.
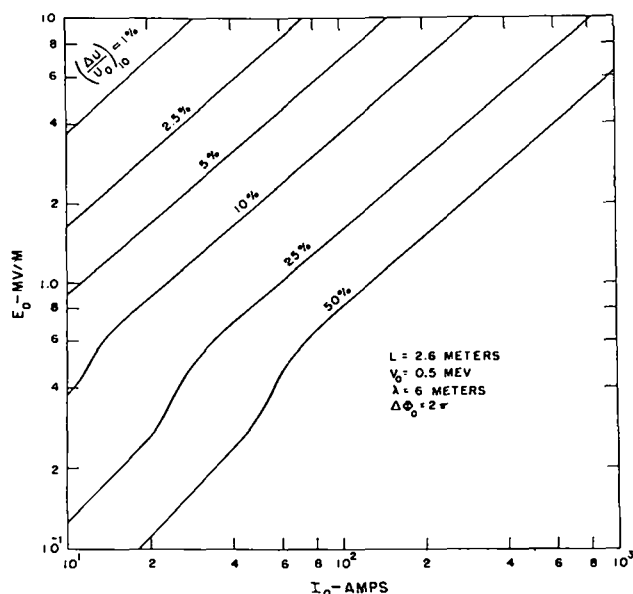
Fig. 3. 8. Fractional energy depletion for ten-cycle injection.

103
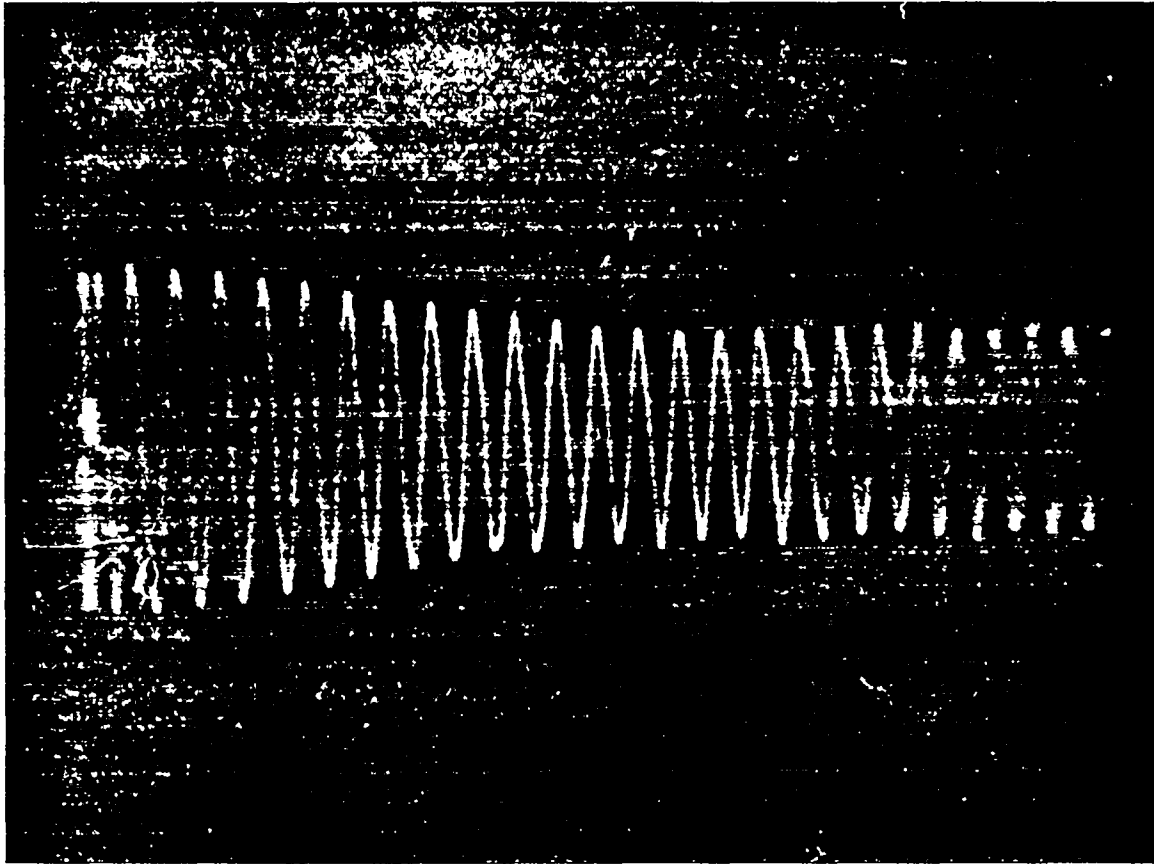
Fig. 3. 9. Oscilloscope trace showing cavity field depletion with injection current.

IV. EQUATIONS OF MOTION

Two previous relevant papers have discussed the dynamics of charged particles in multicavity accelerators.[3.7,3.8] Gabor limited his treatment to very low current relativistic paraxial beams lying near the axis with negligible beam loading of the accelerator.[3.8] Linearizing the equations of motion was accomplished by assuming that both the beam convergence and the changes in beam convergence were everywhere very small. Solution of his final equations also inherently implied that the particle energy gain per cavity was a small fraction of the mean particle energy. Space focusing, phase focusing, transit time considerations, and first-order aperture effects were examined in the absence of space charge. In effect, he treated each cavity as an optical entity possessing characteristics that contributed to both stability and instability of the beam. Mathematical strictures imposed upon his analysis were sufficiently severe that the resulting beam stability criterion sharply limited the range of useful design parameters.

Somewhat over a decade later, Khizhnyak et al. published their study of a multicavity linear accelerator.[3.7] These authors added two considerations: weak space charge fields and energy depletion. Space charge effects were included in the radial equation of motion assuming a constant charge density consistent with highly paraxial beams. Although Khizhnyak et al. approximately matched the nonrelativistic and relativistic regimes, their treatment, like Gabor's, is essentially aimed at highly relativistic electrons.

104

In both these papers, the resulting equations of motion, linearized in a similar way, are two dimensional in r and z. Neither axial nor radial components of possible superimposed magnetic fields were considered, so that no account could be made of azimuthal motion. Thus, neither of these earlier treatments could cope with the effects on space and phase focusing of various magnetic field configurations that might facilitate high current beam confinement within an accelerator. Furthermore, adherence to strictly paraxial motion, although perhaps both desirable and necessary for accelerators with very many cavities, constrained the defined design parameters in both studies to a more restricted range than is necessary in a high current electron accelerator having only a few cavities, such as PHERMEX. In neither of these papers was the space and time distribution of momentum among particles given serious consideration. Yet the capability to focus ejected charge, one of the primary design objectives of PHERMEX, is completely dependent upon the spatial distribution of momentum and charge density at the time of beam ejection.

The restriction to highly paraxial optics, where azimuthal motion has been precluded, is one of several limitations necessary to linearize the equations of motion given by Gabor and Khizhnyak. However, that this restriction is unnecessary and often much more severe than required for actual design purposes has been borne out by experimental diagnostic work at Los Alamos.

Approximate PHERMEX design criteria of operating wavelength, cavity length, minimum field strength, and maximum number of cavities appropriate to the desired machine specifications have been determined by rather simple energy considerations in earlier sections. Energy considerations alone do not constitute a complete or sufficient description of the machine properties; for example, trajectories of energetic electrons that are accessible to the target are not defined. Therefore, it is necessary to determine an achievable time-space distribution of momentum among injected electrons such that, consistent with these design criteria, a maximum useful radiation flux is obtained from a target of fixed size. If the predicted maximum does not satisfy the radiographic demands of the machine, then the design criteria must be readjusted, and the computational pro-

cedure must be repeated. To this end, both particle dynamics and beam energetics were simulated by high speed computer techniques. The three vector components of the Lorentz force equation, expressed in cylindrical coordinates, were solved simultaneously with digital computers. The electromagnetic fields used in the computer codes accounted for the cavity fields of the TM_{010} mode, space charge forces, self-magnetic fields, and certain externally imposed but azimuthally symmetrical confining fields. Aperture defects were also included. Thus, in principle, one can synthesize various momentum distributions among the injected electrons, since it is possible to follow representative points throughout their trajectories within the accelerator and to determine which of those electrons accessible to the target lie within a desirable range of terminal momenta. In essence, the computer can follow representative particles from the electron gun to their termini.

Aperture dimensions were kept small in comparison to the operating wavelength, so that the aperture field defect, confined to the immediate vicinity of the aperture, could then be described by a variation of Davisson's weak lens formula.[3.9] A more elaborate treatment of the aperture field, similar to that suggested by Coleman,[3.10] was also devised. However, this latter scheme offered no useful improvement over the analytically simpler aperture approach. The aperture defect is highly localized, as illustrated in Fig. 3.10, which shows the distribution of the on-axis field and its first space derivative in the vicinity of the injection aperture for an accelerative field
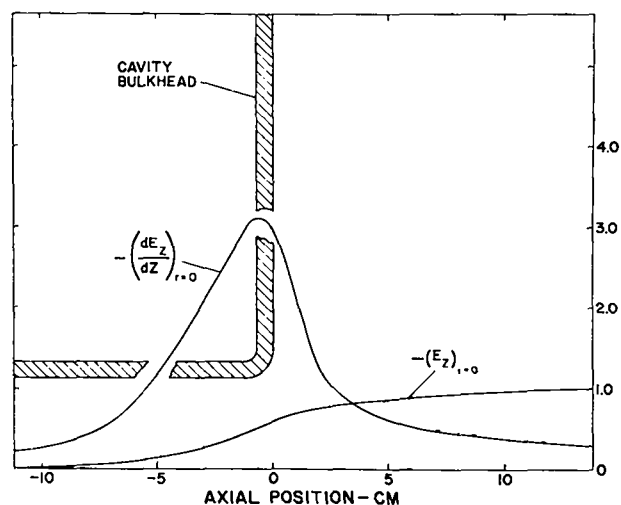
Fig. 3.10. Aperture field distribution.

105

configuration. The computer codes were so arranged that an aperture defect could be introduced in the plane of each aperture. Thus, depending upon the direction of the electric field of the cavity and upon the injection phase angle, an electron could receive a positive or negative contribution to its initial radial momentum according to Eq. (3.17).

$$\Delta \dot{r} = \frac{cr}{2\mu}\left[\left(\frac{V}{\mu} + 1\right)^2 - 1\right]^{-\frac{1}{2}}(E_2 - E_1)$$

$$(3.17)$$

where E_1 and E_2 are the axial components of the electric field strength which would exist on the upstream and downstream sides, respectively, of the aperture (in the absence of the aperture); and where V is the energy of the particle upon entering the aperture. Equation (3.17), a relativistic modification of Davisson's lens formula, shows that the higher the injection energy the less important the aperture defect.

Because the cavity is excited in the TM_{010} mode, the accelerating fields are independent of the cavity length. Thus, the cavity fields can be described by the following two equations:

$$E_z = E_0 J_0\left(2\pi \frac{r}{\lambda}\right) \sin \omega t$$

$$(3.18)$$

and

$$B_\theta = \frac{E_0}{c} J_1\left(2\pi \frac{r}{\lambda}\right) \cos \omega t$$

$$(3.19)$$

Space charge effects are accounted for as a trajectory perturbation, not necessarily small, for those electrons which are injected over a favorable range of injection phase angles. The group of electrons lying within these favored injection phase angles can be treated as a cylinder of charge having a large length-to-diameter ratio.

This assumption is also reasonable for paraxial, but not necessarily parallel, flow in small diameter beams. Indeed, laboratory measurements of the time-average current and current density distribution within ejected beams demonstrated the validity of trajectory predictions for those

electrons emerging from the exit aperture of a single cavity, even when the implied paraxial constraint was neglected.

Internal field distributions were computed for long, cylindrical bunches of electrons having a uniform charge density.[3,11] The results of these determinations indicated that end effects were not serious if the diameter-to-length ratio, when viewed from a frame at rest with respect to the electron bunch, was kept small. Figure 3.11, illustrating the topology of space charge fields, shows surfaces of constant space charge field components, E_r and E_z, for a right circular cylinder of uniform charge density. Except for the charge located very near the ends of such a bunch, the trajectories of the remaining charges are affected primarily by radial space charge forces and negligibly by axial space charge forces. Thus, the space charge perturbation field existing over most of the bunch length can be described adequately by the approximation

$$E_r = \frac{I_0}{2\pi r}\sqrt{\frac{\mu_0}{k_0}}\left[1 - \left(\frac{V_0}{\mu} + 1\right)^{-2}\right]^{-\frac{1}{2}}$$

$$(3.20)$$

where I_0 is the injected current situated within the radius, r, at an energy V_0. Axial space charge fields associated with the nonparallelism of the beam are insignificant. Self-magnetic fields, described by the relation $\mathbf{B} = \mathbf{u} \times \mathbf{E}/c^2$, were accounted for. Forces arising from these magnetic fields tend to reduce the effect of the radial space charge of Eq. (3.20). Because of axial space
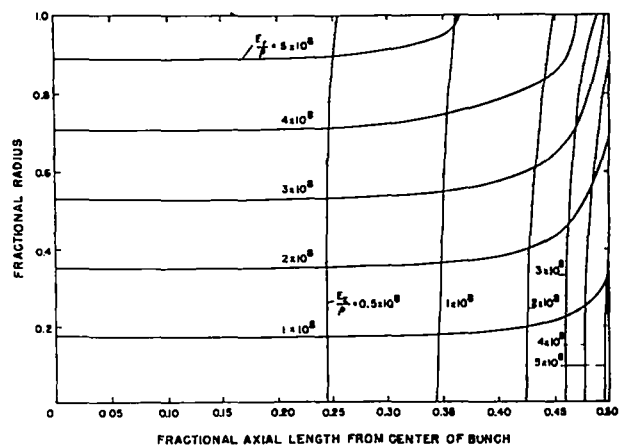
Fig. 3.11. Electric field topology within a cylindrical charge of uniform charge density.

charge forces associated with end effects, as shown in Fig. 3.11, one necessary consideration in choosing the injected bunch length is that the length, measured in terms of injection phase angles, must be somewhat greater than the favorable range of injection phase angles.

The computer codes describing beam trajectories also accounted for externally imposed, beam-confining magnetic fields; these included fields arising from two separate sources: one, a simple, time-constant, spatially uniform axial magnetic field; and the other, a time-constant field also, generated by two multiturn loops whose axes were coincident with the cavity axis. Furthermore, the location outside each cavity and the radius of each coil were arbitrary. This geometric arrangement, as well as a typical distribution of the axial component of the magnetic field, is shown in Fig. 3.12. Thus, with sufficiently large coils, one placed at each end of a cavity, a fairly realistic beam-confining magnetic field distribution graded from injection to ejection could be described analytically and included within the equations of motion.

The computer code description of the Lorentz force equation included aperture defects, cavity fields defined by the TM_{010} mode, space charge and self-magnetic fields, various magnetic-confining fields, cavity length, operating wavelength, and particle specific charge. The resulting radial, azimuthal, and axial force equations were solved by a Runge-Kutta scheme using high speed digital computers.

The computer output gave the representative particle positions, in three-space and time; the three momentum components and energies; and the various electromagnetic fields sensed by the particle in that position at that instant. Thus, the complete trajectory of a representative injected electron having an arbitrary initial position in time (or injection phase angle), configuration, and momentum space could be studied in detail. Furthermore, from these data one could obtain information on field depletion by virtue of the injected electrons as well as by multipactoring.
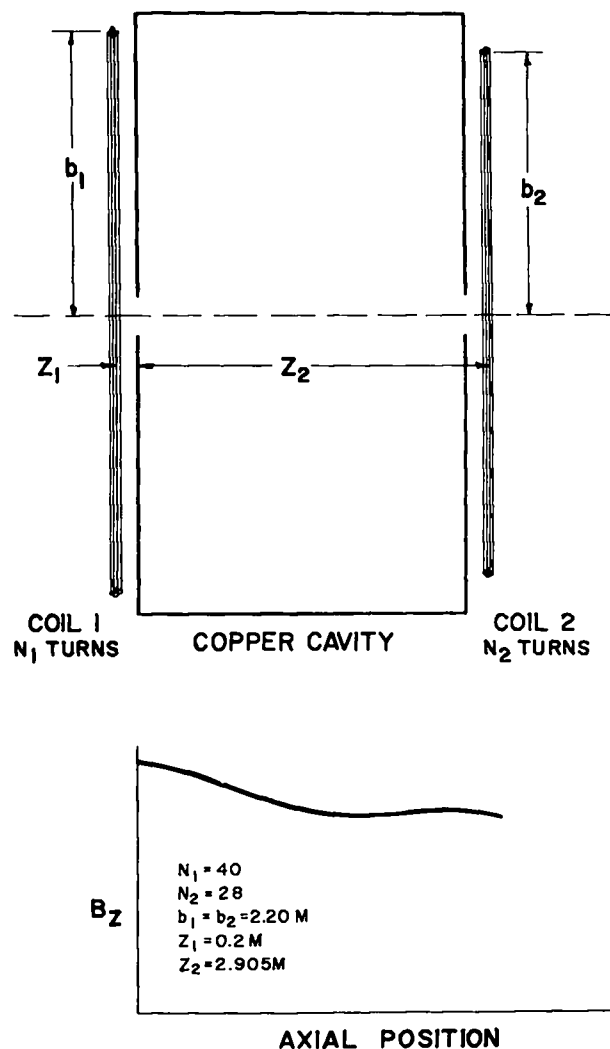
Fig. 3.12. Typical magnetic confining coil configuration and magnetic field distribution.

Thus, the field depletion due to off-axis particles was determined and was found to be very nearly equal to that of the on-axis particles when their radial position was always small compared with a wavelength. Numerical studies and experimental work indicated that multipactoring at design fields in the nominal half-wave cavities of PHERMEX is negligible. The three equations of motion employed in the computer code to describe the beam properties are given below in terms of the cavity fields and the externally impressed magnetic fields:

$$\frac{d}{dt}\left(\frac{\dot{r}}{\sqrt{1-\beta^2}}\right)$$

$$-\frac{r\dot{\theta}^2}{\sqrt{1-\beta^2}} = \eta\left[E_r\left(1-\frac{r^2\dot{\theta}^2}{c^2}\right.\right.$$

$$\left.\left.-\frac{\dot{z}^2}{c^2}\right) + r\dot{\theta}B_z - \dot{z}B_\theta\right]$$

$$(3.21)$$

$$\frac{1}{r}\frac{d}{dt}\left(\frac{r^2\dot{\theta}}{\sqrt{1-\beta^2}}\right) = \eta\left[\frac{r\dot{r}\dot{\theta}}{c^2}E_r\right.$$

$$\left. + \dot{z}B_r - \dot{r}B_z\right]$$

$$(3.22)$$

$$\frac{d}{dt}\left(\frac{\dot{z}}{\sqrt{1-\beta^2}}\right) = \eta\left[E_z\right.$$

$$\left. + \frac{\dot{r}\dot{z}}{c^2}E_r + \dot{r}B_\theta - r\dot{\theta}B_r\right]$$

$$(3.23)$$

where E_z, B_θ, and E_r are given by Eqs. (3.18), (3.19), and (3.20), respectively; and B_r and B_z are the radial and axial components of the externally applied magnetic fields. The B_r and B_z are functions of the on-axis component of B_z, and for this two-lens system have the following forms:

$$B_r(r,z) = -\frac{B_{z0}^I}{2}r$$

$$+ \frac{B_{z0}^{III}}{2^24}r^3 - \frac{B_{z0}^V}{2^24^26}r^5 + \cdots$$

$$(3.24)$$

$$B_z = B_{z0} - \frac{B_{z0}^{II}}{2^2}r^2 + \frac{B_{z0}^{IV}}{2^24^2}r^3 - \cdots$$

$$(3.25)$$

where the on-axis field has the form

$$B_{z0} = B_{00}$$

$$+ 2\pi \times 10^{-7}\sum_1^j \frac{(NI)_i b_i^2}{[b_i^2 + (z-z_i)^2]^{3/2}}$$

$$(3.26)$$

and

B_{00} = superposed constant axial field
$(NI)_i$ = ampere-turns in the ith lens coil
z_i = axial position of the ith lens coil
b_i = radius of the ith lens coil
j = number of lens coils

Beam models and the computational method for solving the equations of motion are described in Chapter 4. Numerical solutions of the equations are presented in Chapter 5, together with discussions of injection, orbit stability, and space charge effects.

V. BEAM COLLIMATION AND OUTPUT RADIATION

The emerging electron beam is collimated with a short, strong-focusing magnetic lens that directs the most useful electrons to the focusing lens. Many electrons are eliminated by this process. Therefore, instead of permitting them to terminate on the stainless steel vacuum walls of the drift tube, beryllium collimators are used. The final beryllium collimator, located just upstream from the target, has a tapered hole, with the smaller diameter being 3 mm. Thus, the beam impinging upon the target is no larger than this minimum diameter.

Engineering details of the overall optical system, including the beryllium collimators and the target blast shielding, are discussed in Chapter 6. Typical radiation intensity angle distributions were discussed in Chapter 2. Figure 3.13 shows the variation of the forward intensity bremsstrahlung as a function of beam energy. Data from the literature and a measured point for PHERMEX are included in the figure.

Calculations had demonstrated clearly that higher injection energies and higher accelerating fields concomitantly enhance the electron optical efficiency in high current, standing wave electron accelerators. Although the initial design fields were chosen to be 4×10^6 V/m in each cavity, to be attained by means of two amplifiers on each of the three cavities, provisions were made for installing a total of nine amplifiers, in the event that three more amplifiers were deemed worthwhile. In the first development phase of PHERMEX the beam energy was about 20 MeV, with 75 A ejected from the last cavity and with about 15 A delivered to a target located 10 m away.
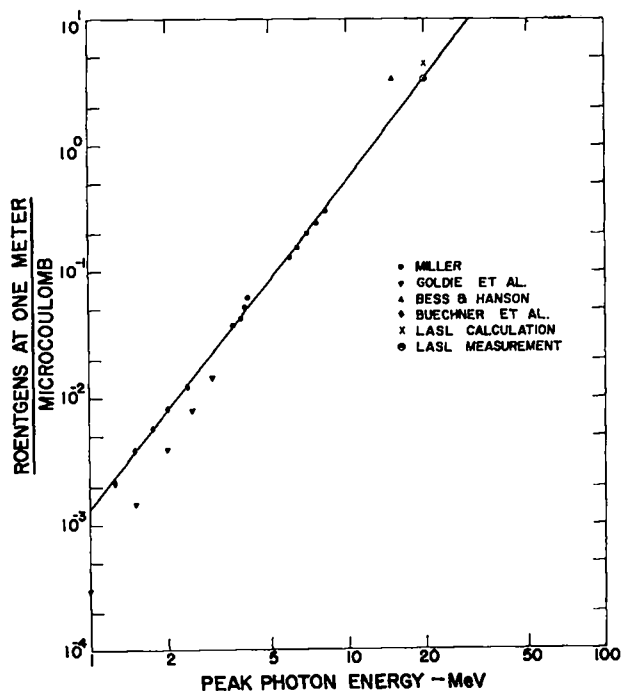
Fig. 3.13. Roentgen per coulomb vs peak photon energy.

PHERMEX operated very satisfactorily for almost 2 years under these conditions, occasionally providing as high as 10 R/0.2 μsec pulse or 5 R/0.1 μsec pulse. However, there were many worthwhile and needed experiments that were marginal with this available flux and intensity. Therefore, three more amplifiers were added so that fields would be 6×10^6, 5×10^6, and 4×10^6 V/m in the first, second, and third cavities, respectively. Although this work is not quite completed, it can be reported that the beam energy is about 27 MeV and an on-axis radiation intensity as high as 30 R/0.2 μsec pulse has been measured 1 m from the target.

With regard to this kind of device as a generator of bremsstrahlung, the following remarks, although specifically applicable to single-cavity devices, are also germane to multicavity, standing wave accelerators. The total radiation flux varies as the production efficiency and as the delivered charge. The production efficiency is a function of particle energy; hence, it is a function of the electric field, too, whereas the ejected charge varies as the square of the accelerating field. On the other hand, the on-axis radiation intensity varies as the production efficiency, and as the charge delivered, and approximately as the square of the beam energy.

Thus, the total radiation flux varies as the product of the radiation production efficiency and the square of the accelerating field strength; the on-axis radiation intensity varies as the product of the radiation production efficiency and the fourth power of the accelerating field strength. It is to be noted that, to a first approximation, the cost of a standing wave device varies as the square of the field strength. Therefore, one can make a rough comparison of cost versus need for standing wave bremsstrahlung generators.

REFERENCES

3. 1. L. B. Snoddy and J. W. Beams, *Phys. Rev.* **74**, 126 (1948); *Phys. Rev.* **75**, 1324 (1949).

3. 2. B. Y. Mills, *Proc. Instn. Elec. Engrs. (London)* Pt. 3, **97**, 423 (1950).

3. 3. H. L. Schultz and W. G. Wadey, *Rev. Sci. Instr.* **22**, 383 (1951).

3. 4. B. J. Polyakov, B. T. Zarubin, and V. V. Kushin, Intern. Conf. High Energy Accelerators, CERN, 670 (1950).

3. 5. W. D. Kilpatrick, *Rev. Sci. Instr.* **28**, 824 (1957).

3. 6. Douglas Venable, *Rev. Sci. Instr.* **33**, 456 (1962).

3. 7. N. A. Khizhnyak, V. T. Tolok, V. V. Chechkin, and N. I. Nazarov, *Soviet J. At. Energy* **11**, 34 (1961).

3. 8. Dennis Gabor, *Rev. Opt.* **29**, 209 (1950).

3. 9. C. J. Davisson and C. J. Calbick, *Phys. Rev.* **38**, 585 (1931); **42**, 580 (1932).

3.10. P. D. Coleman, *Electron Acceleration and Bunching with a Single Microwave Cavity To Energies of 1 to 1.5 Million Electron Volts*, Electrical Engineering Research Laboratory, Engineering Experimental Station, University of Illinois, Urbana, Illinois, Engineering Report No. 2 (AD-3184).

3.11. Ivan Cherry and Douglas Venable, *Am. J. Phys.* **33**, 243 (1956).

3.12. C. W. Miller, *Atomics* **5**, 254 (1954).

3.13. C. H. Goldie, K. A. Wright, J. H. Anson, R. W. Cloud, and J. C. Trump, ASTM Bull. No. 201, 49 (1954).

3.14. Leon Bess and A. O. Hanson, *Rev. Sci. Instr.* **19**, 108 (1948).

3.15. W. W. Buechner, R. J. Van de Graaff, E. A. Burrill, and A. Sperduto, *Phys. Rev.* **74**, 1348 (1948).

Chapter 4

COMPUTATIONAL MODEL:
GRAPE SEED III

by
D. O. Dickman

Several computational models have been employed to describe various aspects of charged particle trajectories in standing wave accelerators, such as PHERMEX, which operate in the TM_{010} mode. These schemes, summarized in the introductory chapter, have provided considerable survey data with regard to both phase and space focusing of high current electron streams. Indeed, thorough examination of these problems, by means of early models, indicated that phase focusing of the higher energy portion of the particle spectrum was ordinarily not important in a standing wave accelerator containing only a few cavity sections. For this reason, the simpler model, described fully in Chapter 3, has been adequate to provide most of the useful computational data.

The computer code for this model is discussed in detail in this chapter. Not only has this model provided beam trajectories in both configuration space and momentum space, but it has also provided information on the irreversible exchange of energy between the electromagnetic fields of the cavities and the injected electrons. This latter computational contribution has agreed with experimental measurements of energy depletion of cavities which has been as great as 10% per cycle.

The computer code for this model is named GRAPE SEED III. With the exception of the Runge-Kutta integration routine, the entire code is written in FORTRAN IV language. The present code was designed to run on the IBM-7094 computer under the IBSYS operating system. A complete listing of GRAPE SEED III is given in Appendix 4A. The code considers a representative particle and follows its path through an accelerator cavity, computing the attendant fields at each point. Provisions are made for aperture corrections and for various instability tests. To determine when any given problem is completed, provisions are made for testing the axial position and radius of the particle, and the phase angle of the fields. One may test all three criteria or just the axial position alone. In instability cases (such as the particle crossing the axis or turning around) three possibilities are offered: (a) continue the problem, (b) go to the next problem within the set, or (c) proceed to the next set. In any given run, there can be many sets (or only one); and in any given set, there can be many problems (or, again, only one). Provision is made in the output to label each set and problem and to print out the date the run was made.

Various checks are made throughout the code for instability and errors. The Runge-Kutta integration routine determines the interval in time that is best suited to the problem. It also determines when output is needed. The two read subroutines assure that all cards necessary for a run are present. The main code determines when all problems within a set are completed and when all sets for that particular run are finished. The main code is also responsible for the introduction of aperture corrections when specified in the input data. The user will always know if he has inadvertently left out an input data card because GRAPE SEED III will print out a message saying which card is missing. If data crucial to the Runge-Kutta are missing, the entire run is terminated via LABRT (the error routine).

I. THE MAIN CODE

GRAPE SEED III is composed of a main code and several subroutines. Thus, it is possible to modify one section of the code without recompiling the entire program. In fact, this was precisely the route taken to yield the "backward" version of GRAPE SEED III. The backward version allows the user to take as input a set of ejection conditions, run the representative particle backward through the cavity, and thus determine what initial conditions would be required to achieve the desired output. In formulating this particular version of GRAPE SEED, only the main code was recompiled. The subroutines that were used for the "forward" version of the code were perfectly adequate for the backward version.

The main code ties the various subroutines together, adds the aperture corrections, and performs the tasks listed below:

1. Calls on the routines that read in set and problem data.

2. Determines the last problem in each set and the last set in a run.

3. Computes the constants needed during the run.

4. Sets up the initial conditions.

5. Determines if aperture corrections are needed and inserts them at the proper time.

6. Calls the Runge-Kutta and the print routines when the Runge-Kutta indicates it is time for output.

7. Makes the various tests specified in the input data concerning errors and end of run.

It can thus be seen that most of the controls and decision-making take place in the main code.

The following subroutines are controlled by the main code:

1. The Runge-Kutta integration routine which, in turn, controls the derivative routine.

2. The initial condition print routine which prints out the initial conditions for a set; this routine uses the FORTRAN IV I/O package.

3. The read "set" data routine.

4. The problem print routine, which provides the output during the running of each problem at intervals selected by the user. (see discussion of input data).

5. The read problem data routine, which reads the input data for each problem within a set.

6. The B_{z_0} routine, which computes B_{z_0} each time an output print is required.

7. The Bessel function routine (which is used only initially), after which the Bessel function is integrated.

The main code also calls on the FORTRAN sine and cosine routines when setting up the initial conditions. The Runge-Kutta integration routine, the derivative routine, and the input data are discussed in succeeding sections.

II. THE INTEGRATION METHOD

The integration scheme used to handle the 14 differential equations of GRAPE SEED III is a fourth-order Runge-Kutta with certain modifications. For a description of the method, refer to Fig. 4.1.
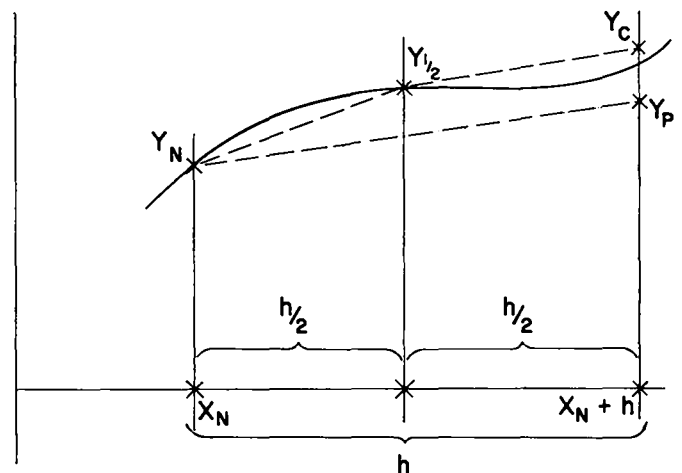
Fig. 4. 1. Runge-Kutta integration model.

Consider one cycle of integration:

Y_N = value of dependent variable at X_N

Y_N' = value of derivative of Y_N at X_N

h = discrete value in X that one wants to advance the integration

Y_P = predicted value of dependent variable at $X_N + h$

Y_C = corrected value of dependent variable at $X_N + h$

Let:
$$K_1 = hY'(X_N, Y_N)$$
$$K_2 = hY'(X_N + h/2, Y_N + K_1/2)$$
$$K_3 = hY'(X_N + h/2, Y_N + K_2/2)$$
$$K_4 = hY'(X_N + h, Y_N + K_3)$$

Then:
$$Y_P = Y_N + 1/6(K_1 + 2K_2 + 2K_3 + K_4)$$

Replacing the value h by h/2, we integrate from X_N to $X_N + h/2$ to yield $Y_{1/2}$. Then, using $Y_{1/2}$ as the initial value, we integrate from $X_N + h/2$ to $X_N + h$. This yields Y_C. Based on an accuracy criterion provided by the user, a comparison is made to determine if Y_P and Y_C are sufficiently close. If not, the cycle is discarded. If the test is passed, the Y_N is replaced by Y_C, and X_N is replaced by $X_N + h$. If Y_P and Y_C are very close to each other, the interval h is replaced by 2h for the next cycle and an indication is given to the user. Also, if the integration was not successful, h is replaced by h/2 for the next cycle. Again, the user is notified of this change.

The testing section on Y_P and Y_C uses a combination of unnormalized arithmetic and bit-by-bit-compare. If either Y_P or Y_C is zero, or if both are zero, that cycle is treated as a special case.

As a special feature, the Runge-Kutta can integrate from X_N to some value, say X_F, taking as many cycles as it needs. It will always integrate to X_F *exactly*. This can be very useful for printout purposes. GRAPE SEED III utilizes this feature.

While the time needed for a single cycle is long compared with some other methods (twelve evaluations of the derivatives are computed), experience has shown that the total running time for a given problem in GRAPE SEED III will be,

on the average, 30 percent less than when using other integration methods. Further, uncertainty concerning the accuracy of the results has been considerably lessened.

III. DERIVATIVE ROUTINE

GRAPE SEED III is made up of a series of subroutines. One of these routines computes the derivatives for the Runge-Kutta integration. Because this routine is utilized 12 times each cycle, ordering and efficiency are essential. For this reason, Bessel functions and sine and cosine functions are integrated instead of computed. Thus, eight of the 14 integrated values provide these quantities. The other six values are the running results of GRAPE SEED, and their derivative equations are obtained from the equations of motion for the beam. It is also in the derivative routine that the electric and magnetic fields are computed. These fields are used in the derivative equations of motion. This section describes how the number of dependent variables was established and how the order of computation evolved. Time, t, is the independent variable.

Now, let Y_i equal the integrated dependent variables and YP_i be their derivatives. The subscript i will assume values from 1 to 14. The dependent variables, for which we need derivative expressions, are as follows:

$$Y_1 = R$$
$$Y_2 = \theta$$
$$Y_3 = Z$$
$$Y_4 = \cos(\omega_1 t + \psi_1)$$
$$Y_5 = \sin(\omega_1 t + \psi_1)$$
$$Y_6 = \cos(\omega_2 t + \psi_2)$$
$$Y_7 = \sin(\omega_2 t + \psi_2)$$
$$Y_8 = J_0(2\pi R/\lambda)$$
$$Y_9 = (2\pi R/\lambda)[J_1(2\pi R/\lambda)]$$
$$Y_{10} = \sin(\omega t)$$
$$Y_{11} = \cos(\omega t)$$
$$Y_{12} = \dot{R}/\delta$$
$$Y_{13} = R^2\dot{\theta}/\delta$$
$$Y_{14} = \dot{Z}/\delta$$

The order of computation for the derivative routine will now be considered, with comments inserted as needed.

The first quantity needed is δ which is equal to $\sqrt{1 - \beta^2}$.

Let

$$\beta^2 = \frac{\dot{R}^2 + R^2\dot{\theta}^2 + \dot{Z}^2}{c^2}$$

(4.1)

where c = speed of light. Using variables Y_{12}, Y_{13}, and Y_{14}, an expression for $\dot{R}^2 + R^2\dot{\theta}^2 + \dot{Z}^2$ is developed:

$$\dot{R}^2 + R^2\dot{\theta}^2 + \dot{Z}^2 = \delta^2\left(Y_{12}^2 + \frac{Y_{13}^2}{R^2} + Y_{14}^2\right)$$

(4.2)

or, from Eqs. (4.1) and (4.2),

$$\beta^2 c^2 = (1 - \beta^2)\left(Y_{12}^2 + \frac{Y_{13}^2}{R^2} + Y_{14}^2\right)$$

(4.3)

Let

$$Y_{12}^2 + \frac{Y_{13}^2}{Y_1^2} + Y_{14}^2 = A$$

where $Y_1^2 = R^2$.

Then

$$\frac{\beta^2}{1 - \beta^2} = A \quad \text{and} \quad \beta^2 = \frac{A}{1 + A}$$

(4.4)

Having an expression for δ, one can now write the equations for the first three derivatives:

$$YP_1 = \delta Y_{12}$$
$$YP_2 = \delta Y_{13}/Y_1^2$$
$$YP_3 = \delta Y_{14}$$

The next eight derivation equations are derived by playing one against the other as follows:

$$YP_4 = -\omega_1 Y_5$$
$$YP_5 = \omega_1 Y_4$$
$$YP_6 = -\omega_2 Y_7$$
$$YP_7 = \omega_2 Y_6$$
$$YP_8 = -YP_1 Y_9/Y_1$$
$$YP_9 = (2\pi/\lambda)^2 Y_1 YP_1 Y_8$$
$$YP_{10} = \omega Y_{11}$$
$$YP_{11} = -\omega Y_{10}$$

Of course, to have values to start with, dependent variables Y_4 through Y_{11} are calculated initially and then integrated thereafter.

The last three derivative equations are taken directly from the equations of motion as described in Chapter 3. However, before these equations can be set down, the **B** and **E** fields have to be computed.

The expression for the radial component of the electric field is everywhere

$$E_R = -59.958\,\frac{I}{\beta_0 Y_1}$$

(4.5)

If the representative particle is not in the cavity, then

$$E_Z = E_1 \quad \text{and} \quad B_\theta = 0$$

If the particle is in the cavity, then the following equations hold:

$$E_Z = E_1 + E_0 Y_8 Y_{10}$$

(4.6)

$$B_\theta = \frac{E_0 \lambda Y_9 Y_{11}}{2\pi c Y_1}$$

(4.7)

The fields B_R and B_Z are space variable. That is to say, they take on different values depending on where the representative particle is. Six test values for Z are read in: Z_{11}, Z_{21}, Z_{12}, Z_{22}, Z_{13}, and Z_{23}. Associated with these are three U values, namely U_1, U_2, and U_3. These U's have the value of either zero or one, based on the following relationship:

$$U_i = \begin{cases} 0 \\ 1 \\ 0 \end{cases} \text{if} \begin{cases} Z < Z_{11} \\ Z_{11} \le Z \le Z_{21} \\ Z_{21} < Z \end{cases}$$

(4.8)

where $i = 1, 2,$ and 3.

One can now write the equations for B_R and B_Z in steps and then put the steps together as follows:

113

$$k = \frac{2\pi \times 10^{-7}(NI)_1 Y_4 b_1^2}{[b_1^2 + (Y_3 - Z_1)^2]^{3/2}}$$

(4.9)

$$l = \frac{2\pi \times 10^{-7}(NI)_2 Y_6 b_2^2}{[b_2^2 + (Y_3 - Z_2)^2]^{3/2}}$$

(4.10)

$$K_1 = \frac{3}{2}\left[\frac{Y_1(Y_3 - Z_1)}{b_1^2 + (Y_3 - Z_1)^2}\right]$$

(4.11)

$$K_2 =$$

$$\frac{15}{16}\left\{\frac{(Y_3 - Z_1)Y_1^3 [3b_1^2 - 4(Y_3 - Z_1)^2]}{[b_1^2 + (Y_3 - Z_1)^2]^3}\right\}$$

(4.12)

$$L_1 = \frac{3}{2}\left[\frac{Y_1(Y_3 - Z_2)}{b_2^2 + (Y_3 - Z_2)^2}\right]$$

(4.13)

$$L_2 =$$

$$\frac{15}{16}\left\{\frac{(Y_3 - Z_2)Y_1^3 [3b_2^2 - 4(Y_3 - Z_2)^2]}{[b_2^2 + (Y_3 - Z_2)^2]^3}\right\}$$

(4.14)

Then

$$B_R = U_1 [k(K_1 + K_2)] + U_2[l(L_1 + L_2)]$$

(4.15)

To obtain the equation for B_Z, the same expressions for k and l are used as in B_R. Subscripted K's and L's take on different values as follows:

let

$$K_1 = \frac{3}{4}\left\{\frac{Y_1^2[b_1^2 - 4(Y_3 - Z_1)^2]}{[b_1^2 + (Y_3 - Z_1)^2]^2}\right\}$$

(4.16)

$$K_2 = \frac{3}{4}\left\{\frac{Y_1^2[b_2^2 - 4(Y_3 - Z_2)^2]}{[b_2^2 + (Y_3 - Z_2)^2]^2}\right\}$$

(4.17)

$$L_1 = \frac{45}{64}\left\{\frac{Y_1^4[b_1^4 - 12b_1^2(Y_3 - Z_1)^2 + 8(Y_3 - Z_1)^4]}{[b_1^2 + (Y_3 - Z_1)^2]^4}\right\}$$

(4.18)

$$L_2 = \frac{45}{64}\left\{\frac{Y_1^4[b_2^4 - 12b_2^2(Y_3 - Z_2)^2 + 8(Y_3 - Z_2)^4]}{[b_2^2 + (Y_3 - Z_2)^2]^4}\right\}$$

(4.19)

Then

$$B_Z = U_1[k(1 + K_1 + K_2)]$$

$$+ U_2[l(1 + L_1 + L_2)] + B_{00}U_3$$

(4.20)

With these expressions computed for the **E** and **B** fields, the derivative expressions for Y_{12}, Y_{13}, and Y_{14} are calculated as follows:

$$YP_{12} = \eta\left\{E_R\left[1 - \frac{(Y_1 YP_2)^2}{c^2}\right.\right.$$

$$\left.\left. - \frac{(YP_3)^2}{c^2}\right] - YP_3 B_\theta + Y_1 YP_2 B_z\right\}$$

$$+ \frac{Y_1 YP_2^2}{\delta}$$

(4.21)

$$YP_{13} = Y_1\eta\left(B_R YP_3 - B_Z YP_1 - \frac{E_R Y_1 YP_1^2}{c^2}\right)$$

(4.22)

$$YP_{14} = \eta\left(E_Z + E_R \frac{YP_1 YP_3}{c^2}\right.$$

$$\left. + YP_1 B_\theta - Y_1 YP_2 B_R\right)$$

(4.23)

This completes the equations computed by the derivative routine. It will be noted that some expressions are used more than once. These are, of course, computed only once and saved. Also, the value of U_1 in the **B** fields is checked before any computation is performed. If the value is zero, that portion of the calculation is skipped.
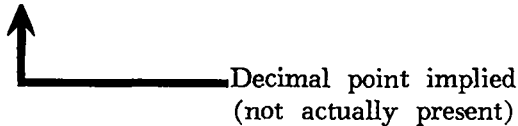
IV. INPUT CARDS

All input to GRAPE SEED III is in floating point. Each card has six fields of 12 digits. Some fields on the cards are not used and are, thus, reserved for future expansion. The FORTRAN IV format for each card is

$$6 \text{ E } 12.7$$

which implies the following form for each number:

$$\pm X.XXXXXXX \pm EE$$

Decimal point implied (not actually present)

The first field of each card is the card number. This is used by GRAPE SEED III as a check to be sure all cards are present. Cards 1 - 9 are "set" input cards and are present only once in a given "set." Cards 10 - 12 are problem input cards and may be repeated many times within a set. In a given run, GRAPE SEED III will handle more than one set. Thus, one could have three sets (or more, or less) in a given run, each set containing several problems. The last set in a run is denoted by a -1.0 in field 1 of card 1.

The card contents are listed below. A sample coded input sheet, included as Fig. 4.2, follows.

CARD 1: set input card
- Field 1: 1.0 (-1.0 for last set in run)
- Field 2: month
- Field 3: day
- Field 4: current year
- Field 5: set number
- Field 6: last problem number in current set

CARD 2: set input card
- Field 1: 2.0
- Field 2: accuracy desired in the Runge Kutta (usually 1.0 E-5)
- Field 3: Δt; interval in independent variable for use by the Runge-Kutta

Field 4: print interval; used to print out results when wanted, based on value of independent variable

Field 5: branching directions in case of error:
- 0.0 — go to next problem in set
- 1.0 — go to next set

Field 6: what to test during run in order to terminate problem:
- 0.0 — test Z_{max}, R_{max}, ϕ_{max}
- 1.0 — test Z_{max} only

CARD 3: set input card

- Field 1: 3.0
- Field 2: whether or not there is an input aperture correction:
  - 0.0 — no input aperture
  - ΔZ — aperture correction within $\pm \Delta Z$
- Field 3: whether or not there is an output aperture correction:
  - 0.0 — no output aperture
  - ΔZ — aperture correction within $\pm \Delta Z$
- Field 4: radius negative decision:
  - 0.0 — continue if R goes negative
  - 1.0 — terminate if R goes negative
- Field 5: β_0
- Field 6: I — injected beam current

CARD 4: set input card
- Field 1: 4.0
- Field 2: Z_1 } positions of lens coils
- Field 3: Z_2 } relative to injection aperture
- Field 4: b_1 } radii of lens coils
- Field 5: b_2 }
- Field 6: L — length of cavity

CARD 5: set input card
- Field 1: 5.0
- Field 2: $(NI)_1$ } ampere turns in lens coils
- Field 3: $(NI)_2$ }
- Field 4: ψ_1 } phase angles for lens coils
- Field 5: ψ_2 }
- Field 6: η — specific charge for particles

IVY FORM II

PROGRAMMER DICKMAN   PROBLEM G. S. III   CODE INPUT   DATE   PAGE 1 of 1

	7–12	13–18 19–24	25–30 31–36	37–42 43–48	49–54 55–60	61–66 67–72	73–80
−1	+00+5	+00+25	+01+1964	+03+1	+00+1	+00	CARD 1
+2	+00+1	−05+1	−10+1	−09+1	+00+1	+00	CARD 2
+3	+00+2	−02+2	−02+0	+00+97908	−01+3	+02	CARD 3
+4	+00−2	−01+2905	+00+22	+00+22	+00+26	+00	CARD 4
+5	+00+0	+00+0	+00+0	+00+0	+00−17592	+11	CARD 5
+6	+00+0	+00+0	+00+299791	+08+6	+00−1	+00	CARD 6
+7	+00+33	+00−1	+00+33	+00−1	+00+33	+00	CARD 7
+8	+00−6	+06+0	+00+33	+00+0	+00+0	+00	CARD 8
+9	+00+0	+00					CARD 9
+1	+01+1	+00					CARD 10
+11	+01+0	+00+2	−02+0	+00+0	+00		CARD 11
+12	+01+0	+00+0	+00+29351949+08				CARD 12

Fig. 4. 2. Typical sheet from which data cards are prepared.

116

CARD 6:   set input card
   Field 1:   6.0
   Field 2: f_1 ⎫ drive frequency for lens
   Field 3: f_2 ⎬ coils
   Field 4:   c — speed of light
   Field 5: λ — operating wavelength of cavity
   Field 6: Z_{11}

CARD 7:   set input card
   Field 1:   7.0
   Field 2: Z_{21}
   Field 3: Z_{12}
   Field 4: Z_{22}
   Field 5: Z_{13}
   Field 6: Z_{23}

   Note: Z_{i1} (i = 1, 2, 3) values are used to turn off and on, spatially, the various B fields

CARD 8:   set input card
   Field 1:   8.0
   Field 2: E_0 — effective inside cavity only
   Field 3: E_1 — constant field
   Field 4: Z_{max}
   Field 5: ϕ_{max}
   Field 6: R_{max}

CARD 9:   set input card
   Field 1:   9.0
   Field 2: B_{00} — constant field

CARD 10:   problem input card
   Field 1:   10.0
   Field 2:   problem number

CARD 11:   problem input card
   Field 1:   11.0
   Field 2: t_0
   Field 3: R_0
   Field 4: θ_0
   Field 5: Z_0

CARD 12:   problem input card
   Field 1:   12.0
   Field 2: $\dot{R}_0$
   Field 3: $\dot{\theta}_0$
   Field 4: $\dot{Z}_0$

Note: Cards 11 and 12 contain the initial conditions for the problem. These values specify the radius, angle, and position of the peripheral electrons relative to the cavity, as well as their initial velocities.

All linear dimensions are in meters; time is in seconds; and angular measure is in radians. Electric and magnetic fields are expressed in volts per meter and webers per square meter, respectively.

Appendix 4A

GRAPE SEED III LISTINGS AND SUBROUTINES

This appendix contains the following detailed information:

1. FORTRAN listing of GRAPE SEED III, including all subroutines except the Runge-Kutta.*

2. FORTRAN listing of the recompiling of the main code to yield "backward" GRAPE SEED.*

3. Writeup of the Runge-Kutta integration subroutine, describing its use.

4. Writeup of LABRT.

---

*Each of these listings contains the output of an actual problem that was run.

B •   1OJCB,CICKMAN,O   GR.SD.3TO1
        $EXECUTE   IBJOR
IBJCB VERSION 5 HAS CCNTROL.
$IBJCB   GO,MAP
$•
$•   VENABLE - GRAPE SEED 3
$•
$IBFTC GS3   LIST,REF

        GS3   - EFN   SOURCE STATEMENT - IFN(S) -


```
C
C     MAIN CODE FOR GRAPE SEED 3
C
      EXTERNAL FY
C
      DIMENSION YI(14),YP(14),Y4(56),BESTEM(100),TEMP(5)
C
      COMMON /NAMED/ EZERO,E1,ZMAX,PHIMAX,RMAX,Z11,Z21,Z12,
     2Z22,Z13,Z23,B00,B1,B2,CENGTH,ETA,CMU,DLAMB,
     3BETAZ,CAPI,Z1,Z2,FPNO,ENDNO,TEST,RIN,ROUT,
     4PINTER,SHIFT,SWITST,PROBNO,TZ,RZ,THETAZ,ZZ,
     5RZDOT,THZDOT,ZZDOT,CSQ,CON1,OMEGA1,OMEGA2,
     6CON5,OMEGA,CON7,CON8,CON9,CON10,CON11,CON12,
     7CON13,CON14,ER,BTHETA,EZ,BR,BZ,T,PHI,PHIZ,
     8PHI1,TZ1,Z,ZDOT,R,RDOT,THETA,THEDOT,BZO,CT1,
     9BETASQ,BETA,DELTA,SETNO,DMONTH,DAY,YEAR,ACC,
     ADT,DNI1,DNI2,PSI1,PSI2,FREQ1,FREQ2,
     BC,CON2,CON3,CON4,CON6
C
C              SET CONSTANTS AND ENDSET FLAG
      FPNO=0.0                                          EQ 13
C
C              INITIALIZE READS AND TESTS
    1 IF(FPNO)2,3,3                                     LASTSET
    2 CALLEXIT
C                                                              5
    3 CALL READ1                                        SETREAD   7
      PRGBNO=0.0                                        EQ 14
C
C     COMPUTE VALUES FOR SET
C
      CSQ=C**2                                          EQ 2
      CMU=ABS(CSQ/ETA)                                  EQ 2.1
      CON1=1.0/C                                        EQ 3
      CON2=3.14159                                      EQ 4
      CON3=6.28318                                      EQ 5
      CON4=39.47842                                     EQ 6
      CON6=CON3*C                                       EQ 7
      CON10=1.5                                         EQ 8
      CON11=15.0/16.0                                   EQ 9
      CON12=0.75                                        EQ 10
      CON13=45.0/64.0                                   EQ 11
      CON15=CON3*(1.0E-7)                               EQ 12
      OMEGA1=CON3*FREQ1
      OMEGA2=CON3*FREQ2
      CON5=CON4/(DLAMB**2)
      OMEGA=CON6/DLAMB
      CON7=EZERO/C
      CON8=DLAMB/CON3
      CON9=CON15*DNI1
      CON14=CON15*DNI2
C
      CALL PRINT1                                       SETPRT
C                                                              9
    4 IF(PROBNO-ENDNO)5,1,5                             LASTPROB
C
    5 CALL READ2                                        PROREAD
C                                                              13
      CALL SUBA                                         BZOCALC  15
      DTZ=DT                                            SAVEDT
C
```

```
C                  SET INITIAL CONDITIONS
        YI(1)=R                                                    EQ 15
        YI(2)=THETA                                               EQ 16
        YI(3)=Z                                                   EQ 17
        YI(4)=COS((OMEGA1*T)+PSI1)                                EQ 18        17
        YI(5)=SIN((OMEGA1*T)+PSI1)                                EQ 19        18
        YI(6)=COS((OMEGA2*T)+PSI2)                                EQ 20        19
        YI(7)=SIN((OMEGA2*T)+PSI2)                                EQ 21
C                                                                              20
        ARGA=(CON3*R)/DLAMB                                       EQ 22
        BESANS=0.0                                                EQ 23
        NBES=0                                                    EQ 24
C
        CALL BESJN(ARGA,NBES,BESTEM,BESANS)                       J(ZERO)
C                                                                              22
        YI(8)=BESANS                                              EQ 25
C
        BESANS=0.0                                                EQ 26
        NBES=1                                                    EQ 27
C
        CALL BESJN(ARGA,NBES,BESTEM,BESANS)                       J(ONE)
C                                                                              25
        YI(9)=ARGA*BESANS                                         EQ 28
        YI(10)=SIN(OMEGA*T)                                       EQ 29        27
        YI(11)=COS(OMEGA*T)                                       EQ 30        28
        BETASQ=((RDOT**2)+((R**2)*(THEDOT**2))+(ZDOT**2))/CSQ     EQ 31
        BETA=SQRT(BETASQ)                                         EQ 32        29
        DELTA=SQRT(1.0-BETASQ)                                    EQ 33        30
        YI(12)=RDOT/DELTA                                         EQ 34
        YI(13)=((R**2)*THEDOT)/DELTA                              EQ 35
        YI(14)=ZDOT/DELTA                                         EQ 36
        N=14                                                      EQ 37
C
        CALL FY(T,YI,YP,N)                                        FYSUB
C                                                                              32
        PHIZ=OMEGA*TZ                                             EQ 38
C
        CALL PRINT2                                               PROPRT
C                                                                              34
        XF=T+PINTER                                               EQ 39
        SH=DT*1.0E-5                                              EQ 40
        NF=0                                                      EQ 41
        IND=0                                                     EQ 42
        CRDOTF=0.0                                                EQ 14.5
        ZFLAG=-1.0                                                EQ 14.6
C
        CALL RKA(T,DT,YI,YP,Y4,FY,ACC,XF,SH,NF,IND,N)            CALLRKA
C                                                                              38
        IF(RIN)100,100,10                                         ZAPER
     10 IF(YI(3))11,200,20
     20 IF(YI(3)-RIN)200,200,100
C
     11 TEMP(1)=ABS(YI(3))
        IF(TEMP(1)-(2.0*PINTER*ZDOT))250,250,32
C
    250 XF=0.0
        TEMP(1)=T+PINTER
C
    251 IND=0
        TEMP(2)=ABS(YI(3))
        IF(T-TEMP(1))255,252,252
C
    252 Z=YI(3)
        ZDOT=YI(14)*DELTA
        R=YI(1)
        RDOT=YI(12)*DELTA
        THETA=YI(2)
        THEDOT=(YI(13)*DELTA)/(R**2)
C
        CALL SUBA                                                              52
        CALL PRINT2                                                            54
        TEMP(1)=TEMP(1)+PINTER
C
    255 IF(TEMP(2)-PIN)256,256,257
C
    257 CALL RKB                                                               59
        GO TO 251
```

119

```
C
  256 XF=TEMP(1)
      GO TO 200
C
   32 CALL RKB
C                                                                    64
      Z=YI(3)                                              EC 46
      ZDCT=YI(14)*DELTA                                    EQ 47
      R=YI(1)                                              EQ 48
      RDCT=YI(12)*CELTA                                    EQ 49
      THETA=YI(2)                                          EU 50
      THEDOT=(YI(13)*CELTA)/(R**2)                         EQ 51
C
      CALL SUBA                                                       66
      CALL PRINT2                                          PROPRT
C                                                                    68
      XF=XF+PINTEP                                         EC 52
      CT=DTZ                                               EQ 53
      INC=0                                                EQ 54
      GC TO 11                                             TO INTE
C
  2CC WRITE(9,2C1)PROBNO                                                71
  2C1 FCRMAT(25H0      PROBLEM NUMBER     ,F1O.O,          APERTURE
     A45H         ADC APERTURE CCRRFCTION, NFXT CYCLF)      COMMENT
C
      V=CMU*((1.O/CELTA)-1.0)                              EQ 55
C
      AINCR=(ETA*YI(1)*DELTA*EZERC*YI(1C))                 EC 56
     A/(2.O*CSC*BETASC)
C
      TEMP(1)=(YP(1)/YP(3))-AINCR                          EQ 57
      TEMP(2)=(TEMP(1)**2)+I10                             EQ 58
      TEMP(3)=(YP(1)**2)+(YP(3)**2)                        EQ 59
      TEMP(3)=TEMP(3)/TEMP(2)                              EQ 60
      TEMP(5)=SQRT(TEMP(3))                                EQ 61       72
      YI(14)=TEMP(5)/DELTA                                 EQ 61.1
      TEMP(3)=TEMP(5)*TEMP(1)                              EQ 61.2
      YI(12)=TEMP(3)/DELTA                                 EQ 61.3
      TEMP(4)=TEMP(3)-YP(1)                                EQ 62
C
      WRITE(9,202)TEMP(4),YI(3)                                       73
  202 FORMAT(23H        DELTA R DOT =,1PE16.7,
     A15H            Z= ,1PE16.7)
C
  1CO IF(Z)110,111,111
  111 ZFLAG=1.0                                            EQ 62.1
      GO TO 102
  110 IF(ZFLAG)102,50,50
  102 IF(DRDOTF)300,101,300
  101 IF(ROUT)300,300,40
C
   40 DTEST=CENGTH-(2.0*PINTER*ZDOT)
C
      IF(YI(3)-DTEST)300,275,275
C
  275 XF=0.0
      TEMP(1)=T+PINTER
C
  276 IND=0
      IF(T-TEMP(1))278,277,277
C
  277 Z=YI(3)
      ZDOT=YI(14)*DELTA
      R=YI(1)
      RDOT=YI(12)*DELTA
      THETA=YI(2)
      THEDOT=(YI(13)*DELTA)/(R**2)
C
      CALL SUBA                                                       91
      CALL PRINT2                                                     93
      TEMP(1)=TEMP(1)+PINTER
C
  278 IF(YI(3)-(CENGTH-ROUT))279,280,280
C
  279 CALL RKB                                                        98
      GO TO 276
```

120

```
C
  280 XF=TEMP(1)
      GO TO 41
C
   41 WRITE(9,201)PROBNO                                  APERCOMM
C                                                                      102
      V=CMU*((1.0/DELTA)-1.0)                             EQ 64
C
      AINCR=(ETA*YI(1)*DELTA*FZERO*YI(10))               EQ 65
     B./(2.0*CSQ*BETASQ)
C
      TEMP(1)=(YP(1)/YP(3))*AINCR                        EQ 66
      TEMP(2)=(TEMP(1)**2)+1.0                           EQ 67
      TEMP(3)=(YP(1)**2)+(YP(3)**2)                      EQ 68
      TEMP(3)=TEMP(3)/TEMP(2)                            EQ 69
      TEMP(5)=SQRT(TEMP(3))                              EQ 70      103
      YI(14)=TEMP(5)/DELTA                               EQ 70.1
      TEMP(3)=TEMP(5)*TEMP(1)                            EQ 70.2
      YI(12)=TEMP(3)/DELTA                               EQ 70.3
      TEMP(4)=TEMP(3)-YP01)                              EQ 71
      DRDOTF=1.0                                         EQ 71.1
C
      WRITE(9,202)TEMP(4),YI(3)                           DRDOT
C                                                                      104
  300 CALL RKB
C                                                                      106
      Z=YI(3)                                            EQ 72
      ZDOT=YI(14)*DELTA                                  EQ 73
      R=YI(1)                                            EQ 74
      RDOT=YI(12)*DELTA                                  EQ 75
      THETA=YI(2)                                        EQ 76
      THEDOT=(YI(13)*DELTA)/(R**2)                       EQ 77
C
      CALL SUBA                                          BZO CALC
C                                                                      108
      CALL PRINT2                                        PROPRT
C                                                                      110
      XF=XF+PINTER                                       EQ 78
      DT=DTZ                                             EQ 79
C
C              THE R, Z, PHI, AND SH TESTS
C
      IF(IND-2)301,50,301
C
   50 IF(SHIFT)1,4,1
C
  301 IND=0                                              EQ 80
      IF(Z-ZMAX)302,4,4
C
  302 IF(R)320,303,303
C
  303 IF(TEST)100,304,100
C
  304 IF(R-RMAX)305,4,4
C
  305 IF(PHI-PHIMAX)100,4,4
C
  320 IF(SWITST)50,303,50
C
      STOP


      END
```

121

```
        FY        -  EFN    SOURCE STATEMENT  -  IFN(S)  -

C
C     FY - FUNCTIONAL EVALUATION FOR GRAPE SEED 3
C
      SUBROUTINE FY(T,YI,YP,N)
C
      DIMENSION YI(14),YP(14),TEMP(5)
C
      COMMON /NAMED/ EZERO,E1,ZMAX,PHIMAX,RMAX,Z11,Z21,          COMMON02
     1Z12,Z22,Z13,Z23,B00,B1,B2,CENGTH,ETA,CMU,                 COMMON03
     2DLAMB,BETAZ,CAPI,Z1,Z2,FPNO,ENDNO,TEST,                   COMMON04
     3REN,ROUT,PINTER,SHIFT,SWITST,PROBNO,                      COMMON05
     4TZ,RZ,THETAZ,ZZ,RZDOT,THZDOT,ZZDOT,                       COMMON06
     5CSQ,CON1,OMEGA1,OMEGA2,CON5,OMEGA,CON7,                   COMMON07
     6CON8,CON9,CEN10,CON11,CON12,CON13,CON14,                  COMMON08
     7ER,BTHETA,EZ,BR,BZ,T,PHI,PHIZ,PHI1,TZ1,                   COMMON09
     8Z,ZDOT,R,RDOT,THETA,THEDOT,BZO,CT1,                       COMMON10
     9BETASQ,BETA,DELTA,SETNO,DMONTH,DAY,YEAR,                  COMMON11
     AACC,DT,DNI1,DNI2,PSI1,PSI2,FREQ1,FREQ2,
     BC,CON2,CON3,CON4,CON6
C
      N=N
      T=T
C
      SMH=YI(1)**2                                              EQ 1
      TEMP(1)=YI(12)**2                                         EQ 2
      TEMP(2)=(YI(13)**2)/SMH                                   EQ 3
      TEMP(3)=YI(14)**2                                         EQ 4
      CAPA=(TEMP(1)+TEMP(2)+TEMP(3))/CSQ                        EQ 5
C
      BETASQ=CAPA/(1.0+CAPA)                                    EQ 6
      BETA=SQRT(BETASQ)                                         EQ 7       3
      DELTA=SQRT(1.0-BETASQ)                                    EQ 8
C                                                                          4
      YP(1)=DELTA*YI(12)                                        EQ 9
      YP(2)=(DELTA*YI(13))/SMH                                  EQ 10
      YP(3)=DELTA*YI(14)                                        EQ 11
C
      SMA=YI(1)*YP(1)                                           EQ 12
      SMB=YI(3)-Z1                                              EQ 13
      SMD=SMB**2                                                EQ 14
      SMC=SQRT(SMH*SMD)                                         EQ 15
C                                                                          5
      YP(4)=-(OMEGA1*YI(5))                                     EQ 17
      YP(5)=OMEGA1*YI(4)                                        EQ 18
C
      SME=YI(3)-Z2                                              EQ 19
      SMF=SME**2                                                EQ 20
      SMG=SQRT(SMH*SMF)                                         EQ 21
C                                                                          6
      YP(6)=-(OMEGA2*YI(7))                                     EQ 23
      YP(7)=OMEGA2*YI(6)                                        EQ 24
C
      SMJ=YI(9)/YI(1)                                           EQ 25
      YP(8)=-(SMJ*YP(1))                                        EQ 26
      YP(9)=CON5*SMA*YI(8)                                      EQ 27
C
      YP(10)=OMEGA*YI(11)                                       EQ 28
      YP(11)=-(OMEGA*YI(10))                                    EQ 29
C
      ER=-(2.0E-7*C)*(CAPI/(BETAZ*YI(1)))                       EQ 30
C
      IF(YI(3))3,2,1                                            EQ 31
    1 IF(CENGTH-YI(3))3,2,2                                     EQ 32
    2 TEMP(1)=EZERO*YI(8)*YI(10)                                EQ 33
      BTHETA=CON7*CON8*SMJ*YI(11)                               EQ 34
      GO TO 4                                                   EQ 35
    3 TEMP(1)=0.0                                               EQ 36
      BTHETA=0.0                                                EQ 37
    4 EZ=E1+TEMP(1)                                             EQ 38
C
```

```
      CAPF=(B1**2)+SMD                                          EQ 39
      CAPG=(B2**2)+SMF                                          EQ 40
      CAPH=CAPF**2                                              EQ 41
      CAPK=CAPH*CAPF                                            EQ 42
      CAPL=CAPH**2                                              EQ 43
      CAPM=SQRT(CAPK)                                           EQ 44      14
      CAPN=CAPG**2                                              EQ 45
      CARO=CAPN*CAPG                                            EQ 46
      CAPP=CAPN**2                                              EQ 47
      CAPQ=SQRT(CAPC)                                           EQ 48      15
      CAPR=SMH*YI(1)                                            EQ 49
C
      IF(YI(3)-Z11)23,21,21                                     EQ 50
   21 IF(Z21-YI(3))23,22,22                                     EQ 51
   22 SMM=B1**2                                                 EQ 52
      SMC=SMM**2                                                EQ 53
      SMK=(CCN9*YI(4)*SMM)/CAPM                                 EQ 54
C
      TEMP(1)=CCN10*((SMB*YI(1))/CAPF)                          EQ 55
      TEMP(2)=(3.0*SMM)-(4.0*SMD)                               EQ 56
      TEMP(3)=SMB*CAPR                                          EQ 57
      TEMP(4)=(TEMP(2)*TEMP(3))/CAPK                            EQ 58
      TEMP(5)=CCN11*TEMP(4)                                     EQ 59
      BR=SMK*(TEMP(1)+TEMP(5))                                  EQ 60
C
      TEMP(1)=(SMM-(4.0*SMD))*SMH                               EQ 61
      TEMP(2)=(CON12*TEMP(1))/CAPH                              EQ 62
      TEMP(3)=SMO-(12.0*SMM*SMD)+(8.0*(SMD**2))                 EQ 63
      TEMP(4)=(SMH**2)*TEMP(3)                                  EQ 64
      TEMP(5)=(TEMP(4)/CAPL)*CON13                              EQ 65
      BZ=SMK*(1.0+TEMP(2)+TEMP(5))                              EQ 66
      GO TO 24                                                  EQ 67
C
   23 SMK=0.0                                                   EQ 68
      BR=0.0                                                    EQ 69
      BZ=0.0                                                    EQ 70
C
   24 IF(YI(3)-Z12)33,31,31                                     EQ 71
   31 IF(Z22-YI(3))33,32,32                                     EQ 72
C
   32 SMN=B2**2                                                 EQ 73
      SMP=SMN**2                                                EQ 74
      SML=(CON14*YI(6)*SMN)/CAPQ                                EQ 75
C
      TEMP(1)=((SME*YI(1))/CAPG)*CON10                          EQ 76
      TEMP(2)=((3.0*SMN)-(4.0*SMF))*SME*CAPR                    EQ 77
      TEMP(3)=(TEMP(2)*CON11)/CAPO                              EQ 78
      BR=BR+(SML*(TEMP(1)+TEMP(3)))                             EQ 79
C
      TEMP(1)=(SMN-(4.0*SMF))*SMH                               EQ 80
      TEMP(2)=(CON12*TEMP(1))/CAPN                              EQ 81
      TEMP(3)=SMP-(12.0*SMN*SMF)+(8.0*(SMF**2))                 EQ 82
      TEMP(4)=((SMH**2)*TEMP(3))*CON13)/CAPP                    EQ 83
      BZ=BZ+(SML*(1.0+TEMP(2)+TEMP(4)))                         EQ 84
C
   33 IF(YI(3)-Z13)43,41,41                                     EQ 85
   41 IF(Z23-YI(3))43,42,42                                     EQ 86
   42 BZ=BZ+BOO                                                 EQ 87
C
   43 SMR=YI(1)*YP(2)                                           EQ 88
C
      TEMP(1)=(1.0-((SMR**2)/CSQ)-((YP(3)**2)/CSQ))*ER          EQ 89
      TEMP(2)=BTHETA*YP(3)                                      EQ 90
      TEMP(3)=BZ*SMR                                            EQ 91
      TEMP(4)=ETA*(TEMP(1)-TEMP(2)+TEMP(3))                     EQ 92
      TEMP(5)=(SMR*YP(2))/DELTA                                 EQ 93
      YP(12)=TEMP(4)+TEMP(5)                                    EQ 94
C
      TEMP(1)=BR*YP(3)                                          EQ 95
      TEMP(2)=BZ*YP(1)                                          EQ 96
      TEMP(3)=ER*((SMR*YP(1))/CSQ)                              EQ 97
      YP(13)=(ETA*YI(1))*(TEMP(1)-TEMP(2)-TEMP(3))              EQ 98
C
      TEMP(1)=ER*((YP(1)*YP(3))/CSQ)                            EQ 99
      TEMP(2)=BTHETA*YP(1)                                      EQ 100
      TEMP(3)=BR*SMR                                            EQ 101
      YP(14)=ETA*(EZ+TEMP(1)+TEMP(2)-TEMP(3))                   EQ 102
C
      RETURN
      END
```

123

```
C
C      PRINT1 - INITIAL CONDITIONS FOR A SET
C
       SUBROUTINE PRINT1
C
       COMMON /NAMED/ EZERO,E1,ZMAX,PHIMAX,RMAX,Z11,Z21,
      AZ12,Z22,Z13,Z23,B00,B1,B2,CENGTH,ETA,CMU,                      COMMON2
      BDLAMB,BETAZ,CAPI,Z1,Z2,FPNO,ENDNO,TEST,                        COMMON3
      CRIN,ROUT,PINTER,SHIFT,SWITST,PROBNO,                          COMMON4
      DTZ,RZ,THETAZ,ZZ,RZDOT,THZDOT,ZZDOT,                           COMMON5
      EC6C,CON1,CMEGA1,OMEGA2,CON5,OMEGA,CON7,                       COMMON6
      FCCN8,CCN9,CCN10,CON11,CON12,CON13,CON14,                      COMMON7
      GER,BTHETA,EZ,BR,BZ,T,PHI,PHIZ,PHI1,TZ1,                       COMMON8
      HZ,ZDOT,R,RDOT,THETA,THEDOT,BZO,CT1,                           COMMON9
      IBETASQ,BETA,DELTA,SETNO,DMONTH,DAY,YEAR,                      COMMON10
      JACC,DT,DNI1,DNI2,PSI1,PSI2,FREQ1,FREQ2,                       COMMON11
      KC,CCN2,CON3,CON4,CON6
C
       WRITE(9,100)                                             TITLE       1
  100 FORMAT(40H1              GRAPE SEED 3            VENABLE)
       WRITE(9,101)                                             SPACE       2
  101 FORMAT(1H0)
C
       WRITE(9,102)DMONTH,DAY,YEAR,SETNO                        LINE 1      3
  102 FORMAT(13H0      MONTH =,F5.0,10H      DAY =,
      AF5.0,11H      YEAR =,F5.0,
      B22H           SET NUMBER =,F10.0)
C
       WRITE(9,103)ACC,DT,BETAZ                                 LINE 2      4
  103 FORMAT(24H0      ACCURACY DESIRED =,1PE16.7,
      119H      DELTA T =,1PE16.7,21H           BETA ZERO =,
      C1PE16.7)
C
       WRITE(9,104)CAPI,Z1,Z2,CENGTH                           LINE 3      5
  104 FORMAT(14H0      I =,1PE16.7,9H     Z1 =,1PE16.7,
      29H     Z2 =,1PE16.7,9H      L =,1PE16.7)
C
       WRITE(9,105)RIN,ROUT,B1,B2                              LINE 4      6
  105 FORMAT(14H0        IN =,1PE16.7,9H    OUT =,1PE16.7,
      39H     B1 =,1PE16.7,9H     B2 =,1PE16.7)
C
       WRITE(9,106)DNI1,DNI2,PSI1,PSI2                         LINE 5      7
  106 FORMAT(14H0       NI1 =,1PE16.7,9H    NI2 =,1PE16.7,
      49H   PSI1 =,1PE16.7,9H   PSI2 =,1PE16.7)
C
       WRITE(9,107)ETA,FREQ1,FREQ2,CMU                         LINE 6      8
  107 FORMAT(14H0      ETA =,1PE16.7,9H   FREQ1 =,
      51PE16.7,9H  FREQ2 =,1PE16.7,9H     MU =,1PE16.7)
C
       WRITE(9,108)DLAMB,B00,Z11,Z21                           LINE 7      9
  108 FORMAT(14H0    LAMDA =,1PE16.7,9H    B00 =,1PE16.7,
      69H    Z11 =,1PE16.7,9H    Z21 =,1PE16.7)
C
       WRITE(9,109)Z12,Z22,Z13,Z23                             LINE 8      10
  109 FORMAT(14H0      Z12 =,1PE16.7,9H    Z22 =,1PE16.7,
      79H    Z13 =,1PE16.7,9H    Z23 =,1PE16.7)
C
       WRITE(9,110)EZERO,E1,ZMAX                               LINE 9      11
  110 FORMAT(24H0       EZERO =,1PE16.7,
      824H              E1 =,1PE16.7,
      A24H             Z MAX =,1PE16.7)
C
       WRITE(9,111)PHIMAX,RMAX                                 LINE 10     12
  111 FORMAT(44H0                        PHI MAX =,1PE16.7,
      944H                         R MAX =,1PE16.7)
C
       WRITE(9,101)                                            SPACE       13
       RETURN
       END
```

```
$IBFTC R01      LIST,REF

        R01        -  EFN   SOURCE STATEMENT  -  IFN(S)  -

C
C     READ1 - READS SET DATA
C
      SUBROUTINE READ1
C
      DIMENSION TEMPA(6)
C
      COMMON /NAMED/ EZERO,E1,ZMAX,PHIMAX,RMAX,Z11,Z21,               COMMON B
     A Z12,Z22,Z13,Z23,B00,B1,B2,CENGTH,ETA,CMU,                      COMMON C
     1 DLAMB,BETAZ,CAPI,Z1,Z2,FPNO,ENDNO,TEST,                        COMMON C
     B RIN,ROUT,PINTER,SHIFT,SWITST,PROBNO,                           COMMON D
     2 TZ,RZ,THETAZ,ZZ,RZDOT,THZDOT,ZZDOT,                            COMMON E
     C CCSQ,CON1,OMEGA1,OMEGA2,CON5,OMEGA,CON7,                       COMMON F
     3 CON8,CON9,CON10,CON11,CON12,CON13,CON14,                       COMMON G
     D ER,BTHETA,EZ,BR,BZ,T,PHI,PHIZ,PHI1,TZ1,                        COMMON H
     4 Z,ZDOT,R,RDOT,THETA,THEDOT,BZO,CT1,                            COMMON I
     E BETASQ,BETA,DELTA,SETNO,DMONTH,DAY,YEAR,                       COMMON J
     5 ACC,DT,DNI1,DNI2,PSI1,PSI2,FREQ1,FREQ2,                        COMMON K
     F C,CON2,CON3,CON4,CON6
C
C
    2 READ(10,300)TEMPA(1),DMONTH,DAY,YEAR,SETNO,ENDNO               CARD 1       1
  300 FORMAT(6E12.7)
C
      IF(TEMPA(1)-1.0)4,3,2
    4 FPNO=TEMPA(1)                                                  LASTSET
C
    3 READ(10,300)TEMPA(1),ACC,DT,PINTER,SHIFT,TEST                  CARD 2       4
      IF(TEMPA(1)-2.0)102,5,102
C
    5 READ(10,300)TEMPA(1),RIN,ROUT,SWITST,BETAZ,CAPI                CARD 3       6
      IF(TEMPA(1)-3.0)103,6,103
C
    6 READ(10,300)TEMPA(1),Z1,Z2,B1,B2,CENGTH                        CARD 4       8
      IF(TEMPA(1)-4.0)104,7,104
C
    7 READ(10,300)TEMPA(1),DNI1,DNI2,PSI1,PSI2,ETA                   CARD 5      10
      IF(TEMPA(1)-5.0)105,8,105
C
    8 READ(10,300)TEMPA(1),FREQ1,FREQ2,C,DLAMB,Z11                   CARD 6      12
      IF(TEMPA(1)-6.0)106,9,106
C
    9 READ(10,300)TEMPA(1),Z21,Z12,Z22,Z13,Z23                       CARD 7      14
      IF(TEMPA(1)-7.0)107,10,107
C
   10 READ(10,300)TEMPA(1),EZERO,E1,ZMAX,PHIMAX,RMAX                 CARD 8      16
      IF(TEMPA(1)-8.0)108,11,108
C
   11 READ(10,300)(TEMPA(I),I=1,6)                                   CARD 9      18
      IF(TEMPA(1)-9.0)109,12,109
C
   12 B00=TEMPA(2)
      GO TO 500
C
  102 CARD=2.0                                                       NOCD 2
      GO TO 200
C
  103 CARD=3.0                                                       NOCD 3
      GO TO 200
C
  104 CARD=4.0                                                       NOCD 4
      GO TO 200
C
  105 CARD=5.0                                                       NOCD 5
      GO TO 200
C
  106 CARD=6.0                                                       NOCD 6
      GO TO 200
C
  107 CARD=7.0                                                       NOCD 7
      GO TO 200
```

```
C
  108 CARD=8.0                                              NOCD 8
      GO TO 200
C
  1C9 CARD=9.0                                              NOCD 9
      GO TO 200
C
  200 WRITE(9,201)SETNO,CARD                                CARD N        44
  201 FORMAT(13H1      SETNO =,F10.0,14H          CARD,     IS
     1F5.0,10H  MISSING,21H      SKIP TO NEXT SET)          NOT
      WRITE(9,202)                                          THERE,        45
  202 FORMAT(1H1)                                           SKIP
C
      GO TO 2
C
  500 RETURN
      END



      $IBFTC PRT2     LIST,REF

          PRT2           EFN   SOURCE STATEMENT  -  IFN(S)  -

C
C     PRINT2 - OUTPUT FOR PROBLEM DURING RUN
C
      SUBROUTINE PRINT2
C
      COMMON /NAMEO/ EZERO,E1,ZMAX,PHIMAX,RMAX,Z11,Z21,
     1Z12,Z22,Z13,Z23,B00,B1,B2,CENGTH,ETA,CMU,             COMMON2
     ADLAMB,BETAZ,CAPI,Z1,Z2,FPNO,ENDNO,TEST,               COMMON3
     2RIK,ROUT,PINTER,SHIFT,SWITST,PROBNO,                  COMMON4
     BTZ,RZ,THETAZ,ZZ,RZDOT,THZDOT,ZZDOT,                   COMMON5
     3CSG,CON1,OMEGAI,OMEGA2,CON5,OMEGA,CON7,               COMMON6
     CCON8,CON9,CCN10,CON11,CON12,CON13,CON14,              COMMON7
     4ER,BTHETA,EZ,BR,BZ,T,PHI,PHIZ,PHI1,TZ1,               COMMON8
     DZ,ZDOT,R,RDOT,THETA,THEDOT,BZO,CT1,                   COMMON9
     5BETASQ,BETA,DELTA,SETNO,DMONTH,DAY,YEAR,              COMMON10
     EACC,DT,DNI1,DNI2,PSI1,PSI2,FREQ1,FREQ2,
     FC,CON2,CON3,CON4,CON6
C
      PHI=OMEGA*T
      PHI1=PHI-PHIZ
      TZ1=T-TZ
      CT1=C*T
      TEMPA=BETA/DELTA
      V=CMU*((1.0/DELTA)-1.0)
C
      WRITE(9,200)PHI,Z,R,THETA                             LINE 1        2
  200 FORMAT(14H0          PHI =,1PE16.7,14H               Z =,1PE16.7,
     114H          R =,1PE16.7,14H        THETA =,1PE16.7)
C
      WRITE(9,201)PHI1,ZDOT,RDOT,THEDOT                     LINE 2        3
  201 FORMAT(14H      PHI-PHIZ =,1PE16.7,14H           Z DOT =,
     21PE16.7,14H        R DOT =,1PE16.7,14H    THETA DOT =,
     31PE16.7)
C
      WRITE(9,202)T,EZ,ER,BTHETA                            LINE 3        4
  202 FORMAT(14H         TIME =,1PE16.7,14H              EZ =,1PE16.7,
     414H           ER =,1PE16.7,14H      B THETA =,1PE16.7)
C
      WRITE(9,203)DT,BZ,BR,V                                LINE 4        5
  203 FORMAT(14H      DELTA T =,1PE16.7,14H              BZ =,1PE16.7,
     514H           BR =,1PE16.7,14H            V =,1PE16.7)
C
      WRITE(9,204)TZ1,BZO,TEMPA,CT1                         LINE 5        6
  204 FORMAT(14H         T-TZ =,1PE16.7,14H             BZO =,1PE16.7,
     614H   BETA/DELTA =,1PE16.7,14H          C*T =,1PE16.7)
C
      RETURN
      END
```

```
C
C      READ2 - READS PROBLEM DATA WITHIN SETS
C
       SUBROUTINE READ2
C
       DIMENSION TEMPB(6)
C
       COMMON /NAMED/ EZERO,E1,ZMAX,PHIMAX,RMAX,Z11,Z21,        COMMON B
      AZ12,Z22,Z13,Z23,B00,B1,B2,CENGTH,ETA,CMU,               COMMON C
      BDLAMB,BETAZ,CAPI,Z1,Z2,FPNO,ENDNO,TEST,                 COMMON D
      CRIN,ROUT,PINTER,SHIFT,SWITST,PROBNO,                    COMMON E
      DTZ,RZ,THETAZ,ZZ,RZDOT,THZDOT,ZZDOT,                     COMMON F
      ECSQ,CON1,OMEGA1,OMEGA2,CON5,OMEGA,CON7,                 COMMON G
      FCON8,CON9,CCN10,CON11,CON12,CON13,CON14,                COMMON H
      GER,BTHETA,EZ,BR,BZ,T,PHI,PHIZ,PHI1,TZ1,                 COMMON I
      IZ,ZDOT,R,RDOT,THETA,THEDOT,BZO,CT1,                     COMMON J
      JBETASQ,BETA,DELTA,SETNO,DMONTH,DAY,YEAR,                COMMON K
      KACC,DT,DNI1,DNI2,PSI1,PSI2,FREQ1,FREQ2,
      LC,CON2,CON3,CON4,CON6
C
     1 READ(10,400)TEMPB(1),PROBNO                             CARD 10        1
   400 FORMAT(6E12.7)
       IF(TEMPB(1)-10.0)1,2,1
C
     2 READ(10,400)TEMPB(1),TZ,RZ,THETAZ,ZZ                    CARD 11        3
       IF(TEMPB(1)-11.0)111,3,111
C
     3 READ(10,400)TEMPB(1),RZDOT,THZDOT,ZZDOT                 CARD 12        5
       IF(TEMPB(1)-12.0)112,20,112
C
   111 WRITE(9,211)PROBNO                                                     7
   211 FORMAT(22H1      PROBLEM NUMBER =,F10.0,
      145H            CARD 11 MISSING, GO TO NEXT PROBLEM)
       GO TO 1
C
   112 WRITE(9,212)PROBNO                                                     9
   212 FORMAT(22H1      PROBLEM NUMBER =,F10.0,
      245H            CARD 12 MISSING, GO TO NEXT PROBLEM)
       GO TO 1
C
    20 T=TZ
       Z=ZZ
       ZDOT=ZZDOT
       R=RZ
       RDOT=RZDOT
       THETA=THETAZ
       THEDOT=THZDOT
C
       WRITE(9,21)PROBNO,DMONTH,DAY,YEAR                       PROBLEM       12
    21 FORMAT(22H1      PROBLEM NUMBER =,F10.0,                HEADING
      316H      DATE =,3F5.0)
C
       RETURN
       END
```

```
C
C      COMPUTE BZO FOR PRINT
C
       SUBROUTINE SUBA
C
       COMMON /NAMED/ EZERO,E1,ZMAX,PHIMAX,RMAX,Z11,Z21,
      1Z12,Z22,Z13,Z23,B00,B1,B2,CENGTH,ETA,CMU,
      2DLAMB,BETAZ,CAPI,Z1,Z2,FPNO,ENDNO,TEST,
      3RIN,ROUT,PINTER,SHIFT,SWITST,PROBNO,
      4TZ,RZ,THETAZ,ZZ,RZDOT,THZDOT,ZZDOT,
```

```
           5CSO,CON1,OMEGA1,OMEGA2,CON5,OMEGA,CON7,
           6CON8,CON9,CON10,CON11,CON12,CON13,CON14,
           7ER,BTHETA,EZ,BR,BZ,T,PHI,PHI2,PHI1,TZ1,
           8Z,ZDOT,R,RDOT,THETA,THEDOT,BZO,CT1,
           9BETASQ,BETA,DELTA,SETNO,DMONTH,DAY,YEAR,
           AACC,DT,DNI1,DNI2,PSI1,PSI2,FREQ1,FREQ2,
           BC,CON2,CON3,CON4,CON6
      C
      C
           CAPA1=DNI1*(B1**2)                                    EQ 1
           CAPA2=(B1**2)+((Z-Z1)**2)                             EQ 2
           CAPA2=SQRT(CAPA2**3)                                  EQ 3          2
           CAPA3=COS((OMEGA1*T)+PSI1)                            EQ 4          3
           CAPA=(CAPA1/CAPA2)*CAPA3                              EQ 5
      C
           CAPB1=DNI2*(B2**2)                                    EQ 6
           CAPB2=(B2**2)+((Z-Z2)**2)                             EQ 7
           CAPB2=SQRT(CAPB2**3)                                  EQ 8          4
           CAPB3=COS((OMEGA2*T)+PSI2)                            EQ 9          5
           CAPB=(CAPB1/CAPB2)*CAPB3                              EQ 10
      C
           CAPC=(CON3*(1.0E-7))*(CAPA+CAPB)                      EQ 11
      C
           BZO=BOO+CAPC                                          EQ 12
      C
           RETURN
           END



    $IBFTC BESJN


          BESJN       -. EFN    SOURCE STATEMENT  -  IFN(S)  -


     SUBROUTINEBESJN(X,N,T,B)
     EQUIVALENCE(ATEX,TWOX),(C(1),B7,T1),(FT,AP),(N1,IC)
    1,(S,APS),(T2,C4),(BET,ENU)
     DIMENSIONAO(6),BO(6)
     DIMENSIONC(4)
     DIMENSIONGTC(8)
     DATA(GTC(I),I=1,8)      /48HBESJN THE N SUPPLIED IS GREATER THAN 20
    1             /
     LOGICALSET
     DIMENSIONT(N)
     DATAPH/1.57079633/
     DATA(AO(I),I=1,6)/-1.1476882112E+11,98124896.,-142304.,424,-4.,1./
     DATA(BO(I),I=1,6)/-3.150778311E+9,3435232.,-6867.2,
    13.33333333E+1,-1.,.125/
     SET=.TRUE.
     Y=ABS(X)
     XN=IABS(N)
     N2=XN
     IF(XN.LE.20.)GOTO1
   2 CALLLABRT(1,GTC,23.                                              7
     RETURN
   1 IF(Y.NE.0.)GOTO10
   3 IF(N2.EQ.0)GOTO5
   4 B=0.
     RETURN
   5 B=1.
     RETURN
  10 IF(Y.LT.50.)GOTO100
   6 IF(N2.EQ.0)GOTO150
   7 IF(Y/XN.LT.3.)GOTO100
   8 ATEX=8.*Y
     ASYM1=-(XN+.5)*PH+Y
     C(3)=SIN(ASYM1)                                                 27
     C(2)=COS(ASYM1)                                                 28
     C(1)=-C(3)
     C(4)=-C(2)
     IC=2
     AP=17.
     APS=33.
     ASYM1=C(1)
     ENU=1.
     FN2=2*N
```

128

```
      DO15I=1,17
      FMR=((FN2-APS)/AP)*((FN2+APS)/ATEX)
      ASYM1=C(IC)+ASYM1*FMP
      AP=AP-1.
      APS=APS-2.
   15 IC=1+MOD(IC,4)
      ASYM1=(ASYM1      )/SQRT(PH*Y)                            38
   14 IF(MOD(N2,2).EQ.0)GOTO18
   17 IF(N.LT.0)ASYM1=-ASYM1
   20 IF(X.LT.0.)ASYM1=-ASYM1
   18 B=ASYM1
      RETURN
  100 IF(Y.LE..001)GOTO200
      TWOX=2.*Y
      N1=(6+MAX1(TWOX,XN)/2)*2
      B7=2./Y
      T(1)=0
      T(2)=1.E-19
      DO101I=2,N1
      FT=N1-I
      FT=FT*B7
  101 T(I+1)=T(I)*FT-T(I-1)
      SET=.FALSE.
      IF(Y.GE.50.)GOTO150
  102 S=0.
      N3=N1-2
      DO103I=2,N3,2
  103 S=S+T(I)
      J=N1-N2
      ASYM1=T(J)/(2.*S+T(N1))
      GOTO14
  150 BET=A0(1)
      T1=(8.*Y)**2
      T2=B0(1)
      DO151I=2,6
      BET=A0(I)+(BET/T1)
  151 T2=B0(I)+(T2/T1)
      T2=T2+(8.*Y)-PH/2.
      FT=BET*COS(T2)                                            87
      ASYM1=FT/SQRT(PH*Y)                                       88
      IF(SET)GOTO14
      J=N1-N2
      ASYM1=T(J)*ASYM1/T(N1)
      GOTO14
  200 T1=Y/2.
      T2=T1**2
      S=0.
      DO201I=1,3
  201 S=(S+(-1.)**I*T2/FLOAT(N2+4-I)                            101
      ASYM1=(1.+S)
      IF(N2.EQ.0)GOTO18
      N1=1
      DO202I=1,N2
  202 N1=I*N1
      S=N1
      ASYM1=ASYM1*(T1**N2)/S                                    115
      GOTO14
      END
```

129

MONTH = 5.   DAY = 25.   YEAR =1964.   SET NUMBER =   1.

ACCURACY DESIRED = 1.0000000E-05   DELTA T = 1.0000000E-10   BETA ZERO = 9.7908000E-01

   I = 3.0000000E 02   Z1 = -2.0000000E-01   Z2 = 2.9050000E 00   L = 2.6000000E 00

   IN = 2.0000000E-02   OUT = 2.0000000E-02   B1 = 2.2000000E 00   B2 = 2.2000000E 00

   NI1 = 0.   NI2 = 0.   PSI1 = 0.   PSI2 = 0.

   ETA = -1.7592000E 11   FREQ1 = 0.   FREQ2 = 0.   MU = 5.1088359E 05

   LAMDA = 6.0000000E 00   BOO = 0.   Z11 = -1.0000000E 00   Z21 = 3.3000000E 00

   Z12 = -1.0000000E 00   Z22 = 3.3000000E 00   Z13 = -1.0000000E 00   Z23 = 3.3000000E 00

      EZERO = -6.0000000E 06   E1 = 0.   Z MAX = 3.3000000E 00

               PHI MAX = 0.   R MAX = 0.

PROBLEM NUMBER =   1.

```
    PHI =      0.                Z =    0.              R =    2.0000000E-02      THETA =    0.
PHI-PHIZ =     0.            Z DOT =    2.9351949E 08   R DOT =    0.          THETA DOT =    0.
    TIME =     0.               EZ =   -0.              ER =   -9.1858989E 05    B THETA =   -2.0957384E-04
 DELTA T =     1.0000000E-10    BZ =    0.              BR =   -0.                    V =    1.9999243E 06
    T-TZ =     0.              BZO =    0.       BETA/DELTA =    4.8118258E 00        C*T =    0.
```

PROBLEM NUMBER   1.   ADD APERTURE CORRECTION, NEXT CYCLE
    DELTA R DOT =   0.   Z =   0.

```
    PHI =      3.1394013E-01       Z =    2.9394019E-01      R =    1.9592572E-02      THETA =    0.
PHI-PHIZ =     3.1394013E-01   Z DOT =    2.9470330E 08   R DOT =   -7.8882230E 05   THETA DOT =    0.
    TIME =     1.0000000E-09      EZ =   -1.8526562E 06      ER =   -9.3769197E 05    B THETA =   -1.9527054E-04
 DELTA T =     3.0000000E-10      BZ =    0.                 BR =   -0.                    V =    2.2742777E 06
    T-TZ =     1.0000000E-09     BZO =    0.          BETA/DELTA =    5.3591555E 00        C*T =    2.9979100E-01

    PHI =      6.2788026E-01       Z =    5.8967870E-01      R =    1.8522669E-02      THETA =    0.
PHI-PHIZ =     6.2788026E-01   Z DOT =    2.9673046E 08   R DOT =   -1.2840488E 06   THETA DOT =    0.
    TIME =     2.0000000E-09      EZ =   -3.5242515E 06      ER =   -9.9185481E 05    B THETA =   -1.5707599E-04
 DELTA T =     3.0000002E-10      BZ =    0.                 BR =   -0.                    V =    3.0752051E 06
    T-TZ =     2.0000000E-09     BZO =    0.          BETA/DELTA =    6.9477888E 00        C*T =    5.9958199E-01

    PHI =      9.4182038E-01       Z =    8.8716731E-01      R =    1.7157672E-02      THETA =    0.
PHI-PHIZ =     9.4182038E-01   Z DOT =    2.9811368E 08   R DOT =   -1.3889869E 06   THETA DOT =    0.
    TIME =     3.0000000E-09      EZ =   -4.8513895E 06      ER =   -1.0707629E 06    B THETA =   -1.0577497E-04
 DELTA T =     3.0000005E-10      BZ =    0.                 BR =   -0.                    V =    4.3301145E 06
    T-TZ =     3.0000000E-09     BZO =    0.          BETA/DELTA =    9.4228220E 00        C*T =    8.9937299E-01

    PHI =      1.2557605E 00       Z =    1.1856856E 00      R =    1.5828385E-02      THETA =    0.
PHI-PHIZ =     1.2557605E 00   Z DOT =    2.9884023E 08   R DOT =   -1.2421074E 06   THETA DOT =    0.
    TIME =     4.0000000E-09      EZ =   -5.7043181E 06      ER =   -1.1606868E 06    B THETA =   -5.1393072E-05
 DELTA T =     3.0000005E-10      BZ =    0.                 BR =   -0.                    V =    5.9172865E 06
    T-TZ =     4.0000000E-09     BZO =    0.          BETA/DELTA =    1.2542655E 01        C*T =    1.1991640E 00

    PHI =      1.5697006E 00       Z =    1.4847290E 00      R =    1.4706894E-02      THETA =    0.
PHI-PHIZ =     1.5697006E 00   Z DOT =    2.9920575E 08   R DOT =   -9.9221884E 05   THETA DOT =    0.
    TIME =     4.9999999E-09      EZ =   -5.9996385E 06      ER =   -1.2491964E 06    B THETA =   -1.6886910E-07
 DELTA T =     1.5000007E-10      BZ =    0.                 BR =   -0.                    V =    7.6804580E 06
    T-TZ =     4.9999999E-09     BZO =    0.          BETA/DELTA =    1.6002460E 01        C*T =    1.4989550E 00
```

130

131

PHI = 1.8836408E 00   Z = 1.7840396E 00   R = 1.3851747E-02   THETA = 0.
PHI-PHIZ = 1.8836408E 00   Z DOT = 2.9939539E 08   R DOT = -7.1730573E 05   THETA DOT = 0.
TIME = 5.9999999E-09   EZ = -5.7084693E 06   ER = -1.3263163E 06   B THETA = 4.4672917E-05
DELTA T = 3.0000008E-10   BZ = 0.   BR = -0.   V = 9.4460632E 06
T-TZ = 5.9999999E-09   BZO = 0.   BETA/DELTA = 1.9463987E 01   C*T = 1.7987460E 00

PHI = 2.1975809E 00   Z = 2.0834912E 00   R = 1.3270924E-02   THETA = 0.
PHI-PHIZ = 2.1975809E 00   Z DOT = 2.9949743E 08   R DOT = -4.4572387E 05   THETA DOT = 0.
TIME = 6.9999999E-09   EZ = -4.8592693E 06   ER = -1.3843646E 06   B THETA = 8.1568233E-05
DELTA T = 3.0000008E-10   BZ = 0.   BR = -0.   V = 1.1040657E 07
T-TZ = 6.9999999E-09   BZO = 0.   BETA/DELTA = 2.2588781E 01   C*T = 2.0985370E 00

PHI = 2.5429149E 00   Z = 2.4129749E 00   R = 1.2940679E-02   THETA = 0.
PHI-PHIZ = 2.5429149E 00   Z DOT = 2.9955662E 08   R DOT = -1.5589248E 05   THETA DOT = 0.
TIME = 8.0999995E-09   EZ = -3.3811466E 06   ER = -1.4196935E 06   B THETA = 1.1202116E-04
DELTA T = 2.0000000E-10   BZ = 0.   BR = -0.   V = 1.2411381E 07
T-TZ = 8.0999995E-09   BZO = 0.   BETA/DELTA = 2.5274177E 01   C*T = 2.4283070E 00

PROBLEM NUMBER   1.   ADD APERTURE CORRECTION, NEXT CYCLE
    DELTA R DOT = 3.4436713E 05   Z= 2.5927146E 00

PHI = 2.8254611E 00   Z = 2.6825872E 00   R = 1.2999893E-02   THETA = 0.
PHI-PHIZ = 2.8254611E 00   Z DOT = 2.9957548E 08   R DOT = 3.5484174E 05   B THETA = 0.
TIME = 8.9999998E-09   EZ = 0.   ER = -1.4132269E 06   THETA DOT = 0.
DELTA T = 7.5685791E-11   BZ = 0.   BR = -0.   V = 1.2949210E 07
T-TZ = 8.9999998E-09   BZO = 0.   BETA/DELTA = 2.6327709E 01   C*T = 2.6981190E 00

PHI = 3.1394013E 00   Z = 2.9821623E 00   R = 1.3361457E-02   THETA = -0.
PHI-PHIZ = 3.1394013E 00   Z DOT = 2.9957507E 08   R DOT = 3.6822738E 05   THETA DOT = -0.
TIME = 9.9999998E-09   EZ = 0.   ER = -1.3749846E 06   B THETA = 0.
DELTA T = 1.0000034E-10   BZ = 0.   BR = 0.   V = 1.2949732E 07
T-TZ = 9.9999998E-09   BZO = 0.   BETA/DELTA = 2.6328731E 01   C*T = 2.9979099E 00

PHI = 3.4533414E 00   Z = 3.2817374E 00   R = 1.3736226E-02   THETA = -0.
PHI-PHIZ = 3.4533414E 00   Z DOT = 2.9957552E 08   R DOT = 3.8124810E 05   THETA DOT = -0.
TIME = 1.1000000E-08   EZ = 0.   ER = -1.3374706E 06   B THETA = 0.
DELTA T = 3.0000024E-10   BZ = 0.   BR = 0.   V = 1.2950219E 07
T-TZ = 1.1000000E-08   BZO = 0.   BETA/DELTA = 2.6329686E 01   C*T = 3.2977009E 00

PHI = 3.7672815E 00   Z = 3.5813125E 00   R = 1.4123833E-02   THETA = -0.
PHI-PHIZ = 3.7672815E 00   Z DOT = 2.9957526E 08   R DOT = 3.9390919E 05   THETA DOT = -0.
TIME = 1.2000000E-08   EZ = 0.   ER = -1.3007657E 06   B THETA = 0.
DELTA T = 3.0000024E-10   BZ = 0.   BR = 0.   V = 1.2950741E 07
T-TZ = 1.2000000E-08   BZO = 0.   BETA/DELTA = 2.6330709E 01   C*T = 3.5974919E 00

EXECUTION BEGAN - 180617
2584 LINES OUTPUT. - 180627
$IBSYS

```
    ■ ■     5JCB, DICKMAN,D.  GS3    G11      GRAPE SEED 3
            $EXECUTE      IBJOB
IBJCB VERSION 5 HAS CONTROL.
$IBJOB          GO,MAP
$■
$■            VENABLE ■ BACKWARD GRAPESEED 3
$■
$IBFTC GS3     LIST,REF
        GS3        -  EFN   SOURCE STATEMENT  -  IFN(S)  -

C
C    MAIN CODE FOR GRAPE SEED 3
C
     EXTERNAL FY
C
     DIMENSION YI(14),YP(14),Y4(56),BESTEM(100),TEMP(5)
C
     COMMON /NAMED/ EZERO,E1,ZMAX,PHIMAX,RMAX,Z11,Z21,Z12,
    2Z22,Z13,Z23,B00,B1,B2,CENGTH,ETA,CMU,DLAMB,
    3BETAZ,CAPI,Z1,Z2,FPNO,ENDNO,TEST,RIN,ROUT,
    4PINTER,SHIFT,SWITST,PROBNO,TZ,RZ,THETAZ,ZZ,
    5RZDOT,THZDOT,ZZDOT,CSQ,CON1,OMEGA1,OMEGA2,
    6CON5,OMEGA,CON7,CON8,CON9,CON10,CON11,CON12,
    7CON13,CON14,ER,BTHETA,EZ,BR,BZ,T,PHI,PHIZ,
    8PHI1,TZ1,Z,ZDOT,R,ROOT,THETA,THEDOT,BZO,CT1,
    9BETASQ,BETA,DELTA,SETNO,DMONTH,DAY,YEAR,ACC,
    ADT,DNI1,DNI2,PSI1,PSI2,FREQ1,FREQ2,
    BC,CON2,CON3,CON4,CON6
C
C          SET CONSTANTS AND ENDSET FLAG
     FPNO=0.0                                               EQ 13
C
C          INITIALIZE READS AND TESTS
   1 IF(FPNO)2,3,3                                          LASTSET
   2 CALLEXIT
C                                                                   5
   3 CALL READ1                                             SETREAD  7
     PROBNO=0.0                                             EQ 14
C
C    COMPUTE VALUES FOR SET
C
     CSQ=C**2                                               EQ 2
     CMU=ABS(CSQ/ETA)                                       EQ 2.1
     CON1=1.0/C                                             EQ 3
     CON2=3.14159                                           EQ 4
     CON3=6.28318                                           EQ 5
     CON4=39.4.7842                                         EQ 6
     CON6=CON3*C                                            EQ 7
     CON10=1.5                                              EQ 8
     CON11=1.5L0/16.0                                       EQ 9
     CON12=0.75                                             EQ 10
     CON13=45.0/64.0                                        EQ 11
     CON15=CON3*(1.0E-7)                                    EQ 12
     OMEGA1=CON3*FREQ1
     OMEGA2=CON3*FREQ2
     CON5=CON4/(DLAMB**2)
     OMEGA=CON6/DLAMB
     CON7=EZERO/C
     CON8=DLAMB/CON3
     CON9=CON15*DNI1
     CON14=CON15*DNI2
C
     CALL PRINT1                                            SETPRT
C                                                                    9
   4 IF(PROBNO-ENDNO)5,1,5                                  LASTPROB
C
   5 CALL READ2                                             PROREAD
C                                                                   13
     CALL SUBA                                              BZOCALC  15
     DTZ=DT                                                 SAVEDT
     ZFLAG=0.0
C
C          SET INITIAL CONDITIONS
     YI(1)=R                                                EQ 15
     YI(2)=THETA                                            EQ 16
     YI(3)=Z                                                EQ 17
     YI(4)=COS((OMEGA1*T)+PSI1)                             EQ 18    17
     YI(5)=SIN((OMEGA1*T)+PSI1)                             EQ 19    18
     YI(6)=COS((OMEGA2*T)+PSI2)                             EQ 20    19
     YI(7)=SIN((OMEGA2*T)+PSI2)                             EQ 21
```

132

```
G                                                                    20
      ARGA=(CCN3*R)/DLAMB                              EQ 22
      BESANS=0.0                                       EQ 23
      NBES=0                                           EQ 24
C
      CALL BESJN(ARGA,NBES,BESTEM,BESANS)              J(ZERO)
C                                                                    22
      YI(8)=BESANS                                     EQ 25
C
      BESANS=0.0                                       EQ 26
      NBES=1                                           EQ 27
C
      CALL BESJN(ARGA,NBES,BESTEM,BESANS)              J(ONE)
C                                                                    25
      YI(9)=ARGA*BESANS                                EQ 28
      YI(10)=SIN(OMEGA*T)                              EQ 29        27
      YI(11)=COS(OMEGA*T)                              EQ 30        28
      BETASQ=((RDOT**2)+((R**2)*(THEDOT**2))+(ZDOT**2))/CSQ  EQ 31
      BETA=SQRT(BETASQ)                                EQ 32        29
      DELTA=SQRT(1.0-BETASQ)                           EQ 33        30
      YI(12)=RDOT/DELTA                                EQ 34
      YI(13)=((R**2)*THEDOT)/DELTA                     EQ 35
      YI(14)=ZDOT/DELTA                                EQ 36
      N=14                                             EQ 37
C
      CALL FY(T,YI,YP,N)                               FYSUB
C                                                                    32
      PHIZ=OMEGA*TZ                                    EQ 38
C
      CALL PRINT2                                      PROPRT
C                                                                    34
      XF=T+PINTER                                      EQ 39
      SH=DT*1.0E-5                                     EQ 40
      NF=0                                             EQ 41
      IND=0                                            EQ 42
C
      CALL RKA(T,DT,YI,YP,Y4,FY,ACC,XF,SH,NF,IND,N)    CALLRKA
C                                                                    38
      IF(ROUT)300,300,41
C
   41 WRITE(9,201)PROBNO                               APERCOMM
C                                                                    41
      V=CMU*((1.0/DELTA)-1.0)                          EQ 64
C
      AINCR=(ETA*YI(1)*DELTA*EZERO*YI(10))             EQ 65
     B/(2.0*CSQ*BETASQ)
C
      TEMP(1)=(YP(1)/YP(3))-AINCR                      EQ 57
      TEMP(2)=(TEMP(1)**2)+1.0                         EQ 67
      TEMP(3)=(YP(1)**2)+(YP(3)**2)                    EQ 68
      TEMP(3)=TEMP(3)/TEMP(2)                          EQ 69
      TEMP(5)=SQRT(TEMP(3))                            EQ 70        42
      YI(14)=TEMP(5)/DELTA                             EQ 70.1
      TEMP(3)=TEMP(5)*TEMP(1)                          EQ 70.2
      YI(12)=TEMP(3)/DELTA                             EQ 70.3
      TEMP(4)=TEMP(3)-YP(1)                            EQ 71
      WRITE(9,202)TEMP(4),YI(3)                        DRDOT
C
C                                                                    43
  300 CALL RKB
C                                                                    45
      Z=YI(3)                                          EQ 72
      ZDOT=YI(14)*DELTA                                EQ 73
      R=YI(1)                                          EQ 74
      RDOT=YI(12)*DELTA                                EQ 75
      THETA=YI(2)                                      EQ 76
      THEDOT=(YI(13)*DELTA)/(R**2)                     EQ 77
C
      CALL SUBA                                        BZO CALC
C                                                                    47
      CALL PRINT2                                      PROPRT
C                                                                    49
      XF=XF+PINTER                                     EQ 78
      CT=DTZ                                           EQ 79
C
      IF(ZFLAG)301,221,221
  221 IF(Z-RIN)200,200,301
```

133

```
C
   260 WRITE(9,201)PROBNO                                                               54
   201 FORMAT(25H0       PROBLEM NUMBER       ,F10.0,            APERTURE
       A45H             ADC APERTURE CORRECTION, NEXT CYCLE)    COMMENT
C
       V=GMU*((1.0/DELTA)-1.0)                                 EQ 55
C
       AINCR=(ETA*YI(1)*DELTA*EZERO*YI(10))                    EQ 56
       A/(2.0*CSQ*BETASC)
C
       TEMP(1)=(YP(1)/YP(3))+AINCR                             EQ 66
       TEMP(2)=(TEMP(1)**2)+1.0                                EQ 58
       TEMP(3)=(YP(1)**2)+(YP(3)**2)                           EQ 59
       TEMP(3)=TEMP(3)/TEMP(2)                                 EQ 60
       TEMP(5)=SQRT(TEMP(3))                                   EQ 61      55
       YI(14)=TEMP(5)/DELTA                                    EQ 61.1
       TEMP(3)=TEMP(5)*TEMP(1)                                 EQ 61.2
       YI(12)=TEMP(3)/DELTA                                    EQ 61.3
       TEMP(4)=TEMP(3)-YP(1)                                   EQ 62
C
       WRITE(9,202)TEMP(4),YI(3)                                           56
   202 FORMAT(23H        DELTA R DOT =,1PE16.7,
       A15H          Z= ,1PE16.7)
C
       ZFLAG=-1.0                                              EQ 14.6
   301 IF(IND-2)302,50,302
    50 IF(SHIFT)1,4,1
   302 IND=0
       IF(Z)4,4,303
   303 IF(TEST)300,304,300
   304 IF(R-RMAX)305,4,4
   305 IF(PHI-PHIMAX)300,4,4
       STOP

       END
```

MCNTH = 2   DAY = 9.   YEAR =1965.   SET NUMBER = 1.

ACCURACY DESIRED = 1.0000000E-05   DELTA T = -1.0000000E-11   BETA ZERO = 8.8794539E-01

     J = 3.0000000E 02   Z1 = -1.0000000E-01   Z2 = 1.4000000E 00   L = 1.3000000E 00

     IN = 1.0000000E-02   OUT = 1.0000000E-02   B1 = 1.1000000E 00   B2 = 1.1000000E 00

     NI1 = 0.   NI2 = 0.   PSI1 = 0.   PSI2 = 0.

     ETA = -1.7587960E 11   FREQ1 = 0.   FREQ2 = 0.   MU = 5.1100606E 05

     LAMDA = 3.0000000E 00   BOO = 0.   Z11 = -5.0000000E-01   Z21 = 1.8000000E 00

     Z12 = -5.0000000E-01   Z22 = 1.8000000E 00   Z13 = -5.0000000E-01   Z23 = 1.8000000E 00

     EZERO = -4.0000000E 06   E1 = 0.   Z MAX = 1.6000000E 00

     PHI MAX = 1.0000000E 02   R MAX = 1.1500000E 00

PROBLEM NUMBER = 1.

     PHI = 2.8254753E 00   Z = 1.2987730E 00   R = 4.2674270E-02   THETA = 0.
PHI-PHIZ = 0.   Z DOT = 2.9799922E 08   R DOT = -3.0173558E 06   THETA DOT = 0.
     TIME = 4.4999999E-09   EZ = -1.2410324E 06   ER = -4.7470046E 05   B THETA = 5.6614661E-04
     DELTA T = -1.0000000E-11   BZ = 0.   BR = -0.   V = 4.1879289E 06
     T-TZ = 0.   BZO = 0.   BETA/DELTA = 9.1409218E 00   C*T = 1.3490662E 00

PROBLEM NUMBER   1.   ADD APERTURE CORRECTION, NEXT CYCLE
     DELTA R DOT = -1.7024730E 06   Z= 1.2987730E 00

     PHI = 2.7626870E 00   Z = 1.2689770E 00   R = 4.3164946E-02   THETA = 0.
PHI-PHIZ = -6.2788337E-02   Z DOT = 2.9793998E 08   R DOT = -5.0954272E 06   THETA DOT = -0.
     TIME = 4.3999999E-09   EZ = -1.4765942E 06   ER = -4.6930432E 05   B THETA = 5.5976190E-04
     DELTA T = -3.0000002E-11   BZ = 0.   BR = -0.   V = 4.1476609E 06
     T-TZ = -1.0000001E-10   BZO = 0.   BETA/DELTA = 9.0616465E 00   C*T = 1.3190870E 00

     PHI = 2.6998986E 00   Z = 1.2391851E 00   R = 4.3693702E-02   THETA = 0.
PHI-PHIZ = -1.2557667E-01   Z DOT = 2.9789584E 08   R DOT = -5.4815577E 06   THETA DOT = -0.
     TIME = 4.3000000E-09   EZ = -1.7063079E 06   ER = -4.6362506E 05   B THETA = 5.5133288E-04
     DELTA T = -3.0000002E-11   BZ = 0.   BR = -0.   V = 4.1004788E 06
     T-TZ = -2.0000001E-10   BZO = 0.   BETA/DELTA = 8.9687483E 00   C*T = 1.2891077E 00

     PHI = 2.6371103E 00   Z = 1.2093980E 00   R = 4.4261625E-02   THETA = 0.
PHI-PHIZ = -1.8836504E-01   Z DOT = 2.9784413E 08   R DOT = -5.8788642E 06   THETA DOT = -0.
     TIME = 4.1999999E-09   EZ = -1.9292655E 06   ER = -4.5767626E 05   B THETA = 5.4081295E-04
     DELTA T = -3.0000002E-11   BZ = 0.   BR = -0.   V = 4.0465769E 06
     T-TZ = -3.0000002E-10   BZO = 0.   BETA/DELTA = 8.8626049E 00   C*T = 1.2591285E 00

     PHI = 2.5743219E 00   Z = 1.1796164E 00   R = 4.4869865E-02   THETA = 0.
PHI-PHIZ = -2.5115338E-01   Z DOT = 2.9778453E 08   R DOT = -6.2879972E 06   THETA DOT = -0.
     TIME = 4.0999999E-09   EZ = -2.1445856E 06   ER = -4.5147216E 05   B THETA = 5.2815480E-04
     DELTA T = -3.0000002E-11   BZ = 0.   BR = -0.   V = 3.9861696E 06
     T-TZ = -4.0000003E-10   BZO = 0.   BETA/DELTA = 8.7436321E 00   C*T = 1.2291492E 00

     PHI = 2.5115336E 00   Z = 1.1498412E 00   R = 4.5519636E-02   THETA = 0.
PHI-PHIZ = -3.1394172E-01   Z DOT = 2.9771625E 08   R DOT = -6.7095902E 06   THETA DOT = -0.
     TIME = 3.9999999E-09   EZ = -2.3514169E 06   ER = -4.4502762E 05   B THETA = 5.1331061E-04
     DELTA T = -3.0000002E-11   BZ = 0.   BR = -0.   V = 3.9195041E 06
     T-TZ = -5.0000004E-10   BZO = 0.   BETA/DELTA = 8.6123095E 00   C*T = 1.1991700E 00

```
RHI   =    2.4487452E 00        Z =    1.1200733E 00         R =    4.6212216E-02      THETA  =   0.
PHI-PHIZ = - 3.7673008E-01    Z DOT =    2.9763855E 08     R DOT =   -7.1442630E 06   THETA DOT =  -0.
TIME  =    3.8999999E-09       EZ =   -2.5489415E 06        ER =   -4.3835802E 05     B THETA  =   4.9623229E-04
DELTA T =  -3.0000002E-11      BZ =    0.                   BR =   -0.                       V  =   3.8468503E 06
T-TZ  =   -6.0000005E-10      BZO =    0.              BETA/DELTA =    8.4691601E 00       C•T  =   1.1691907F 00

RHI   =    2.3859569E 00        Z =    1.0903137E 00         R =    4.6948941E-02      THETA  =   0.
PHI-PHIZ =   -4.3951842E-01   Z DOT =    2.9755077E 08     R DOT =   -7.5926117E 06   THETA DOT =  -0.
TIME  =    3.7999999E-09       EZ =   -2.7363783E 06        ER =   -4.3147928E 05     B THETA  =   4.7687188E-04
DELTA T =  -3.0000002E-11      BZ =    0.                   BR =   -0.                       V  =   3.7684996E 06
T-TZ  =   -7.0000005E-10      BZO =    0.              BETA/DELTA =    8.3147489E 00       C•T  =   1.1392115E 00

RHI   =    2.3231685E 00        Z =    1.0605634E 00         R =    4.7731209E-02      THETA  =   0.
PHI-PHIZ =   -5.0230676E-01   Z DOT =    2.9745179E 08     R DOT =   -8.0551833E 06   THETA DOT =  -0.
TIME  =    3.6999999E-09       EZ =   -2.9129859E 06        ER =   -4.2440776E 05     B THETA  =   4.5518181E-04
DELTA T =  -3.0000002E-11      BZ =    0.                   BR =   -0.                       V  =   3.6847718E 06
T-TZ  =   -8.0000006E-10      BZO =    0.              BETA/DELTA =    8.1496954E 00       C•T  =   1.1092372E 00

RHI   =    2.2603802E 00        Z =    1.0308236E 00         R =    4.8560466E-02      THETA  =   0.
PHI-PHIZ =   -5.6509510E-01   Z DOT =    2.9734055E 08     R DOT =   -8.5324732E 06   THETA DOT =  -0.
TIME  =    3.5999999E-09       EZ =   -3.0780659E 06        ER =   -4.1716024E 05     B THETA  =   4.3111534E-04
DELTA T =  -3.0000002E-11      BZ =    0.                   BR =   -0.                       V  =   3.5960051E 06
T-TZ  =   -9.0000007E-10      BZO =    0.              BETA/DELTA =    7.9746544E 00       C•T  =   1.0792530F 00

PHI   =    2.1975918E 00        Z =    1.0010957E 00         R =    4.9438204E-02      THETA  =   0.
PHI-PHIZ =   -6.2788346E-01   Z DOT =    2.9721577E 08     R DOT =   -9.0248975E 06   THETA DOT =  -0.
TIME  =    3.4999999E-09       EZ =   -3.2309651E 06        ER =   -4.0975387E 05     B THETA  =   4.0462711E-04
DELTA T =  -3.0000002E-11      BZ =    0.                   BR =   -0.                       V  =   3.5025597E 06
T-TZ  =   -1.0000001E-09      BZO =    0.              BETA/DELTA =    7.7903231E 00       C•T  =   1.0492737E 00

PHI   =    2.1348035E 00        Z =    9.7138093E-01         R =    5.0365955E-02      THETA  =   0.
PHI-PHIZ =   -6.9067180E-01   Z DOT =    2.9707595E 08     R DOT =   -9.5327694E 06   THETA DOT =  -0.
TIME  =    3.3999999E-09       EZ =   -3.3710787E 06        ER =   -4.0220612E 05     B THETA  =   3.7567369E-04
DELTA T =  -3.0000002E-11      BZ =    0.                   BR =   -0.                       V  =   3.4048156E 06
T-TZ  =   -1.1000001E-09      BZO =    0.              BETA/DELTA =    7.5974360E 00       C•T  =   1.0192945F 00

RHI   =    2.0720152E 00        Z =    9.4168098E-01         R =    5.1345275E-02      THETA  =   0.
PHI-PHIZ =   -7.5346014E-01   Z DOT =    2.9691957E 08     R DOT =   -1.0056276E 07   THETA DOT =  -0.
TIME  =    3.2999999E-09       EZ =   -3.4978526E 06        ER =   -3.9453475E 05     B THETA  =   3.4421427E-04
DELTA T =  -3.0000002E-11      BZ =    0.                   BR =   -C.                       V  =   3.3031680E 06
T-TZ  =   -1.2000001E-09      BZO =    0.              BETA/DELTA =    7.3967575E 00       C•T  =   9.8931521E-01

RHI   =    2.0092268E 00        Z =    9.1199759E-01         R =    5.2377729E-02      THETA  =   0.
PHI-PHIZ =   -8.1624850E-01   Z DOT =    2.9674456E 08     R DOT =   -1.0595430E 07   THETA DOT =  -0.
TIME  =    3.1999999E-09       EZ =   -3.6107851E 06        ER =   -3.8675780E 05     B THETA  =   3.1021151E-04
DELTA T =  -3.0000002E-11      BZ =    0.                   BR =   -0.                       V  =   3.1980326E 06
T-TZ  =   -1.3000001E-09      BZO =    0.              BETA/DELTA =    7.1890901E 00       C•T  =   9.5933596E-01

PHI   =    1.9464385E 00        Z =    8.8233271E-01         R =    5.3464872E-02      THETA  =   0.
PHI-PHIZ =   -8.7903682E-01   Z DOT =    2.9654884E 08     R DOT =   -1.1150037E 07   THETA DOT =  -0.
TIME  =    3.0999998E-09       EZ =   -3.7094297E 06        ER =   -3.7889355E 05     B THETA  =   2.7363239E-04
DELTA T =  -3.0000002E-11      BZ =    0.                   BR =   -0.                       V  =   3.0898363E 06
T-TZ  =   -1.4000001E-09      BZO =    0.              BETA/DELTA =    6.9752573E 00       C•T  =   9.2935671F-01

RHI   =    1.8836501E 00        Z =    8.5268853E-01         R =    5.4608232E-02      THETA  =   0.
PHI-PHIZ =   -9.4182518E-01   Z DOT =    2.9632989E 08     R DOT =   -1.1719636E 07   THETA DOT =  -0.
TIME  =    2.9999999E-09       EZ =   -3.7933967E 06        ER =   -3.7096047E 05     B THETA  =   2.3444937E-04
DELTA T =  -3.0000002E-11      BZ =    0.                   BR =   -0.                       V  =   2.9790213E 06
T-TZ  =   -1.5000001E-09      BZO =    0.              BETA/DELTA =    6.7561121E 00       C•T  =   8.9937745E-01
```

```
        PHI =    1.8208618E 00        Z =    8.2306753E-01        R =    5.5809270E-02        THETA =    0.
   PHI-PHIZ =   -1.0046135E 00     Z DOT =    2.9608497E 08    R DOT =   -1.2303446E 07    THETA DOT =   -0.
       TIME =    2.8999998E-09        EZ =   -3.8623542E 06        ER =   -3.6297726E 05    B THETA =    1.9264163E-04
    DELTA T =   -3.0000002E-11        BZ =    0.                   BR =   -0.                     V =    2.8660389E 06
       T-TZ =   -1.6000001E-09       BZO =    0.           BETA/DELTA =    6.5325234E 00        C*T =    8.6939819E-01

        PHI =    1.7580734E 00        Z =    7.9347246E-01        R =    5.7069352E-02        THETA =    0.
   PHI-PHIZ =   -1.0674019E 00     Z DOT =    2.9581081E 08    R DOT =   -1.2900277E 07    THETA DOT =   -0.
       TIME =    2.7999998E-09        EZ =   -3.9160305E 06        ER =   -3.5496277E 05    B THETA =    1.4819653E-04
    DELTA T =   -3.0000002E-11        BZ =    0.                   BR =   -0.                     V =    2.7513525E 06
       T-TZ =   -1.7000001E-09       BZO =    0.           BETA/DELTA =    6.3053828E 00        C*T =    8.3941895E-01

        PHI =    1.6952851E 00        Z =    7.6390642E-01        R =    5.8389701E-02        THETA =    0.
   PHI-PHIZ =   -1.1301902E 00     Z DOT =    2.9550377E 08    R DOT =   -1.3508451E 07    THETA DOT =   -0.
       TIME =    2.6999998E-09        EZ =   -3.9542145E 06        ER =   -3.4693611E 05    B THETA =    1.0111135E-04
    DELTA T =   -3.0000002E-11        BZ =    0.                   BR =   -0.                     V =    2.6354319E 06
       T-TZ =   -1.8000001E-09       BZO =    0.           BETA/DELTA =    6.0755934E 00        C*T =    8.0943969E-01

        PHI =    1.6324967E 00        Z =    7.3437290E-01        R =    5.9771342E-02        THETA =    0.
   PHI-PHIZ =   -1.1929786E 00     Z DOT =    2.9515984E 08    R DOT =   -1.4125698E 07    THETA DOT =   -0.
       TIME =    2.5999998E-09        EZ =   -3.9767572E 06        ER =   -3.3891652E 05    B THETA =    5.1395234E-05
    DELTA T =   -3.0000002E-11        BZ =    0.                   BR =   -0.                     V =    2.5187521E 06
       T-TZ =   -1.9000002E-09       BZO =    0.           BETA/DELTA =    5.8440667E 00        C*T =    7.7946044E-01

        PHI =    1.5697084E 00        Z =    7.0487580E-01        R =    6.1215041E-02        THETA =    0.
   PHI-PHIZ =   -1.2557669E 00     Z DOT =    2.9477432E 08    R DOT =   -1.4749028E 07    THETA DOT =   -0.
       TIME =    2.4999998E-09        EZ =   -3.9835716E 06        ER =   -3.3092350E 05    B THETA =   -9.2851334E-07
    DELTA T =   -3.0000002E-11        BZ =    0.                   BR =   -0.                     V =    2.4017935E 06
       T-TZ =   -2.0000001E-09       BZO =    0.           BETA/DELTA =    5.6117243E 00        C*T =    7.4948119E-01

        PHI =    1.5069201E 00        Z =    6.7541953E-01        R =    6.2721220E-02        THETA =    0.
   PHI-PHIZ =   -1.3185553E 00     Z DOT =    2.9434199E 08    R DOT =   -1.5374593E 07    THETA DOT =   -0.
       TIME =    2.3999998E-09        EZ =   -3.9746343E 06        ER =   -3.2297675E 05    B THETA =   -5.5819809E-05
    DELTA T =   -3.0000002E-11        BZ =    0.                   BR =   -0.                     V =    2.2850380E 06
       T-TZ =   -2.1000002E-09       BZO =    0.           BETA/DELTA =    5.3794892E 00        C*T =    7.1950194E-01

        PHI =    1.4441317E 00        Z =    6.4600908E-01        R =    6.4289868E-02        THETA =    0.
   PHI-PHIZ =   -1.3813436E 00     Z DOT =    2.9385712E 08    R DOT =   -1.5997534E 07    THETA DOT =   -0.
       TIME =    2.2999998E-09        EZ =   -3.9499847E 06        ER =   -3.1509624E 05    B THETA =   -1.1321879E-04
    DELTA T =   -3.0000002E-11        BZ =    0.                   BR =   -0.                     V =    2.1689664E 06
       T-TZ =   -2.2000002E-09       BZO =    0.           BETA/DELTA =    5.1482818E 00        C*T =    6.8952268E-01

        PHI =    1.3813434E 00        Z =    6.1665002E-01        R =    6.5920432E-02        THETA =    0.
   PHI-PHIZ =   -1.4441319E 00     Z DOT =    2.9331323E 08    R DOT =   -1.6611793E 07    THETA DOT =   -0.
       TIME =    2.1999998E-09        EZ =   -3.9097255E 06        ER =   -3.0730222E 05    B THETA =   -1.7304237E-04
    DELTA T =   -3.0000002E-11        BZ =    0.                   BR =   -0.                     V =    2.0540588E 06
       T-TZ =   -2.3000002E-09       BZO =    0.           BETA/DELTA =    4.9190198E 00        C*T =    6.5954343E-01

        PHI =    1.3185550E 00        Z =    5.8734857E-01        R =    6.7611685E-02        THETA =    0.
   PHI-PHIZ =   -1.5069203E 00     Z DOT =    2.9270332E 08    R DOT =   -1.7209930E 07    THETA DOT =   -0.
       TIME =    2.0999998E-09        EZ =   -3.8540225E 06        ER =   -2.9961530E 05    B THETA =   -2.3518040E-04
    DELTA T =   -3.0000002E-11        BZ =    0.                   BR =   -0.                     V =    1.9407898E 06
       T-TZ =   -2.4000002E-09       BZO =    0.           BETA/DELTA =    4.6926106E 00        C*T =    6.2956418E-01

        PHI =    1.2557667E 00        Z =    5.5811173E-01        R =    6.9361573E-02        THETA =    0.
   PHI-PHIZ =   -1.5697086E 00     Z DOT =    2.9201978E 08    R DOT =   -1.7782913E 07    THETA DOT =   -0.
       TIME =    1.9999998E-09        EZ =   -3.7831041E 06        ER =   -2.9205646E 05    B THETA =   -2.9949132E-04
    DELTA T =   -3.0000002E-11        BZ =    0.                   BR =   -0.                     V =    1.8296276E 06
       T-TZ =   -2.5000002E-09       BZO =    0.           BETA/DELTA =    4.4699496E 00        C*T =    5.9958493E-01
```

```
RHI =      1.1929785E 00      Z =     5.2894726E-01      R =     7.1167062E-02      THETA =     0.
PHI-PHIZ =  -1.6324970E 00    Z DOT =  2.9125448E 08     R DOT =  -1.8319917E 07    THETA DOT =  -0.
TIME =      1.8999998E-09     EZ =    -3.6972599E 06     ER =     -2.8464707E 05    B THETA =   -3.6579735E-04
DELTA T =   -3.0000002E-11    BZ =     0.                BR =     -0.               V =          1.7210315E 06
T-TZ =      -2.6000002E-09    BZO =    0.                BETA/DELTA =  4.2519164E 00   C*T =    5.6960568E-01

RHI =      1.1301900E 00      Z =     4.9986378E-01      R =     7.3023926E-02      THETA =     0.
PHI-PHIZ =  -1.6952853E 00    Z DOT =  2.9039910E 08     R DOT =  -1.8808139E 07    THETA DOT =  -0.
TIME =      1.7999998E-09     EZ =    -3.5968406E 06     ER =     -2.7740901E 05    B THETA =   -4.3387938E-04
DELTA T =   -3.0000002E-11    BZ =     0.                BR =     -0.               V =          1.6154487E 06
T-TZ =      -2.7000002E-09    BZO =    0.                BETA/DELTA =  4.0393692E 00   C*T =    5.3962643E-01

RHI =      1.0674016E 00      Z =     4.7087070E-01      R =     7.4926559E-02      THETA =     0.
PHI-PHIZ =  -1.7580737E 00    Z DOT =  2.8944522E 08     R DOT =  -1.9232633E 07    THETA DOT =  -0.
TIME =      1.6999997E-09     EZ =    -3.4822561E 06     ER =     -2.7036468E 05    B THETA =   -5.0347133E-04
DELTA T =   -3.0000002E-11    BZ =     0.                BR =     -0.               V =          1.5133128E 06
T-TZ =      -2.8000002E-09    BZO =    0.                BETA/DELTA =  3.8331438E 00   C*T =    5.0964717E-01

RHI =      1.0046133E 00      Z =     4.4197826E-01      R =     7.6867750E-02      THETA =     0.
PHI-PHIZ =  -1.8208620E 00    Z DOT =  2.8838492E 08     R DOT =  -1.9576240E 07    THETA DOT =  -0.
TIME =      1.5999997E-09     EZ =    -3.3539738E 06     ER =     -2.6353699E 05    B THETA =   -5.7425463E-04
DELTA T =   -3.0000002E-11    BZ =     0.                BR =     -0.               V =          1.4150396E 06
T-TZ =      -2.9000002E-09    BZO =    0.                BETA/DELTA =  3.6340477E 00   C*T =    4.7966792E-01

RHI =      9.4182494E-01      Z =     4.1319746E-01      R =     7.8838460E-02      THETA =     0.
PHI-PHIZ =  -1.8836504E 00    Z DOT =  2.8721127E 08     R DOT =  -1.9819591E 07    THETA DOT =  -0.
TIME =      1.4999997E-09     EZ =    -3.2125171E 06     ER =     -2.5694940E 05    B THETA =   -6.4585256E-04
DELTA T =   -3.0000002E-11    BZ =     0.                BR =     -0.               V =          1.3210257E 06
T-TZ =      -3.0000002E-09    BZO =    0.                BETA/DELTA =  3.4428589E 00   C*T =    4.4968867E-01

RHI =      8.7903659E-01      Z =     3.8453992E-01      R =     8.0827607E-02      THETA =     0.
PHI-PHIZ =  -1.9464387E 00    Z DOT =  2.8591919E 08     R DOT =  -1.9941292E 07    THETA DOT =  -0.
TIME =      1.3999997E-09     EZ =    -3.0584626E 06     ER =     -2.5062595E 05    B THETA =   -7.1782518E-04
DELTA T =   -3.0000002E-11    BZ =     0.                BR =     -0.               V =          1.2316440E 06
T-TZ =      -3.1000002E-09    BZO =    0.                BETA/DELTA =  3.2603211E 00   C*T =    4.1970941E-01

RHI =      8.1624825E-01      Z =     3.5601762E-01      R =     8.2821888E-02      THETA =     0.
PHI-RHIZ =  -2.0092270E 00    Z DOT =  2.8450655E 08     R DOT =  -1.9918299E 07    THETA DOT =  -0.
TIME =      1.2999997E-09     EZ =    -2.8924380E 06     ER =     -2.4459108E 05    B THETA =   -7.8966532E-04
DELTA T =   -3.0000002E-11    BZ =     0.                BR =     -0.               V =          1.1472415E 06
T-TZ =      -3.2000003E-09    BZO =    0.                BETA/DELTA =  3.0871415E 00   C*T =    3.8973016E-01

RHI =      7.5345990E-01      Z =     3.2764255E-01      R =     8.4805635E-02      THETA =     0.
PHI-PHIZ =  -2.0720154E 00    Z DOT =  2.8297539E 08     R DOT =  -1.9726559E 07    THETA DOT =  -0.
TIME =      1.1999997E-09     EZ =    -2.7151183E 06     ER =     -2.3886968E 05    B THETA =   -8.6079599E-04
DELTA T =   -3.0000002E-11    BZ =     0.                BR =     -0.               V =          1.0681354E 06
T-TZ =      -3.3000003E-09    BZO =    0.                BETA/DELTA =  2.9239879E 00   C*T =    3.5975091E-01

RHI =      6.9067155E-01      Z =     2.9942622E-01      R =     8.6760763E-02      THETA =     0.
PHI-PHIZ =  -2.1348037E 00    Z DOT =  2.8133337E 08     R DOT =  -1.9341952E 07    THETA DOT =  -0.
TIME =      1.0999997E-09     EZ =    -2.5272232E 06     ER =     -2.3348683E 05    B THETA =   -9.3057028E-04
DELTA T =   -3.0000002E-11    BZ =     0.                BR =     -0.               V =          9.9461083E 05
T-TZ =      -3.4000003E-09    BZO =    0.                BETA/DELTA =  2.7714873E 00   C*T =    3.2977166E-01

RHI =      6.2788321E-01      Z =     2.7137905E-01      R =     8.8666824E-02      THETA =     0.
PHI-PHIZ =  -2.1975921E 00    Z DOT =  2.7959544E 08     R DOT =  -1.8741572E 07    THETA DOT =  -0.
TIME =      9.9999969E-10     EZ =    -2.3295127E 06     ER =     -2.2846759E 05    B THETA =   -9.9827478E-04
DELTA T =   -3.0000002E-11    BZ =     0.                BR =     -0.               V =          9.2691724E 05
T-TZ =      -3.5000003E-09    BZO =    0.                BETA/DELTA =  2.6302224E 00   C*T =    2.9979240E-01
```

```
     PHI =    6.6509487E-01      Z =    2.4350953E-01         R =    9.0501204E-02      THETA =      0.
PHI-PHIZ =   -2.2603804E 00      Z DOT =    2.7778513E 08     R DOT =   -1.7905294E 07   THETA DOT =   -0.
    TIME =    8.9999969E-10      EZ =    -2.1227834E 06        ER =   -2.2383675E 05     B THETA =   -1.0631366E-03
  DELTA T =  -2.9999996E-11      BZ =     0.                   BR =   -0.                      V =    8.6526723E 05
    T-TZ =   -3.6000003E-09      BZO =    0.            BETA/DELTA =    2.5007321E 00         C*T =    2.6981316E-01


     PHI =    5.0290653E-01      Z =    2.1582332E-01         R =    9.2239486E-02      THETA =      0.
PHI-PHIZ =   -2.3231688E 00      Z DOT =    2.7593573E 08     R DOT =   -1.6817590E 07   THETA DOT =   -0.
    TIME =    7.9999969E-10      EZ =    -1.9078634E 06        ER =   -2.1961848E 05     B THETA =   -1.1243356E-03
  DELTA T =  -2.9999996E-11      BZ =     0.                   BR =   -0.                      V =    8.0983472E 05
    T-TZ =   -3.7000003E-09      BZO =    0.            BETA/DELTA =    2.3835086E 00         C*T =    2.3983391E-01


     PHI =    4.3951819E-01      Z =    1.8832223E-01         R =    9.3856020E-02      THETA =      0.
PHI-PHIZ =   -2.3859571E 00      Z DOT =    2.7409075E 08     R DOT =   -1.5469432E 07   THETA DOT =   -0.
    TIME =    6.9999969E-10      EZ =    -1.6856083E 06        ER =   -2.1583587E 05     B THETA =   -1.1810222E-03
  DELTA T =  -2.9999996E-11      BZ =     0.                   BR =   -0.                      V =    7.6075518E 05
    T-TZ =   -3.8000003E-09      BZO =    0.            BETA/DELTA =    2.2789969E 00         C*T =    2.0985466E-01


     PHI =    3.7672985E-01      Z =    1.6100325E-01         R =    9.5324647E-02      THETA =      0.
PHI-PHIZ =   -2.4487455E 00      Z DOT =    2.7230316E 08     R DOT =   -1.3860091E 07   THETA DOT =   -0.
    TIME =    6.9999968E-10      EZ =    -1.4568964E 06        ER =   -2.1251057E 05     B THETA =   -1.2323399E-03
  DELTA T =  -2.9999996E-11      BZ =     0.                   BR =   -0.                      V =    7.1812757E 05
    T-TZ =   -3.9000002E-09      BZO =    0.            BETA/DELTA =    2.1875944E 00         C*T =    1.7987541E-01


     PHI =    3.1394150E-01      Z =    1.3385766E-01         R =    9.6619614E-02      THETA =      0.
PHI-PHIZ =   -2.5115338E 00      Z DOT =    2.7063357E 08     R DOT =   -1.1998062E 07   THETA DOT =   -0.
    TIME =    4.9999968E-10      EZ =    -1.2226237E 06        ER =   -2.0966235E 05     B THETA =   -1.2774528E-03
  DELTA T =  -2.9999996E-11      BZ =     0.                   BR =   -0.                      V =    6.8201748E 05
    T-TZ =   -4.0000002E-09      BZO =    0.            BETA/DELTA =    2.1096493E 00         C*T =    1.4989616E-01


     PHI =    2.5115316E-01      Z =    1.0687043E-01         R =    9.7716600E-02      THETA =      0.
PHI-PHIZ =   -2.5743221E 00      Z DOT =    2.6914685E 08     R DOT =   -9.9046482E 06   THETA DOT =   -0.
    TIME =    3.9999968E-10      EZ =    -9.8370047E 05        ER =   -2.0730864E 05     B THETA =   -1.3155772E-03
  DELTA T =  -2.9999999E-11      BZ =     0.                   BR =   -0.                      V =    6.5246244E 05
    T-TZ =   -4.1000003E-09      BZO =    0.            BETA/DELTA =    2.0454600E 00         C*T =    1.1991691E-01


     PHI =    1.8836482E-01      Z =    8.0020033E-02         R =    9.8593792E-02      THETA =      0.
PHI-PHIZ =   -2.6371105E 00      Z DOT =    2.6790745E 08     R DOT =   -7.6086837E 06   THETA DOT =   -0.
    TIME =    2.9999968E-10      EZ =    -7.4104702E 05        ER =   -2.0546421E 05     B THETA =   -1.3460137E-03
  DELTA T =  -2.9999999E-11      BZ =     0.                   BR =   -0.                      V =    6.2947855E 05
    T-TZ =   -4.2000003E-09      BZO =    0.            BETA/DELTA =    1.9952737F 00         C*T =    8.9937655E-02


     PHI =    1.2557648E-01      Z =    5.3278731E-02         R =    9.9232936E-02      THETA =      0.
PHI-PHIZ =   -2.6998988E 00      Z DOT =    2.6697391E 08     R DOT =   -5.1511878E 06   THETA DOT =   -0.
    TIME =    1.9999968E-10      EZ =    -4.9559073E 05        ER =   -2.0414084E 05     B THETA =   -1.3681790E-03
  DELTA T =  -2.9999997E-11      BZ =     0.                   BR =   -0.                      V =    6.1306763E 05
    T-TZ =   -4.3000002E-09      BZO =    0.            BETA/DELTA =    1.9592850E 00         C*T =    5.9958405E-02


     PHI =    6.2788143E-02      Z =    2.6613471E-02         R =    9.9620261E-02      THETA =      0.
PHI-PHIZ =   -2.7626871E 00      Z DOT =    2.6639319E 08     R DOT =   -2.5810540E 06   THETA DOT =   -0.
    TIME =    9.9999685E-11      EZ =    -2.4826351E 05        ER =   -2.0334714E 05     B THETA =   -1.3816342E-03
  DELTA T =  -2.9999999E-11      BZ =     0.                   BR =   -0.                      V =    6.0322464E 05
    T-TZ =   -4.4000002E-09      BZO =    0.            BETA/DELTA =    1.9376343E 00         C*T =    2.9979155E-02


     PHI =   -1.9714594E-07      Z =   -1.2705577E-05         R =    9.9747183E-02      THETA =      0.
PHI-PHIZ =   -2.8254755E 00      Z DOT =    2.6619572E 08     R DOT =    4.5337739E 04   THETA DOT =   -0.
    TIME =   -3.1398495E-16      EZ =     0.                   ER =   -2.0308839E 05     B THETA =      0.
  DELTA T =  -1.8539427E-14      BZ =     0.                   BR =   -0.                      V =    5.9994332E 05
    T-TZ =   -4.5000002E-09      BZO =    0.            BETA/DELTA =    1.9304054E 00         C*T =   -9.4130332E-08
```

```
PROBLEM NUMBER              .1.        ADD APERTURE CORRECTION, NEXT CYCLE
    DELTA R DOT =  -1.5966797E-01            Z=  -1.2705577E-05


    EXECUTION BEGAN - 180690
838 LINES OUTPUTJ  - 180713
    $IBSYS                                                          ENDTAP     E
    *      END TAPE
    ;
    PERIPHERAL UNIT POSITIONS AT END OF JOBS :
    SYSPP1  IS   B4    REC. 00039, FILE 00004
    SYSOU1  IS   A3    REC. 03171, FILE 00000
    SYSIN1  IS   A2    REC. 00001, FILE 00006:
    END OF JOBS :1
```

```
LA DA15 A *                    DON DICKMAN        T-1                        64
LA DA15 O *RK - INTERVAL DETERMINING RUNGE-KUTTA
LA DA15 B *INTEGRATION    D1 D2        MAP              SR7094      IBSYS
LA DA15 C *                    LABRT        SW 6              LS 22
LA DA15 D *MAP SOURCE CARDS     637BCDRELOCATABLE BINARY      42BIN
LA DA15 S **RK*INTERVAL*DETERMINING*RUNGE-KUTTA
LA DA15 10*ON DISK    FA COMPAT     WU 09/20/65 REV DECK 10/28/64


LA DA15 11*INITIALIZING CALL —
LA DA15 12*       CALL RKA(XZ, HZ, YI, YP, YY, FY, ACC, XF, SH, NF, IND, N)
LA DA15 13*INTEGRATION CALL —
LA DA15 14*       CALL RKB
LA DA15 15*PURPOSE —
LA DA15 16*        TO INTEGRATE N SIMULTANEOUS FIRST ORDER
LA DA15 17*        DIFFERENTIAL EQUATIONS. ROUTINE IS SELF TESTING
LA DA15 18*        AND DETERMINES OWN INTERVAL.
LA DA15 19*STORAGE — 699 LOCATIONS PLUS DATA IN CALL SEQ.
LA DA15 20*USES-LABRT
```

RKA is entered once, at the beginning of a particular integration, to set up addresses. It also checks the calling sequence (RKA calling sequence has 12 arguments). If IND is set minus prior to entering RKA, no doubling of HZ is permitted (RK can still cut HZ). RKB is entered to carry integration forward.

The calling sequences are:

FORTRAN IV
    CALL RKA (XZ, HZ, YI, YP, Y4, FY, ACC,
                  XF, SH, NF, IND, N)

    CALL RKB

   MAP
  OP   FIELD
CALL   RKA (XZ, HZ, YI, YP, Y4, FY, ACC,
                  XF, SH, NF, IND, N)
CALL   RKB

An explanation of symbols follows. In all cases, a symbol in calling sequence denotes a location where the value of symbol may be found. All values are in floating point unless otherwise specified. No zero locations are permitted.

XZ: Value of independent variable.

HZ: Interval size of independent variable. It cannot be zero, but can be initially small (RK will double it if it is too small).

YI: Values of dependent variables. YI is a block of storage N words long (YI is FWA of block).

YP: Block of storage, N words long, which will contain the derivatives for the YI as determined by user's functional evaluation routine (YP is FWA of block).

Y4:   Block of temporary storage, 4N words long, which RK uses (Y4 is FWA of block).

FY: Location of user's functional evaluation routine.

ACC: Specified maximum relative error for a given cycle of integration, pertains to all YI. As RK uses only exponent of this number, accuracy of cycle will be to nearest power of 2. Thus number must be less than 0.5 and positive (a number like 1.0E-5 will give approximately five decimal digits of accuracy per cycle).

XF: Final value of the independent variable. If XF = 0, one cycle of integration is performed. When more than one cycle is wanted upon entry to RKB, RK will integrate to XF exactly. Thus the last value of HZ could be small.

SH: Smallest value that HZ can become at any time during integration. If |HZ| becomes less than SH during run, RKB will return to user with a comment printed via LABRT and a 2 in IND as a FORTRAN IV integer. SH must be greater than zero.

NF: A FORTRAN IV integer denoting the number of single pass integration cycles (with no testing) per stabilization. If NF = 0, RK stays in dual pass. If NF is not zero, RK first stabilizes on HZ. HZ is considered stabilized when two successive integration cycles yield the same HZ. RK then goes to single pass integration for NF cycles. After NF cycles, RK returns to dual pass to stabilize on HZ again. This process is repeated until XF is reached (thus in order for NF to be nonzero, XF must also be nonzero).

IND: RKB indicator test cell, a FORTRAN IV integer. Possible contents and meaning are described below.

N: Number of dependent variables as a FORTRAN IV integer.

User must supply routine at FY to evaluate derivatives for the YI. These derivatives are stored in the YP block. Control must return to 1,4. RK calls FY as follows:

OP   FIELD
CALL   FY (XZ, YI, YP, N)

In FORTRAN IV, FY must be a subroutine preceded by a subroutine card as follows:

SUBROUTINE FY (XZ, YI, YP, N)
Subroutine must end with a "Return" statement.

When the first error is detected in the calling sequence by RKA, a comment is printed out via LABRT and the job is terminated. In RKB, when subroutine returns to user, a FORTRAN IV integer is put in IND with the following meanings:

Integer	Meaning
0	Normal return for XF = 0. No doubling next cycle.
1	XF = 0, HZ cut, no integration has taken place (HZ already set to one half of former value).
2	For either XF = 0, or XF not equal to zero. HZ cut and new HZ less than SH (comment also printed via LABRT).
3	XF = 0, RK will double next cycle. HZ already set to twice previous HZ.
4	Normal return for XF not zero. Integration has been completed to exactly XF.

The restrictions are:

1. If XF is used, user must be careful when calling RKB again, as HZ could be quite small when RK has integrated to XF exactly.

2. RK uses XR1 and XR2. It does not save them on entering FY. If the user codes FY in MAP and uses XR1 or XR2, he must save and restore them. If FY is a FORTRAN IV subroutine, the XR's will be saved.

3. The error routine, LABRT, is required for proper operation of RK.

4. RK is compatible to MAP or FORTRAN IV only. Routine will also be available for the 7030.

5. For proper integration
$$hY_i' \geq 1.0E-7Y_i$$

The method used is a straight dual pass fourth-order Runge-Kutta, with none of the variations currently available. RK integrates over the interval HZ twice, the first time in a single step, and the second time in two steps. The results are compared, based on the accuracy required by the user to determine if the integration was successful.

SAMPLE PROBLEM

```
C
C      DICKMAN, RK TEST 8
C
       INTEGER TEST
       REAL MH,MZ
       EXTERNAL FS8
       DIMENSION YZ(5),YP(5),Y4(20)
   100 FORMAT(22H1 BACKWARD INTEGRATION)
   102 FORMAT(7HC TEST=,I2)
   101 FORMAT(5HC XZ=,E16.8,5H  HZ=,E16.8)
   103 FORMAT(25H       YZ              YP)
   104 FORMAT(2E16.8)
       WRITE(9,100)                                              1
       XZ=1.5
       HZ=-0.01
       ACC=1.0E-7
       XF=0.0
       MH=1.0E-8
       MZ=0.0
       TEST=0
       N=5
       YZ(1)=1.125
       YP(1)=2.25
       YZ(2)=-0.07074
       YP(2)=0.99749
       YZ(3)=4.4817
       YP(3)=4.4817
       YZ(4)=3.0
       YP(4)=2.0
       YZ(5)=-0.22313
       YP(5)=0.22313
       CALL RKA(XZ,HZ,YZ,YP,Y4,FS8,ACC,XF,MH,MZ,TEST,N)          4
       IF(TEST)3,2,3
     3 WRITE(9,102)TEST                                          7
       PAUSE 77777
     2 WRITE(9,101)XZ,HZ                                         8
       WRITE(9,103)                                              9
       WRITE(9,104)(YZ(I),YP(I),I=1,5)                           10
     5 CALL RKB                                                  19
       IF(XZ)6,6,7
     6 PAUSE 77777
     7 IF(TEST)4,2,4
     4 GO TO(5,6,2,2)TEST

ERROR MESSAGE NUMBER    1
       STOP

ERROR MESSAGE NUMBER    2
       END



       SUBROUTINE FS8(XZ,YZ,YP,N)
       DIMENSION YZ(5),YP(5)
       M=N
       YP(1)=XZ**2
       YP(2)=SIN(XZ)                                             3
       YP(3)=EXP(XZ)                                             4
       YP(4)=2.0
       YP(5)=EXP(-XZ)                                            5
       R=YZ(1)
       RETURN
       END
```

BACKWARD INTEGRATICN

XZ= 0.15000000E 01   HZ= -C.10000000E-C1
    YZ   YP
0.11250000E C1   0.22500000.E 01
-0.70740000E-01 0.99749000E 00
0.44817000E 01   0.448170C0E C1
0.30000000E 01   0.200000C0E 01
-0.22313000E C0 0.22313000E 00

XZ= 0.1490000CE 01   HZ= -0.20000000E-C1
    YZ   YP
0.11026497E 01   0.22201000E 01
-0.80711246E-01 0.99673775E 00
0.44371064E 01   0.44370955E 01
0.29800000E 01   0.200000C0E 01
-0.22537249E 00 0.22537266E C0

XZ= 0.14699999E 01   HZ= -C.40000000E-01
    YZ   YP
0.10588410E 01   0.21608999E C1
-0.10062853E 00 0.99442434E C0
0.43492460E 01   0.43492350E 01
0.29399999E 01   0.2000C000E C1
-0.22992532E C0 0.22992549E C0

XZ= 0.14299999E 01   HZ= -0.80000000E-C1
    YZ   YP
0.97473565E 00   0.20448999E 01
-0.14033440E C0 0.99010455E 00
0.41787099E 01   0.41786990E 01
0.28599999E C1   0.20000000E C1
-0.23930875E 00 0.23930893E 00

XZ= 0.13499999E 01   HZ= -0.16000000E CC
    YZ   YP
0.82012499E C0   0.18224999E C1
-0.21900947E CC 0.97572335E 00
0.38574388E C1   0.38574350E C1
0.26999998E 01   0.2000C000E C1
-0.25924009E C0 0.25924028E C0

XZ= 0.11900CC0E 01   HZ= -C.16000000E C0
    YZ   YP
0.56171968E C0   0.14160998E 01
-0.37166265E CC 0.92836855E C0
0.32870189E C1   0.32870810E C1
0.23799998E C1   0.2000C000E C1
-0.30422109E C0 0.30422128E C0

XZ= 0.10300000E 01   HZ= -0.16000000E CC
    YZ   YP
0.36424237E C0   0.10608999E 01
-0.51482162E CC 0.85729896E C0
0.28010766E 01   0.28010656E C1
0.20599997E C1   0.2000C0C0E C1
-0.35700679E 00 0.35700698E 00

XZ= 0.86999994E CC   HZ= -0.16000000E CC
    YZ   YP
0.21950105E 00   0.75689989E C0
-0.64482930E C0 0.76432889E C0
0.23869216E C1   0.238691C6E C1

0.17399998E C1   0.2000C0C0E C1
-0.41895138E C0 0.41895158E C0

XZ= 0.70999993E CC   HZ= -0.16000000E CC
    YZ   YP
0.11930373E 00   0.50409991E C0
-0.75836462E C0 0.65183371E C0
0.20340020E 01   0.20339911E 01
0.14199997E C1   0.2000CC00E C1
-0.49164403E C0 0.49164423E C0

XZ= 0.54999993E 00   HZ= -0.16000000E C0
    YZ   YP,
0.55458422E-01   0.30249992E 00
-0.85252725E C0 0.52268717E C0
0.17332638E 01   0.17332529E 01
0.10999997E C1. 0.200000C0E 01
-0.57694964E C0 0.57694986E C0

XZ= 0.38999993E 0C   HZ= -0.32000000E 00
    YZ   YP
0.19773100E-01   0.15209994E 00
-0.92491176E C0 0.38018835E C0
0.14769916E 01   0.14769807E 01
0.77999969E 00   0.2000C000E 01
-0.67705671E C0 0.67705692E 00

XZ= 0.22999993E 0C   HZ= -0.16000000E 00
    YZ   YP
0.40557745E-02   0.52899967E-C1
-0.97366907E C0 0.22797745E C0
0.12586107E 01   0.12585999E 01
0.45999968E 00   0.2000C000E 01
-0.79453344E 00 0.79453367E C0

XZ= 0.14999992E 0C   HZ= -0.80000000E-01
    YZ   YP
0.11251101E-02   0.22499979E-01
-0.98877374E C0 0.14943806E 00
0.11618450E 01   0.11618342E C1
0.29999968E 00   0.20000000E 01
-0.86070781E C0 0.86070804E 00

XZ= 0.10999992E 00   HZ= -0.80000000E-C1
    YZ   YP
0.44377751E-03   0.12099984E-01
-0.99395875E 00 0.10977823E C0
0.11162780E C1   0.11162780E C1
0.21999967E C0   0.2000C000E 01
-0.89583396E 00 0.89583421E C0

XZ= 0.69999930E-01   HZ= -0.40000000E-01
    YZ   YP
0.11444470E-03   0.48999901E-02
-0.99755364E 00 0.69942776E-C1
0.10725081E C1   0.10725081E C1
0.13999967E C0   0.2000C000E 01
-0.93239365E 00 0.93239389E.00

XZ= 0.29999929E-01   HZ= -C.40000000E-01
    YZ   YP
0.91116531E-05   0.89999576E-C3
-0.99955266E 00 0.29995430E-C1

0.10304653E C1   0.10304545E C1
0.59999675E-C1   0.2000C0C0E C1
-0.97044536E C0 0.S7044560E C0

XZ= -0.10000071E-01   HZ= -C.80000000E-C1
    YZ   YP
-0.22162362E-C6 0.1000C141E-C3
-0.99995261E CC -0.99999037E-C2
0.99006057E C0   0.S9004976E 00
-0.20000324E-C1 0.2000C000E 01
-0.10100500E 01 0.101005C2E C1

XZ= -0.90000071E-01   HZ= -0.16000000E C0
    YZ   YP
-0.24288885E-C3 0.8100C127E-02
-0.99595533E C0 -0.89878619E-01
0.91394192E C0   0.S1393113E C0
-0.18000032E 00 0.200000C0E C1
-0.10941741E 01 0.10941744E 01

144

XZ= -0.25000007E 0C HZ= -C.160000C0E C0
       YZ   YP
-0.52082259E-C2 0.62500035E-C1
-0.96891500E 00 -0.24740402E 00
 0.77881152E C0 3.77880074E 00
-0.50000031E 00 0.2000G0000E 01
-0.12840252E C1 0.12840255E C1

XZ= -0.41000007E 0C HZ= -0.3?000000E 0C
       YZ   YP
-0.22973566E-C1 0.16810CC5E C0
-0.91712338E 00 -0.3986093?E C0
 0.66366099E C0 0.66365021E C0
-0.82000031E C0 0.2000C0C0E 01
-0.15068176E 01 0.15068179E C1

XZ= -0.57000007E.0C HZ= -C.16000000E CC
       YZ   YP
-0.61730909E-01 0.32490008E C0

```
LA NA03 A *            CHERRY           T-1                    64
LA NA03 O *LOS ALAMOS ABORTER AND MESSAGE PRINTER
LA NA03 B *MATH SR ERRORS N1         MAP        SR7094    IBSYS
LA NA03 C *                          SW 3    LS 6
LA NA03 D *MAP SYMBOLIC CARDS    57BCDIBLDR REL BIN CDS       9BIN
LA NA03 S **ERROR*TERMINATION*COMMENT
LA NA03 10*ON DISK    F4 COMPAT    WU 08/21/64 REV DECK 08/19/64 REV

LA NA03 11*CALL LABRT (ISW, LHOL, INT)
LA NA03 12*PRINTS MESSAGES, CALL LOCATIONS, SETS LINE COUNT,
LA NA03 13*AND CAUSES JOB TERMINATION ACCORDING TO ISW SETTINGS.
LA NA03 14*USED WITH MATH SUBROUTINES FOR ERROR MESSAGES AND/OR
LA NA03 15*JOB TERMINATION. 64 WORDS REQUIRED
LA NA03 16*USES-EXIT,.FWRD.,SYSLOC,.UN09.,.FSLO.,.FCNU.,FFIL
```

The purpose of this routine is to handle FORTRAN IV library subroutine errors and to print double spaced error messages under count control with option to terminate job or printing. By use of the various entries, one may determine whether (a) a message is to be produced, (b) the error is to be ignored, (c) the print limit is to be reset, or (d) the job is to be terminated. The routine prints 48 Hollerith characters plus six octal digits. In library usage, the name of the routine using LABRT is placed left adjusted in the first word of the message.

USAGE: CALL LABRT (ISW, LHOL, INT)

ISW is the location of a FORTRAN IV integer, LHOL is the location of 48 Hollerith characters, and INT is the location of a FORTRAN IV integer.

If ISW equals:

1, the 48 Hollerith characters specified by LHOL and the octal integer by INT will be printed and the print limit reduced by one if the print switch is on and if the print limit has not been attained. If the termination switch is on, the job will be terminated after any message.

2, set the print switch off; subsequent entries with ISW = 1 cause no printing.

3, set the print switch on; set the print limit equal to the value of INT.

4, set the termination switch on; subsequent entries with ISW = 1 cause job termination.

5, set the termination switch off.

0, (> 5) a return is made with no other action taken.

Normally, library subroutines enter LABRT having ISW equal to one. The programmer may enter using other values of ISW to control actions of LABRT upon error conditions. The program is completely FORTRAN IV compatible. Thus, one may simply write his own LABRT routine in FORTRAN IV if he wishes a different reaction to error conditions. Initial conditions are:

Print switch is on.

Print limit is set to 10.

Termination switch is off.

145

Chapter 5

PARAMETER VARIATIONS

by
J. N. Hardwick and Douglas Venable

This chapter is based primarily upon the work found in Chapters 3 and 4, in which the mutual relationships among the operating parameters such as initial beam radius, energy, current, and cavity accelerating fields were surveyed over a significant range of injection phase angles by exploiting the versatility of a computer code that solves the equations of motion.

The function of PHERMEX is to provide a high intensity pulse of bremsstrahlung that has adequate total flux appropriately directed in space, and a suitable distribution of quantum energy to satisfy certain flash radiographic requirements. Specifically, this flux corresponds to that which would be developed by 5 to 10 μcoul of electrons, having energies of at least 20 MeV, delivered with nearly zero convergence to a tungsten target. The desired electron orbits are those which terminate on the target and which also have the appropriate energy and convergence. With unbunched injection, the electrons ejected from this kind of accelerator have a significant distribution in momentum; furthermore, energy-dependent refractive optics is needed to focus the beam to a distant target. Depending upon ejection radii and convergences, there are many particles which are inaccessible to the target.

Therefore, a parametric study was made to determine stable orbits of electrons injected into the accelerator, where a stable orbit is one which terminates on the target regardless of the electron momentum. The next step was to extract the useful stable orbits, i.e., those which when incident upon the target also have the desired energy and convergence to assure the proper gamma-ray spectrum and intensity angle distribution. In addition to the injected beam current, energy, radius, convergence, and cavity fields, externally imposed magnetic field distributions were also considered. Some computational work was done with azimuthally uniform but radially dependent current densities. The independent variable for each trajectory was taken to be the injection phase angle or injection time. This problem then became an iterative computational process using the computer code GRAPE SEED III, described in Chapter 4, which determined each of the three vector momentum components and energy at each spatial point on a given trajectory beginning with an initial vector momentum and position in space and time. The iteration was made to converge upon a spatial distribution of momentum among ejected electrons that assures subsequent delivery of at least the prescribed amount of charge to the target within the permissible convergence and energy ranges. Account was made of space charge effects. The cycle-to-cycle depletion of the cavity fields was considered when injection occurs over more than one cycle, since particle trajectories are strongly dependent upon the accelerating field strength, especially when space charge defocusing is important. From these studies it was found that the conditions of stability suggested in the literature may be more restrictive than necessary for an accelerator having a small number of cavities. Subsequent experiments have demonstrated the validity of these computations within the range of PHERMEX operational parameters.

The spatial momentum distribution of the ejected electrons depends strongly upon the injection parameters and, less strongly, upon beam loading. Therefore, two widely different injection schemes were investigated extensively in this computational study. One consists of injecting a constant current into the accelerator continuously over the number of cycles which fall within a prescribed pulse length. Although this method is extremely simple and inexpensive in practice, it suffers from one serious defect: When the injection energy is considerably less than the possible energy gain of the cavity, as with the first cavity

of PHERMEX, only about one-third of the injected charge can reach the ejection aperture of a half-wavelength cavity. Of this quantity of charge only a small portion can become accessible to the target because of its unfavorable spatial distribution of momentum. The second injection scheme involves injecting bunches of electrons whose initial momentum among electrons is optimally prepared. This latter method is by far the most efficient optically in that parameters can be selected for which virtually all of the injected electrons are accessible to the target at the desired energy. The disadvantage of bunched injection lies in the cost, complexity, and reduced operational reliability.

Time variation of the beam convergence upon both injection and ejection is feasible. If properly phased with the electric fields of the respective cavities, the variation of the angular dispersion of the ejected electrons can be reduced significantly. Like beam bunching, this added method of beam preparation was considered in the design studies, but only continuous injection has been used up to now simply because of its practical advantages.

The study of particle orbits for continuous injection showed that to a first approximation an injected beam convergence of zero was nearly optimum for most of the parameters considered with both time invariant injection and ejection. Hence those parameters which were varied extensively in this study were the beam radius, current, and energy, cavity field strength, cavity length, and the externally imposed magnetic field distribution. Parameter variations ranged below and above nominal design values but covered values that were considered as physically feasible, although not necessarily economically practical, so that the estimated output radiation flux per pulse also bracketed the desired value by a significant margin. Thus, the study included the potential growth aspect, too.

One of the first parameters to be examined and established early for design purposes was the cavity length. Considerations of beam energy, momentum, practically attainable cavity field strengths, and useful stable orbits indicated that a noncritically defined optimum cavity length was about 2.6 m for a sharply prebunched beam. All subsequent design consideration was fixed upon this length. This same length is very nearly optimal for a continuously injected beam.

An additional point was examined. Calculations demonstrated that streamline flow exists for each of the cases shown. Only a slight departure from laminar flow occurs for large negative injection phase angles when phase focusing becomes important. This property of laminar flow permits one to estimate the time average of the current density distribution in the beam. Precise experimental verifications of this aspect of the analysis would be extremely difficult. However, measurements of the time average current density distributions of beams ejected from a single cavity have demonstrated that the computations are correct within the error of measurements.

The equations of motion are also used to describe simple short strong-focusing magnetic lenses which are located in various positions along the optical path of PHERMEX. Therefore, including the aperture defect and lenses, the computer code served as the exploratory tool with which most of the optical components of PHERMEX were designed.

The computer code is used to describe particle trajectories in three-space, momentum components, energy, time and phase angle, and the instantaneous value of fields sensed by the electron. From these data one also obtains the energy extracted from the electromagnetic fields in the cavity.

Section I deals with typical trajectories in the first cavity for different values of injected beam radius, energy, current, and electric fields when the injected beam is parallel. Accessibility of electrons to the target depends very strongly upon the flow conditions in the first cavity. Then the effect of confining magnetic fields is examined in Section II. The most favorable trajectories found in Section I are carried throughout the three cavities of PHERMEX as shown in Section III. Energy depletion plays a part in beam trajectories. Section IV discusses this phase of the study. Section V provides an illustration of the injection aperture defect in the first cavity. The utility of time variable injection is shown in Section VI. In Section VII momentum and energy distribution among ejected electrons is discussed. Phase and space instabilities in PHERMEX beams

147

are also important over certain ranges of parameters, as demonstrated in Section VIII.

I. USEFUL BEAM TRAJECTORIES WITHIN FIRST CAVITY

The computational explorations displayed in this section pertain to variations in the following parameters: beam radius, current, energy upon injection, and cavity field strength. Aperture defects are included in all of the calculations of this section. There are no externally imposed magnetic fields considered here. Instead the effects of confining fields are shown in Section II. Results of beam trajectory calculations in the first cavity with no superposed magnetic fields are best presented in the form of graphs found in Figs. 5.1 through 5.33. The pertinent parameters are listed on each illustration. In these calculations the running variable was ϕ_0, the injection phase angle. Only those ϕ_0's, hence only those trajectories, are presented here which, upon reaching the downstream wall of the first cavity, have useful terminal energies.

Space charge effects are seen to be depressed most strongly by increasing both the injection radius and injection energy, whereas practicably achievable increases in the strength of the accelerating fields are not quite so effective. An initial convergence of zero was found to be sufficiently close to the optimum injection convergence over the range of all other parameters that no results of injection convergence variations are shown here.

These calculations were based only upon values of parameters that are considered to be among those that are both physically feasible and applicable to PHERMEX.

II. EFFECTS OF SUPERPOSED MAGNETIC FIELDS

The effect of superposed magnetic fields in confining the electron beam in the accelerator was the subject of careful consideration. As constructed, PHERMEX incorporates large diameter coils at each end of each cavity section. These coils, having unequal numbers of turns, were designed to provide axial **B**-fields within the cavities varying in intensity with axial position, if the coils are energized in series. A normalized plot of the on-axis B_z field within the first cavity is shown in Fig. 3.12. In the legends of the figures accompanying this section "NONUNIFORM" refers to B_z fields which vary with axial position in this manner. The value of magnetic field intensity noted on the legends is the value at the input aperture, and decreases with increasing axial position. Where the fields are described as "UNIFORM" in the legends, they are considered as having the same B_z value throughout the cavity with no B_r component.

Since the optical properties of the accelerator in the region of the first cavity affect the total charge deliverable to the target to a far greater extent than do the optical properties of other regions, it is best to demonstrate the effects of magnetic fields on beam trajectories in this cavity. Account is taken of both B_r and B_z components, as discussed in Chapters 3 and 4. In Figs. 5.34 to 5.45 typical trajectories of peripheral electrons in the first cavity with superposed magnetic fields are shown for nonuniform on-axis B_z fields of 100 and 1000 gauss, and for uniform fields of 1000 gauss.

Although magnetic field confinement exciting coils were built into PHERMEX to provide up to 100 gauss in the "NONUNIFORM" field distribution, it has not been necessary to make use of these fields with injected beam currents of 300 A or less.

III. TRAJECTORIES THROUGH THREE PHERMEX CAVITIES

Typical trajectories of peripheral particles in a 300 A beam flowing through all three PHERMEX cavities for the cavity fields now being used and those originally planned are illustrated in Fig. 5.46. Figure 5.47 shows the trajectories for a 300 A beam passing through the present distribution of cavity field strengths but with an injection energy of 2 MeV. Figure 5.48 presents the predicted trajectories for 600 A beams accelerated with the existing cavity field strengths, but with enhanced injection energies. Figure 5.49 represents trajectories for a 1000 A beam with an injection energy of 3 MeV.

148

IV. EFFECTS OF ENERGY DEPLETION

Particle trajectories are a function of the peak acceleration field strength. As energy is extracted from a cavity its field strength decreases. Consquently there exists a trajectory change which occurs from cycle to cycle. Energy depletion was determined using the same computational model that was used in determining trajectories. The agreement between energy depletion computed by use of the model and the energy depletion actually measured has been surprisingly good — so good, in fact, that measurements of energy depletion in the first cavity have since been used to determine the amount of injected charge, with sufficient accuracy for day-to-day machine operation. A careful computational survey was made to determine whether or not the effects of energy depletion were sufficient to make the trajectories of particles on the tenth cycle significantly different from corresponding trajectories in the first cycle. It was concluded that the effects of energy depletion did not significantly degrade the optical efficiency of PHERMEX when the electrons extract 5 percent or less of the stored energy.

V. INJECTION APERTURE DEFECTS

Aperture defects are most pronounced at the injection aperture of the first cavity. Upon passing from a region where the electric field intensity has one value, E_0, through an aperture, into another region where the electric field intensity has a different value, E_1, an electron beam experiences a change of convergence given by

$$\triangle C = \frac{\eta}{2c^2} \frac{\delta}{\beta^2} (E_1 - E_0)$$

(5.1)

In the case of PHERMEX, the field within the cavity is varying sinusoidally while the field outside the cavity is zero; therefore Eq. (5.1) is modified to become

$$\triangle C = \frac{\eta}{2c^2} \frac{\delta}{\beta^2} E_1 \sin(\omega t)$$

(5.2)

where again $\delta = \sqrt{1 - \beta^2}$

It is apparent that when β is small, as is the case upon injection into the first cavity, the change of convergence will be the most pronounced; when β approaches unity, as is the case upon ejection

from the first cavity, and at both injection and ejection from subsequent cavities, the change of convergence will be of much less consequence. Also, the aperture defect will be greater for low injection energies, (e.g., 600 keV now being used) than for higher injection energies such as the 2 MeV or higher energies projected as a goal in plans for an improved injector. Equation (5.2) also reveals that the change of convergence of electrons injected into a region of time-varying electric field will be different at different injection phase angles. Thus electrons injected at 0° suffer no change of convergence, while those injected at 90° undergo a maximum change.

Figure 5.50a shows trajectories for a 300 A, 600 keV, 2 cm radius electron beam injected into the first PHERMEX cavity where the peak electric field strength is 4 MV/m. This corresponds to initially planned operating parameters. The change of convergence due to the aperture defect is indicated. Figure 5.50b shows trajectories for the same injection parameters, but assuming no aperture defect.

A 3 cm radius, 300 A, 600 keV beam injected into a cavity having a peak electric field strength of 6 MV/m is illustrated in Figs. 5.51a and 5.51b for the cases with and without aperture defect, respectively. This last set of injection parameters corresponds to those that have now been achieved.

The results of this study demonstrate that in most cases for very high current injection the aperture defect performs a very useful function by providing a certain degree of focusing without which the beam would suffer an unacceptably large divergence. In the absence of large space charge forces the aperture defect introduces serious space defocusing forces such that Alvarez windows or grids must be used.

VI. TIME-VARIABLE INJECTION

If both the radius and convergence of the beam were made time-variable upon injection, significant gains in useful charge delivered to the target could be realized. Computations were made to determine optimum injection radius and convergence for several injection phase angles for a 300 A, 0.6 MeV beam injected into a cavity excited to 4 MV/m. Useful trajectories were then computed through the other two cavities.

Results of these computations are shown in Figs. 5.52 and 5.53. For comparison purposes, computations for a 5 cm radius 300 A, 0.6 MeV beam are shown in Fig. 5.54. The potential benefits of time-variable injection are obvious.

Most of the preceding sections demonstrate that the cavities themselves act as time-variable lenses. However, if the injection radius and injection convergence are suitably chosen and kept static, and the cavity fields are made appropriately strong, useful trajectories converge at about the ejection aperture of the third cavity. Since it is within reach of the present day state of the art to achieve these latter injection parameters and field values, efforts to enhance bremsstrahlung output of PHERMEX are being directed along these lines at this time rather than toward achieving time-variable injection. It is no easy matter to vary the injection parameters of a 300 A, 0.6 MeV electron beam at a 50 Mc/sec rate. Though technically possible, engineering difficulties make this approach unattractive at present.

VII. ENERGY AND MOMENTUM DISTRIBUTIONS AMONG EJECTED ELECTRONS

About 70 A have been collected upon ejection from the last cavity where the peak energy was above 20 MeV. These emerging electrons follow trajectories which, although nearly parallel, have a sufficient distribution in radial momentum and energy that only a fraction of these electrons is accessible to the 3 mm diameter target located about 11 m away. Currents in excess of 20 A, indeed almost 35 A, have been collected at the target, having passed through a 3 mm diameter beryllium collimator. Figures 5.55 and 5.56 illustrate typical computed distributions in energy and normalized radial momentum for peripheral ejected electrons when the machine is operating under the conditions indicated in Fig. 5.46a. Another set of distributions is found in Figs. 5.57 and 5.58 where the machine parameters are identical with those used in Fig. 5.48c.

VIII. BEAM INSTABILITIES

Here beam instability refers to those conditions of both radial and phase defocusing by which electrons become inaccessible to the target. The four illustrated cases of a 100 A beam, Figs. 5.59 to 5.62, provide examples of gross defocusing phenomena where the injection energies are 0.25, 0.50, 1.0, and 3.0 MeV respectively. The so-called aperture defect is included in the apertures of each cavity; each cavity provides an accelerating field strength of 4 MV/m. Figures 5.59a, 5.60a, 5.61a, and 5.62a represent trajectories in r-z space. These are similar to those shown in Section III of this chapter. Electrons injected at large negative phase angles do not reach the downstream wall of the first cavity, but instead space charge forces cause the beam to expand and the deceleration fields force them to return to the upstream wall. In a similar manner those electrons that are injected too late are turned around before reaching the downstream wall and excessive space charge forces cause the beam to blow up.

These instabilities are diminished as the injection energy is increased. The trend in phase defocusing is seen in the Minkowski representations of Figs. 5.59b, 5.60b, 5.61b, and 5.62b, whereas radial defocusing is illustrated by the corresponding Minkowski diagrams of Figs. 5.59c, 5.60c, 5.61c, and 5.62c. The important result is that both space and phase focusing are improved by increasing the injection energy.
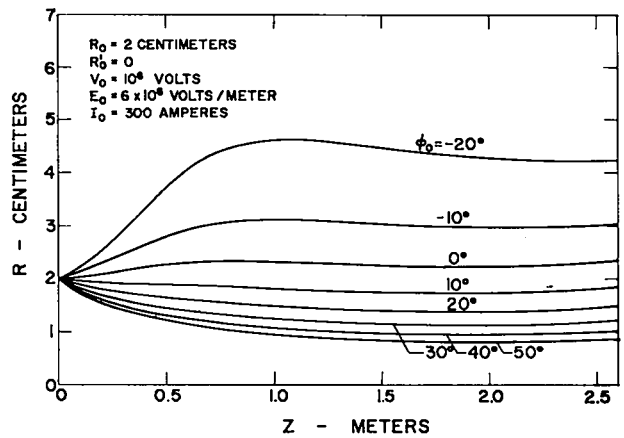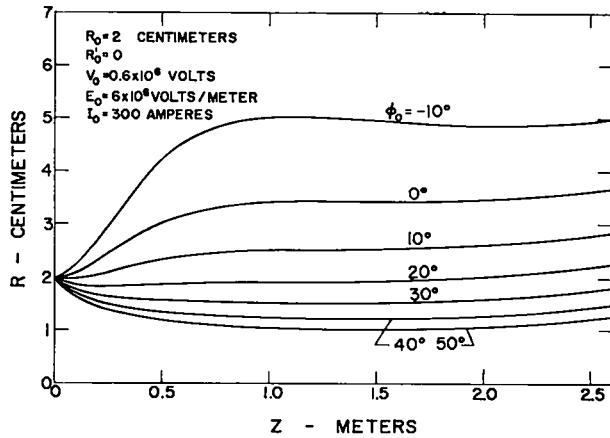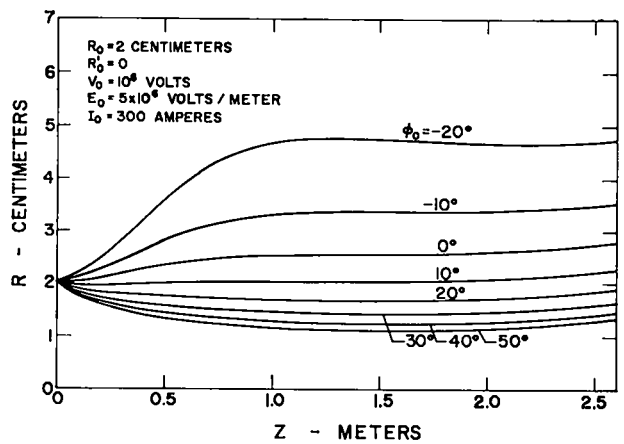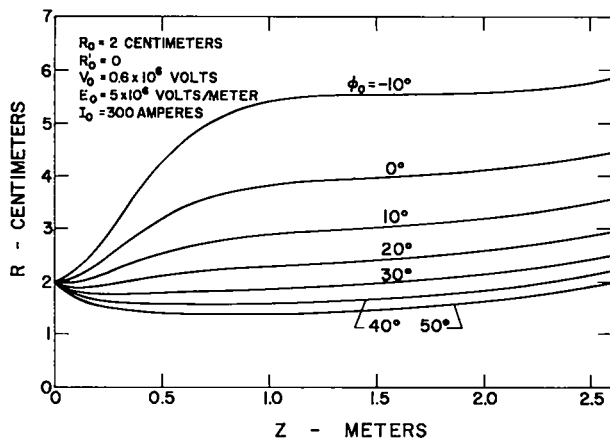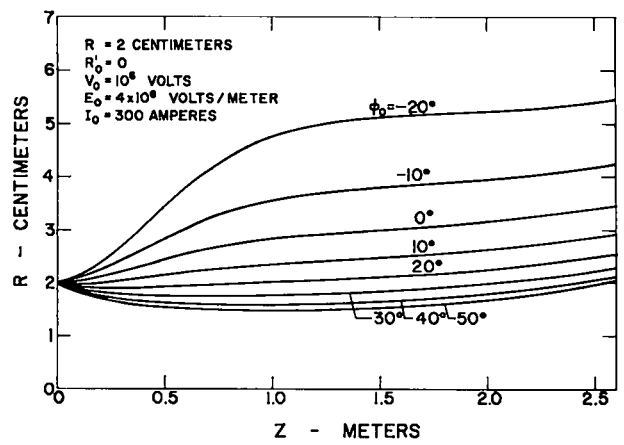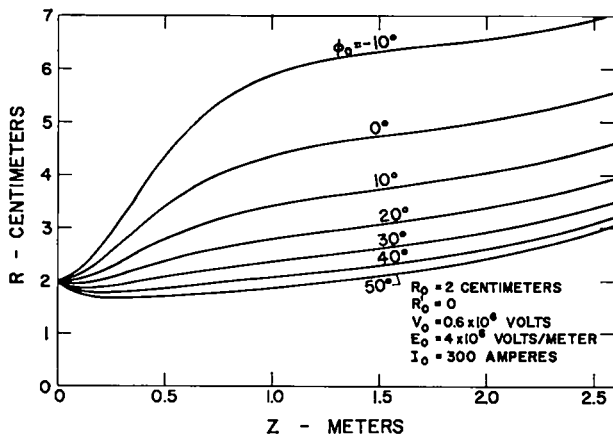
Fig. 5. 1. Beam trajectories in first cavity with no superposed magnetic fields.

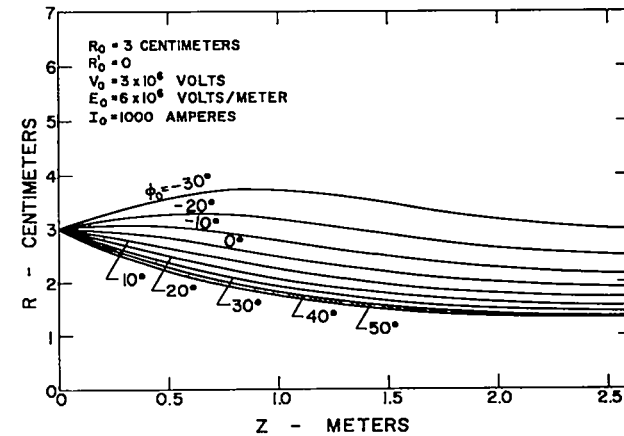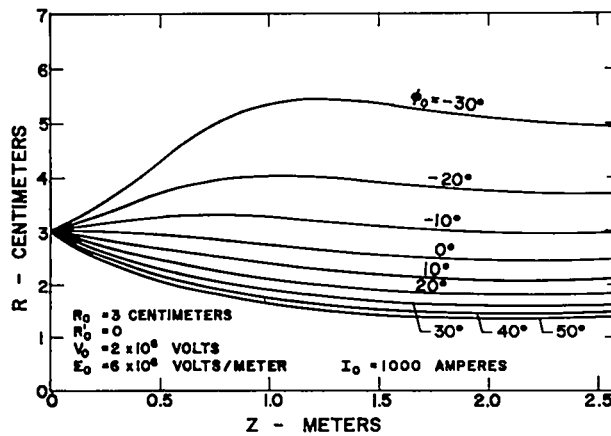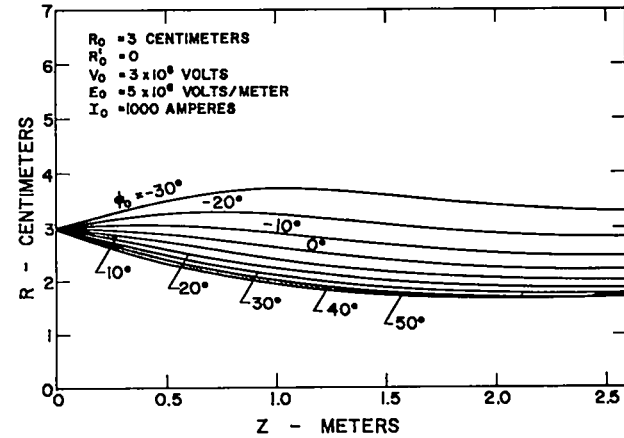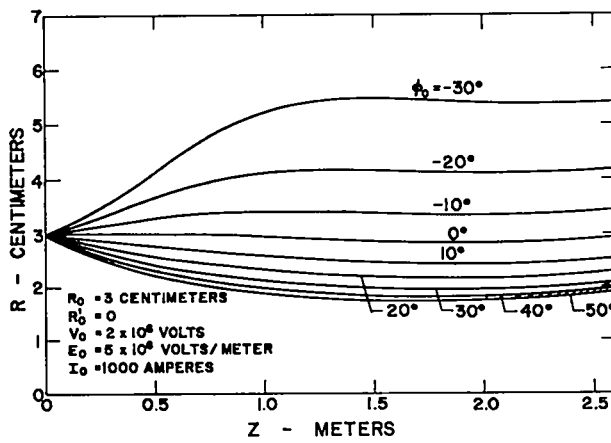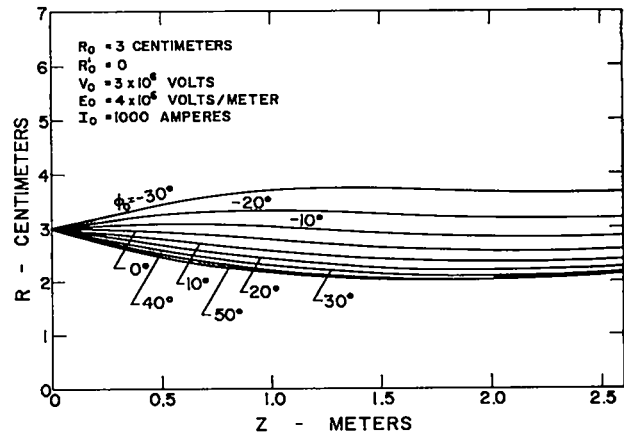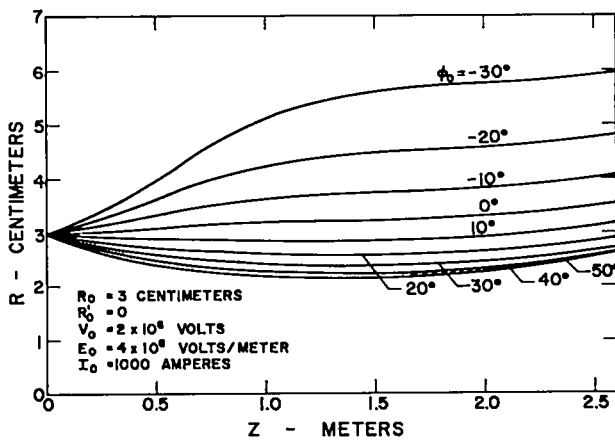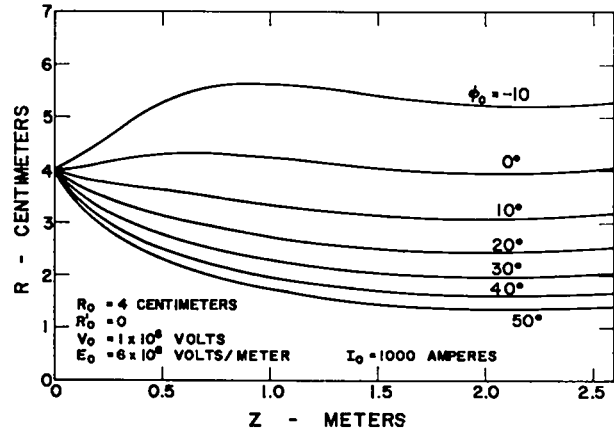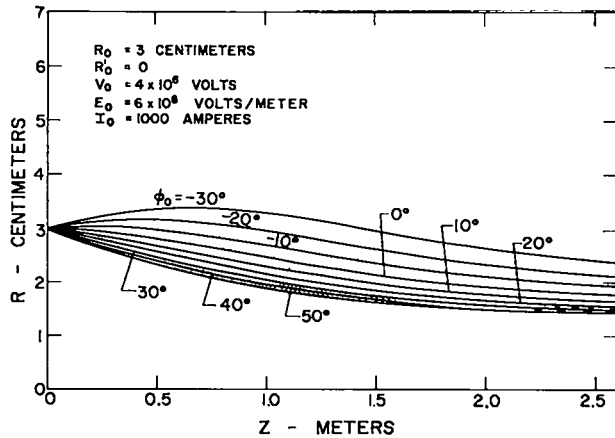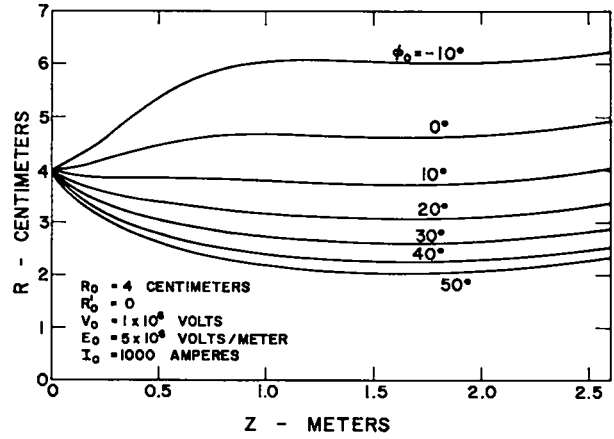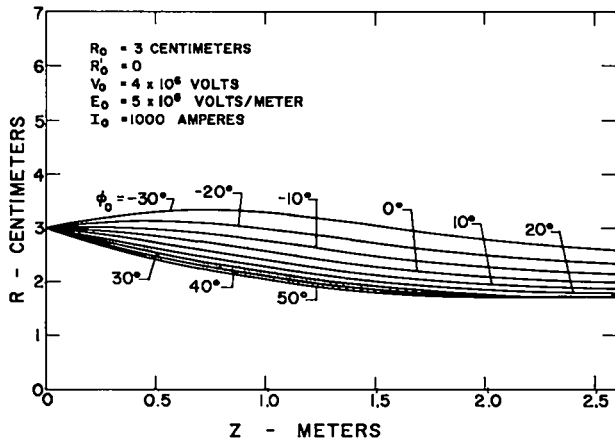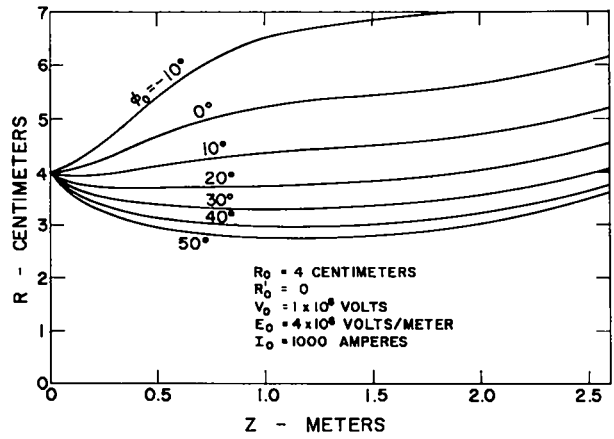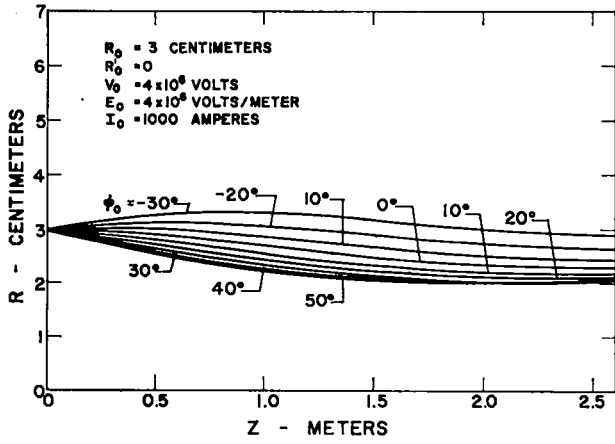Fig. 5. 2. Beam trajectories in first cavity with no superposed magnetic fields.
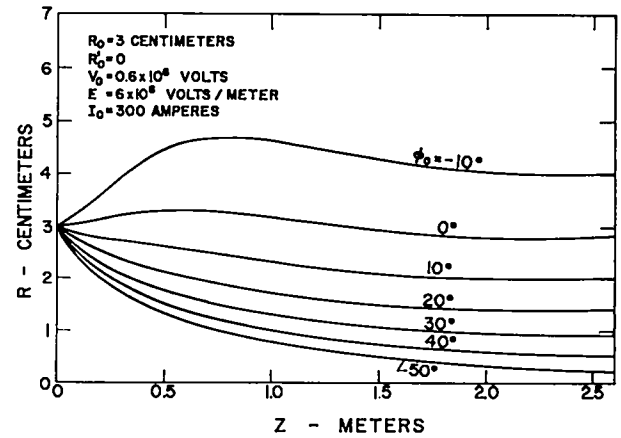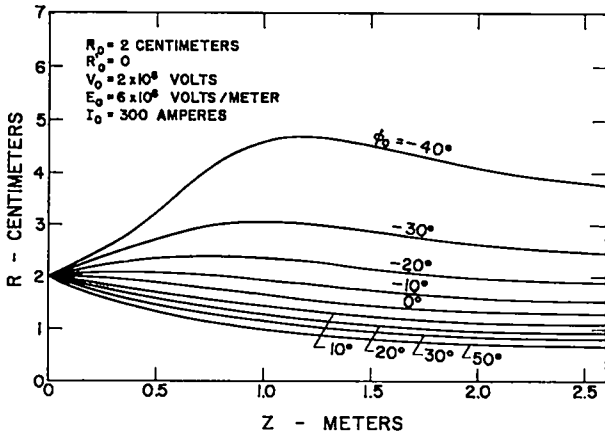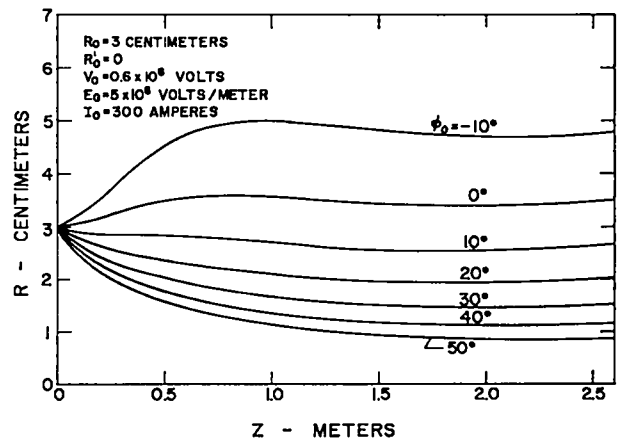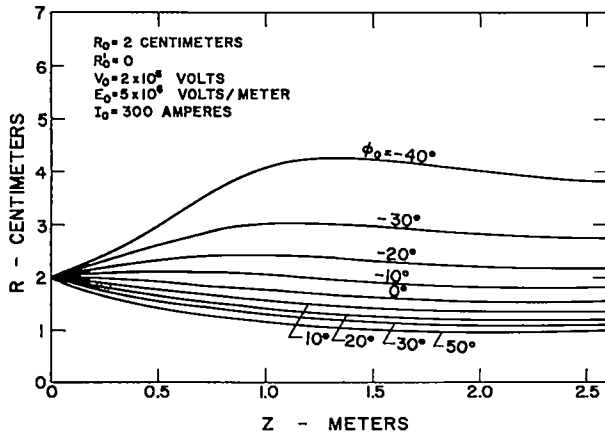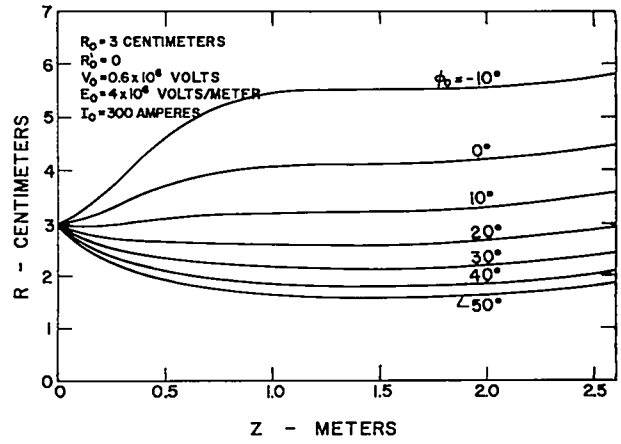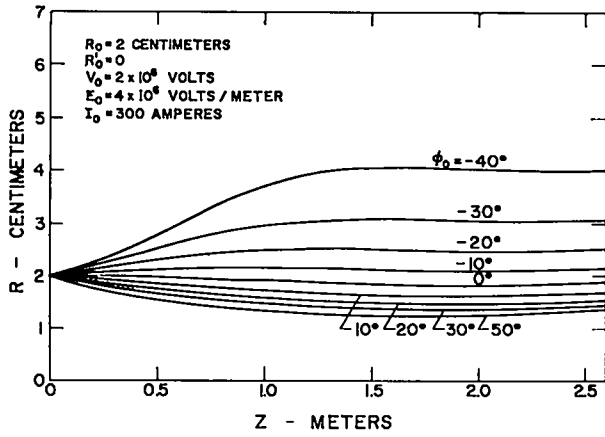
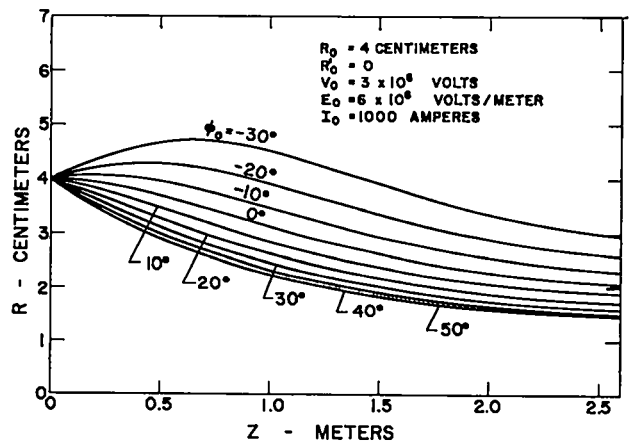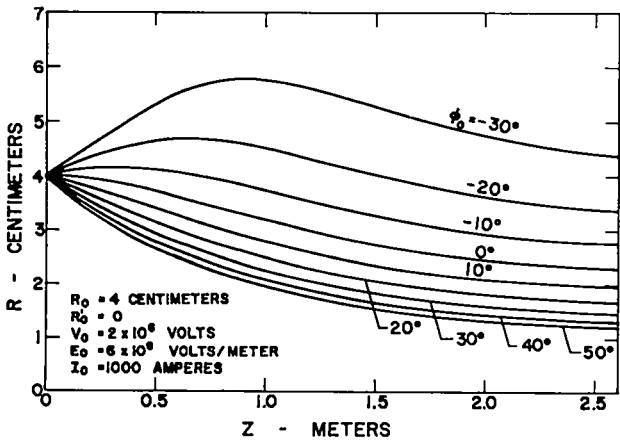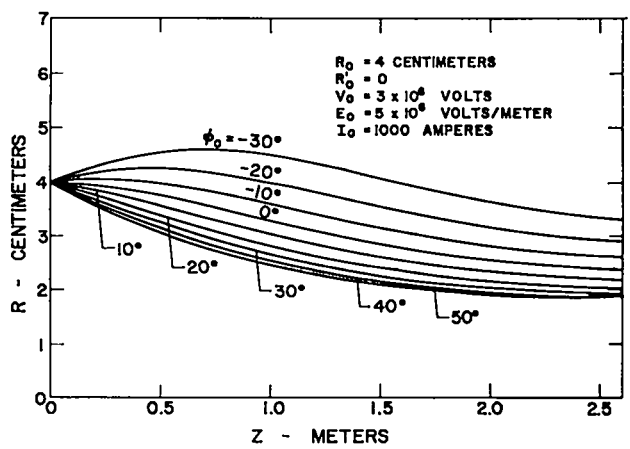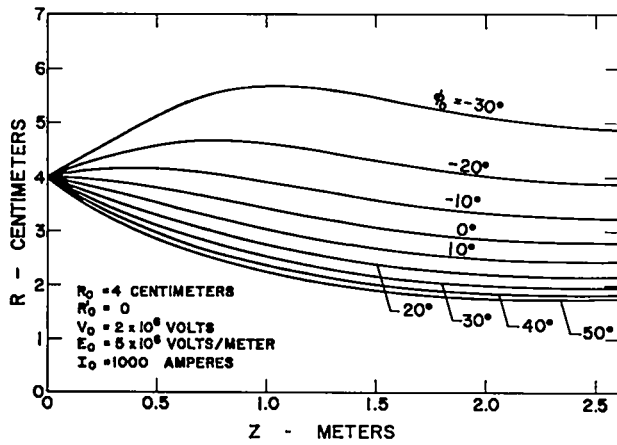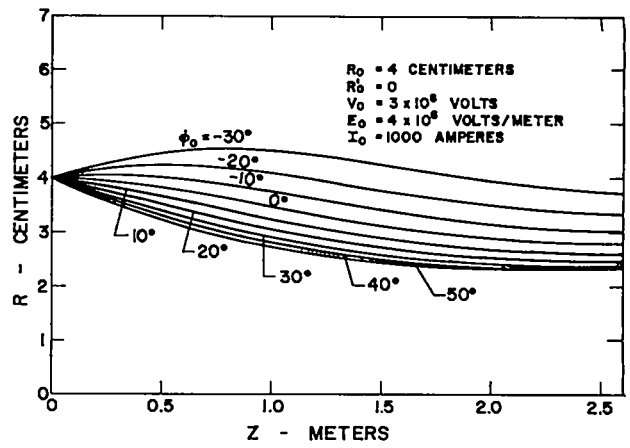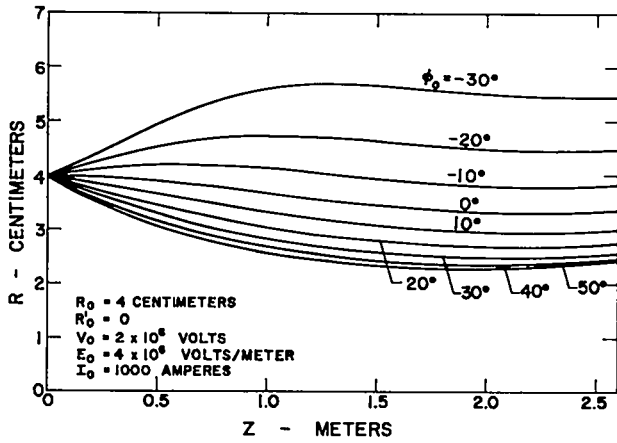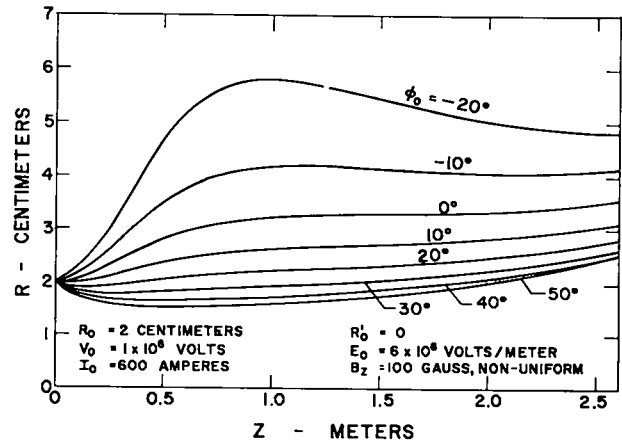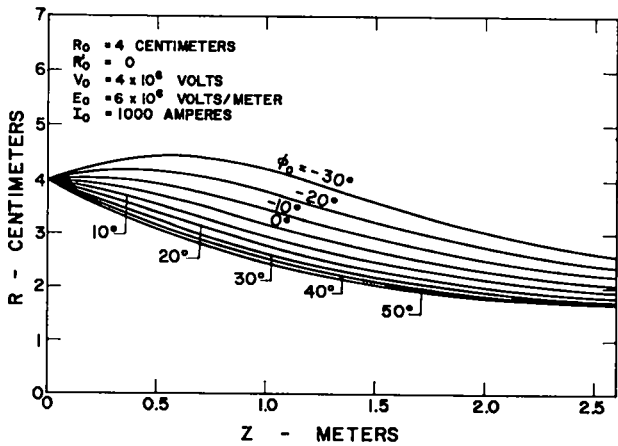Fig. 5. 3. Beam trajectories in first cavity with no superposed magnetic fields.

Fig. 5. 4. Beam trajectories in first cavity with no superposed magnetic fields.
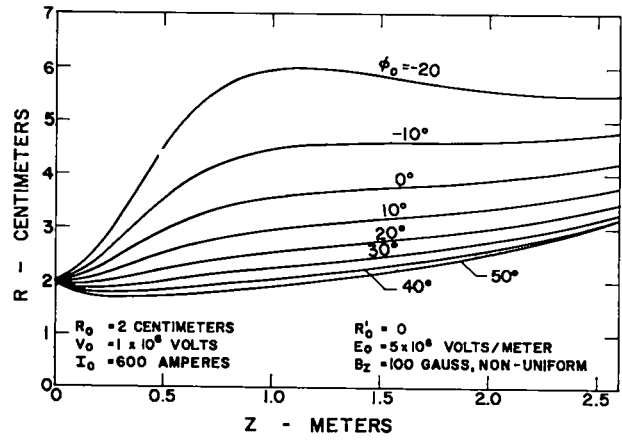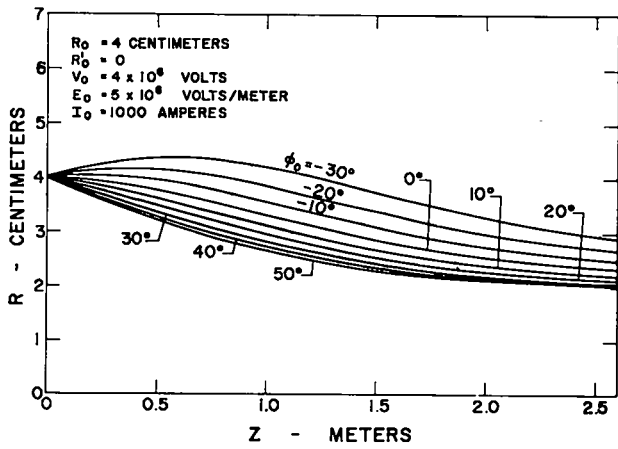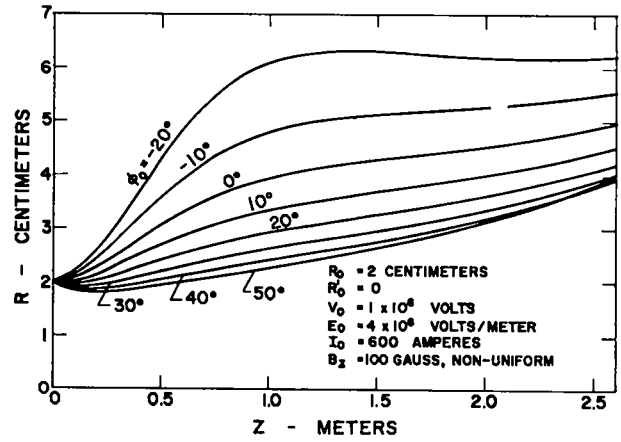
152
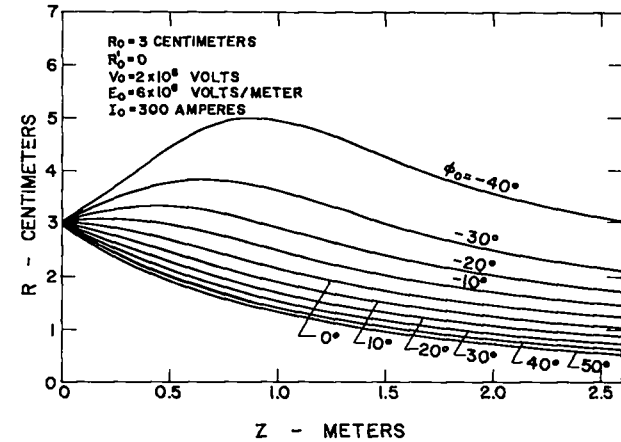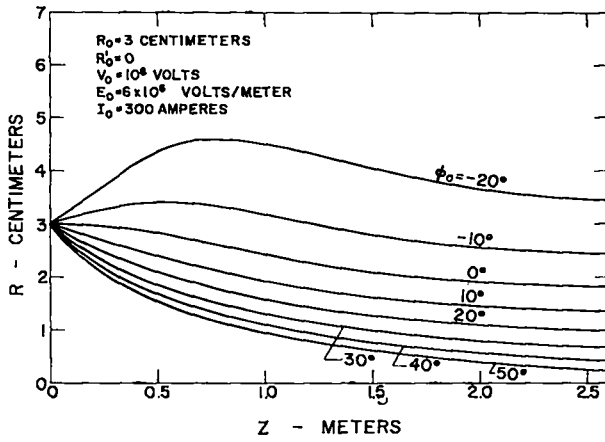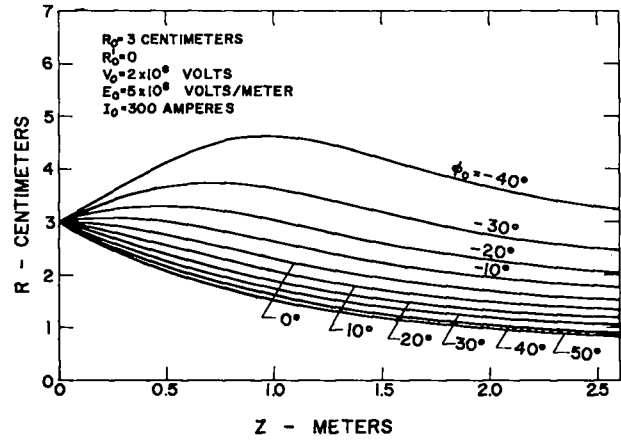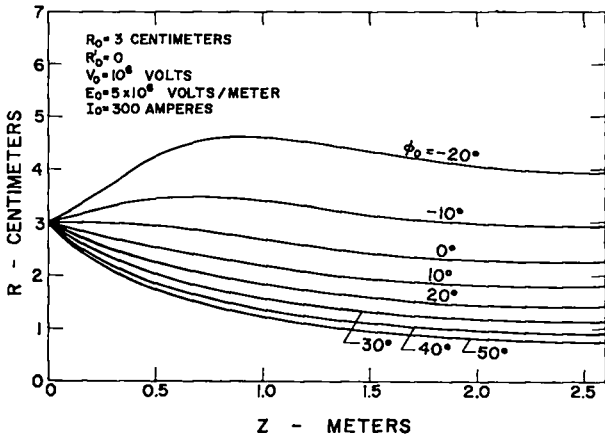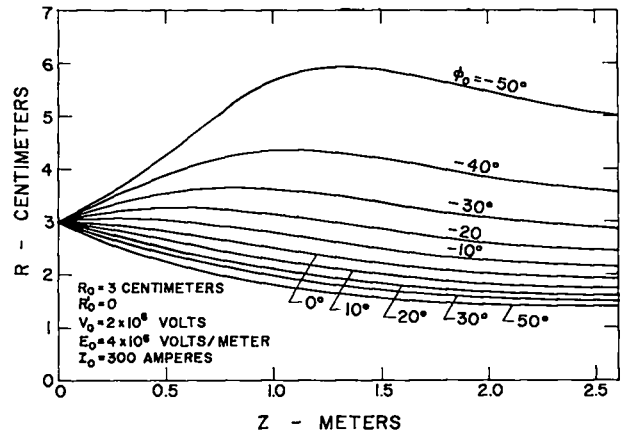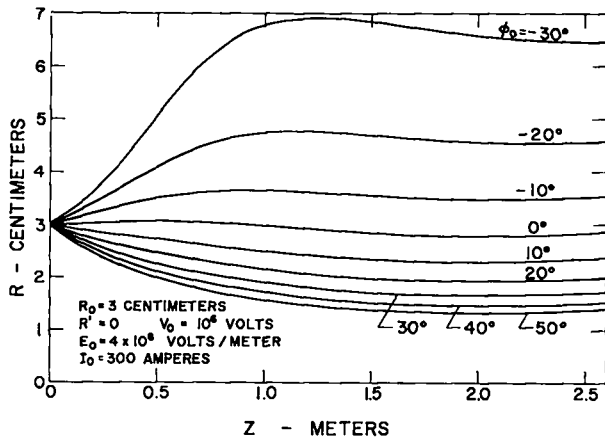
Fig. 5. 5.   Beam trajectories in first cavity with no
             superposed magnetic fields.

Fig. 5. 6.   Beam trajectories in first cavity with no
             superposed magnetic fields.
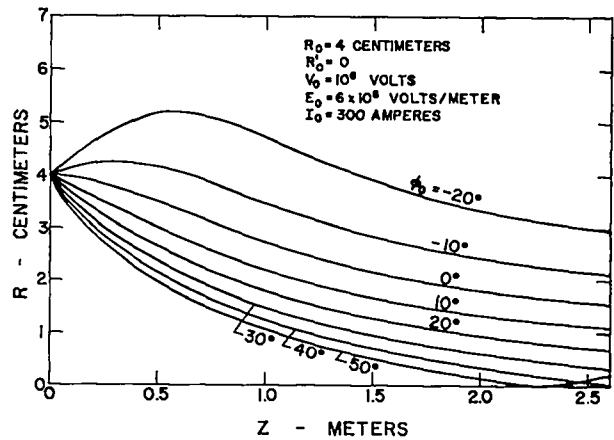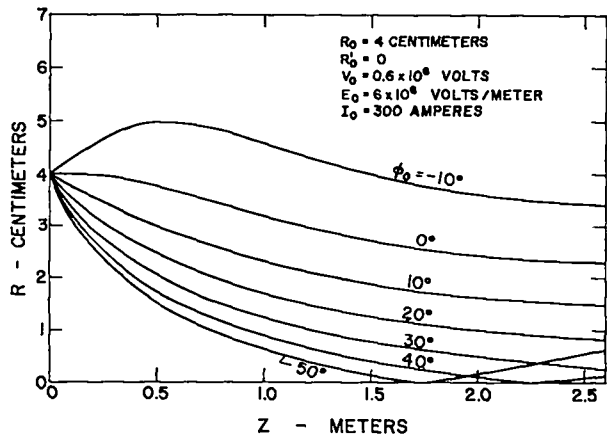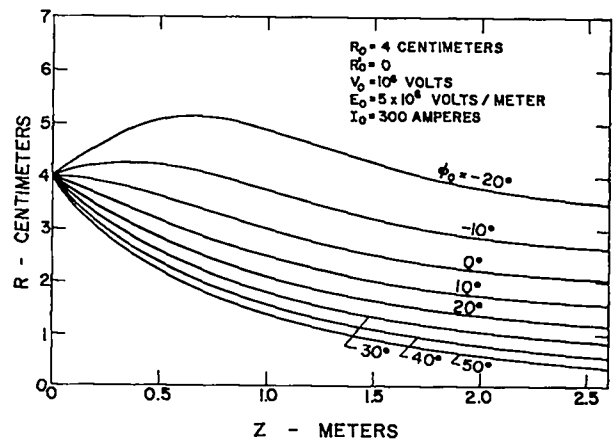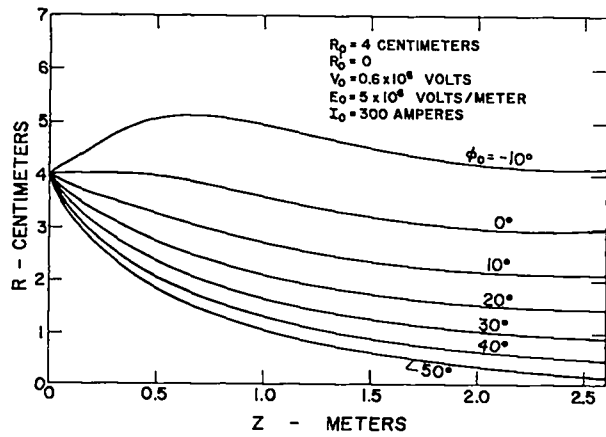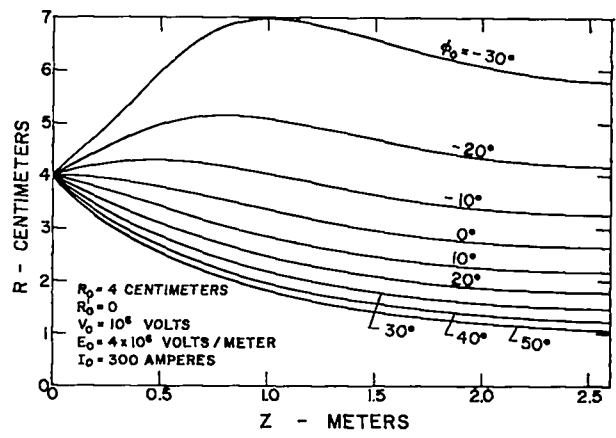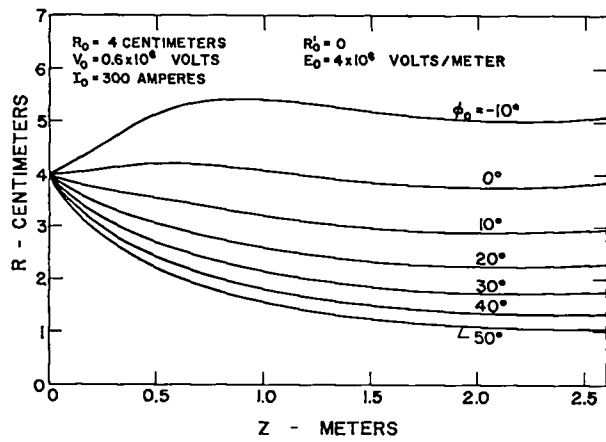
Fig. 5. 7. Beam trajectories in first cavity with no superposed magnetic fields.

Fig. 5. 8. Beam trajectories in first cavity with no superposed magnetic fields.
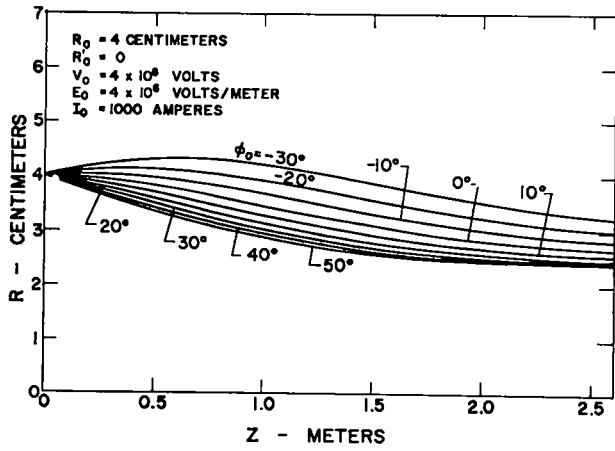
154
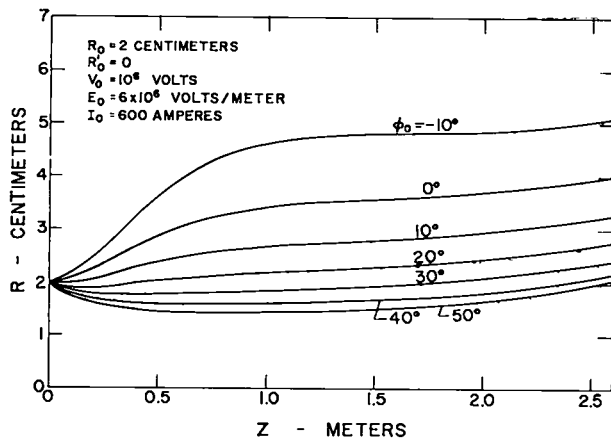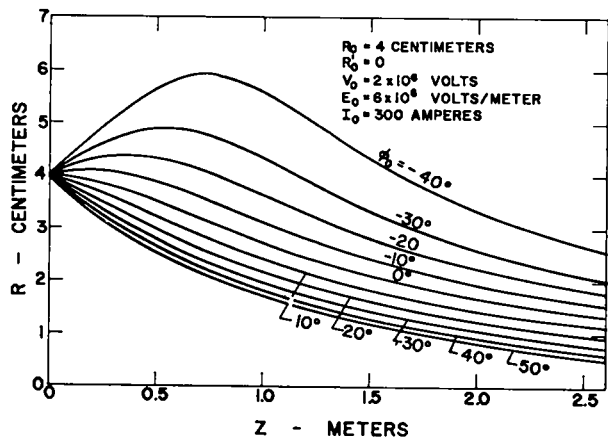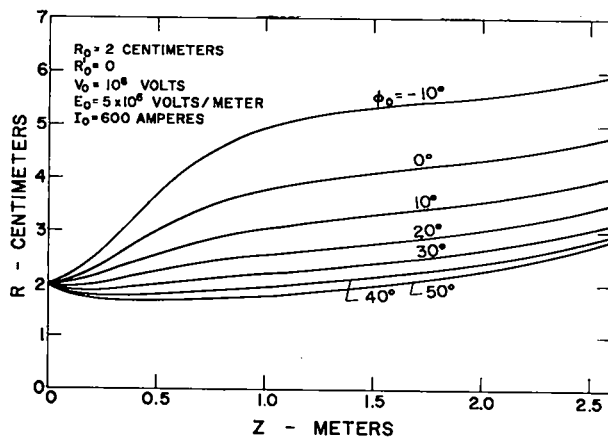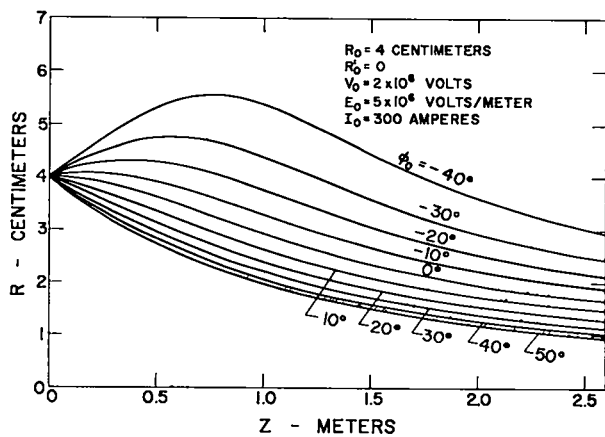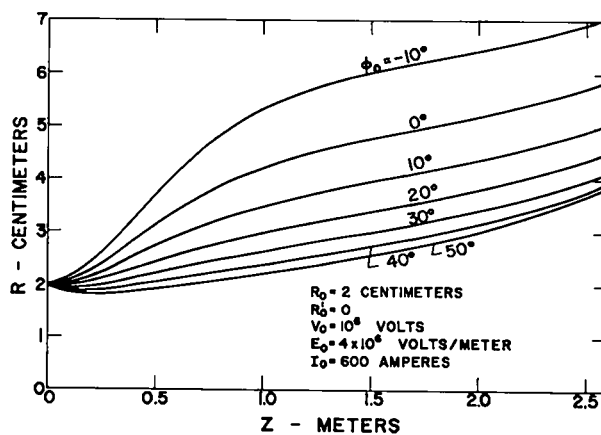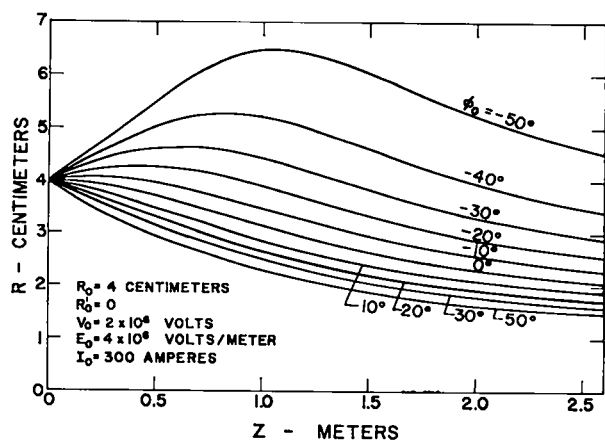
Fig. 5. 9.   Beam trajectories in first cavity with no
superposed magnetic fields.

Fig. 5.10.   Beam trajectories in first cavity with no
superposed magnetic fields.
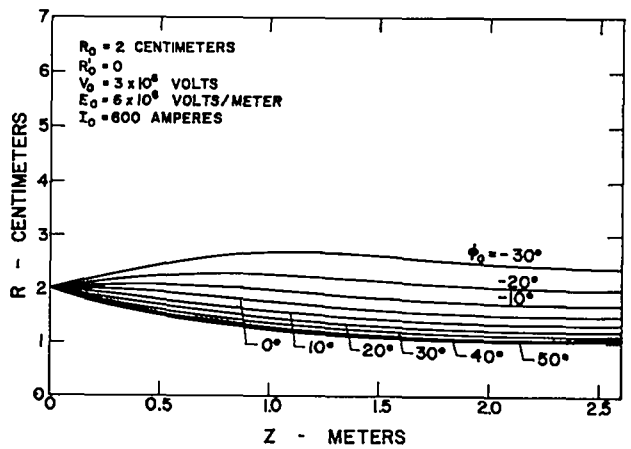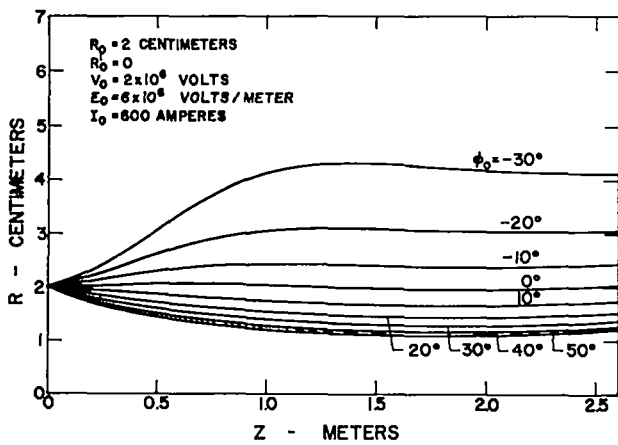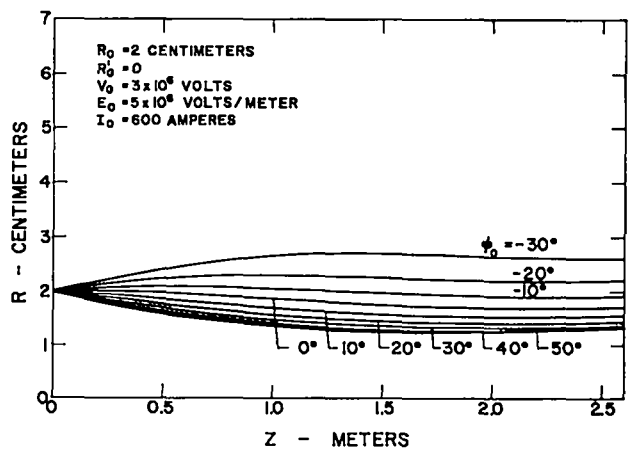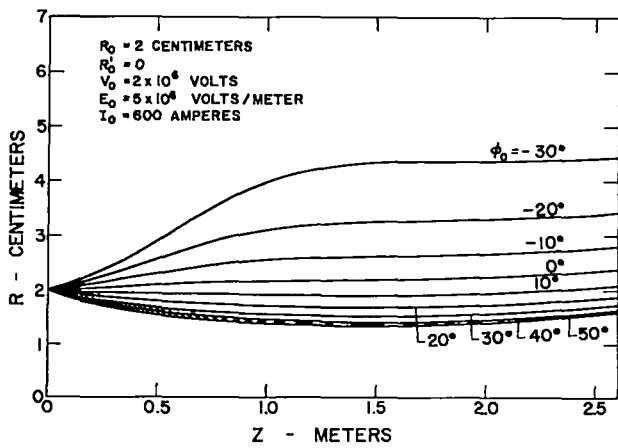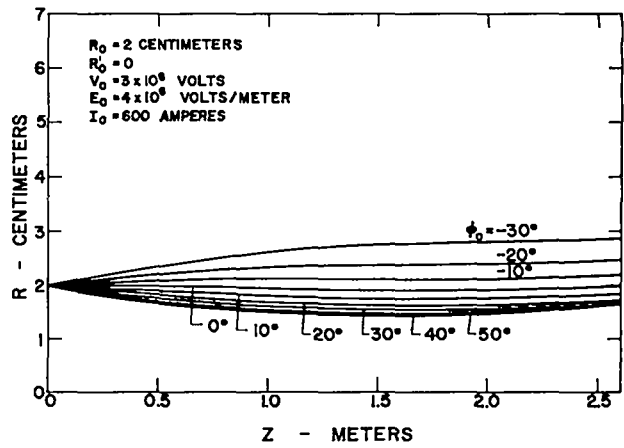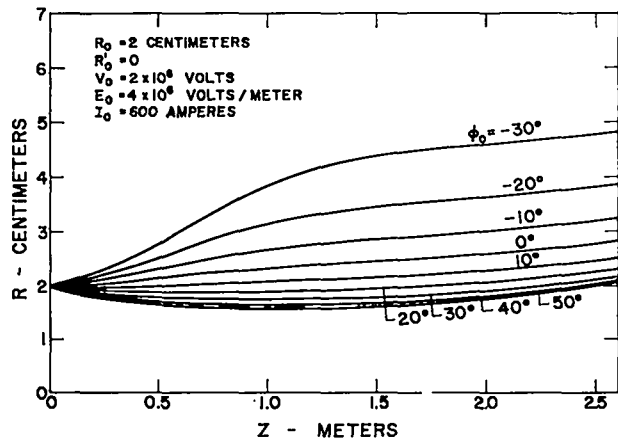
Fig. 5.11. Beam trajectories in first cavity with no   Fig. 5.12. Beam trajectories in first cavity with no
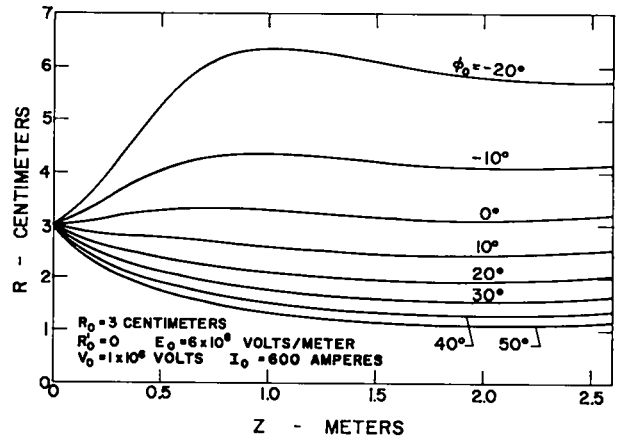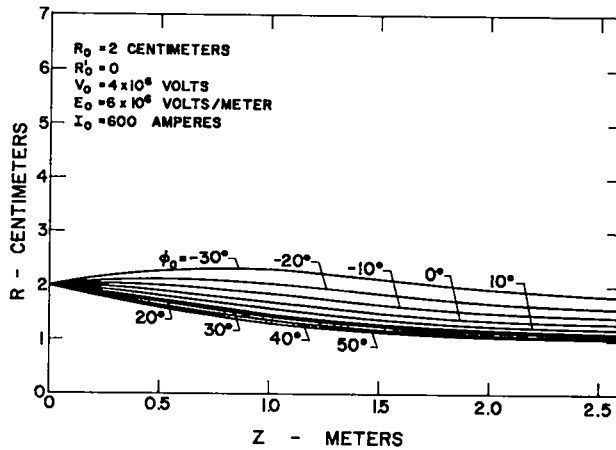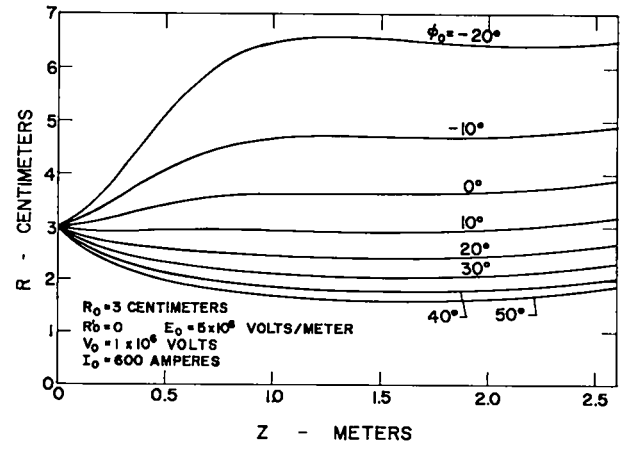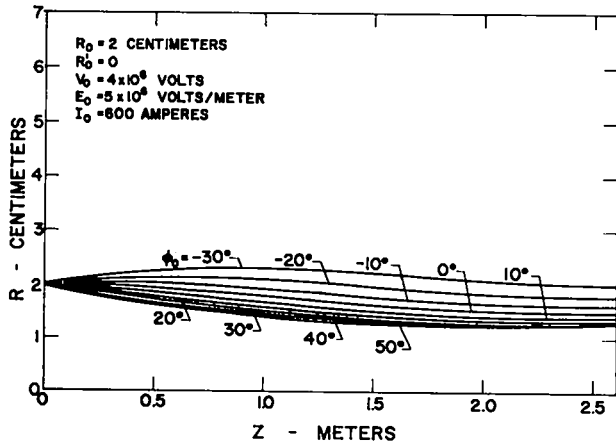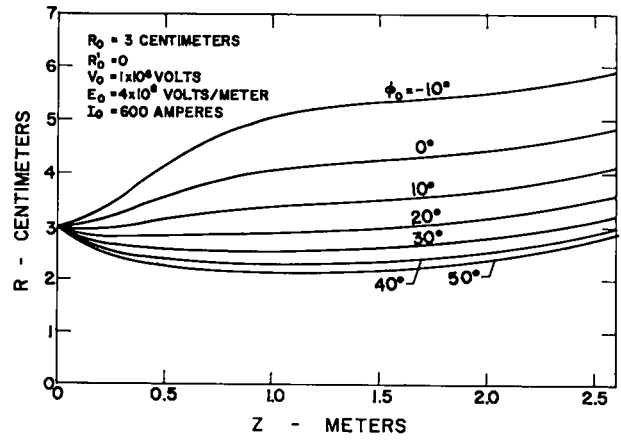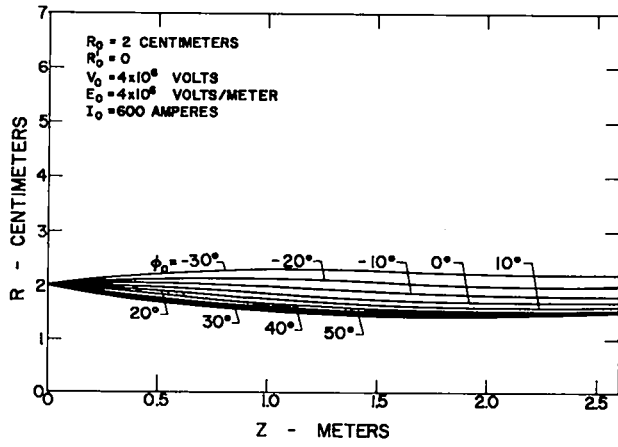
Fig. 5.13. Beam trajectories in first cavity with no superposed magnetic fields.

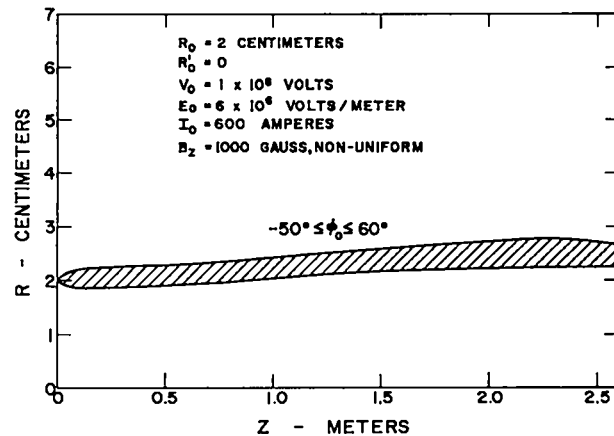**Fig. 5.14.** Beam trajectories in first cavity with no superposed magnetic fields.

157
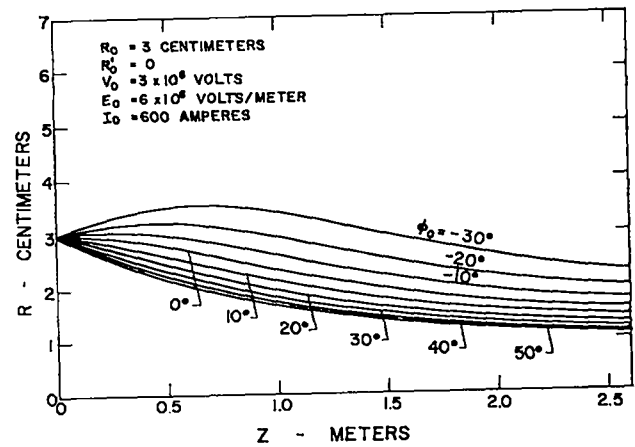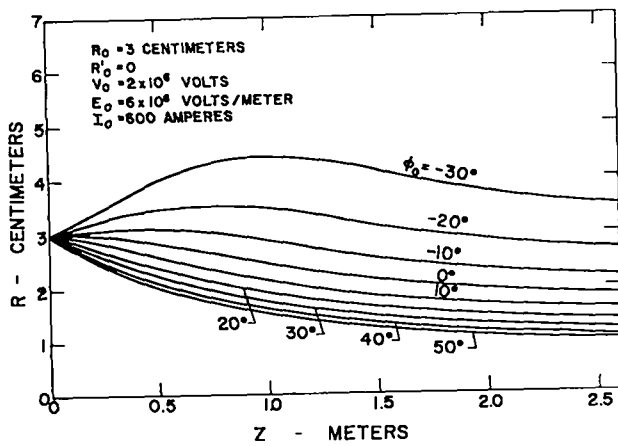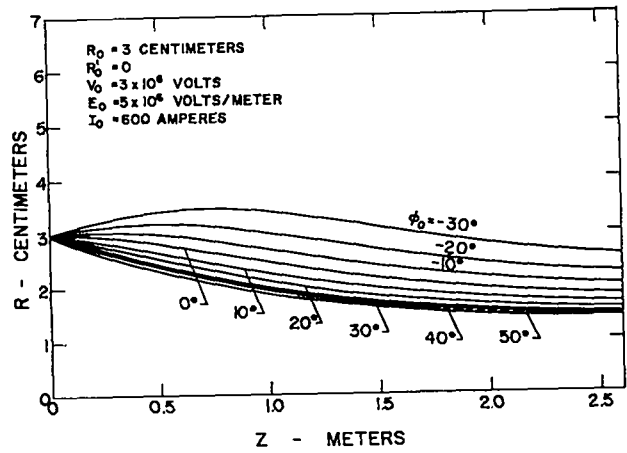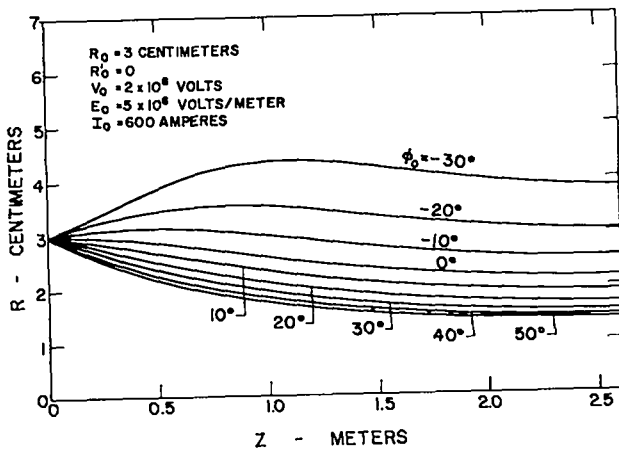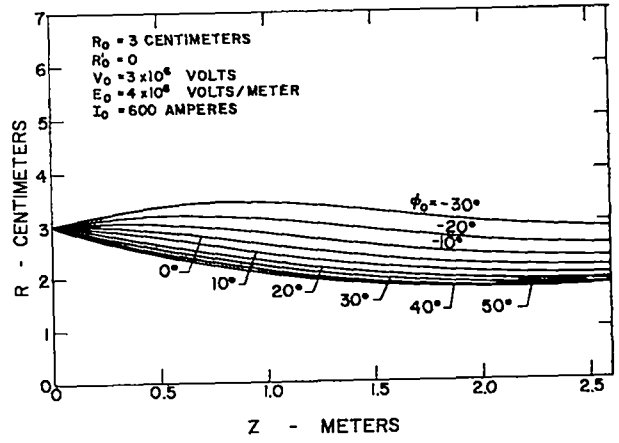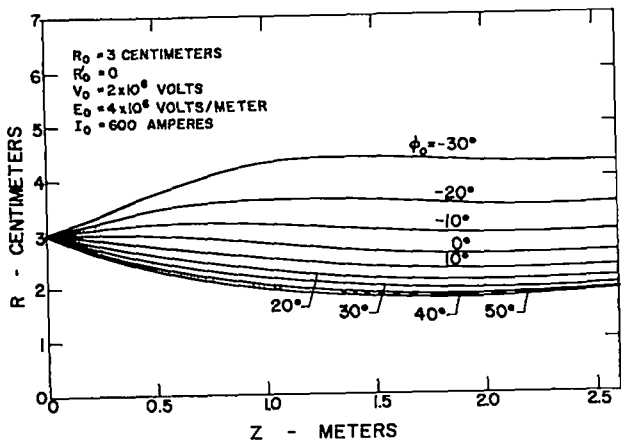
Fig. 5.15. Beam trajectories in first cavity with no superposed magnetic fields.

Fig. 5.16. Beam trajectories in first cavity with no superposed magnetic fields.
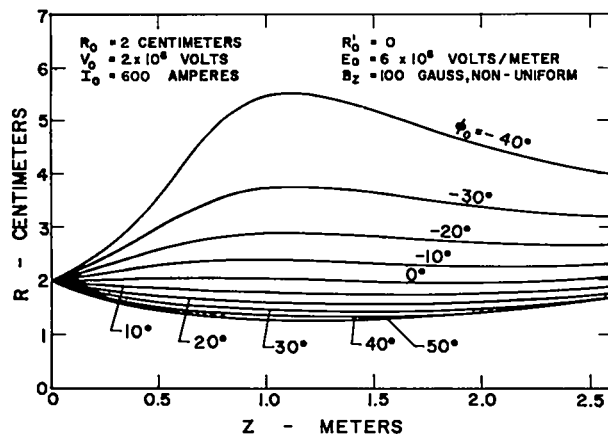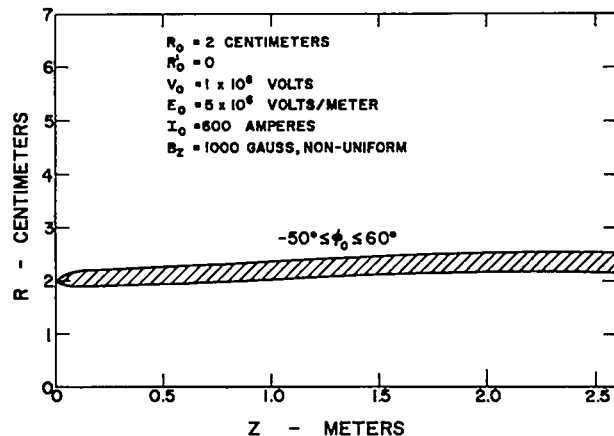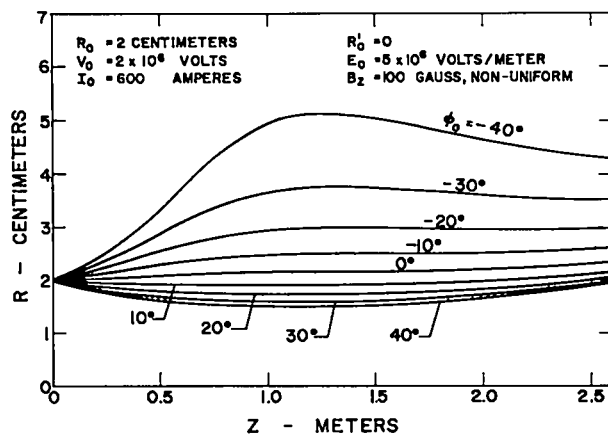
158
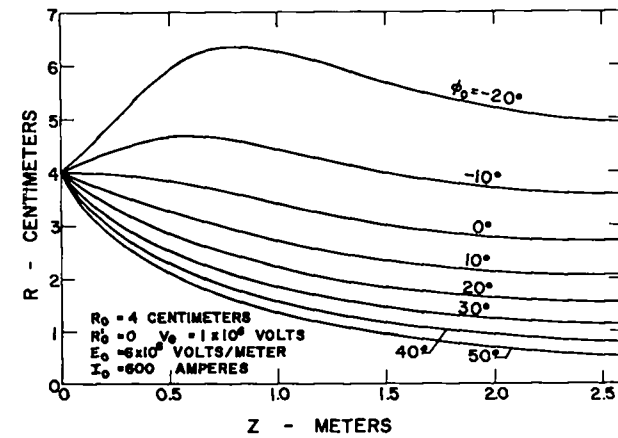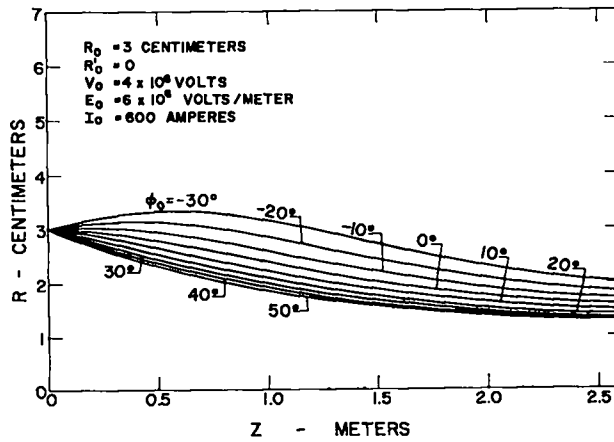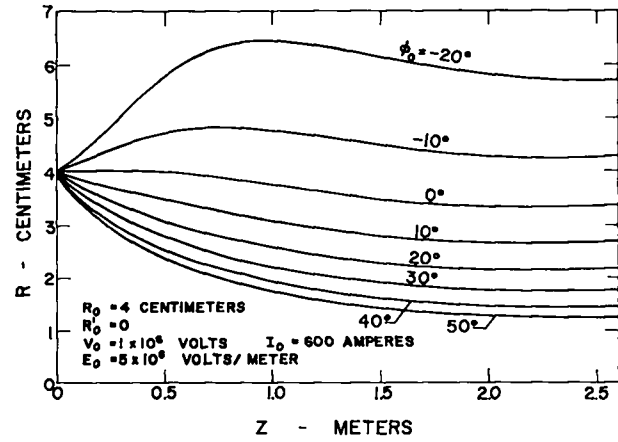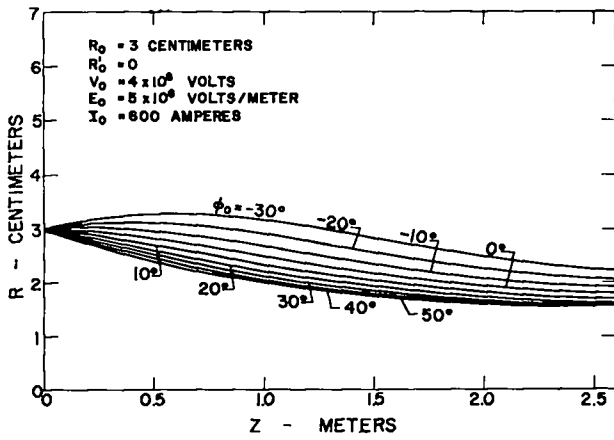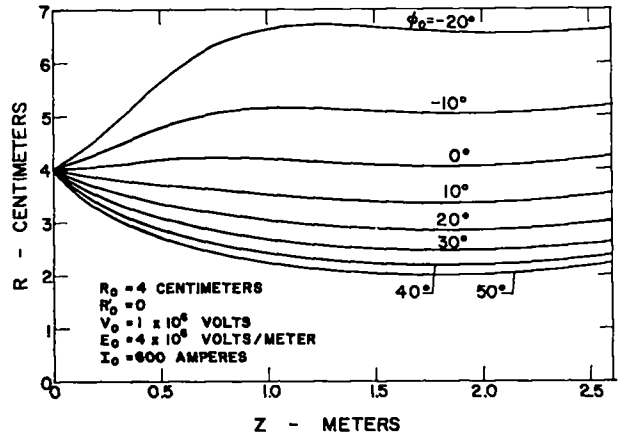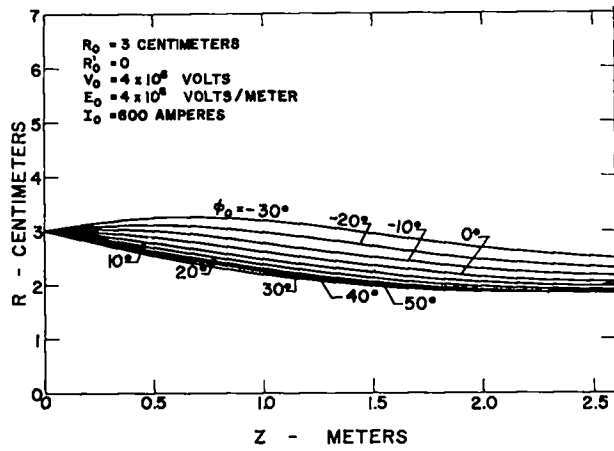
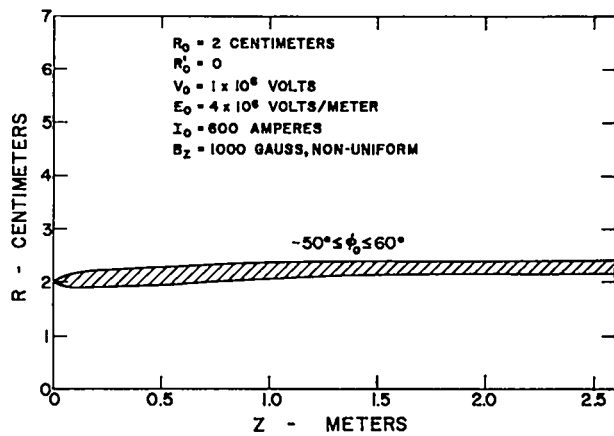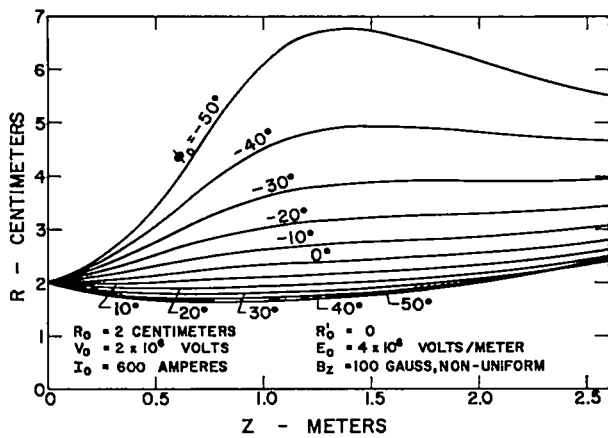Fig. 5.17. Beam trajectories in first cavity with no superposed magnetic fields.

Fig. 5.18. Beam trajectories in first cavity with no superposed magnetic fields.

159
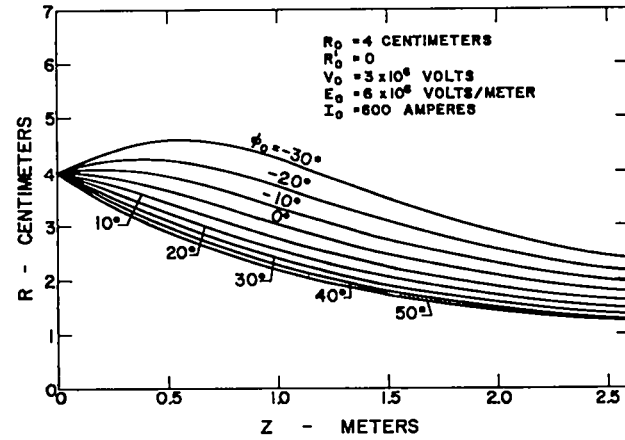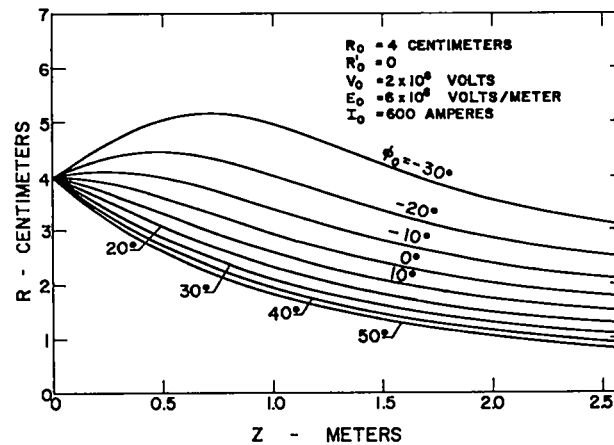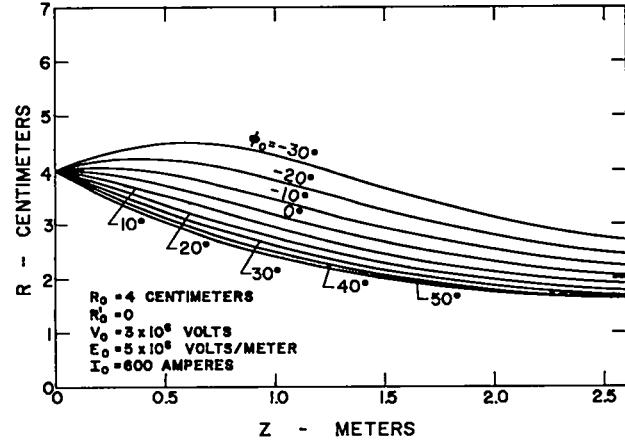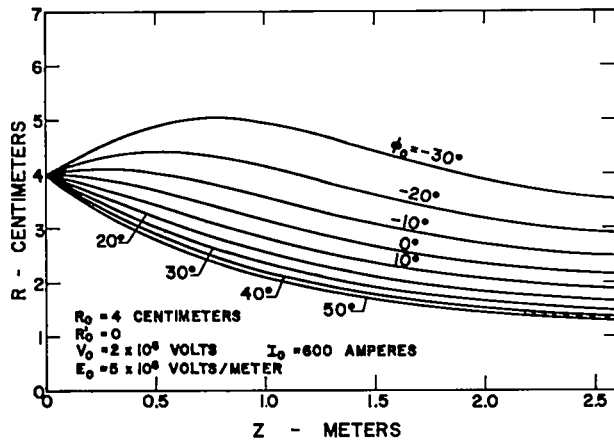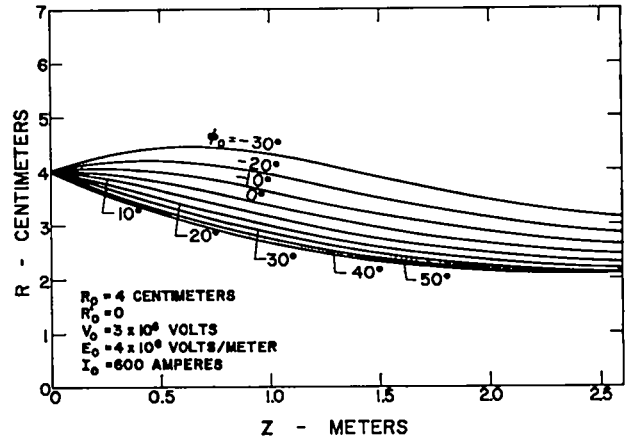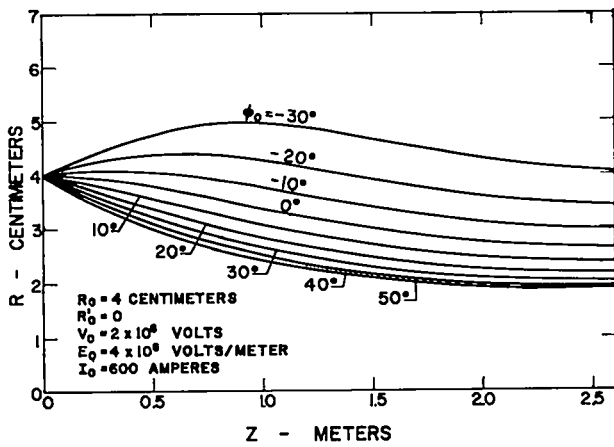
Fig. 5.19. Beam trajectories in first cavity with no superposed magnetic fields.

Fig. 5.20. Beam trajectories in first cavity with no superposed magnetic fields.

160
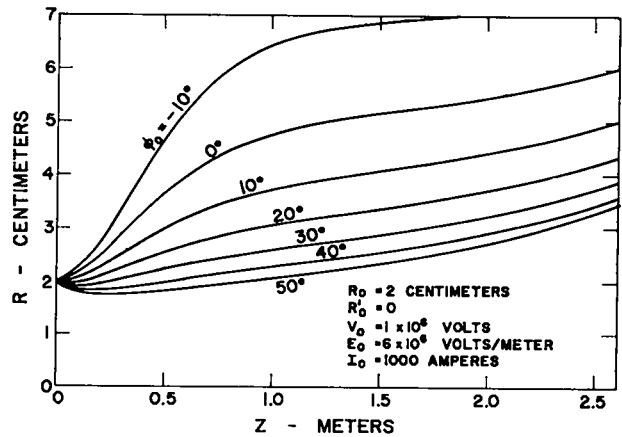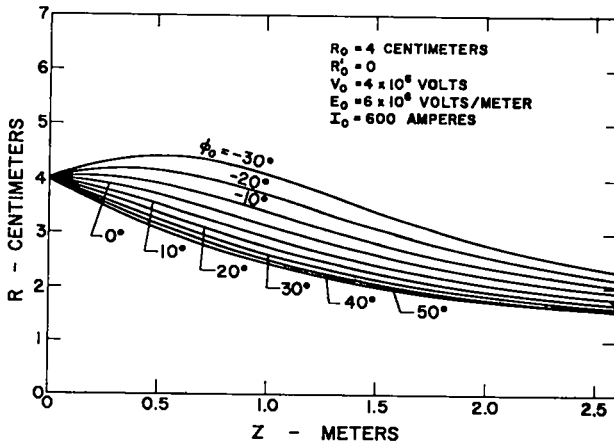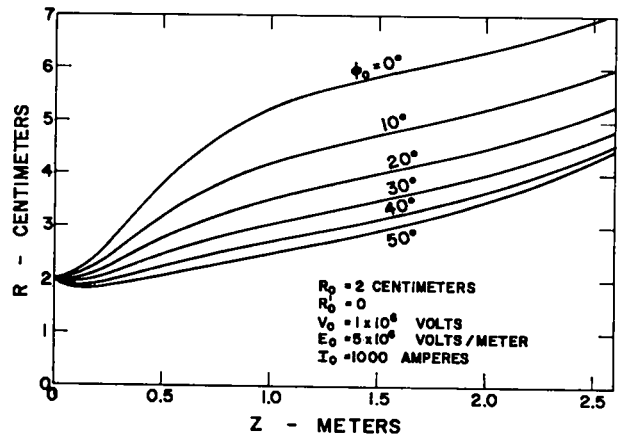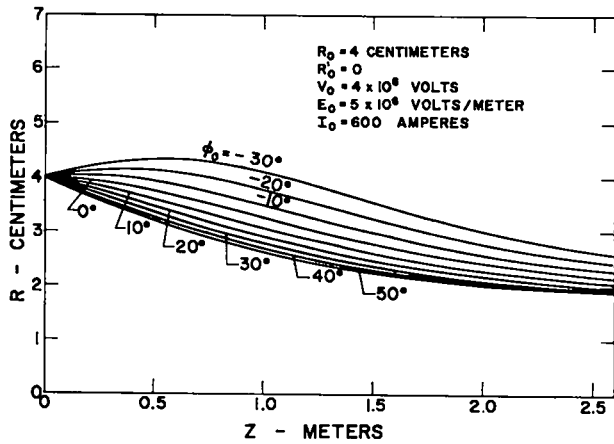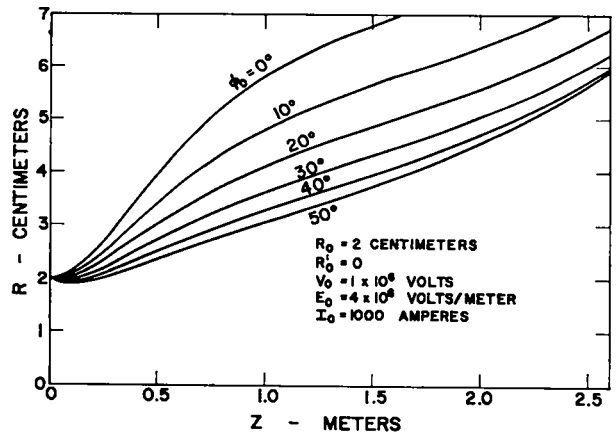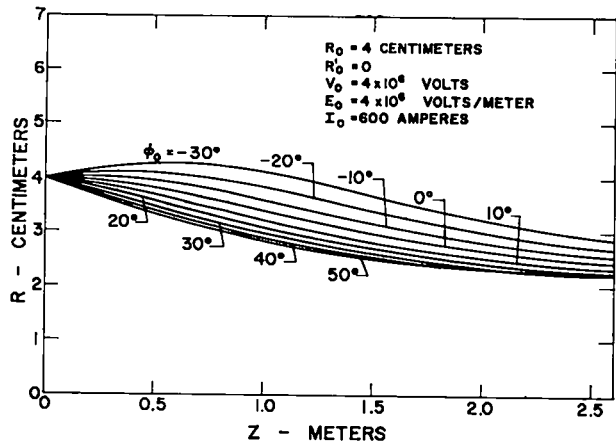
Fig. 5.21. Beam trajectories in first cavity with no superposed magnetic fields.

Fig. 5.22. Beam trajectories in first cavity with no superposed magnetic fields.

161
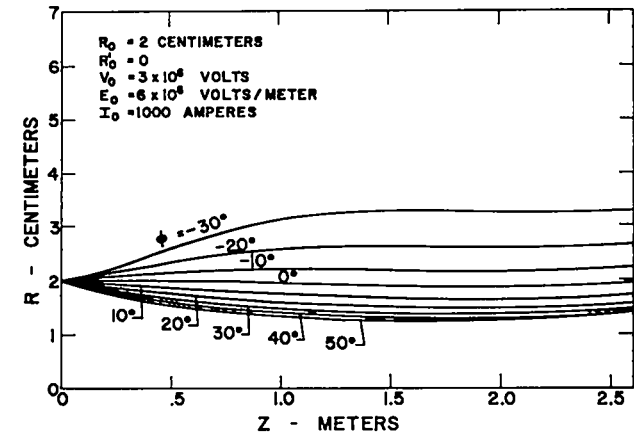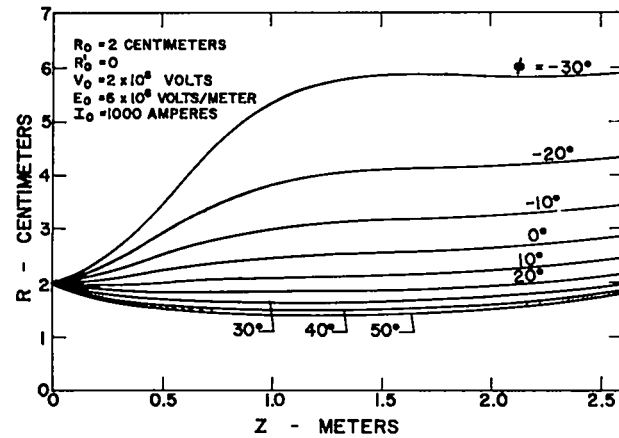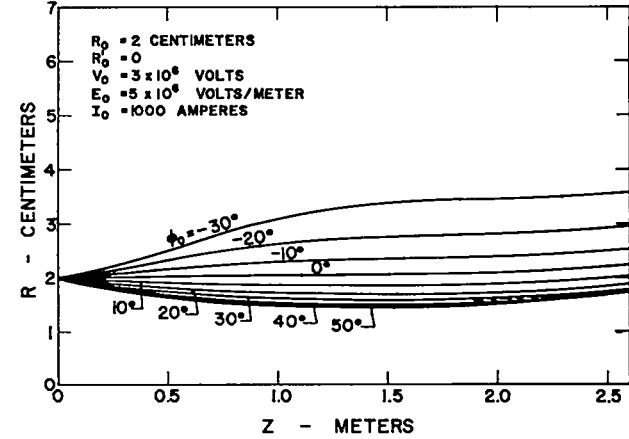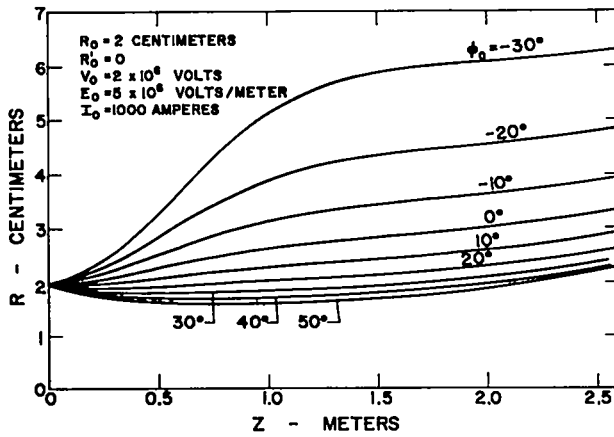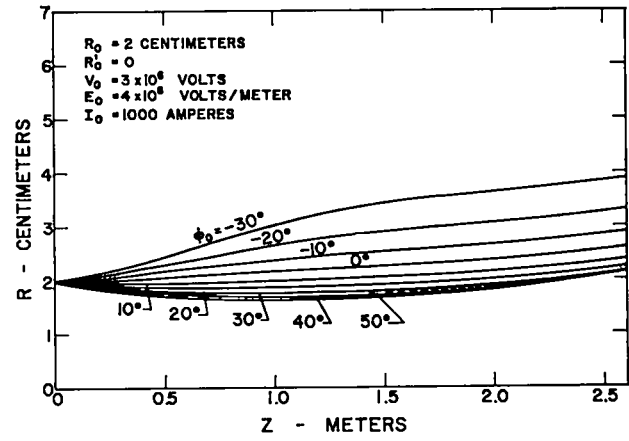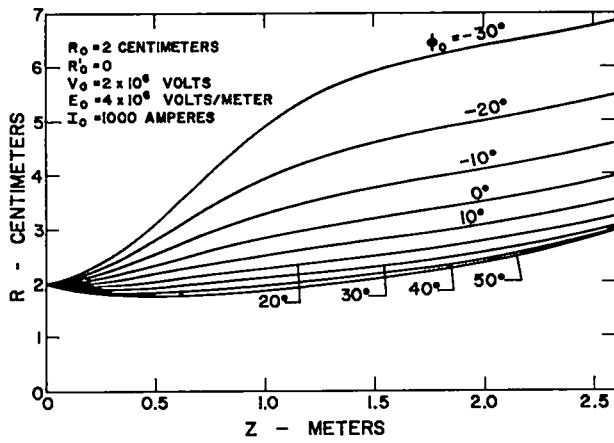
Fig. 5.23.   Beam trajectories in first cavity with no superposed magnetic fields.

Fig. 5.24.   Beam trajectories in first cavity with no superposed magnetic fields.

162
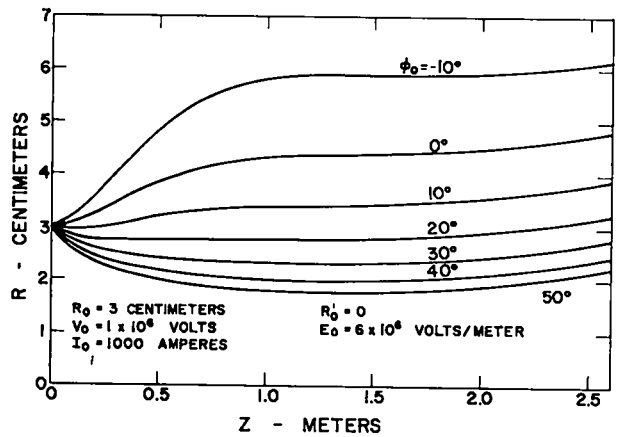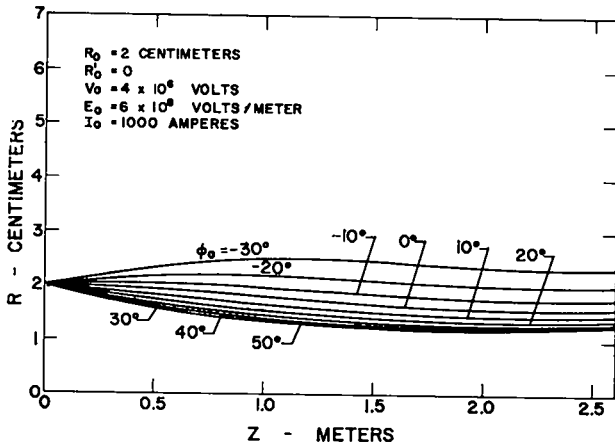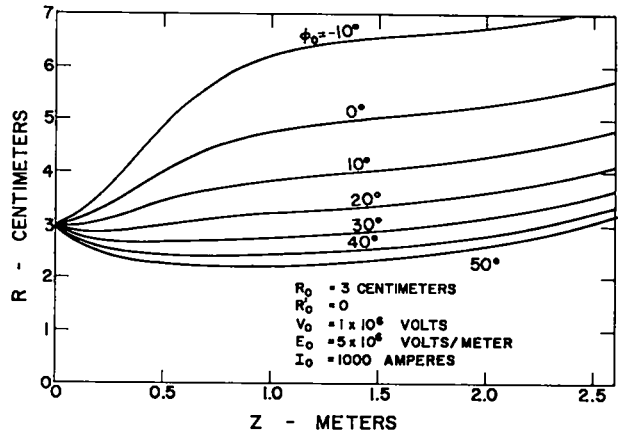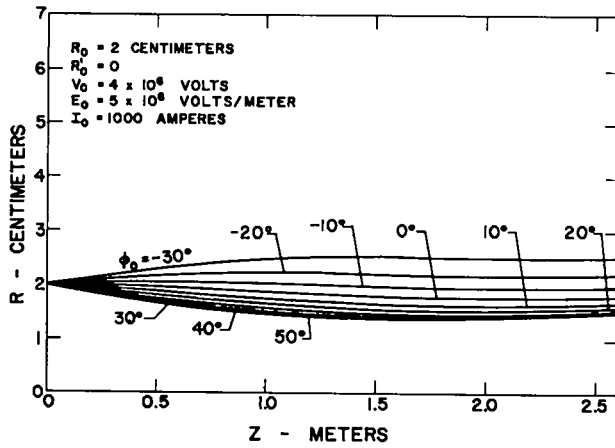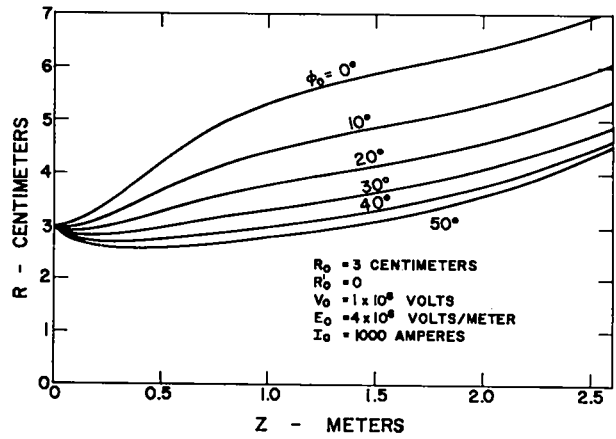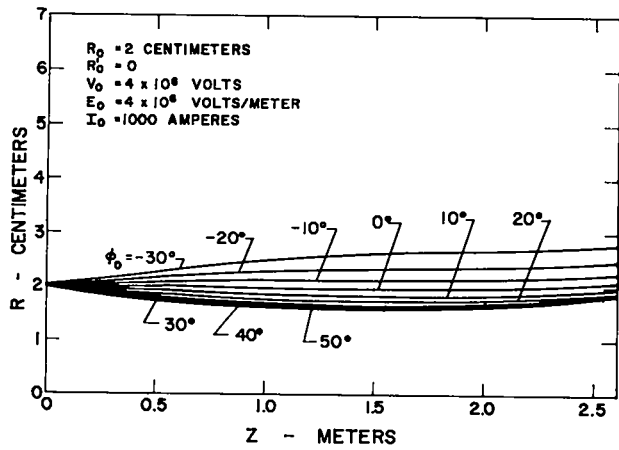
Fig. 5.25. Beam trajectories in first cavity with no superposed magnetic fields.

Fig. 5.26. Beam trajectories in first cavity with no superposed magnetic fields.
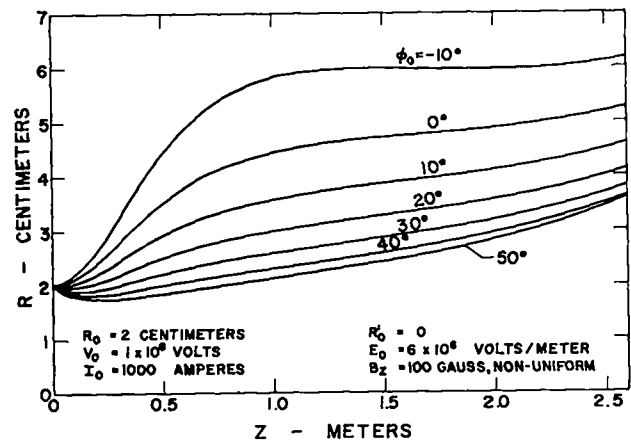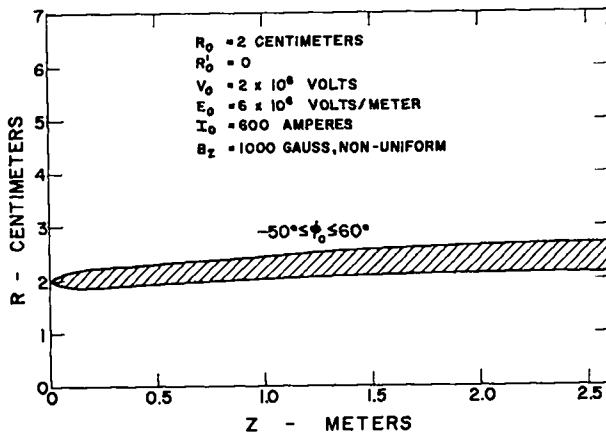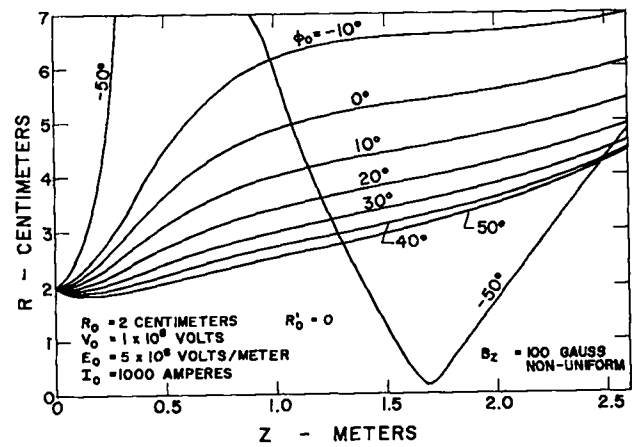
Fig. 5.27. Beam trajectories in first cavity with no superposed magnetic fields.

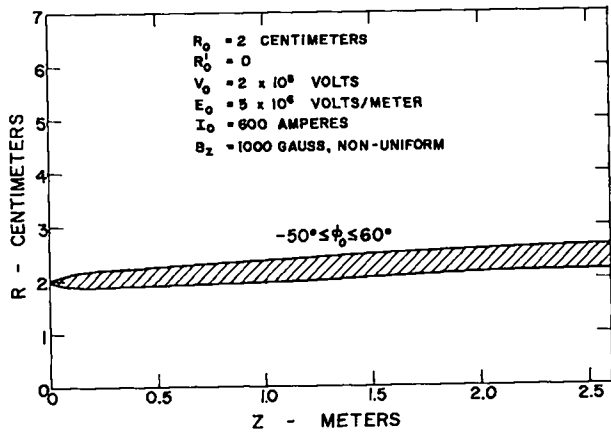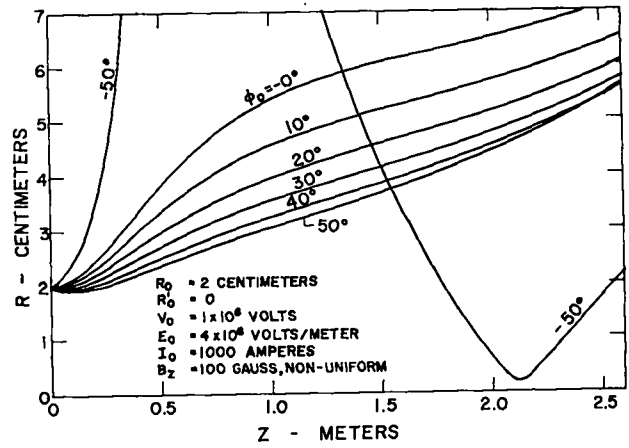Fig. 5.28. Beam trajectories in first cavity with no superposed magnetic fields.

164

Fig. 5.29. Beam trajectories in first cavity with no
superposed magnetic fields.

Fig. 5.30. Beam trajectories in first cavity with no
superposed magnetic fields.

165

Fig. 5.31. Beam trajectories in first cavity with no superposed magnetic fields.

Fig. 5.32. Beam trajectories in first cavity with no superposed magnetic fields.
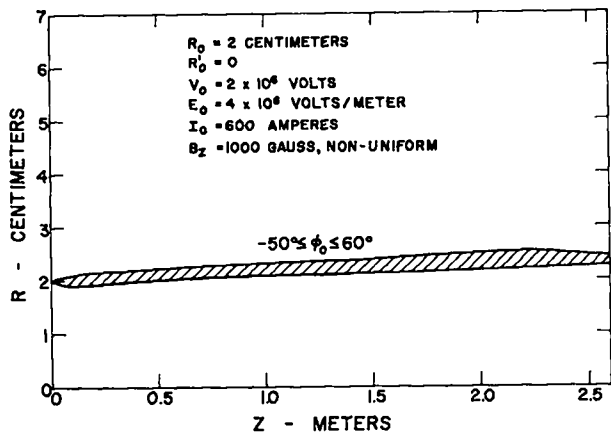
166

Fig. 5.33. Beam trajectories in first cavity with no superposed magnetic fields.

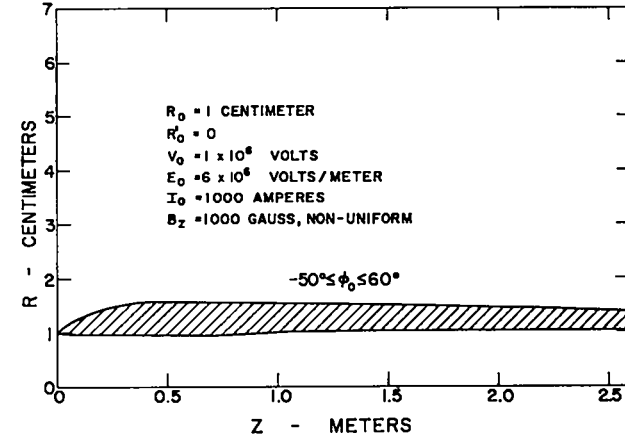Fig. 5.34. Beam trajectories in first cavity with superposed magnetic fields.

167

Fig. 5.35. Beam trajectories in first cavity with super-
posed magnetic fields.

Fig. 5.36. Beam trajectories in first cavity with super-
posed magnetic fields.

168

Fig. 5.37. Beam trajectories in first cavity with super-
posed magnetic fields.

Fig. 5.38. Beam trajectories in first cavity with super-
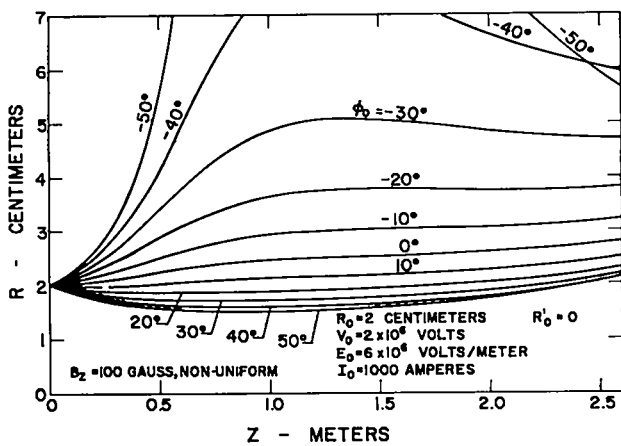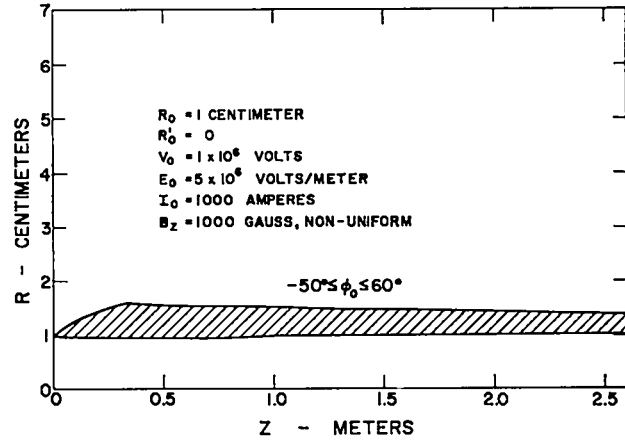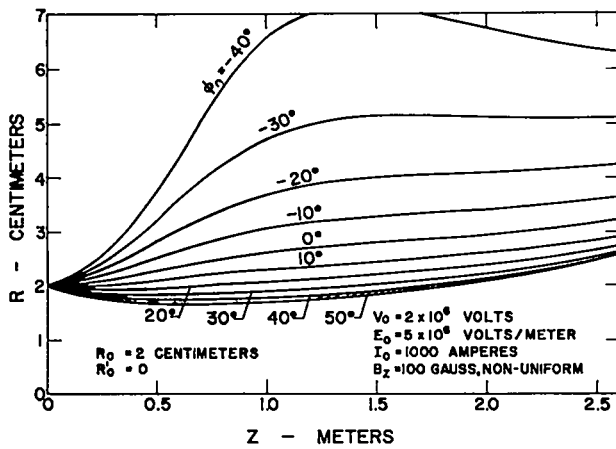posed magnetic fields.

169

Fig. 5.39. Beam trajectories in first cavity with super-
posed magnetic fields.

Fig. 5.40. Beam trajectories in first cavity with super-
posed magnetic fields.
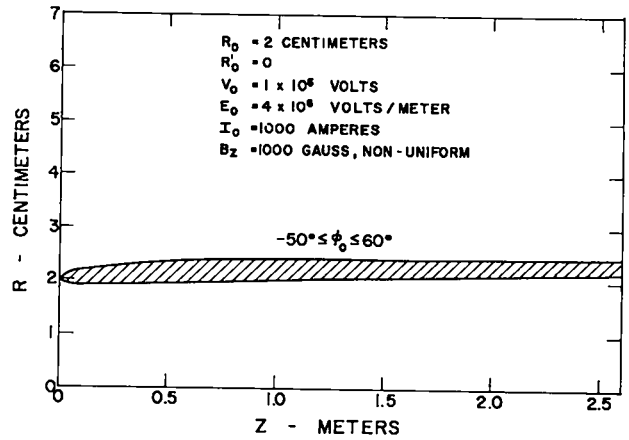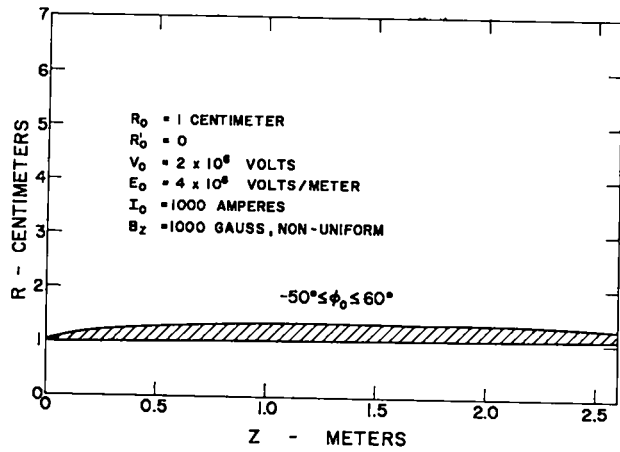
Fig. 5.41. Beam trajectories in first cavity with super-
posed magnetic fields.

Fig. 5.42. Beam trajectories in first cavity with super-
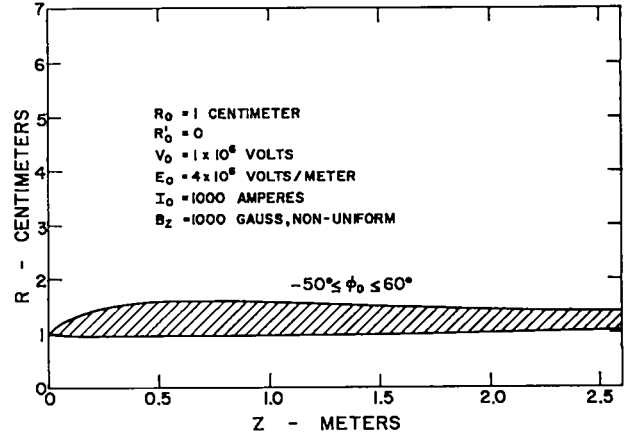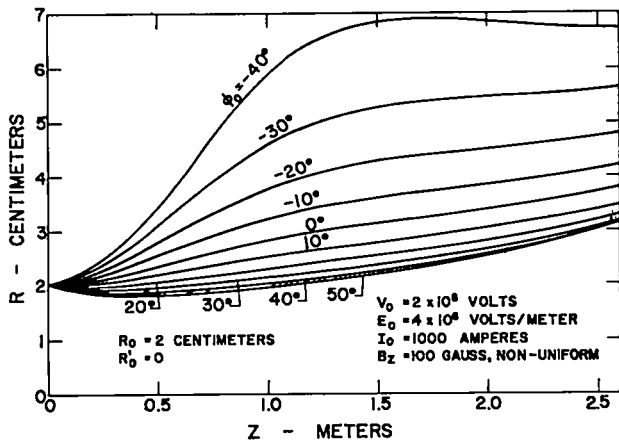posed magnetic fields.
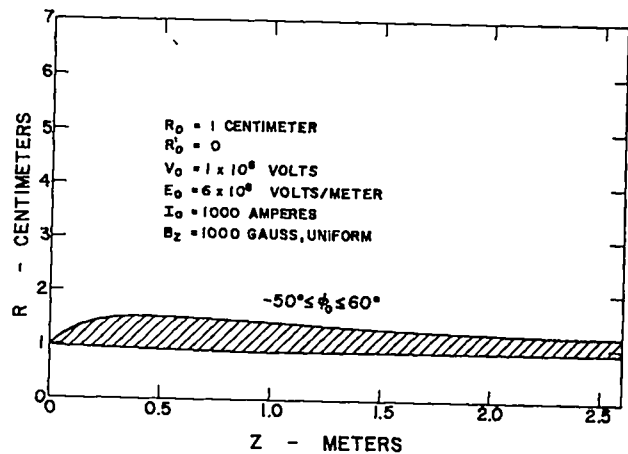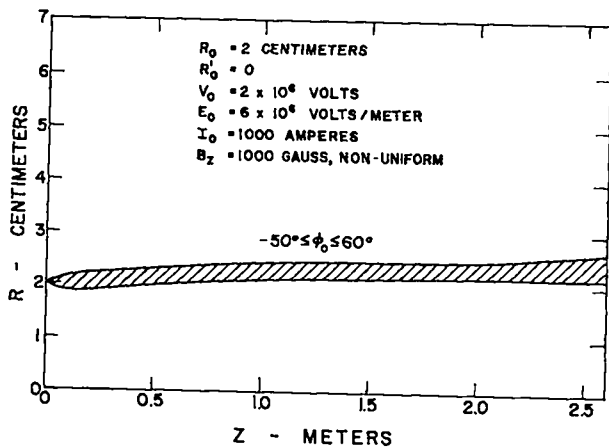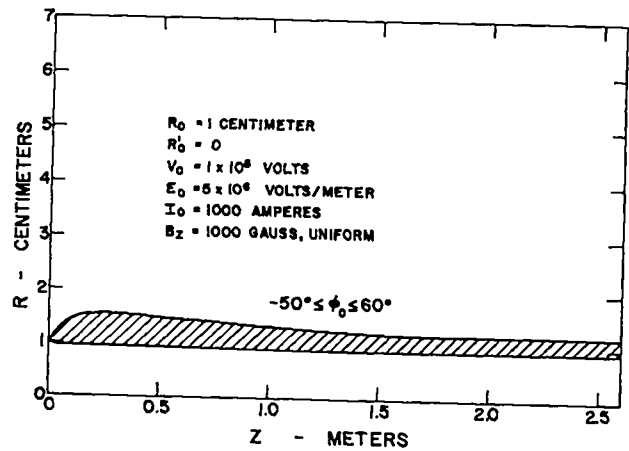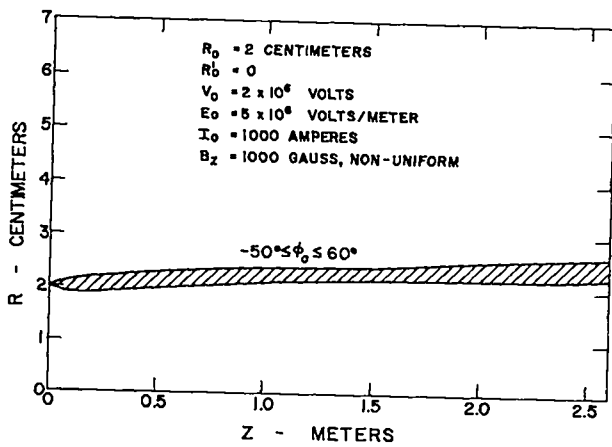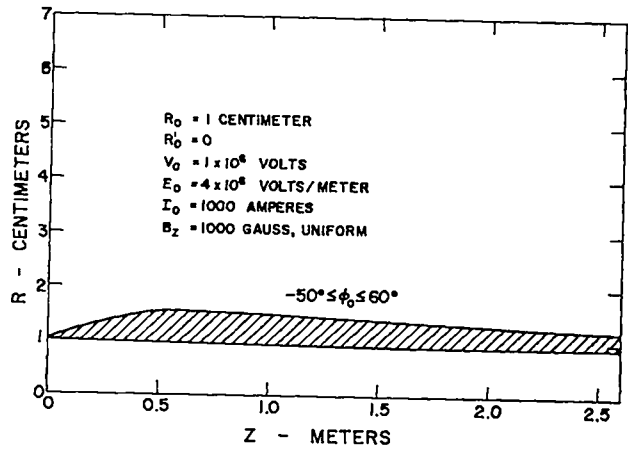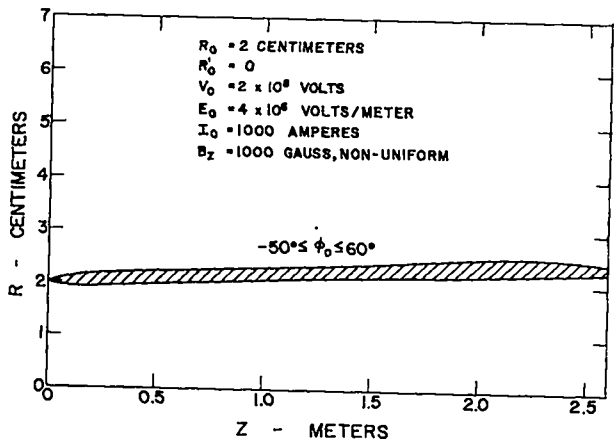
Fig. 5.43. Beam trajectories in first cavity with super-
posed magnetic fields.

Fig. 5.44. Beam trajectories in first cavity with super-
posed magnetic fields.
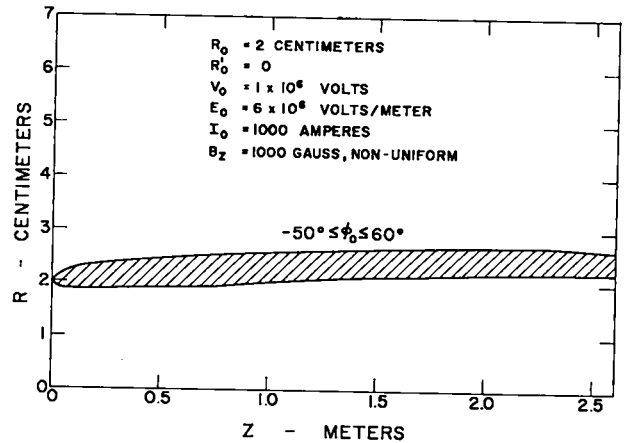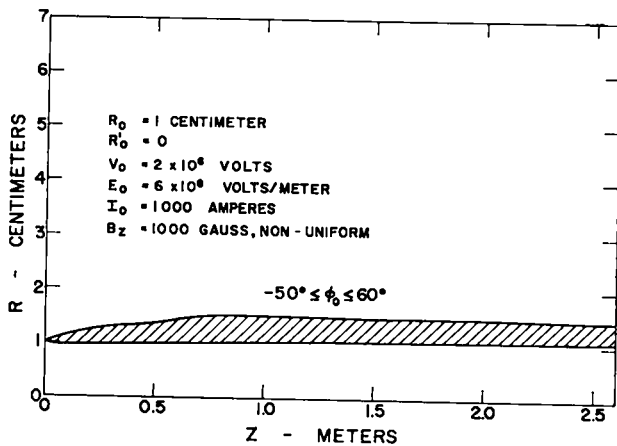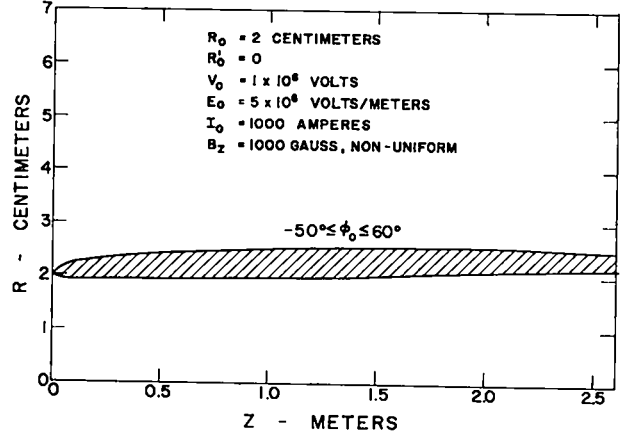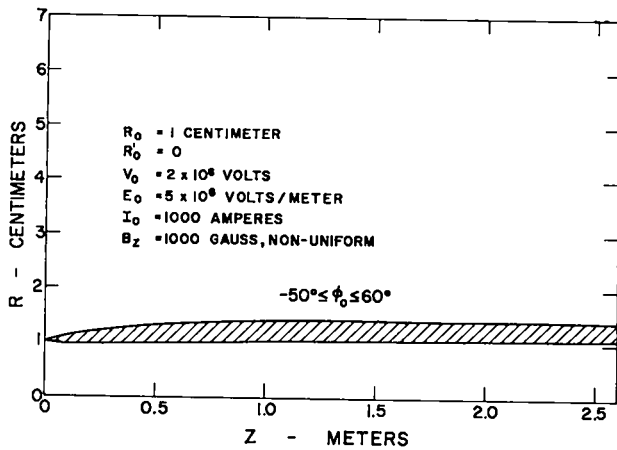
172
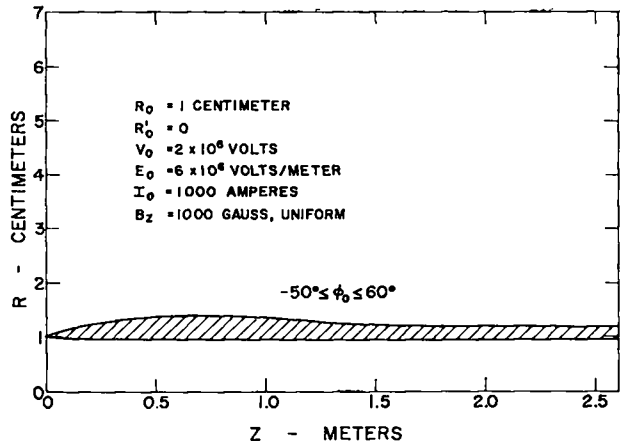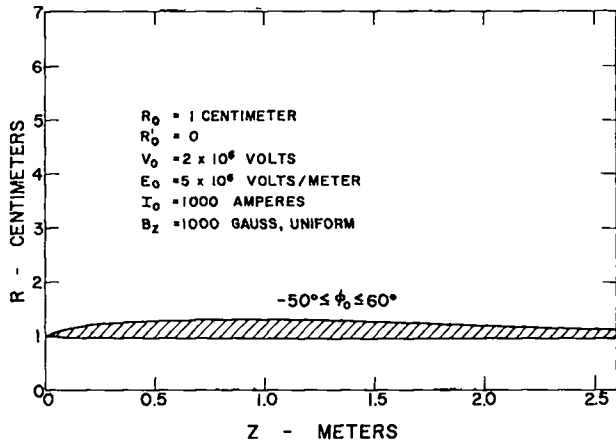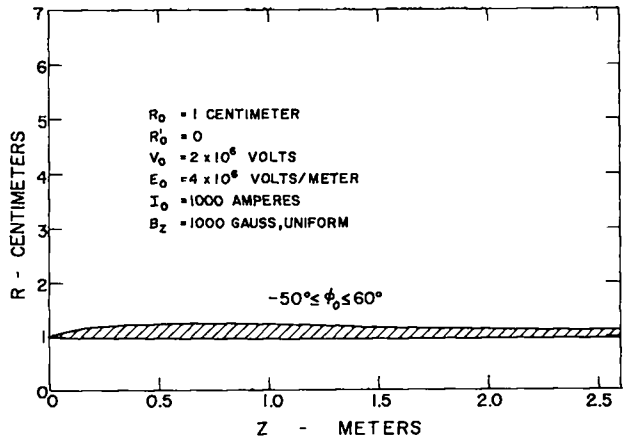
Fig. 5.45. Beam trajectories in first cavity with super-
posed magnetic fields.

173
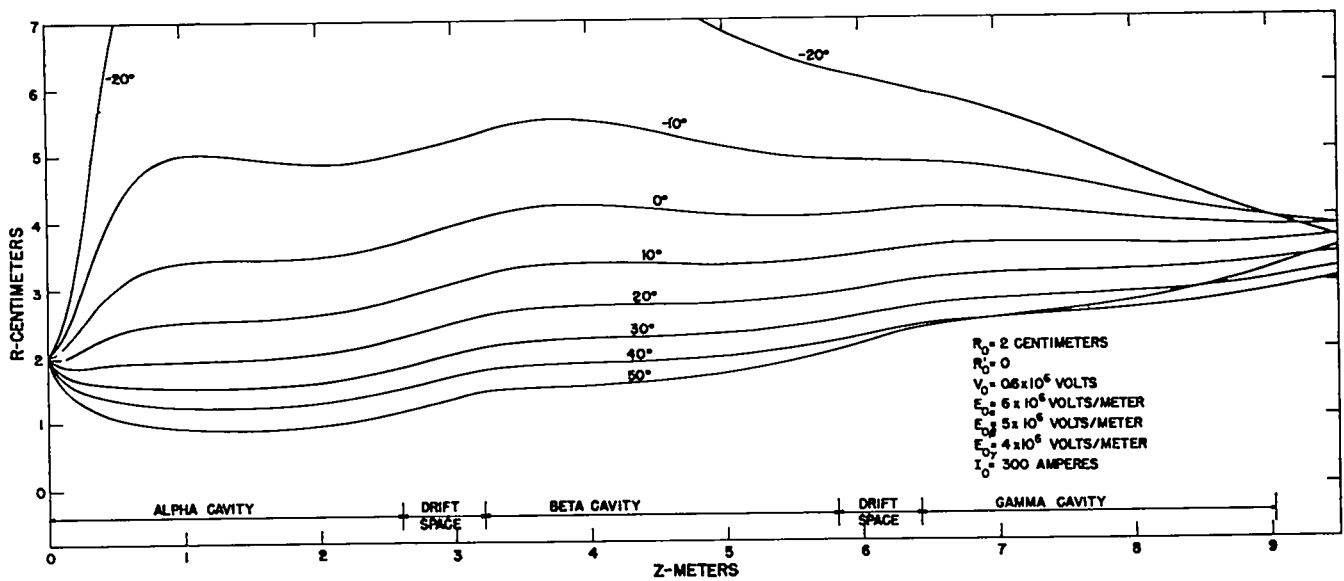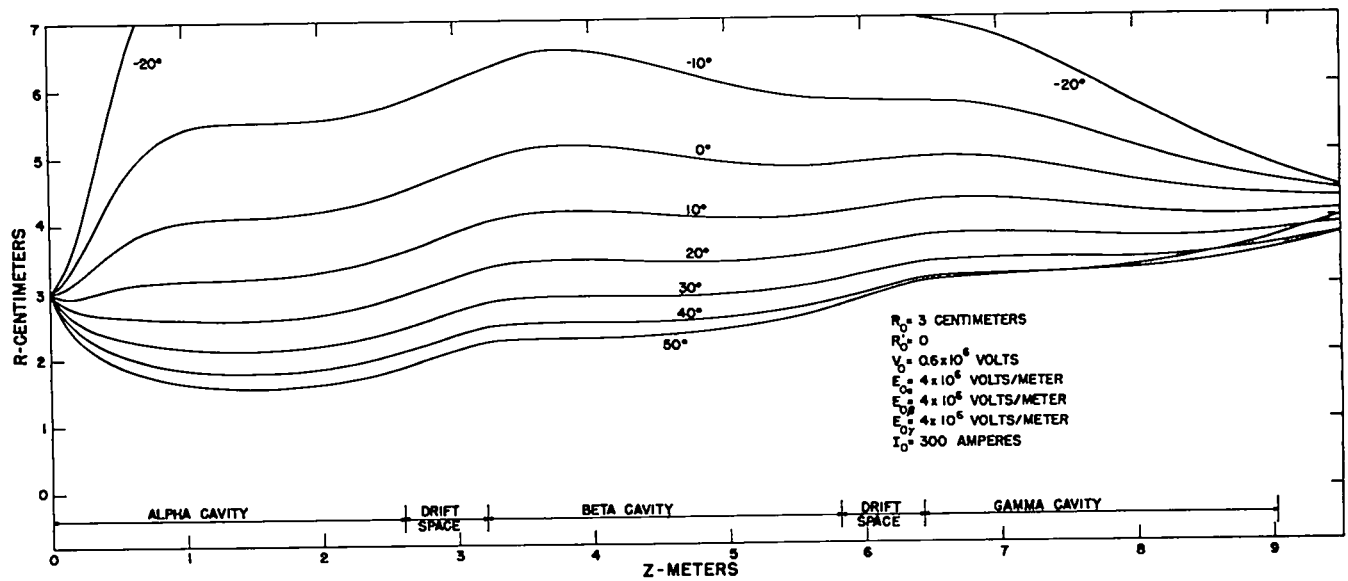
Fig. 5.46. Trajectories through three cavities.
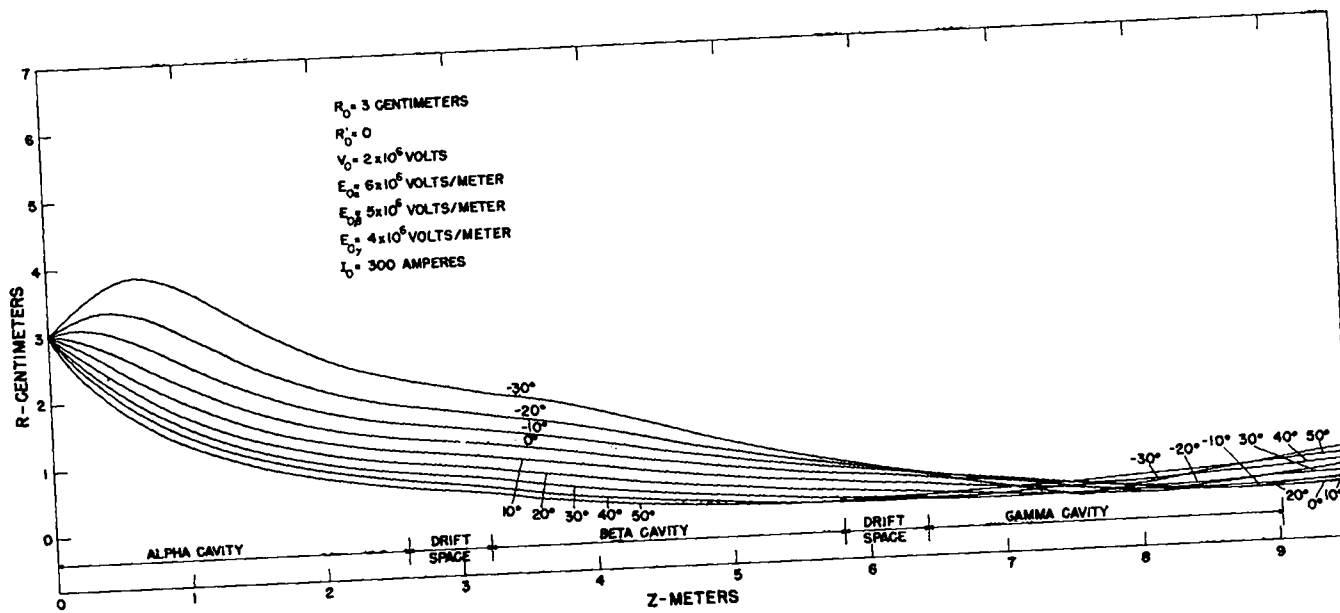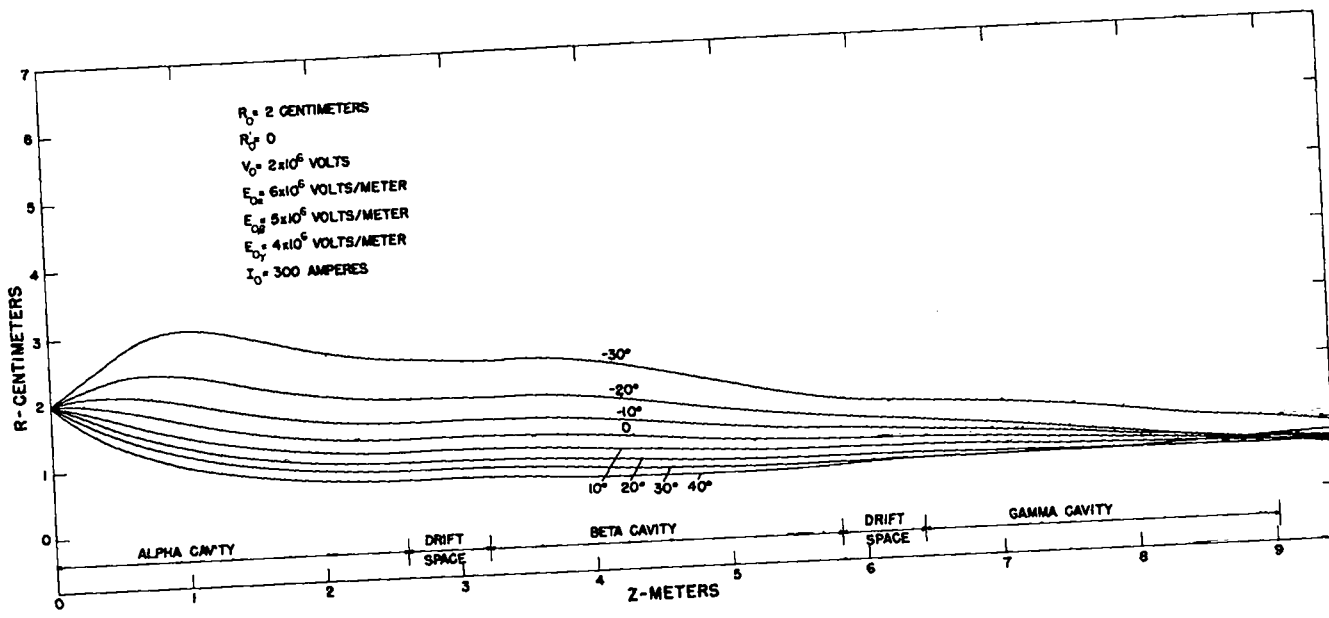
Fig. 5.47. Trajectories through three cavities.
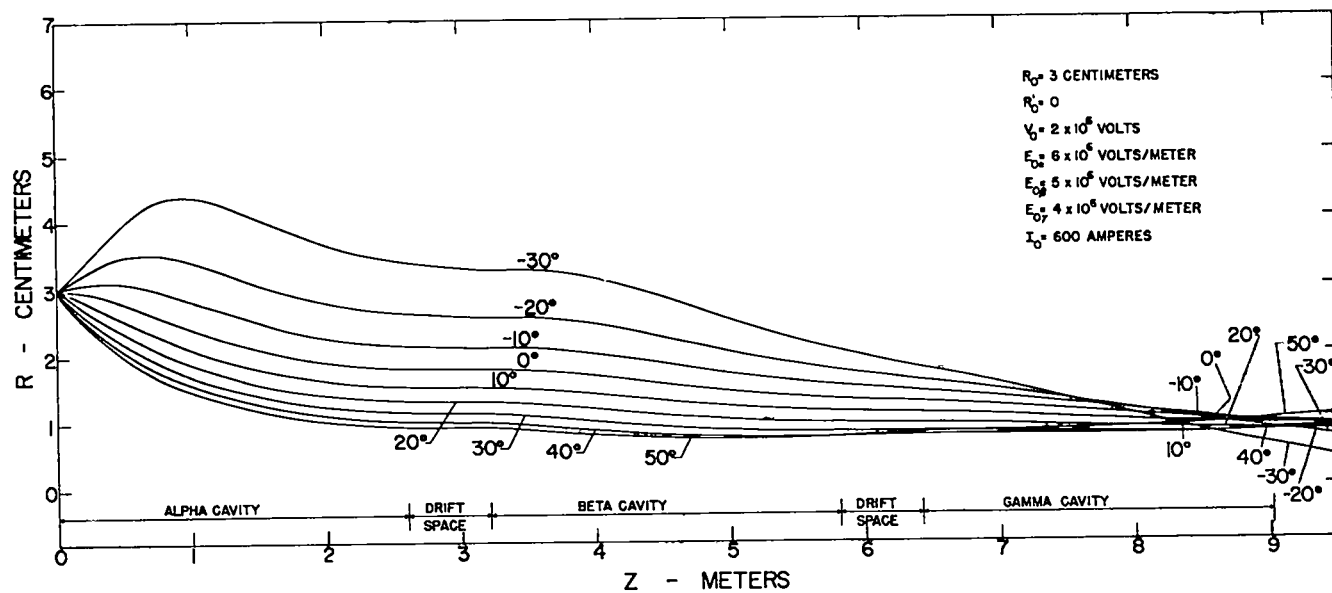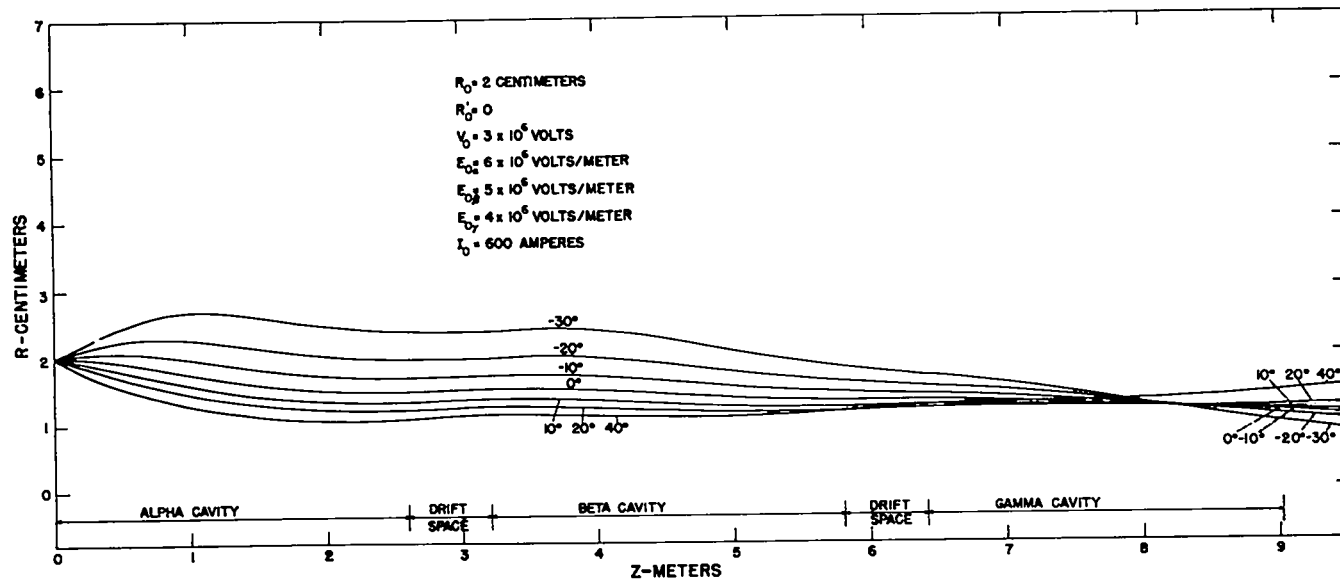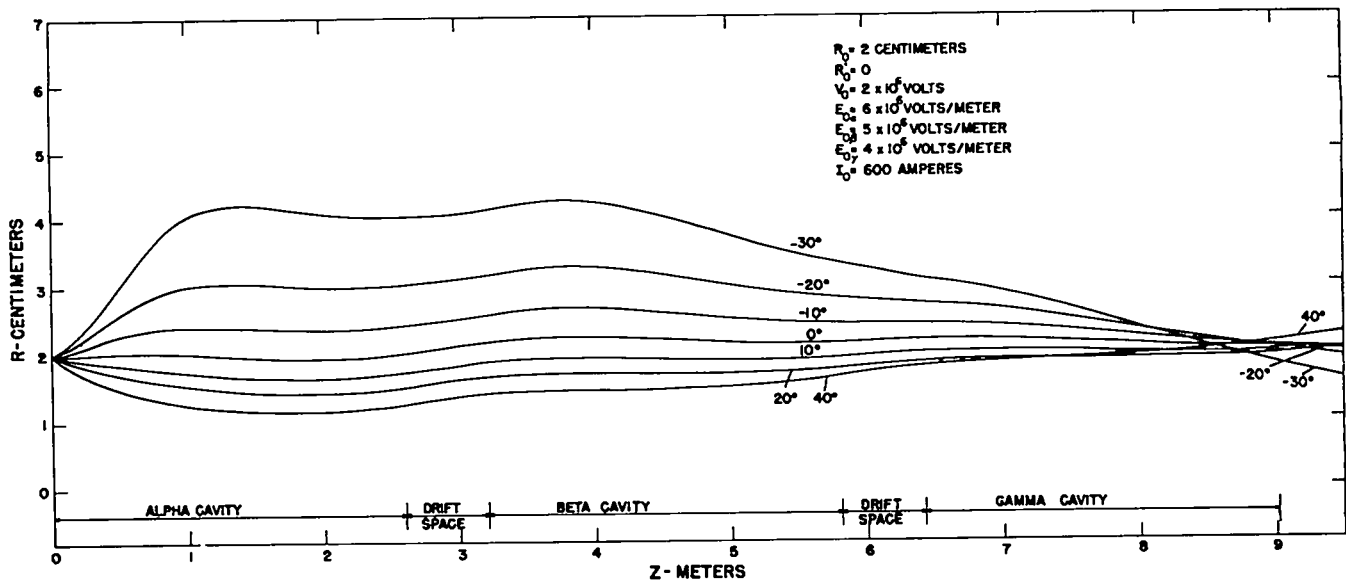
Fig. 5.48. Trajectories through three cavities.
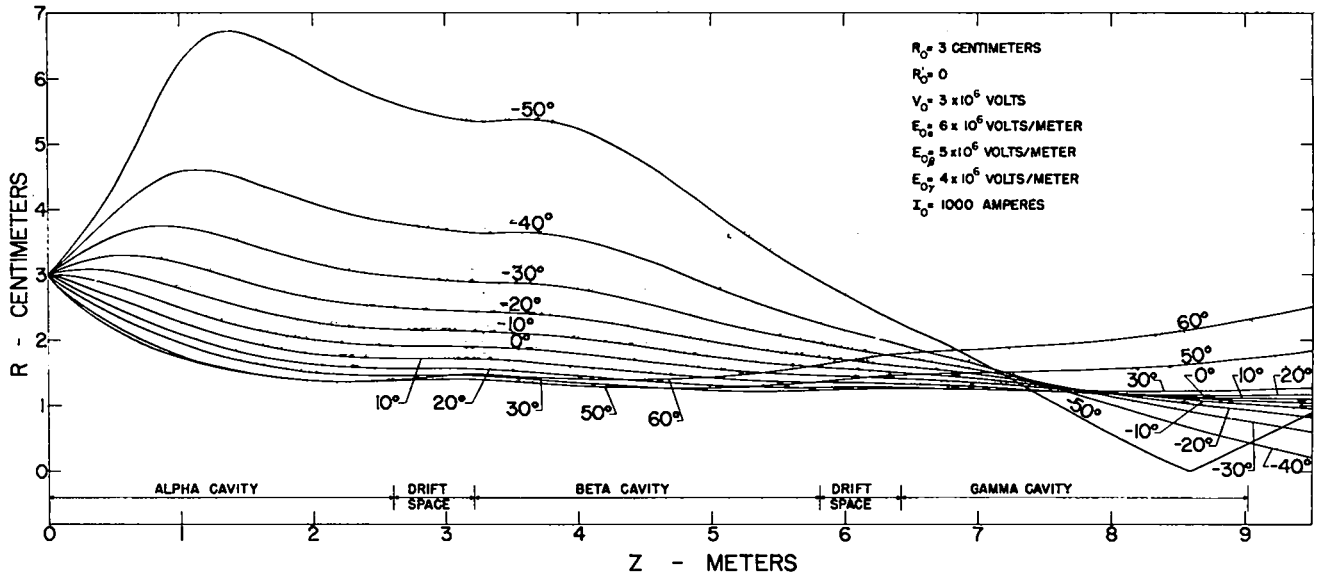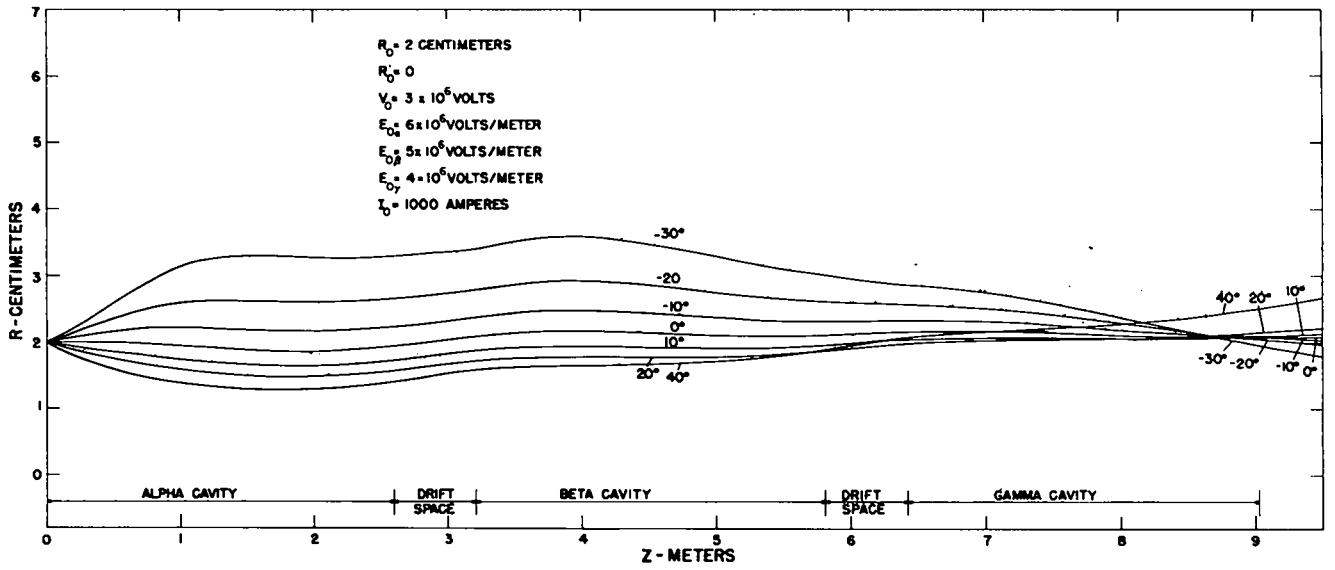
Fig. 5.49.   Trajectories through three cavities.
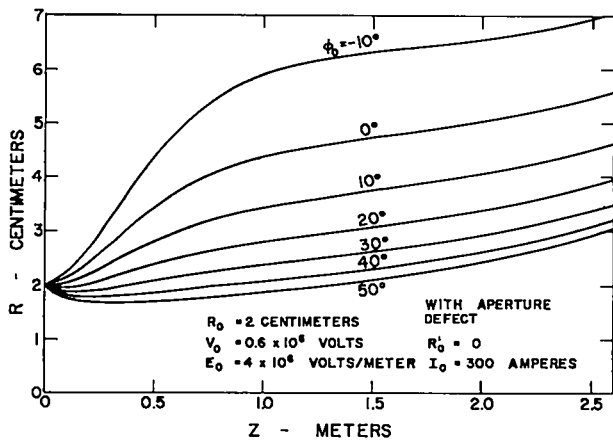
Fig. 5.50a. First cavity trajectories with aperture defect.
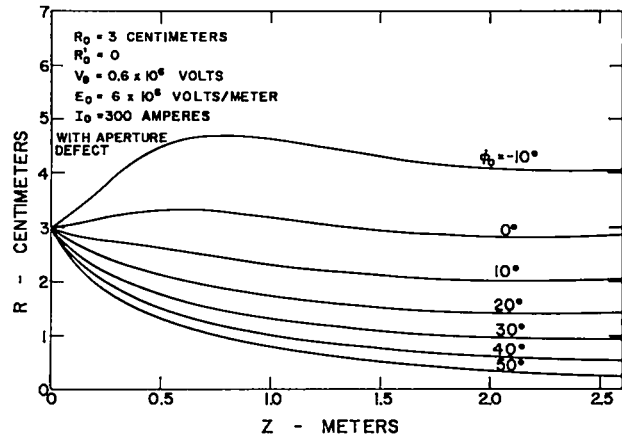
Fig. 5.51a. First cavity trajectories with aperture defect.
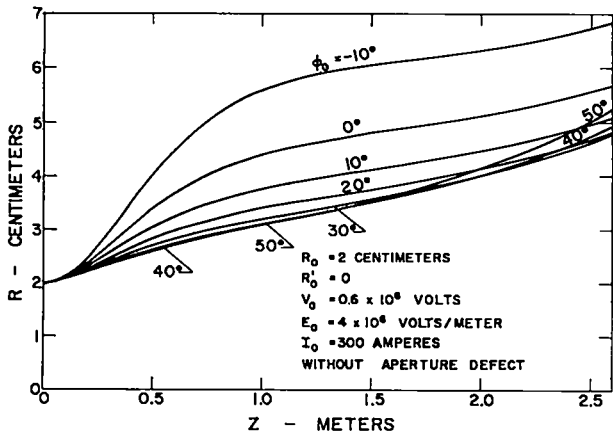
Fig. 5.50b. First cavity trajectories without aperture defect.
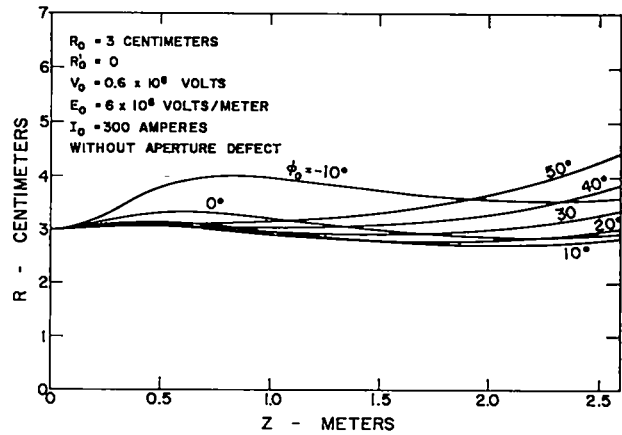
Fig. 5.51b. First cavity trajectories without aperture defect.
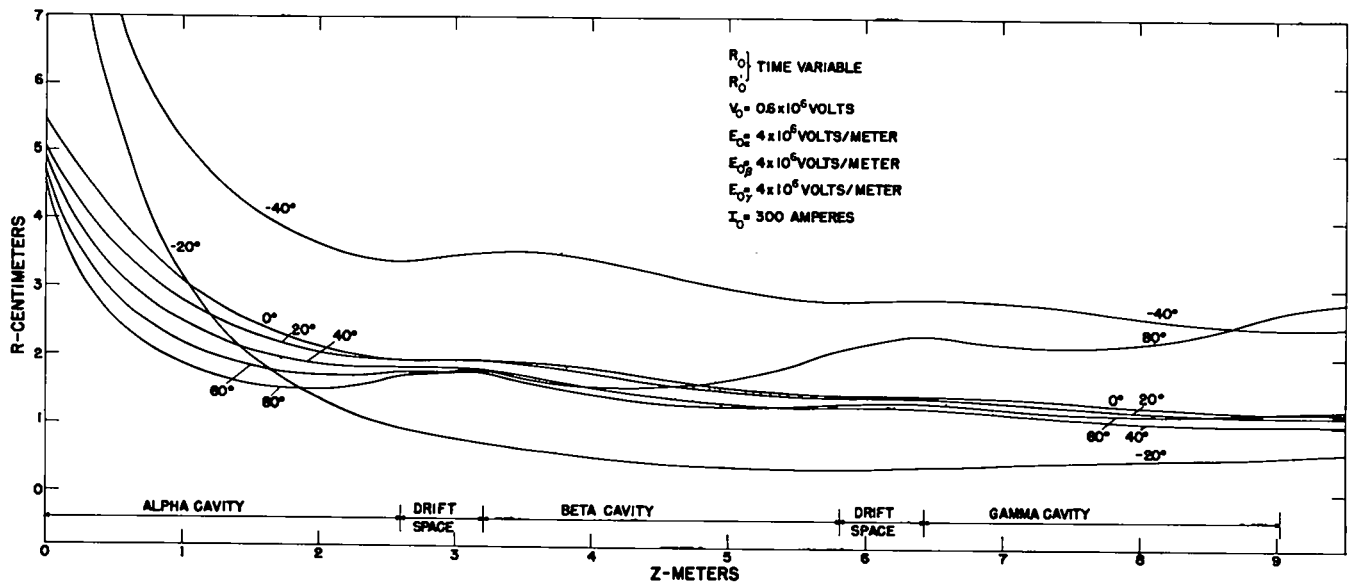
Fig. 5.52.   Three cavity trajectories with time-variable injection radius and convergence.
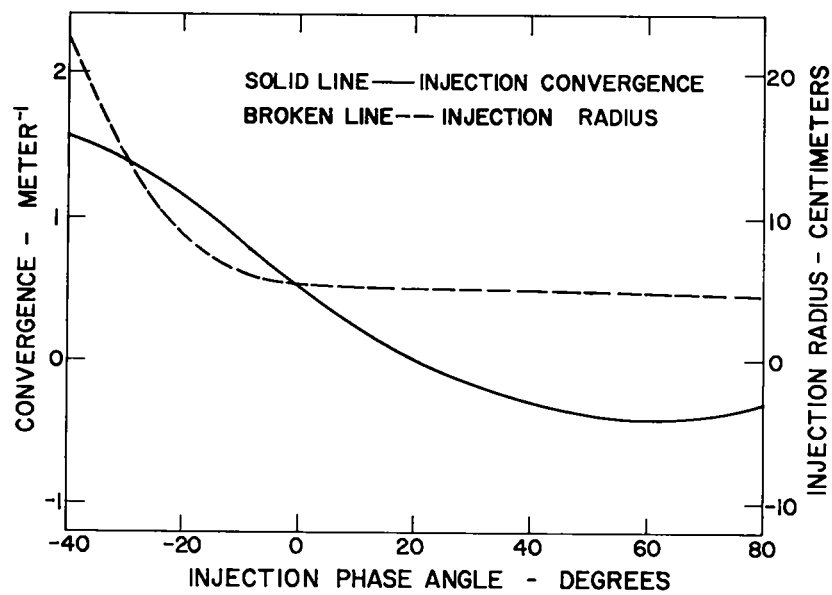
Fig. 5.53.   Radius and convergence variation for time-variable injection.

179
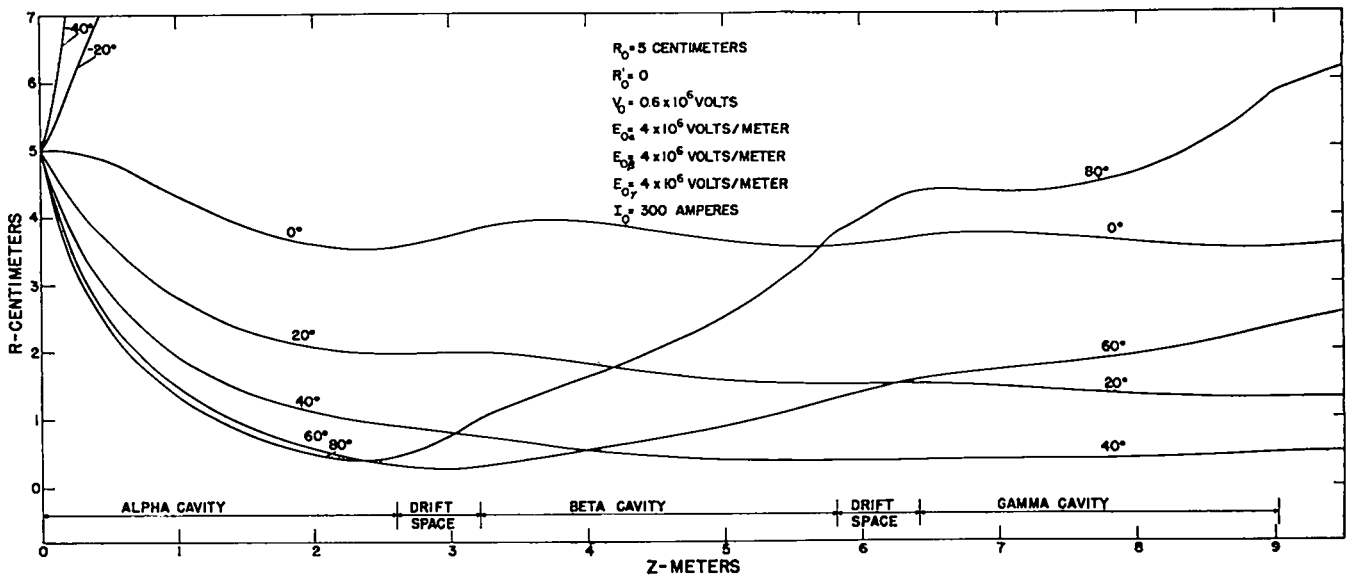
Fig. 5.54. Three cavity trajectories for 5 cm injection radius.
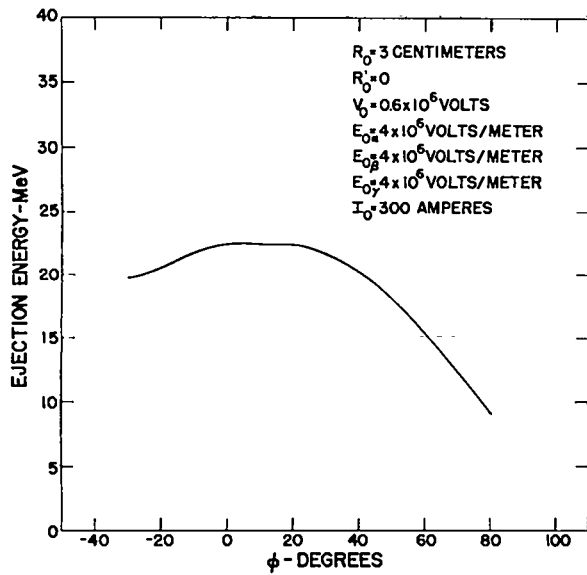
Fig. 5.55. Ejection energy vs injection phase angle.
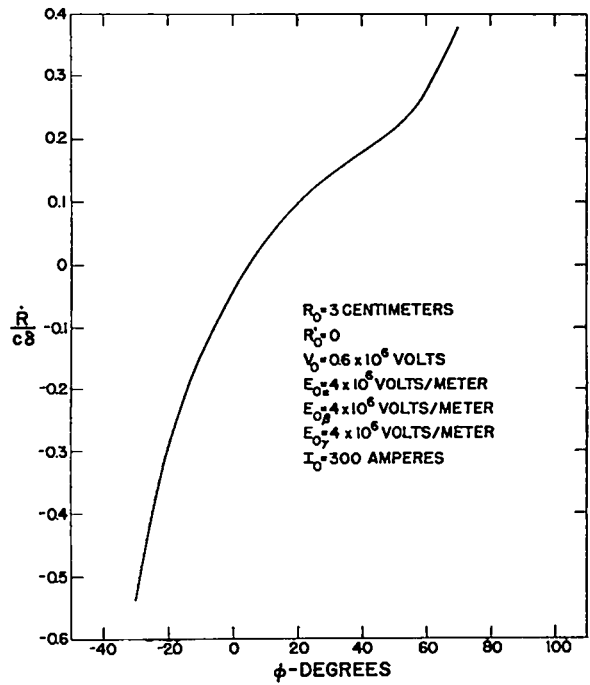
Fig. 5.56. Normalized radial momentum vs injection phase angle.

180
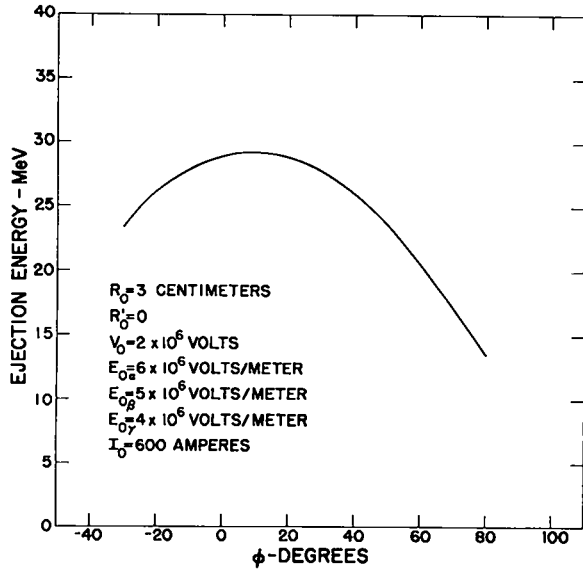
Fig. 5.57. Ejection energy vs injection phase angle.
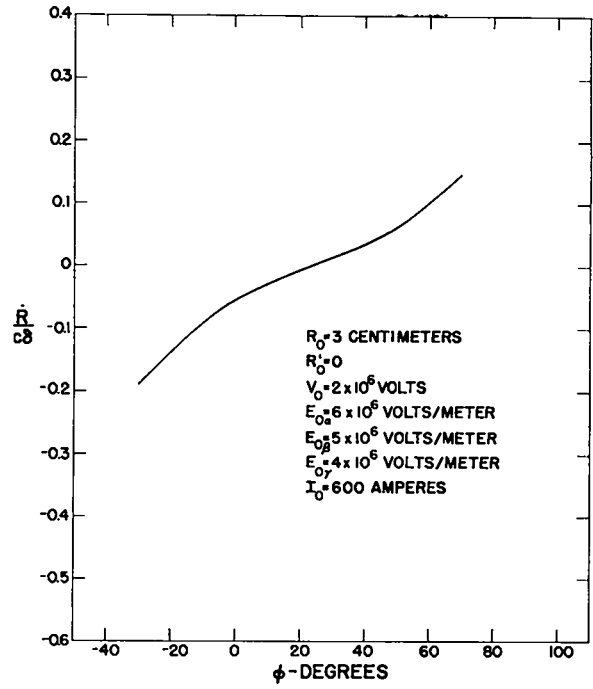
Fig. 5.58. Normalized radial momentum vs injection phase angle.
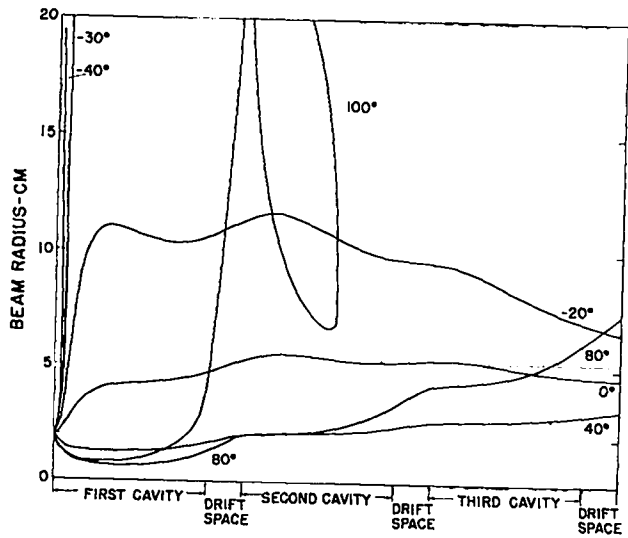
Fig. 5.59a. Radial instabilities in R-Z space.
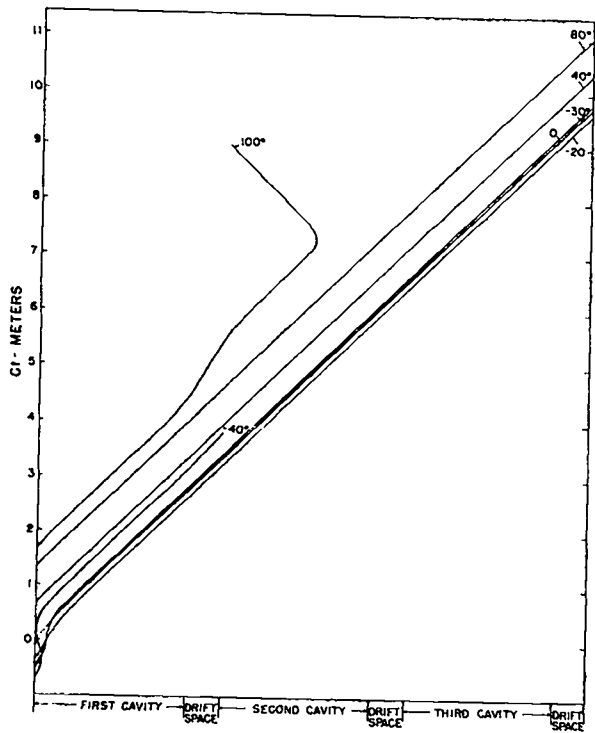
Fig. 5.59b. Phase focusing and defocusing.
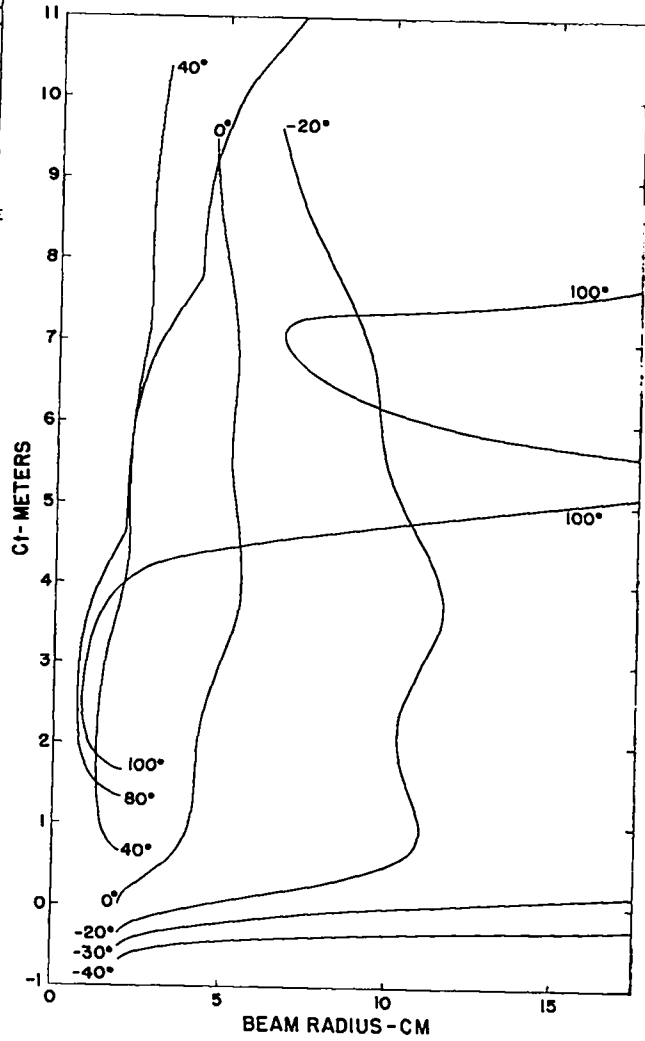
Fig. 5.59c. Radial defocusing.
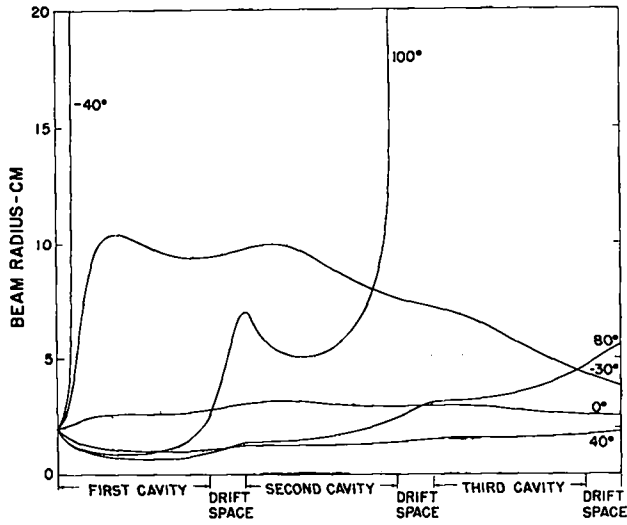
Fig. 5.60a. Radial instabilities in R-Z space.

Fig. 5.60b. Phase focusing and defocusing.

Fig. 5.60c. Radial defocusing.

183
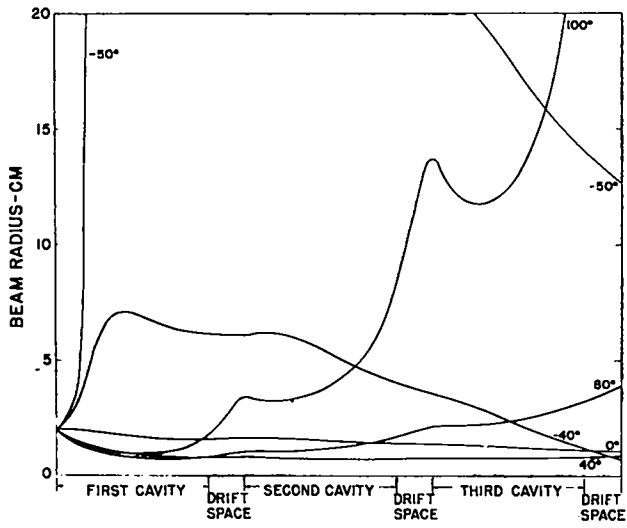
Fig. 5.61a. Radial instabilities in R-Z space.
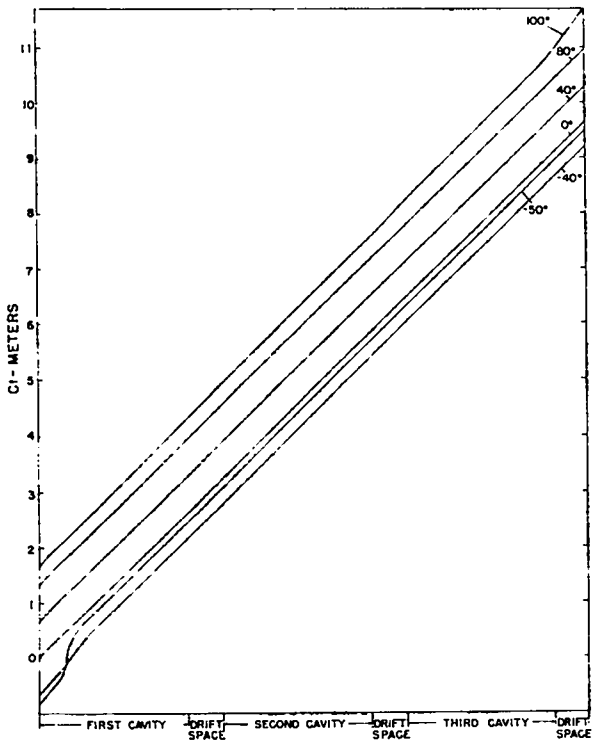
Fig. 5.61b. Phase focusing and defocusing.
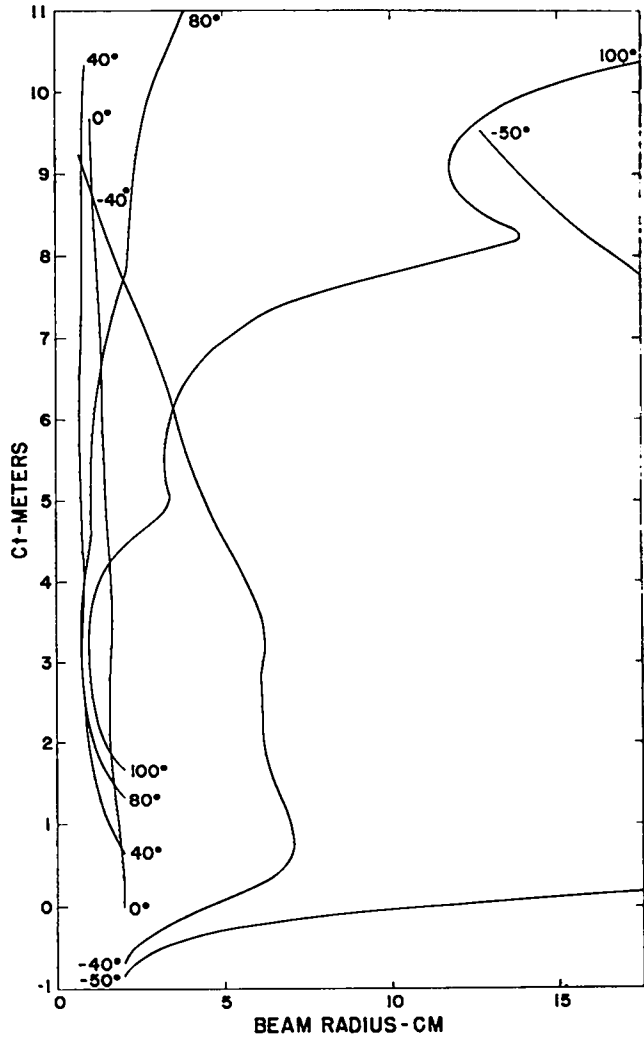
Fig. 5.61c. Radial defocusing.
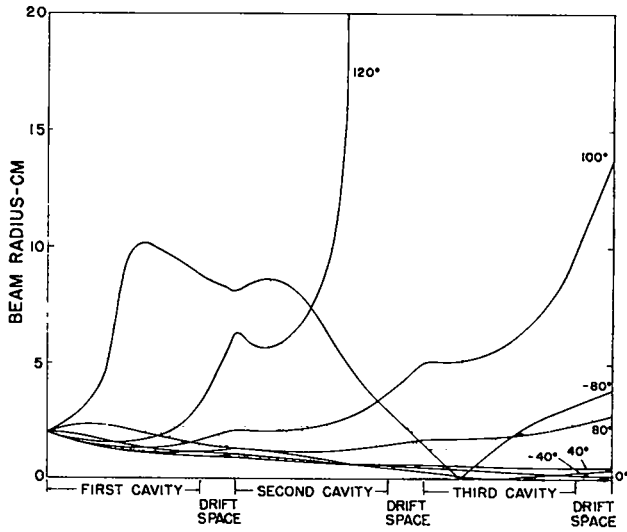
Fig. 5.62a. Radial instabilities in R-Z space.

Fig. 5.62c. Radial defocusing.

Fig. 5.62b. Phase focusing and defocusing.

Chapter 6

ELECTRON OPTICAL SYSTEM

by
E. D. Bush, Jr., J. N. Hardwick,
R. W. Taylor, and Douglas Venable

Results of calculations pertaining to the flow of electrons through the three-cavity accelerator were presented in Chapter 5. This study indicates that, for charge injected with a suitable energy, a modest degree of space focusing is effected. This has been observed.

Discussions of development details of the 10 cm diameter cathode electron gun and its magnetostatic lenses are presented in Section I of Chapter 6. Also discussed in this section are fabrication and inspection techniques, the electron gun vacuum system, and the high voltage pulser associated with the electron gun.

Section II of this chapter describes the ejector optical system and its development.

Output current of the machine delivered to a 3 mm diameter target has exceeded 30 A. About 30 R of bremsstrahlung per pulse have been measured at 1 m from the tungsten target.

I. INJECTOR

A. Electron Gun Design

The purpose of this subsection is to present the salient design features and fabrication techniques employed to develop the present electron beam injector. Although this injector incorporates features developed on preliminary models, using from 1.25 to 10 cm diameter impregnated cathodes, essentially all major prototype work was accomplished on a 5 cm diameter cathode gun. The cathode and anode field forming electrodes of this model were half-scale versions of those of the 10 cm gun. All other components, if not to scale, incorporate the same design principles.

1. Cathode

Much of the mechanical design of the injector was dictated by the type of cathode selected. Cathode choice hinged upon the following considerations: emission current density, uniformity of emission current density under space-charge-limited flow, low operating temperature, long service life, surface smoothness, resistance to poisoning, and ease of fabrication. An impregnated cathode was selected for the PHERMEX injector primarily for its reasonably high and uniform emission current density, long lifetime, smooth surface, and relatively low susceptibility to poisoning. A higher operating temperature of 1100°C is required, in contrast to about 900°C for the oxide-coated cathode.

Since most of the thermal loss of the gun is by radiation, the power required to heat the cathode is proportional to the fourth power of temperature. Therefore, more serious design and fabrication considerations had to be given to materials used in the heater assembly than would have been necessary with a coated cathode operating at a lower temperature.

2. Cathode field forming electrode and anode

Cathode and anode field forming electrode profiles were established experimentally using an electrolytic tank, subject to conditions described in Appendix 6A. The final anode profile deviates somewhat from the theoretical design as shown in Fig. 6.1. This modification was made to reduce the possibility of electrical breakdown. First-order calculations were performed with these profiles to determine the thermal operating environment.
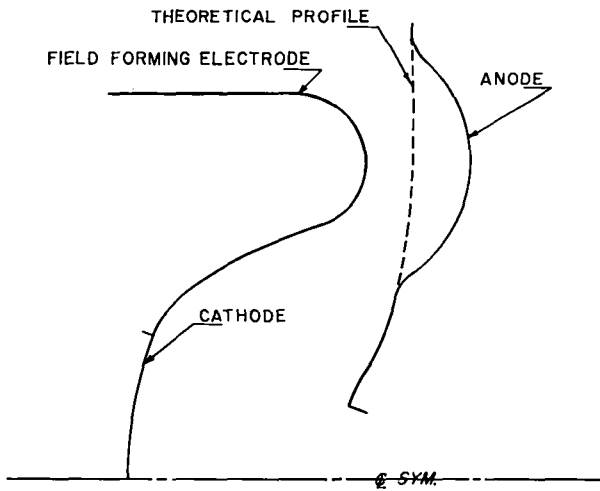
Fig. 6. 1. Comparison of actual and theoretical anode profiles.

Previous experience showed that clean, low vapor pressure materials are necessary to insure long cathode lifetimes. Although inconsistent with long cathode lifetimes, prototype field forming electrodes were made of Type 304-L stainless steel for initial studies. Final design components were made of molybdenum. With a cathode operating at 1100°C in a vacuum of 1×10^{-7} torr, alloying elements, which evaporate from the stainless steel, impair cathode life seriously. Figure 6.2 shows a typical cathode field forming electrode of stainless steel after a short period of operation.

Fig. 6. 2. Stainless steel cathode field forming electrode.

The prototype cathode and anode field forming electrodes were machined on a milling machine using matching radii to simulate the desired profile as shown in Figs. 6.3 and 6.4. This technique proved adequate for prototype fabrication.
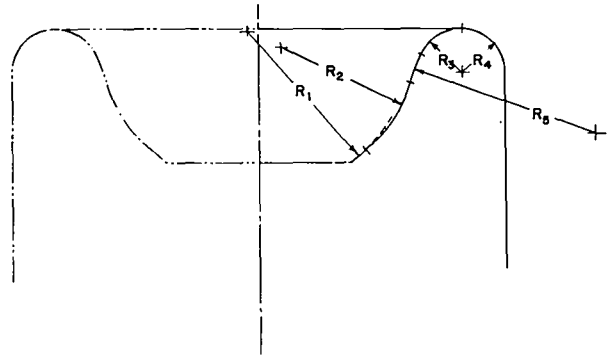
Fig. 6. 3. Cathode field forming electrode profile approximation.
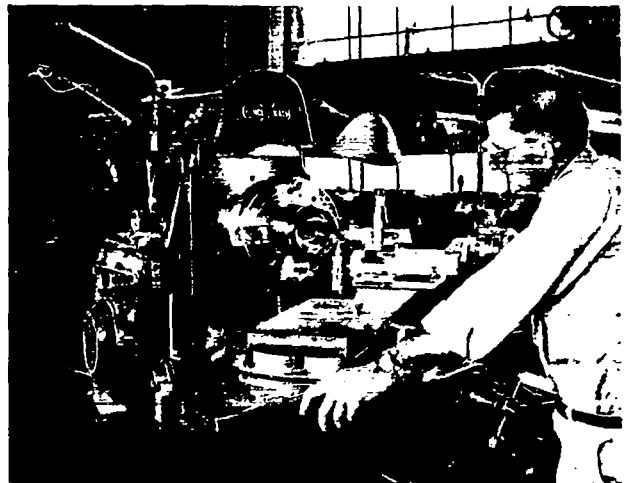
Fig. 6. 4. Two-inch cathode field forming electrode in milling machine.

For final models the coordinates, obtained experimentally from electrolytic tank data, were smoothed, using the seven-point moving method of least squares. Since these parts were fabricated on a tracer lathe, a master cam or template had to be provided. The template, representing a cross section of the figure of revolution, was made on a jig bore. At each of the 147 smoothed points the jig bore tool location was established by determining a position at distance r on a line normal to a given profile coordinate (see Fig. 6.5). The value r is the radius of the jig bore tool.

187
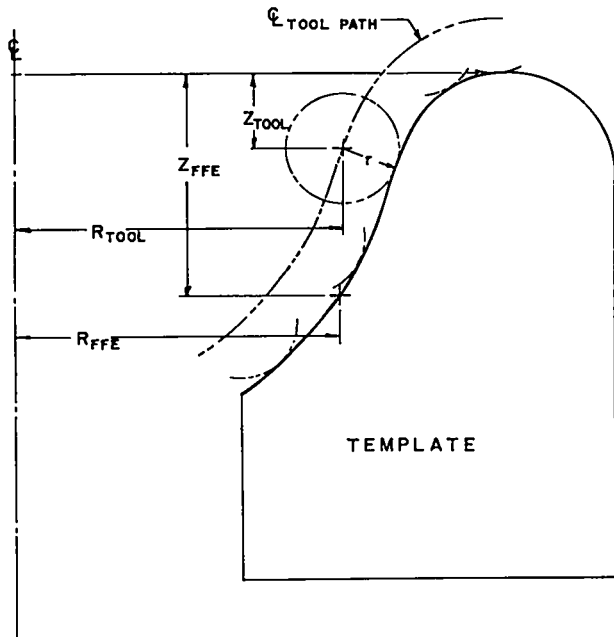
Fig. 6. 5. Cathode field forming electrode tracer template layout.

Fig. 6. 6. Cathode field forming electrode in tracer lathe.

For stability, the template was made of Pioneer Aluminum tooling plate. Upon completion, the template was inspected on a Jones and Lamson Model ER-30 contour projector. Prior to machining the molybdenum billets, full scale aluminum models were made and inspected to verify further the accuracy of the calculations and the template.

Molybdenum cathode and anode field forming electrodes were machined in a 16 in. Monarch lathe equipped with a Tru-Trace hydraulic tracer attachment, Mark 2A, as shown in Figs. 6.6 and 6.7. The completed cathode field forming electrode is shown in Fig. 6.8.

Fig. 6. 7. Cathode field forming electrode in tracer lathe.

3. Cathode heater

The following method of analysis, applied with considerable success on the half-scale gun, was also used on the full-scale gun. The heater was designed assuming negligible convection and conduction, using the following form of the Stefan-Boltzmann equation:

$$P_R = KF_\epsilon F_a A(T_2^4 - T_1^4)$$
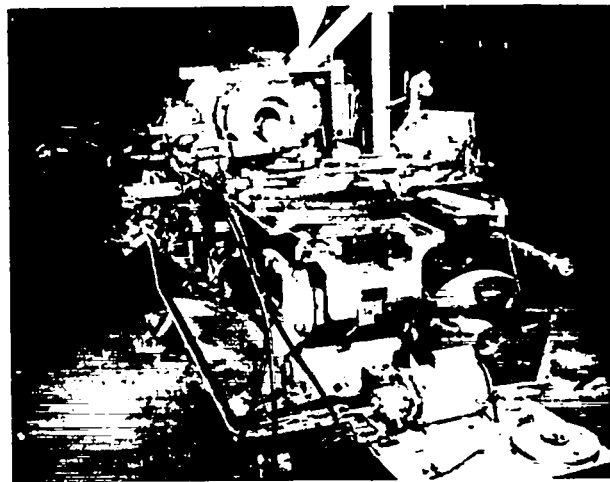
(6.1)
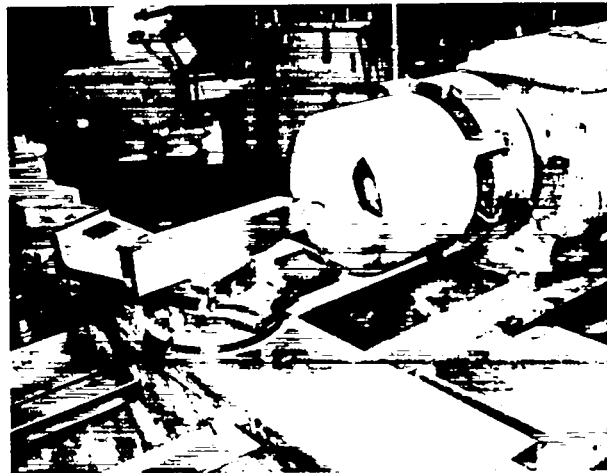
where P_R is the power radiated in watts, K combines the Stefan-Boltzmann constant and appropriate factors to convert to units of watts, A is the radiating area, and T_2 and T_1 are the temperatures of the radiating area and cool area, respectively. The terms F_ϵ, function of emissivities, and F_a, a factor depending on the system shape and arrangement, can be found in most standard texts on heat transfer.

188
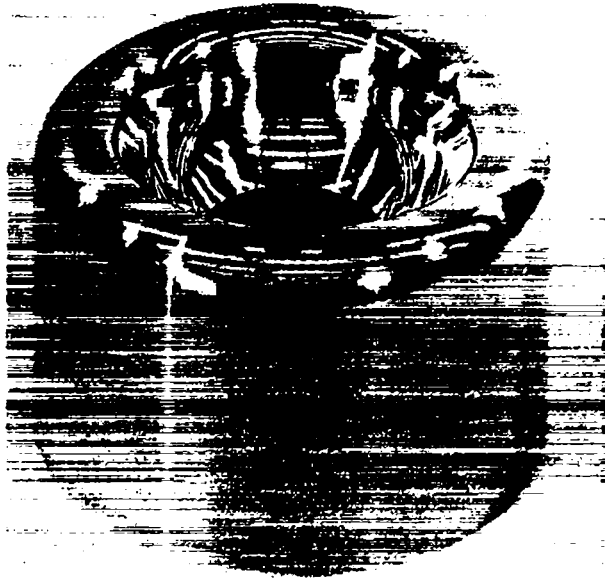
Fig. 6. 8. Completed cathode field forming electrode.

The power radiated by the cathode and its field forming electrode was assumed to be equal to the power dissipated by the filament:

$$P_R = P_F$$
(6.2)

Because of the relatively high operating temperature of the filament, $\varepsilon_F \sim 1$, and because of the small volume of the inner heat shield, it can be conservatively assumed that

$$P_F = K A_F T_F^4$$
(6.3)

A filament operating temperature of 2000°C was selected; thus the radiating area of the filament, A_F, was determined by Eq. (6.3). From this radiating area and the operating temperature, the filament length and diameter can be adjusted to match the impedance of the filament power supply.

$$R_F = \frac{\rho_T L}{a}$$
(6.4)

The filament resistance at operating temperature R_F is a function of the resistivity ρ (at T_F), cross sectional area a, and length L.

The values of T_1 and T_2 in Eq. (6.1) can be estimated reasonably well; however, since radiated power varies as the fourth power of temperature, any error could affect the results significantly. The terms F_ε and F_a are notoriously nebulous. Estimates of the configuration factor, emissivities, and operating temperatures of the components must be selected judiciously to obtain realistic power requirements. Blackbody radiation was assumed to obtain an upper limit for the power required.

This approach proved adequate for the design of the heater on the 10 cm gun. The original choice of filament radiating area has never been modified, and its measured operating temperature is about 1950°C. The filament is mounted in an "S" shape, Fig. 6.9, to facilitate more uniform thermal coupling.
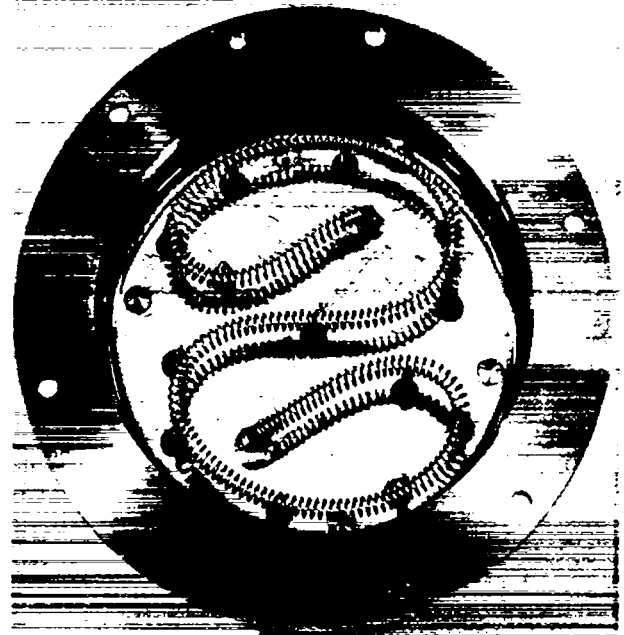
Fig. 6. 9. Cathode heater filament.

Heat shields, filament supports, cathode support, and insulators, Figs. 6.10 to 6.12, were developed from designs used in earlier guns. Molybdenum was used for all metal components of this assembly, and either high quality alumina or sapphire was used for the insulators. Parts in this area are subjected to high temperatures and vacua in the 10^{-8} torr region. Recrystallization occurs in those molybdenum parts subjected to higher temperatures. This process takes place between 885° and 1265°C; however, it is also time-dependent, increasing with time. Filaments have

189

operated satisfactorily for as long as 2500 hr; consequently the molybdenum becomes very brittle because of recrystallization. In this application molybdenum was chosen for its refractory qualities and inherent cleanliness rather than strength, since the mechanical loads are insignificant on those parts subjected to extreme heating.

Fig. 6.11. Cathode heater assembly.
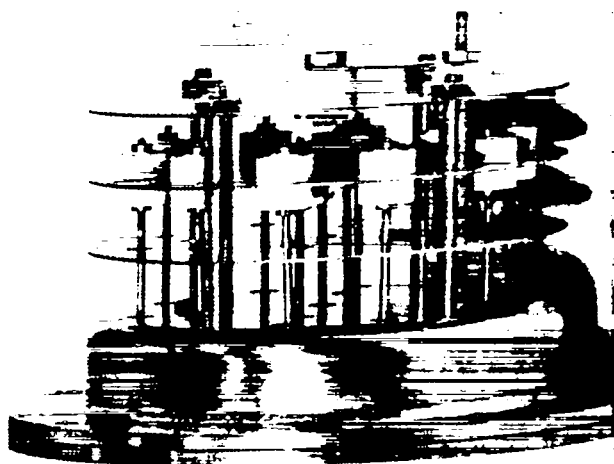
Fig. 6.12. Cathode heater assembly.

Other refractory materials display certain advantages but were avoided because of cost, machining difficulties, or more severe embrittlement.

Hydrogen embrittlement of molybdenum, like all body centered cubics, was another area of concern. As indicated in Chapter 10, an established

Fig. 6.10. Cathode heater assembly.

operating procedure has been to purge with hydrogen the three accelerator cavity sections during pumpdown, and periodically thereafter to improve the vacuum achieved by the ion pumps. The cavities are purged only after the filament has cooled for at least 12 hr and the valve between the gun and cavities has been closed. This may seem unnecessarily conservative; however, disastrous results, because of hydrogen embrittlement, were experienced with an early generation tantalum gun (Fig. 6.13). To date no failures attributed to hydrogen embrittlement have been experienced with existing guns.

the effect of SF_6 as a breakdown inhibiting atmosphere was also studied. This information was used to determine the insulator length required to inhibit electrical breakdown for the 10 cm gun. Under high vacuum conditions, breakdown has never been experienced on the inner insulator, even though that path length is considerably shorter. To hold off 600 kV in air, an outside length of at least 43 cm would have been required. However, in the interest of economy and to keep the component size within reason, a length of 33 cm was chosen and provisions were made to maintain an atmosphere of SF_6 around this insulator by means of a plastic bag.

Fig. 6.13. Hydrogen embrittlement of early 1 in. gun.

Fig. 6.14. Cathode field forming electrode support.

4. Cathode field forming electrode support

Injector design requirements called for a cathode-anode potential of 600 kV. Figure 6.14 shows the method of insulating the cathode field forming electrode. It is supported by two aluminum oxide ceramic cylinders. The breakdown path length was determined experimentally, using cylindrical ceramic insulators with rings pressed over the insulator at various axial distances. A 0.2 μsec high voltage pulse was applied to these rings. The voltage was increased until breakdown occurred. It is to be noted that even when breakdown occurred it was always at the very end of the 0.2 μsec pulse. At the same time,

The cathode field forming electrode is cantilevered from the rear cavity flange within the vacuum system (Figs. 6.15 and 6.16). The support consists of two 94% aluminum oxide insulators (Frenchtown Type 4462) fixed to the rear cavity flange and loaded by the internal tension member. The inner ceramic cylinder has two Type 304-L stainless steel rings assembled over the ends with an interference sufficient to load the rings slightly beyond their yield point. By maintaining the stainless rings in tension and the ceramic in compression, each material is loaded in its optimum manner. Stainless steel was selected for its nonmagnetic properties and its relative cleanliness at modestly elevated temperatures in a high vacuum. Initially, the rings were pressed over the ends of the ceramic cylinder with

191
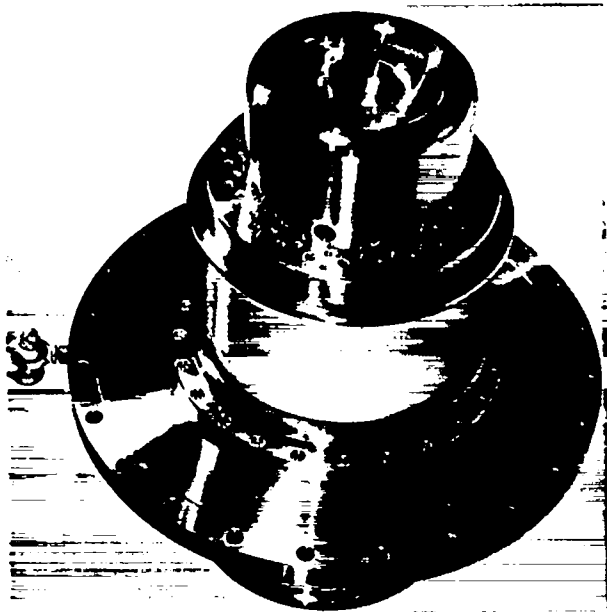
Fig. 6.15. Cathode field forming electrode support.
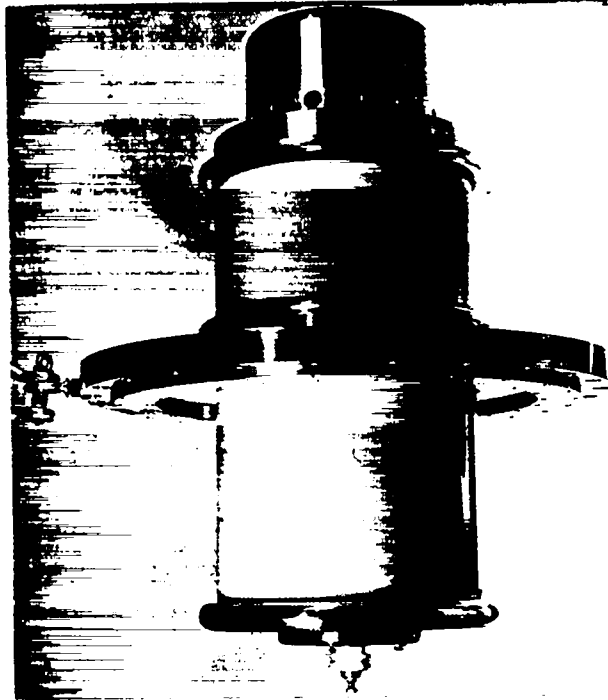
Fig. 6.16. Cathode field forming electrode support.

a hydraulic press. The load was raised to about 1.8 × 10⁵ N (20 tons) to assure adequate bottoming. More recently, the procedure has been to place the rings and the cylinder in a furnace, and raise the temperature gradually to 345°C over a period of 6 hr. At terminal temperature, because of differential expansion, the rings slip in place over the ceramic. After assembly, the furnace temperature is progressively lowered and the part

is furnace-cooled overnight. The furnace technique seems to be less severe on the ceramic; however, both methods have proved satisfactory.

The terminal temperature was determined by applying the expansion equation

$$\Delta r_2 = r_2 \int_{T_1}^{T_2} \alpha_m(T) \ dT - r_2 \int_{T_1}^{T_2} \alpha_c(T) \ dT \tag{6.5}$$

In Eq. (6.5), r_2 is the radius of the metal-ceramic interface, α is the instantaneous coefficient of expansion, and T is the temperature. The subscripts m and c refer to metal and ceramic.

The analytical approach used to determine resulting stresses and deflections utilizes the conventional cylindrical shell approach. [6,1,6,2] It combines several thick-wall cylinder expressions to achieve parameters of interest for this particular application. Figure 6.17 shows an enlarged view of the joint with the notation used herein. Equation (6.6) gives the tangential stress in the metal ring at any radius b.
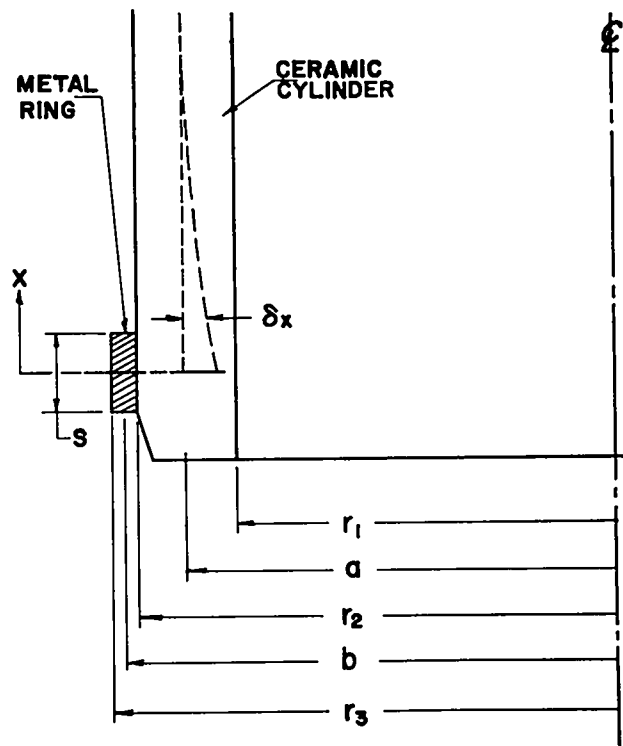
Fig. 6.17. Metal-ceramic joint.

192

$$\sigma_m = \frac{Pr_2{}^2}{r_3{}^2 - r_2{}^2}\left(1 + \frac{r_3{}^2}{b^2}\right)$$

(6.6)

where P is the interface pressure applied by the metal ring for a given stress in the metal, σ_m, at any value of the radius b, where $r_2 < b < r_3$.

The radial deflection, δ, at a distance x from the edge, can be derived from

$$\frac{d^4\delta}{dx^4} + 4\lambda^4\delta = 0$$

(6.7)

$$\delta_x = $$
$$-\frac{\sigma_{m2}S(r_3{}^2 - r_2{}^2)(r_2 + r_1)^2}{2E_c(r_2{}^2 + r_3{}^2)(r_2 - r_1)}\, \lambda e^{-\lambda x}\cos(\lambda x)$$

(6.8)

where

$$\lambda = \left[\frac{12(1 - \mu_c{}^2)}{(r_2 + r_1)^2(r_2 - r_1)^2}\right]^{1/4}$$

(6.9)

E_c is Young's modulus and μ_c is Poisson's ratio for the ceramic cylinder. The tangential stress distribution between r_1 and r_2 is described by

$$\sigma_c = $$
$$-\frac{2E_c\delta_x(r_1 + r_2)\left(1 + \frac{r_1{}^2}{a^2}\right)}{[(r_1 + r_2)^2 + 4r_1{}^2] + \mu_c[(r_1 + r_2)^2 - 4r_1{}^2]}$$

(6.10)

The axial moment of the mean radius of the inner cylinder is given by

$$M_x = \frac{\sigma_{m2}S(r_3{}^2 - r_2{}^2)}{\lambda(r_2{}^2 + r_3{}^2)}\, e^{-\lambda x}\sin(\lambda x)$$

(6.11)

with M_x maximum occurring at $x = \pi/4$.

The above equations are reasonably accurate for cylinders as short as $l = \pi/\lambda$ loaded at one end or $l = 2\pi/\lambda$ loaded at both ends. The metal rings are assumed to be loaded by a uniform internal pressure at their inner radius, r_2. The ceramic cylinder is assumed to be radially loaded by the metal ring at the end of the cylinder. No end moments or differential pressures are assumed to exist.

If the metal ring is sufficiently long so that $ds/dx \cong 0$, the following equation can be applied:

$$\sigma_{ca} = -\frac{Pr_2{}^2}{(r_2{}^2 - r_1{}^2)}\left(1 + \frac{r_1{}^2}{a^2}\right)$$

(6.12)

where σ_{ca} is the tangential stress in the ceramic cylinder wall at any radius a, and $r_1 < a < r_2$.

The radial deflection of the metal ring at r_2 is

$$\delta_{m2} = \frac{Pr_2}{E_m}\left[\frac{(r_3{}^2 + r_2{}^2)}{(r_3{}^2 - r_2{}^2)} + \mu_m\right]$$

(6.13)

and for the ceramic

$$\delta_{c2} = -\frac{Pr_2}{E_c}\left[\frac{(r_2{}^2 + r_1{}^2)}{(r_2{}^2 - r_1{}^2)} - \mu_c\right]$$

(6.14)

The minus sign in Eq. (6.14) indicates deflection opposite that of the metal ring.

By combining Eqs. (6.13) and (6.14), the total radial interference can be written

$$\delta = Pr_2\left[\frac{(r_3{}^2 + r_2{}^2)}{E_m(r_3{}^2 - r_2{}^2)} + \frac{\mu_m}{E_m}\right.$$
$$\left. + \frac{(r_2{}^2 + r_1{}^2)}{E_c(r_2{}^2 - r_1{}^2)} - \frac{\mu_c}{E_c}\right]$$

(6.15)

These equations were verified by measuring the induced strains and radial deflections on a half-scale electron gun support. The radial deflections along the meridian of the ceramic were measured with a Brown and Sharpe electronic indicator set for ±0.001 in. full-scale deflection and calibrated with gauge blocks. The assembly was moved under the indicator head on a micrometer carriage. Figure 6.18 shows the measured and analytical radial deflections along the meridian of the ceramic cylinder.
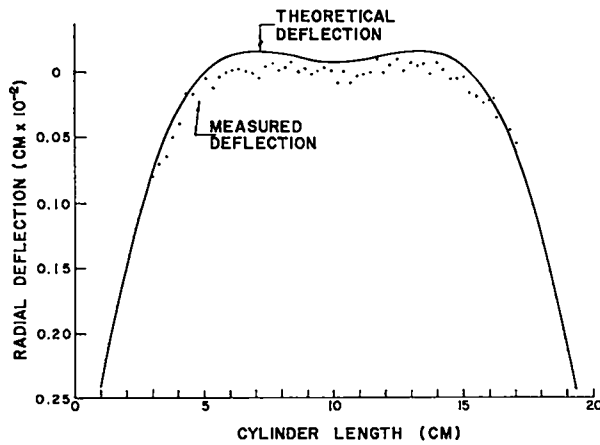
Fig. 6.18. Comparison of analytical and measured deflection.

Prior to assembly, Baldwin-Lima-Hamilton Type A-7 strain gauges were affixed to the components. The gauges were connected, temperature compensated, and balanced with a B-L-H SR-4, Type N, strain indicator and balancing unit. Upon assembly in the hydraulic press, strain readings were recorded after the load was removed from the ram. The comparison of measured and theoretical stresses is

Station x = 1.8 cm

Radius	Measured (N/m²)	Theoretical (N/m²)
r_1	2.375×10^7	2.435×10^7
r_2	1.975×10^7	2.200×10^7

The support assembly is completed by the external ceramic cylinder and the tension tube. The tube serves two purposes: to hold the components of the internal ceramic cylinder in compression and to provide a continuous load on the two vacuum seals of the external insulator during thermal transients. Convaseal, a high vacuum elastomer manufactured by Consolidated Vacuum Corporation, and reputed to have very low outgassing properties up to 260°C, has been used successfully for these seals. The tension tube and external insulator are held together in a fixture and are assembled on the gun support as a unit. Allenuts are used to hold the tension tube in place and are tightened with a long wrench through the center of the tube. The filament feedthrough insulator flange serves as a cover plate on the tube end.

5. Gun cavity

The gun support and anode mounting flange, Fig. 6.19, are assembled on the ends of the cavity that provides the proper cathode-anode spacing and ties the gun to the vacuum system, Fig. 6.20. Cooling water is circulated in a series circuit through the gun support flange, anode support and connecting flange, and the gun cavity, respectively. Cooling in this manner keeps the Convaseal at a minimum temperature. Water connections on the gun cavity utilize standard copper gasket vacuum seals. While this may at first appear a luxury, its purpose is to provide a positive means for leak-checking the vacuum system through the water jacket.
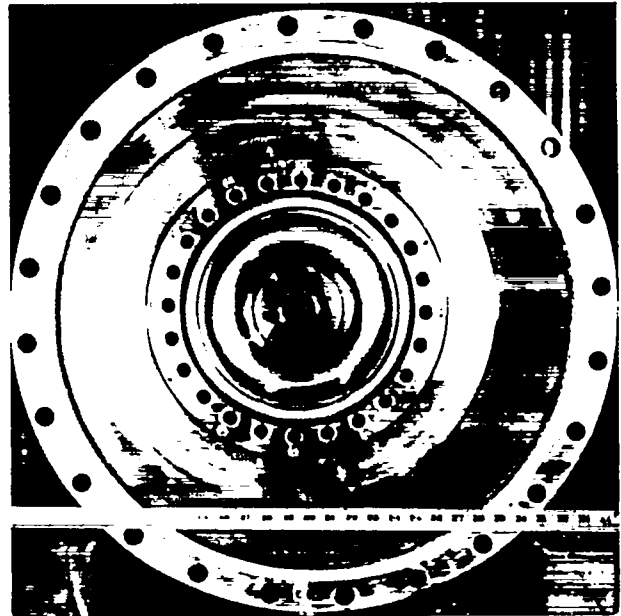
Fig. 6.19. Anode and mounting flange.
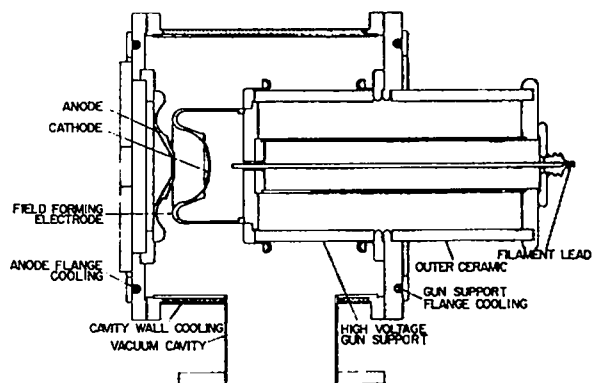
Fig. 6.20. Cross section of gun cavity.

194

6. Thermal studies

Several questions arose regarding the conditions existing during transient heating and cooling and at thermal equilibrium. The areas of concern were: (a) time-temperature measurements during heating and cooling, (b) vacuum seal capabilities, (c) stability of the metal-ceramic structural support for the field forming electrode, and (d) the cathode-anode spacing variations.

To investigate these problems, a conventional 10 cm electron gun was instrumented with 33 Chromel-Alumel thermocouples located at specific stations on all critical components of the assembly (Fig. 6.21). The system was evacuated and power applied to the cathode, thus simulating cathode operating conditions. Temperatures were measured after the system had reached thermal equilibrium
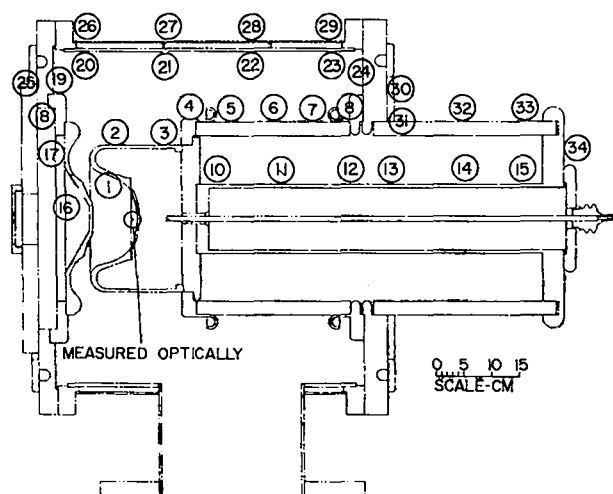
when subjected to various water cooling conditions. To study the transient conditions, temperatures were recorded hourly for 8 hr after the cathode power had been applied, and hourly for 7 hr after the cathode power was shut off. The gun was not pulsed, and a Pyrex window was used in the flange downstream from the anode; otherwise the experimental setup was a duplicate of the operational assembly. These variations had a negligible effect on the thermal environment of the unit. Cathode temperature was measured with a Pyro Micro-Optical pyrometer. The temperature recorded with this instrument was brightness temperature. Ideal blackbody conditions were assumed. Furthermore the temperature was not corrected for the emissivity of the cathode material nor the light transmission through the glass window.

The thermocouples were cemented in place with B-L-H PBX high temperature strain gauge cement after preparing the surface with an S.S. White abrasive unit. On the stainless steel areas operating at lower temperatures, the thermocouples were affixed with Kirkson stainless steel soft solder. Steatite thermocouple beads were used to insulate the wire within the vacuum envelope between the measuring junctions and the Kovar-to-glass feedthrough bushings. The external junctions were taped in place with lead foil tape and thermally insulated to reduce convection and radiation losses.

Although this setup involved several tens of feet of thermocouple beads, soft solder, and only a moderate degree of cleanliness during assembly, pressures of 2.5×10^{-6} torr at operating temperature and 3.0×10^{-8} torr cold were achieved.

Data were collected for each of the following cooling conditions:

Fig. 6.21. Thermocouple stations.

Condition	Anode Flange	Cavity	Gun Support
I	cooled	cooled	not cooled
II	not cooled	cooled	cooled
III	not cooled	cooled	not cooled
IV	cooled	cooled	cooled
V	cooled	not cooled	cooled
VI	cooled	not cooled	not cooled
VII	not cooled	not cooled	cooled

For transient thermal measurements the three typical water cooling conditions selected were:

Condition	Anode Flange	Cavity	Gun Support
A	cooled	cooled	cooled
B	not cooled	cooled	cooled
C	not cooled	cooled	not cooled

Because of the relatively low thermal conductivity of stainless steel [0.039 compared with 0.92 cal/(sec)(cm^2)(°C/cm) for copper] and the poor thermal coupling between the three water cooled sections, results indicate that the presence or absence of water cooling on one section has very little effect on the adjacent section. Figures 6.22 through 6.24 show the temperature distribution in the inner and outer cavity walls, the ceramic insulators, and the center tension tube. For clarity, only the curves for water cooling conditions IV and VI are shown. Graphs illustrating the transient heating and cooling of the cathode field forming electrode and support are shown in Figs. 6.25 and 6.26 for the thermocouple stations
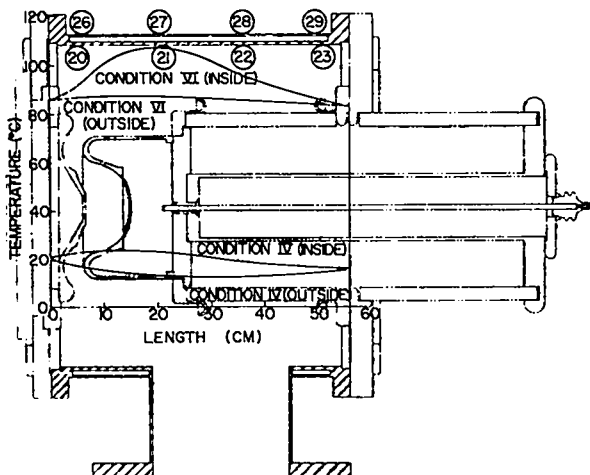
Fig. 6.22. Temperature distributions of cavity walls.
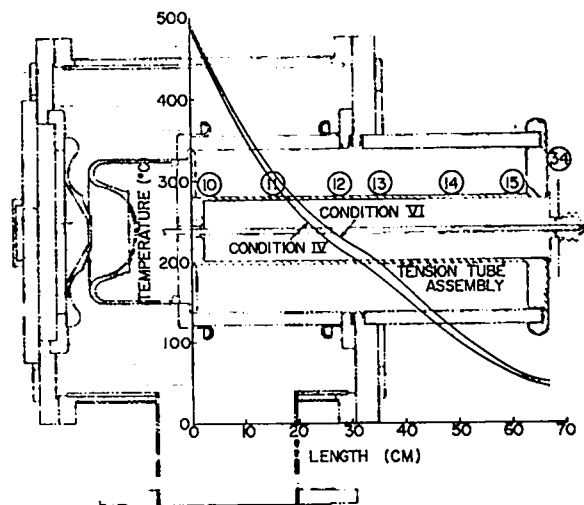
Fig. 6.24. Temperature distribution of center tube.
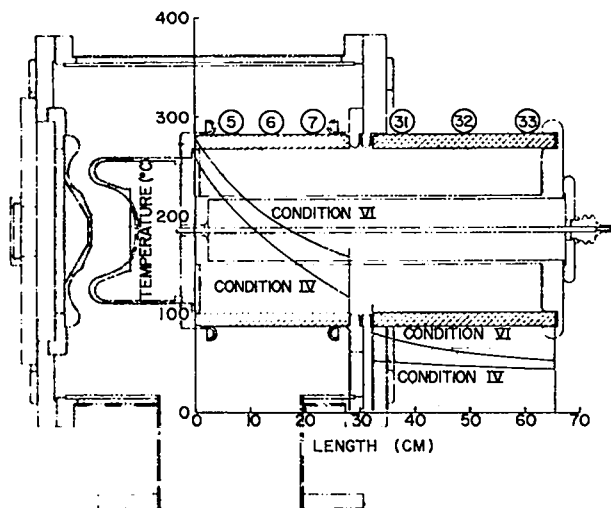
Fig. 6.23. Temperature distribution of ceramic insulators.
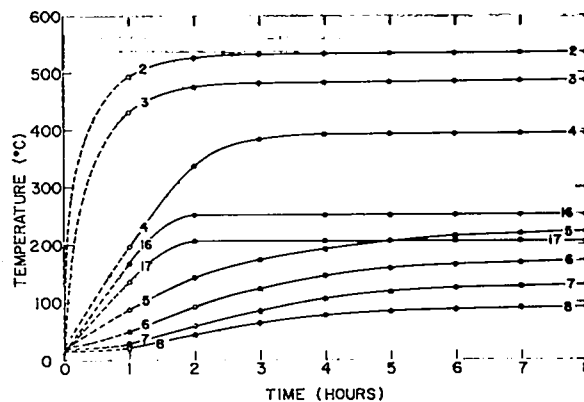
Fig. 6.25. Heating rate.

196
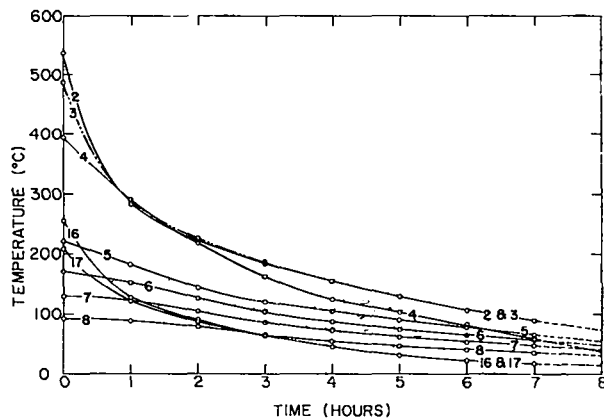
Fig. 6.26. Cooling rate.

noted. Only condition A is shown. It can be seen that the system begins to approach temperature equilibrium only after full power has been applied for 4 hr; after 6 hr the unit has essentially reached thermal equilibrium.

Figure 6.27 shows the sealing scheme utilized in Varian-type vacuum seals. The nominal 0.12 cm thick copper gasket is plastically deformed in bearing at the overlapping sealing surfaces of the male and female flanges. Concentric alignment is

ENLARGED VIEW OF SEAL
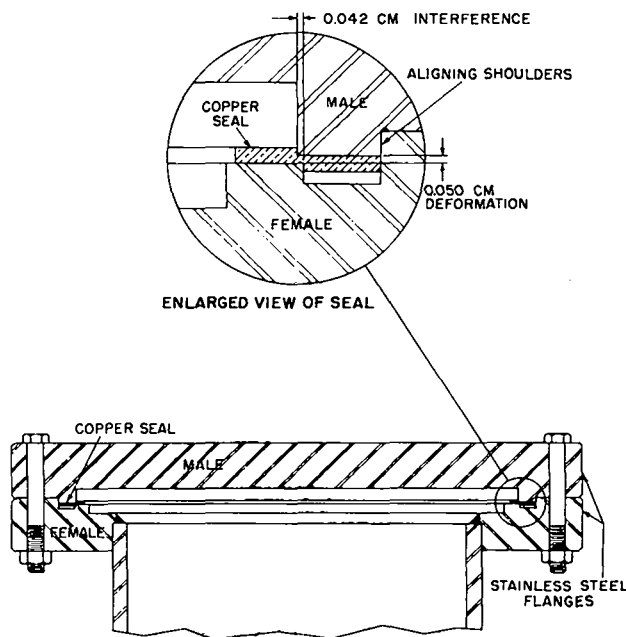
Fig. 6.27. Varian type vacuum seal.

accomplished by providing a close fit between the aligning shoulders on the mating flanges. Dowel pins are incorporated where precise angular alignment is required. When the reference shoulders are in contact, the sealing edges compress the copper to 0.05 cm. The maximum temperature differential recorded during this series of tests occurred during the transient heating run under water cooling condition C. At this time, the anode flange reached a maximum temperature of 84°C, while the corresponding ring on the cavity was at 30°C. The total radial expansion described by Eq. (6.16)

$$\Delta r = r \int_{T_1}^{T_2} \alpha(T) \, dT$$

(6.16)

was found to be 0.0292 cm. While this leaves an interference of only 0.0127 cm, these seals function properly even with a clearance of as much as 0.117 cm.

Measurements showed the maximum temperature in the area of the Convaseal gaskets to be 17°C below the maximum temperature tolerance of the material. The seals are compressed from an initial nominal thickness of 0.318 to 0.157 cm upon assembly. Using the temperature gradients of the inner and outer ceramics and the tension tube together with the temperatures measured at adjoining stations, the resultant load release was computed. Numerical analysis techniques were applied to determine the total expansion of each component:

$$\delta_n = l \int_{T_1}^{T_2} \alpha(T) \, dt$$

(6.17)

where δ_n is the resulting expansion of the nth component. The length in question was divided into increments and treated numerically, since the coefficient of expansion is a function of temperature and the temperature varies with length. The total expansion of each path is

$$\delta_t = \Sigma \; \delta_n$$

(6.18)

197

The resulting compression for water cooling condition VI is plotted against time in Fig. 6.28. The total seal deformation is tabulated below for the three typical water cooling combinations:

Cooling Condition	Deformation (cm)
II	0.0647
III	0.0662
IV	0.0702

Applying the load-stroke curve of Convaseal, as shown in Fig. 6.29, the initial and final minimum axial loads encountered are 7.17×10^4 and 1.65×10^4 N, respectively, for the seal area of 137 cm^2.

By loading the rings beyond their yield point, the maximum radial load is achieved for the materials with their particular cross sections. This design facilitates assembly and replacement of cathodes by removing the cathode field forming electrode after removing the outer ceramic cylinder. However, at operating temperature, the conditions are such that the stainless steel ring near the gun expands to a larger value than that of the

Fig. 6.29. Convaseal load-stroke curve.

ceramic, thus relieving the preload. This relief is due to the lower coefficient of expansion of the ceramic compared with that of the stainless steel and to the poor thermal coupling at the ceramic-stainless steel interface. Figure 6.30 represents the expansion-time characteristic of this assembly during heating from ambient to operating temperature. The ring nearest the field forming electrode reaches maximum radial clearance of 0.0724 cm from the ceramic cylinder 3 hr after the filament power has been applied and it stabilizes at 0.0686 cm upon reaching thermal equilibrium. While this clearance is certainly undesirable, it is felt that no serious radial misalignment is encountered, since the axial load never falls below 1.65×10^4 N. Also, when the assembly is cooled, the unit undergoes a radial realignment due to the nature of the design.

Fig. 6.28. Convaseal deformation.
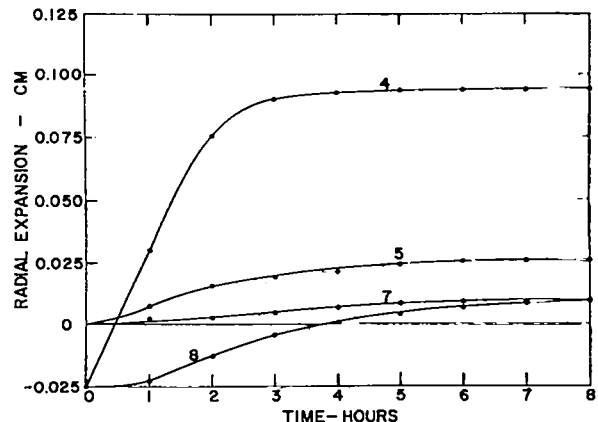
Fig. 6.30. Gun support expansion curves.

198

The cathode-anode spacing from ambient temperature through the transient heating period was calculated for the water cooling conditions A, B, and C. The problem was treated numerically as described previously, and the spacing was determined for each hour of the 8 hr heating period. Figure 6.31 shows the cathode-anode spacing variations as measured axially from the center of the cathode to the edge of the anode.

It can be seen that water cooling condition A induces the maximum variation of 0.0315 cm, while cooling condition C yields the minimum of 0.0168 cm. This situation is caused by the improved temperature compensation when operating the cavity walls at a higher temperature. The dip in the curve for condition A is caused by the cavity reaching thermal equilibrium and then remaining at a relatively constant temperature early in the cycle while the other parts continue to expand.
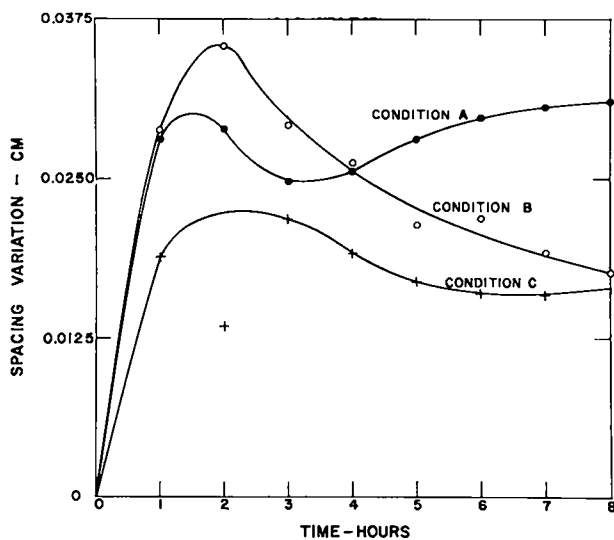
Fig. 6.31. Cathode-anode spacing variations.

B. Injector Lens Design

The PHERMEX magnetostatic lens design evolution is discussed here. A prototype injector lens was built with its pole pieces and coils located within the vacuum system. The reason that pole pieces were initially placed within the vacuum was to reduce the effective diameter and hence to minimize the demanded ampere turns. While valuable design and operation information was collected, problems were encountered evacuating the lens and sealing it off,

since it was not continuously pumped. The second-generation prototype lens utilized coils external to the vacuum system with pole pieces forming part of the vacuum envelope. This assembly technique necessitated vacuum welds of stainless steel to Armco iron, causing undesirable magnetic hard spots in the iron. In the interest of economy and fabrication time, prototype test lenses utilized a built-up external magnetic circuit of mild steel. These lenses have proved sucessful; however, owing to the magnetic inhomogeneity of the material and nature of construction, appreciable on-axis transverse magnetic field aberrations were encountered. That is, the magnetic fields were found to be azimuthally asymmetrical. These deviations from azimuthal symmetry were intolerable for PHERMEX injection energies. While modified versions of these lenses were made later, the injector test lenses were in service on the PHERMEX machine for over a year.

The modified lenses were designed to minimize on-axis transverse magnetic fields. Pole pieces were machined from solid Armco ingot iron billets. To eliminate the necessity of fasteners penetrating and disturbing the magnetic circuit, the two pole piece halves were joined by a clamp ring at the outside equator of the lens as shown in Fig. 6.32. Use of the clamp ring precluded perforating the pole pieces for fasteners, and it also provided an eye for handling equipment. Each injector lens weighs nearly 270 kg. A stainless
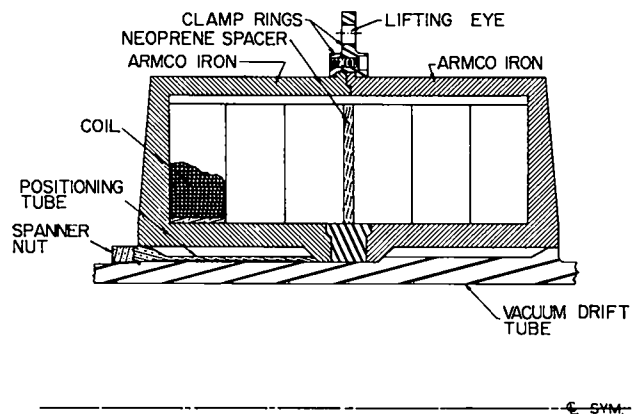
Fig. 6.32. Injector lens construction.

199

steel spacer is used in the gap. The coils, each with 900 turns of No. 14 wire, are wound over a machined phenolic ring and potted in Epocast-202 (with D-40 hardener). The phenolic ring, with 0.32 cm fiber glass Glastic end discs, formed the coil spool. Upon curing, the coil sections were machined flat and parallel with the center ring as a reference (Fig. 6.33). A close fit of the coil inside diameter on the pole piece halves provides positive alignment. These lenses fit over the nonmagnetic stainless steel evacuated drift tube. They are positioned axially and radially, and are locked in place with a spanner nut. Each lens has provisions for installation of a permanent gaussmeter probe in the gap between the pole pieces for continuous monitoring during machine operation. Internal cooling is unnecessary since the power dissipation in each injector lens is less than 25 W.
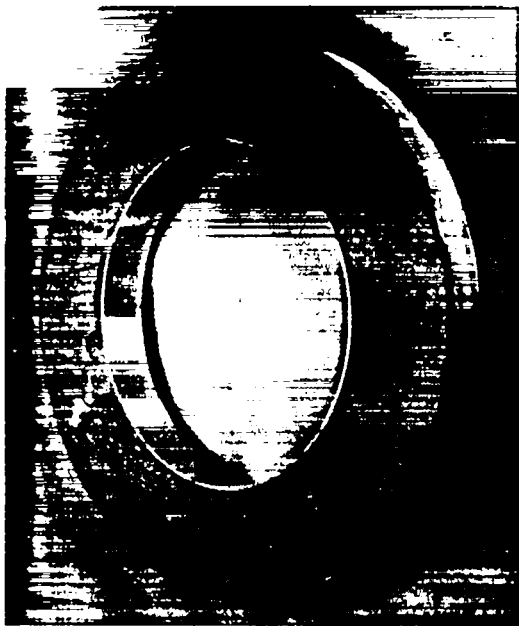
Fig. 6.33. Lens coil section.

Lens focal length, axial position, and ampere-turns requirements were theoretically determined from the paraxial ray optical analyses described in Chapter 1 and in Appendix 6B. Using these design criteria, the governing geometry of the injector beam, and the space available in the head of the first cavity, the magnetic circuit design was established.

Treating the lens as a simple series magnetic circuit, the flux density in any element j can be described by

$$B_j = \frac{4\pi \times 10^{-7}(NI)}{A_j \left(\dfrac{l_1}{\mu_1 A_1} + \dfrac{l_2}{\mu_2 A_2} + \cdots + \dfrac{l_j}{\mu_j A_j} \right)}$$

(6.19)

where A_j is the cross sectional area, l_j is the path length, and μ_j is the permeability of the jth element. By performing a series of successive approximations, the cross sectional area of each component was established such that the flux density was well below the knee of the saturation curve.

Optimum pole piece contours at the gap were established approximately by field plotting techniques with conducting paper. Comparison of the normalized conducting paper field plots and the measured axial magnetic field distribution (Fig. 6.34) indicates relatively good agreement.

Axial and transverse fields were measured at 2.5 cm increments on center through the entire lens and valve assembly (Fig. 6.35) with an F. W. Bell "120" gaussmeter. Magnitudes of the axial fields, and both magnitude and angular direction of the on-axis transverse fields were recorded at current settings from 0 to 20 A. Maximum transverse residual fields of less than 0.4 gauss were found in the new lenses, compared
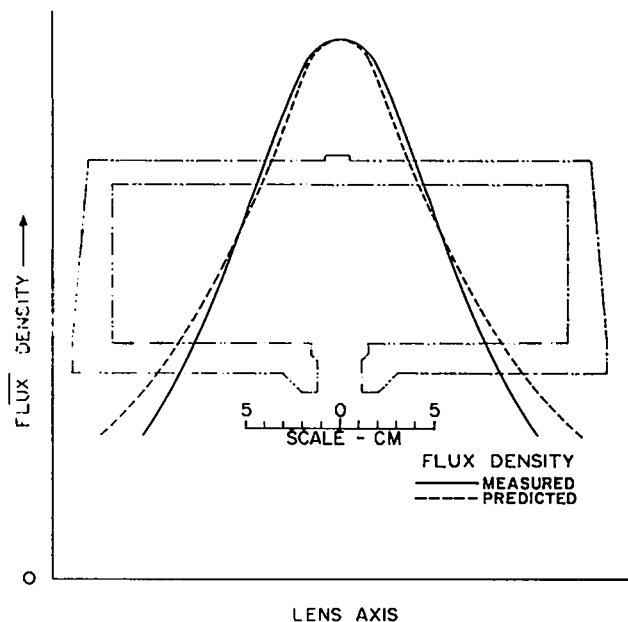
Fig. 6.34. Comparison of conducting paper plot with actual field measurements.

200
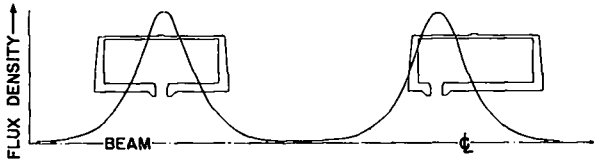
Fig. 6.35. Axial field distribution.

with more than two times that value in the old lenses. At four times the normal operating current in the new lenses, transverse fields of 2.1 gauss were measured, an improvement of 50% over the old lenses at their normal operating current. To evaluate the effect of reversing current polarity, the four possible current polarity combinations were imposed and data recorded. No measurable variation could be detected.

The lens assembly is supported within the cavity nozzle liner at three points: at the cavity wall, at the upstream end of the second lens, and at the upstream end of the valve. This supporting sequence allows the upstream lens and valve to be removed without removing the nozzle liner. Each supporting member consists of a split aluminum ring installed in the nozzle liner and locked into position by an expansion device. Three equally spaced high load, short stroke springs are threaded radially into the ring to permit alignment of the drift tube. With the different loading conditions imposed, the springs must be flexible to avoid redundancy, and must have different load stroke characteristics at each support. The springs, of nonmagnetic material, consist of a piston, cylinder, and a neoprene pad (Fig. 6.36). A predetermined load is applied to each spring assembly. Static load-stroke measurements show the characteristics to be reproducible, and prolonged load application results in negligible creep.

The injector assembly (Figs. 6.37 and 6.38) is shown with valve and supports within the nozzle liner connected to the gun cavity.

C. Inspection Procedures

Early beam analysis, confirmed by experimental work on the half-scale injector, showed the importance of precise axial and radial alignment of gun components. Each element of the injector assembly is individually inspected to assure that it is within allowable tolerances. The number
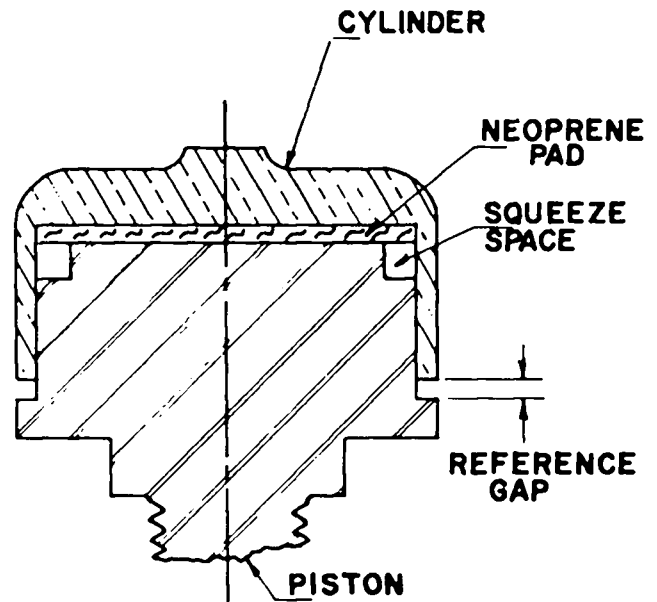
Fig. 6.36. Lens support spring.
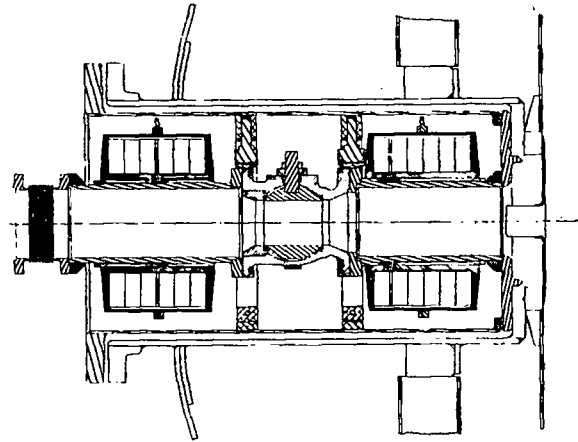
Fig. 6.37. Injector lens assembly.
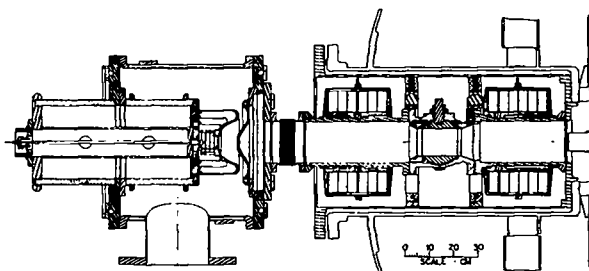
Fig. 6.38. Injector assembly.

and nature of the parts allows the possibility for the assembly to be grossly out of tolerance, simply by virtue of the addition of allowable errors of the components. In order to produce a sufficiently precise assembly and yet specify parts with realistic tolerances, a rigorous inspection routine has been established. After the components have been inspected, mating symmetrical parts are oriented angularly to minimize radial and axial errors. With the exception of the cathode and anode field forming electrodes, all subassemblies are located with dowel pins unequally spaced, to prevent possible assembly 180° from the desired position.

An inspection report for each injector assembly is completed. This report includes the axial and radial misalignment of each component during assembly. Cathode-anode spacing is the final measurement made prior to placing the injector in service. All cathode field forming electrodes and anodes are interchangeable; however, they are numbered and have similar inspection records. Upon completion the injector is given an ARRAY number that identifies the specific gun cavity, support, cathode field forming electrode, anode, and cathode. Experience has proved the inspection effort to be well justified, since burrs or pulled threads on parts can seriously impair injector performance.

D. Cleaning

To maintain maximum current emission and prolong service life of cathodes, a high degree of cleanliness and a high vacuum are required. Parts in the vicinity of the hot gun were machined dry or with water to avoid any possibility of cathode contamination by cutting oil. Other parts in cooler areas were machined with sulfur-free cutting oil. All components of appropriate size are cleaned in a Pangborn Model EZ-3 Hydrofinisher, using 620 grit abrasive in a water slurry. Parts are then rinsed in clear water and cleaned in an ultrasonic cleaner. Large vacuum components are electro-polished. None of the vacuum components is baked, other than by the progressive heating of the cathode during activation. This technique has proved adequate, since the injector operates hot at about 8×10^{-8} torr and has been in the 10^{-9} torr range cold.

E. Vacuum System

Figure 6.39 shows the general layout of the injector vacuum system. The system is rough-pumped by a Central Scientific Co. Hypervac Model-100 pump through a liquid nitrogen cold trap and valve to the 1000 liter/sec VacIon pump and gun cavity. Trapping serves primarily to minimize backstreaming of pump oil but also improves the ultimate vacuum. The injector can be evacuated while separated from the accelerator cavities for beam diagnostic studies, or it can be isolated from the cavities during cathode activation or maintenance.
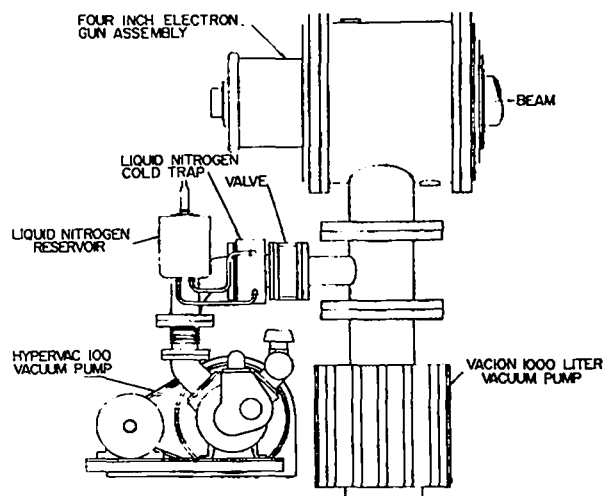
Fig. 6.39. Injector vacuum system.

The Hypervac pumps the system from atmospheric pressure to 10^{-4} torr in less than 10 min, at which time the VacIon pump can be started. Upon staring the ion pump at this pressure, a glow discharge occurs, causing the pressure to rise. Roughing is continued with the ion pump off. After cycling the system a few times in this manner, this ion pump can be started and the valve to the rough pump closed. This system has been repeatedly pumped from atmospheric pressure to 10^{-6} torr in about 30 min. Pumpdown time has been minimized by flooding the system with water-pumped nitrogen before opening it to the atmosphere.

Convaseal gaskets are used in the gun support, neoprene "O" rings in the roughing pump valve, and Teflon in the isolation valve between the lenses; all other seals are metal. Flat copper gaskets, described earlier, are used on the injector flanges, and aluminum wire is used in the pumping system. Aluminum wire seals are used in conjunction with standard ASA Schedule-40 steam flanges. The only modification of this flange consists of a 1 μ lathe finish on sealing surfaces. Inherent advantages of these flanges are interchangeability (no male and female parts), relatively low cost, and ease of removing scratches. Soft aluminum wire, 0.16 cm in diameter, is butt-welded with a Utica Koldwelder to form the proper diameter ring. Aluminum foil strips hold the wire seal in place on flange faces during assembly. This seal has proved to be valuable and has been used since in numerous vacuum systems with a high order of reliability. The major disadvantage is that precise axial, radial, and angular alignment cannot be attained unless locating pins or reference shoulders are incorporated. Tightening the bolts to a predetermined torque value has proved to be unnecessary, although load-stroke characteristics have been recorded for design purposes.

F. Cathode Activation

Cathode activation commences when a pressure less than 10^{-6} torr is achieved. During activation the pressure is never permitted to rise above 10^{-6} torr. Typical activation takes about 30 hr before operating power and emission are reached. Power is raised gradually, limited by the pressure criterion. The system is set to shut off the filament power if the pressure rises above 10^{-6} torr when left unattended. Pressure is continually monitored by a strip recorder in order to have a permanent record of the activation history. Also recorded, in the form of handwritten notes on the strip chart, are filament power, pulse voltage, and any circumstances known to affect the cathode environment. When operating power is reached, the gun is pulsed and total current collected at the focal point of the beam. Although emission continues to increase gradually for the first 100 hr or so, maximum emission is approached after the first few hundred pulses.

G. Beam Trajectory Measurements

The purpose of beam trajectory determination experiments was to evaluate the final lens design of the 10 cm injector. Current density distribution, beam radius, and beam slope were measured at three axial stations: downstream from the anode (near the focal point of the cathode), at the center position of the valve, and at the position of the cavity wall.

Prior to conducting this series of tests, the total emission was carefully measured. A variable aperture device, Figs. 6.40 and 6.41, was designed so that the beam can be masked off by preselected-diameter apertures. The beam current

Fig. 6.40. Beam aperture device.
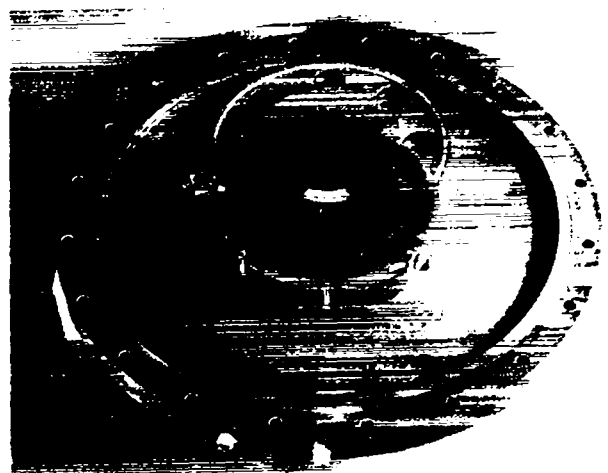
Fig. 6.41. Beam aperture device.

passes through an aperture and falls on a 0.32 cm thick beryllium plate. Eight apertures mask equal-area increments of the beam. In other words, the area of the largest aperture is eight times that of the smallest hole. The effective current, for a 0.2 μsec pulse, was determined by measuring the charge collected on a capacitor connected between the beryllium plate and ground.

Data were collected at each of the three axial stations for each aperture setting, holding the cathode filament power constant and pulsing at 400, 500, and 600 kV. At the two downstream stations, lens currents were adjusted to achieve maximum current through the large aperture. Current density distributions at the three axial stations are plotted in Figs. 6.42, 6.43, and 6.44.

To measure the beam radius and slope (convergence), three photographs of the beam were taken at 1 in. increments for each of the axial stations. A DuMont scope camera was adapted to a window, Fig. 6.45, through which a P-11 fluor-coated 0.075 cm molybdenum sheet was photographed. The screen was so designed that the beam image could be photographed at each of the required positions. Photographs of the beam were made holding all parameters identical to those of the variable aperture runs. These photographs provided views of the beam which showed fair symmetry, and from which the beam radius was measured, the beam slope at each of the three axial positions was determined from these data.

Fig. 6.43. Current density distribution, valve position.
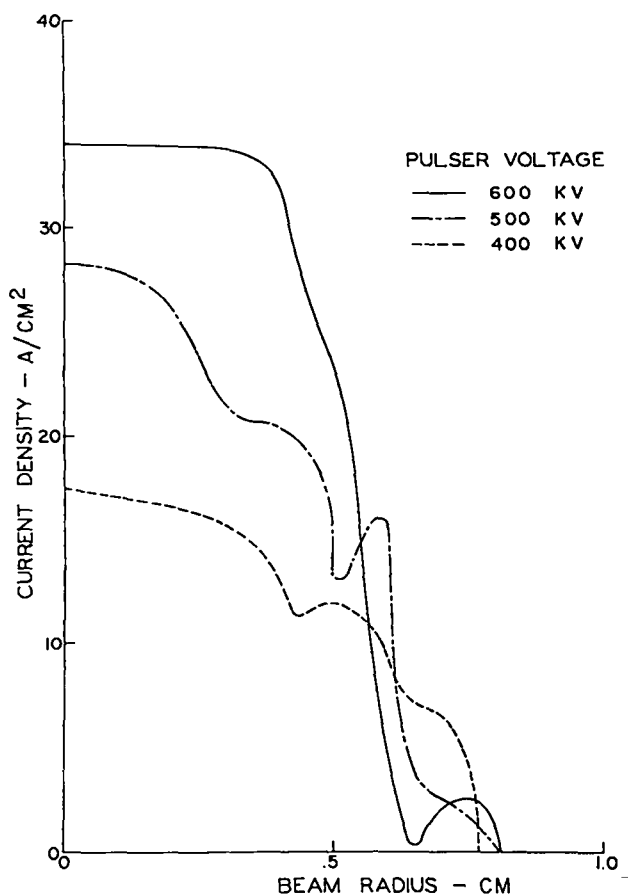
Fig. 6.44. Current density distribution, cavity position.

Fig. 6.42. Current density distribution, anode position.

204
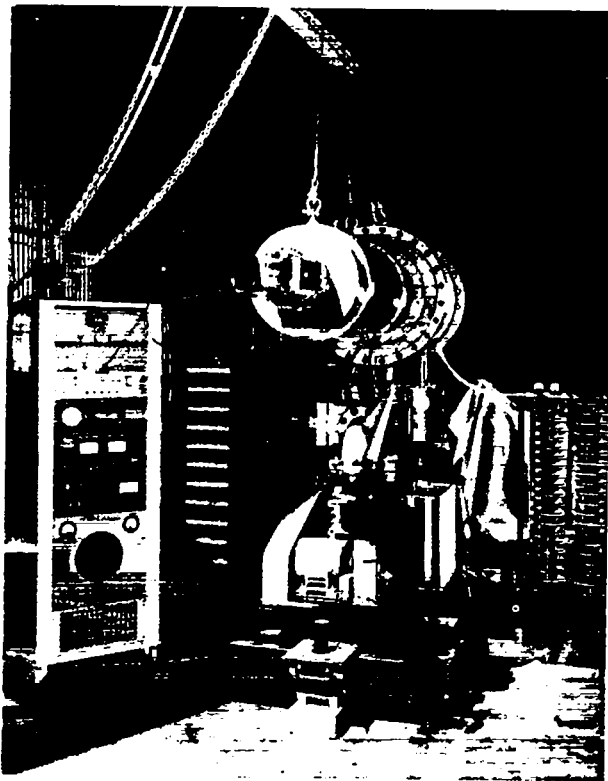
Fig. 6.45. DuMont camera installation.

The measured beam radius and slope are compared with the anticipated theoretical profile in Fig. 6.46.
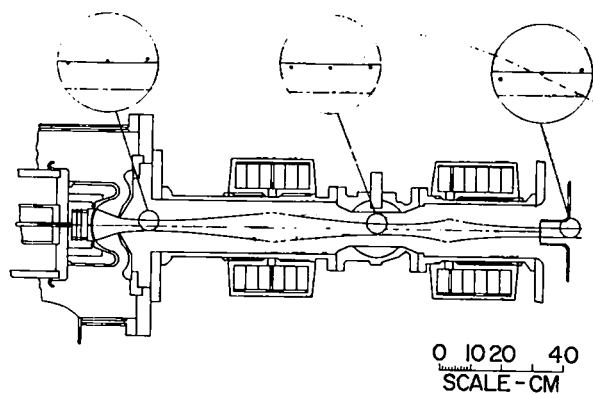
Fig. 6.46. Injector with beam profiles.

H. Pulser

All gun tests were made using Femcor 300 and 600 kV line pulsers, shown in Figs. 6.47 and 6.48. At present a 600 kV Femcor pulser is used to drive the 10 cm electron gun on the PHER-MEX machine.
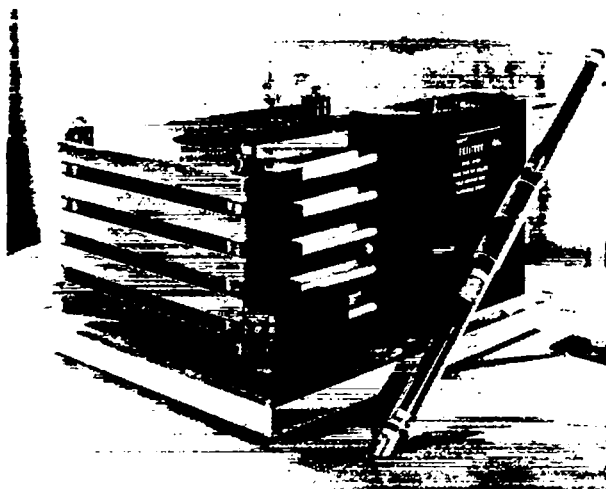
Fig. 6.47. 300 kV pulser.
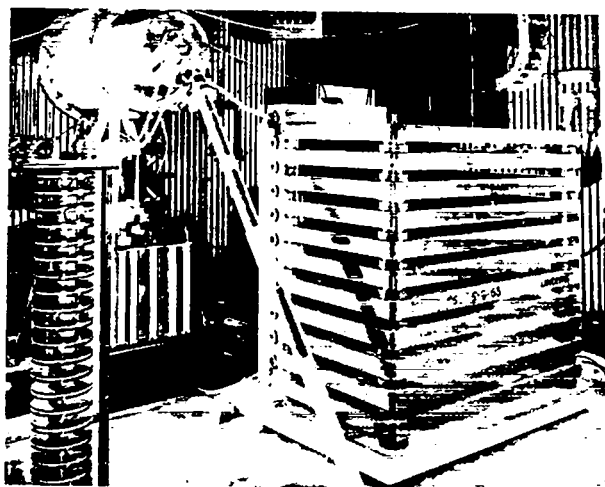
Fig. 6.48. 600 kV pulser.

The choice of pulser was influenced by several factors; among these, availability, dependability, and serviceability were pre-eminent. At the time high voltage tests of the 5 cm electron gun began, the Femcor 300 kV line pulser was the only commercially available unit having appropriate peak voltage, rise time, and pulse duration. Lumped-constant artificial-line pulsers, while perhaps feasible, were dropped from consideration, since none was commercially available then, and it was undesirable to enter into a program of pulser development at that time.

The Femcor line pulsers are Marx generators, using transmission lines as energy storage elements. Each energy storage element originally consisted of two RG-19/U transmission lines in parallel, potted in an epoxy to form a rigid module. Early module failures almost invariably occurred due to puncture of the line dielectric at the open (unterminated) end of these transmission lines. At the suggestion of LASL Group GMX-11, Field Emission Corporation modified the design to use a single length of RG-19/U folded back upon itself. The failure rate of these new-style modules has been gratifyingly low.

In PHERMEX service, the Femcor pulsers are charged negatively with respect to ground, to deliver a negative pulse to the cathode of the electron gun (gun anode is at ground potential). This charging polarity is the reverse of that for which the pulser was designed, and seems to have caused a small reduction in module lifetime. Far more serious consequences of the negative charging polarity were a decrease in triggering reliability and a greatly increased triggering jitter. These disadvantages, inconsequential in gun tests but prohibitive in PHERMEX operation, were completely overcome by replacing the Femcor trigger pulse transformer and trigger pulse amplifier with a larger pulse transformer and a GMX-11-designed trigger pulse amplifier delivering a more energetic trigger spark.

The 300 kV Femcor pulser delivers a 0.2 μsec pulse into a 125 Ω load. This output impedance was quite fortuitous, being low enough to give an acceptably short pulse rise time at the gun, yet sufficiently high to damp out any ringing due to the L and C of the gun. This situation was demonstrated later by means of computations

with a computer code called TAP. Since the 5 cm gun represents a real load impedance of approximately 2000 Ω, it does not present a matched load to the pulser. Therefore it was necessary to add a resistive load in parallel with the electron gun to match the pulser output impedance. This resistive load for the 300 kV pulser is made up of three Resistance Products Co. Type GZZ high frequency resistors having a total series resistance of about 125 Ω. These resistors, the best known to be available for the purpose, invariably demonstrate a decrease in resistance after being subjected to repeated high voltage pulses. The resistance eventually stabilizes at some lower value; thus it was necessary to "age" the load resistance by applying several hundred pulses before reproducible results could be obtained in gun tests. Pulser waveshape and, hence, charge delivered by the gun are somewhat sensitive to pulser load. Pulser waveshape for the 300 kV pulser, measured at the resistive load, is shown in Fig. 6.49.

The 0.2 μsec, 600 kV pulser used with the 10 cm gun has an internal impedance of 275 Ω. As with the smaller pulser, it was necessary to add a matching load resistance in parallel with the gun. The waveshape of the 600 kV pulser is definitely inferior to that from the 300 kV pulser. This degradation is attributed to the greater number of modules and spark gap switches in the system. The 275 Ω impedance is higher than optimum and limits the voltage rise time at the gun electrodes. Since the gun has a finite capacitance (about 100 pF) the gun voltage cannot rise instantaneously to its peak value. Pulser waveshape for the 600 kV pulser, measured at the resistive load, is shown in Fig. 6.50 for the optimum value of load resistance.

The period of the rf cycle in the cavities is 2×10^{-8} sec. Each 0.2 μsec gun pulse therefore covers 10 rf cycles. Ideally, the current pulse from the gun would rise in a time interval short compared with one rf period, maintain a constant current-value for 10 cycles, and then fall to zero in a time comparable with its rise time.

The gun current pulse shape is a function of the gun voltage pulse shape, current varying as the 3/2 power of voltage when Child's law is valid. If the rise time of the voltage pulse is short in comparison with its duration, the current and voltage pulse shapes will be very nearly identical.
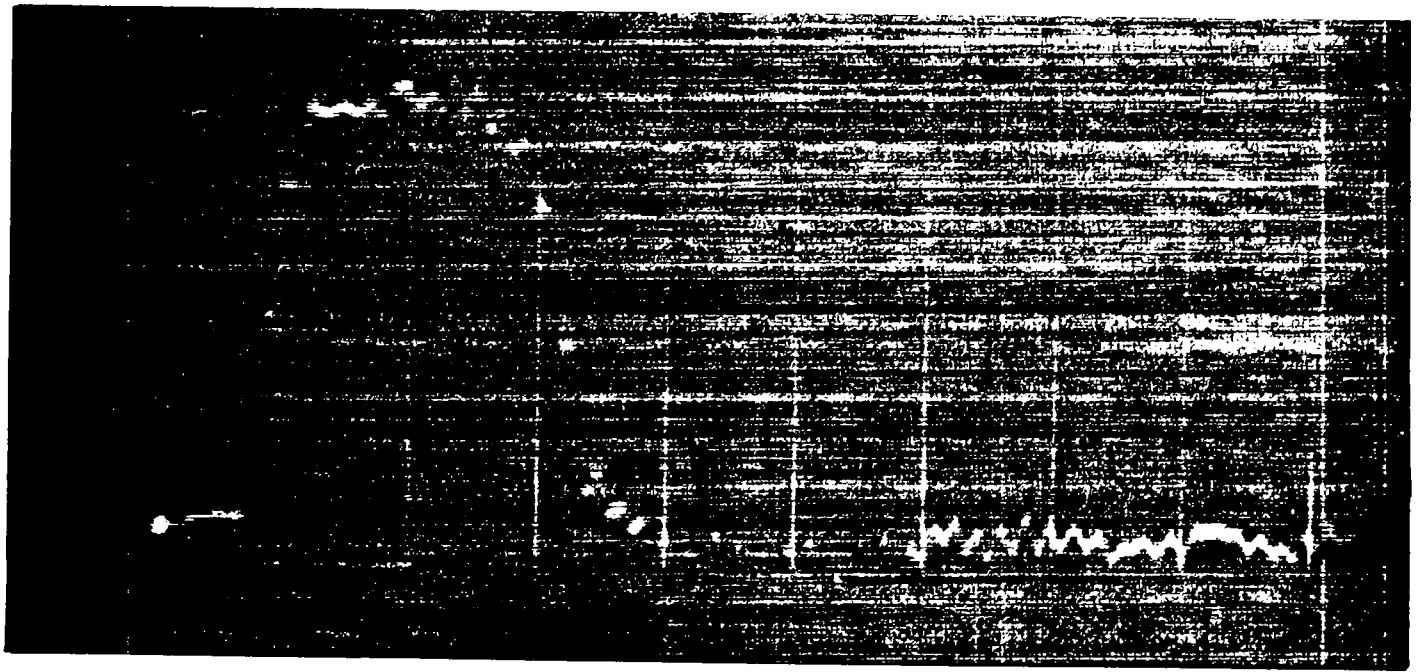
Fig. 6.49.   300 kV pulser wave form.
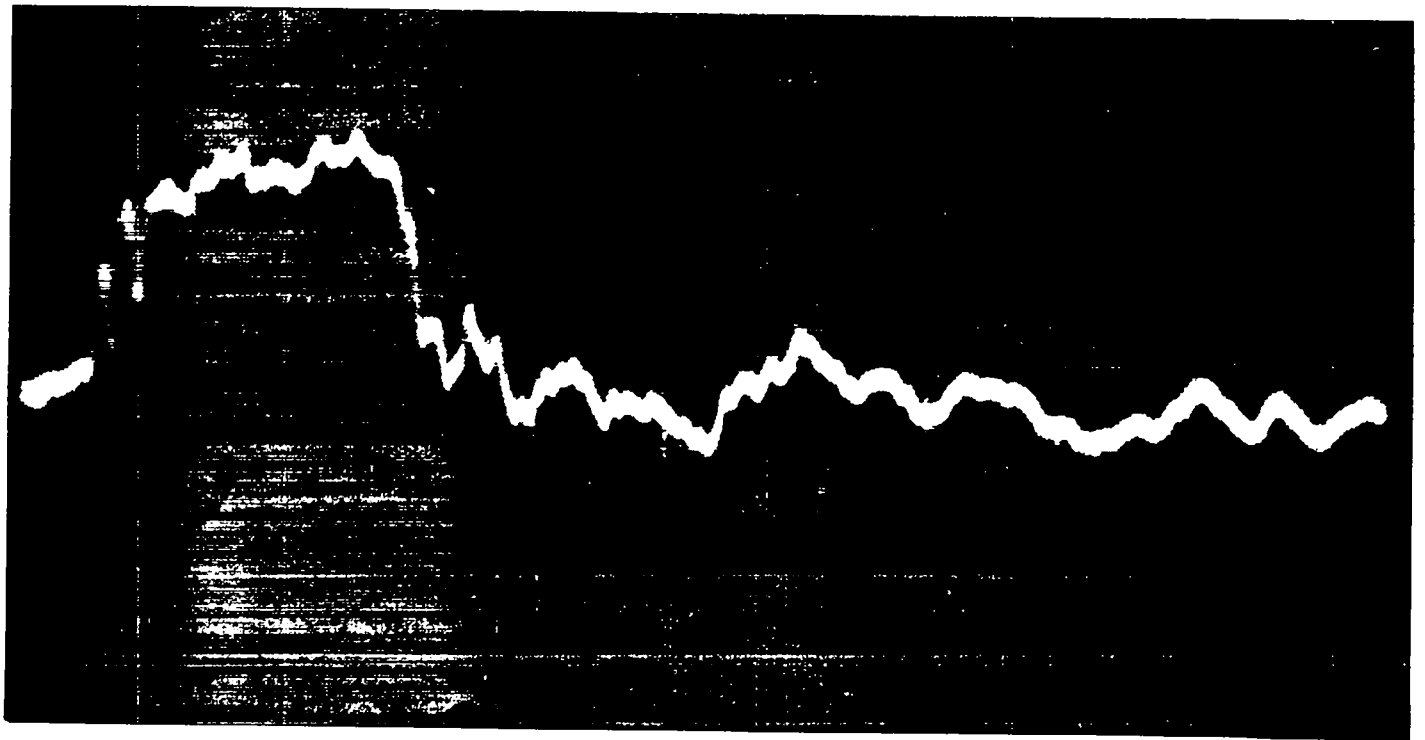
Fig. 6.50.   600 kV pulser wave form.

It is recognized that the voltage pulse shape at the gun electrodes is not identical to the voltage pulse delivered by the pulser, as the gun represents a nonlinear resistive load having a parallel capacitance and a series lead inductance both inside and outside the gun.

II. EJECTION

As seen in the illustration of the ejection optical system, Fig. 6.51, the beam emerging from the last cavity is crudely collimated by means of a magnetic lens. This lens, similar in design to the injector lenses, directs the maximum number of useful electrons toward the final focusing lens, located about 10 m away. Just downstream from the collimating lens is a set of steering magnets that can be used to effect small shifts in the radial position of the beam. From here, the beam traverses a magnetically shielded drift tube to the focusing lens.

Since the beam emerging from the last cavity is far from being monoenergetic, a large fraction of its electrons are inaccessible to the target when static lenses are employed. As a result, the trajectories of these particles terminate on the drift

tube wall or other internal structures. If not adequately attenuated, the radiation background that arises from these electrons would be intolerable for good radiography. Therefore, instead of trying to attenuate bremsstrahlung, it is best to collimate the electron beam in such a way to prevent this spurious radiation from being generated. Beryllium collimators have been found most satisfactory. One, with a 2.5 cm diameter on-axis hole, is located about 1.5 m upstream from the focusing lens; three more collimators are located downstream, as is shown in Fig. 6.59. Since the beam current density distribution is roughly bell-shaped, most of the beam passes through the 3 mm diameter collimator leading to the target.

A. Collimating Lens

The original collimating lens was designed with radial and angular alignment capability. Mechanical tolerances in the manufacture of the cavities left the exact position of the electron optical axis uncertain; therefore, the position of the electron beam upon ejection was not known exactly. At the time, it was felt that alignment capability would allow the lens to be positioned on the beam and the maximum current to be focused through the 2.5 cm diameter aperture located upstream from the focusing lens. The lens focal length, axial position, and ampere-turn requirements were theoretically determined from paraxial optics considerations described in Appendix 6B. Normalized flux field values were obtained for various ampere-turns; the results are shown in Fig. 6.52. Considerable saturation was recorded for the higher ampere-turn values. However, this was thought not to be unduly harmful to the high energy beam.

Fig. 6.51. Ejection optical system.
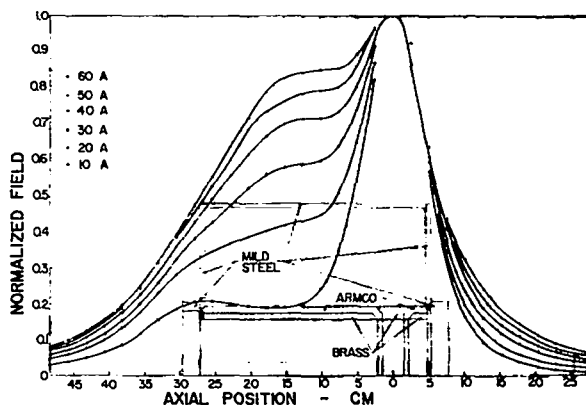
Fig. 6.52. Axial field distribution in first version of collimating lens.

An interim lens, which was a modification of the original collimating lens, was fabricated. This lens had a larger cross section, type 1020 mild steel magnetic circuit. Water cooling was also installed between coil sections to remove the heat. Plots of the flux field distribution, Fig. 6.53, show that saturation at the higher ampere-turn values was decreased. Because of the extremely critical problem of aligning this lens, and since the electron beam was found to be close to the optical center of the ejection aperture, the interim lens was permanently aligned on the beam axis and had no mechanical adjustments of its own. This modified lens was used on PHERMEX for over a year while an improved lens was designed and fabricated.

The present collimating lens has an Armco iron magnetic circuit, water cooling, a Hall-effect gaussmeter probe, and a thermocouple. Normalized axial field distributions for various ampere-turns are shown in Fig. 6.54. Slight asymmetry still occurs about the equatorial plane of the lens. Figure 6.55 shows the collimating lens and vacuum valve in position in the downstream port of the ejector nozzle liner assembly.

Fig. 6.54. Axial field distribution in present collimating lens.
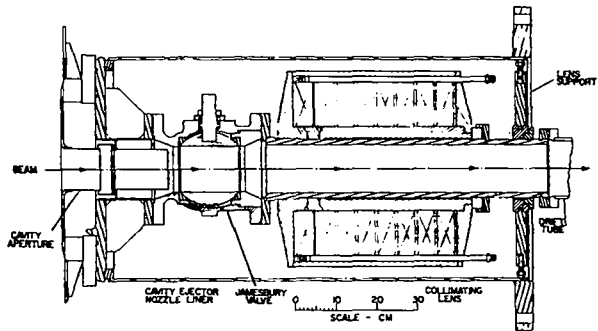
Fig. 6.55. Collimating lens and vacuum valve in ejector nozzle liner.

B. Drift Tube Space and Steering Magnets

Drift tube space consists of 10 m of type 304-L stainless steel tubing with a set of steering magnets on the upstream end. Magnetic shielding was used throughout most of the system to eliminate perturbing fields. A vacuum pump, incorporated in the assembly, is located on the downstream end of the drift tube. The steering magnets have the capability of moving the electron beam transversely in the target plane by about 3 mm without serious aberrations. A cutaway detail of the steering magnet assembly is shown in Fig. 6.56.

Fig. 6.53. Axial field distribution in second collimating lens.
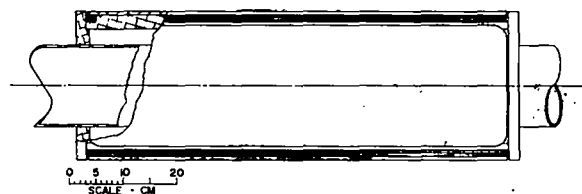
Fig. 6.56. Cross section of steering quadrupole.

209

The magnetic shielding, shown in Fig. 6.51, is capable of reducing the intensity of the perpendicular components of local magnetic fields by a factor of about 2500. The shielding was fabricated in the form of a nest of three concentric thin-wall tubes of specially heat-treated mumetal. Concentricity of these tubes is maintained by felt spacers. The units were made in 61 cm long sections for ease of assembly and simple replacement of damaged components.

C. Focusing Lens

The original focusing lens was designed with external pole pieces, with the vacuum tube serving as both the support and the permanent mechanical aligning mechanism. Normalized axial field measurements, Fig. 6.57, show a relatively good field distribution. Ampere-turn requirements for this prototype lens were determined from paraxial optics considerations for a focal length of 1 m. This lens was designed for intermittent operation and, thus, had no provisions for water cooling. When, later, it was found necessary to run the lens continuously for optimum machine operation, heat dissipation became a problem; but by careful use, the prototype was kept in operation for over a year while a new lens was being designed and fabricated.

The present focusing lens also has an Armco iron magnetic circuit, water cooling, a Hall-effect gaussmeter probe, and a thermocouple. Normalized axial field values for various ampere-turns are shown in Fig. 6.58. The new focusing lens is positioned 0.5 m from the target and is aligned by radial movement of the heavy-wall center tube, which is also the vacuum enclosure. The focusing lens and target assembly are enclosed in a protective envelope and protected by a blast-resistant nose. As shown in Fig. 6.59, the blast-resistant nose assembly is hinged for easy access to the target area and to facilitate maintenance of the focusing lens.
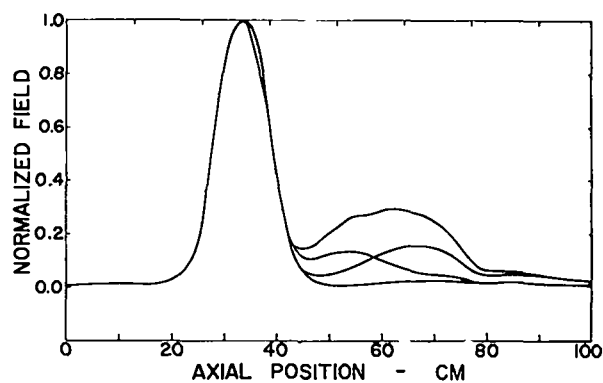
Fig. 6.58. Axial field distribution in final focusing lens.
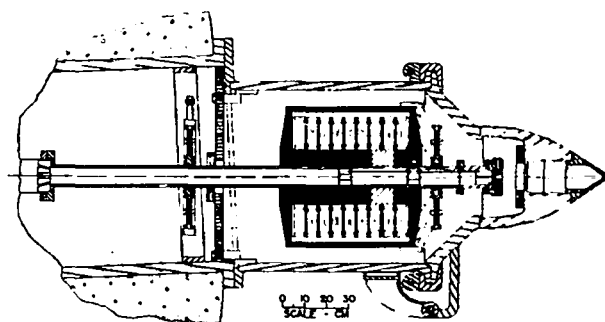
Fig. 6.59. Blast protective system housing focusing lens and target assembly.

REFERENCES

6. 1. W. M. Coates, *Trans. ASME*, **52**, APM-52-12-117 (1930).

6. 2. F. B. Seely and J. O. Smith, *Advanced Mechanics of Materials*, John Wiley and Sons, New York, 1955, 2nd Ed., 295-327.

Fig. 6.57. Axial field distribution in first version of focusing lens.

Appendix 6A

INJECTOR GUN DESIGN

I. DESIGN PROCEDURES

There are two beam current extremes in electron gun design. One is the case of emission limited flow where no space charge influences the beam trajectories. In this case the equipotential distributions are defined by Laplace's equation. Only beams of very low current density can be considered. Therefore, in order to achieve the required peak currents it is necessary to use very large diameter electron beams.

Cathode current densities of less than 10^{-8} A/cm^2 begin to satisfy the condition that space charge is negligible. Clearly, for a beam current of 250 A, the cathode radius must be about 290 cm. This beam could be "focused" to perhaps a radius of 50 cm after it has been accelerated to its maximum energy without serious loss in current. Even so, a beam radius of 50 cm is intolerable when it is accelerated through PHERMEX cavities. The resulting loss of target current would be prohibitive.

The other extreme in gun design makes use of space-charge-limited flow. Here, in the absence of residual gas effects, one can produce maximum current density beams for a given acceleration potential. This means that Poisson's equation, instead of Laplace's, holds. One such gun type is based upon rectilinear flow between two concentric spheres, the outer sphere being the cathode. From this type we may write Poisson's equation as

$$\frac{1}{r^2} \frac{d}{dr} \left(r^2 \frac{dV}{dr} \right) = -\frac{q_v}{k_0}$$

(A.1)

Here the beam current is a constant

$$I = 4\pi r^2 J = -4\pi r^2 q_v u = -4\pi r^2 q_v \sqrt{2\eta V}$$

(A.2)

where

J = current density, A/m^2
u = particle velocity, m/sec
η = specific charge, 1.759×10^{11} coul/kg

Substituting Eq. (A.2) into Eq. (A.1) we have

$$\frac{d}{dr} \left(r^2 \frac{dV}{dr} \right) = \frac{IV^{-1/2}}{4\pi k_0 \sqrt{2\eta}}$$

(A.3)

Let I have the following form, based upon the analogous form of space-charge-limited flow across a planar diode,

$$I = \frac{16\pi k_0 \sqrt{2\eta}}{9} \frac{V^{3/2}}{(-\alpha)^2} = 29.3 \times 10^{-6} \frac{V^{3/2}}{(-\alpha)^2}$$

(A.4)

and

$$V = \left(\frac{9I}{16\pi k_0 \sqrt{2\eta}} \right)^{2/3} (-\alpha)^{4/3}$$

(A.5)

Thus

$$\frac{d}{dr} \left(r^2 \frac{dV}{dr} \right) = \frac{4}{9} \frac{V}{(-\alpha)^2}$$

(A.6)

Further, let

$$\gamma = \ln \frac{r}{r_c}$$

(A.7)

and substitute Eqs. (A.5) and (A.7) into Eq. (A.6) to give the equation defining the dimensionless function $(-\alpha)^2$

$$3\alpha \frac{d^2\alpha}{d\gamma^2} + 3\alpha \frac{d\alpha}{d\gamma} + \left(\frac{d\alpha}{d\gamma} \right)^2 - 1 = 0$$

(A.8)

This equation was first studied by Langmuir and Blodgett in 1923. Their published results were tabulated giving $(-\alpha)^2$ as a function of r_c/r, where r_c is the radius of the cathode. There are other functions of $(-\alpha)^2$, such as $d(-\alpha)^2/d(r_c/r)$ which were needed for gun design. Equation (A.8) was solved numerically, checking Langmuir (to three places), and at the same time the other useful functions were generated.

Now consider the current flowing radially from only a sector of the sphere so that the actual current becomes

$$I = 14.7 \times 10^{-6} \frac{1 - \cos\theta}{(-\alpha)^2} V^{3/2}$$

(A.9)

where θ is the semi-cone angle of the electron beam. This relationship is valid when there is no aperture in the anode and only approximately so for finite size apertures. Theory and practice are in best accord when the anode-to-cathode distance is large compared with the aperture diameter. In order to develop approximate formulae to establish numerical values of electron gun parameters, one assumes that Davisson's lens formula is adequate here so that the convergence effect of the aperture may be written

$$\Delta C = \frac{1}{f} = -\frac{E_a}{4V_a}$$

(A.10)

where

$f =$ focal length of aperture lens, m
$\Delta C =$ convergence change of the aperture lens, m^{-1}
$E_a =$ electric field at anode, V/m
$V_a =$ anode potential, V

Assume thin lens, paraxial optics here, even though the assumption is not rigorously valid. Hence, the convergence C_e of the beam emerging from the gun is

$$C_e = C_i + \Delta C_i = \frac{1}{r_a} - \frac{E_a}{4V_a}$$

(A.11)

where $C_i =$ convergence of beam incident on anode aperture. Then Eq. (A.5) defines V in terms of constants and the function $(-\alpha)^2$. Hence

$$E_a = -\left(\frac{\partial V}{\partial r}\right)_{r_a} = -\left[\frac{dV}{d(-\alpha)^2} \frac{d(-\alpha)^2}{dr}\right]_{r_a}$$

$$= \frac{2}{3} \frac{V_a}{(-\alpha)^2} \frac{r_c}{r_a^2} \left[\frac{d(-\alpha)^2}{d(r_c/r_a)}\right]_{r_a}$$

(A.12)

From Eq. (A.10) the net change in convergence of the electron beam passing through the aperture lens is

$$\Delta C_i = \left\{-\frac{1}{6(-\alpha)^2} \frac{r_c}{r_a^2} \left[\frac{d(-\alpha)^2}{d(r_c/r_a)}\right]\right\}_{r_a} = \frac{1}{f}$$

(A.13)

Thus the exit convergence becomes

$$C_e = \frac{1}{r_a}\left\{1 - \frac{1}{6(-\alpha)^2} \frac{r_c}{r_a} \left[\frac{d(-\alpha)^2}{d(r_c/r_a)}\right]\right\}_{r_a}$$

(A.14)

Before pursuing the problem of the net convergence of the electron beam, examine Eq. (A.13) graphically, substituting

$$\varepsilon = r_c/r_a$$

This is illustrated in Fig. 6A.1 where

$$\frac{f}{r_c} = \left\{\frac{6(-\alpha)^2}{\varepsilon^2} \left[\frac{d(-\alpha)^2}{d\varepsilon}\right]^{-1}\right\}_{r_a}$$

(A.15)

is plotted as a function of ε. Here the maximum focal length f occurs for a cathode-anode radius of
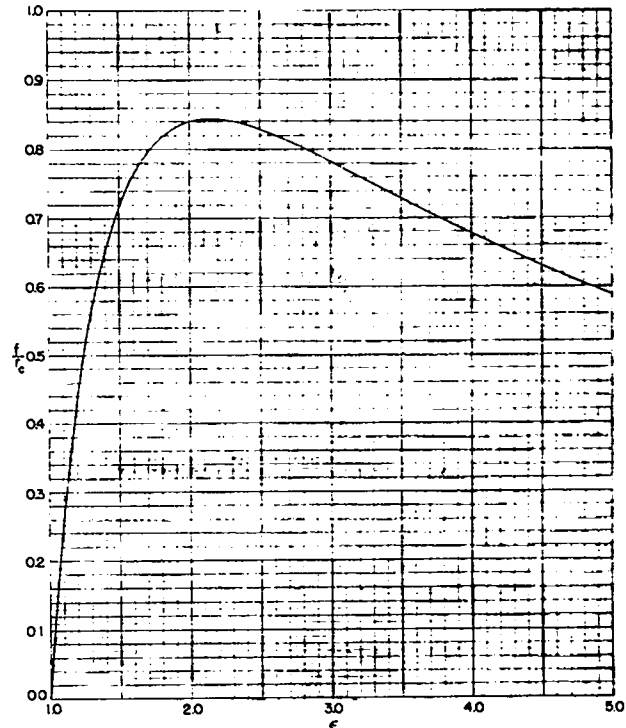
Fig. 6A. 1. Aperture convergence change vs r_c/r_a.

$$\frac{r_c}{r_a} \cong 2.15$$

(A.16)

Now return to Eq. (A.14) which is rewritten as Eq. (A.17). The trend in the net convergence is indicated in Fig. 6A.2 where

$$C_e r_c = \varepsilon \left\{ 1 - \frac{\varepsilon}{6(-\alpha)^2} \left[\frac{d(-\alpha)^2}{d\varepsilon} \right] \right\} r_a$$

(A.17)
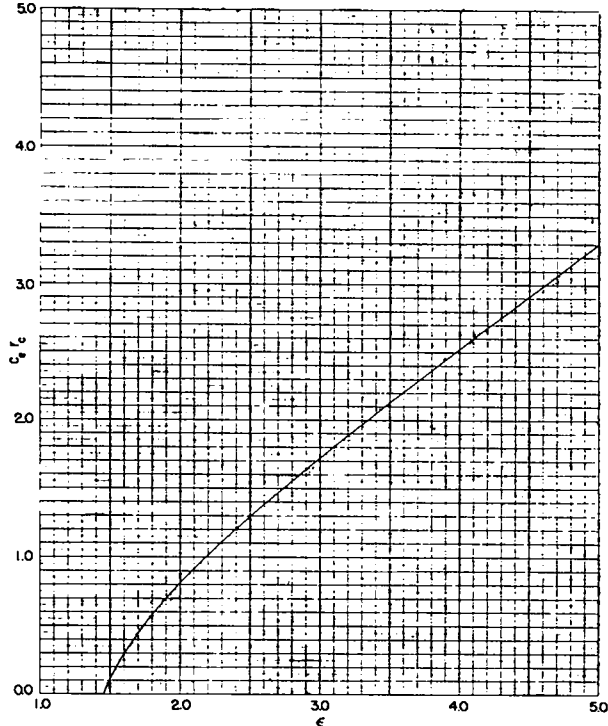
Fig. 6A. 2. Exit aperture convergence vs r_c/r_a.

The beam emerging from the anode aperture enters a region free of externally applied electric fields. Hence, in the absence of magnetic fields, the relativistic paraxial ray equation is Eq. (B.1) whose solutions are given in Appendix 6B.

The first integration of Eq. (B.1) yields

$$(R')^2 = \ln R + (R_0')^2$$

(A.18)

where R_0' is the value of the reduced slope on the exit side of the anode aperture. When

$$R' = 0$$

(A.19)

R reaches a minimum

$$R_{min} = e^{-(R_0')^2}$$

(A.20)

A second integration of Eq. (B.1) yields

$$Z = \int_1^R \frac{dR}{R'}$$

(A.21)

In addition to the solutions plotted in Appendix 6B, Fig. A.3 illustrates several typical reduced trajectories where R has been plotted for various values of R_0' as a function of Z.
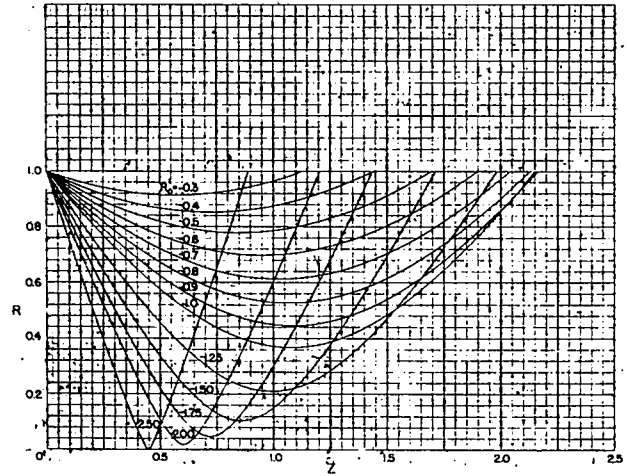
Fig. 6A. 3. Reduced ray trajectories.

Consider the value of Z at which R becomes unity again, and ask, "Is there a maximum Z for some specific choice of R_0'?" Figure A.3 indicates (a) that all reduced rays with negative values of R_0' pass through the unity R line at points other than $R = 1$, $Z = 0$, and (b) indeed there is a maximum in Z when

$$Z \cong 2.15$$

occurring for

$$R_0' \cong -0.9225$$

The locus of R_{min} versus Z is shown in Fig. 6A.4.

213
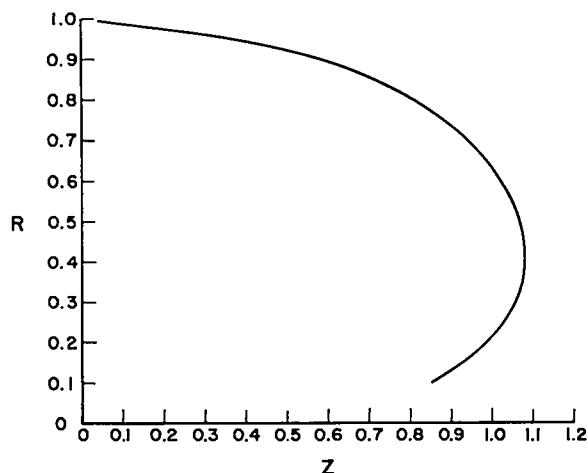
Fig. 6A. 4. Locus of R_{min} vs Z.

As a result of these considerations, one finds that there is a maximum current which can be passed through a constant diameter tube whose length is L. If the tube diameter is D, then

$$I_{max} = 38.5 \times 10^{-6}[V(1 + 0.98 \times 10^{-6}V)]$$

$$\times \left(\frac{D}{L}\right)^2$$

(A.22)

It is clear that a similar expression can be obtained for the case of unequal aperture diameters by using the information found in Fig. 6A.3. The difference between the solid line and the dashed (nonrelativistic) line in Fig. 6A.5 indicated the relativistic effect on I_{max}, the relativistic term being
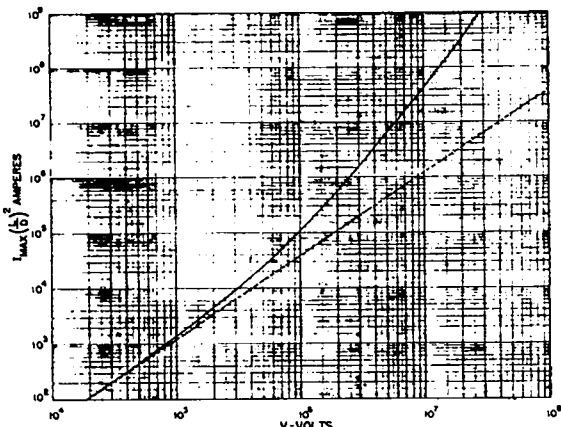
Fig. 6A. 5. Maximum current passable through a constant diameter tube of length L.

$$\left(1 + \frac{V}{2\mu}\right)^{3/2} = (1 + 0.98 \times 10^{-6}V)^{3/2}$$

(A.23)

This is considered since apertures are found in various regions of the entire system.

It has been tacitly assumed that to a useful approximation the anode aperture could be treated as a thin lens so that we may describe the ray optics as shown in the diagram of Fig. 6A.6. Thus one uses the thin lens equation, recognizing it is only an approximation,

$$\frac{1}{f} = \frac{1}{b} - \frac{1}{r_a}; \qquad \frac{b}{r_a} = \left(\varepsilon - \frac{r_o}{f}\right)^{-1}$$

(A.24)

f being the focal length of the aperture lens in the absence of space charge effects for paraxial optics.
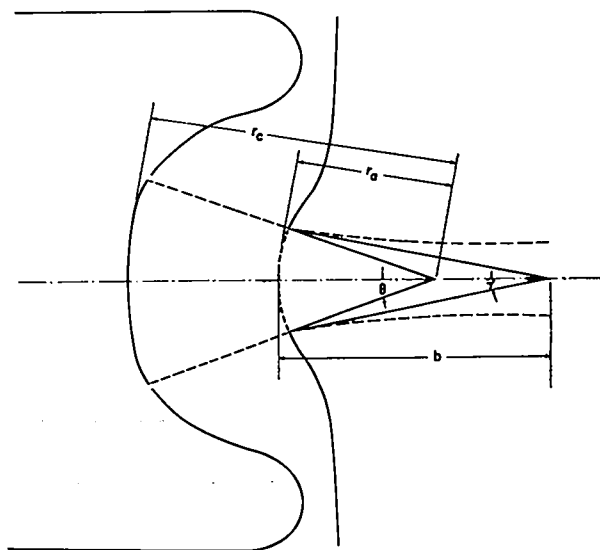
Fig. 6A. 6. Simplified schematic of ray optics in gun.

Figure 6A.6 indicates that

$$\sin \theta \propto \frac{1}{r_a}; \qquad \sin \gamma \propto \frac{1}{b}$$

(A.25)

214

By Snell's law the index of refraction becomes

$$n = \frac{\sin \theta}{\sin \gamma} = \frac{b}{r_a} = \frac{b}{r_c} \frac{r_c}{r_a}$$

$$(A.26)$$

Plot Eq. (A.24) as a function of r_c/r_a in Fig. 6A.7, where r_c/f has been given by Eq. (A.15).
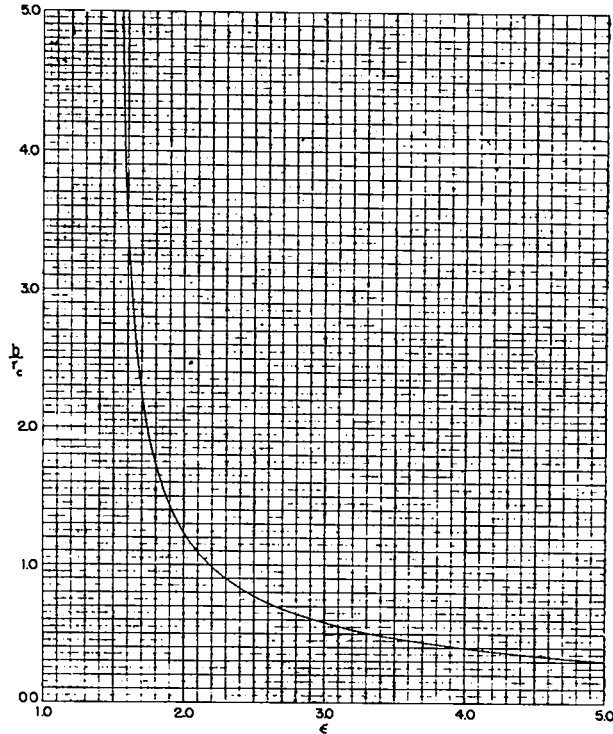
Fig. 6A. 7. Thin lens properties: b/r_c vs r_c/r_a.

It will be noticed that as r_c/r_a approaches about 1.45 the ratio b/r_c goes to infinity; that is, the emerging beam is parallel.

Now one can also plot the index of refraction Eq. (A.26) to relate the semi-cone angle θ of the incident beam to the semi-cone angle α of the exit beam. This is shown in Fig. 6A.8. Incident angle θ and exit cone angle α are plotted parametrically for various ε's in Fig. 6A.9. Equation (A.9) has been plotted in Figs. 6A.10 and 6A.11 for reference. It is recognized that Eq. (A.9) is valid only for nonrelativistic flow and that a correction must be made to the perveance equation for very high energy electrons.
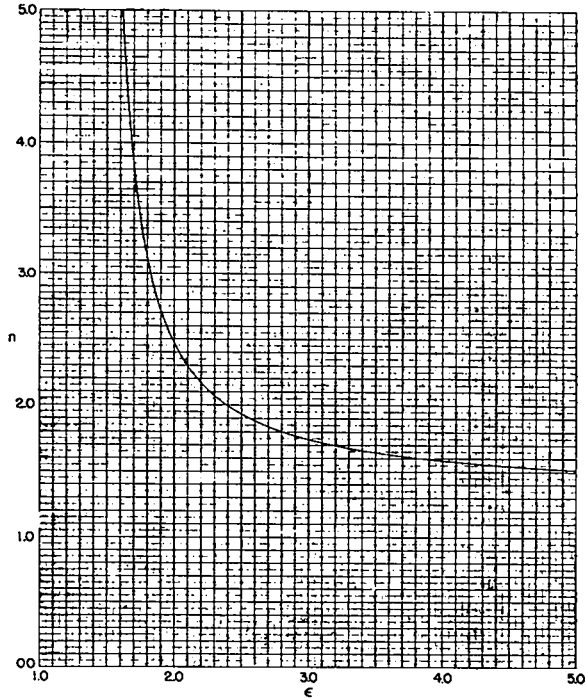
Fig. 6A. 8. Index of refraction.
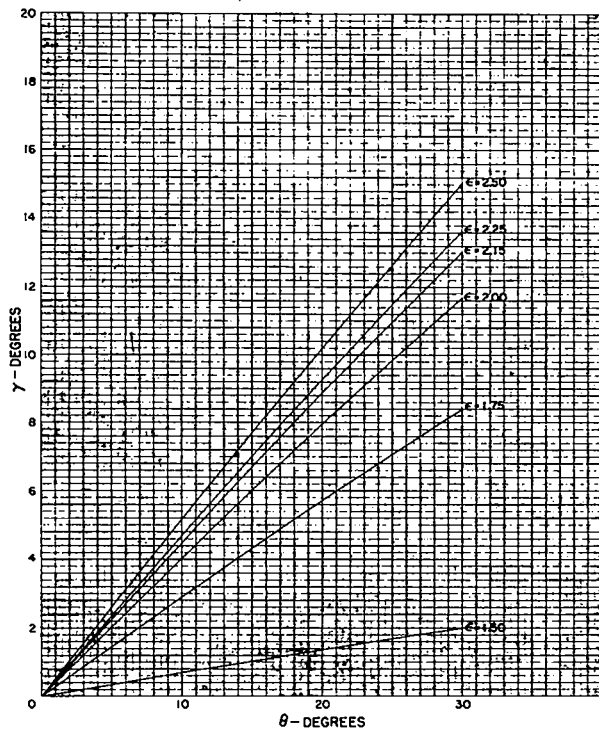
Fig. 6A. 9. Exit cone angle γ vs incident cone angle θ.
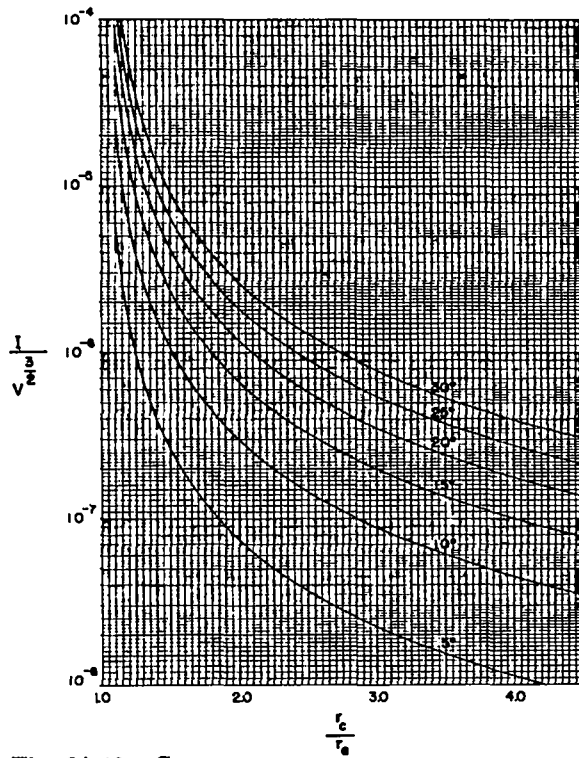
Fig. 6A.10. Gun perveance.
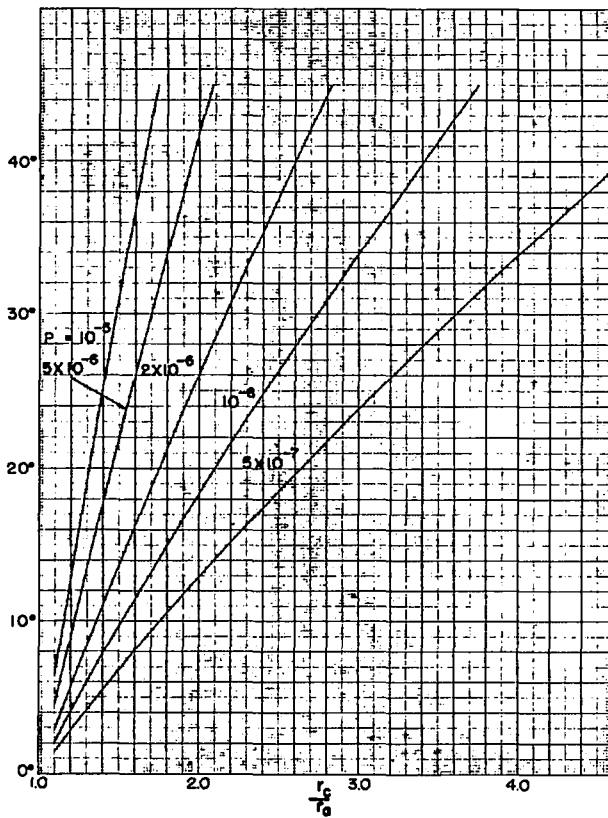
Fig. 6A.11. Gun perveance.

II. MODEL I GUN CHARACTERISTICS

Model I gun was designed to satisfy the following requirements:

$$I = 16 \text{ A}$$
$$V = 70 \text{ kV}$$
$$P = 0.82 \times 10^{-6}$$
$$\delta = 0.15$$

and a cathode diameter of 5 cm. The symbol δ is defined in Appendix 6B. Because of the space charge instability it is necessary to choose a geometry such that the focal spot lies a maximum distance Z_{max} from the anode aperture. This corresponds to

$$Z = \frac{\delta z}{r_0} = 2.15$$

$$R_0' = \frac{r'}{\delta} = -0.9225$$

Furthermore, r_c/r_a was chosen to be about 2 where the focal length of the aperture lens is a maximum. One bit of arbitrariness arises. That is the cathode-anode gap whose choice is based upon the uncertainty in electric breakdown for 70 kV. A gap of about 1 cm was chosen. This now defines an incident cone angle of about 20°. Hence the remaining characteristics become

$$z_{max} = 18.3 \text{ cm}$$
$$r_{min} = 0.533 \text{ cm}$$
$$r' = 0.139$$
$$\theta = 20°$$
$$\alpha = 8°$$

There is one unique electrode configuration which is able to form the field configuration needed to support the electron flow. Fortunately for the experimenter there is an infinitude of approximations which may be used. In order to facilitate our design work, electrode shapes known to approximate our needs were used initially. A study of the structure was made with an electrolytic tank, then the necessary modifications were made to satisfy our explicit requirements. In the electrolytic tank study, space charge was accounted for and the resulting potential distribution was compared with the same system in the absence of space charge. In both cases the plots were for three-dimensional systems of cylindrical symmetry. These potential distributions are shown in Figs. 6A.12 and 6A.13 for the structures that were actually fabricated for the Model I gun.

216
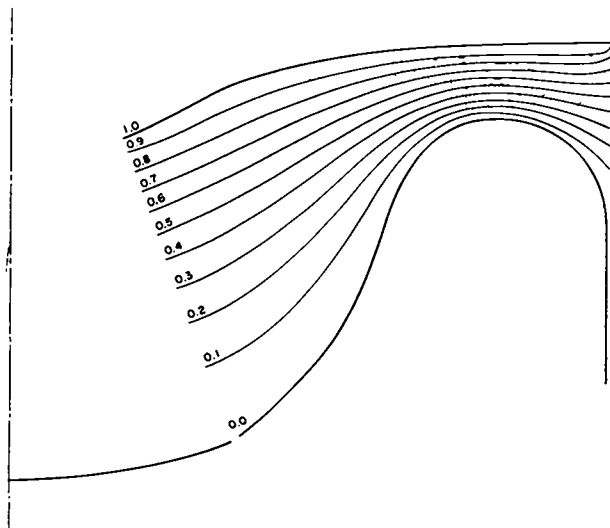
Fig. 6A.12. Potential distribution with space charge limited flow.

Fig. 6A.14. Comparison of theoretical Poisson and Laplace potential distributions without apertures.

Based upon these calculations, the dynamic effect of the aperture was computed graphically (neglecting space charge) to give an indication of the electron loss. This did not appear too important; however, experimental confirmation was obtained later.

Figure 6A.15 compares the analog solutions (electrolytic tank) of Laplace's equation for our gun configuration with and without the aperture.

The flow is governed primarily by Poisson's equation, and since we have assumed that in the neighborhood of the anode Laplace's and Poisson's equations give nearly the same results, we compare, in Fig. 6A.16, the electrolytic tank potential solutions of Laplace's and Poisson's equations. Prior to experimental confirmation, these results indicated that a fair approximation to a proper choice of electrode configurations had been achieved. Initial design was based upon these values. Later experiments demonstrated their validity.

Fig. 6A.13. Potential distribution with emission limited flow.

Although the aperture effect could not be accounted for in the space-charge case, calculations of the axial potentials for both the Poisson (space charge) and the Laplace (no space charge) cases, shown in Fig. 6A.14, indicate that the aperture fields should be roughly the same in both cases.

217

REDUCED PARAXIAL RAY EQUATION

The time-dependent equation of radial motion can be transformed to a space equation for flow in field-free regions. This equation becomes

$$r'' = -\frac{\eta I}{2\pi k_0 c^8 r}\left[\left(\frac{V}{\mu}+1\right)^2-1\right]^{-3/2}$$

(B.1)

If the following transformations are made

$$R = \frac{r}{r_0} \qquad Z = \delta\frac{z}{r_0}$$

(B.2)

where

$$\delta = \frac{5.58 \times 10^6\sqrt{I}}{[V(V+2\mu)]^{8/4}}$$

(B.3)

then Eq. (B.1) becomes

$$R'' = \frac{1}{2R}$$

(B.4)

with

$$R' = \frac{\partial R}{\partial Z} = \frac{1}{\delta}\frac{\partial r}{\partial z}$$

(B.5)

These equations become tools appropriate for approximating designs of high current electron beams. Equation (B.4), recognized as being the same as Eq. (1.1), has been solved by means of electronic digital computers. The function δ, Eq. (B.3), is plotted in Fig. 6B.1, and values of the solutions R(Z) and dR/dZ of Eq. (B.5) are found in Figs. 6B.2 through 6B.11.
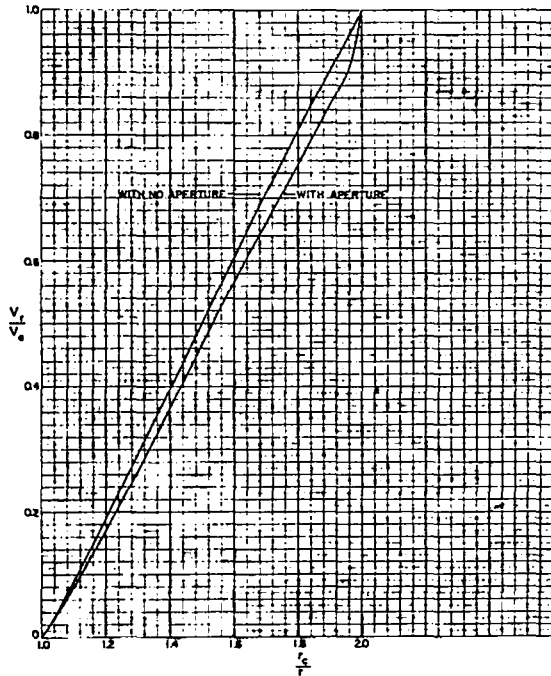
Fig. 6A.15. Comparison of electrolytic tank solutions of Laplace's equation with and without apertures.

Fig. 6A.16. Comparison of electrolytic tank solutions of Laplace's equation without apertures.
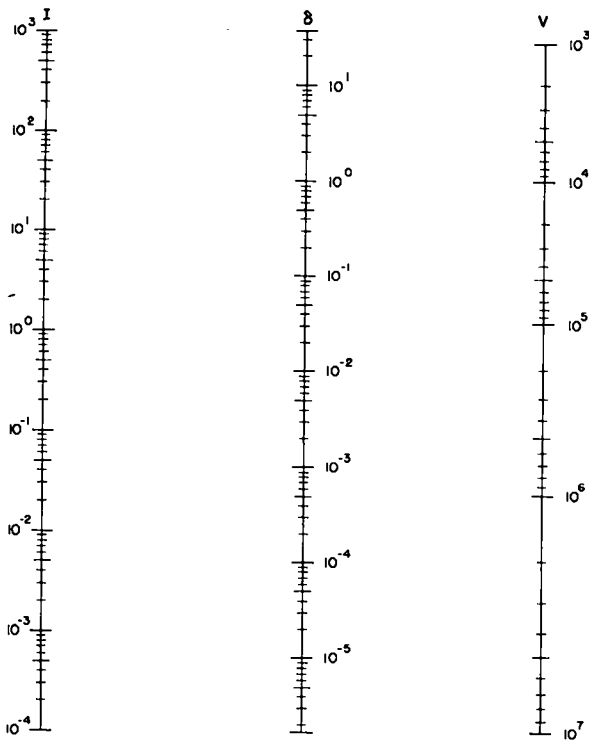
Fig. 6B. 1. Nomograph for normalizing function δ.
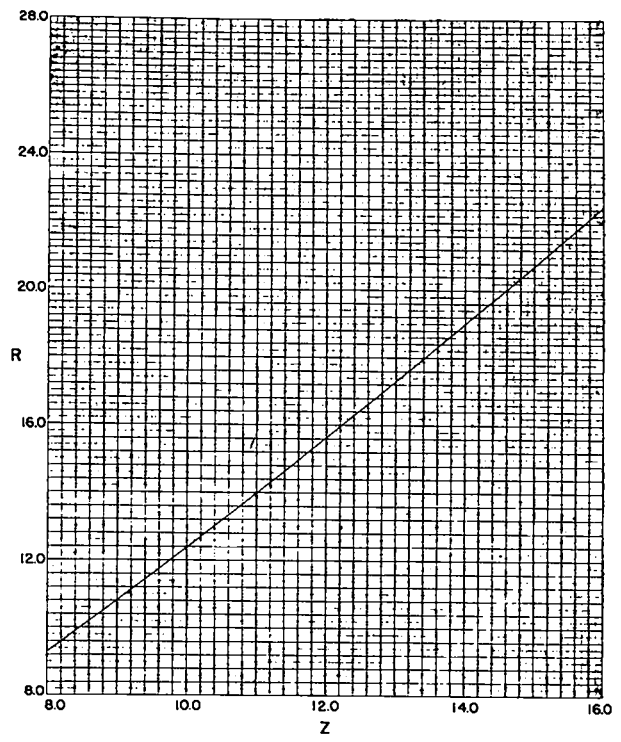
Fig. 6B. 3. Normalized trajectory.
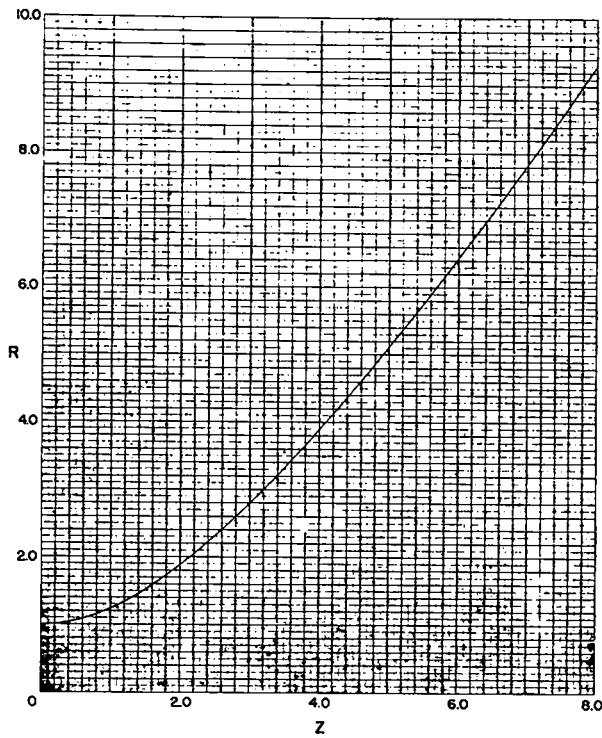
Fig. 6B. 2. Normalized trajectory.
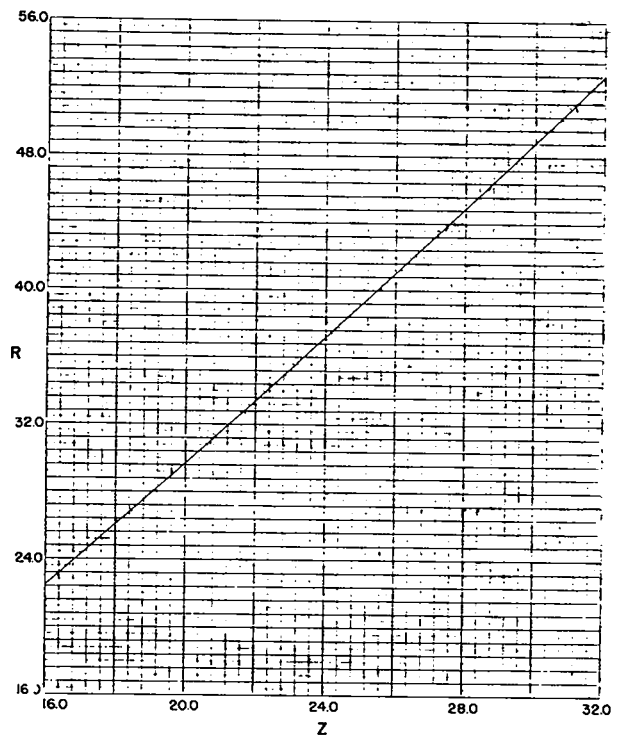
Fig. 6B. 4. Normalized trajectory.

219
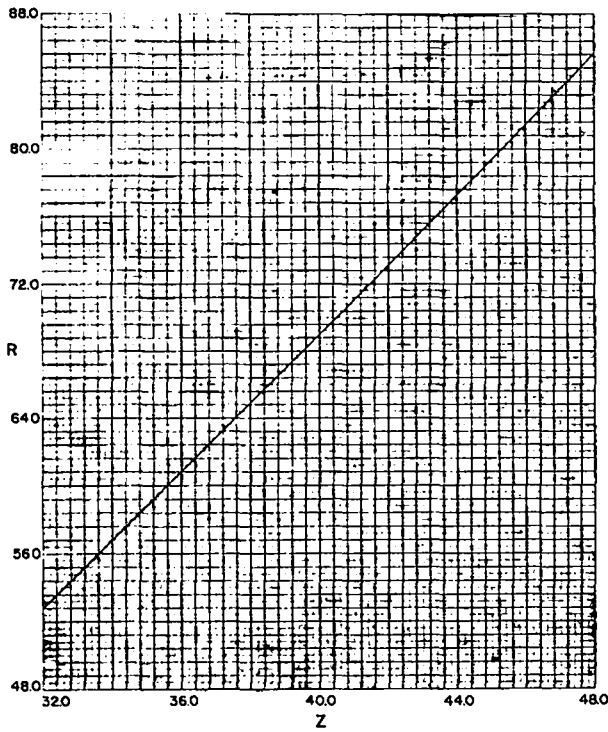
Fig. 6B. 5. Normalized trajectory.
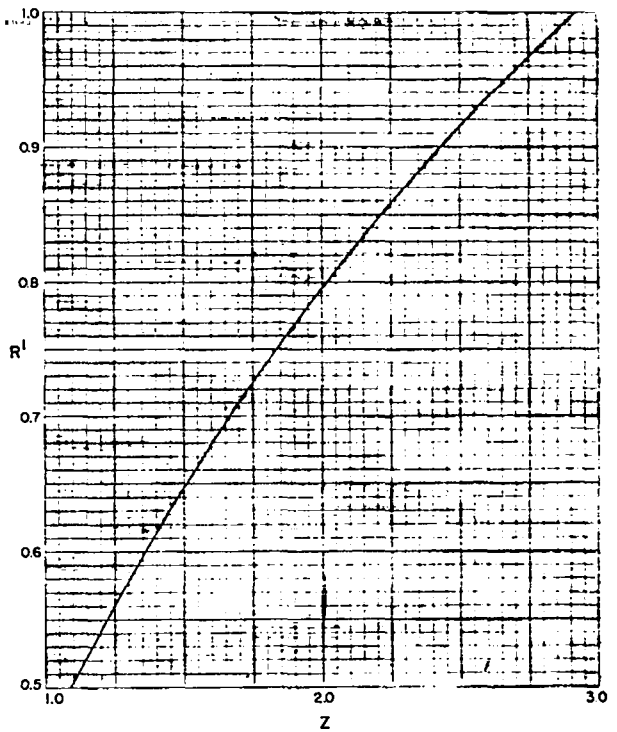
Fig. 6B. 7. Normalized trajectory slope.
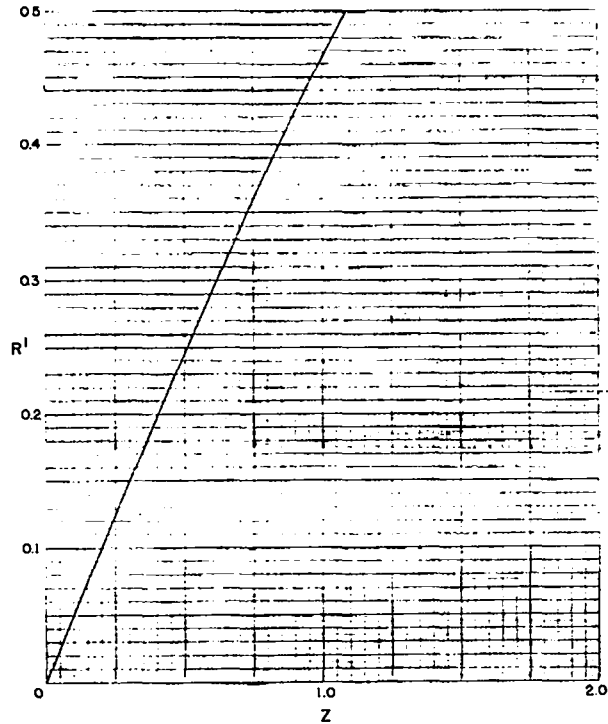
Fig. 6B. 6. Normalized trajectory slope.
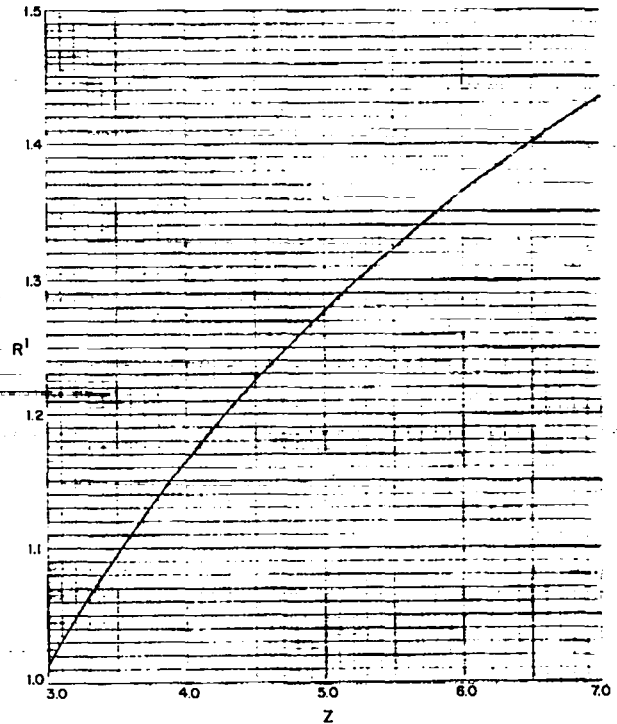
Fig. 6B. 8. Normalized trajectory slope.

220
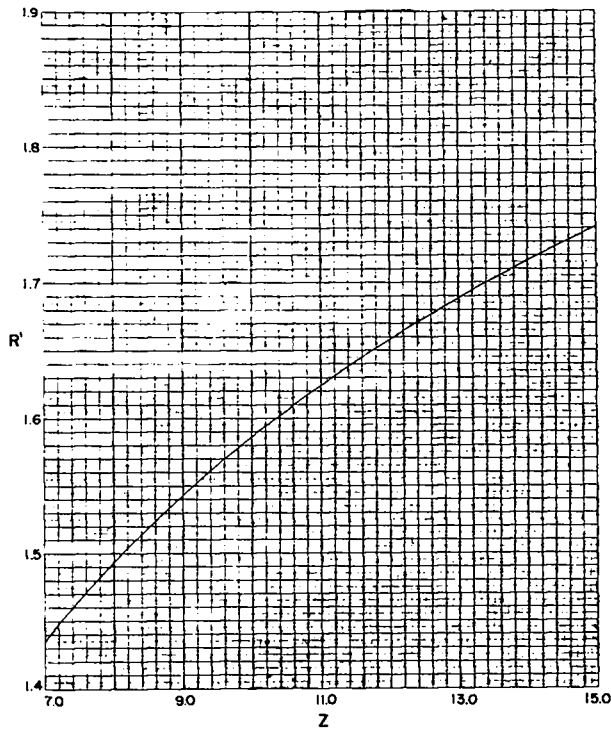
Fig. 6B. 9.   Normalized trajectory slope.
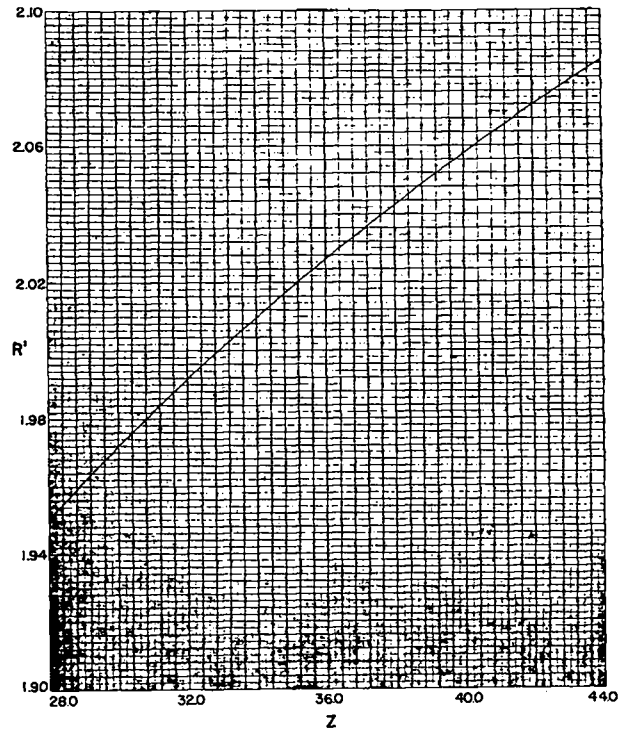
Fig. 6B.11.   Normalized trajectory slope.
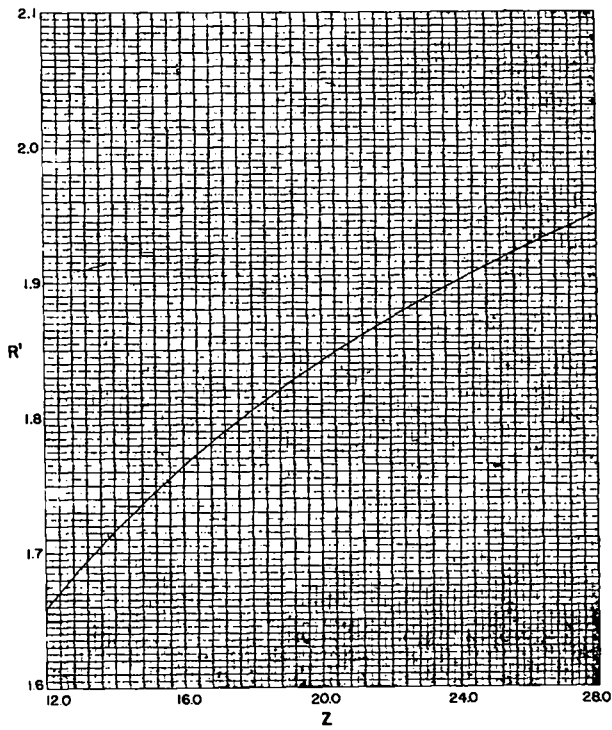
Fig. 6B.10.   Normalized trajectory slope.

221

Chapter 7

THE RADIOFREQUENCY POWER SOURCE

by
T. J. Boyd, J. N. Hardwick, J. R. Ruhe,
and E. J. Schneider

It was extremely fortunate that adequate high power radiofrequency generators had been developed successfully by other workers before this project began. Although their frequencies differed from that needed for PHERMEX, they were sufficiently close that a simple mechanical scaling of several basic components would have been almost satisfactory if no other requirements had entered the scene.

Consistent with the specific needs for PHERMEX, several modifications and innovations were made by this Laboratory. These are discussed below. For continuity, a broader description of the overall rf power system is presented also.

I. ACCELERATOR SECTIONS

PHERMEX is a standing wave electron accelerator consisting of three right circular cylindrical accelerator cavities. Each cavity is excited in its TM_{010} mode at 50 Mc/sec. The mode and frequency define a cavity diameter of 4.6 m. The cavity length and minimum useful electric field strength were fixed at 2.6 m and 4×10^6 V/m. An unloaded Q of 1.3×10^5 is consistent with these values for each of the copper-lined cavities.

During the early period of operation each cavity was energized to this same minimum field strength. Accordingly, the peak energy of the ejected electron beam was about 20 MeV. The electromagnetic fields in each cavity contained about 800 J, consistent with the dimensions and field strength of 4×10^6 V/m. Concomitantly, the wall losses amounted to 2 MW per cavity.

Recently an upgrading program has been completed by which the fields have been increased to 6×10^6 V/m in the first upstream cavity and 5×10^6 V/m in the second, with the fields in the third cavity remaining at 4×10^6 V/m. The corresponding stored energies are now 1600, 1200, and 800 J, respectively, with a peak electron energy of about 26 MeV.

II. RADIOFREQUENCY SYSTEM

A. Power Amplifiers

The rf power to drive the cavities is supplied by high level amplifiers, each using one RCA A-15041 shielded grid beam triode.[7.1] Figure 7.1 illustrates a typical high level amplifier. These
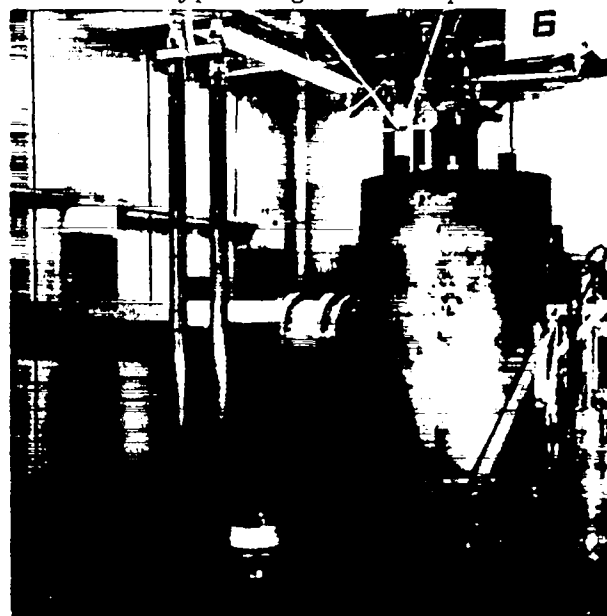
Fig. 7. 1. High level amplifier in operating position.

amplifiers are similar to those used in the Berekeley/Yale HILAC[7,2] but are scaled from 70 to 50 Mc/sec. Other modifications to the Berkeley/Yale design include an internal neutralization circuit and an enhanced spacing of elements in anticipation of pulsed operation up to perhaps 40 kV. At a 20 kV plate potential, each amplifier is capable of delivering 1 MW peak power for 3 msec at a maximum repetition rate of 15 pulses/sec. The tubes are operated in Class B with a plate efficiency of about 60%. The A-15041 operating parameters are summarized in Table 7.1.

Fig. 7. 2. Low level drive chain.

Table 7.1
Typical Operating Parameters of Final Amplifier

Tube	A-15041
Operation	grounded cathode
Cathode	multistrand thoriated tungsten
Filament potential	7.3 V
Filament current	1140 A
Dc plate voltage	20,000 V
Dc grid voltage	−600 V
Dc plate current	91 A
Dc grid current	0.9 A
Peak rf grid drive	3200 V
Driving power	2900 W*
Plate dissipation	690,000 W
Plate power input	1,820,000 W
Plate power output	1,130,000 W
Plate efficiency	62%
Cooling	air and water

*Less reactive losses

Four amplifiers drive the first cavity. Energy for the second and third cavities is supplied by three and two amplifiers, respectively. Transmission lines between the amplifiers and cavities have electrical lengths that are integral multiples of a half wavelength, to within about 5 cm. Coupling to the azimuthal magnetic fields in the cavities is achieved through rotatable loops.

B. Drive Chains

Each of the nine high level amplifiers is driven with an individual low level pulsed rf chain that terminates in a grounded grid stage using an Eimac 3W5000-A3 tube, as is shown in the block diagram of Fig. 7.2. The relative phase

between individual drive chains is adjusted by an appropriately matched variable delay line located in the grid circuit of each 8072 amplifier. The nine delay lines are fed from the output of a single amplifier, the 4CX1000A common drive stage.

Drive for the 4CX1000A stage is provided by a reactance-loaded crystal oscillator and a frequency multiplier stage. A nominal crystal frequency of 3.125 Mc/sec is used in the variable frequency oscillator. This frequency is then multiplied to the 50 Mc/sec cavity operating frequency. The master oscillator can be tuned ±250 cycles around the crystal frequency, thus providing a frequency excursion of ±4 kc/sec about the natural frequency of the cavities.

The rf drive for all stages beyond the master oscillator is pulsed for approximately 3 msec. Cavity fields attain essentially steady state conditions in about 1 msec. A portion of the remaining time is used to sample the cavity fields for amplitude and phase. If these parameters are favorable for proper beam acceleration, a permissive signal is generated which triggers the electron injector and the irrevocable explosive experiment.

C. Frequency and Phase Tuning

During operation, the master oscillator is tuned to the natural frequency of the first cavity. Tuning slugs are then used to adjust the frequencies of the remaining cavities to match that of the first. These tuning slugs have a tuning range of 7.5 kc/sec, a range similar to that of the oscillator, which is more than adequate to

cope with the cavity frequency drifts resulting from changes in ambient temperature. A frequency drift of 3 cps per minute is typical during normal working hours.

Once the drive frequency and the resonant frequencies of the three cavities have been adjusted to a common value, the inter-cavity phasing is adjusted to maximize the electron beam output, as observed by charge collected at the target. The desired phase between the first and second cavities is set by adjusting the delay lines in the drive chains to the first cavity. The desired phase between the second and third cavities is set by adjusting the delay lines in the drive chains to the third cavity. Delay lines in the first and third cavity drives provide unique inter-cavity phase adjustments. Those delay lines in the drive chains to the second cavity are used only for intra-chain phase adjustment. Once phases between cavities have been set, it is seldom necessary to readjust them; it is necessary only to keep the drive and cavity frequencies locked to a common, albeit constantly changing, value.

D. Power Supplies

The dc plate power demand of each high level rf amplifier is supplied by a 100 μF energy storage bank. At present, each bank is charged to 20 kV, thus providing a 20 kJ energy reservoir. A typical rf pulse extracts 30% of the stored energy with an attendant voltage slump of about 15%.

Capacitor banks are charged by three 0 to 45 kV, three phase, full wave rectifier units, now set at the 23 kV output tap. These rectifier units are each capable of handling a 0.5 MW peak load at 100% duty cycle. A water cooled triode, type ML-6696, is used as a series regulator between the rectifiers and each energy storage bank. The grid of the regulating triode is programmed to re-establish the initial anode operating voltage at the bank and to maintain a constant charging rate consistent with the pulse frequency, thereby maintaining an essentially constant demand on the incoming power lines.

The bias, screen, and anode supplies of the remaining pulsed rf stages consist of capacitor energy storage banks. The capacity of each bank is such that bias and screen voltage variations over the 3 msec pulse interval are held to 1% and the anode slump to 10%.

III. CONTROL AND MONITORING

Because of the nature and size of PHERMEX, flexible systems for control and monitoring are essential. These systems are housed in two main buildings: the Power Control building and the PHERMEX chamber.

The Power Control building has three rooms on the first floor: the Energy Storage room, containing nine equipment racks and nine capacitor banks; the Control room, with 52 racks and a control console; and the RF room, with 34 racks and nine high level amplifier stations. The basement houses the Motor Control center, the water and air cooling systems, and electrical patch centers for control and monitoring.

The PHERMEX chamber contains the accelerator cavities, electron gun, electron optical system, vacuum systems, and an auxiliary electrical patch system for both control and monitoring.

A. Control Wiring

All equipment racks and control stations are permanently connected to the control patch center with 32 conductor cables. At the rear of each rack is a terminating board that handles up to six cables. The patch center accommodates 900 of these cables, or approximately 29,000 conductors. Cables between buildings and racks are laid in trays and are readily accessible for repairs or replacement.

To install a circuit, three patch wires are required: one from the control panel to the terminal board in the control rack, one from the unit to be controlled to the terminal board at the base of its rack, and one connecting the two racks at the patch center.

B. Monitoring

All rf system monitoring is done through a coaxial cable system similar to the control system. This permits the display of any function at any one of several positions on the control console. To reduce the number of monitors required, most function signals are channeled into a switching system that allows selection of a specific function. More critical functions, such as A-15041 grid and plate currents that are closely observed during run-up, are displayed on individual monitors.

Functions that may be monitored through-out the rf amplifier system are: filament voltages, dc control grid voltages, screen grid and anode voltages, grid and anode currents, and rf grid drives. Currents drawn by the VacIon pumps are also remotely monitored in the Control room and these currents give an indication of pressure.

In the basement of the Power Control build-ing there are inlet and outlet monitors for cooling water flow, pressure, and temperature. Inlet cool-ing water pressure and outlet flow on the 3W5000-A3 and A-15041 tubes are interlocked on an individual circuit basis. A fault must exist for 10 sec before it will trip the interlock, in order to avoid making the circuit inoperable because of momentary variations. Monitoring in the Control room is limited to a "go—no go" indication for these interlocked functions.

C. Operation

PHERMEX is divided into three sections for control purposes: the electron gun, the low level rf, and the high level rf. There are four modes of operation covering the various combinations of different sections as follows:

> Mode 1. Electron gun
> Mode 2. Low level rf
> Mode 3. High level rf
> Mode 4. Full operation

Modes 1 and 2 can be run simultaneously. To operate in a higher mode, the machine must be run up in sequence from Mode 2. When Mode 3 is energized, Mode 1 is automatically dropped out, permitting complete rf operation without pro-ducing radiation. Mode 4 returns the electron gun control for full operation.

D. Personnel Safety

Motors and pumps that may be controlled from the Control room are also equipped with controls and a disconnect switch located within sight of the unit to allow personnel to lock out or control the unit locally for maintenance or service purposes.

All doors, exterior and interior, are inter-locked with the machine controls. One interior door into each area has a bypass control to per-mit entrance for trouble-shooting. When the by-pass has been energized, visual and audible in-dication is given in the Control room. Doors equipped with a bypass control, but not within sight of the control console, are locked as a part of the operating procedure. The only keys for these doors are kept in an interlock panel in the Control room. Removal of a key from the inter-lock panel initiates an audible alarm.

The radiation hazard zone is under constant surveillance through a closed circuit TV system. This TV circuit is run through the coaxial cable patching system so that cameras can be set up throughout the site to observe any hazardous operation.

IV. COOLING AND PROTECTION

A. Cooling Water System

Four basic cooling circuits provide the necessary cooling water and air for the electronic components. Three of these, the tube cooling deionized water system, a chilled water system, and an auxiliary water system, are located in the basement of the Power Control building. The fourth, a cooling tower system, is located at a distance sufficient to provide protection from blast damage during explosive experiments.

The deionized water system for cooling tubes is a closed system that supplies cooling water for the high level rf amplifier tubes and for the series-regulator tubes in the energy storage facility. The specific resistivity of the water is maintained at 5 $M\Omega$-cm by continuous circulation through a deionizing circuit. The system includes an 18.9 m^3 stainless steel storage tank. All piping is copper tubing with silver soldered joints.

The chilled water system supplies 4.4°C water to three air handling units that feed cool air to the electronic equipment racks. The temperature of the air supplied to the racks is maintained at 20°C by controlling the chilled water flow through the unit. The water is chilled by a hermetically sealed centrifugal refrigeration unit.

The auxiliary water system supplies cooling water for circulation through the water cooling jackets on the accelerator cavities. Water is pumped from the basement of the Power Control building to a manifold in the PHERMEX chamber. From the manifold, water is distributed to cavity jackets and bulkhead cooling coils. The water is exhausted into an open drain, enters a collection tank, and is pumped back to the basement for reprocessing. However, for low repetition rates, this cooling system is not required.

The cooling tower system is conventional. Water from the tower is circulated through the condenser of the chilled-water-system refrigeration unit and through two heat exchangers to cool the deionized and auxiliary cooling water.

B. Protection

The water to each rf amplifier chain is controlled and monitored at a water control panel. Each amplifier chain has five water circuits. The flow rate, pressure, and temperature are monitored at each circuit. For protection of the tubes, the inlet pressure and outlet flow on each circuit are interlocked to provide power shutoff to the tubes in the event of a water failure.

Should the 20 kJ stored in the individual energy storage banks be allowed to discharge into an amplifier tube as a result of a fault in the tube or its associated circuitry, it could seriously damage the tube. In order to protect the tube from such damage, a spark gap is used to divert the stored energy from the tube to an energy sink. A current transformer in the plate lead of the amplifier tube is used to sense any fault and to supply a triggering signal to a commercially made, triggered spark gap. In the event of a fault, virtually all the stored energy is diverted through the gap to be dissipated in a sink resistor.

NOTE AND REFERENCE

7. 1. The commercial version of this tube is designated RCA 6949, and, when tested for pulsed operation, it is A-15041.

7. 2. E. L. Hubbard *et al*, *Rev. Sci. Instr.* 32, 621, (1961).

Chapter 8

MECHANICAL PROBLEMS

by
B. T. Rogers

PHERMEX not only includes the electrical and mechanical aspects of a very high current electron accelerator but also includes the blast proof structures which inclose it. However, the design of such impulse resistant structures is not discussed here since the procedures that were used have been fairly well worked out and the fundamental concepts are covered in the available unclassified literature.[8.1-8.13] Instead, a brief description of the design features of important components of the accelerator is presented.

I. PRELIMINARY CONSIDERATIONS

The basic design of the vessel was executed in detail by the mechanical engineering staff of Group GMX-11. The vessel system was made completely compatible with the physics of the situation and the major engineering problems were resolved. A complete stress analysis constituted a part of this basic design. The result of this design effort was a set of drawings from which, for all practical purposes, a complete vessel system could be fabricated. A set of preliminary specifications was drafted. One important provision of these specifications was that the vessel should be constructed in strict accordance with the Code for Unfired Pressure Vessels (Section VIII, ASME Boiler and Pressure Vessel Code) and should be so stamped.

These specifications also required that the vendor provide a complete set of shop drawings for prior approval by LASL. This is more or less standard practice in projects of this scale, since the vendor must state clearly and precisely what he proposes to do and how he intends to do it. This step was very important, particularly so in the case of the fabrication of a large vacuum vessel.

Many experienced vendors think in terms of standard fabrication procedures, some of which are completely incompatible with good vacuum practice. These unacceptable details must be detected and corrected before the part is fabricated. Therefore, prior approval of shop drawings is one of the methods used to eliminate these unacceptable procedures.

A final, and perhaps most important, procedure to insure a satisfactory vessel was the appointment of a senior engineer to serve as resident engineer and inspector during the construction phase. This representative worked with the vendor's engineers and craftsmen during the production phase and was vested with approval and rejection authority of all details. He coordinated the work of independent inspection services retained to perform radiography and leak testing and evaluated the results of these service groups and, in general, observed and, in many cases, directed every critical phase of vessel fabrication. The fact that a highly successful vessel was produced is in large part the direct result of his careful attention to every detail, no matter how minor, of fabrication procedure.

A large number of materials were required in the fabrication of the PHERMEX vessel assembly. The major critical item was copper clad steel plate. This was required for the shells of the hard vacuum accelerator sections and represented a major expense item. While the vendor was required to purchase most of the materials for the vessel, it was made mandatory that he use plates supplied by LASL for the shell sections. This process assured a high quality inspection of one of the most important structural components. For the PHERMEX vessel system, all shell plates were subjected to 100% ultrasonic inspection.

Group GMX-1 of the Los Alamos Scientific Laboratory developed a special automatic ultrasonic scanning machine that made it feasible and practicable to inspect an entire plate with an overlapping crystal traverse path. The system was truly 100% inspected. As a result, some plates, or parts of plates, were rejected for laminations, porosity, or poor copper-to-steel bond. A lamination that terminated in a weld-root crack could produce a leak so tenuous that it would probably escape detection by means of the common techniques. Thus this inspection, consistent with our allowable leak rate specifications which required that no detectable leaks of any sort would be accepted, was most important.

The copper clad plates were delivered to Los Alamos with the copper surface protected by a film of plastic that was well bonded to the surface and very hard to remove. The surface was further contaminated by lubricants used in the fabricating mill, probably palm oil. As the efficient functioning of a resonant cavity accelerator is directly related to the surface conductivity of the cavities, a very thorough cleaning process was necessary. It was required that the surface of the cleaned plate have a conductivity equal to OFHC copper when measured at 50 Mc, the operating frequency of the cavity.

Plate cleaning was arduous and long. A variety of reagents was used to produce the desired cleanliness and electrical conductivity, depending on the condition of the particular plate. Solvents were used to cut the plastic coating. A typical copper etchant recipe was:

> 25 g $FeCl_3 \cdot 6H_2O$
> 90 ml H_2O
> 10 ml conc. HCl
> 1 to 2 g $NaClO_8$

This is representative only of a large number of "brews" that were used.

II. VESSEL DESIGN

The primary structural element of PHERMEX proper is a large vacuum vessel. This vessel is about 15 ft in diameter and 35 ft long, and consists of a number of sections. Some sections must operate at a pressure of the order of 10^{-7} torr.

Other sections that are primarily structural in character operate at about 70 μ. In view of the fact that large vacuum vessels present a somewhat specialized area of pressure vessel design, it would seem proper to discuss the design of this vessel.

From a mechanical engineering standpoint a vessel of this sort can be broken down into three major parts: the two heads that close the ends of the shell assembly; the shell, consisting of five discrete sections in this case; and the support structure for the entire assembly. These elements are considered in the above order.

In addition to satisfying the basic physics requirements of vessel performance, a minimum standard for quality of construction was established. A vacuum vessel of this volume, when evacuated and surrounded by atmospheric pressure, represents a nontrivial store of potential energy. This energy, if accidentally released through structural failure, could present a major hazard to life and property. Therefore the vessel was constructed in complete compliance with the ASME Boiler and Pressure Vessel Code, Section VIII (Unfired Pressure Vessels), inspected by an independent inspection agency, and so stamped.

A. Heads

In considering heads for a machine in which the resonant cavities are to be right circular cylinders with the ends held to a plane surface, the natural reaction is to design a flat head. Higher frequency machines have been built in this fashion. Thick section flat head designs were studied but were rejected because of their impracticality.

Successful flat heads of thin material provided with exterior stays have been designed, constructed, and placed in use by GMX-11. These heads performed well in service and were reconsidered as potential candidates for the problem at hand. There have been two designs; the first being a crossed "T" beam form of stiffening in which structural Tee sections were welded to the thin head in such a manner that the head material became effective as part of the structural system. The second system used a radial array of wide flange beams that terminated in an annulus

around the center port. The annulus absorbed the fixed end moments of the beams and was very sturdy for this reason. The shell was welded to the flange of the beams and served as a vacuum barrier with some secondary structural contribution. Both of these heads were nominally 15 ft in diameter and served their purpose well. The crossed beam array was an early design executed by the writer, and the radial array was the work of H. G. Worstell, a member of the engineering staff of GMX-11. Figure 8.1 shows the crossed beam head and Fig. 8.2 shows the radial beam stiffened head. It should be pointed out that the flat, externally stayed heads may be easily constructed of copper clad steel with cladding on the inside and thus avoid the problems of copper plating.

When the design of the PHERMEX vessel was being established, it became apparent that the ends of the resonant cavities should not be part of the structural system of the vessel. This decision was dictated by the requirement that the ends be water cooled and that there be space for beam confining coils of large size within the head structure and between the cavities. The cavities were terminated by copper diaphragms hung from the shell sections. Electrical continuity between the shell (fabricated from copper clad steel)
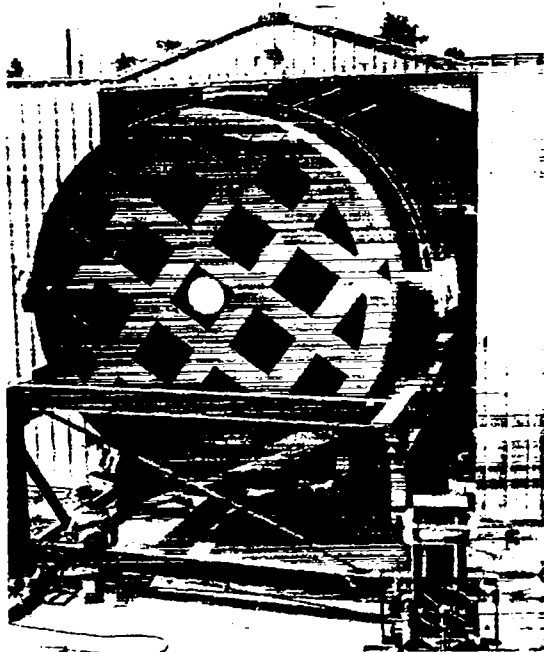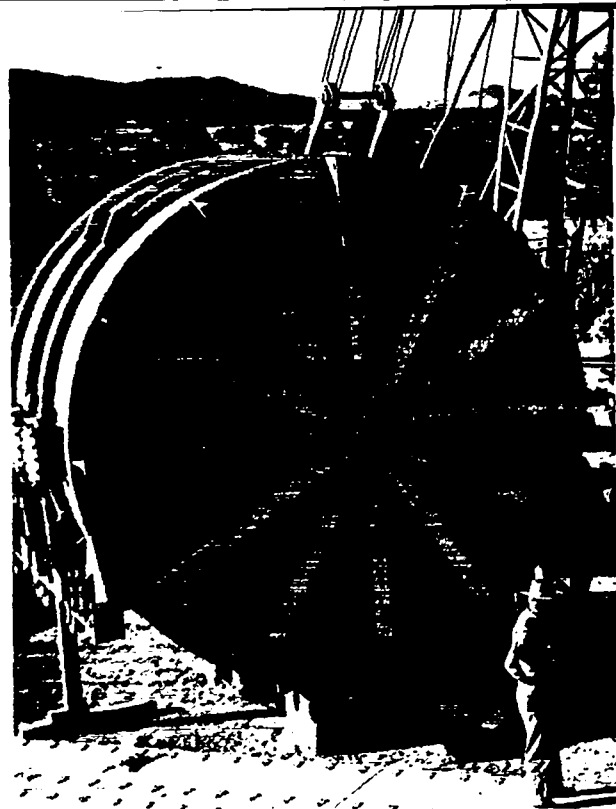
Fig. 8. 2. Radial beam head.

and the diaphragm was established by a thin preformed copper fillet welded to both the shell copper and the suspended diaphragm. This part of the system is described later.

To satisfy the closure requirements, in which the heads were required to house field confining coils, standard ASME torispherical heads were recommended by the writer and accepted. A standard ASME torispherical head is defined as a head proportioned as shown in Fig. 8.3, in which the values of r, L, and material thickness are established in keeping with the rules of Section VIII of the ASME Boiler and Pressure Vessel Code.

Fig. 8. 1. Crossed beam head.

L = INSIDE CROWN RADIUS
r = KNUCKLE RADIUS
s = SKIRT
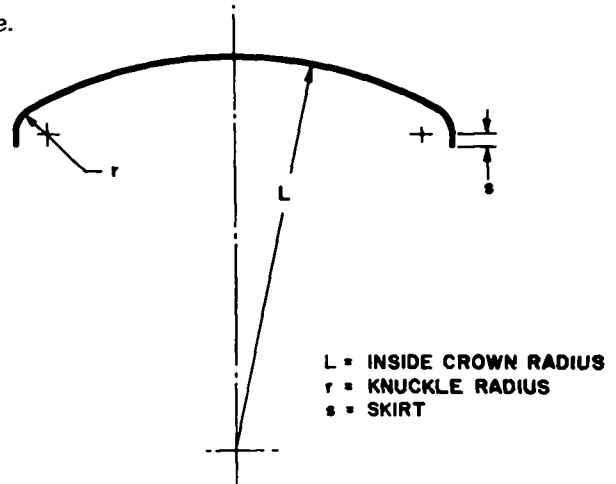
Fig. 8. 3. ASME torispherical head.

Heads of this proportion when subjected to external pressure fail by elastic instability; that is, the head fails from progressive deflections that start well within the elastic range of the material. A vessel under internal pressure will deform within the elastic range and when the pressure is removed will return to its original dimensions. Similar elastic deformations in a vessel subjected to external pressures may lead to buckling and catastrophic failure. Straightforward design procedures have been developed on a semiempirical basis (backed by theoretical analysis and model tests, and further supported by extensive field experience) to cover the design of heads under external pressure. These methods make use of design charts constructed for various materials, and the charts and procedures have been made a part of the ASME Code. Typical design computations can be found in Section VIII of the ASME Boiler and Pressure Vessel Code and its appendixes:

Simple flat heads without stays become very thick even of strength alone is considered. When severe deflection limitations are imposed, a flat head becomes very thick indeed.

Some comparative data further illustrates the point:

Table 8.1.

Comparative Properties of Flat and Torispherical Heads

	Simple flat head limited by strength only	ASME torispherical head
Thickness	3.86 in.	0.625 in.
Wt/ft²	157.5 lb	25.5 lb
Wt of head	27,833 lb	5452 lb

The cost of spinning a 180 in. diameter head from the material supplied by the customer is listed at about $200, so it can be seen that the cost of spinning a torispherical head is a minor item on a project of this sort.

B. Shells

In the design of large vacuum vessel shells, considerable advantage may be gained by making use of fairly thin materials and providing adequate stiffening to prevent collapse of the vessel. The situation is somewhat parallel to the design of an externally stayed head. The mode of failure is again an elastic instability condition.

If we consider a ring under uniform external loading, it can be shown that there is a critical pressure at which the ring becomes unstable, and further that the number of nodes the ring will go into can be computed. The two-node mode results in the lowest value for the critical pressure and governs the design calculations. The higher number of nodes, 4, 6, 8, etc., are of interest in studying vessels with other conditions of constraint.

However, the simple ring approach is inadequate since a cylindrical structure with stiffening rings represents an entirely different configuration of forces.

Because this vessel was to be constructed according to ASME code standards, the code requirements for shell thickness and stiffening rings are examined and the shell stability requirements are computed by use of the code design charts mentioned in the discussion of head design. An acceptable design can be shown to be one in which the space between the stiffening rings is 36 in. The dimensions of the ring are 2 in. by 5 in., with the longer dimension normal to the shell surface. Data obtained from the design charts indicate that these design dimensions provide the necessary support and include a safety factor.

C. Vessel Support

While the structural steel work used to support the PHERMEX vessel is of strictly conventional design, the elastic support of the cavity system is worthy of some comment. The vessel

sections were provided with Vee groove casters and the top member of the support structure had an inverted angle bar welded to it to provide a rail for the casters. When the sections were inserted into the chamber they were rolled into position along the rails. This design was adopted to minimize the size of the removable section of the chamber.

Two problems of support were involved. It was necessary to allow for differential expansion between the support structure and vessel proper. It was necessary to prevent excessive deflection of the vessel assembly due to its own weight. Further, there was the problem of dealing with the shock loading from explosive experiments and the possibility of plastic deflection at the support points under the influence of this shock loading.

The design finally adopted made use of a rigidly welded assembly front-support for the system, a "soft" suspension at each caster, and a sliding shoe type of bearing at the rear to accommodate thermal excursions. The front of the vessel is the end nearest to the explosive experiment.

The "soft" suspension was provided by placing a pack of Belleville spring washers of robust proportions under each of the 16 caster spindles. Load stroke curves were run for each pack of matched washers and the back-up plates were adjusted so that each caster carried just the right part of the total load of the vessel. The result is that the vessel is rigidly supported at the ends (four points) and floats on 16 elastic supports that just compensate for any tendency of the shell to sag.

The suspension has provided excellent service and there has been no detectable tendency of the machine to sag between rigid supports.

III. COPPER DIAPHRAGM

As was mentioned before, the electrical termination of the cavities was established with a copper diaphragm or bulkhead. The design of these bulkheads was complicated by the requirements that they be of OFHC copper, that they have a continuous electrical and mechanical bond with the copper surface of the cavity shell, that they be provided with passages for water cooling, and that they be very flat. A number of practical considerations dictated a thickness of $\frac{1}{4}$ inch, forming a disc of copper $\frac{1}{4}$ in. thick with a diameter of about 15 ft. The conductivity requirements made it necessary that the bulkhead be in the dead soft condition.

The dry weight of these subassemblies was 2790 lb. The cooling water in the channels added about 180 lb to this total for an in-service weight of almost 3000 lb. It is difficult to lift such a disc without yielding or buckling it from the action of its own weight. Furthermore when in place in the cavity assembly, it must be free to expand or contract without bowing or bulging. It should be pointed out that these bulkheads are subject to no loading from atmospheric pressure. The cavities are at a pressure on the order of 1×10^{-7} torr and the pressure in the heads and coil sections is about 70 μ; so the loading from this differential is trivial.

H. G. Worstell worked out a design for dealing with the above conditions. This was adopted and has given trouble-free service since the machine was placed in operation. In essence the scheme involves a radial array of some 40 leaf springs that carry the bulkhead and are in turn supported by a back-up flange welded to the inside of the vessel shell. A system of shoulder bolts provides axial constraint and at the same time provides enough clearance so that the bulkhead is free to move in the radial direction. A 1/16 in. thick copper membrane forms the conducting fillet between the copper diaphragm and the copper interior surface of the cavity shell. This membrane was formed with segmental discs and TIG welded in place with copper welding rod. The whole system was leak tested. Leaks were eliminated to avoid any gas migration between the hard and soft vacuum systems.

Water cooling for the bulkheads was provided by two circuits of copper tubing of rectangular cross section. These circuits were fabricated by copper welding and applied to the bulkheads with soft solder to establish a thermal bond. The whole assembly, with solder preforms, was set up in a large furnace; the furnace was slowly and uniformly brought up to soldering temperature and slowly cooled. Extensive tooling and weighting was required to perform this operation satisfactorily.

Figure 8.4 shows one of these bulkheads in place. The multitude of leaf springs that support the diaphragm can be seen around the periphery of the copper bulkhead just inside of the main assembly flange.
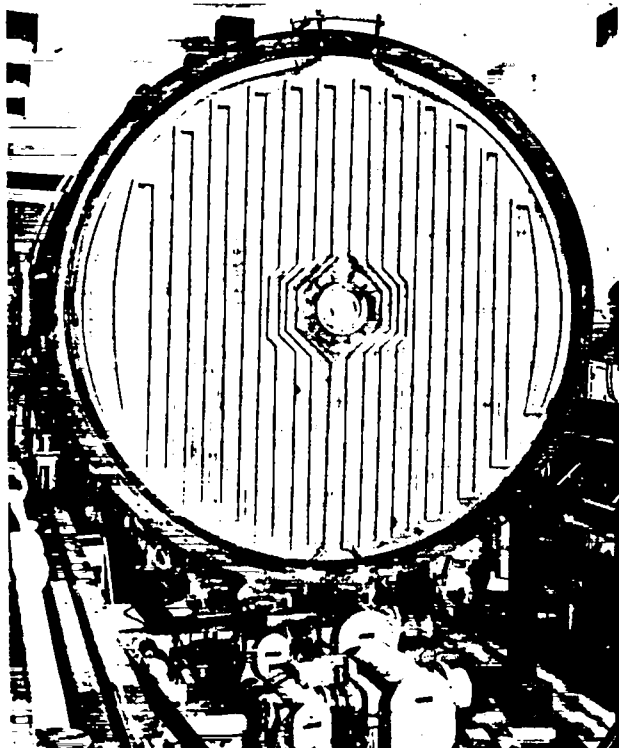

Fig. 8. 4. Copper bulkhead in place.

IV. PHERMEX MECHANICAL SYSTEM

It was necessary to construct a major ancillary mechanical system to support the PHERMEX plant. The primary function of this system was to dissipate waste heat, some 8,700,000 Btu/hr. Most of the electrical energy input to the machine appears as heat to be rejected to atmosphere; only a trivial portion appears in the electron beam.

The system can be broken down into three operating systems and a heat rejection system as follows:

1. Deionized water system, plus three subsystems.
2. Chilled water system.
3. Auxiliary cooling water system.
4. Cooling tower recirculating system.

The deionized water system is a two leg design. Four 300 gpm pumps supply water to the electronic load through three supply headers operating at pressures that are proper for the cooling circuits they serve; only three of these pumps are operated at any given time, one being held in reserve as a standby. The principal load on this system is nine A-15041 amplifiers. The second leg of this system takes water from the deionized water storage tank (5000 gallon capacity), circulates it through a heat exchanger, and returns it to the storage tank. This is the temperature control leg. A third small system takes water from the storage tank, runs it through the deionizer and returns it to the tank. This system has performed well in service and has a number of advantages over a low capacity series system. The large storage tank results in excellent temperature stability and is capable of absorbing considerable contamination without adversely affecting the conductivity of the water. It has never been required to shut PHERMEX down because of high conductivity troubles. The usual system conductivity is about 0.16 μmho/cm^3. Another advantage of the large capacity parallel system is that one can clean a fouled strainer in the heat exchanger raw water supply with the machine in operation. As a result of the large mass of deionized water in the storage tank, only a minor system-temperature rise is experienced during this emergency operation. The large storage capacity also permits an orderly shutdown procedure in the event of a major leak in one of the amplifiers or other system components. This has never happened, but it is a comfortable sort of insurance.

The chilled water system provides water for the cooling coils in the air handling units. All rack-mounted electronic gear is air cooled with a plenum supply below the floor and returns above the ceiling. Some idea of the total anticipated load to be handled by this system may be visualized by considering the centrifugal water chilling

unit. It is sized to handle a load of 174 tons with 45°F supply water and 72°F return. The heat rejected by this unit is taken by the cooling tower recirculating system.

The auxiliary cooling water system is a closed series system with a heat exchanger and is also piped for cooling tower water. This system is used for cooling components that do not require deionized or chilled water. Typical items are the cavity shells and heads.

The cooling tower recirculating system is served by two 1050 gpm pumps. The tower is designed for 83°F inlet water and 72°F outlet water at 62°F wet bulb temperature. It is an induced draft unit with two-speed reversible fans and a deep sump to deal with the low operating temperatures that occur from time to time at Los Alamos during the winter months. The tower was designed to withstand 50 lb/ft² wind loads to avoid damage from the abuse that it is subjected to when explosive experiments are fired nearby.

Some idea of the general character of mechanical installation can be gained by examining Fig. 8.5. This is a general view of the mechanical equipment room; the graphic control panel for the system can be seen in the left foreground, and one of the nine amplifier water control panels is visible at the end of the operating aisle (center background).
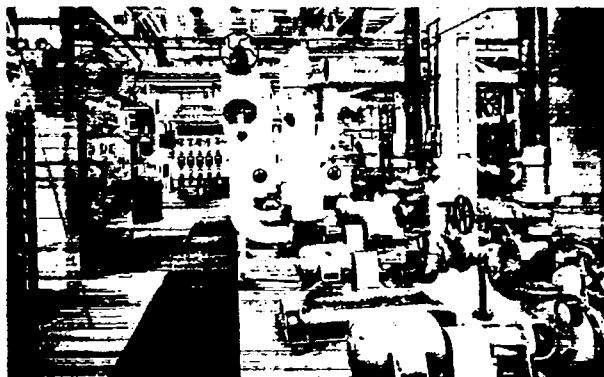

Fig. 8. 5. PHERMEX mechanical equipment room.

REFERENCES

8. 1. Joseph Lipka, *Graphical and Mechanical Computations*, John Wiley and Sons, Inc., New York, 1918.

8. 2. W. F. Cassie, *Structural Analysis*, Longmans, Green and Co., Ltd., London, 1961.

8. 3. L. C. Urquhart, C. E. O'Rourke, and G. Winter, *Design of Concrete Structures*, McGraw-Hill Book Co., Inc., New York, 1958.

8. 4. P. G. Hodge, Jr., *Plastic Analysis of Structures*, McGraw-Hill Book Co., Inc., New York, 1959.

8. 5. S. F. Borg and J. J. Gennaro, *Advanced Structural Analysis*, D. Van Nostrand Co., Inc., Princeton, 1959.

8. 6. A. S. Niles and J. S. Newell, *Airplane Structures*, Vols. I and II, John Wiley and Sons, Inc., New York, Vol. I 1954, Vol. II 1958.

8. 7. S. Timoshenko, *Strength of Materials*, Vols. I and II, D. Van Nostrand Co., Princeton, 1956.

8. 8. B. W. Boguslavsky, *Design of Reinforced Concrete*, The Macmillan Co., New York, 1956.

8. 9. R. J. Roark, *Formulas for Stress and Strain*, McGraw-Hill Book Co., Inc., New York, 1954.

8.10. *Steel Construction*, American Institute of Steel Construction, New York, 1957, 5th Ed.

8.11. H. L. Callahan, *Structural Design to Resist Dynamic Loads*, (an address presented at the University of Kansas Structural Conference, Lawrence, Kansas, December 4, 1959).

8.12. *Fundamentals of Protective Design*, (Engineer Manual for War Department Construction), Corps of Engineers, Office of the Chief of Engineers, 1946.

8.13. *Design of Structures to Resist the Effects of Atomic Weapons*, Corps of Engineers, U.S. Army (a series of manuals):

EM 1110-345-414, "Strength of Materials and Structural Elements," 15 March 1957.

EM 1110-345-415, "Principles of Dynamic Analysis and Design," 15 March 1957.

EM 1110-345-416, "Structural Elements Subjected to Dynamic Loads," 15 March 1957.

EM 1110-345-419, "Shear Wall Structures," 15 January 1958.

EM 1110-345-420, "Arches and Domes," 15 January 1960.

EM 1110-345-421, "Buried and Semiburied Structures," 15 January 1960.

Chapter 9

MECHANICAL ALIGNMENT

by
B. T. Rogers

Mechanical alignment of PHERMEX concerns the precise positioning of all its electron optical components with respect to the electro-mechanical axis of the cavity accelerator sections. This is done in such a way that radial displacements lie within 0.01 in. of the axis and angular displacements are held within 3 milliradians of the axis over the entire optical path of about 90 ft. The electron optical system has been discussed in Chapter 6, so that it is unnecessary to review its details here. The need for the precision indicated here has been established by practice, not theory. Therefore, only the alignment procedures are presented; theory is omitted.

There are two areas of importance: internal alignment of components during assembly or during periods when the machine is opened to atmospheric pressure, and external alignment which concerns locating experiments precisely on the axis of the radiation beam, as well as the realignment of the radiation target without disturbing the vacuum of the machine proper. These two alignment operations are discussed below.

I. INTERNAL ALIGNMENT

Before PHERMEX cavities were installed, the PHERMEX chamber was carefully measured and all critical grades checked. The hypothetical center line of the machine was established, and the support structure was erected with reference to the established line and grade and carefully checked.

At the rear of the chamber, the intersection of the PHERMEX centerline with the 2 ft thick rear chamber wall was established and the point of intersection scribed on the inside surface of the wall. At the front of the chamber, the face of the 3 ft diameter nozzle was scribed with the vertical and horizontal centerlines.

Alignment during assembly was accomplished by observing optical alignment targets mounted on the different components of PHERMEX. The components were jacked and shimmed into position as the machine was assembled. When alignment was satisfactory, each component was bolted in place, and in some cases assembly welds between parts of the mounting pads were made. In the case of the welds, it was necessary to estimate weld shrinkage and allow for this in the initial alignment of the component.

The alignment targets were observed through a Keuffel and Esser alignment telescope mounted on a special removable fixture specifically designed for this function, Fig. 9.1. Grade was maintained with a 1 sec of arc striding level that was indexed on the hardened and ground cylindrical barrel of the telescope. Because of extensive rigging activity nearby, the fixture was designed around a kinematic system to be removable, having only two small assemblies and a pressure
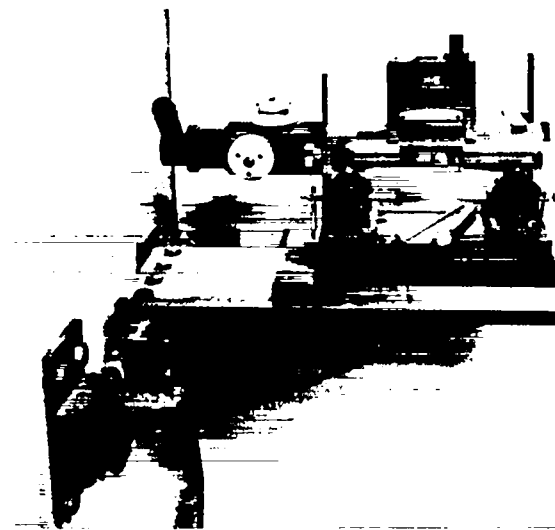

Fig. 9. 1. Removable alignment telescope fixture.

plate attached to the wall. The kinematic system consisted of a ball and cup, a cylinder and Vee, and a pressure point; the whole fixture and telescope can be removed and replaced with excellent reproducibility of alignment.

Inspection of Fig. 9.1 reveals that the telescope is mounted on four independently adjustable conical supports that reduce to two effective Vee blocks of zero axial thickness. Plumb lines were ranged on the nozzle centerlines and the telescope was then bucked in on the centerline of PHERMEX. This was done by successively reversing the telescope in the cone mounts and observing the fiducial scribed on the rear wall and the ranged lines at the nozzle in succession. The mounts were adjusted until the telescope was exactly on the centerline.

The striding level was used to monitor the diurnal variations in the massive rear wall. When a significant change in the vertical of this wall occurred, the observer would remove all targets and would then reset on the ranged lines by adjusting the front set of cones. The diurnal variation of the wall from the vertical amounted to about ±6 sec of arc. The error introduced by sighting on the rear fiducial was nearly zero because of the short base distance. While the use of ranged plumb lines for the fiducial at the nozzle rather than, say, taut wires or a glass target, might seem a bit pedestrian, plumb lines provided, in fact, a most satisfactory target. Orange plumb lines were used and, at the distance existing between the telescope and the lines, they subtended a slightly larger angle than the cross hairs. When the system was aligned well, one observed a black cross hair with an orange border — a very sensitive and easily observed target.

After the massive major components of PHERMEX had been completely assembled and all assembly welds had been made, the vessel was allowed to settle for a few days, after which the base centerline was shifted to the actual physical axis of the assembled PHERMEX — a trivial adjustment. The minor components were then located on the "machine" centerline, which was tied, by reference, to the construction centerline.

During the initial phases of machine operation a similar system of optical alignment was repeated each time PHERMEX was opened to atmospheric pressure. The wall-hung telescope mount was used to check alignment, and minor changes in the relation between the machine centerline and the construction centerline were observed as the normal progression of explosive experiments, fired in near proximity to the front of the chamber, slowly shook PHERMEX into a more and more stable location.

After the initial "shakedown" operation of PHERMEX had nominally put the machine into a stable location, a less cumbersome system of alignment was devised. This was initially proposed in an internal document by the author which described the external control methods and recommendations for construction of internal monuments. The final selection of the internal method of control was deferred until the in-service development of PHERMEX had reached a state when massive concrete monuments could be constructed within the chamber, without jeopardizing the operation of the facility.

Before discussing the final alignment scheme it is necessary to describe a few of the tools and principles of optical tooling technique. We will describe first some of the tools:
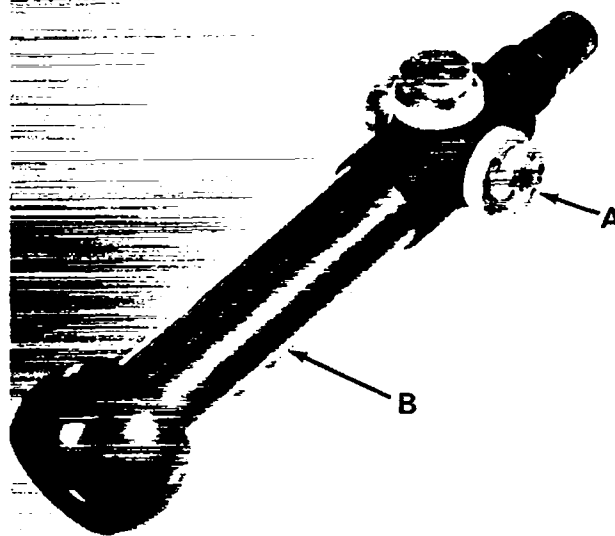
1. Optical alignment telescope (Fig. 9.2).

Fig. 9. 2. Optical alignment telescope.

This telescope is characterized by a hardened and precisely ground cylindrical barrel (B), micrometers that can displace the line-of-sight with respect to the cross hairs (A), and a line-of-sight

that at 0-0 micrometer setting exactly coincides with the centerline of the barrel. The diameter of the barrel is 2.2498 in. (+0, —0.0003 in.).

2. Spherical adapter with collet (Fig. 9.3).

Fig. 9. 3. Spherical adapter with collet.

This adapter is a 3-½ in. diameter spherical sector with a concentric collet that accommodates the barrel of the alignment telescope so that the centerline of the telescope exactly intersects the center of the sphere. An alignment target can also be inserted into the collet so that the center of the pattern is exactly centered in the sphere.

3. Alignment target (Fig. 9.4).
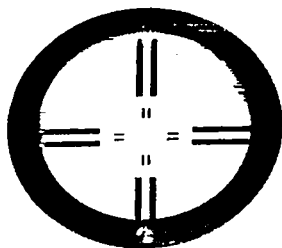
Fig. 9. 4. Alignment target.

This target usually consists of a glass disc with an aluminum alignment pattern deposited on the glass. The pattern is designed to optimize pointing accuracy when observed through the alignment telescope. It is mounted in a steel ring which fits the spherical adapter described above.

4. Adjustable cup mount (Fig. 9.5).
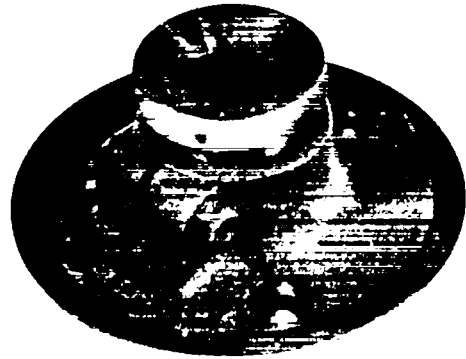
Fig. 9. 5. Adjustable cup mount.

The cup of this mount is designed to support a spherical adapter in such a manner that the location of the center of the sphere is uniquely defined for any given position of the height adjustment. The truncated conical base will accommodate a support fixture for the alignment telescope (alignment telescope bracket). By this means the alignment telescope, when fitted with a spherical adapter, can be adjusted through a fairly wide range at horizontal and vertical angles, with its axial centerline at all times passing through a uniquely defined point in space. In internal alignment practice, the cup mount is bolted to a heavy steel plate which is in turn bolted to a massive concrete monument. The height adjustment is locked in a location that puts the "uniquely defined point in space" on the centerline of the PHERMEX cavity system.

Figure 9.6 shows the whole assembly in place. The striding level can be seen resting on the barrel.

The other alignment tool that is unique to the PHERMEX internal alignment scheme is the straddle gauge. As the projected centerline of the machine would be surrounded by the drift tube for the emergent electron beam, a special target had to be designed. This system, shown in Fig. 9.7, consists of a concrete monument with two pillars so located that the machine centerline passes between them.

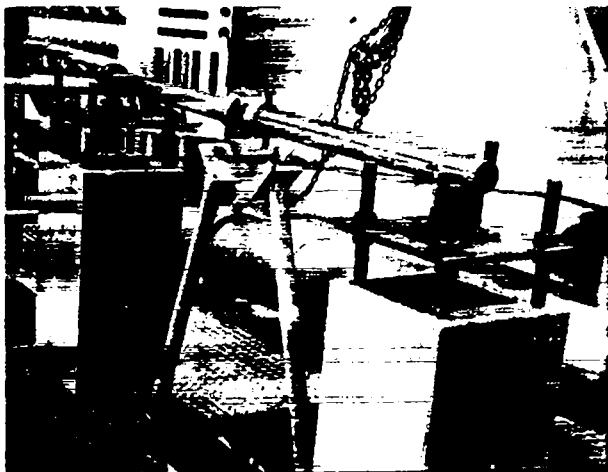Fig. 9. 6. Alignment telescope assembly in use.

Fig. 9. 7. Straddle gauge.

One pillar is fitted with an adjustable cup mount and the other with a narrow Vee support. The straddle gauge has a spherical adapter with a collet fitted to one end and a bore for an optical alignment target at the center. The target is set vertical with a level, the ball and cup define the lateral location, the Vee supports the other end, and vertical adjustments are made by moving the cup and Vee up and down by means of screws. When the target has been set on the centerline of the machine, all adjustments are locked and

the straddle gauge becomes a primary alignment standard. The gauge is removable and replaceable at will so the machine can be assembled and subsequently put into service. When machine alignment is next checked, the drift tube is removed and the gauge replaced. The alignment telescope with its sphere and cup mount and the target in the straddle gauge precisely define the machine axis. It should be pointed out that the center bore for the alignment target places the target face on the common centerline of the straddle gauge shafts. Minor deviations from the vertical of the target face do not introduce a parallax error into the centerline location.

In setting the location of the adjustable cup mount for the alignment telescope, an alignment procedure was used that greatly simplified the operation. The alignment telescope was placed on the adjustable cone wall mount and carefully positioned in so that it lay exactly on the cavity centerline. This was done by observing targets located in the upstream and downstream nozzles of the PHERMEX cavity system in rotation. The cones of the mount were adjusted until the axis of the telescope and the center of the targets all lay on a common line. A spherical adapter with target was then placed on an adjustable cup mount on the steel mounting plate of the rear monument. This was adjusted until the target also lay on the cavity centerline as observed through the telescope. Bolt holes were drilled and the cup mount was locked in place. After rechecking, all adjustments were locked in their final position. The telescope was then fitted with a spherical adapter, the cup mount on the monument was fitted with an alignment telescope bracket and the telescope transferred to the monument. The cavity targets were observed from the new location of the telescope as a final check on this operation.

The system of internal monuments was first placed in use on October 27, 1964. At that time the concrete was still slightly green and it was anticipated that some shrinkage would be observed after the monuments had fully cured and come to equilibrium with the conditions existing in the chamber. A check of the system on November 30, 1965, revealed that the cavity system appeared to be uniformly 0.090 in. above the line-of-sight. This was interpreted as monument

shrinkage. A check of the Portland Cement Institute shrinkage chart showed good agreement with this interpretation. The monuments are nominally 12.323 ft high and the anticipated shrinkage in inches per 100 ft for a six-sack per cubic yard mix, and a water-cement ratio of six gallons per sack of cement, would be 0.69 in./100 ft. The shrinkage measured would equal 0.73 in. per 100 ft. These figures are in surprisingly good agreement and well within normal batching tolerances for concrete mixes. Figure 9.8 shows the referred-to chart with the batch characteristics and shrinkage plotted on it.

6×10^{-7}. If we assume that there is a temperature difference of 30°F between the steel system and the concrete monuments and we use an approximate centerline elevation of 148 in., we find:

$$30 \times 148 \times 6 \times 10^{-7} = 0.00266 \text{ in.}$$

A 0.003 in. error from this rather extreme case is not a major cause of concern. A similar argument applies to the centering of the straddle gauge on the two-pillar monument; however in this case the base dimension is only 24 in. Thermal gradients from one end of the PHERMEX chamber to the other, as well as throughout the monument cross section, could present a severe source of error. The great mass of the chamber and its installed equipment, plus the fact that the space is thermostated for winter heating, seems to have made errors from this source small. However, the matter is scheduled for further investigation.

Figure 9.9 shows a photograph of a model of the PHERMEX bunker with the top removed. The monument for the alignment telescope and the straddle gauge monument are indicated on this illustration.

Fig. 9. 8. Concrete shrinkage nomogram.

Superficial examination of the alignment scheme raises the question of thermal effects, in view of the fact that we have a steel system with concrete monuments and no system of temperature compensation. A few comments are in order. The usually accepted coefficient of linear expansion for concrete is 55×10^{-7} per deg F and for steel, 61×10^{-7} per deg F, a difference of

Fig. 9. 9. Monument locations in PHERMEX chamber.

238

II. EXTERIOR SYSTEM

The interior system is devised to provide a high order of optical alignment precision. Once the optical axis is established, one has the capability of determining planes perpendicular to the axis by means of autoreflection for those planes which are distant from the telescope and by means of autocollimation techniques for planes close to the instrument. Thus one can accurately establish line, grade, and angular error of the various machine components. For critical components, such as the electron gun, this is done with great pains and to a high order of accuracy. This work is undertaken at the infrequent times when the machine is opened to atmospheric pressure, and it is not uncommon to spend several days checking machine geometry and locating replacement parts in exact optical alignment.

The problem of establishing external alignment presents an entirely different situation. There are two rather different objectives. In one case the external alignment is defined by the projected optical axis of the machine, extending beyond the bremsstrahlung target to any point that may be of interest for locating experiments. In the other case, one is interested in accurately establishing a line in space from the valve in the downstream nozzle of·the PHERMEX cavity to some instrument station located beyond the end of the blast-resistant bull nose. This operation is required when it is desired to change the downstream drift tube hardware without disrupting the vacuum in PHERMEX; i.e., when the downstream vacuum isolation valve is closed.

In the first case a rapid, accurate experiment alignment is required. The system also must be adaptable to programmatic experimental work executed in keeping with a tight schedule. The alignment should be a normal step in the experiment setup procedures. These setup procedures are designed to maximize the efficient use of the machine time. An inefficient, time-consuming alignment system or one of such sensitivity that much time is wasted would be intolerable. The system must be satisfactorily usable by technicians who have primary competence in the areas of electronics and explosive technology.

The aluminum blast tip of the bull nose is attached by a bayonet-type locking device and is usually replaced on each shot. An adjustable cradle for supporting a modest alignment telescope is attached in place of the blast tip, making use of the bayonet locking device. The telescope is placed in the cradle pointing first toward the machine and a center mark on the beryllium electron catcher is observed. This check is made to assure that the cradle has not been improperly inserted or that its adjustment has not been tampered with. The telescope is then reversed so that the observer is now looking away from the machine and down the firing pad; a distant target is observed. This target is set on the centerline of the machine. At this time a minor adjustment of the front screws of the telescope cradle may be required to center the target in the reticule. The axis of the telescope is now assumed to be on line, as the effect of minor adjustment of the front screws on the short back sight alignment is trivial. The experiment is now set in place and aligned with respect to the axis of PHERMEX. This method provides rapid and accurate alignment, well within the requirements of the experimental program. It is not necessary to perturb the machine to establish alignment.

Figure 9.10 illustrates the procedure and shows the alignment telescope in place on the adjustable cradle, all mounted on the front of the bull nose and ready to align an experiment.

Fig. 9.10. External alignment telescope.

The various steps involved in establishing external alignment of the machine (as distinguished from alignment of experiments) are covered in detail in an internal document by the author. Most of the elements of these procedures had been implemented at this writing; the rest will probably be brought into use when the need arises. In general, the alignment philosophy has been to stay at least an order of magnitude ahead of the demonstrated precision requirements of the system. This is obviously a converging process. Although the machine has been operational since August 1963, there is still a generous supply of techniques of increasing elegance that have not yet been called upon.

The current technique makes use of the straddle gauge as a target and a number of isolated concrete monuments that have been set into the undisturbed tuff of the firing mound at various locations along the axis of the machine. Offset monuments have also been placed on the mound and some of the on-line monuments are hundreds of feet from any point at which an explosive experiment has been fired. These monuments are brass-capped and protected by a concrete slab with a steel cover. When not in actual use they are further protected by a layer of sandbags. Figure 9.11 illustrates the details of a typical monument.
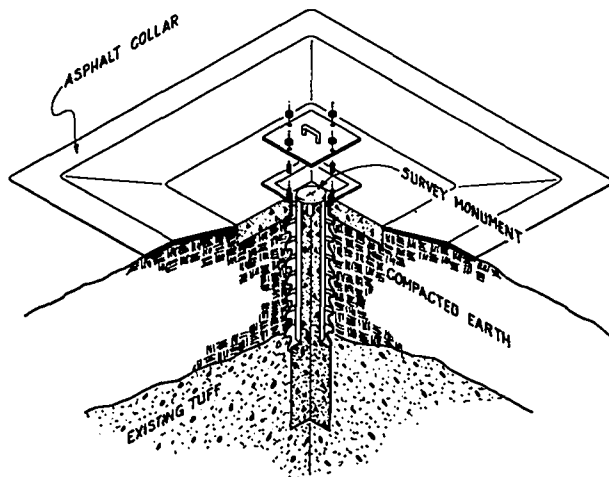
Fig. 9.11. Typical external monument.

The brass caps have been marked for line by observing a target with the alignment telescope when the telescope had been accurately set on the machine axis.

The procedure that is used to locate those critical machine parts that lie downstream from the exit aperture of the cavity system, without perturbing the hard vacuum of the machine proper, is as follows:

1. Close the downstream ball valve between the cavity system and the drift tube.

2. Remove the drift tube section that passes over the straddle gauge monument.

3. Put the straddle gauge in place.

4. Remove the bull nose tip, electron catcher, target, window, and any other obstructing hardware.

5. Set a jig transit over an appropriate monument on an instrument stand.

6. Sight on the straddle gauge target and elevate the instrument until the reticle is sighted on the center of the straddle gauge and the instrument is level.

7. Recheck to assure that the instrument is still centered over the monument mark, and that the instrument is level when centered on the straddle gauge target.

8. Repeat steps 5, 6, and 7 until the three conditions are satisfied, i.e., centered over monument, level, and on target.

9. Proceed to locate parts by means of alignment targets centered in the part and autoreflection mirror placed normal to the face of the part or, in the case of long tubes, a target at each end.

A few comments are in order. It should be pointed out that a jig transit can be plunged and then rotated about the vertical axis in such a manner that the monument mark can be observed through the hollow vertical spindle. When the

well-leveled instrument shows no relative motion between the reticle and the monument marking while being rotated about the vertical axis, and the mark is centered in the reticle, the condition that the center of the instrument is over the mark is satisfied. (In optical tooling practice this is referred to as optically plumbing the instrument.) Further, an instrument stand, unlike a surveyor's tripod, allows one to raise and lower the instrument so that the procedure of step 6 is possible.

The accelerator section of the machine is not exactly level. The deviation from horizontal has been measured and found to be on the order of 1-$\frac{1}{2}$ to 2 sec of arc. In the above procedure this error has been ignored. The reasoning is as follows:

1. The straddle gauge is set on the axis of the machine and should be a stable reference now that the monuments are fully cured.

2. It is seldom necessary to align a part that lies more than 25 ft from the straddle gauge.

3. One second of arc subtends a little more than 0.001 in. at 25 ft.

In the event that this error seems important in the future, the level error of the machine will be determined precisely, and then an appropriate correction will be made in alignment procedure. At this time it is not a matter of serious concern; effort spent in this direction could probably be better expended in correlating the relationship between the electromagnetic and mechanical axis of the machine.

III. SUMMARY

The practical day-to-day methods to keep PHERMEX mechanically aligned have been outlined. These methods are in keeping with the basic philosophy, previously stated, of maintaining the elegance of mechanical alignment about an order of magnitude ahead of demonstrated need for precision, and to do this with a minimum of disruption of machine operation. In most cases time charged to alignment has been effectively zero as other considerations, such as maintenance, require the machine to be out of service on occasions. Alignment procedures are usually exercised during these routine maintenance operations.

Chapter 10

A HYDROGEN PURGING TECHNIQUE TO ENHANCE PUMPING SPEED AND ULTIMATE VACUUM

by
B. T. Rogers and H. G. Worstell

This chapter describes the vacuum system design, the bases for component selection, the system performance, the development of a hydrogen purge technique, and the outgassing data that have been obtained from system operations. The purpose of these descriptions is to make available to those contemplating the construction of large vacuum systems the techniques and methods used for PHERMEX. This system has presented no operating problems since the first pump was started on the newly assembled machine and has exceeded the minimum performance specifications in every category.

The PHERMEX vacuum vessel is approximately 11.1 m long and 4.56 m in diameter. The complete assembly weighs approximately 10^5 kg and consists of seven sections, each of which is 4.56 m i.d. Figure 10.1 is a conceptual drawing of the completed assembly.
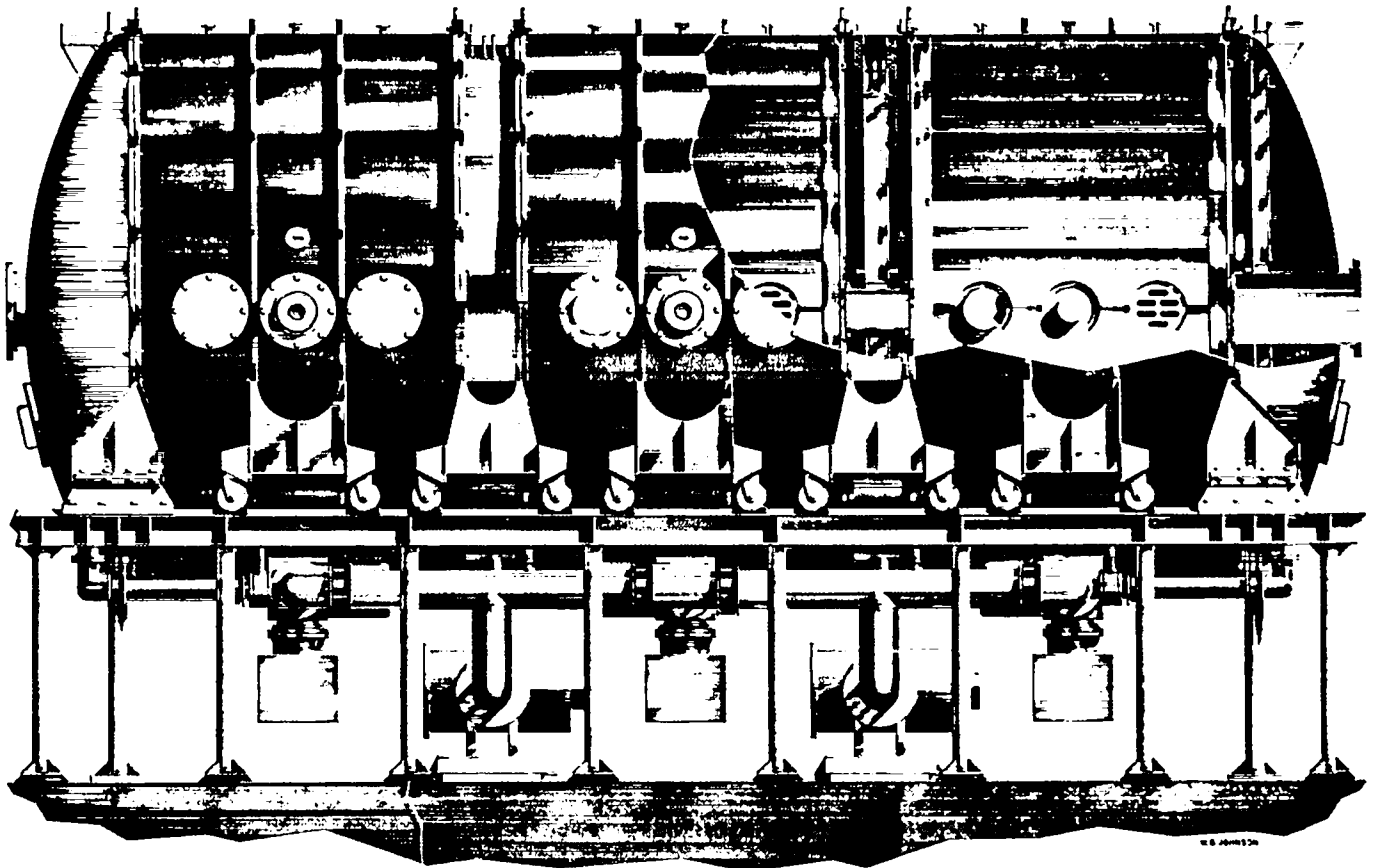
Fig. 10.1. Conceptual drawing of PHERMEX.

The three identical high vacuum accelerator sections were fabricated from copper-clad steel. There is a 4.56 m diameter, 6 mm thick, water-cooled copper bulkhead at each end which serves as a highly conducting surface for rf currents. These bulkheads also separate the high vacuum and soft vacuum regions. Each accelerator section contains six 45 cm diameter nozzles, a 43 × 61 cm manhole, and four 30 cm diameter nozzles; each section is encased by a steel water jacket to maintain the temperature near 21 °C. The total high vacuum volume of the three sections is 132 m^3 with a surface area of 2.4×10^2 m^2 of which 99% is OFHC copper. The balance of the surface area is comprised of carbon steel, stainless steel, aluminum, and elastomer seals. There are 47 m of metal seals, 25 m of Viton-A seals, and 410 m of welds in the high vacuum system. This system has never been baked out and is evacuated with six 1000 liter/sec ion pumps.

The four soft vacuum sections consist of two 51 cm thick coil sections and two end heads, and have a total volume of about 40 m^3. A pressure of approximately 70 μ is maintained in the entire soft vacuum system during operation by a small Welch pump, Model 1397. The heads and the coil sections contain coils for generating beam-confining magnetic fields. The hard vacuum system threads these coils from bulkhead-to-bulkhead by means of stainless steel spools in the case of the coil sections, and by nozzles in the heads. An electron gun at one end of the vessel and a drift tube and target at the other end complete the hard vacuum envelope.

The original design specifications called for a copper-lined vessel with three cavity-accelerator sections and necessary ancillary sections. This vessel was to be evacuated from local atmospheric pressure to 1×10^{-6} torr in 16 hr by a pumping system that would introduce no hydrocarbon or mercury contamination. Further requirements were that the system use metal seals where possible and that the linear feet of elastomer seals be kept to an absolute minimum.

When the project was started, titanium sput-tering pumps were available commercially and small VacIon pumps were just appearing on the market. A primitive test setup, known locally as the Standard Dirty Volume (SDV), was assembled and used for comparative testing of pumps. The SDV consisted of about 6.1 m of 25 cm diameter brass tubing fitted with flanges and ion gauges, all assembled with soft solder. It was a vacuum system that consistently represented the most adverse conditions to be expected. A few runs from atmospheric pressure quickly provided a comparative figure of merit representing pump capability under anticipated, adverse, nonlaboratory conditions. Several models of sputtering pumps were tested and found to be incapable of performing satisfactorily under these conditions. By this time, high capacity VacIon pumps had become available, and tests using the SDV indicated that such pumps would be satisfactory. Time has shown this conclusion to be correct. Other ion pumps were tested and rejected for various reasons, such as inadequate capacity or inability to withstand shipping.

Experience soon showed that ion pumps were susceptible to "swamping" when looking into very large volumes. Swamping describes a pressure situation (usually about 7×10^{-5} torr in the case of PHERMEX volumes) at which the pump heats and outgasses faster than it can reduce the system pressure. Swamping results in excessive heating, and if allowed to continue results in irreversible pump damage. To avoid swamping, it was decided to select a roughing system that could pump the hard vacuum system below this critical pressure. The system chosen consists of two parallel arrays of pumps, each composed of a Heraeus VPR-6000, a VPR-1600, and a two-stage Heraeus DK-180 in series. As the DK-180 has a rather small throughput, the system is valved so that the initial evacuation of the entire vessel (to approximately 1 torr in both the hard and soft systems) is handled by two Kinney KD-310 pumps operating in parallel. A schematic diagram of the evacuation equipment is shown in Fig. 10.2. This system exhausts the hard vacuum volume to a pressure of 2×10^{-5} torr; however, in practice the ion pumps are usually started at 5×10^{-5} torr. After the ion pumps have started, the roughing system is valved off from the hard vacuum sections and is not used again until a hydrogen purge is introduced, as described later.

243
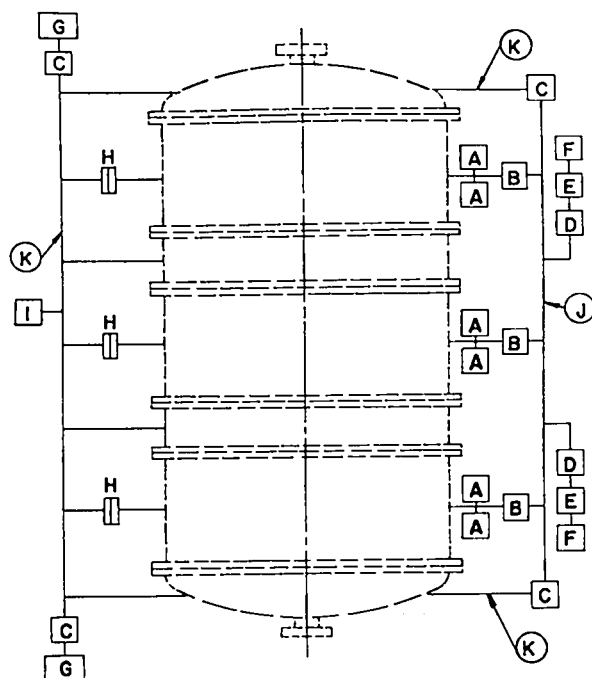
(A) 1000 LITER/SEC ION PUMP
(B) 12 INCH VALVE
(C) 6 INCH VALVE
(D) VPR 6000 PUMP
(E) VPR 1600 PUMP
(F) DK 180 PUMP
(G) KD 310 PUMP
(H) 12 INCH RUPTURE DISC
(I) 1397 WELCH PUMP
(J) 12 INCH MANIFOLD
(K) 6 INCH MANIFOLD

Fig. 10.2. Schematic diagram of evacuation equipment.

To recapitulate, a typical pumpdown procedure representative of current practice is outlined. The description starts where the Kinney KD-310 pumps have been isolated from the hard-vacuum side of the system, and the Heraeus series-parallel arrays of mechanical pumps are in operation. The hard vacuum system is then at a pressure of about 1 torr. Pumping continues to a pressure of 1.5 to 2×10^{-4} torr. Then, the high vacuum system is purged with hydrogen and exhausted to 8×10^{-5} torr. At this point, the ion pumps are energized and allowed to heat to a temperature of 65°C. They are then shut off and allowed to cool. After the ion pumps have cooled to nearly ambient temperature, the system is repurged with hydrogen. The ion pumps are started and usually pick up the pumping load, without heating, at this point. After the ion pumps are stabilized, the roughing packages are valved off from the hard vacuum system and let up to air.

These are not started again until a later hydrogen purge is introduced. Typically, the time required to go from atmospheric pressure to 1×10^{-6} torr is about 5-½ hr.

In keeping with the original specifications, most of the seals in the hard vacuum volume are metal. After some study, a seal was developed consisting of 150 psi ASA flanges separated by a gasket made from 16 gauge, 2S aluminum wire, butt-welded by the Utica "Koldweld" process. The flanges, as purchased, have a cold water finish, and about 80% of those received have surfaces adequate for hard vacuum service. A minimum of refurbishing makes even the unsatisfactory flanges adequate for hard vacuum applications.

Electron gun and drift tube seals are made with conventional flat copper gasket crush seals. In normal practice, the gun seals are opened more frequently than the other parts of the machine.

The general scheme for evacuating PHERMEX has evolved as the result of a number of years of actual experience with large, unbaked, copper-lined volumes, and represents what is believed to be sound operating practice. A great deal of experimental effort has been spent in developing and verifying these methods.

It is common knowledge among ion pump users that these pumps are rather fussy about the kind of gas they digest. Pumping speeds for noble gases and outgassing materials may be reduced to nearly zero. As the system is pumped down, the ion pump selectively pumps the gases for which it has an appetite and leaves the distasteful components. This process continues until the system becomes saturated with gases that cannot be consumed efficiently. A state is reached where further reduction in pressure becomes a very slow process.

This dilemma arose about 7 years ago in conjunction with work on a prototype single-cavity accelerator. At that time ion pumps were considerably smaller than those commercially available today. A great deal of trouble was experienced in starting the pumps on the prototype accelerator with a volume of 39 m³. Also it took as long as 2 weeks to reach a base pressure of 3×10^{-6} torr, a pressure still too high for satisfactory accelerator operation.

A purging technique was developed at this time which very effectively eliminated the undesirable residual gases and significantly improved the ion pump starting characteristics. Generally, hydrogen is used as the purge gas because of ion pump avidity for this gas. However, trapped air or nitrogen is nearly as effective, although these gases extend the pumpdown time. Furthermore, purging with air or nitrogen does not mitigate the ion pump starting problem nearly so much as does hydrogen in a system as large as the one described here.

Figure 10.3 illustrates the procedure now employed in purging the high vacuum sections in the form of a plot of the average data obtained for several pumpdown periods during early stages of machine operation. Briefly the technique is as follows:

1. At the end of the roughing cycle and just prior to starting the ion pumps, hydrogen is admitted to the system with the 30 cm valves closed (see Fig. 10.2) to increase the high vacuum section pressure to about 100 μ. This provides a residual gas dilution of one part in about 10^5.

2. The three 30 cm valves are then opened to the roughing pump system manifold; the rough pumps exhaust the system to the starting pressure of the ion pumps, and the ion pumps are started. The three valves are then closed, and the rough pumps are turned off.

3. The vessels are purged again when the pumping speed has been reduced by the evolution of outgas materials, and a base pressure plateau is impending. The vacuum system is designed so that purging may be accomplished at any time and as often as necessary.

To further evaluate the ion pump performance on outgas materials and to examine differential pumping characteristics, data were obtained from which the curves in Fig. 10.4 are plotted. This information was recorded some 6 months after initial evacuation, when pressures as low as 1.5×10^{-8} torr were observed and the surfaces were known to be moderately clean. The pumpdown time on air would have been considerably longer, and the system base pressure would have been much higher if these data had been obtained during initial evacuation and prior to rf heating of the copper surfaces.
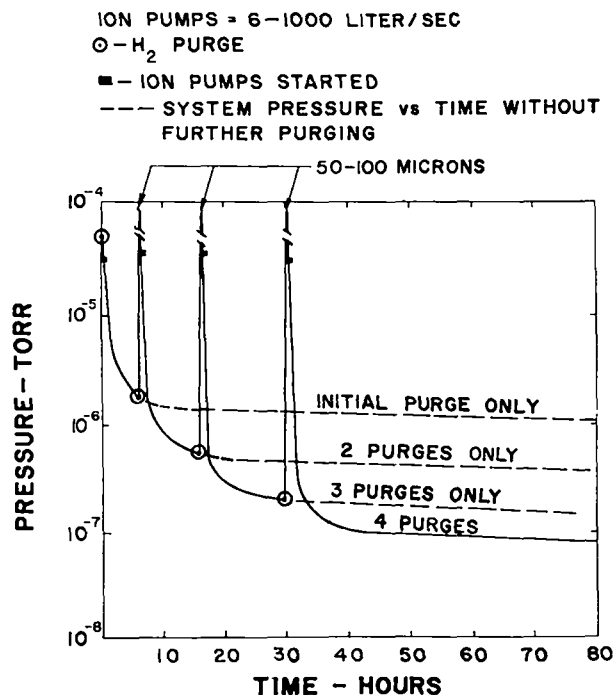
Fig. 10.3. Plots of data obtained during pumpdown operations.
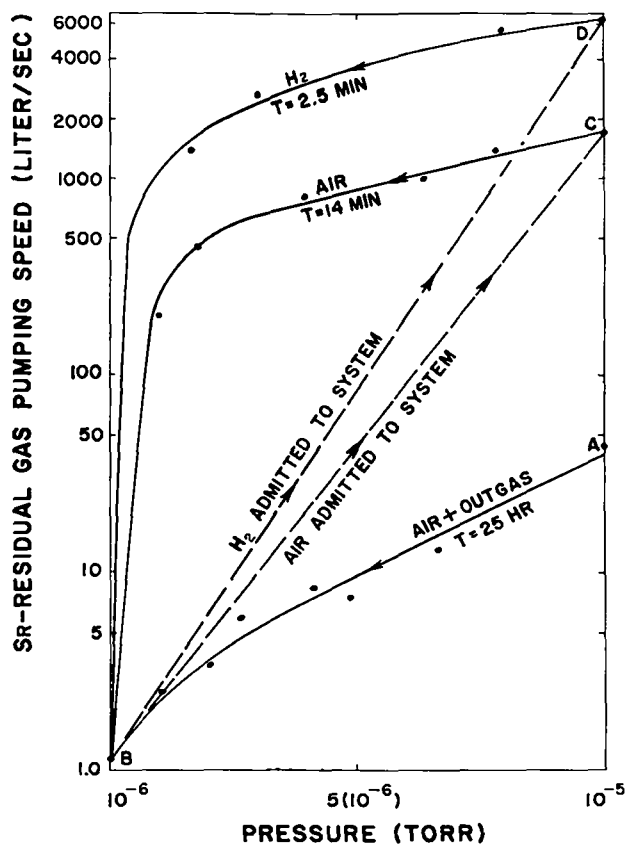
Fig. 10.4. Residual gas pumping speed vs pressure.

The vessel had been standing at air for 4 days prior to starting the roughing pumps. The ion pumps were started in the conventional manner and allowed to evacuate the system from point A, in Fig. 10.4, to 1×10^{-6} torr at point B, requiring 25 hr of pumping time. The pumps were then turned off; ambient air was admitted to the system from B to C, and the ion pumps were restarted at point C. The evacuation from C to B required 14 min. Hydrogen was then admitted to the system from B to D; the ion pumps were restarted at D; and again the pressure was reduced to point B, requiring 2.5 min of pumping time. Note that all three pumping curves converge at B. This pressure plateau near 1×10^{-6} torr has been observed on numerous occasions.

The balance equation for the pumping speed of the system at any pressure may be defined as:

$$S_p = S_o + S_R$$

(10.1)

where

S_p = total rate or speed of gas removal from the system by the ion pumps (liters/sec).

S_o = speed of outgassing plus leakage speed (liters/sec), which may be determined with reasonable accuracy by the rate-of-rise method. (The total leakage rate is known to be less than 6×10^{-6} std cm^3 air/sec from outgas rate determinations.)

S_R = speed at which pumps remove residual gas from the system, equal to:

$$\frac{2.3V}{t} \log_{10}\left(\frac{P_1}{P_2}\right) \quad \text{liters/sec}$$

(10.2)

V = volume of high vacuum system, 132,000 liters.

t = time (in sec) required for the system pressure to change from P_1 to P_2.

If one examines the pumping curves in Fig.

10.4, it seems reasonable to assume that essentially all the free air and nitrogen have been removed from the residual gas within a few hours after the pumps are started at point A. As the pump-down continues from A to B, the pumps remove most of the normal surface outgas materials and some of the residual gases. There are some outgas constituents, however, for which the ion pumps have practically no appetite; and these gases remain as part of the residual gas load. The process continues until, at point B, the residual gas is primarily composed of outgas components that the ion pumps find very distasteful, and S_R approaches zero. There are now 132,000 liters of gas in the system to be removed at the rate of a mere fraction of a liter per second, if the system pressure is to be reduced. It is indeed fortunate that outgassing diminishes with time.

If the system were purged at point B as described previously, the volume of residual gas might be removed in approximately 15 min and a new pumpdown curve similar to curve A-B obtained, except that starting point A is near 10^{-6} torr rather than 10^{-5} torr (see Fig. 10.3). Thus, the cycle is restarted, and a new pressure plateau is reached at some pressure considerably lower than point B of Fig. 10.4.

After S_R was obtained for the pumpdown from D to B, the pumps were turned off, and S_o was determined by rate of rise to be 55 liters/sec and equal to S_p, since S_R is virtually zero. In the lower 10^{-8} torr range, S_o was observed to be 310 liters/sec.

Outgas rates (including leakage) have been obtained for several conditions by turning off the pumps, observing the rate of rise, and calculating the outgas rate K:

$$K = \frac{V(P_1 - P_2)}{tA} \quad \text{torr-liters/sec/cm}^2$$

(10.3)

where P_1, P_2, V, and t are defined above, and A is the area of the outgassing surface, 2.4×10^6 cm^2. The results are shown in Table 10.1.

Note: All pressures are the average readings from three separate Veeco RG-75 ion gauges calibrated for air, and no correction has been made for any other gas.

Table 10.1
Outgas Rates

P_2 torr	P_1 torr	Time Under Vacuum	Time of Rise sec	Min K torr-liters/sec/ cm^2	Max K torr-liters/sec/ cm^2
1.5×10^{-5}	5.7×10^{-4}	100 min	1800	- - -	1.3×10^{-8}
1.0×10^{-6}	3.0×10^{-5}	30 hr	63900	2.5×10^{-11}	2.7×10^{-11}
7.8×10^{-8}	1.1×10^{-6}	60 days	13500	4.0×10^{-12}	4.6×10^{-12}
2.6×10^{-8}	3.3×10^{-7}	80 days	4500	2.4×10^{-12}	4.4×10^{-12}
1.7×10^{-8}	2.3×10^{-6}	5 months	57600	1.8×10^{-12}	4.1×10^{-12}

NAME INDEX

Adams, G. D. 17, 23

Al'tshuler, L. V. 23

Anson, J. H. 109

Bainbridge, K. T. 24, 90

Balchan, A. S. 23

Beams, J. W. 109

Bennett, S. D. 23

Bess, Leon 109

Bethe, H. 90

Bloch, F. 90

Boguslavsky, B. W. 233

Borg, S. F. 233

Boyd, T. J. 222

Buechner, W. W. 109

Burrill, E. A. 109

Bush, E. D. Jr. 186

Calbick, C. J. 109

Callahan, H. L. 233

Cassie, W. F. 233

Chechkin, V. V. 109

Cherry, Ivan 109

Clark, J. C. 23

Cloud, R. W. 109

Coates, W. M. 210

Coleman, P. D. 105, 109

Cowan, G. R. 23

Davisson, C. J. 105, 106, 109, 212

Dickman, D. O. 110

Dyke, W. P. 23

Emigh, C. Robert 31, 90

Gabor, Dennis, 104, 105, 109

Gennaro, J. J. 233

Goldhaber, M. 24, 90

Goldie, C. H. 109

Greisen, K. 90

Grundhauser, F. J. 23

Hanson, A. O. 56, 90, 109

Hardwick, J. N. 146, 186, 222

Hawkins, David 23

Heitler, W. 90

Herrmann, K. H. 23

Hess, W. N. 23

Hodge, P. G. Jr. 233

Hubbard, E. L. 226

Kerst, D. W. 17, 23

Khizhnyak, N. A. 103-105, 109

Kilpatrick, W. D. 98, 109

Kulenkampff, H. 90

Kushin, V. V. 109

Lanzl, L. 56, 90

Lawson, J. D. 90

Levi, Roberto 23

Lichtblau, H. 90

Lipka, Joseph 233

Manakov, M. A. 23

Martin, M. D. 23

McFarland, G. C. 23

Miller, C. W. 109

Miller, N. C. 23

Mills, B. Y. 109

Moliere, G. 90

Muirhead, E. G. 90

Nazarov, N. I. 109

Newell, J. S. 233

Niles, A. S. 233

O'Rourke, C. E. 233

Perry, Leo F. 23, 90

Petrunin, A. P. 23

Polyakov, B. J. 109

Roark, R. J. 233

Rogers, B. T. 227, 234, 242

Rossi, B. 90

Ruhe, J. R. 222

Rutz, W. A. 23

Schaaffs, W. 23

Schall, R. 23

Scheer, M. 90

Schiff, L. I. 90

Schittenhelm, R. 90

Schneider, E. J. 222

Shultz, H. L. 109

Seay, Glenn E. 23

Seely, F. B. 210

Segre, E. 90

Siegbahn, K. 90

Simon, L. E. 23

Smith, J. O. 210

Snoddy, L. B. 109

Spencer, B. M. 90

Sperduto, A. 109

Steely, J. D. 23

Taylor, R. W. 186

Thomer, G. 23

Timoshenko, S. 233

Tolok, V. T. 109

Trendelenburg, F. 23

Trump, J. C. 109

Urquhart, L. C. 233

Van de Graaff, R. J. 109

Venable, Douglas 5, 15, 24, 90, 91, 109, 146, 186

Wadey, W. G. 109

Welch, J. A. 23

Williams, E. J. 90

Wilson, E. 24, 90

Winter, G. 233

Worstell, H. G. 229, 231, 242

Wright, K. A. 109

Zarubin, B. T. 109

Zukerman, V. A. 23

SUBJECT INDEX